THE SYNTHESIS, SOLID STATE STRUCTURES AND

PROPERTIES OF SOME LOW-DIMENSIONAL

COORDINATION COMPOUNDS OF IRON AND PLATINUM

by

Riaan Büchner B.Sc. (Hons.), (Natal)

A thesis submitted in partial fulfilment of the requirements for the

degree Doctor of Philosophy in the Faculty of Science,

University of Natal, Pietermaritzburg.

Department of Chemistry and Chemical Technology

University of Natal

Pietermaritzburg

December 1995

DECLARATION

I hereby certify that this research is the result of my own investigation which has not already been accepted in substance for any degree and is not being submitted in candidature for any other degree.
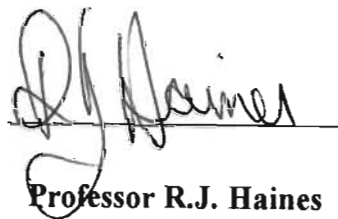
R. Büchner

We hereby certify that this statement is correct.

Professor J.S. Field

Co-Supervisor

Professor R.J. Haines

Supervisor

Department of Chemistry and Chemical Technology

University of Natal

Pietermaritzburg

December 1995

TO MY PARENTS

In recognition of everything they have done to provide me with the best opportunities in life...

ACKNOWLEDGEMENTS

INDEX

CHAPTER 2

Charge transfer salts of the dinuclear metallocene donor complex [Fe$_2$Cp$_2$*(CO)$_2$(μ-SEt)$_2$] and the electron acceptor molecules Tetracyanoquino-dimethane (TCNQ), Tetracyanoethylene (TCNE) and the Dicyanoquinone-diimines (DCNQI's)

CHAPTER 3

Square planar bipyridyl and terpyridyl complexes of platinum(II)

APPENDIX A

General experimental details

APPENDIX B

REFERENCES

SUMMARY

The first chapter of this thesis serves as an introduction to the low-dimensional coordination compounds of iron and platinum, described in chapters two and three. The chapter thus describes the structure, bonding and function of representative examples of low-dimensional materials, as reported in the literature. These materials are discussed under the headings: (i) metal chain compounds, (ii) stacked metallomacrocycles, (iii) ligand bridged complexes and (iv) electron transfer salts. The dominant interactions between the molecular units constituting these materials are explored and the impact of these interactions on the solid state properties of the bulk materials are described.

The second chapter describes the results obtained from an investigation involving the synthesis, characterization and study of the physical properties of some low-dimensional dinuclear metallocene-based charge transfer salts. Initial studies focused on the electron transfer reactions involving $[Fe_2Cp_2(CO)_2(\mu-SEt)_2]$ and dicyanoquinonediimine (DCNQI) molecules. The reaction involving 2,5-Me$_2$-DCNQI was shown to afford a product which is prone to disproportionation to the neutral starting materials. In an attempt to overcome this problem, $[Fe_2Cp_2(CO)_2(\mu-SEt)_2]$ was reacted with the more electron accepting molecule, 2,5-Cl$_2$-DCNQI, but the product resulting from this reaction was found to be inherently unstable.

Based on reports that decamethyl substitution on the donor molecule imparts some stability to ferrocene-based charge transfer salts, the previously unsynthesized complex, $[Fe_2Cp_2^*(CO)_2(\mu-SEt)_2]$ (Cp* = pentamethylcyclopentadienyl), was prepared. Contrary to expectation, the bulky Cp* ligands in this molecule are arranged in a cis configuration with respect to the Fe-Fe vector, as confirmed by X-ray diffractometric studies. These studies also revealed that the Cp* ligands of neighbouring $[Fe_2Cp_2^*(CO)_2(\mu-SEt)_2]$ molecules occur in a face-to-face arrangement in the crystal lattice, with the neutral molecules being arranged in extended rows within the crystal lattice. However, due to a substantial offset of the face-to-face arranged Cp* ligands with respect to each other, there are no orbital interactions between the ligands on

neighbouring molecules, and thus no extended interactions between the $[Fe_2Cp_2^*(CO)_2(\mu\text{-}SEt)_2]$ molecules in the solid state.

The reaction between $[Fe_2Cp_2^*(CO)_2(\mu\text{-}SEt)_2]$ and 2,5-Me$_2$-DCNQI, affords the electron transfer salt $[Fe_2Cp_2^*(CO)_2(\mu\text{-}SEt)_2](2,5\text{-}Me_2\text{-}DCNQI)$. X-ray diffractometric studies revealed that the Fe-Fe distance in the cation of this salt in significantly shorter than that associated with the neutral molecule, and that it is comparable to the Fe-Fe distance established for the $[Fe_2Cp_2^*(CO)_2(\mu\text{-}SMe)_2]^+$ cation. It was thus concluded that the reaction between $[Fe_2Cp_2^*(CO)_2(\mu\text{-}SEt)_2]$ and 2,5-Me$_2$-DCNQI involves the complete transfer of an electron from the donor to the acceptor molecule. It was also found that the salt crystallizes with extended stacks of alternating donor and acceptor molecules, in which the (2,5-Me$_2$-DCNQI)$^-$ anion lies between the Cp* ligands of the cations which, as in the case of the neutral molecule, are arranged with their faces parallel to each other. Although this salt meets both the prerequisites for the stabilization of ferromagnetic interactions between the unpaired electrons on the radical cations and anions, variable temperature magnetic susceptibility measurements indicated that only very weak, if any, ferromagnetic interactions are present between the unpaired electrons.

In an attempt to obtain charge transfer salts with different packing architectures to that of $[Fe_2Cp_2^*(CO)_2(\mu\text{-}SEt)_2](2,5\text{-}Me_2\text{-}DCNQI)$, $[Fe_2Cp_2^*(CO)_2(\mu\text{-}SEt)_2]$ was also reacted with the non-centrosymmetric acceptor molecules 2-Cl-5-Me-DCNQI and 2-Me-DCNQI. These afforded $[Fe_2Cp_2^*(CO)_2(\mu\text{-}SEt)_2](2\text{-}Cl\text{-}5\text{-}Me\text{-}DCNQI)$ and $[Fe_2Cp_2^*(CO)_2(\mu\text{-}SEt)_2](2\text{-}Me\text{-}DCNQI)$, respectively. Both of these salts were found to be inherently unstable and to decompose in the solid state, even when stored under dry, inert conditions. The salt $[Fe_2Cp_2^*(CO)_2(\mu\text{-}SEt)_2](H_4\text{-}DCNQI)$, obtained from the reaction between $[Fe_2Cp_2^*(CO)_2(\mu\text{-}SEt)_2]$ and the unsubstituted dicyanoquinonediimine H$_4$-DCNQI, was also found to be unstable.

Following these observations, $[Fe_2Cp_2^*(CO)_2(\mu\text{-}SEt)_2]$ was reacted with tetracyanoquinonedimethane (TCNQ) and tetracyanoethylene (TCNE).

The reaction with TCNQ affords a stable salt, of stoichiometry [Fe₂Cp₂*(CO)₂(μ-SEt)₂]₂(TCNQ)₂. Based on the wavenumbers of the C≡N stretching peaks in the solid state infrared spectrum of this salt, it was concluded that this reaction involves the complete transfer of a single electron from the donor to the acceptor molecule. This was confirmed by X-ray diffractometric studies which revealed that the Fe-Fe distance in the cation is analogous to that observed in the 2,5-Me₂-DCNQI salt and substantially different from that associated with the neutral donor molecule. These studies also revealed that the crystal lattice of the salt consists of isolated tetradic [Fe₂Cp₂*(CO)₂(μ-SEt)₂]⁺, (TCNQ)₂²⁻, [Fe₂Cp₂*(CO)₂(μ-SEt)₂]⁺ units with the (TCNQ)₂²⁻ dianions being "slipped in" between the Cp* ligands of the cations and forming part of a Cp*, (TCNQ)₂²⁻, Cp* arrangement. Only one of the Cp* ligands of each cation participates in this mode of packing, with the mean plane of the other Cp* ligand being almost perpendicular to that of the analogous Cp* ligand from the closest neighbouring cation. The electron spins on the (TCNQ)₂²⁻ dianions are paired, as confirmed by room temperature magnetic susceptibility measurements from which an effective magnetic moment of 2.76 μB was obtained. This value is consistent with two unpaired electrons per tetradic unit, *i.e.* one electron on each of the cations in the unit.

The reaction between [Fe₂Cp₂*(CO)₂(μ-SEt)₂] and TCNE affords [Fe₂Cp₂*(CO)₂(μ-SEt)₂](TCNE). As in the case of the reaction with TCNQ, infrared spectroscopy revealed that this reaction involves the complete transfer of a single electron form the donor to the acceptor molecule. The crystal lattice of [Fe₂Cp₂*(CO)₂(μ-SEt)₂](TCNE) consists of isolated trimeric [Fe₂Cp₂*(CO)₂(μ-SEt)₂]⁺, TCNE⁻, [Fe₂Cp₂*(CO)₂(μ-SEt)₂]⁺ units, which are separated by TCNE⁻ anions. The TCNE⁻ anions within these trimeric units participate in a face-to-face arrangement with the Cp* ligands of the cations. The TCNE⁻ anions separating the trimeric units are also located between the Cp* ligands of neighbouring cations, but the dihedral angles between the mean planes of these anions and that of the Cp* ligands are such that no orbital interactions are possible between these moieties. Consequently, the ferromagnetic interactions between the unpaired electrons on the radical ions in [Fe₂Cp₂*(CO)₂(μ-SEt)₂](TCNE) are negligible, as was confirmed by variable temperature magnetic susceptibility measurements.

The third chapter of this thesis focuses on the synthesis, solid state structures and luminescent behaviour of some polypyridyl coordination complexes of platinum.

The yellow complex salt $[Pt(terpy)(CH_3CN)](SbF_6)_2$, which was obtained by substituting the Cl^- ligand in $[Pt(terpy)Cl](SbF_6)$ with CH_3CN, crystallizes with a lattice structure which consists of sheets in which rows of cations and anions alternate. Furthermore, there is no evidence of any orbital interactions between the $[Pt(terpy)(CH_3CN)]^{2+}$ chromophores in the crystal lattice, as evidenced by X-ray diffractometric analysis. Samples of $[Pt(terpy)(CH_3CN)](SbF_6)_2$, both in the solid state and in dilute butyronitrile glass at 77 K, exhibit simultaneous emission from both an intraligand $^3(\pi\text{-}\pi^*)$ and a unimolecular ^{3}MLCT excited state. The $^3(\pi\text{-}\pi^*)$ component of the emission is suppressed in CH_3CN solution at room temperature, with only the ^{3}MLCT component being observed under these conditions. Attempts at preparing analytically pure samples of $[Pt(terpy)(CH_3CN)](CF_3SO_3)_2$ and $[Pt(terpy)(CH_3CN)]$-$(BF_4)_2$, were unsuccessful.

The next part of the study focused on the salts of $[Pt(terpy)Cl]^+$, and in particular, on the influence the steric demands of the counterion has on the luminescent properties of this chromophore in the solid state. In this regard the SbF_6^-, $CF_3SO_3^-$ and BF_4^- salts of this species were prepared and their luminescent behaviour studied. The SbF_6^- salt exhibits polymorphic behaviour. When freshly precipitated, and as long as it is in contact with the mother liquid, the salt is bright orange in colour. However, as soon as it is isolated from the mother liquid, a slow transition to a yellow phase sets in. The yellow modification of this salt exhibits weak luminescence in the solid state at room temperature. The intensity of this luminescence increases with decreasing sample temperature, but the position of the emission maximum is independent of the sample temperature. The $CF_3SO_3^-$ and BF_4^- salts do not exhibit polymorphic behaviour and are respectively orange and orange-red in colour. Both salts are emissive in the solid state, the intensity of the emission increasing on decreasing the sample temperature. In contrast to the emission behaviour of the SbF_6^- salt however, the solid state emission spectra of these salts display distinct red-shifts of the emission maxima on decreasing the temperature of the salts. The difference in the solid state emission behaviour of the three salts is believed to be a consequence of differences between the solid state

packing architectures of the salts. The red-shift of the emission maxima in the solid state spectra of the $CF_3SO_3^-$ and BF_4^- salts is typical of the emission behaviour of linear chain compounds with metal-metal interactions between the chromophores and where the emission originates from the radiative decay of a $^3(d_{\sigma^*} \rightarrow \pi^b)$ excited state. The emission from solid samples of the SbF_6^- salt may also originate form a $^3(d_{\sigma^*} \rightarrow \pi^b)$ excited state, the lattice architecture of the salt being such that a decrease in sample temperature does not affect a decrease in the Pt-Pt separation and consequently, no red-shift is observed. Alternatively, the emission may originate from a unimolecular ^{3}MLCT excited state if there are no orbital interactions between the $[Pt(terpy)Cl]^+$ chromophores.

The complex salts $[Pt(bipy)_2](SbF_6)_2$ and $[Pt(bipy)_2](CF_3SO_3)_2$ were synthesized to further investigate the influence of the steric demands of the counterion on the solid state emission behaviour of square planar platinum polypyridyl chromophores. Single crystal X-ray diffractometric studies revealed that the crystal lattice of the SbF_6^- salt is such that there would be no effective orbital interactions between the individual $[Pt(bipy)_2]^{2+}$ chromophores. In the case of the $CF_3SO_3^-$ salt however, the chromophores are arranged in extended stacks with ligand-ligand overlap between neighbouring chromophores. The solid state emission spectra of both salts were recorded and found to consist of two overlapping components. The high energy side of the band envelopes exhibit vibrational structure which originate from the radiative decay of $^3(\pi-\pi^*)$ excited states. The low energy side of the band envelopes each exhibit a partly obscured broad, structureless feature, which other workers have previously observed in the solid state emission spectra of $[Pt(bipy)_2](ClO_4)_2$ and which they suggested to originate from an excimeric excited state. This assignment is disproved by the fact that this feature also appears in the solid state emission spectrum of the SbF_6^- salt. Unfortunately, an accurate assignment of this feature could not be attempted without the aid of more sophisticated photophysical experiments.

The emission behaviour of chromophores incorporating ligands which exhibit deviations from planarity, was also investigated. One of the complexes synthesized in this regard is $[Pt(4'-Ph-terpy)Cl](SbF_6)$. Uncrushed samples of this salt exhibit bright yellow luminescence in the solid state which, based on the vibrational structure

observed in the solid state emission spectrum, can be assigned to the radiative decay of a $^3(\pi-\pi^*)$ excited state. On crushing the salt, its emission in the solid state at room temperature, changes from bright yellow to bright orange. The solid state emission of such a crushed sample, recorded at room temperature, consists of a single broad band. On reducing the temperature of the sample, the colour of the luminescence changes from orange to yellow. This change is associated with the broad feature in the solid state emission spectrum undergoing a red-shift; also noticable on lowering the temperature is the development of a $^3(\pi-\pi^*)$ component, of the type observed in the spectrum of the uncrushed sample. This $^3(\pi-\pi^*)$ component is superimposed on the high energy side of the broad feature. The latter is assigned to the radiative decay of a $^3(d_{\sigma^*} \to \pi^b)$ excited state, based on the red-shift of its emission maximum with decreasing sample temperature. Two scenarios are proposed to explain the luminescent behaviour of crushed samples of [Pt(4'-Ph-terpy)Cl](SbF$_6$). The first involves the [Pt(4'-Ph-terpy)Cl]$^+$ chromophores existing in two crystallographically distinct environments, with the $^3(\pi-\pi^*)$ and $^3(d_{\sigma^*} \to \pi^b)$ components of the emission originating from the chromophores in the different environments. The second scenario involves all the chromophores existing in the same crystallographic environment and exhibiting simultaneous emission from both the $^3(\pi-\pi^*)$ and $^3(d_{\sigma^*} \to \pi^b)$ excited states, the two states being coupled by thermally activated vibrational interactions.

The final part of this investigation focused on the [Pt(terpy)(C≡CPh)](SbF$_6$) and [Pt(4'-Ph-terpy)(C≡CPh)](SbF$_6$) salts, which were synthesized by displacing the Cl⁻ ligand from [Pt(4'-R-terpy)Cl](SbF$_6$) (R = H or Ph) with the phenylacetylide ligand. X-ray diffractometric studies revealed that in both salts the [Pt(4'-R-terpy)(C≡CPh)]$^+$ chromophores are arranged in extended stacks with the interplanar spacing between neighbouring chromophores being uniform and less than, or comparable to, the Van der Waal's separation for π-aromatic species in a face-to-face arrangement. Furthermore, each of the two salts exhibit two different Pt-Pt separations which alternate along the extended stacks. Both the [Pt(terpy)(C≡CPh)]$^+$ and the [Pt(4'-R-terpy)(C≡CPh)]$^+$ chromophore exhibit emission form a unimolecular ^{3}MLCT excited state in degassed CH$_2$Cl$_2$ or CH$_3$CN solution at room temperature. Quenching studies did, however, confirm that the emission form both chromophores is partially quenched

by CH_3CN. The solid state emission spectra of the two salts were recorded at various temperatures and found to consist of two overlapping components originating from two different excited states. The component of lower energy exhibits distinct red-shifts of its emission maximum on decreasing the temperature of the salt and is thus believed to originate from the radiative decay of a $^3(d_{\sigma^*} \rightarrow \pi^b)$ excited state. Unfortunately, the currently available data is insufficient to make an unequivocal assignment of the component of higher energy in the solid state emission spectra of the [Pt(terpy)(C≡CPh)](SbF$_6$) and [Pt(4'-Ph-terpy)(C≡CPh)](SbF$_6$) salts.

CHAPTER ONE

Low-dimensional Materials : Structure, Bonding and Function

1.1 Introduction

Low dimensionality is ascribed to organic and inorganic materials which, in the solid state, exhibit a high degree of anisotropy in their inherent physical properties. These properties include, for instance, optical, electrical and/or magnetic behaviour. A pseudo one-dimensional material thus possesses enhanced properties in one direction compared to the orthogonal directions. Similarly, a pseudo two-dimensional material has enhanced physical properties in two directions when compared to the remaining direction.

The above-mentioned anisotropy in physical properties arises from cooperative interactions occurring within linear chain (for pseudo one-dimensional) or layer (for pseudo two-dimensional) structures. It is these cooperative interactions that span the gap between the structural characteristics of a low-dimensional material and the bulk properties of that material in the solid state.

Based on their solid state structures and the dominant interactions present in the solid state, low dimensional solids can be divided into four broad categories:

i)   Metal chain compounds (the dominant interaction being between the p_z and d_{z^2} orbitals of neighbouring metal atoms in the chain).

ii)   Stacked metallomacrocycles (the dominant interactions being π-π interactions between the flat π-conjugated ligands or, in certain cases between the metal atoms of neighbouring molecules, as well).

iii) Ligand bridged complexes (interaction occurs between metal orbitals and those of the bridging ligand).

iv)   Electron transfer salts (interactions involve π-π interactions and spin-spin interactions of unpaired electrons).

This chapter is aimed at introducing the reader to representative examples of low-dimensional materials from each of the above four categories and, where possible, will highlight the correlation between the solid state structure and the bulk properties of the materials. Instead of attempting to be comprehensive, examples illustrating fundamental principles will be discussed and although attention will largely focus on low-dimensional materials containing transition metal atoms, occasional reference will be made to purely organic substances. As such it will serve as an introduction to the work discussed in this thesis.

1.2 Metal chain compounds

In general, metal chain compounds possess a columnar structure comprised of planar, or near planar monomeric units, stacked one on top of the other to form extended metal atom chains. Most metal chain compounds are formed from square planar monomers (see Figure 1.1), which implies that these compounds are mainly confined to
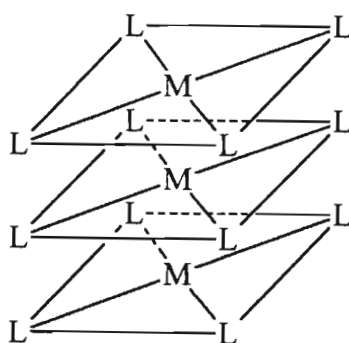
Figure 1.1: *A typical metal chain arrangement: monomeric ML₄ units stacked one on top of the other*

d^8 metal complexes.[1] Table 1.1 lists metals with accessible d^8 electron configurations.

Table 1.1: *Metals with accessible d^8 electron configurations*

Configuration	Metal (oxidation state)			
$3d^8$	Fe (O)	Co(I)	Ni(II)	Cu(III)
$4d^8$	Ru(O)	Rh(I)	Pd(II)	Ag(III)
$5d^8$	Os(O)	Ir(I)	Pt(II)	Au(III)

Complexes formed from zero-valent iron, ruthenium and osmium favour trigonal bipyramidal geometries, which obviously cannot accommodate stacking and thus extended metal-metal interactions. Of the remaining metals with accessible d^8 configurations, a quick overview of the literature reveals that one-dimensional metal chain structures are predominantly formed by Pt(II), Pd(II), Ni(II), Ir(I) and Rh(I) (in an approximate order of decreasing occurrence). Within the wealth of metal chain compounds, there are three main categories, *viz.*:

i)   Divalent and partially oxidized metal cyanides

ii)   Partially oxidized bis (oxalato) platinate salts

iii)   Linear chain platinum haloamines

In order to gain a fundamental understanding of the underlying principles associated with the above compounds, it is necessary to consider the intermolecular interactions occurring in extended metal chain compounds.

1.2.1 Intermolecular interactions in extended metal chain compounds

1.2.1.1 Metal-metal orbital overlap

This approach, developed by Rundle[2] and Miller[3], considers first the interaction of the $5d_{z^2}$ and $6p_z$ orbitals of two metal atoms, Pt in this case. The interacting $5d_{z^2}$ orbitals of a_{1g} symmetry give rise to a bonding and an antibonding molecular orbital of a_{1g} and a_{2u} symmetries respectively. Similarly, the interacting $6p_z$ orbitals with a_{2u} symmetry result in the formation of an a_{1g} bonding and an a_{2u} antibonding orbital [see Figure 1.2 (a)].
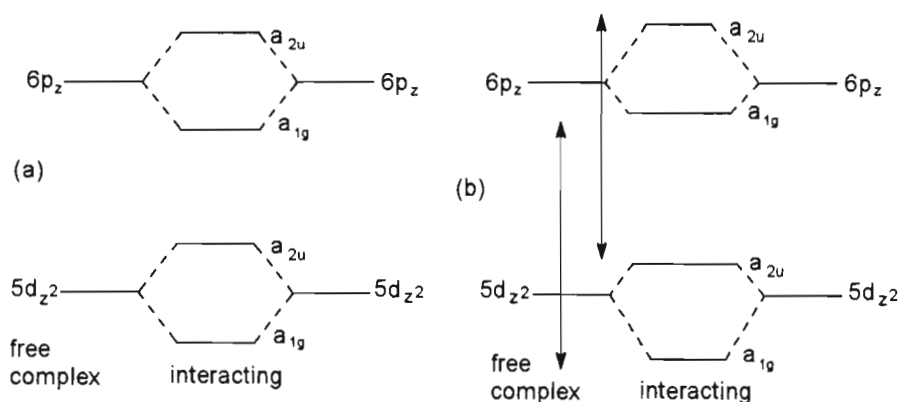
Figure 1.2:   *Molecular orbital scheme showing orbital interaction*

(a) without and (b) with configuration interaction

3

For a d^8 system, such as Pt(II), four electrons have to be accommodated in these molecular orbitals, resulting in the population of the two lower orbitals (one bonding and one antibonding), the overall effect being nonbonding. However, since non-degenerate molecular orbitals of the same symmetry "repel" each other, the lower a_{1g} molecular orbital is displaced to lower energies and the upper to higher energies [see Figure 2 (b)]. The same applies to the a_{2u} molecular orbitals. This results in a decrease in the energy of the electrons in the lower two molecular orbitals and thus the total energy of the system, with the net effect being bonding in character.

In moving from two atoms to an extended chain of metal atoms, the discrete energy levels are replaced by bands. Decreasing the distance between atoms in the chain results in a widening of the bands and a concomitant decrease in the energy gap between the highest occupied level in the d_{z^2} band and the lowest unoccupied level in the p_z band. The smaller this gap, the lower the energy required for a transition between the highest occupied d_{z^2} level and the lowest unoccupied p_z level and the more feasible electrical conduction, for instance, becomes along the chain.

1.2.1.2 Electrostatic interaction

In contrast to the model involving metal-metal orbital overlap, chain formation in this model is electrostatically enforced since neighbouring complexes are oppositely charged. There is no orbital overlap between the metal atoms in the chain and all spectroscopic changes in moving from isolated monomers to the chain structure are ascribed to intramolecular transitions being modified by the presence of the electrostatic crystal field of the neighbouring molecules in the chain. An example of this behaviour is provided by the Magnus green salts discussed in Section 1.2.2.3.

1.2.2 The three main categories of metal chain compounds

1.2.2.1 Divalent and partially oxidized metal cyanides

The metal cyanide salts with mono- or divalent counterions have attracted attention due to their varying colours and highly anisotropic optical properties.

X-ray diffraction studies[4] on $Mg[Pt(CN)_4].7H_2O$ revealed a columnar stacked chain structure of $[Pt(CN)_4]^{2-}$ units with a Pt-Pt distance of 3.155Å and a torsion angle of

45°, i.e. successive $[Pt(CN)_4]^{2-}$ units are rotated by 45° about the Pt-Pt axis relative to each other. The metal-metal distances in a wide variety of $[Pt(CN)_4]^{2-}$ salts possessing such columnar structures have been determined[5] and have been found to be crucially dependent on the cation's size and charge and on the degree of hydration of the compound. (For example, $Sr[Pt(CN)_4].3H_2O$ has a Pt-Pt separation of 3.09Å compared to 3.60Å for $Sr[Pt(CN)_4].5H_2O$.) However, there is no obvious trend governing the relationship between the cation size/charge or the extent of hydration of the compound and the intrachain Pt-Pt separation. Furthermore, as illustrated by the series: $Ca[M(CN)_4].5H_2O$ (M = Ni, Pd, Pt; M-M distances (Å): Ni 3.38[1]; Pd 3.42[6]; Pt 3.38[7]) or $Sr[M(CN)_4].5H_2O$ (M = Ni, Pd, Pt; M-M distances (Å): Ni 3.65[1]; Pd 3.63[8]; Pt 3.60[7]), the intermetallic distances are hardly affected by the presence of different transition-metal atoms. It has however been found[5] that Pt-chain compounds with a short Pt-Pt separation have a staggered configuration of $[Pt(CN)_4]^{2-}$ units, i.e. a torsion angle of ~45°, whereas compounds with a long Pt-Pt distance have an eclipsed configuration, i.e. a torsion angle of ~0°. (Compare e.g. $Mg[Pt(CN)_4].7H_2O$, Pt-Pt distance = 3.155 Å, torsion angle = 45° and $Na_2[Pt(CN)_4].3H_2O$, Pt-Pt distance = 3.691Å, torsion angle = 0°). This difference is not unexpected, since the staggered configuration minimizes the repulsive interactions between the CN groups and thus allows for close approach of the $[Pt(CN)_4]^{2-}$ units.

Following the determination of the structures of some fully hydrated $[Pt(CN)_4]^{2-}$ salts, Yamada[9] recognized a relationship between the Pt-Pt distance and the colour associated with the compound. In studying the polarized crystal spectra of $Ca[Pt(CN)_4].5H_2O$, $Mg[Pt(CN)_4].7H_2O$ and $Ba[Pt(CN)_4].4H_2O$, he observed a very strong perpendicular polarized band and a much sharper parallel polarized band both occuring at lower frequencies than any of the bands in the solution spectrum. He was also able to show that there exists an approximately linear relationship between the Pt-Pt distance and the position of the parallel polarized band. These observations were confirmed by studies[7] performed on dehydrated alkaline earth metal tetracyanoplatinates. The above studies have also shown that the intense colours of the $[Pt(CN)_4]$ compounds with Pt-Pt distances less than 3.25Å, are due to the presence of these strong absorbtion bands in the visible region of the spectrum. However, the

5

absence of such intense colours, does not indicate the total absence of metal-metal interactions. Moncuit and Poulet[10] have proven that weak Pt-Pt interactions exist in $Sr[Pt(CN)_4].5H_2O$, a colourless compound with a Pt-Pt distance of 3.60Å.

The dc electrical conductivities parallel to the metal atom chain ($\sigma_|$) have been determined[11] for several tetracyanoplatinate salts and were found to be strongly dependent on the nature of cation. Furthermore, $\sigma_|$ was shown to vary with the reciprocal of the Pt-Pt distance. However, the divalent tetracyanoplatinates (at best) behave as semiconductors (*e.g.* $\sigma_|$ for $Li_2[Pt(CN)_4].xH_2O = 3\times10^{-1}$ S.cm^{-1},[12] Pt-Pt = 3.18Å), because of a band gap between the highest occupied d_{z2} level and the lowest unoccupied p_z level. It has also been suggested that the observed electrical conductivities could be due to the presence of Pt(IV) impurities.

For all of the above divalent metal cyanides, the metal atom has a d^8 configuration, implying that all of the energy levels of the d_{z2} band are filled [see Figure 1.3(b)]

Energy

(a)   (b)   (c)
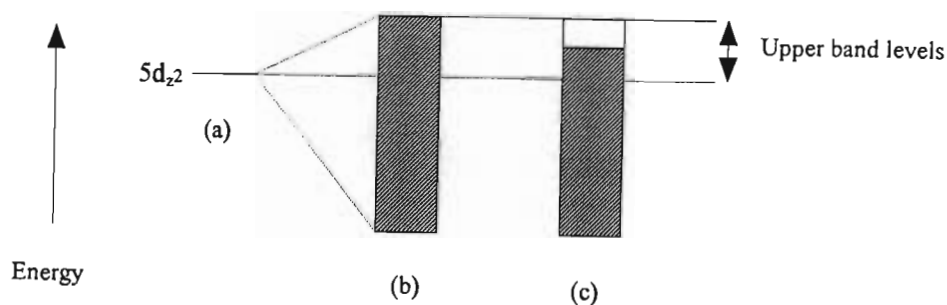
Figure 1.3:   *Diagrammatic representation of the band structure of d^8 metal*
        chain compounds:
        (a) Isolated monomer
        (b) Divalent metal atom chain
        (c) Partially oxidized metal atom chain
        (Shading implies filled levels)

The upper levels of the d_{z2} bands possess higher energies than the energy of the d_{z2} level in the isolated monomeric unit [see Figure 1.3 (a) and (b)]; and electron occupation of these levels thus has an antibonding effect on the chain. On this basis Krogmann[1] suggested that bonding in the chain would be strengthened if electrons are

removed from the upper band levels of the d_{z^2} band. In practice this implies partial oxidation of the metal atoms in the chain. [see Figure 1.3(c)].

In the partial oxidation of the metal chain atoms, the preservation of electrical neutrality of the lattice dictates that an appropriate number of anions have to be introduced into the lattice or an appropriate number of cations removed. This gives rise to the classification of the partially oxidized tetracyanoplatinates as either anion deficient (e.g. $K_2[Pt(CN)_4]Cl_{0.32}.2.6H_2O)^{(1)}$ or cation deficient (e.g. $M_{1.75}[Pt(CN)_4].xH_2O$; $M = Li^+, K^+, Rb^+, Cs^+)^{(13)}$. Of these two groups that of the anion deficient salts is the more extensively studied group.

The molecular geometries associated with the partially oxidized tetracyanoplatinates are fairly predictable, since they are guided by three factors as summarized[14] below:

a)   The basic integrity of the Pt-Pt chains once partial oxidation has occurred.

b)   The columnar stacking of the square planar $[Pt(CN)_4]^{-x}$ moieties.

c)   The limited range of allowed Coulombic and hydrogen bonding crystal binding parameters.

Furthermore, the Pt-Pt distance (d_{Pt-Pt}) is related to the degree of partial oxidation (DPO), as expressed by the equation:[15]

$$d_{Pt-Pt} (\text{Å}) = 2.59 - 0.60 \log_{10}(DPO)$$

(The degree of partial oxidation is determined through room temperature diffuse X-ray scattering.[16])

Based on the differences in their structural type, the anion deficient salts are subdivided into type P, primitive, which are normally hydrated and type I, body centred, usually anhydrous. At room temperature, both groups behave as one-dimensional conductors (e.g. $(NH_4)_2(H_3O)_{0.17}[Pt(CN)_4]Cl_{0.42}.2.83H_2O$ (Type P), $\sigma_{R.T.} = 0.45$ S.cm^{-1} [17] and $Cs_2[Pt(CN)_4](FHF)_{0.39}$ (Type I), $\sigma_{R.T.} = 1.6 \times 10^3$ S.cm^{-1} [18]), their conductivity largely being governed by d_{Pt-Pt}. However, upon lowering the temperature, type P salts undergo a transition to a semi-conducting state at higher temperatures than that associated with type I. Compare $(NH_4)_2(H_3O)_{0.17}[Pt(CN)_4]Cl_{0.42}.2.83H_2O$ (Type P) and $Cs_2[Pt(CN)_4](FHF)_{0.39}$ (Type I) with transition temperatures of 195 K and 80 K

respectively. This difference in behaviour stems directly from structural differences between type P and I salts.

Type P hydrated salts crystallize in primitive tetragonal lattices (*P4mm*) with the counter cations situated on planes between those of the anionic $[Pt(CN)_4]^{-x}$ moieties.[19-22] The Pt chains, which are ~10Å apart, are held together by a complex bonding network which depends partly on weak hydrogen bonding interactions including the H_2O molecules of crystallization. In contrast, type I (usually anhydrous) salts, crystallize with body centred tetragonal lattices (*I4/mcm*).[22-25] Here the counter cations (B^+) are situated on the same plane as the $[Pt(CN)_4]^{-x}$ anions, thus maximising the B^+-$N\equiv C$ interactions, resulting in an interchain separation which is about 1Å shorter than that in the type P salts.

The above structural differences need to be kept in mind when considering the structural changes that occur in a one-dimensional conductor on lowering the temperature. As predicted by Peierls,[26] there is a mean field temperature T_p, associated with any one-dimensional conductor, below which critical fluctuations occur. The extent of these fluctuations (Peierls distortions) increase as the temperature is decreased and create one-dimensional correlated domains which, with decreasing temperature, extend over increasing portions of the Pt atom chain. Interchain Coulombic interactions also increase with decreasing temperature until at a certain temperature, T_{3D}, the Coulombic interactions are strong enough to cause a three-dimensional ordering of the one-dimensional lattice distortions, resulting in a band gap being created at the Fermi (highest occupied) level of the d_{z2} band (see Figure 1.4). At
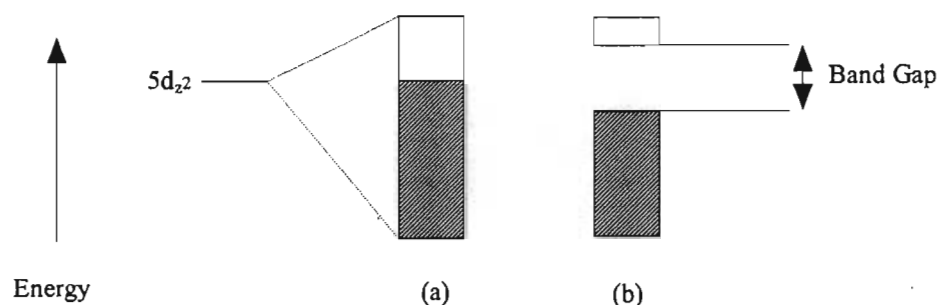
Figure 1.4: (a) Partially filled d$_{z2}$ band

(b) Splitting of the d$_{z2}$ band due to Peierls distortion

(Shading implies filled levels)

this temperature the transition to semiconducting behaviour is complete.

Interchain interactions depend considerably on the extent of hydrogen bonding between the Pt atom chains. An increase in the extent of hydrogen bonding will thus promote the three-dimensional coupling of the one-dimensional Peierls distortions. This explains the difference of T_{3D} and thus the difference in the low-temperature conductivity behaviour of the type P and I anion deficient salts.

Cation deficient tetracyanoplatinates are less well documented than anion deficient salts. Probably the best known example of a cation deficient salt is $K_{1.75}[Pt(CN)_4].1.5H_2O$. Like its Rb and Cs analogues, $K_{1.75}[Pt(CN)_4].1.5H_2O$ behaves as a one-dimensional metal,[27] its room temperature conductivity being ~100 $S.cm^{-1}$.[28,29] However, variable temperature conductivity studies revealed two three-dimensional ordering temperatures, T_{3D}'s, *viz.* 308K[28] and 50K.[29] Further studies[30] indicated that the transition at 50K is due to a Peierls instability, the high temperature transition being assigned to a non-Peierls transition.

1.2.2.2. Partially oxidized bis(oxalato)platinate salts

Interest in the bis(oxalato)platinate salts arose when Krogmann found that, like the partially oxidized tetracyanoplatinates, the partially oxidized bis(oxalato)platinate salts show one-dimensional metallic properties.[31-32] Generally these salts are synthesized by oxidizing samples of bis(oxalato)platinum(II) salts with smaller amounts of oxidant than that required to facilitate the complete oxidation to the Pt(IV) species.[31,32-37]

Structural studies[38] of the partially oxidized bis(oxalato) plantinate salts have mainly centred on the potassium and rubidium salts and have revealed that crystalline samples often consist of several phases.
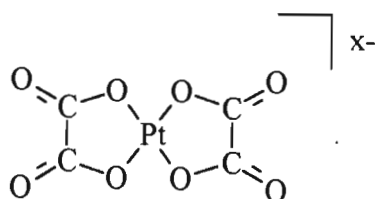
$[Pt(C_2O_4)_2]^{x-}$

The γ phase of $K_{1.81}[Pt(C_2O_4)_2].2H_2O$ has four $[Pt(C_2O_4)_2]^{1.81-}$ units arranged in a zigzag chain along the stacking axis in the unit cell, the Pt-Pt distances being 2.837Å

and 2.868Å with a torsion angle of 45° between adjacent $[Pt(C_2O_4)_2]^{1.81-}$ units.[33] Furthermore, the Pt chains are sinusoidally modulated at room temperature, the wave period (29.92Å) closely matching the expected value (30Å) for a Peierls superlattice distortion.[38] The same distortion occurs in $Rb_{1.67}[Pt(C_2O_4)_2].1.5H_2O$. The partially oxidized bis(oxalato)platinates also display non-Peierls distortions which occur at temperatures above 273K.

The room temperature conductivities of the partially oxidized bis(oxalato)platinate salts along the chain direction ($\sigma_|$ in the range 1 to 100 S.cm^{-1}) are considerably lower than those observed for the analogous tetracyanoplatinates with similar Pt-Pt separations. Compare e.g. $\sigma_|$(300K) for $Cs[Pt(CN)_4](FHF)_{0.39}$ $\approx 2 \times 10^3$ S.cm^{-1},[5] d_{Pt-Pt} = 2.833Å, with $\sigma_|$(300K) for $Zn_{0.81}[Pt(C_2O_4)_2].6H_2O$ = 94 S.cm^{-1},[39] d_{Pt-Pt} = 2.838Å. Bullett[40] has predicted these differences in conductivity through band structure calculations. It has also been suggested that the occurrence of Peierls superstructures in these compounds may play an important part in their room temperature electrical conductivities.

1.2.2.3. Linear chain platinum(II)haloamines

Although the first examples of platinum compounds with halogens and/or amines as ligands were synthesised in the late 1800's, the first detailed study of their physical properties was only undertaken in 1951, when Yamada[41] investigated the anisotropic optical behaviour of $[Pt(NH_3)_4][PtX_4]$ (X$^-$ = Cl$^-$ or Br$^-$). Recent interest in these compounds centred on the possibility of high electrical conductivities, but this interest was short-lived, since most linear chain platinum haloamines display semiconducting or insulating behaviour.[42] The optical properties of these compounds, however remain of interest.

The linear chain platinum(II) haloamines can be ordered with respect to the number of amine or ammonia ligands coordinated to the platinum centre.

The best known example of the tetraamine or -ammonia type is $[Pt(NH_3)_4]Cl_2.2H_2O$, the lattice of which has been suggested to consist of linear arrays of $[Pt(NH_3)_4]^{2+}$ units. These units are arranged in an eclipsed configuration, the Pt-Pt distance in the chain being 4.21Å.[43] As in the case of most of the other compounds from this group

{excluding those with $[PtX_4]^{2-}$ (X = Cl⁻ or Br⁻) anions}, the large Pt-Pt distance in $[Pt(NH_3)_4]Cl_2.2H_2O$ results in very weak intermolecular Pt-Pt interactions, thus precluding the possiblity of any unusual physical properties.

The triaminehaloplatinum(II) salts are represented by two types of compounds. In the first, the triamine portion comprises three separate ligands *e.g.* $[Pt(NH_3)_3Cl]Cl$. With the exception of salts containing $[PtX_4]^{2-}$(X = Cl⁻ or Br⁻), none of the salts from this type shows any unusual physical properties. The second type of triamine-haloplatinum(II) salt possesses a tridentate ligand representing the triamine section, *e.g.* [Pt(terpy)Cl]Cl (terpy = 2,2',6',2''-terpyridine). Many of the salts of this type crystallize with structures allowing intermolecular interaction and consequently possess unusual physical properties. The Pt-terpy complexes and their properties are discussed in Chapter 3 and will thus not be discussed here in any further detail.

The neutral diaminedihaloplatinum(II) salts can also be divided into two types. Of the first type, represented as $[Pt(NH_3)_2X_2]$ (X = halogen), the cis isomer of $[Pt(NH_3)_2Cl_2]$ has attracted the most attention. It crystallizes with linear stacks of the neutral molecules extending through the crystals. The Pt-Pt distances within these stacks alternate, the two distances being 3.37 and 3.41Å.[44] Oxidizing *cis*-$[Pt(NH_3)_2Cl_2]$ with $(NH_4)_2S_2O_8$[45] results in a product, single crystals of which are able to polarize light between 850 and 350 nm.[46] (The corresponding values for Polaroid® are 620 and 400 nm.) Subsequent investigations[47] have revealed that different solids are formed upon oxidation of *cis*-$[Pt(NH_3)_2Cl_2]$, the structures obtained depending on the reaction conditions and any additional ions in solution. In contrast to the cis isomer, the shortest Pt-Pt distance in *trans*-$[Pt(NH_3)_2Cl_2]$ is about 5Å.[44] Furthermore, it is not possible to obtain partially oxidized products from this isomer. In the second type of neutral diaminodihaloplatinum(II) compounds, the diamine portion consists of a single bidentate ligand. An example of this type of compound is $[Pt(en)X_2]$ (en = 1,2 diaminoethane, X = Cl⁻, Br⁻). Here, the $[Pt(en)X_2]$ units are arranged in extended chains, the Pt-Pt separation being 3.39Å for $[Pt(en)Cl_2]$[48] and 3.50Å for $[Pt(en)Br_2]$.[49] Spectroscopic studies[48,49] revealed that, despite the reasonably short Pt-Pt distances, the metal-metal interactions are insufficient to give rise to a delocalisation of the platinum d electrons along the chain. Instead, an electron transfer

11

model resulting in the formation of ion pairs in a bound ionic state has been invoked to explain those bands in the crystal spectra which do not originate from intermolecular electronic transitions. In this model the energies of transitions to the ionic states increase strongly with the molecular separation because of the greater separation of charge which occurs in the excited state. This explains the observed increase in energy of the charge transfer excitation bands in moving from [Pt(en)Cl$_2$] to [Pt(en)Br$_2$]. Another example of a linear chain diaminodihaloplatinum(II) salt with the diamine portion consisting of a single bidentate ligand, is [Pt(bipy)Cl$_2$] (bipy = 2,2′-bipyridine). This and related compounds, along with their properties will be discussed in Chapter 3, and thus will not be discussed here in any further detail.

Probably the best known of the extended linear chain platinum(II)haloamine salts are Magnus' Green Salt [Pt(NH$_3$)$_4$][PtCl$_4$], and its analogues. The general structure of these salts consist of linear arrays of alternating planar [PtX$_4$]$^{2-}$ and [PtL$_4$]$^{2+}$ ions.[3,50] In [Pt(NH$_3$)$_4$][PtCl$_4$] the alternate ions are staggered by 28°, thus allowing close approach of the Pt atoms (Pt-Pt distance = 3.25Å) along the chain.[51] Since the green colour of [Pt(NH$_3$)$_4$][PtCl$_4$] cannot arise due to a superposition of the colour of the cation (colourless) and that of the anion (pink), the optical properties of this compound and others with unusual colours have attracted attention.

The absorption spectrum of [Pt(NH$_3$)$_4$][PtCl$_4$] consists of 4 main bands, 3 originating from the anion, the fourth only occuring in compounds containing Pt in both the cation and the anion and which in addition, have short Pt-Pt distances. Miller[3] has proposed that interaction of the 5d$_{z2}$ and 6p$_z$ orbitals on the alternating cations and anions gives rise to a band structure consisting of four bands (see Figure 1.5).

The origin of the fourth band was thus assigned to a transition from the highest occupied d band to the lowest unoccupied p band. On a chemical level this corresponds to a partial electron transfer from, in the case depicted below, the anion 5d$_{z2}$ orbital to the cation 6p$_z$ orbital. The fact that this fourth band is not observed in [Pt(NH$_3$)$_4$][PdCl$_4$] for instance, is attributed to insufficient overlap of the relevant d- and p orbitals.
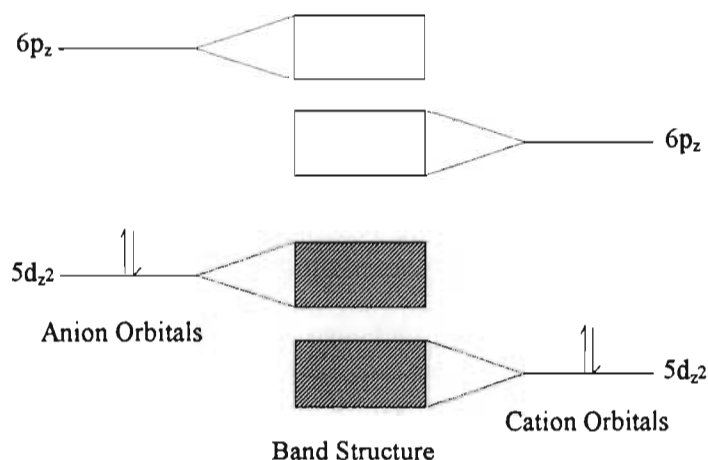
Figure 1.5: *Simplified schematic diagram of relative energies in e.g.*
[Pt(NH₃)₄][PtCl₄] (shading implies filled bands)

The green colour of *e.g.* [Pt(NH₃)₄] [PtCl₄], does not arise from the above-mentioned transition. Instead, it has been suggested to result from a red-shift of the three absorption bands originating from transitions from the anion d_{yz}, d_{xz} and d_{z^2} orbitals to the anion $d_{x^2-y^2}$ orbitals.[52] This shift occurs as a result of the d_{z^2} electrons of the cations perturbing the d_{xz}, d_{yz} and d_{z^2} orbitals of the adjacent $[PtCl_4]^{2-}$ anions. The effect of increasing the amine size on the visible spectra of $[PtA_4][PtX_4]$ (A = amine) can also be explained by applying this model.

Studies on the electrical conductivity of [Pt(NH₃)₄][PtCl₄] revealed that it behaves as a anisotropic semiconductor, the ratio of the conductivity in the stacking direction to that perpendicular to the stacks being 100:1.[53]

1.3 Stacked metallomacrocycles

1.3.1 Introduction

For this discussion, a metallomacrocycle is regarded as a metal atom surrounded by an essentially square planar array of four coordinating nitrogen atoms which form part of a flat, ring-shaped π-conjugated ligand system.

The bulk physical properties of all of the metal chain compounds discussed in the previous section are essentially determined by the disposition of the d orbitals of the

metal chain atoms in the solid state. The equatorial ligands do play a definite part in determining the properties of the material, but ultimately their influence on the bulk properties is still directed through a perturbation of the d orbitals of the metal chain atoms. In the case of the metallomacrocycles and especially the partially oxidized derivatives, the coordinated ligand molecules are directly involved in determining the nature of the bulk properties of the materials.

Based on the ligand system employed in the formation of these compounds, metallomacrocycles can be divided into three broad groups, namely:

a)   Metal bis(dioximates) where the ligand system consists of 2 dioximate molecules held together by hydrogen bonding.

b)   Porphyrinic metal complexes, the ligand system consisting of a single porphyrin molecule.

c)   Tetraazaannulene metal complexes, the ligand system consiting of a single tetraazaannulene molecule.

1.3.2   Metal bis(dioximates)

Probably the best-known example of the metal bis(dioximates) is bis(dimethyl-glyoximato)nickel, [Ni(dmg)$_2$], in which the monomeric units, depicted below, are arranged face-to-face in extended columns in the solid state.[54, 55] Similar structures have been reported for the bisdimethylglyoximato complexes of Pd[55] and Pt.[56]
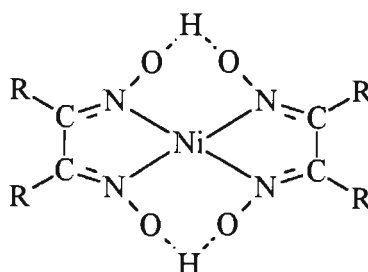
[Ni(dmg)₂] (R = Me) and [Ni(dpg)₂] (R = Ph)

The two dimethylglyoxime ligands in each monomer of the derivative, are held in a rigid square planar configuration by short hydrogen bonds (2.40Å) to the oxygen atoms from each of the two ligands, as seen above. Within each column, successive

monomeric units adopt torsion angles of 90° to each other, allowing the methyl groups, which protrude the furtherest from the plane defined by the metal atom and the rest of the ligands, to interlock. Through this interlocking process, close approach of the monomeric units is possible, as indicated by the short metal-metal distances in the following compounds: 3.245Å for [Ni(dmg)$_2$],[54,55] 3.253Å for [Pd(dmg)$_2$][55] and 3.23Å for [Pt(dmg)$_2$].[56] These short distances have been interpreted[57] in terms of metal-metal bonds being present in these complexes, such bonds leading to a further stabilization of the columnar structures.

The above-mentioned interlocking of substituents seems to be essential for the bis(glyoximato) metal complexes to adopt structures with extended columnar stacks in the solid state. The Ni(II), Pd(II) and Pt(II) complexes of glyoxime (R = H) for instance are planar, yet these complexes do not adopt the [Ni(dmg)$_2$] structure.[58-60] The bis(methylethylglyoximato) nickel molecule is also planar, but the crystal structure[61] of the complex is such that the possibility of close approach of the monomeric units is precluded.

Interest in the absorption spectra of [Ni(dmg)$_2$] has centred mainly on the lowest energy visible absorption band which is polarized in the stacking direction and is only present in the solid state spectra. The origin of this band was initially thought to result from a ($3d_{z^2} \rightarrow p_z$) transition, which was subsequently confirmed by Ohasi and co-workers.[63] They concluded that the band is mainly due to the ($3d_{z^2} \rightarrow p_z$) transition within a nickel atom, but that it also includes some interatomic ($3d_{z^2}$[atom a]$\rightarrow$ $4p_z$[atom b]) charge transfer excitation. There is also a close relationship between the energy associated with this band and the metal-metal distances in the compounds. This correlation was previously observed by Zahner and Drickamer,[64] who found that increased pressure caused a shortening of the metal-metal distances in [M(dmg)$_2$] (M= Ni, Pd, Pt). This shortening of the metal-metal distance manifests itself in a decrease in the energy of the $d_{z^2} \rightarrow p_z$ transition.

[Ni(dmg)$_2$] behaves as an ohmic semiconductor; the single crystal conductivity[65] at 323 K being 3.8×10^{-10} S.cm^{-1} along the needle/stacking axis. This conductivity is roughly 10^5 times greater than that observed for compressed powder measurements,

and was interpreted as suggesting some delocalization of electrons along the stacking direction.

The reaction of bis(diphenylglyoximato)nickel, [Ni(dpg)$_2$], with molecular iodine results in a partial oxidation of the complex, to afford a product [Ni(dpg)$_2$]I, the pressed pellet conductivity[66] of which is 10^3 to 10^4 times greater than that of [Ni(dpg)$_2$]. This result sparked a series of studies focussing on partially oxidized metallomacrocycles.

With regard to the metallomacrocycle, the crystal structure[67] of [Ni(dpg)$_2$]I is virtually identical to that of the parent compound, the only structural variation being that the Ni-Ni distance decreases from 3.547Å to 3.223Å on oxidation. This distance is still comparable with the 3.25Å observed in unoxidized [Ni(dmg)$_2$] and is considerably greater than that in Ni metal (2.49Å). The iodine atoms occur in extended chains which run parallel to the stacking axis and are situated in channels between the chains of macrocyclic units. However, the iodine chains are one-dimensionally ordered so that the exact species of iodine present cannot be determined from X-ray scattering data. The diffuse X-ray scattering pattern was found to be suggestive of I_5^-, as was subsequently confirmed by resonance Raman and ^{129}I Mössbauer spectroscopy.[67] [Ni(dpg)$_2$]I, [Ni(dpg)$_2$]Br, [Pd(dpg)$_2$]I and [Pd(dpg)$_2$]Br have been found to be isomorphous, with nearly identical unit cell dimensions,[68] thus suggesting that all four of these compounds possess the same basic crystal structure. This is further supported by the fact that the Br species in [M(dpg)$_2$]Br (M = Ni, Pd) have been shown to be Br_5^-,[69] exactly as in the case of the iodine derivatives. These studies also revealed that for the bromine derivatives, the [M(dpg)$_2$] units are formally in the fractional oxidation states + 0.20(2) for M = Ni and + 0.22(2) for M = Pd.[69] In the case of [M(dpg)$_2$]I (M = Ni, Pd), the fractional oxidation state is +0.20(4).[67]

Electrical conductivity studies [67, 69] on single crystals of [M(dpg)$_2$](X) (M = Ni, Pd; X = Br, I) have shown a linear dependence of ln(σ) versus $^1/_T$ (where σ = conductivity) with a room temperature conductivity σ_{293K} of 10^{-3} to 10^{-2} S.cm^{-1}. This represents a 10^7 to 10^8 fold increase in conductivity when compared to the parent compounds. Various possibilities for a conduction pathway which allows for the observed conductivity have

16

been suggested. The possibility that the halogen chains constitute the major pathway was discarded since the conductivity is independent of whether bromine or iodine is used as the oxidant. Had the halogen chains been the major pathway, the iodine chains would be expected to be far more efficient charge carriers than the bromine chains.[69] Based on the relatively large metal-metal separations and the insensitivity of the conductivity to whether the metal is Ni or Pd, the possibility of a metal-centred pathway has also been suggested to be less likely.[67] It would thus appear that the charge carriers could be transported through the π-systems of the ligands.

In an attempt to decrease the metal-metal separation and to study the influence of increased conjugation of the ligand system when compared to the glyoximes, the
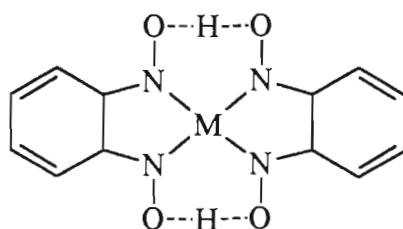
[M(bqd)₂]

partially oxidized nickel and palladium bis-benzoquinonedioximates, $[M(bqd)_2]I_x.nS$ (S = solvent) were synthesized.[70] The crystal structures of $[Pd(bqd)_2]I_{0.50}.0.52o$-dichlorobenzene[70] and $[Ni(bqd)_2]I_{0.52}.0.32toluene$ consist of stacks of rigorously planar, partially staggered $[M(bqd)_2]$ units, with two differently sized channels between them. The smaller of these channels is occupied by chains of I atoms, which from Raman and ^{129}I Mössbauer spectroscopy have been determined to be present as I_3^-. The larger channels are occupied by disordered solvent molecules. The metal-metal distances in these compounds (3.153Å, M = Ni; 3.184Å, M = Pd) are shorter than that in either the parent $[M(bqd)_2]$ or the analogous $[M(dpg)_2]I$ compounds.

From the $[M(bqd)_2]$:I ratio, and the fact that the iodine is present as I_3^-, it follows that the partial oxidation state of the $[M(bqd)_2]^{x+}$ units is +0.17, similar to the +0.20 observed in the $[M(dpg)_2]I$ materials. Despite this and the shorter metal-metal distance in $[M(bqd)_2]I_x.nS$, the room temperature thermally activated single crystal conduc-

tivities of the $[M(bqd)_2]I_x.nS$ compounds are slightly lower than that of the corresponding $[M(dpg)_2]I$ crystals.[70]

1.3.3 Porphyrinic metal complexes

This category of metal complexes encompasses those metallomacrocycles derived from the metalloporphine skeleton depicted below.
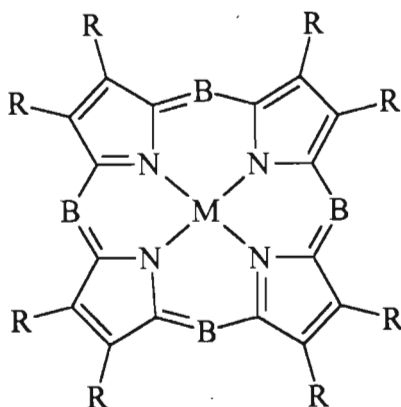
The metalloporphine skeleton

When B represents a nitrogen atom, the metalloporphine skeleton constitutes the backbone of the metallophthalocyanines, whereas if B represents =CH–, the metalloporphyrins are introduced.

1.3.3.1 Metallophthalocyanines

Interest in the synthesis and study of these compounds arose due to the highly conjugated planar structure of the phthalocyanines, the accessibility of multiple redox sites and the chemical flexibility associated with the phthalocyanine ligand.

Partial oxidation of the metallophthalocyanines and the metal-free macrocycle with molecular iodine (see reaction outline below), was found to result in an extensive range of highly conducting molecular materials.[72]

$$M(Pc) + {}^x/_2 I_2 \leftrightarrow M(Pc)(I)_x$$

M = Fe, Co, Ni, Cu, Zn, Pt, H_2, Pc = Phthalocyanine
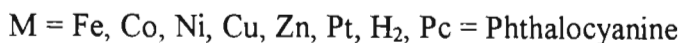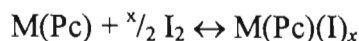
The I:MPc ratios were found to be variable, the composition of the final product depending on the experimental conditions. Furthermore, the iodination is reversible such that the iodine can be completely removed by heating the products *in vacuo*. The exact nature of the iodine species present, and confirmation that partial oxidation had occurred, was obtained from ^{129}I Mössbauer and Raman spectroscopic studies. Both techniques revealed that for $x \leq 3$ (see reaction outline) the iodine is present as I_3^- only, whereas for $x > 3$ both techniques revealed the presence of I_5^- and other coordinated I_2 species.

$H_2(Pc)I^{(73)}$ and $Ni(Pc)I^{(74)}$ both crystallize in the space group P4/mcc. Both structures consist of stacked planar M(Pc) units (M = H_2 or Ni) with disordered chains of I_3^- counter ions situated in channels occurring between and running parallel to the M(Pc) stacks. The intermolecular separation for $H_2(Pc)I$ within the M(Pc) stacks, was found to be $3.251(2)Å^{(75)}$ which is slightly, but not significantly, longer than that associated with Ni(Pc)I, *viz*. $3.244(7)Å.^{(74)}$ Furthermore, consecutive molecules within each stack are staggered, the torsion angles being 40.0 and 39.5° for $H_2(Pc)I$ and Ni(Pc)I, respectively.

The room temperature electrical conductivity for $H_2(Pc)I$ (2.3 S.cm^{-1})$^{(73)}$ is marginally higher than that of Ni(Pc)I (0.7 S.cm^{-1} measured for a compressed pellet). This result, together with the fact that $H_2(Pc)I$ and Ni(Pc)I have virtually identical structures, establishes that a coordinated metal atom is not a prerequisite for high electrical conductivity to be observed in this class of compounds. It is also clear that the conduction pathway in these compounds is not metal-centred. Analysis of the g-values and the line widths of the EPR signals associated with the charge carrying hole species of Ni(Pc)I$^{(74)}$ revealed that the charge carriers resulting from the partial oxidation, are in fact ligand-based. Thus, the metal does not contribute directly to the carrier orbital or to the charge transport process, but acts solely as an internal substituent that influences the electronic properties of the ring.

Initial variable temperature studies$^{(74)}$ established the electrical conductivity of Ni(Pc)I to be metal-like, the conductivity increasing with decreasing temperature until a metal to semiconductor transition was reached at *ca*. 50 K. It was speculated that this

transition results from a subtle structural rearrangement resulting in a change in carrier mobility. In a subsequent study[75] however, Ni(Pc)I was found to maintain its metal-like conductivity to temperatures of 100 mK, with σ ~2000 to 5000 S.cm^{-1} for T $\leq$ 25 K. At temperatures below 25 K the conductivity decreased gradually before levelling off to an asymptotic value ranging from 0.5 to 2 times the room temperature value as the temperature approached 0 K. Ni(Pc)I was in fact the first reported low-temperature molecular metal, based on a metallo-organic complex.

Modifications to the M(Pc)I system have been made, these include methyl substitution in the 3 or 4 position on the phthalocyanine to produce M(3-Me)$_4$Pc or M(4-Me)$_4$Pc respectively.[76, 77]
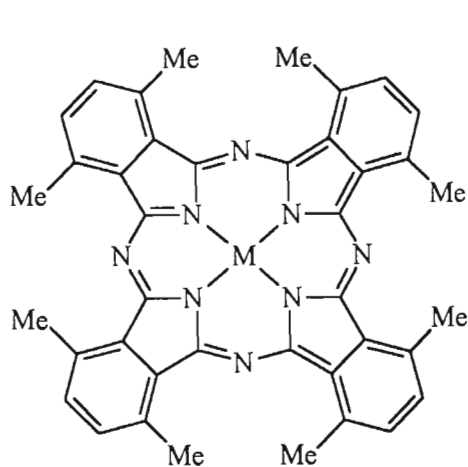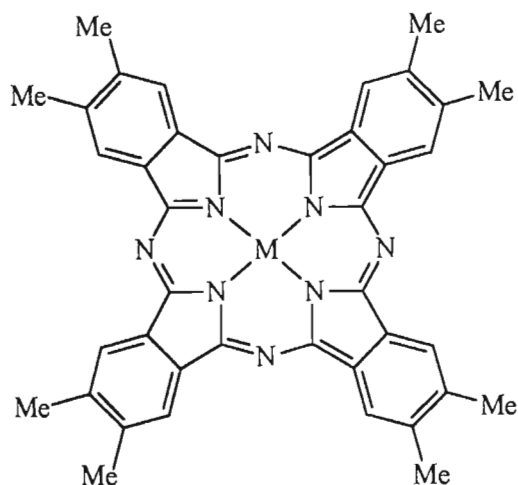
M(3-Me)₄Pc   *M(4-Me)₄Pc*

Partial oxidation of these metallophthalocyanines afforded products containing the I$_5^-$ moiety, even at low iodine concentrations. This was attributed to the alkylated derivatives requiring a higher iodine concentration than the unsubstituted phthalocyanine derivatives to reach a given degree of partial charge transfer. Electrical conductivity studies revealed that these partially oxidized substituted metal phthalocyanines exhibit metallic conductivity; the conductivity of the [M(3-Me)$_4$Pc]I$_x$ compounds being higher than that of the [M(4-Me)$_4$Pc]I$_x$ compounds. A possible explanation for the different conductivities is that for [M(3-Me)$_4$Pc]I$_x$, the methyl substituents extend into the surrounding lattice to a lesser extent, thus maintaining the conductivity requisites of close stacking and delocalization of electrons.

A further variation involves the electro-oxidation of Ni(Pc) in the presence of $Bu_4N^+BF_4^-$ to produce halogen-free $Ni(Pc)(BF_4)_{0.33}$.[78] The crystal structure of this compound is very similar to that of Ni(Pc)I and $H_2(Pc)I$, the structure consisting of $Ni(Pc)^{+0.33}$ ions stacked in columns with an interplanar separation of 3.240(5)Å and surrounded by BF_4^- counterions. EPR measurements confirmed that the oxidation is ligand-centred. $Ni(Pc)(BF_4)_{0.33}$ crystals exhibit a room temperature conductivity of ~1000 S.cm^{-1} in the stacking direction, but unlike Ni(Pc)I and $H_2(Pc)I$, the metallic temperature dependence of $Ni(Pc)(BF_4)_{0.33}$ does not exhibit a sharp peak. Instead it was found to possess a broad metal-to-semiconductor transition at ~80 K [compared to ±15 K for $H_2(Pc)I$].

1.3.3.2 Metalloporphyrins

Porphyrins are closely related to phthalocyanines both with regard to electronic and molecular structure. As for the metallophthalocyanines M(Pc), iodine-oxidation of the metalloporphyrins, ML (L = porphyrin), affords partially oxidized metallomacrocycles, MLI_x, in this case.[79-83] The crystal structures of these iodinated metalloporphyrins closely resemble that of e.g. Ni(Pc)I; consisting of stacks of the oxidized metallomacrocyclic molecules with chains of polyiodide anions occurring between and parallel to these stacks. The molecular structures of some representative examples of the metalloporphyrins are depicted below.
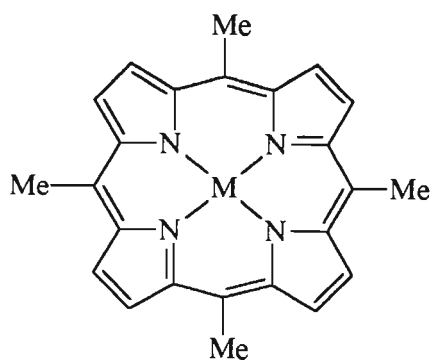
M(tmp)

(tmp = tertramethylporphyrin)
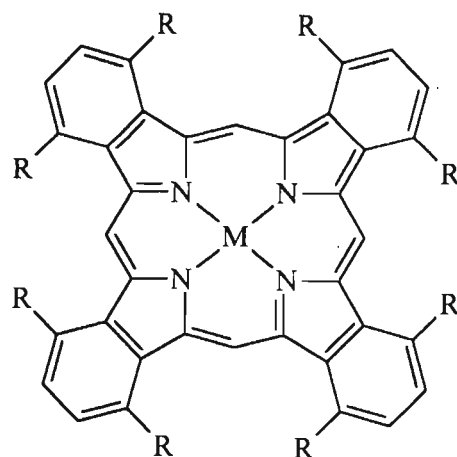
M(tbp) (R=H) and M(omtbp) (R=Me)

(tbp = tetrabenzoporphyrin)

(omtb = octamethyltetrabenzoporphyrin)
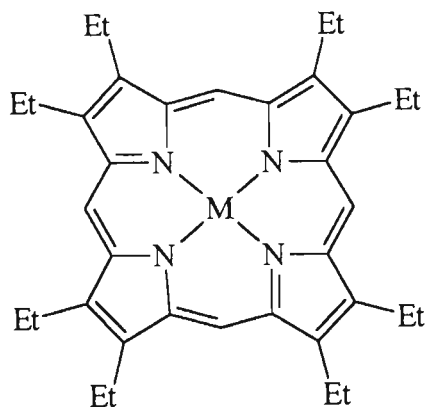
M(oep)

(oep = octa-ethylporphyrin)

A comparison of the conductivities of the iodinated metalloporphyrins with the analogous phthalocyanines, reveals that at room temperature, the porphyrin compounds have conductivities close to [$\sigma_{R.T}$ (single crystal) for Ni(tmp)I = 40 to 270 S.cm^{-1}; $\sigma_{R.T}$ (single crystal) for Ni(tbp)I = 150 to 350 S.cm^{-1} [83]] or less [$\sigma_{R.T}$ (compressed pellet) for Ni(oep)I$_{5.7}$ = 2.8 x 10^{-2} S.cm^{-1} [84]] than that of *e.g.* Ni(pc)I, [$\sigma_{R.T}$ (single crystal) = 260 to 750 S.cm^{-1}[85]; $\sigma_{R.T}$ (compressed pellet) = 0.7 S.cm^{-1} [72]]. The low-temperature conductivity behaviour of the iodinated metalloporphyrins is similar to that of the phthalocyanines, both groups exhibiting a metal-like increase in conductivity upon lowering the temperature. However, Ni(Pc)I has a relatively sharp conductivity maximum (σ_{max} = 2000 to 5000 S.cm^{-1}) at $T_m \approx$ 25K, whereas the conductivities of the porphyrin compounds go through broad maxima, the temperatures at which these maxima occur (T_m) being higher than that for the phthalocyanines and the associated conductivity (σ_{max}) being lower [for Ni(tmp)I, σ_{max} ~80 to 540 S.cm^{-1} at T_m ~115 $\pm$ 10 K,[83] for Ni(tbp)I, σ_{max} ~600 S.cm^{-1} at T_m ~95 K[82]].

A very interesting and important concept originating from the study of Ni(tbp)I, is that of double mixed valency. Upon iodination of a metal-containing species ML, various modes of oxidation are possible, the limiting cases being those where electron loss occurs from the metal *e.g.* in the case of the tetracyanoplatinates, or from the ligand, as was discussed for Ni(Pc)I. Examination of the *g*-values and line widths of the EPR

signals associated with the charge-carrying holes, enables the deduction of the mode of oxidation, *i.e.* whether it is metal- or ligand-based. From such examinations it was found that the charge carriers in Ni(Pc)I,[74] Ni(omtbp)I[80,81] and Ni(tmp)I[83] are ligand-based, with only a small contribution from the iodine. In contrast, the carrier spin *g*-values and EPR line widths for Ni(tbp)I indicate that for this compound the oxidation is not purely ligand-based, but rather of a mixed ligand π and metal d character. Furthermore, the interpretation of the room temperature *g*-values of Ni(tbp)I requires a contribution of $\pm^1/_5$ from the [Ni^{III}(tbp)] form of the oxidized parent macrocycle. EPR results also indicate that the carrier holes are not delocalized in orbitals originating from both the metal and the ligand, but that the holes rather have one identity or the other, *i.e.* that they "hop" between the metal and the ligand. In chemical terms, Ni(tbp)I can thus be written as [Ni(tbp)]$_2$[Ni(tbp)]$^+$I where [Ni(tbp)]$^+$ represents the equilibrium [Ni^{III}(tbp)] $\leftrightarrow$ [Ni^{II}(tbp)$^+$]. Schematically, the conduction pathway can thus be represented as seen in Figure 1.6.
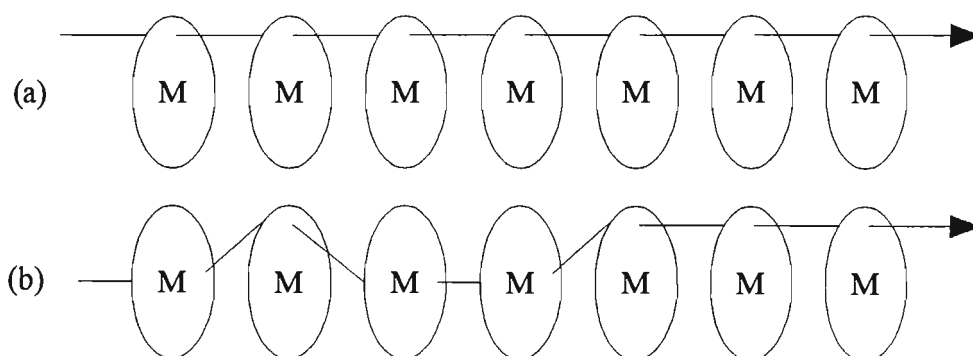
Figure 1.6: *Conduction pathway in a non-integral oxidation state metallomacrocycle stack:*

(a) Mixed valence system created by partial oxidation of the ring.

(b) Double mixed valence stack with carriers hopping between ligand and metal.

A further point well illustrated by the partially oxidized metalloporphyrins is that although the molecular co-crystallization method discussed up to now, is a useful first-generation approach, it does not allow rigorous structural enforcement, thus limiting its applicability.

An example of this limitation is provided by a consideration of attempts to modify the metallomacrocycle by alkylation, for instance. Substitution of the para hydrogens on the benzene fragments of tbp with methyl groups, affords the octa-methyl derivative, omtbp. Ni(omtbp)I$_{1.08}$ crystallizes with the same structural motif as Ni(tbp)I but steric interaction of the methyl substituents causes pronounced ruffling of the porphyrin ring. This results in the Ni-Ni separation in the metallomacrocycle stack increasing from 3.217(5)Å for Ni(tbp)[82] to 3.778(5)Å[81] for Ni(omtbp)I$_{1.08}$. The increase in the intermolecular spacing causes a decrease in the intermolecular orbital overlap which manifests itself in a decrease in the electrical conductivity [$\sigma_{R.T}$ for Ni(tbp)I = 150 to 330 S.cm^{-1},[83] whilst $\sigma_{R.T}$ for Ni(omtbp)I ~10 S.cm^{-1} [79]].

A second example involves changing the acceptor moiety through employing the non-halogen acceptor molecule 7,7,8,8-tetracyanoquinodimethane (TCNQ), for instance.
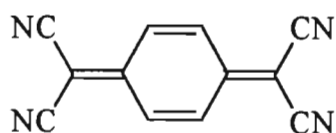
TCNQ

The reaction of Ni(tmp) with TCNQ affords the charge transfer complex [Ni(tmp)](TCNQ),[86] the crystal structure of which consists of stacks of alternating Ni(tmp) and TCNQ moieties. The room temperature conductivity for [Ni(tmp)](TCNQ) was found to be less than 10^{-5} S.cm^{-1}.

From the above two examples, Marks[73] concludes: "Without rigorous structural enforcement of the metallomacrocyclic stacking, it is impossible to effect controllable and informative variations in stacking architecture or in donor-acceptor spatial-electronic relationships. Clearly, the packing forces operative in most molecular conductors are rather delicate."

In order to overcome the proven problem of structural enforcement in metallomacrocyclic compounds, planar charge-carrying molecular subunits were linked in a cofacial orientation. This approach is discussed in full in Section 1.4, and will not be discussed here in any further detail.

1.3.4 Tetraazaannulene metal complexes

The electrically conductive metallophthalocyanines and related porphyrins, discussed above, are all 22π-electron species. In order to understand the role of the metallomacrocycle's molecular and electronic structure in stabilizing the conductive mixed-valent state, the 16π-electron tetraazaannulene metal complexes [M(taa)] and [M(tmtaa)], depicted below, were subjected to partial oxidation through iodination.[87,88]

[M(taa)]: R = H; M = Co, Ni, Cr, Pd, H₂

[M(tmtaa)]: R = Me; M = Ni, Pd, H₂
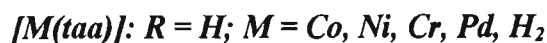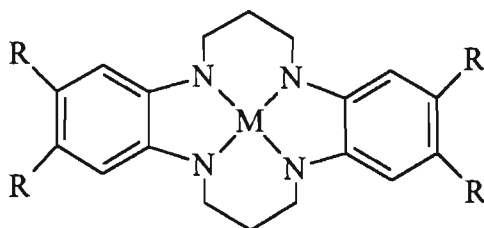
The stoichiometry of the resulting products, $[M(taa)]I_x$ or $[M(tmtaa)]I_y$, can be systematically varied with the reaction conditions. Single crystal diffraction studies on $[Ni(taa)]I_{1.8}$ and $[Ni(tmtaa)]I_{2.44}$ suggested a structure consisting of segregated, partially oxidized metallomacrocylic donor stacks surrounded by parallel chains of acceptor counterions. The nature of the polyiodide ions present in the anion chains depends on the stoichiometry of the product. Resonance Raman spectra indicated that for x, y $\leq$ 3 the I_3^- species is present, whereas for x, y > 3, I_5^- predominates. With respect to the nature of the oxidation, electrochemical studies[89,90] have shown that it involves molecular orbitals which are predominantly ligand centred.

The powder conductivity of $[M(taa)]I_x$ is comparable to that of $[Ni(Pc)]I$,[87] but unlike that for the phthalocyanines, the conductivity of $[H_2(taa)]I_x$ is several orders of magnitude smaller than that of $[M(taa)]I_x$ and $[M(tmtaa)]I_x$. The conductivity of $[M(taa)]I_x$ is also greater than that of $[M(tmtaa)]I_x$, the methyl substituent on [M(tmtaa)] probably interfering with the close packing of the metallomacrocyclic units, thus effecting the decrease in conductivity.

1.4 Ligand bridged complexes

1.4.1 Introduction

As indicated in the above discussion, the metallophthalocyanine and -porphyrin complexes do not allow any structural enforcement. Thus very little, if any control of the solid state stacking architecture is possible by modification of the architecture/composition of these materials on a molecular level. This implies that all synthetic attempts at modification of the bulk solid state properties of the metal phthalocyanines and porphyrins are subject to the packing forces involved in crystallization, these forces being quite delicate, poorly understood and thus, rather unpredictable.

In order to overcome this problem, synthetic attempts were directed to metallomacrocyclic polymers, which are constructed by covalently linking molecular metallomacrocyclic subunits in a cofacial arrangement. This approach allows for rigorous enforcement of the stacking pattern and thus meaningful investigations of, for instance, donor-acceptor relationships for structurally and electronically different dopants and the influence of different interplanar spacings on bulk properties. Furthermore, the polymers are unreactive to air and water, thermally stable and can be processed to obtain conducting fibres.

Based on the bridging ligands employed, the metallomacrocyclic polymers can be divided into 2 groups, *viz.*:

a)   Polymers in which the bridging/linking ligand consists of a single atom, usually oxygen or fluorine.

b)   Polymers with multi-atom bridging/linking ligands.

By far the majority of coordination polymers studied, contain metallophthalocyanines or -porphyrins as the subunits and attention will thus be focused on these materials and their properties.

1.4.2 Single-atom bridged metallomacrocyclic polymers

1.4.2.1 Unoxidized/Virgin polymer

The polysiloxane polymers $[M(Pc)O]_n$ (M = Si, Ge, Sn) can be synthesized by the dehydration of the dihydro derivative $[M(Pc)(OH)_2]$ *in vacuo*.[91] Similar polymers with M = Al or Ga and F as the bridging ligand have been prepared.[92,93] However, the structures of these single-atom bridged polymers were only verified when the single crystal structure of $[Ga(Pc)F]_n$ was obtained in 1981.[94] As expected, the structure consists of octahedral Ga coordinated to the four phthalocyanine nitrogen atoms and two trans arranged fluorine atoms, these atoms linking the Ga(Pc) moieties in a cofacial arrangement.

In the case of polysiloxane polymers $[M(Pc)O]_n$, the degree of polymerization, n, can be varied by varying the polymerization conditions. For typical samples n = 120($\pm$30) (M = Si), 70($\pm$40) (M = Ge), 100($\pm$40) (M = Sn).[95] Furthermore, the interplanar Pc-Pc spacing depends on the coordinated metal, ranging from 3.83(2)Å for M = Si, through 3.53(2)Å or 3.57(2)Å for M = Ge to 3.82(2)Å for M = Sn. The polymers were also found to be extremely robust, polymerization for both the oxygen and fluorine bridged materials typically occurring at about 400°C, while $[Si(Pc)O]_n$ can be dissolved and recovered from concentrated H_2SO_4 without any detectable change.[95]

The partial oxidation of $[M(Pc)O]_n$ (M = Si, Ge) and $[M(Pc)F]$ (M = Al, Ga) results in a sharp increase in electrical conductivity and sparked a series of studies on this topic. The variety of oxidants employed in these studies can be divided into three groups and are discussed below under the following headings:

a)   Halogen and nitrosyl salt oxidants.

b)   Electrochemical oxidation.

c)   Quinone oxidants.

1.4.2.2 Halogen and nitrosyl salt oxidation of metallomacrocyclic polymers

Both the fluorine bridged $[M(Pc)F]_n$ (M = Al, Ga) and the oxygen bridged $[M(Pc)O]_n$ (M = Si, Ge, Sn) polymers have been subjected to partial oxidation/doping by halogens and nitrosyl salts.

Halogen doping of $[M(Pc)F]_n$ (M = Al, Ga) affords materials of composition $\{[M(Pc)F]I_x\}_n$ where x = 0.012 to 3.4 (M = Al) and x = 0.048 to 2.1 (M = Ga) the conductivities being up to 10^7 times greater than that of the undoped/virgin polymers.[92,96,97] (Room temperature compressed powder conductivities are; $\sigma_{R.T} < 10^{-9}$ S.cm^{-1} for $[Ga(Pc)F]_n$, $\sigma_{R.T} = 0.12$ S.cm^{-1} for $\{[Ga(Pc)F]I_{0.93}\}_n$.) Raman spectroscopy indicated that for all of these materials, except those prepared by heating $\{[Al(Pc)F]I_{3.4}\}_n$ to temperatures less than 200°C, both I_3^- and I_5^- are present, with I_5^- predominating. (I_3^- predominates in $\{[Al(Pc)F]I_{3.4}\}_n$ derivatives.) Using (NO)(BF$_4$) and (NO)(PF$_6$), the partially oxidized $\{[M(Pc)F](X)_x\}_n$ polymers (M = Al, Ga; X$^-$ = BF$_4^-$, PF$_6^-$) were synthesized[98] and found to be electrically conductive.[99] Furthermore, the halogen-oxidized materials can be undoped by heating *in vacuo*, whereas the nitrosyl-oxidized fluorine-bridged polymers were found to be highly stable to both high temperatures and exposure to air.

Halogen- and nitrosyl-oxidation[100,101] of the polysiloxane polymers $[M(Pc)O]_n$ proceeds as outlined by the following equations:

$$[M(Pc)O]_n + 0.53n\ X \rightarrow \{[M(Pc)O](X_3)_y\}_n \text{ (M = Si, Ge; X = Br, I; y} \approx 0.35)$$

$$[M(Pc)O]_n + 0.35\ NO^+Z^- \rightarrow \{[M(Pc)O](Z)_{0.35}\}_n + 0.35\ NO$$

$$(M = Si, Z^- = BF_4^-, PF_6^-, \text{ and } SbF_6^-)$$
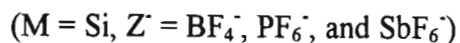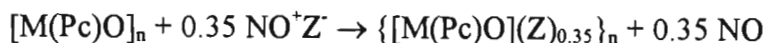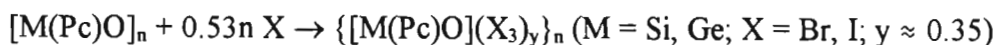
Whereas the halogen-oxidation of the Si and Ge polymers proceed smoothly, it would seem that for the Sn analogue, the Sn-O bonds are lost upon doping. A similar situation prevails when nitrosyl salts are employed to effect oxidation, the Si polymer being partially oxidized, but the Ge analogue decomposes. However, if oxidation does occur, the resulting products were found to be indefinitely stable in air. The above equations also show that for all halogen and nitrosyl oxidants, the ultimate degree of partial oxidation, ρ, is $\approx$ +0.35. This observation is in accordance with the theoretical values obtained from Born-Haber cycle calculations.[101] An interesting feature of the halogen and nitrosyl salt oxidation is that, as deduced from X-ray powder diffraction studies,[100, 101] the doping process is inhomogeneous. This implies that the dopant is not homogeneously dispersed throughout the lattice, but rather that as the amount of

oxidant available increases, varying amounts of the fully doped phase and the virgin polymer coexist within the same lattice. Only once full uptake of the oxidant dopant is achieved, does the material become homogeneous again. This inhomogeneity of the doping process was further confirmed by transmission electron microscopy.[102,103]

The fully doped polysiloxane polymers, $\{[M(Pc)O](X_3)_{0.35}\}_n$, have tetragonal crystal structures, but similar to the fluorine-bridged halogenated polymers, can be undoped by heating *in vacuo*. The undoped material obtained in this way is best modelled by a tetragonal structure, whereas the virgin polymer possesses an orthorhombic structure. As such, thermally undoped $[Si(Pc)O]_n$ represents a new $[Si(Pc)O]_n$ phase.

The series $[Ni(Pc)](I_3)_{0.33}$, $\{[Si(Pc)O](I_3)_{0.35}\}_n$ and $\{[Ge(Pc)O](I_3)_{0.35}\}_n$ provides an illustrative example of how variation of the Pc-Pc interplanar spacing can modify the bulk properties of the material. The crystal structures of these three materials are virtually the same, the only difference being a variation in the Pc-Pc interplanar spacing, which increases from 3.244(2)Å for $[Ni(Pc)](I_3)_{0.33}$[74] to 3.30(2)Å for $\{[Si(Pc)](I_3)_{0.35}\}_n$[100] to 3.48(2)Å for $\{[Ge(Pc)](I_3)_{0.35}\}_n$.[100] Accompanying this increase in Pc-Pc interplanar spacing, is a decrease in conductivity from $\sigma = 250$ to 600 $S.cm^{-1}$ for $[Ni(Pc)](I_3)_{0.33}$ and $\sigma \approx 100$ $S.cm^{-1}$ for $\{[Si(Pc)](I_3)_{0.35}\}_n$ to $\sigma \approx 10$ $S.cm^{-1}$ for $\{[Ge(Pc)](I_3)_{0.35}\}_n$.[100] Even though the above conductivities of the doped polysiloxane polymers are only estimates, supporting evidence for the decrease in conductivity is provided by an increase in the Pauli magnetic susceptibility ($\chi_{Ni} < \chi_{Si} < \chi_{Ge}$) and a decrease in the optical reflectivity plasma frequency ($\omega_{Ni} > \omega_{Si} > \omega_{Ge}$).[100] The decrease in conductivity associated with the increasing Pc-Pc interplanar spacing is attributable to a diminution of the efficiency of charge transport, resulting from decreasing overlap between the adjacent macrocycle π-systems.

A graph of the electrical conductivity of the doped polysiloxane polymers as a function of the doping level,[100] exhibits a sharp increase in conductivity with increased doping at low dopant concentrations, followed by a levelling off as the dopant concentration is further increased. This behaviour is a consequence of the inhomogeneity of the doping process resulting in the product consisting of a mixture of conductive and non-conductive "particles". At low dopant levels, increasing the volume fraction of

conductive "particles", results in a sharp increase in conductivity. However, a critical volume fraction exists beyond which the conductive particles form a continuous network. At this point, the percolation threshold, the material becomes highly conductive and the conductivity as a function of dopant concentration, levels off. The electrical conductivity, σ, of these materials has also been found to be temperature dependent,[100,101] a linear relationship existing between $-1/\ln(\sigma/\sigma_0)$ and temperature (σ_0 is a constant characteristic of the material). This relationship suggests that the temperature dependence of the conductivity can be explained by the fluctuation-induced tunnelling model. In this model, electrical conduction is modulated by small non-conducting junctions separating longer high-conductivity regions.

A further question addressed by these studies involves the influence counter/dopant anions with different sizes and polarizabilities,[104] have on the polymer composition and structure in general, and on the charge carriers in particular.

With regard to polymer composition/structure it was found that the degree of incomplete charge transfer, the inhomogeneity of the doping process and the geometries (interplanar spacings and ring-ring staggering angles) of the partially oxidized polymers are almost independent of the counter/dopant anion present. Differing size and polarizability of the counter anions also have little or no influence on the charge carriers. Magnetic susceptibility data failed to reveal any effect of the counterions on Coulombic enhancement, whereas optical reflectivity studies proved that the optical bandwidth parameters are virtually independent of the counterion. Differences in the variable temperature conductivity data corresponding to the different dopants are explicable in terms of different interparticle resistances and chain-packing densities. Finally ESR data for the various $\{[Si(Pc)O]X_y\}_n$ polymers revealed that the oxidation is ligand-based, with the absence of any heavy atoms in extensive communication with the charge carriers.

This insensitivity of the polymer electronic properties to the nature of the dopant, has been suggested to arise from the essentially frozen character of the stacking structure so that counterion-based band structure modifications can basically only take place through Coulombic interactions or modifications of the Pc-Pc ring staggering angles. A

second and less important factor has been suggested to originate from the unique M(Pc) electronic structure.

1.4.2.3 Electrochemical oxidation

The electrochemical oxidation of $[Si(Pc)O]_n$ in the presence of a supporting electrolyte, AX ($X^- = BF_4^-$, PF_4^-, SbF_6^-, tosylate, $CF_3(CF_2)_n SO_3^-$ n = 0, 3, 7 and SO_4^{2-}) was found to reversibly afford the oxidized polymers $\{[Si(Pc)O]X_y\}_n$.[105,106] However, attempts to effect the same oxidation of $[Ge(Pc)O]_n$ failed, due to suggested polymer decomposition involving cleavage of the Ge-O bonds.[106]

A comparison of, for example, the electrochemically produced oxidized polymer $\{[Si(Pc)O](BF_4\}_n$ with that produced via the nitrosyl salt oxidation, reveals that the two methods yield material with the same tetragonal crystal structure, but that for the electrochemical process the highest degree of partial oxidation, $y_{max} = 0.50$, whereas for the nitrosyl salt oxidation, y_{max} is restricted to ≈ 0.35. Furthermore, X-ray diffractometric studies have revealed that, in contrast to chemical oxidation, the electrochemical doping process is homogeneous, thus allowing for smooth tuning of the extent of partial charge transfer/oxidation.

A further feature of electrochemical doping is that the initial oxidation/doping of the virgin polymer is accompanied by a large overpotential/kinetic barrier, whereas subsequent undoping and doping cycles do not exhibit any overpotential. This behaviour, referred to as "break in" behaviour, is a direct consequence of the structural rearrangements associated with the redox behaviour of the polysiloxane polymers. As was pointed out for the halogen and nitrosyl salt oxidation of these polymers (see section 1.4.2.2), doping of the virgin polymer involves an orthorhombic to tetrahedral phase transformation which implies a reorganisation of the $[Si(Pc)O]_n$ chains and an expansion of the crystal lattice. This reorganization necessitates the large overpotential. Undoping the doped polymer affords a tetragonal phase of $[Si(Pc)O]_n$, implying that subsequent electrochemical cycling involves interconversion between the structurally similar tetragonal doped and undoped phases. These cycles only require anion migration through the "channels" between the $[Si(Pc)O]_n$ chains, implying minimal reorganization of the chains themselves, and thus no associated large overpotential.

The maximum doping stoichiometry and hence the extent of partial oxidation/band depletion, has been suggested to be largely determined by the anion size. This suggestion is based on simple packing calculations employing Van der Waal's radii which revealed that there is good agreement between the maximum possible occupancy of the anion "channels" between the $[Si(Pc)O]_n$ chains and the doping level achieved.[106] An illustrative example of this sensitivity of the extent of partial oxidation to the dopant/anion structure is provided by the homogenous $CF_3(CF_2)_n SO_3^-$ series. For n = 0, 3 and 7 the maximum degrees of partial oxidation, y_{max}, achieved are, to a first approximation, 0.57, 0.35 and 0.26 respectively.[106] In the case of the extremely large anions, for example, $[Mo_8O_{26}]^{4-}$, the ultimate degree of doping/partial oxidation decreases to even lower values of $y_{max} \approx 0.06$.

As illustrated by the series $\{[Si(Pc)O](BF_4)_n$, $\{[Si(Pc)O](tosylate)_y\}_n$ and $\{[Si(Pc)O](SO_4)_y\}_n$, the electrical conductivities of the doped polysiloxane polymers for a fixed degree of partial oxidation (y) is not counteranion dependent.[107] The conductivity does however vary with the degree of doping/partial oxidation.[107] At low levels of partial oxidation, y < 0.20, a steep increase in conductivity accompanies increased partial oxidation. This is followed by a levelling off at y $\approx$ 0.20-0.30 whereafter the conductivity is virtually independent of the extent of partial oxidation, up to y $\approx$ 0.67. Based on thermoelectric power measurements, magnetic susceptibilities and ESR data, it has been suggested that the change in conductivity behaviour upon incremental doping at y $\approx$ 0.20 stems from a transition from p-type semiconducting behaviour to p-type molecular metallic behaviour. Such a transition implies drastic changes in the electronic structure and carrier mobilities of the oxidized polymer. As evidenced by X-ray diffraction and electrochemical data, this change in electronic properties is not accompanied by a similarly drastic change on a structural level. In fact, the diffractometric and electrochemical data rather suggest a smooth evolution in structure as a function of y. The observed transition in conductivity behaviour was thus explained[107] by utilizing an electronic structural model which focuses on the effect disorder and defects have on quasi one-dimensional band structures. In terms of this model charge carriers (holes) have low mobilities at very low and very high doping/partial oxidation levels.

1.4.2.4 Quinone-oxidation

The highest degree of partial oxidation, y_{max}, achieved upon employing electrochemical oxidation of the polysiloxane polymers, is limited to *ca.* +0.70. Utilization of the strong
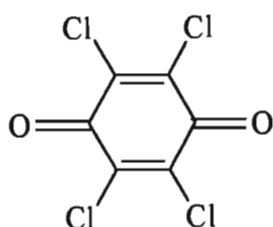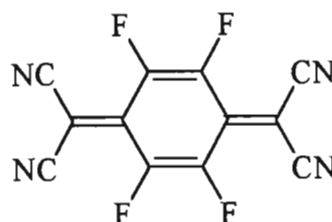
$$DDQ \qquad\qquad TCNQF_4$$

oxidizing agents 2,3-dichloro-5,6-dicyano-*p*-benzoquinone (DDQ) or 2,3,5,6-tetrafluoro-7,7,8,8-tetracyanoquinodimethane (TCNQF$_4$), depicted above, allows for oxidation of [Si(Pc)O]$_n$ to levels with $y \approx 1.65$ [108,109] (see reaction scheme below).

$$[Si(Pc)O]_n + yn\ Q \leftrightarrow \{[Si(Pc)O]Q_y\}_n \quad (Q = DDQ, TCNQF_4)$$

Spectral data indicated that most, if not all, of the quinone molecules in $\{[Si(Pc)O]Q_y\}_n$ exist as radical anions. However, as revealed by X-ray diffractometry, the doping process is partly inhomogeneous. Furthermore, as with the halogen-oxidized polymers, $\{[Si(Pc)O]Qy\}_n$ can be undoped by heating the product *in vacuo*.

The electrical and optical properties of the quinone-doped polysiloxane polymers closely resemble those of the other oxidized polymers discussed above, but are markedly different to those of the quinone-oxidized molecular metalloporphyrins (see section 1.3.3.2). This is not surprising since the quinone-oxidized metalloporphyrins have an integrated stacked structure, whereas for the polysiloxane polymers, "segregated stacking" is structurally enforced.

In considering the electronic properties of these materials it was found, as confirmed by optical reflectivity and thermoelectric power data, that there is a steep rise in conductivity as the level of partial oxidation is increased to $y \approx 0.20$. Beyond $y \approx 0.20$ the room temperature conductivity remain virtually constant until $y \approx 0.50$ to 0.60 is

reached. At this point the conductivity starts decreasing. Increasing y further, to ≈ 0.90, results in the conductivity decreasing to a value 10^7 times smaller than that associated with $y \approx 0.40$. The conductivity associated with $y \approx 0.90$ is also lower than that associated with the unoxidized parent material. Thus it is evident that $\{[Si(Pc)O]Q_y\}_n$ approaches a metal-to-insulator transition as y approaches ≈ 1.00. Utilizing $TCNQF_4$ it is possible to increase the level of partial oxidation beyond $y \approx 1.00$. This affects another increase in conductivity with the oxidation products exhibiting conductivities analogous to those observed in the $0.20 \leq y \leq 0.60$ region.

1.4.2.5 Electronic structure

In order to gain insight into the electronic structure of the oxidized $[Si(Pc)O]_n$ polymers, electronic structure calculations have been performed on $Si(Pc)(OR)_2$ and $ROSi(Pc)OSi(Pc)OR$ $\{R = Si[C(CH_3)]_3(CH_3)_2\}^{[110]}$ and $[Si(Pc)(OH)_2]$ where the phthalocyanine, Pc, is octafluoro- or octacyano-substituted.[111]

Considering the HOMO of $[Si(Pc)(OH)_2]$, the calculations revealed that the greatest orbital amplitude is situated near the core of the metallomacrocycle with lesser contributions from the orbitals of the fused aromatic rings and an almost negligible contribution from the orbitals which will be involved in the $-(Si-O)_n-$ chain. From this result it follows that the conduction band in the oxidized polymers is mainly composed of carbon $p\pi$ orbitals located close to the macrocycle core. Bearing in mind the spatial extent of the Pc ring and thus the remoteness of the conduction band orbitals from the dopant counteranions, it is not unexpected that the collective properties of the oxidized $\{[Si(Pc)O]X_y\}_n$ polymers show little to no dependence on the nature of X.

Calculations on dimeric structures $e.g.$ $ROSi(Pc)OSi(Pc)OR$ $\{R = Si[C(CH_3)]_3-(CH_3)_2\}$, were performed to study the influence of interplanar eclipsing/twist angle and ring-ring interplanar spacing on π-π interactions between the rings.[110,112] As far as interplanar eclipsing is concerned, the studies revealed that two possible overlap maxima exist, $viz.$ at $0°$ and at $45°$; experimentally observed angles being $ca.$ $40°$. The $0°$ option is possibly avoided due to accompanying non-bonded repulsions. Furthermore, zero π-π overlap will occur for angles approaching $\approx 20°$. In exact accordance with experimental observations (see discussion of conductivity versus

interplanar spacing, section 1.4.2.2), the calculations also revealed a rapid decrease in π-π interactions as the ring-ring separation increases for a fixed twist angle.

1.4.3 Multi-atom ligand bridged metallomacrocyclic polymers

1.4.3.1 Introduction

As discussed in the previous section, the conduction pathway in the single-atom bridged metallomacrocyclic polymers is ligand-based with negligible, if any, contribution from the metal-bridging-ligand backbone. In the case of the multi-atom ligand bridged metallomacrocyclic polymers however, this situation is reversed with the metal backbone playing a much more significant part in the conduction process. Thus, analogous to the metal chain compounds (see section 1.2), the conduction process for this class of compounds is not derived from the supporting ligand(s), but from overlap of the transition metal d orbitals. The difference between the multi-atom ligand bridged metallomacrocyclic polymers and the metal chain compounds lies in the fact that whereas for the metal chain compounds direct metal-metal interaction takes place, the metallomacrocyclic polymers participate in indirect interaction mediated through the bridging ligand.

The multi-atom ligand bridged metallomacrocyclic polymers consist of three basic independent building blocks, systematic variation of which allows for modification of the bulk physical properties of the polymer. These building blocks are: [113]

a)   The metal. Here it has been found that the more easily oxidized strongly π-bonding 4d and 5d metals are the best candidates for use in these materials.

b)   The bridging ligand which, depending on its nature, can be axially linked to the metal atoms in one of three ways:[114]

      i)   Through two coordinate bonds *e.g.* pyrazine (pyz), 1,4-diisocyanobenzene (dib), 4,4'-bipyridine (4,4'-bipy), tetrazine (tz) and 1,4-diazabicyclo[2.2.2]octane (dabco)

      ii)   Through one σ and one coordinate bond *e.g.* CN⁻

      iii)   Through two σ bonds *e.g.* $C{\equiv}C^{2-}$, $N{=}C{=}N^{2-}$

c)   The supporting macrocyclic ligand. The majority of the multi-atom ligand bridged polymers reported in the literature utilize one of two marocyclic ligand types, *viz.:*

i)   Porphyrin and its derivatives

ii)   Phthalocyanine (Pc) and its derivatives.

Subsequent discussion of these polymers will be conducted based on this differentiation.

1.4.3.2 Multi-atom ligand bridged metalloporphyrin polymers

Probably the most extensively researched and thus representative group of compounds typifying the multi-atom ligand bridged metalloporphyrin polymers, is the series $[M(oep)L]_n$ (where M = Fe, Ru, Os; oep = octaethylporphyrin and L = pyz, 4,4'-bipy and dabco)

The undoped/virgin polymers $[M(oep)L]_n$[115] are sythesized by reacting *e.g.* $[Ru(oep)]_2$ with the relevant bridging ligand, the chain length, n, of the resulting polymer depending on the experimental conditions employed. However, infrared red end group analysis has shown typical values of n for $[M(oep)(pyz)]_n$ to be n = 40 ($\pm$10) for M = Fe, n = 25 ($\pm$5) for M = Ru and n = 20 ($\pm$5) for M = Os.

When compared to their related $[M(oep)(pyz)_2]$ monomers, the undoped polymers show significant increases in conductivity [115] {*e.g.* for $[Os(oep)(pyz)_2]$, $\sigma_{R.T.} = 8 \times 10^{-11}$ S.cm^{-1} whilst for $[Os(oep)(pyz)]_n$, $\sigma_{R.T.} = 3.2 \times 10^{-7}$ S.cm^{-1}}. It has also been suggested that the $[M(oep)(pyz)]_n$ polymers exhibit increased conductivities as M varies from Fe down the triad to Os. Upon moving down the Fe triad however, the $[M(oep)(pyz)]_n$ polymers become increasingly sensitive to adventitious oxygen doping resulting in large conductivity increases, so that the "trend" towards greater conductivity as one moves down the triad, becomes less clear-cut.

Various dopants including I_2, $[FeCp_2](PF_6)$ (Cp = cyclopentadiene) and $(NO)(PF_6)$ have been utilized in the partial oxidation of $[M(oep)(pyz)]_n$, typically resulting in conductivity increases of 10^5 when compared to the undoped polymers {for $[Os(oep)(pyz)]_n$, $\sigma_{R.T.} = 3.2 \times 10^{-7}$ S.cm^{-1} for $[Os(oep)(pyz)I_{1.0}]_n$, $\sigma_{R.T.} = 5 \times 10^{-2}$ S.cm^{-1}

and $[Os(oep)(pyz)(PF_6)_{0.2}]_n$, $\sigma_{R.T.} = 2.3 \times 10^{-2}$ $S.cm^{-1}$ }.[113] Resonance Raman spectroscopy revealed that the dominant form of iodine present in the iodine doped materials is I_3^-. As in the case of the doped single-atom bridged $[M(Pc)X]_n$ (X = O, F) polymers, the doped $[M(oep)(pyz)]_n$ compounds show a steep increase in conductivity with initial incremental doping, the conductivity maximum being reached as the doping level, y, approaches y = 0.2 to 0.4. Unlike the doped $[M(Pc)X]_n$ polymers though, doped $[M(oep)(pyz)]_n$ exhibits a decrease in conductivity as y is increased beyond y = 0.2 to 0.4. At these doping levels, the results of any possible adventitious oxidation doping becomes negligible. Considering the conductivities of the doped $[M(oep)L]_n$ series in this light, reveals a genuine increase in conductivity upon descending the Fe traid. Accompanying this increase, is an increase in conductivity as the bridging ligand, L, is varied from dabco through 4,4'-bipy to pyz. It is believed that the bridging ligands' ability to mediate electron exchange between the M(III) sites along the chain, constitutes a cardinal part of the origin of these trends. The interaction in question involves the mixing of the metal's d_π (d_{xz}, d_{yz}) with the π^* level of the bridging ligand. Thus, better π-bonding metals (Os > Ru > Fe) and more π-acidic bridging ligands (pyz > bpy >> dabco) allow for the formation of polymers with greater metal-metal communication and thus greater electrical conductivities.[115]

The partial oxidation of these $[M(oep)(pyz)]_n$ polymers is metal-centred. Direct evidence for this assignment was obtained from electrochemical studies[115] revealing transition metal-centred oxidation waves occurring at potentials less positive than those corresponding to the oxidation of the porphyrin ring. This implies that during oxidative doping, the metal, rather than the macrocyclic ligand will be oxidized. Further supporting evidence for this assertion was provided by ESR,[113] UV/visible and near infrared[115] studies which suggest that oxidation of the polymers does not appreciably alter the electron distribution of the porphyrin π-electron system.

Cyclic voltammetric studies on $[Os(oep)(pyz)]_n$ in the presence of ClO_4^-, BF_4^- and PF_6^- [115] revealed a moderate dependence of the shape of the redox waves on the nature of the anion present. This effect has been suggested to originate from structural changes operative in the system and/or electrostatic screening and/or pinning of the conduction electrons by the dopant anions.

1.4.3.3 Multi-atom ligand bridged metallophthalocyanine polymers

The majority of studies involving the multi-atom ligand bridged metallophthalocyanine polymers centre on one of two types of bridging ligands: those coordinating to "neighbouring" metal atoms of the polymer through two coordinate bonds *e.g.* 1,4-diisocyanobenzene (dib), 4,4′-bipyridine (4,4′-bipy), pyrazine (pyz) and its derivatives and s-tetrazine (tz). The second group constitutes ligands coordinating through one σ and one coordinate bond *e.g.* CN⁻.

The undoped polymers [M(Pc)L]$_n$ (M = Fe, Ru, Os; L = pyz, tz and for M = Fe, Ru; L = dib and 4,4′-bipy) are accessible via one of two synthetic routes, the first involving the reaction of the metalphthalocyanine with an equivalent amount of the bridging ligand as employed for the synthesis of [Fe(Pc)(pyz)]$_n$,[116] [M(Pc)(dib)]$_n$ (M = Fe,[117] Ru,[118] [Fe(Pc) (4,4′-bipy)]$_n$[117] and [M(Pc)(tz)]$_n$ (M = Fe,[119] Ru[119] and Os[120]). The second route involves the thermal splitting off of one of the coordinated ligands from the monomeric [M(Pc)L$_2$] species and is utilized in the synthesis of [M(Pc)(pyz)]$_n$ (M = Ru,[118] Os[120]) and [Ru(Pc)(4,4′-bipy)]$_n$.[118] Compared to the related monomeric species, the undoped polymers typically exhibit increases in conductivity between 10^3 {*e.g.* for [Ru(Pc)(4,4′-bipy)$_2$], $\sigma_{R.T.}$ = 1 x 10^{-11} S.cm⁻¹;[118] while for [Ru(Pc)(4,4′-bipy)]$_n$, $\sigma_{R.T.}$ = 2 x 10^{-8} S.cm⁻¹[118]} and 10^9 fold {*e.g.* for [Ru(Pc)(tz)$_2$], $\sigma_{R.T.}$ = 1 x 10^{-11} S.cm⁻¹;[119] while for [Ru(Pc)(tz)]$_n$, $\sigma_{R.T.}$ = 1 x 10^{-2} S.cm⁻¹ [119]}. A further interesting observation is that the conductivity of the undoped polymers does not appear to be dependent, or if so only slightly, on the length of the bridging ligand employed.[117] This observation is supported by both the Fe[121] and Ru[118] series [M(Pc)L$_2$]$_n$ (L = pyz, dib, 4,4′-bipy) where the conductivity decreases in the order $\sigma_{R.T.}$(dib) > $\sigma_{R.T.}$(pyz) > $\sigma_{R.T.}$(4,4′-bipy). For this [M(Pc)L$_2$]$_n$ series, (M = Fe, Ru; L = pyz, dib, 4,4′-bipy) it has also been found that the conductivities of the Ru polymers are slightly reduced compared to those of the analogous Fe polymers.[118]

Attempts at gaining insight into the structure of [Fe(Pc)(pyz)]$_n$ utilizing quantitative infrared spectroscopic measurements,[122] have revealed that the degree of polymerization, n, is *ca.* 20. Furthermore, from attempts at indexing the powder diffraction data obtained for the [Fe(Pc)(pyz)]$_n$ polymers, it is clear that these

compounds are not isostructural with the single atom bridged $[M(Pc)O]_n$ or $[M(Pc)F]_n$ polymers.[123]

Iodine doping of the multi-atom ligand bridged $[M(Pc)L]_n$ (M = Fe, Ru; L = pyz, dib) polymers affords stable compounds with the general stoichiometry $[M(Pc)(L)I_y]_n$ (y lies in the range 0 to 2.6, with the exact value of the upper limit depending on the nature of M). Although a number of the doped polymers have been synthesized[114, 117, 118, 123] the most extensive studies centred on $\{[Fe(Pc)(pyz)]I_y\}_n$.[123] ^{57}Fe Mössbauer data indicated that the polymeric structure remains intact upon doping, the iodine dopant being present as I_5^-, as evidenced by Resonance Raman spectroscopy. As in the case of the single atom bridged polymers e.g. $[M(Pc)O]_n$, incremental iodine doping of $[Fe(Pc)(pyz)]_n$ results in a rapid and roughly parallel increase in conductivity, the conductivity maximum of $\sigma \approx 10^{-1}$ to 10^{-2} S.cm^{-1} [123] for $\{[Fe(Pc)(pyz)]I_y\}_n$, being reached at y $\approx$ 2 (for $\{[M(Pc)O]I_y\}_n$, the conductivity maxima of $\sigma \approx 1$ S.cm^{-1} (M = Si) and $\sigma \approx 10^{-1}$ S.cm^{-1} (M = Ge) are reached at y ≈ 1.1;[100] for the undoped polymer $[Fe(Pc)(pyz)]_n$, $\sigma = 2 \times 10^{-5}$ S.cm^{-1} [117]). Mössbauer spectroscopy also revealed that the iodine-oxidation involves orbitals, which as in the case of the $\{[M(Pc)O]I_y\}_n$ (X = O, F) and Ni(Pc)I systems, are predominantly ligand-based. However, from specular reflectance spectroscopy it became clear that for $\{[Fe(Pc)(pyz)]I_y\}_n$, partial oxidation does not produce the type of phthalocyanine π-electron band structure as is found in the partially oxidized $\{[M(Pc)O]I_y\}_n$ (M = Si, Ge) polymers.

An example of multi-atom ligand bridged $[M(Pc)L]_n$ polymers where the central metal atoms are linked by a ligand utilizing one σ and one coordinate bond, is provided by the cyano-bridged $[M(Pc)(CN)]_n$ polymers (M = Co(III), Fe(II), Fe(III), Mn(III) and Cr(III))[114, 124, 125]. A general route leading to the $[M(Pc)(CN)]_n$ polymers, involves the splitting off of alkali metal cyanide from the monomeric $M'[M(Pc)(CN_2)]$ complexes (M' = Na, K; M = Co, Mn, Fe, Cr). Alternative routes involve the displacement of an axial X^- ion (X = halogen) by CN^- in the coordinatively unsaturated compounds PcMX, as was utilized in the synthesis of $[Fe(Pc)(CN)]_n$ and $[Mn(Pc)(CN)]_n$, or a reduction-polymerization reaction involving the reaction of $[Co(Pc)Cl_2]$ and $[Cr(Pc)Cl_2]$ with aqueous alkali metal cyanide to afford the $[Co(Pc)(CN)]_n$ and $[Cr(Pc)(CN)]_n$ polymers.

X-ray diffraction studies have revealed that the $[M(Pc)(CN)]_n$ polymers (M = Co, Fe, Mn, Cr, Rh) are all isostructural.

The undoped polymer, $[Co(Pc)(CN)]_n$ exhibits an electrical conductivity of $\sigma = 2 \times 10^{-2}$ $S.cm^{-1}$, which is comparable to that observed for the doped single atom bridged $\{[M(Pc)X]I_y\}_n$ (X = O, F) and the doped two coordinate bond multi-atom bridged $\{[M(Pc)L]I_y\}_n$ (L = pyz, dib, 4,4'-bipy) polymers. Treatment of $[Co(Pc)(CN)]_n$ with competing ligands e.g. pyridine however, destroys the polymeric structure, affording monomeric $[Co(Pc)(CN)(pyr)]$ with an accompanying 10^{10} fold decrease in conductivity (for $[Co(Pc)(CN)(pyr)]$, $\sigma = 3 \times 10^{-12}$ $S.cm^{-1}$). $[Fe(Pc)(CN)]_n$ has a conductivity of $\sigma = 3 \times 10^{-3}$ $S.cm^{-1}$ comparable with that of the Co polymer, with lower values of $\sigma = 1 \times 10^{-5}$ $S.cm^{-1}$ and 3×10^{-6} $S.cm^{-1}$, observed for $[Mn(Pc)(CN)]_n$ and $[Cr(Pc)(CN)]_n$ respectively. Attempts at doping $[Co(Pc)(CN)]_n$ with I_2, afforded the stable product $\{[Co(Pc)(CN)]I_y\}_n$ (y = 1.6). The conductivity is, however, only slightly increased by doping, to $\sigma_{R.T.} = 0.6$ $S.cm^{-1}$.

The exact conduction pathway associated with the comparatively high conductivities observed for $[Co(Pc)(CN)]_n$ and $[Fe(Pc)(CN)]_n$ is still unknown. EPR spectra obtained for polycrystalline $[Co(Pc)(CN)]_n$, exhibits two signals; one corresponding to an oxidation centred on the macrocyclic ligand, the other suggesting a partial reduction of the metal, bridging-ligand backbone.[114, 125]

1.5 Electron/charge transfer and radical ion salts

1.5.1 Introduction

An electron/charge transfer salt can, in the classic sense of the term, be defined as the product resulting from a reaction in which electron density is transferred from an electron rich donor molecule to an electron acceptor molecule. Such a salt thus consists of open shell cations combined with open shell anions. In contrast, a radical ion salt comprises open shell cations in combination with closed shell anions e.g. $(TMTSF)_2ClO_4$ (TMTSF = tetramethyltetraselenofulvalene, see section 1.5.4.1) or vice versa as demonstrated by $(Me_4N)(2,5-Cl_2-DCNQI)$ (2,5-Cl_2-DCNQI = 2,5-dichlorodicyanquinonediimine, see section 1.5.4.4). A radical ion salt is thus not

generated by charge transfer from a donor to an acceptor molecule, but rather through, for example, electrochemical means as demonstrated by $(TMTSF)_2ClO_4$ where the electrochemical reaction proceeds according to the following scheme:

$$2 \text{ TMTSF} + ClO_4^- \rightarrow (TMTSF)_2ClO_4 + e^-$$
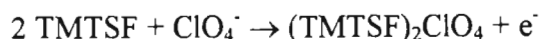
The majority of the materials discussed in the previous section contained transition metal atoms, the influence of these metal atoms on the bulk properties of the materials varying from being of cardinal, to of little, or no importance. In the case of many charge transfer salts, and particularly the very first examples of them, the constituent molecular radical ions contain no transition metal atoms; in other words they are completely organic in their composition.

Despite early predictions by McCoy and Moore[126] suggesting that it might be "possible to prepare composite metallic substances from non-metallic constituents", many were surprised when the reaction between the electron rich donor molecule, tetrathiofulvalene (TTF, depicted below) and the electron acceptor molecule 7,7,8,8-tetracyanoquinodimethane (TCNQ, depicted below) afforded a product,
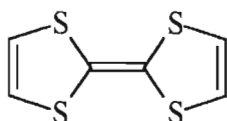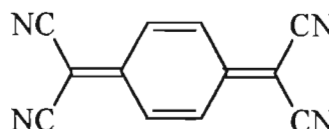
TTF   *TCNQ*

(TTF)(TCNQ), which exhibits genuine metal-like conductivity[127] despite being completely organic. Following this discovery a flurry of studies followed in which a large number of (TTF)(TCNQ) type charge transfer salts were synthesized.[128] All of these however, are so-called pseudo one-dimensional materials, their conductivities being subject to low temperature metal-to-insulator transitions/lattice distortions.

Today interest in charge transfer salts centres mainly on one of two directions. The first involves pseudo two-dimensional charge transfer salts, some of which exhibit superconductivity. The second area is concerned with the reaction between organometallic and in particular, metallocene electron donor molecules, with organic

acceptor molecules. The products from these reactions often exhibit interesting magnetic properties and in some cases, ferromagnetic behaviour has been observed.

In the following discussion, brief attention will be focused on the (TTF)(TCNQ) type pseudo one-dimensional charge transfer salts, the relationship between their structure and conductivity and the metal-to-insulator transitions associated with charge transfer salts. This will be followed by a discussion of the pseudo two-dimensional charge transfer salts and the structure-function relationships observed in these materials. The metallocene-based charge transfer salts are discussed in Chapter 2 (see section 2.3.2.1) and will not be discussed here in any further detail.

1.5.2 Pseudo one-dimensional charge transfer salts

The reaction between TTF and TCNQ[127, 129] affords the 1:1 salt (TTF)(TCNQ), the crystal structure of which[130] consists of separate stacks of planar TTF and TCNQ molecular ions. In each of these stacks the TTF or TCNQ moieties are arranged face-to-face, i.e. like poker chips, the distance between two neighbouring TTF or TCNQ moieties being less than the Van der Waal's radii associated with the constituent atoms of the respective molecules. This arrangement allows for extensive orbital overlap within the stacks, resulting in the formation of extended π-electronic systems. The net charge on the TTF and TCNQ units, resulting from the charge transfer reaction, is partly delocalized in these π-systems, thus enabling electrical conductivity along the stacks. In directions perpendicular to the stacking axis, there is no such interaction between the constituent units of the stacks. This lack of inter-stack interactions also manifests itself in the physical properties of (TTF)(TCNQ), thus explaining why it is referred to as being pseudo one-dimensional.

At room temperature, (TTF)(TCNQ) has a conductivity of 500 S.cm^{-1}, which, analogous to the behaviour in metals, increases upon cooling. This increase is not monotonic however, a maximum value of 10^4 S.cm^{-1} being reached before metal-to-insulator transitions occur at 54 K[131] and 38 K.[132] As expected from the one-dimensional nature of (TTF)(TCNQ), the conductivity is highly anisotropic, the conductivity in the most favourable direction in single crystals being 500 to 1000 times greater than that in the least favourable direction.

Following the discovery of metal-like conductivity in (TTF)(TCNQ), a plethora of related pseudo one-dimensional charge transfer salts, exhibiting conductivities ranging from insulating to metal-like, were synthesized.[128] Based on the knowledge gained form these materials, it became apparent that, in order for a new charge transfer salt to exhibit metal-like conductivity, is has to meet certain minimum criteria, these being:

a)   Partial or incomplete charge transfer from the donor to the acceptor molecule.

b)   Segregated stacking of the donor and acceptor molecular ions in the solid state.

c)   A certain degree of planarity of the constituent molecular ions in order to allow for close approach of the ions to one another within a segregated stack.

d)   The formation of a new aromatic sextet upon formation of the radical ion.

The concept of incomplete or partial charge transfer,[133] suggests that only a fraction of the electron charge (e) is transferred from the donor to the acceptor molecule. Quantitative evidence for partial charge transfer in (TTF)(TCNQ) was provided by both diffuse X-ray [134, 135] and neutron scattering[136, 137] results which indicated that the amount of charge transferred, $\rho = 0.59e$. This implies that on a very short time scale, each of the TTF or TCNQ stacks can be considered to consist of 59% fully ionized molecules, the rest of the molecules, which will be neutral, being interspersed between these.

The need for partial charge transfer can be explained as follows. Consider an ordered uniform chain of radicals, each having one unpaired electron [see Figure 1.7(a)]. In order for the chain to be conductive, charge needs to migrate along the chain, implying that it has to pass through a transition state where two electrons reside on a single site [see Figure 1.7(b)]. For the materials dealt with here, the formation of this transition state is energetically disfavoured, implying that the electrons are localized on the radicals, causing the chain to be electrically insulating. If however, the chain consisted of radicals interspersed with neutral entities [see Figure 1.7(c)], charge transfer can occur along the chain without the need to pass through the high energy intermediate, and electrical conductivity becomes feasible.
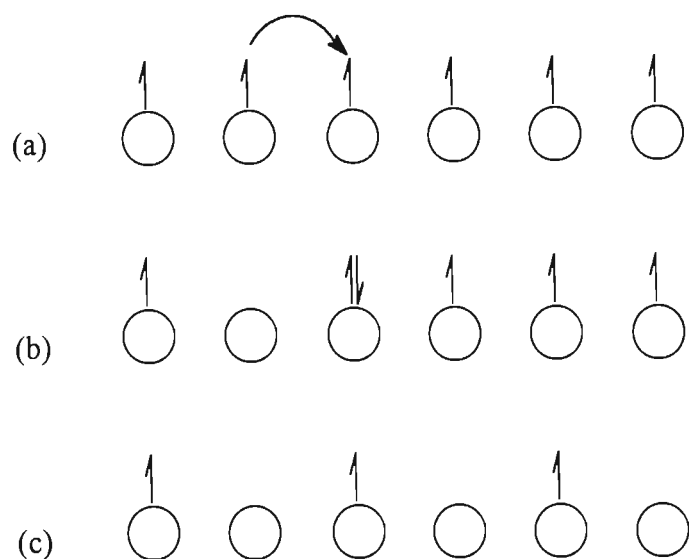
Figure 1.7: (a) Chain of radical ions each possessing one unpaired electron

(b) The high energy intermediate

(c) Chain of radical ions interspersed with neutral entities

As discussed above, crystals of (TTF)(TCNQ) consist of separate donor (D) stacks [...D-D-D-D...] and acceptor (A) stacks [....A-A-A-A.....]. This mode of packing is referred to as segregated stacking. An alternative mode of packing, where the molecular ions are also arranged face-to-face, but alternate within the stack, *i.e.* [....D-A-D-A....], is known as integrated stacking. Since the frontier orbitals on the donor (D) and acceptor (A) molecular ions differ in energy, the extent of orbital overlap in an integrated stack is severely diminished, thus resulting in a localization of the charge carriers and ultimately, low electrical conductivity.

In order for substantial orbital overlap to occur, short intermolecular distances between adjacent molecules within the segregated stacks is necessary. As discussed, the intermolecular distances associated with adjacent TTF or TCNQ molecular ions in (TTF)(TCNQ), is less than the sum of their Van der Waal's radii. Placing substituents in positions ortho to each other on the TCNQ-quinone ring, results in the rigid =C(CN)$_2$ grouping tilting from the plane of the ring (thus destroying the planarity of the molecule)[138, 139] which results in a breakdown in conductivity in the charge transfer salts. In contrast to the above, placement of chains of up to five or six alkyl carbons in positions para to each other on the quinone ring of the TCNQ, has only a minor effect

on the conductivity observed in the associated (TTF)(TCNQ) salts.[140] The reason for this observation stems from the alkyl substituents being able to participate in an interlocking structure, as demonstrated in the crystal structure of (TTF)(TCNQ).[141]

On consideration of a range of charge transfer compounds, Perlstein[142] found that not all of those compounds possessing segregated stacks of planar molecular ions, and where partial charge transfer has occurred, show high electrical conductivity. Close scrutiny revealed that for those that exhibit high conductivity, the donor and/or acceptor molecules form a new aromatic sextet on being transformed to the radical ion. This led to the proposal that the ability of charge to efficiently migrate from one molecule to the next in a segregated stack is linked to the presence of an aromatic sextet that can also migrate between adjacent molecules. This proposal has also been incorporated into a set of guidelines proposed for use in the design of new donor and acceptor molecules for highly conducting charge transfer compounds.[143]

1.5.3 Metal-to-insulator phase transitions

As reported above, the charge transfer materials discussed thus far are pseudo one-dimensional. At low temperature, such systems can not sustain long-range order and are unstable with respect to lattice distortions,[26] the degree of instability depending on the level of band-filling and ultimately on the relative number of radical ions and neutral molecules within the segregated stacks.

For a uniform chain of molecular ions, each having one unpaired electron, [see Figure 1.8(a)] there is an electronic driving force for spin pairing, resulting in the dimerization of the molecular ions [see Figure 1.8(b)]. Each of these dimers has two electrons in the highest occupied orbital, implying that the conduction band is completely filled and resulting in an insulating state. This dimerization is known as the Peierls distortion,[26] the alternating regions of higher and lower charge density in the lattice constituting a charge density wave (CDW). For non-integral fractions of band-filling, as generally results from partial charge transfer, the CDW periodicity is not commensurate with the lattice periodicity, so that in theory it is free to translate to new positions, thus acting as a charge carrier. In practice however, ordering of the CDW's on different stacks

relative to each other can provide a mechanism for the Peierls instability to occur, resulting in a metal-to-insulator transition as observed in (TTF)(TCNQ) at 54 K.
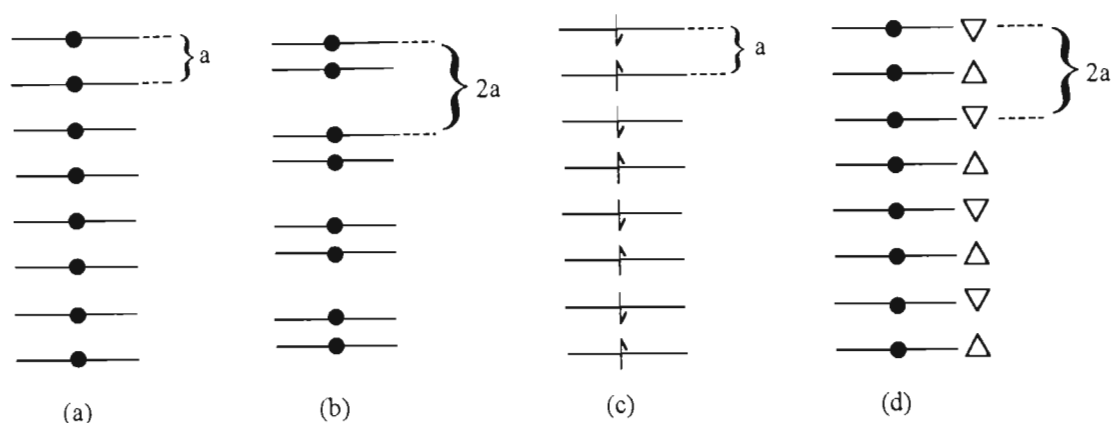
Figure 1.8: *Insulating distortions associated with charge transfer and*

radical ion salts:

(a)   Uniform chain of molecular ions

(b)   Peierls distortion

(c)   Spin density wave

(d)   Anion ordering

The Peierls distortion is most commonly associated with quasi one-dimensional materials. In contrast, the quasi two-dimensional charge transfer salts (see Section 1.5.4), are subject to metal-to-insulator transitions driven either by a spin density wave (SDW) or anion ordering.[144]

The electrons in a pseudo two-dimensional salt containing centrosymmetric anions (*e.g.* PF_6^-, AsF_6^-), become localized on their sites if the Coulombic repulsion between the electrons in the chains of molecular ions is greater than their interaction with the lattice. In this state, the electron spins are aligned antiferromagnetically (alternating spin up and down) resulting in an insulating magnetic state. Such an insulating state is referred to as being spin density wave driven [see Figure 1.8(c)].

Pseudo two-dimensional radical ion salts containing non-centrosymmetric, non-planar anions (*e.g.* ReO_4^-, ClO_4^-) often have these ions arranged in a random order in the crystal lattice at room temperature, *i.e.* the anions are crystallographically disordered. However, on lowering the temperature, the anions can re-orient giving rise to three-dimensional superstructures. Should the periodicity of such a superstructure match that of the electrons in the highest occupied levels in the band structure [see Figure 1.8(d)], an insulating state results. Such a metal-to-insulator transition is referred to as being driven by anion ordering. The above remarks do not imply however, that anion disorder is essential to the stabilization of electrical conductivity. In fact, anion disorder lowers electrical conductivity through electron scattering.

1.5.4 Pseudo two-dimensional charge transfer and radical ion salts

In one-dimensional charge transfer and radical ion salts there is no interaction between the chains of molecular ions constituting the salt. Pseudo two-dimensional salts differ from their one-dimensional analogues in that there are distinct interactions between the chains, thus giving rise to a configuration which can rather be described as "sheet-like" than "chain-like". The strength of the interchain relative to the intrachain interactions can vary from being weak, to situations where the structure is purely sheet-like with no evidence of any chain-like structure.

1.5.4.1 Selenium-based pseudo two-dimensional systems

The origin of pseudo two-dimensional charge transfer salts can be found in a study by Bechgaard,[145, 146] which concentrated on the synthesis of tetramethyltetraselenofulvalene (TMTSF) radical ion salts which do not contain planar organic molecular acceptor anions, but rather monovalent charge compensating anions such as PF_6^- or ClO_4^-.
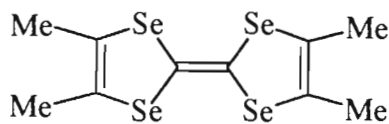
TMTSF

The $(TMTSF)_2X$ salts (X = ReO_4^-, PF_6^-, AsF_6^-, BF_4^-) exhibit high electrical conductivities ($\sigma_{R.T.} \approx 10^5$ S.cm^{-1}) with low temperature metal-to-insulator

transitions.[146] In an attempt to suppress the insulating transition, hydrostatic pressure was applied to $(TMTSF)_2PF_6$. This resulted in the sample becoming superconductive at temperatures less than $T_c \approx 0.9$ K; the first observation of superconductivity in an organic conductor.[145] Shortly after this discovery, ambient pressure superconductivity was observed in $(TMTSF)_2ClO_4$ $(T_c = 1.4$ K).[147, 148]

Investigations into the crystal structures of several of these compounds revealed that they are all iso-structural,[149-151] the nearly planar TMTSF molecules being arranged in a zigzag fashion in pseudo one-dimensional chains which run parallel to the direction of highest conductivity, the [a]-axis.[152] Pseudo two-dimensionality is introduced by an infinite "sheet network" of Se-Se interstack contacts,[149] the contact distances (3.9 to 4.0Å at room temperature) being comparable to the sum of the Van der Waal's radii for two Se atoms (3.9 to 4.0Å). The "sheets" are separated by the anions, thus preventing the formation of a three-dimensional structure. It is this "sheet network" that sustains the observed electrical conductivity. On lowering the temperature, the interstack, Se-Se distances decrease by nearly twice as much as the intrastack distances,[153, 154] leading to considerable increased interchain electronic delocalization through the Se-Se network.

Although the anions (X) play no direct role in the conductivity of the $(TMTSF)_2X$ systems, they indirectly influence it, in that the Se-Se network distances vary systematically with the anion size. The minimum average observed Se-Se interstack distance, d_{av}, is associated with the ambient pressure $(TMTSF)_2ClO_4$ superconductor. In the case of the incipient (applied pressure) superconductors (e.g. X = PF_6^-, ReO_4^-) d_{av} is less than d_{av} for the ambient pressure superconductors (X = ClO_4^-). From these observations and the isostructural nature of all of the $(TMTSF)_2X$ salts, it was concluded that on applying pressure to the incipient superconductors, their Se-Se networks contract until their geometries approximate that of $(TMTSF)_2ClO_4$, at which point they become superconducting.[154, 155]

A further feature concerning the anions in $(TMTSF)_2X$ involves that relating the nature of the low-temperature transitions to the anion symmetry and/or environment. As discussed above, the $(TMTSF)_2X$ salts $(X^- = PF_6^-, AsF_6^-, ReO_4^-, BF_4^-)$ exhibit low

temperature metal-to-insulator transitions. The driving forces for these transitions depend on the symmetry of the anion; for non-centrosymmetric anions (*e.g.* ReO_4^-, BF_4^-) the transition is driven by anion disorder, whilst for centrosymmetric anions (*e.g.* PF_6^-, AsF_6^-) it originates from a spin density wave. It has been found that for $(TMTSF)_2(AsF_6^-)$, an incipient superconductor, there are no short H-F separations between the disordered AsF_6^- anion and the H atoms of the TMTSF methyl groups.[156] This is in contrast to the ambient pressure superconductor, $(TMTSF)_2ClO_4$, where numerous short H-O contacts exist between the ClO_4^- anion and the methyl H atoms. These contacts have been suggested to result in a pinning of the ClO_4^- anion which is associated with a "sluggish" anion ordering at low temperatures. This anion ordering does not result in an increase in lattice periodicity and thus does not drive an insulating transition.[157] In fact, the ordering has been claimed to be a necessary prerequisite for superconductivity since it reduces electron scatter which results from crystallographic disorder.

1.5.4.2 Sulphur-based pseudo two-dimensional systems

The discovery of superconductivity in the $(TMTSF)_2X$ systems prompted research into analogous sulphur-based systems and in particular into salts derived from the donor molecule bis(ethylenedithio)-tetrathiafulvalene (abbreviated BEDT-TTF or ET, and depicted below). The selenium-based pseudo two-dimensional systems have since been overshadowed by the sulphur-based systems and currently most of the ambient pressure superconductors are sulphur-based.
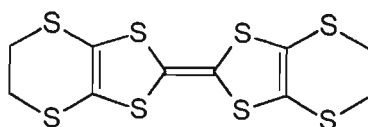
ET (BEDT-TTF)

Superconductivity in an ET salt, was first observed in $(ET)_2ReO_4$.[159] The salt behaves as an incipient superconductor with superconductivity occurring at temperatures below $T \approx 2$ K. The crystal structure of the isostructural $(ET)_2BrO_4$ salt[160] revealed that the ET moiety is decidedly non-planar. This, together with the large thermal vibration of

the peripheral ethylene bridges, impedes good π-overlap along a face-to-face stacking axis. Compared to the known $(TMTSF)_2X$ systems, the $(ET)_2X$ structures show little or no columnar stacking.[160, 161] The ET moieties are rather arranged side-by-side with short "interstack" S-S contact distances (3.3 to 3.7Å). However, as in the case of the $(TMTSF)_2X$ systems, these contacts give rise to a "corrugated sheet network" constituting the main conduction pathway.

The first sulphur-based pseudo two-dimensional material to display superconductivity at ambient pressure, was β-$(ET)_2I_3$[162] ($T_c \approx 1.5$ K). As established for $(ET)_2 BrO_4$, the crystal structure of β-$(ET)_2I_3$ consists of a two-dimensional "corrugated sheet network" of short "interstack" S-S contacts.[162] This network is sandwiched between sheets of linear I_3^- anions, the anions [analogous to those in $(TMTSF)_2X$] being completely surrounded by H atoms from the CH_2-groups on the ET molecules.[163] Furthermore, it was deduced that the S-S "interstack" contact distances can be systematically altered through changing the length of the anion. This led to the synthesis of β-$(ET)_2IBr_2$,[164] which is isostructural with β-$(ET)_2I_3$, but has shorter S-S "interstack" contact distances, due to the shorter linear anion used. This shortening of the S-S contacts manifests itself in an increase in the superconducting transition temperature; for β-$(ET)_2IBr_2$, $T_c \approx 2.5$ K.[165]

Interest in the pseudo two-dimensional sulphur-based systems has since moved away from β-$(ET)_2X$ salts to focus on the κ-phase. κ-Type packing does not comprise stacks or sheets of the ET donor molecules, instead the donor molecules exist as interacting dimers which are positioned approximately orthogonal to each other forming a conducting two-dimensional network of short S-S contacts. For the κ-phase it has also been found that T_c increases concomitantly with an increase in the length of the counterion. It is thus a common structural feature of the κ-$(ET)_2X$ salts with $T_c > 10K$ {e.g. κ-$(ET)_2 Cu[N(CN)_2]$ Br, $T_c = 11.6$ K}, to have the anions arranged in insulating V-shaped polymeric chains.[166]

1.5.4.3 Metal(dmit)₂-based systems

In the sulphur and selenium-based systems, two-dimensionality is introduced by short contact distances between atoms situated on a classical "donor-molecule". In contrast,

two-dimensionality in the M(dmit)$_2$ systems originates from "acceptor molecule"-based interactions.
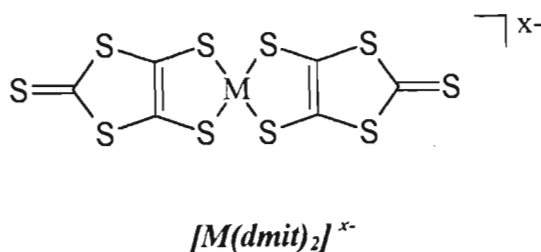
$[M(dmit)_2]^{x-}$

Interest in these systems as building blocks for low-dimensional systems are based on three features:

a)   The $[M(dmit)_2]^{x-}$ anion (depicted above) is nearly planar when the central metal atom has a square planar geometry. Thus, most studies involving $[M(dmit)_2]^{x-}$ are centred on the metals M = Ni(II), Pd(II) or Pt(II).

b) $[M(dmit)_2]^{x-}$ possesses ten peripheral sulphur atoms which can engage in intra- and interstack interactions.

c)   The redox properties of the molecule can be tuned by varying the central metal atom.

As might be expected, the cation involved in a $[M(dmit)_2]^{x-}$ salt plays a crucial part in determining the packing of the $[M(dmit)_2]^{x-}$ anions and thus on the physical properties of the salt. Based on the nature of the cation, the $[M(dmit)_2]^{x-}$ salts can thus be divided into 3 categories, viz.: salts of "open shell organic" (e.g. TTF), "closed shell organic" (e.g. tetraalkylammonium salts) and inorganic (e.g. Na$^+$, Cs^{2+}) cations. Superconductivity has been observed in the first two categories.

The "open shell organic" derivative TTF[Ni(dmit)$_2$]$_2$ was the first compound containing a metal complex anion to exhibit superconductivity (T$_c$ = 1.6 K at 7kbar).[167] The crystal structure consists of segregated stacks of TTF and [Ni(dmit)$_2$]$^{x-}$ moieties, with interstack S-S contact distances less than 3.70Å, observed between the TTF and [Ni(dmit)$_2$]$^{x-}$ and the [Ni(dmit)$_2$]$^{x-}$ stacks themselves.[168] Replacement of Ni by Pd affords α- and α'-TTF[Pd(dmit)$_2$]$_2$, both of which are isostructural with TTF[Ni(dmit)$_2$][169, 170] and exhibit superconductivity.[171] The Pt analogue behaves as a semiconductor and has the stoichiometry, TTF[Pt(dmit)$_2$]$_3$,[169] thus precluding direct

51

comparison with the Ni and Pd derivatives. In both TTF[Ni(dmit)$_2$]$_2$ and α- and α'-TTF[Pd(dmit)$_2$]$_2$ the partially oxidized TTF stacks, as well as the anion stacks contribute to the electrical conduction, thus rendering these materials two-chain conductors. It has also been established that the conduction pathway in all of the [M(dmit)$_2$]$^{x-}$ salts is essentially ligand-based. However, the nature of the metal atom plays an indirect but crucial part in determining the electronic band structure. This is evidenced by the fact that although TTF[Ni(dmit)$_2$]$_2$ and α'-TTF[Pd(dmit)$_2$]$_2$ are isostructural, T$_c$ for TTF[Ni(dmit)$_2$]$_2$ increases with increasing pressure, whereas for the Pd analogue, it decreases with pressure.[172, 173]

It has been found that in the case of the tetraalkylammonium salts, *i.e.* salts with "closed shell" organic cations, the size of the cations prevents the establishment of close inter-anion interactions for salts of large cations and simple stoichiometry. This results in the salts being semiconductors or insulators.[174] For non-stoichiometric compounds with low cation-to-anion ratios, strong inter-anion interactions are possible and do indeed occur, resulting in high electrical conductivities at room temperature. Salts for which this is true, include for example, (n-Bu$_4$N)$_{0.5}$[Pd(dmit)$_2$] (σ$_{R.T.}$ = 12 S.cm^{-1}) and (*n*-Bu$_4$N)$_{0.33}$[Pd(dmit)$_2$] (σ$_{R.T.}$ = 150 S.cm^{-1}).[175] In both of these compounds, the [Pd(dmit)$_2$]$^{x-}$ moieties occur as dimers which are arranged side-by-side to give rise to pseudo two-dimensional sheets, the S-S contact distances between the dimers being less than 3.7Å. The cations occur in layers between the "sheets".[175]

Logic dictates that for smaller "closed shell" cations, the establishment of close inter-anion interactions would be even more feasible. Somewhat unexpectedly, (Me$_4$N)[Ni(dmt)$_2$]$_2$ was the first salt composed of a "closed shell" spectator donor cation and a redox active metal complex anion, to exhibit a superconducting transition under pressure. The structure[176] consists of almost planar [Ni(dmt)$_2$]$^{x-}$ anions arranged face-to-face in columns extending along the [c]-axis. Within these stacks a slight dimerization is prevalent, giving rise to two different alternating interplanar distances (3.58 and 3.53Å). Along the [b]-axis the [Ni(dmt)$_2$]$^{x-}$ anions exist in a close side-by-side arrangement, thus allowing for S-S contact distances (3.49Å) which are shorter than the sum of their Van der Waal's radii. This radical ion salt has a room temperature conductivity in the ab-plane of σ$_{R.T.}$ = 60 S.cm^{-1}. The conductivity perpendicular to this

plane is 10^3 times smaller,[177] and is indicative of the intermolecular interstack S-S interactions constituting the major conduction pathway. On cooling of $(Me_4N)[Ni(dmt)_2]$ the metal-like conductivity persists to 100 K at which point a metal-to-semimetal transition occurs.[176] This transition is not driven by counterion ordering as would be expected for the non-centrosymmetric Me_4N^+ ion. Low temperature X-ray oscillation photography has in fact revealed that there is no change in the lattice periodicity associated with the transition, the low temperature crystal structure being essentially the same as that at room temperature.[178] The application of pressures in excess of 3 kbar results in the suppression of the metal-to-semimetal transition and at low temperatures (3.0 K at 3.2 kbar) a transition to a superconducting state is observed. Increasing the applied pressure results in an increase in the transition temperature, Tc (5.0 K at 7kbar).[177] The Pd analogue, $(Me_4N)[Pd(dmit)_2]_2$, has two polymorphic forms, α and β. Both have solid state structures similar to that of $(Me_4N)[Ni(dmt)_2]_2$ and room temperature conductivities, $\sigma_{R.T.}$ ~50 S.cm^{-1}. Similar to $(Me_4N)[Ni(dmt)_2]_2$, both the α and β forms exhibit a sharp increase in resistivity on cooling to 100K, but on application of pressure the Pd salts undergo a transition to metallic and not superconducting behaviour. [177, 179]

Based on the premise that small size counterions should allow strong inter-anion interactions, the $[Ni(dmt)_2]^{x-}$ salts with small Group I and Group II cations were studied. The salts have, however, been found to be difficult to prepare and generally crystals were not of sufficient quality to allow detailed investigations. Of note, however, is $Na[Ni(dmt)_2]_2$ which has a room temperature conductivity $\sigma_{R.T.}$ ~100 S.cm^{-1}. On cooling, the salt retains its metallic conductivity to a temperature of 2 mK at ambient pressure, with no evidence of a Peierls transition. The application of external pressure at low temperatures results in an increase in conductivity, however no transition to superconducting behaviour is observed.[174]

1.5.4.4 Systems based on DCNQI acceptor molecules

As indicated earlier, (see section 1.5.2), the TCNQ molecule distorts from its planar configuration on extensive substitution on the quinone ring. In order to overcome this problem a new class of acceptor molecules, the N,N'-Dicyanoquinonediimines

53

(DCNQI's)[180, 181], of which the 2,5-dimethyl derivative is depicted below, has been developed.
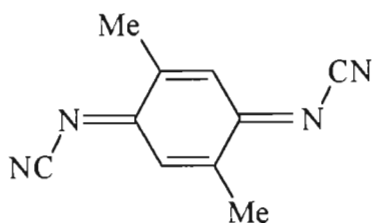
2,5-Me₂-DCNQI

Interest in the DCNQI molecules as acceptors for charge transfer salts centres around the following:

a)   Structure: The =NCN group is flexible and sterically less demanding
                        that the =C(CN)$_2$ group so that planarity of the DCNQI
                        system is retained even upon tetrasubstitution.[182]

b)   Synthesis: DCNQI's are produced in good yields in a one-pot
                        synthesis from the corresponding benzoquinones.[181]

c)   Redox properties: The acceptor strength of DCNQI is similar to that of
                        TCNQ and can be finely tuned by appropriate
                        substitution.[183]

A variety of DCNQI salts have been characterized with π-donors (*e.g.* TTF), organic cations (*e.g.* tetramethylammonium) and metal cations. The first two classes are pseudo one-dimensional materials and only brief attention will be paid to them before discussing the higher dimensional salts derived from metal cations.

A range of charge transfer complexes have been obtained through the interaction of various substituted DCNQI's with the π-donor molecules TTF and TMTSF. Many of these show powder conductivities, $\sigma \sim 0.1$ S.cm^{-1}, which has been interpreted as indicating segregated stacking of donor and acceptor molecules.[184] Segregated stacking has been confirmed for (TTF)(H$_4$-DCNQI).2H$_2$O,[185] which has a room temperature conductivity $\sigma_{R.T.} = 10$ S.cm^{-1}. In contrast to the analogous TCNQ salt (TTF)(TCNQ), where the temperature dependence of the conductivity points to

54

metallic behaviour, $(TTF)(H_4\text{-}DCNQI).2H_2O$ behaves as a metal-like semiconductor.[186]

The compound $(Me_4N)(2,5\text{-}Cl_2\text{-}DCNQI)$ represents one example of a DCNQI radical anion salt containing an organic cation. The salts consists of radical anions arranged equidistant from each other in zigzag stacks which produces channels in which the cations occur.[187] At room temperature the salt has a conductivity of 10^{-2} S.cm^{-1} which decreases with decreasing temperature until a suspected Peierls transition occurs at 17 K. [187]

Radical anion salts of DCNQI metal cations can be represented by the empirical formula $(2\text{-}X\text{-}5\text{-}Y\text{-}DCNQI)_2M$ (where for M = Cu,[188-193] X/Y on DCNQI = CH_3/CH_3. CH_3O/CH_3O, CH_3/Cl, CH_3/Br, CH_3/I, Cl/Cl, Br/Br, Cl/Br; for M = Ag,[190, 194] X/Y = CH_3/CH_3. CH_3/Cl, CH_3/Br, CH_3/I, and for M = Li,[190, 195] Na[190] and K,[190] X/Y = CH_3/CH_3). All of these salts crystallize in the space group I4/a,[190] the metal ions being stacked like a string of pearls and each one being surrounded by a number of DCNQI radicals which are associated with the metal through the N atom of the -C≡N group. Comparison of the sum of the Van der Waal's radii of the nitrogen atom and the metal ion with the metal to N atom distance, reveals that for the alkali metal salts, the metal to nitrogen atom interaction is mainly Coulombic in nature, whereas for the Cu and Ag salts strong orbital interactions are implied.[194] The number of DCNQI molecules associated with the metal ion varies; for Cu, Ag and Li the number of associated DCNQI molecules (n) = 4, for Na, n = 6 and for K, n = 8.[191] Furthermore, each of the two -C≡N groups of the DCNQI molecule is associated with a metal ion, thus resulting in a regular network of alternating metal ions and DCNQI radicals. Within this network, the DCNQI radicals occur in stacks with the exocyclic C=N bond on one radical interacting with the ring of its closest neighbour. The resulting ring-over-exocyclic-double-bond network presents a pathway for electrical conduction to occur along the DCNQI stacks, the metal-metal distance in the metal cation stacks [~3.8Å in $(2,5\text{-}Me_2\text{-}DCNQI)_2$ Cu[188]] being too large to allow for any conductivity.

Based on their conductivities the $(2\text{-}X\text{-}5\text{-}Y\text{-}DCNQI)_2M$ salts are divided into two groups; the copper and non-copper complexes. All of the non-copper DCNQI salts

behave as one-dimensional metal-like semiconductors, the conductivity of the lithium salt (2,5-Me$_2$-DCNQI)$_2$Li, matching that of the silver salts listed above.[194] In contrast to these, the copper salt (2,5-Me$_2$-DCNQI)$_2$Cu, has a room temperature conductivity, $\sigma_{R.T.} \sim 1000$ S.cm^{-1} which steadily increases upon cooling to 1.3 K without any metal-to-insulating or -semiconducting transition. At 3.5 K, $\sigma = 5 \times 10^5$ S.cm^{-1}. This conductivity is pseudo three-dimensional with a value of ~100 S.cm^{-1} perpendicular to the stacking axis, the N-Cu-N bridges providing a channel for conduction in this direction.[196] Similar conductivity behaviour has been noted for (2,5-Me-5-I-DCNQI)$_2$Cu[192] and [2,5-(MeO)$_2$-DCNQI]$_2$Cu.[191] However, the 2,5-Cl$_2$; 2,5-Br$_2$, and 2-Cl-5-Br derivatives undergo phase transitions to become semiconducting at low temperatures.

A further development in this field of study involves the synthesis of binary alloys of the DCNQI radical anion salts, *i.e.* compounds of formula [(2-W-5-X-DCNQI)$_m$(2-Y-5-Z-DCNQI)$_n$]$_2$Cu.[197] As an example, alloying (2-Br-5-Me-DCNQI)$_2$Cu (showing a phase transition at low temperatures) with (2-I-5-Me-DCNQI)$_2$Cu (no phase transition) results in an alloy with only a weak phase transition in the temperature range 90 to 20 K. Further cooling results in an apparent cancellation of this weak transition with a conductivity of ~600 S.cm^{-1} being reached as the temperature approaches 4 K.

Some salts, *e.g.* [2.5-(MeO)$_2$-DCNQI]$_2$Cu, do not exhibit a low temperature metal-to-insulator transition, whereas others *e.g.* (2.5-Cl$_2$-DCNQI)$_2$Cu, do. Initially this difference was thought to be dependent on the size of the substituents, X and Y, on the DCNQI molecule.[198] The occurrence of a low temperature metal-to-insulator transition in the temperature dependent conductivity behaviour of (2,5-X$_2$-DCNQI)$_2$Cu (X = Cl, Br) was attributed to the presence of small substituents on the DCNQI molecules, whereas the absence of such a transition in the conductivity behaviour of *e.g.* [2,5-(OMe)$_2$-DCNQI]$_2$Cu was suggested to be a direct consequence of the presence of the large OMe-substituents on the DCNQI molecules. This model however can not explain why certain systems, *e.g.* (2.5-Me$_2$-DCNQI)$_2$Cu, where the Van der Waal's volume of the methyl group is substantially smaller than that of Br, does not exhibit a low temperature metal-to-insulator transition. Subsequent studies[199] into the

effect of substituting the methyl protons of $[2,5\text{-}Me_2\text{-}DCNQI]_2Cu$ with deuterium, and the influence of such a substitution on the occurrence of low temperature phase transitions, revealed that the steric size of the DCNQI substituents do indeed play a crucial part in determining whether or not these low temperature transitions occur. The steric influence appears to be indirect, occurring as a consequence of a tetragonal distortion of the tetrahedral geometry around the Cu ion, the extent of the distortion reflected by the N-Cu-N coordination angle, α_{co}. For small distortions of α_{co} the interaction between the Cu 3d orbitals and the DCNQI LUMO band is still close to the "optimal" situation both in terms of relative energy and geometrical overlap. This interaction is an essential prerequisite for electrical conduction perpendicular to the stacking axis and along the N-Cu-N bridges. Furthermore, the conduction pathway along the stacking axis is coupled with that perpendicular to the axis, thus introducing pseudo three-dimensionality and a stabilization of the metallic conductivity against low temperature insulating distortions. For large distortions of α_{co}, the interaction of the Cu 3d orbitals with the DCNQI LUMO band is diminished, manifesting itself in a breakdown of the conduction pathway perpendicular to the stacking axis. As a result, there is no stabilization of the conduction pathway along the stacking axis, rendering it prone to low temperature metal-to-insulator transitions.

CHAPTER TWO

Charge transfer salts of the dinuclear metallocene donor complex [Fe₂Cp₂ˉ(CO)₂(μ-SEt)₂] and the electron acceptor molecules Tetracyanoquinodimethane (TCNQ), Tetracyanoethylene (TCNE) and the Dicyanoquinonediimines (DCNQI's)

2.1 Introduction

In attempts to synthesize novel molecular based charge transfer salts exhibiting high electrical conductivity, comparable to or exceeding the conductivity of (TTF)(TCNQ) (see Section 1.5), the electron acceptor molecules TCNX (X = Q or E) and various substituted DCNQI's were not only reacted with a range of electron rich organic molecules, but also with a host of electron rich organometallic molecules. The seminal work in this regard involves the synthesis of [Fe^{III}Cp$_2$*](TCNQ) (Cp* = C$_5$Me$_5$) which was found to possess magnetic properties which are substantially different from that normally associated with ferrocinium salts. This discovery by J.S. Miller and co-workers sparked interest into a totally new area of research, namely the development of molecular based bulk ferromagnetic materials.

2.2 Aims of this work

A consideration of [Fe^{III}Cp$_2$*](TCNQ) and other examples of metallocene based charged transfer salts which exhibit unusual magnetic properties, reveals that all metallocene based molecules employed to date, are mononuclear. It was thus deemed appropriate to utilize a dinuclear metallocene based donor molecule in reactions with the polycyano acceptor molecules and to study the effect such a perturbation would have on the magnetic properties of the resulting charge transfer salts. The donor molecule selected in this context was the electron-rich dinuclear sulphido bridged molecule, [Fe$_2$Cp$_2$*(CO)$_2$(μ-SEt)$_2$].

[Fe$_2$Cp$_2$*(CO)$_2$(μ-SEt)$_2$] when compared to $e.g.$ [FeCp$_2$*] is not only dinuclear, but also possesses two bridging thio-ethyl ligands. Consequently, the steric requirements of the [Fe$_2$Cp$_2$*(CO)$_2$(μ-SEt)$_2$] molecule is dramatically different to that of [FeCp$_2$*]. This

difference can be expected to manifest itself in the solid state structures and physical properties of any charge transfer salts derived from [Fe$_2$Cp$_2$*(CO)$_2$(μ-SEt)$_2$].

The aims of this work thus included the following:

i) The synthesis and characterization of [Fe$_2$Cp$_2$*(CO)$_2$(μ-SEt)$_2$] and the charge transfer salts resulting from its reactions with polycyano electron acceptor molecules.

ii) The determination of the solid state structures of the parent donor molecule and its charge transfer salts.

iii) The investigation of the magnetic properties of these compounds.

iv) The reconciliation of the observed bulk physical properties of these materials with their solid state structures.

With the object of putting the results obtained in this study in context, a brief introduction to molecular based magnetism, outlining some of the fundamental theoretical considerations, is provided next. This is followed by a short discussion of relevant results as found in the literature. No effort is made at attempting to be comprehensive in this regard, instead only results illustrating fundamental principles associated with molecular based magnetism are discussed. The final section will consist of a report and discussion of the results obtained in the study of the donor molecule [Fe$_2$Cp$_2$*(CO)$_2$(μ-SEt)$_2$] and the charge transfer salts resulting from its reactions with TCNX (X = Q or E) and various substituted DCNQI's.

2.3 Background

2.3.1 Fundamental theoretical considerations

Bulk magnetic behaviour arises from the intrinsic spin of electrons and how the spins on adjacent molecules or atoms constituting a material are coupled (aligned). Materials possessing no unpaired electron spin density are diamagnetic. Should a material possess unpaired electron spin density, but the spins are not aligned, the material behaves as a very weak magnet and is referred to as being paramagnetic (see Figure 2.1). Spins which are aligned antiparallel to each other can cancel completely, known as antiferromagnetic coupling, or result in a reduced magnetic moment, known as ferrimagnetic behaviour. In

rare cases the unpaired electron spins may align parallel to each other, resulting in a net magnetic moment. Such behaviour is termed ferromagnetism. In order for a material to exhibit bulk ferromagnetic behaviour, this coupling should not be restricted to isolated domains, but should extend in all directions in the solid.

(a)   (b)

(c)   (d)
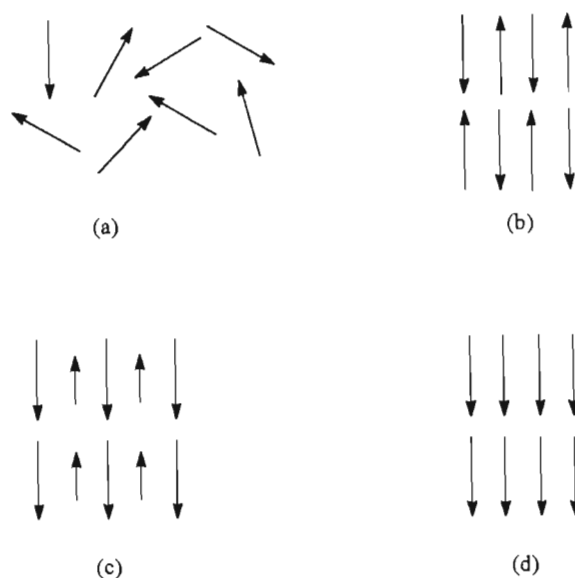
Figure 2.1:   *Electron spin alignment and magnetic behaviour*

(a) Paramagnetic

(b) Antiferromagnetic

(c) Ferrimagnetic

(d) Ferromagnetic

In conventional bulk ferromagnetic materials *e.g.* CrO_2 or γ-Fe_2O_3, unpaired electrons involved in spin-spin coupling reside in metal atom or metal ion-based d-orbitals and couple with each other *via* direct bonds that extend in all three dimensions. In contrast, the organometallic charge transfer salts utilizing organic acceptor molecules (*e.g.* TCNQ), rely on the coupling of spins which are both d-orbital based (from the organometallic constituent) and p-orbital based (the organic acceptor molecule). Furthermore, the charge transfer salts considered here, with possibly the exception of $[V(TCNE)_x].y(CH_2Cl_2)$, do not possess the three dimensional network of direct bonds found in conventional bulk ferromagnetic materials.

A crucial part of the study of molecular based magnetism thus involves ascertaining whether the unpaired electron spins on the molecular units are coupled or not, and if so,

what mode of coupling is operative. This involves studying the material's response to an applied magnetic field. On exposing a material possessing unpaired electron spins to such an applied field, a magnetic moment is induced in the solid. For ideal noninteracting spins the induced magnetic moment, M, is proportional to the applied field strength, H, the proportionality constant χ, being the molar magnetic susceptibility.

$$M = \chi H$$

The molar magnetic susceptibility, in turn varies with temperature, the temperature dependence being chararcterized by the Curie expression:

$$\chi = C.T^{-1}$$

C is the Curie constant associated with the number of unpaired spins per radical in the material. The above relationship applies to materials possessing noninteracting unpaired electron spins. Ferromagnetic (or antiferromagnetic) coupling results in the spins experiencing an effective parallel (or antiparallel) exchange field which increases (or decreases) the measured susceptibility with respect to that predicted from the Curie law for independent spins. In such cases, the high temperature (T > 50 K) susceptibility data can often be fitted to the Curie-Weiss law;

$$\chi = C.(T - \theta)^{-1}$$

where for ferromagnetic (or antiferromagnetic) coupling the Weiss constant, θ, is greater than (or less than) zero. The Weiss-constant, θ, is thus used as an indicator of whether no coupling, ferromagnetic or antiferromagnetic cooperative interactions are operative between the unpaired electron spins of the material.

A critical temperature, below which the interacting unpaired spins of a material order on a microscopic level, exists. If the ordering is such that the spins are aligned parallel to each other (ferromagnetic coupling), a macroscopic spontaneous magnetization results, even if no field is applied, *i.e.* H = 0. In this case the critical temperature is also known as the Curie temperature, T_C. For a material showing such spontaneous magnetization to be commercially useful, the Curie temperature needs to exceed room temperature, as is observed for CrO_2 (T_C = 387 K) and γ-Fe_2O_3 (T_C = 816 K). If in contrast to ferromagnetic

coupling, the material's unpaired electrons undergo a spontaneous antiferromagnetic ordering, no net macroscopic moment results and the critical temperature is referred to as the Néel temperature, T_N.

2.3.2 Molecular based magnetic materials; selected examples from the literature

Molecular based materials exhibiting novel magnetic behaviour will be discussed under the following three headings:

i)   Metallocene based charge transfer salts

ii) $[V(TCNE)_x].y(CH_2Cl_2)$

iii)   Metalloporphyrin based materials

Although there are distinct differences between the materials under the three different headings, they are all interrelated, the metalloporphyrin based materials having evolved from $[V(TCNE)_x].y(CH_2Cl_2)$ which in turn originated from the metallocene based charge transfer salts.

2.3.2.1 Metallocene based charge transfer salts

In an attempt to obtain TCNQ-based sublimable conducting charge transfer salts, Miller and co-workers reacted decamethylferrocene $[FeCp_2^{\bullet}]$ with TCNQ.[200] The reaction was found to afford three different products of varying stoichiometry,[201] with the relative yields being dependent on the reaction conditions. Of these products, the kinetic phase of the 1:1 charge transfer salt $[FeCp_2^{\bullet}](TCNQ)$, crystallizes with one-dimensional integrated stacks of donor and acceptor anions, i.e. ...$D^+A^-D^+A^-$... The magnetic behaviour of this salt obeys the Curie-Weiss law, with $\theta = +3$ K.[202] At temperatures below 2.55 K, $[FeCp_2^{\bullet}](TCNQ)$ behaves as a metamagnet, i.e. the nature of the spin coupling of the unpaired electrons changes between ferromagnetic and antiferromagnetic, depending on the strength of the applied magnetic field, H. In this case, at temperatures below 2.55 K and at field strengths less than 1500 Oe, antiferromagnetic behaviour is observed. Increasing the applied field strength to above 1500 Oe, results in the spin coupling changing to being ferromagnetic.

Based on the supposition that a radical anion smaller than TCNQ would have a greater spin density which could lead to increased spin-spin interactions, $[FeCp_2^{\bullet}](TCNE)$ was synthesized.[203] This salt possesses the same ...$D^+A^-D^+A^-$... motif as $[FeCp_2^{\bullet}](TCNQ)$, its

magnetic behaviour obeying the Curie-Weiss law at temperatures above 60 K. The unpaired electron spins are ferromagnetically coupled, as indicated by the Weiss constant, $\theta = +30$ K. At temperatures below 4.8 K the salt displays the onset of spontaneous magnetization in zero applied field, *i.e.* bulk ferromagnetism is observed.

The results obtained with $[FeCp_2^*](TCNQ)$ and $[FeCp_2^*](TCNE)$ paved the way for the synthesis of new molecular based ferromagnetic materials. With the goal of identifying the combination of steric and electronic features which would stabilize ferromagnetic coupling as well as bulk ferromagnetic behaviour in the metallocene based charge transfer salts, the properties of a variety of these materials were studied. The three variable entities associated with these salts are:

i)   The nature of the acceptor molecule

ii)   The substituents on the metallocene cyclopentadienyl rings

iii)   The metal in the metallocene donor molecule.

One of the first modifications was the replacement of the Me-groups on $[FeCp_2^*]$ with H-atoms. However, ferrocene $[FeCp_2]$ (Cp = C_5H_5), is more difficult to oxidize than $[FeCp_2^*]$,[204] resulting in no electron transfer occurring when it is reacted with TCNE. Nevertheless, the product obtained, $[FeCp_2](TCNE)$, has the same structural motif [205] as that associated with the $[FeCp_2^*]$ analogue, yet it is diamagnetic, since neither $[FeCp_2]^0$ or $(TCNE)^0$ possess unpaired electron spin density.

Subsequent studies [203] centred on charge transfer salts where the salt comprises either a radical donor ion in combination with a spinless acceptor ion *e.g.* $[FeCp_2^*][C_3(CN)_5]$, or *vice versa* as found in $[CoCp_2^*](TCNE)$.
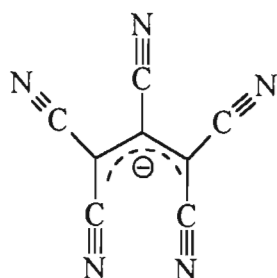
[C₃(CN)₅]⁻ (Pentacyanopropenide)

63

The crystal structure of [FeCp$_2$*][C$_3$(CN)$_5$] consists of integrated stacks of the radical [FeCp$_2$*]$^+$ ion and the spinless [C$_3$(CN)$_5$]$^-$ ion, *i.e.* ...D$^{.+}$A$^-$D$^{.+}$A$^-$... The structure of [CoCp$_2$*](TCNE) has not been reported, however both of these salts exhibit only very weak Curie-Weiss behaviour {θ = -1.2 ± 0.4 K for [FeCp$_2$*][C$_3$(CN)$_5$] and θ = -1.0 ± 0.3 K for [CoCp$_2$*](TCNE)}[203] This is indicative of negligible, if any, cooperative behaviour (spin coupling), thus suggesting that in order to stabilize ferromagnetic coupling and ultimately bulk ferromagnetic behaviour, it is essential that each of the donor and acceptor ions must have unpaired electron spin density, S ≥ ½. This situation can only be achieved if complete charge transfer occurs between the diamagnetic donor and acceptor molecules. At this point it is also interesting to note the contrast between this requirement of complete charge transfer to stabilize bulk ferromagnetic behaviour and that of partial charge transfer (see Section 1.5.2) required for high electrical conductivity to occur in charge transfer salts.

Ferrocene is not oxidized by the TCNE, but reaction with the stronger acceptor 7,7,8,8-tetracyanoperfluoro-p-quinodimethane, TCNQF$_4$,[206] results in the formation of two products [FeCp$_2$*](TCNQF$_4$) and [FeCp$_2$]$_2$(TCNQF$_4$)$_3$. The crystal structure of the 1:1 charge transfer salt consists of segregated one-dimensional chains of S = ½ radical donor and acceptor ions which contrasts with the integrated ...D$^{.+}$A$^-$D$^{.+}$A$^-$... structure observed in [FeCp$_2$*](TCNE). The magnetic properties of [FeCp$_2$](TCNQF$_4$) provide no evidence for ferromagnetic coupling. In fact, the magnetic susceptibility is weakly antiferromagnetic (θ ~ -3 K). A further result which highlights the relationship between the solid state packing motif and the magnetic properties of the metallocene based charge transfer salts, involves the bis(dithiolato)metalate salts of decamethylferrocene, and in particular [FeCp$_2$*][M{S$_2$C$_2$(CF$_3$)$_2$}$_2$] (M = Ni and Pt).
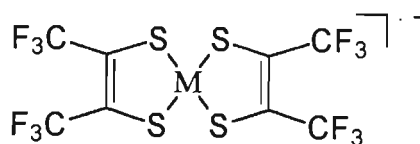
The bis(dithiolate) radical anion [M{S$_2$C$_2$(CF$_3$)$_2$}$_2$]$^-$

The crystal structures of both [FeCp$_2$*][Ni{S$_2$C$_2$(CF$_3$)$_2$}$_2$][207] and [FeCp$_2$*][Pt{S$_2$C$_2$(CF$_3$)$_2$}$_2$][208] consist of stacks of alternating [FeCp$_2$*]$^+$ and [M{S$_2$C$_2$(CF$_3$)$_2$}$_2$]$^-$ radical ions; however, the ...D$^{.+}$A$^-$D$^{.+}$A$^-$... chains in the Pt-containing

salt are strictly linear, whereas the chains in the Ni-analogue exhibits a distinct zig-zag or wavelike nature, resulting in a greater Fe-Fe separation in the Ni-analogue (11.19Å) compared to that observed in the Pt-analogue (10.94Å). The magnetic susceptibilities of both salts approximate to Curie-Weiss behaviour, but differ between the two compounds in that the magnetic coupling in the Pt-analogue (θ = +27 K) is greater than that of the Ni containing salt (θ = +15 K). This difference in ferromagnetic interaction is believed to be the consequence of weaker intrachain coupling in the Ni-analogue as a direct result of the wavelike nature of the ...$D^+A^-D^+A^-$... chains. These results support the necessity of a solid state packing motif consisting of strictly linear integrated ...$D^+A^-D^+A^-$... chains for achieving significant ferromagnetic coupling and ultimately, bulk ferromagnetic behaviour. Again it is interesting to note that the prerequisite for ferromagnetic coupling, *i.e.* integrated stacking, is the exact opposite to that which is required for high electrical conductivity to be observed, *i.e.* segregated stacking (see Section 1.5.2).

A comparison of the magnetic behaviour of [FeCp$_2^*$](TCNQ) (metamagnetic) with that of [FeCp$_2^*$](TCNE) (bulk ferromagnetism below 4.8 K) seems to suggest that ferromagnetic coupling and bulk ferromagnetic behaviour tends to be more associated with charge transfer salts possessing higher spin densities. Further support for this suggestion is obtained by consideration of the ferrocinium(dithiolato)metalate salts [FeCp$_2^*$][M$\{S_2C_2(CN)_2\}_2$] (M = Ni and Pt).

The crystal structure of [FeCp$_2^*$][Ni$\{S_2C_2(CN)_2\}_2$] comprises isolated $D^+(A_2)^{2-}D^+$ dimers and the salt shows no cooperative spin interactions (θ = 0 K).[207] The Pt-analogue, in contrast, crystallizes in two phases, both of which have one dimensional ...$D^+A^-D^+A^-$... strands in one direction and $D^+(A_2)^{2-}D^+$ dimer units in the other direction.[207] The magnetic behaviour of both phases can be described by the Curie-Weiss law, with Weiss-constants (θ = +6.6 K for the α-phase and θ = +9.8 K for the β-phase) intermediate between that of [FeCp$_2^*$][Ni$\{S_2C_2(CN)_2\}_2$], possessing isolated $D^+(A_2)^{2-}D^+$ dimers, and *e.g.* the trifluoro analogue [FeCp$_2^*$][Pt$\{S_2C_2(CF_3)_2\}_2$] possessing ...$D^+A^-D^+A^-$... chains. The reduced Weiss-constants for α- and β-[FeCp$_2^*$][Pt$\{S_2C_2(CN)_2\}_2$], when compared to [FeCp$_2^*$][Pt$\{S_2C_2(CF_3)_2\}_2$], would seem to be a direct consequence of the presence of $D^+(A_2)^{2-}D^+$ dimer units in the crystal lattice. The occurrence of these dimers result in two-thirds of the anions in the [FeCp$_2^*$][Pt$\{S_2C_2(CN)_2\}_2$] lattice existing as diamagnetic, S = 0,

$(A_2)^{2-}$ units, thus reducing the overall unpaired spin density. The suggestion that higher unpaired electron spin density on the constituent donor and acceptor ions of a charge transfer salt could enhance ferromagnetic coupling and bulk ferromagnetic behaviour, is further supported by a study [209] centred on $[MnCp_2^*](TCNQ)$. $[MnCp_2^*]$ was selected as the donor molecule since its cationic form, $[MnCp_2^*]^{+}$, has an unpaired spin density, $S = 1$. Furthermore, the absence of the element Fe removed the possibility of any contribution to the observed magnetism of the charge transfer salt from ferromagnetic metallic iron which might result form decomposition. (Metallic Mn is antiferromagnetic.) The reaction of $[MnCp_2^*]$ with TCNQ involves a complete electron transfer from $[MnCp_2^*]$ to TCNQ. The crystal structure of the salt consists of the integrated $...D^{+}A^{-}D^{+}A^{-}...$ stacks and is isomorphous with the structure reported for $[FeCp_2^*](TCNE)$. [203] The magnetic susceptibility of $[MnCp_2^*](TCNQ)$ can be described by the Curie-Weiss law, the Weiss-constant ($\theta = +10.5 \pm 0.5$ K) being indicative of ferromagnetic spin interactions. Bulk ferromagnetic behaviour was observed at temperatures less than 6.2 ± 0.1 K.

A further prerequisite for the stabilization of bulk ferromagnetic behaviour involves that the required $...D^{+}A^{-}D^{+}A^{-}...$ chains exist as extended chains in the crystal lattice as compared to being of finite length. The importance of this prerequisite is aptly illustrated by a study in which spinless $S = 0$ $[CoCp_2^*]^{+}$ cations were randomly substituted for the $S = \frac{1}{2}$ $[FeCp_2^*]^{+}$ cation in the $[FeCp_2^*](TCNE)$ structure. [210] This resulted in the formation of random finite $...D^{+}A^{-}D^{+}A^{-}...$ chains existing in the crystal lattice, which manifested itself in a dramatic reduction of the Curie Temperature, T_C, with increasing $[CoCp_2^*]^{+}$ content (T_C for $[FeCp_2^*]_x[CoCp_2^*]_{1-x}(TCNE)$: For $x = 1$, $T_C = 4.8$ K; $x = 0.925$, $T_C = 2.75$ K and $x = 0.85$, $T_C = 0.75$ K).

From the above discussion it is clear that in order to stabilize ferromagnetic coupling and bulk ferromagnetic behaviour in a metallocene based charge transfer salt, the solid state structure of the salt has to comprise extended integrated $...D^{+}A^{-}D^{+}A^{-}...$ stacks of donor and acceptor ions. Furthermore, the charge transfer between the donor and acceptor molecules has to be complete. These two conditions are necessary prerequisites for ferromagnetic coupling. However, they do not guarantee that such coupling will occur in the charge transfer salt.

2.3.2.2 [V(TCNE)$_x$].y(CH$_2$Cl$_2$)

The discovery of bulk ferromagnetic behaviour in [MnCp$_2$*](TCNQ), together with the fact that [V^I(C$_6$H$_6$)$_2$]$^+$ like [Mn^{III}Cp$_2$*]$^+$ is a S = 1 cation with ^{3}E$_{2g}$ ground state, led researchers to expect that the charge transfer salt of [V(C$_6$H$_6$)$_2$] and TCNE would also exhibit bulk ferromagnetism. However, the reaction of [V(C$_6$H$_6$)$_2$] with excess TCNE in dichloromethane, did not result in the expected charge transfer salt. Instead an insoluble, black product of empirical composition [V(TCNE)$_x$].y(CH$_2$Cl$_2$) (x ~ 2; y ~ 0.5) was isolated. [211, 212] The product is believed to result from an electron transfer from [V(C$_6$H$_6$)$_2$] to TCNE followed by loss of the benzene ligands, according to the infrared spectroscopic evidence. On the basis of the IR spectral data it was also suggested that the final product, [V(TCNE)$_x$].y(CH$_2$Cl$_2$), contains reduced TCNE with some of its nitrogen atoms coordinated to the vanadium. However, the exact oxidation state of the vanadium and TCNE is still unknown.

[V(TCNE)$_x$].y(CH$_2$Cl$_2$) behaves as a ferromagnet at room temperature and is strongly attracted to a permanent magnet, making it the first example of a molecular or organic-based material exhibiting ferromagnetic behaviour at room temperature. The Curie temperature, T$_C$, exceeds 350 K at which point the material undergoes thermal decomposition. Attempts directed at determining T$_C$ *via* indirect methods, lead to an estimated T$_C$ value of *ca.* 400K.

Based on infrared spectroscopic data, X-ray diffraction studies and the extreme insolubility of [V(TCNE)$_x$].y(CH$_2$Cl$_2$), the compound is believed to comprise vanadium centres, each coordinated by up to six nitrogen atoms from different TCNE moieties. Furthermore, each TCNE molecule can coordinate up to four different vanadium centres through σ N-bonds, thereby enabling the construction of a three-dimensional network which could support the strong three-dimensional spin-spin coupling necessary for a Curie temperature of *ca.* 400K to occur.

[V(TCNE)$_x$].y(solvent) has also been prepared with a variety of S = 0 solvents *e.g.* THF, CH$_3$CN, diethylether and hexane, replacing CH$_2$Cl$_2$.[208] The magnetic properties of the resulting products were found to vary dramatically with the choice of solvent, T$_C$ systematically decreasing with increasing ability of the solvent to coordinate to the

vanadium centre. Several explanations attempting to rationalize the differences in magnetic behaviour with variation of the occluded solvent molecule have been proposed. These include:

i)   Coordinated solvent molecules reduce the number of nearest neighbour spins surrounding the vanadium centre.

ii)   The connectiveness between the vanadium centres and thus the dimensionality of the magnetic state is reduced, since a coordinating solvent molecule can displace a multicoordinating TCNE ion.

iii) Coordinated solvent molecules can affect the degree of crystalline order around each vanadium centre, leading to random anisotropy and random exchange.

Attempts to prepare magnetic materials from the reaction of $[V^0(C_5H_5)(C_7H_7)]$ or $[V^{II}(C_5H_5)_2]$ with TCNE, or $[V(C_6H_6)_2]$ with other acceptor molecules, e.g. TCNQF$_4$, $C_4(CN)_6$, 2,3,5,6-tetrachlorobenzoquinone and 2,3,5,6-tetracyanobenzoquine, afforded insoluble materials of unknown composition. None of these products exhibit bulk ferromagnetic behaviour. In fact, their magnetic behaviour typically is in accordance with that predicted by the Curie-Weiss law with $\theta \sim -1$ K, characteristic of weak antiferromagnetic coupling.

2.3.2.3 Metalloporphyrin based materials

The metalloporphyrin based materials and in particular [Mn(tpp)](TCNE).2(toluene) (tpp = meso-tetraphenylporphine), [Mn(oep)](TCNE) (oep = octaethylporphine) and [Mn(oep)]-[C$_4$(CN)$_6$], represent the third structural class of molecular magnets.

The crystal structure of [Mn(tpp)](TCNE).2(toluene)[213] consists of parallel one-dimensional ...[D]$^{\cdot+}$[A]$^{\cdot-}$[D]$^{\cdot+}$[A]$^{\cdot-}$... chains in which the TCNE$^{\cdot}$ moieties are coordinated to two [Mn(tpp)]$^+$ fragments in a trans-μ_2-N-σ-bound manner. This solid state motif is distinctly different from that observed in the metallocene based materials where the TCNE$^{\cdot}$ radical anion is not coordinated to the metal atom. It does however parallel the proposed structural arrangement in $[V(TCNE)_x].y(CH_2Cl_2)$, which is believed to contain TCNE$^{\cdot}$ moieties coordinated to the vanadium centres. The magnetic susceptibility of [Mn(tpp)](TCNE).2(toluene) is in accordance with Curie-Weiss behaviour with a Weiss-

constant θ of +61 K. Evidence for bulk ferromagnetic behaviour was observed at 5 K and the Curie temperature, T_C, was estimated to be 18 K.

The magnetic behaviour of the analogous [Mn(oep)](TCNE) salt can also be described by the Curie-Weiss law, however it exhibits only weak ferromagnetic coupling ($\theta = + 7$ K) and no evidence for bulk ferromagnetic behaviour was observed. The difference in the magnetic properties of [Mn(tpp)](TCNE).2(toluene) and [Mn(oep)](TCNE) stems from a difference in their solid state structures. Whereas both materials possess parallel one dimensional ...[D]$^{.+}$[A]$^-$[D]$^{.+}$[A]$^-$... chains, the spacing between the metalloporphyrin fragments in [Mn(tpp)](TCNE).2(toluene) is uniform. In contrast, the one-dimensional chains in [Mn(oep)](TCNE) have a dimeric nature with two alternating distances between the metalloporphyrin fragments constituting a chain. Furthermore, the interactions between the π^* orbital on TCNE$^-$ and the Mn^{III} centres is not uniform over all the Mn^{III} centres in [Mn(oep)](TCNE).

In contrast to [Mn(oep)](TCNE), [Mn(oep)][C$_4$(CN)$_6$][214] possesses uniform one dimensional chains with uniform spin couplings with the Mn^{III} centres. Accompanying these features is a Weiss-constant, θ, of +67 K.

Considering the results presented above, it would appear that uniformity in the one-dimensional integrated chains in the metalloporphyrin based materials, is an important contributing factor to the achievement of long-range magnetic order.

2.4 Results and Discussion

2.4.1 Preliminary studies utilizing [Fe$_2$Cp$_2$(CO)$_2$(μ-SEt)$_2$] as the dinuclear donor molecule

The dinuclear molecule [Fe$_2$Cp$_2$(CO)$_2$(μ-SEt)$_2$] forms a part of a series of mercapto-bridged iron compounds which can be represented as [Fe$_2$Cp$_2$(CO)$_2$(μ-SR)$_2$] (R = alkyl or aryl). The first report on a compound of this type, [Fe$_2$Cp$_2$(CO)$_2$(μ-SMe)$_2$], was published in 1961[215] with subsequent reports[216,217] describing the synthesis of several other compounds of the series. Of note is a report by Dessy and co-workers describing the electrochemical oxidation of [Fe$_2$Cp$_2$(CO)$_2$(μ-SMe)$_2$] to afford the mono-cationic

derivative $[Fe_2Cp_2(CO)_2(\mu\text{-}SMe)_2]^{+.(218)}$ It was subsequently discovered that the oxidation of $[Fe_2Cp_2(CO)_2(\mu\text{-}SMe)_2],^{(219)}$ and in fact a large number of the other members of the $[Fe_2Cp_2(CO)_2(\mu\text{-}SR)_2]$ series,$^{(220)}$ can be affected chemically through the use of iodine, silver salts and even oxygen in acidic media. The magnetic susceptibilities of a number of the oxidized products, *e.g.* $[Fe_2Cp_2(CO)_2(\mu\text{-}SEt)_2](BPh_4)$, were measured at room temperature,$^{(220)}$ and found to correspond to one unpaired electron per $[Fe_2Cp_2(CO)_2(\mu\text{-}SR)_2]^+$ cation, *i.e.* a $S = \frac{1}{2}$ system. However, all the compounds containing $[Fe_2Cp_2(CO)_2(\mu\text{-}SR)_2]^+$, studied to date, include a closed shell ($S = 0$) anion in combination with the cation.

Based on these literature results, it was deemed appropriate to utilize $[Fe_2Cp_2(CO)_2(\mu\text{-}SEt)_2]$ as the dinuclear donor molecule in attempts to study the effect of a dinuclear (versus mononuclear) donor molecule on the magnetic properties of charge transfer salts resulting from its reactions with polycyano acceptor molecules. As will be discussed in section 2.4.3.2, the one-electron oxidation of bridged dinuclear complexes containing a M_2X_2 moiety (M = Fe, X = μ-SEt in this case) involves the removal of an electron populating a molecular orbital involving both Fe-atoms. This is in contrast to the mononuclear metallocene donor molecules where oxidation involves electrons populating orbitals originating from a single Fe-atom. However, a preliminary study on the reaction between $[Fe_2Cp_2(CO)_2(\mu\text{-}SEt)_2]$ and 2,5-Me$_2$-DCNQI revealed that the product tends to disproportionate to the starting materials, indicating that 2,5-Me$_2$-DCNQI is not a strong enough electron acceptor molecule to fully oxidize $[Fe_2Cp_2(CO)_2(\mu\text{-}SEt)_2]$ to $[Fe_2Cp_2(CO)_2(\mu\text{-}SEt)_2]^+$.

This was confirmed by cyclic voltammetric studies on the donor and acceptor molecules. The first half-wave potential of the acceptor 2,5-Me$_2$-DCNQI, E_{1A}, *i.e.* the potential corresponding to the half-reaction 2,5-Me$_2$-DCNQI + e$^-$ → (2,5-Me$_2$-DCNQI)$^-$, occurs at +0.008 V (see Table 2.1). On the other hand, the first half-wave potential, E_{1D}, associated with the $[Fe_2Cp_2(CO)_2(\mu\text{-}SEt)_2]/[Fe_2Cp_2(CO)_2(\mu\text{-}SEt)_2]^+$ couple, occurs at -0.07 V, giving a difference in potentials ($|E_{1A} - E_{1D}|$ using Wheland's notation$^{(140)}$) equal to 0.15 V. This value lies within the range of $|E_{1A} - E_{1D}| \leq 0.25$ V$^{(140)}$, associated with charge transfer

salts for which the electron transfer between the donor and acceptor molecules is not complete.

Table 2.1 Redox potentials of selected donor and acceptor molecules

Compound	E_1 (V)		E_2 (V)	
	This Study	Literature	This Study	Literature
$[Fe_2Cp_2(CO)_2(\mu\text{-SEt})_2]$	-0.07	-0.42[220]	Irreversable	-
$[Fe_2Cp_2{}^*(CO)_2(\mu\text{-SEt})_2]$	-0.27	-	+0.47	-
2,5-Me$_2$-DCNQI	+0.08	+0.21[225]	-0.51	-0.38[225]
2,5-Cl$_2$-DCNQI	+0.42	+0.65[225]	-0.26	0.00[225]
2-Cl-5-Me-DCNQI	+0.22	+0.43[225]	-0.41	-0.20[225]
2-Me-DCNQI	+0.12	+0.31[225]	-0.55	-0.31[225]
H$_4$-DCNQI	+0.14	+0.39[225]	-0.49	-0.25[225]
TCNQ	+0.14	+0.39[225]	-0.44	-0.28[225]
TCNE	+0.21	+0.15[234]	-0.85	-0.57[234]

In an attempt to overcome this problem, $[Fe_2Cp_2(CO)_2(\mu\text{-SEt})_2]$ was reacted with 2,5-Cl$_2$-DCNQI, a much stronger electron acceptor molecule than its 2,5-dimethyl analogue; E_{1A} for 2,5-Cl$_2$-DCNQI equals + 0.42 V. However, the product afforded by this reaction was found to be prone to decomposition, thus complicating any further studies of its properties or structure. The reason for the observed instability of $[Fe_2Cp_2(CO)_2(\mu\text{-SEt})_2](2,5\text{-Cl}_2\text{-}$DCNQI) could be attributed to a variety of factors. Firstly, the cyclic voltammogram of $[Fe_2Cp_2(CO)_2(\mu\text{-SEt})_2]$, dissolved in CH_2Cl_2, revealed that the second oxidation wave, corresponding to the $[Fe_2Cp_2(CO)_2(\mu\text{-SEt})_2]^+/[Fe_2Cp_2(CO)_2(\mu\text{-SEt})_2]^{2+}$ couple, is irreversible. A similar observation has been made [220] for the cyclic voltammogram recorded in 1,2-dimethoxyethane where a broad peak was observed for this oxidation as a result of coating of the electrode. Furthermore, the potentials E_{1A} and E_{2A} for the reduction waves of 2,5-Cl$_2$-DCNQI are such that there is partial overlap, albeit very little, of the first reduction wave of the acceptor with the second irreversible oxidation wave of $[Fe_2Cp_2(CO)_2(\mu\text{-SEt})_2]$ and of the second reduction wave of 2,5-Cl$_2$-DCNQI with the first oxidation wave of $[Fe_2Cp_2(CO)_2(\mu\text{-SEt})_2]$. This implies that the product obtained from the

reaction of $[Fe_2Cp_2(CO)_2(\mu\text{-}SEt)_2]$ with 2,5-Cl_2-DCNQI could contain small amounts of the di-ionic $[Fe_2Cp_2(CO)_2(\mu\text{-}SEt)_2]^{2+}$ and $[2,5\text{-}Cl_2\text{-}DCNQI]^{2-}$ species. Dicationic species of the type $[Fe_2Cp_2(CO)_2(\mu\text{-}SR)_2]^{2+}$ (R = Me, Ph, ^nBu for instance) have been reported as consitituent ions of the $[Fe_2Cp_2(CO)_2(\mu\text{-}SR)_2](PF_6)_2$ salts.[220] The report detailing the synthesis and properties of these salts, did not make mention of any unusual instability of the dicationic $[Fe_2Cp_2(CO)_2(\mu\text{-}SR)_2]^{2+}$ moieties or of its PF_6^- salts.

On the other hand, no reports of any stable charge transfer salts involving dianionic dicyanoquinonediimine moieties have been found. Thus it is possible that the instability of the product resulting from the reaction of $[Fe_2Cp_2(CO)_2(\mu\text{-}SEt)_2]$ with 2,5-Cl_2-DCNQI originates from the decomposition of small amounts of the $[2,5\text{-}Cl_2\text{-}DCNQI]^{2-}$ anion (present as a by-product) which catalyses a chain reaction leading to further decomposition of the product. Apart from this possibility, other metallocene based charge transfer salts of the dicyanoquinonediimines, where the possibility of forming the dianionic acceptor species does not exist, have been found and have been reported to be unstable. Further discussion of this instability is provided in section 2.4.6.1.

Considering the fact that the transition-metal decamethylmetallocenes are more readily oxidized than their corresponding metallocene analogues and that methyl substitution on the cyclopentadienyl ring seem to impart some stability to the decamethylmetallocinium ions[204], it was thus decided to utilize the electron-rich decamethyl derivative $[Fe_2Cp_2^*(CO)_2(\mu\text{-}SEt)_2]$, rather than $[Fe_2Cp_2(CO)_2(\mu\text{-}SEt)_2]$ as the donor molecule in electron transfer reactions with TCNQ, TCNE and substituted DCNQI's. The preparation of the decamethyl derivative has not been described previously and its synthesis and characterization is discussed in the following sections.

2.4.2 $[Fe_2Cp_2^*(CO)_2(\mu\text{-}SEt)_2]$ (1)

2.4.2.1 Synthesis and spectroscopic studies on $[Fe_2Cp_2^*(CO)_2(\mu\text{-}SEt)_2]$ (1)

The synthesis of the pentamethyl cyclopentadienyl derivative $[Fe_2Cp_2^*(CO)_2(\mu\text{-}SEt)_2]$ was based on the procedure for the preparation of its cyclopentadienyl analogue, $[Fe_2Cp_2(CO)_2(\mu\text{-}SEt)_2]^{[221]}$ with some modifications. Treatment of the di-carbonyl bridged dimer $[Fe_2Cp_2^*(CO)_4]^{[222]}$ with an excess of the dialkyl disulphide, Et_2S_2, in toluene under

reflux, afforded [Fe$_2$Cp$_2^*$(CO)$_2$(μ-SEt)$_2$] in high yield. The product was isolated by removing the solvent *in vacuo* and extracting the residue with petroleum ether, followed by a crystallization from petroleum ether. Elemental analysis for C and H were consistent with the formulation of the brown-black crystalline material as being [Fe$_2$Cp$_2^*$(CO)$_2$(μ-SEt)$_2$].

The spectroscopic data for [Fe$_2$Cp$_2^*$(CO)$_2$(μ-SEt)$_2$] are presented in Tables 2.2 and 2.3.

The ^{1}H-NMR spectrum of **1**, recorded at room temperature in C$_6$D$_6$, exhibits a single peak corresponding to the methyl protons of the Cp* ligands and the expected pattern of a triplet and quartet assigned to the ethyl groups of the bridging SEt ligands (see Table 2.2). This implies that the chemical environment of the two ethyl groups, and similarly of the two Cp* ligands, is identical and thus that, in solution, the [Fe$_2$Cp$_2^*$(CO)$_2$(μ-SEt)$_2$] molecule is symmetrical about a two-fold axis or a centre of inversion. Cis-trans isomerism is known to occur in [Fe$_2$Cp$_2$(CO)$_2$(μ-SEt)$_2$][221]. However, since the ^{1}H-NMR spectrum of **1** exhibits only a single singlet, triplet and quartet, with no evidence for splitting of these resonances, it follows that only one isomer, either *cis* or *trans*-[Fe$_2$Cp$_2^*$(CO)$_2$(μ-SEt)$_2$] is present in solution, or that if both are present, rapid interconversion between the two isomers occurs.

Table 2.2. *^{1}H-NMR Data for [Fe$_2$Cp$_2^*$(CO)$_2$(μ-SEt)$_2$] (**1**)*

Functional group / ligand	Chemical Shift (δ)[a]	Splitting Pattern
-CH$_2$CH$_3$	2.32	Quartet
-CH$_2$CH$_3$	1.16	Triplet
C$_5$(CH$_3$)$_5$	1.79	Singlet

[a] Relative to tetramethylsilane

The infrared spectrum of **1** measured in cyclohexane exhibits two peaks in the C-O stretching region, a strong peak at 1931 cm^{-1} and a weak peak at 1902 cm^{-1} (see Table 2.3). This pattern (strong, weak) presents an exact match to that of the cis isomer of the cyclopentadienyl derivative [Fe$_2$Cp$_2$(CO)$_2$(μ-SEt)$_2$] and is in marked contrast to the

Table 2.3 *Infrared Spectroscopic Data*[a]

Compound	Wavenumbers and Recording Medium		
	CH_2Cl_2	Cyclohexane	KBr
$[Fe_2Cp_2(CO)_2(\mu\text{-}SEt)_2]$	1944(s), 1909(w,sh)	1954(s), 1928(m)	1948(s), 1930(ms), 1894(w)
$[Fe_2Cp_2*(CO)_2(\mu\text{-}SEt)_2]$ (**1**)	1916(s), 1890(w,sh)	1931(s), 1902(w)	1918(s), 1892(m), 1886(m), 1854(w)
$[Fe_2Cp_2*(CO)_2(\mu\text{-}SEt)_2](2,5\text{-}Me_2\text{-}DCNQI)$ (**2**)	2120(m), 2092(m), 1983(s), 1946(w)	insoluble	2120(ms), 2092(ms), 1967(s), 1926(ms)
$[Fe_2Cp_2*(CO)_2(\mu\text{-}SEt)_2](2\text{-}Cl\text{-}5\text{-}Me\text{-}DCNQI)$ (**3**)	2127(m), 2120(m), 2110(m), 1984(s), 1949(mw)	insoluble	2122(m), 2108(m), 1967(s), 1936(m)
$[Fe_2Cp_2*(CO)_2(\mu\text{-}SEt)_2](2\text{-}Me\text{-}DCNQI)$ (**4**)	2128(mw), 2104(m), 1983(s), 1946(mw)	insoluble	2120(m), 2096(m), 1967(s), 1930(ms)
$[Fe_2Cp_2*(CO)_2(\mu\text{-}SEt)_2](H_4\text{-}DCNQI)$ (**5**)	2164(w), 2124(mw), 2098(m), 1984(s), 1947(mw)	insoluble	2160(w),2124(mw), 2092(m), 1978(s), 1946(ms)
$[Fe_2Cp_2*(CO)_2(\mu\text{-}SEt)_2](TCNQ)$ (**6**)	2182(s), 2154(w), 1984(ms), 1949(w)	insoluble	2178(s), 2156(mw), 1978(ms), 1941(ms)
$[Fe_2Cp_2*(CO)_2(\mu\text{-}SEt)_2](TCNE)$ (**7**)	2187(w), 2147(m), 1983(s), 1947(mw)	insoluble	2188(mw), 2148(m), 1978(s), 1946(s)

[a] Wavenumbers quoted in cm^{-1},

Key: sh = shoulder, s = strong, ms = medium to strong, m = medium, mw = medium to weak, w = weak

74

medium, strong pattern reported for the trans isomer of [Fe$_2$Cp$_2$(CO)$_2$(μ-SEt)$_2$] (see Table 2.4). The infrared spectrum of **1** recorded in CH$_2$Cl$_2$ exhibits essentially the same pattern as that recorded in cyclohexane with a strong peak at 1916 cm^{-1} and a weak shoulder at 1890 cm^{-1}. The solid state spectrum, recorded as a KBr-pellet also exhibits one strong peak at 1918 cm^{-1} with weaker peaks at 1892, 1886, and 1856 cm^{-1}.

From the solution infrared spectra, in conjunction with the NMR evidence, it would thus appear that the [Fe$_2$Cp$_2^*$(CO)$_2$(μ-SEt)$_2$] molecule is present as the cis isomer in solution. A crystal structure determination (see section 2.4.2.2) revealed that only the cis isomer is present in the solid state.

Table 2.4. *Infrared spectroscopic data - Literature results (frequencies quoted in cm^{-1}).*

Compound	Wavenumbers and Recording Medium		Reference
	CH$_2$Cl$_2$	Cyclohexane	
cis-[Fe$_2$Cp$_2$(CO)$_2$(μ-SEt)$_2$]	-	1955(s), 1926(w)	221
trans-[Fe$_2$Cp$_2$(CO)$_2$(μ-SEt)$_2$]	-	1944(ms), 1931(s)	221
cis-[Fe$_2$Cp$_2$(CO)$_2$(μ-SEt)$_2$](SbF$_6$)	2012(s), 1990(m)	-	220

A comparison of the infrared spectra of [Fe$_2$Cp$_2^*$(CO)$_2$(μ-SEt)$_2$] and [Fe$_2$Cp$_2$(CO)$_2$(μ-SEt)$_2$] recorded in CH$_2$Cl$_2$ reveals a shift of 28 cm^{-1} towards lower wavenumbers in going from the cyclopentadienyl to the pentamethylcyclopentadienyl analogue. This is in accordance with theoretical considerations which suggest that since methyl substitution on the cyclopentadienyl ring increases the electron density on the iron centres, the wavenumber of the C-O stretching peaks should decrease as a result of the increased back donation of electron density into the antibonding orbitals of the carbonyl ligands.

Further confirmation for this increased electron density on the iron centres, was obtained from cyclic voltammetric studies. The cyclic voltammogram of **1** consists of 2 reversible one electron oxidation waves, the half-wave potential, E$_{1D}$, corresponding to the [Fe$_2$Cp$_2^*$(CO)$_2$(μ-SEt)$_2$]/[Fe$_2$Cp$_2^*$(CO)$_2$(μ-SEt)$_2$]$^+$ couple occurring at -0.29 V (see Table 2.1). This potential is 0.20 V cathodic with respect to that associated with the corresponding couple for the cyclopentadienyl analogue, thus reflecting the increased

electron density on the $[Fe_2Cp_2^*(CO)_2(\mu\text{-}SEt)_2]$ molecule as brought about by the methyl substituents on the Cp^* ligands. It is also important to note that the difference in the first half-wave potentials ($|E_{1A} - E_{1D}|$) for the combination **1** and 2,5-Me$_2$-DCNQI is 0.35 V. This value is substantially larger than the minimum value of 0.25 V[140] required for complete electron transfer between the donor and acceptor molecule. This is in marked contrast to the cyclopentadienyl analogue, where only partial charge transfer occurred when it was reacted with 2,5-Me$_2$-DCNQI, and again highlights the increased electron density on **1** originating from the methyl substituents on the Cp^* ligands.

2.4.2.2 Structural studies on $[Fe_2Cp_2^*(CO)_2(\mu\text{-}SEt)_2]$ (**1**)

Single crystals of **1** were grown by slow cooling of a saturated petroleum ether solution of the compound and an X-ray diffraction study conducted.

$[Fe_2Cp_2^*(CO)_2(\mu\text{-}SEt)_2]$ was found to crystallize in the monoclinic space group *C2/c* with four molecules per unit cell. The unit cell dimensions, a full list of internuclear distances and angles and other crystallographic data may be found in Tables 2.10 to 2.14 at the end of this chapter.

The structure of $[Fe_2Cp_2^*(CO)_2(\mu\text{-}SEt)_2]$ comprises two crystallographically identical FeCp*(CO) moieties which are linked to each other by the two bridging mercapto-ligands (see Figure 2.2). The two halves of the molecule are related by a crystallographically imposed two-fold rotation axis which passes through the centre of the Fe$_2$S$_2$ rhomboid. This implies that, contrary to what would be expected from purely steric considerations, the bulky Cp* ligands are arranged in a cis configuration with respect to the Fe-Fe vector. Similarly, the two carbonyl groups occur in a cis configuration. Furthermore, as a consequence of the two-fold symmetry, the S-C bonds of the ethyl-mercapto ligands are arranged in a syn-configuration with respect to the S-S vector, but the C-C bonds of the ethyl moiety define an anti-arrangement with respect to this vector. As such the molecular structure of $[Fe_2Cp_2^*(CO)_2(\mu\text{-}SEt)_2]$ is closely related to that reported for the phenyl-mercapto bridged, cyclopentadienyl analogue, $[Fe_2Cp_2(CO)_2(\mu\text{-}SPh)_2]$.[223]

The Fe$_2$S$_2$ rhomboid in $[Fe_2Cp_2^*(CO)_2(\mu\text{-}SEt)_2]$, like that in the $[Fe_2Cp_2(CO)_2(\mu\text{-}SPh)_2]$ molecule, is slightly puckered, the dihedral angle between the two planes defined by the two bridging S-atoms and one Fe-atom being 162.4(3)°. The Fe-Fe distance in
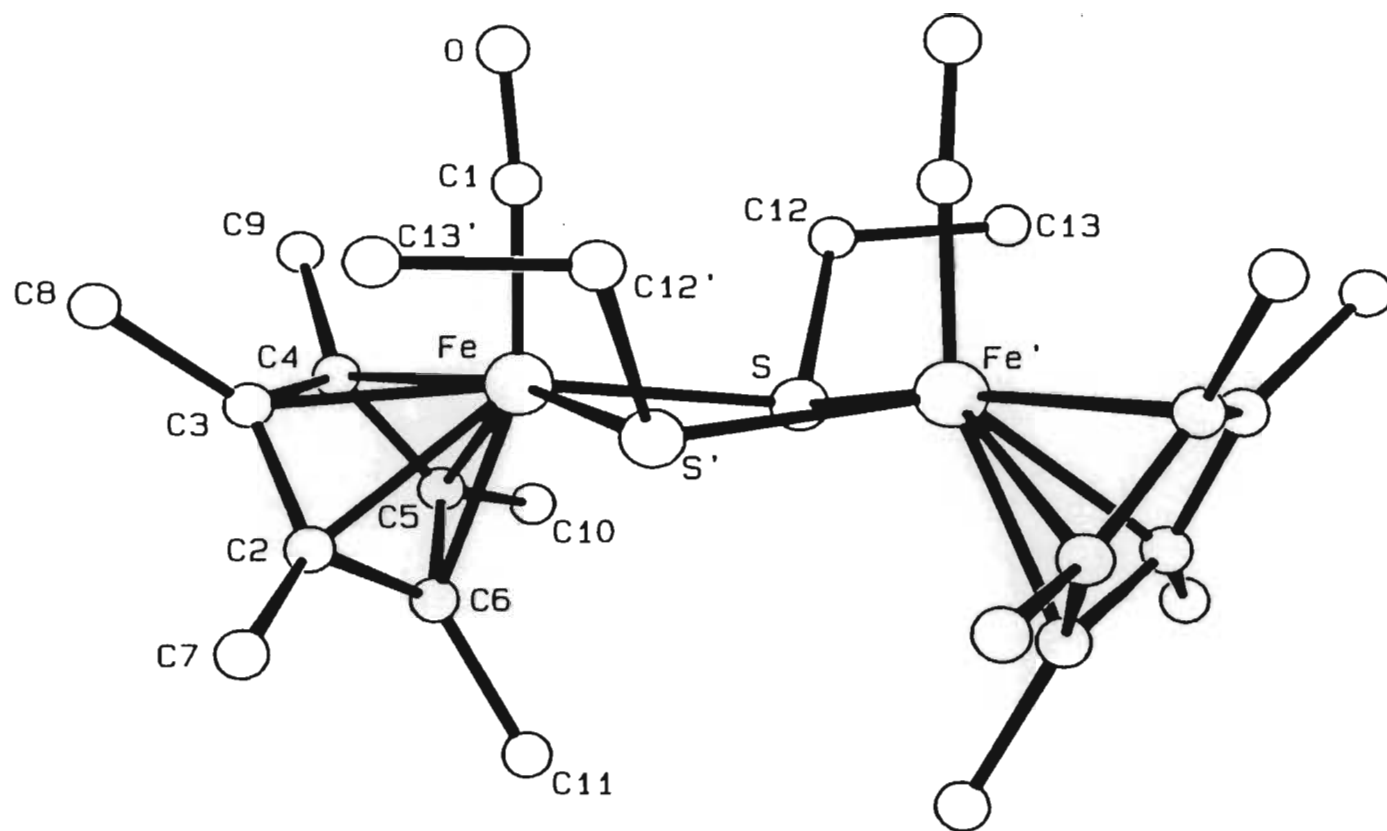
Figure 2.2 *The molecular structure of the neutral molecule [Fe₂Cp₂*(CO)₂(μ-SEt)₂] (**1**).*

$[Fe_2Cp_2^*(CO)_2(\mu\text{-}SEt)_2]$ is 3.444(1)Å, which is slightly longer than that of 3.39Å reported for the phenyl-mercapto bridged cyclopentadienyl analogue. This distance is consistent with no bonding interaction between the Fe atoms as predicted by a simple electron-count, *i.e.* a closed-shell electron configuration is achieved for each Fe atom, without the necessity of any Fe-Fe bonding interaction.

The Fe-S distances in **1** are 2.278(1) and 2.276(1)Å with the Fe-S-Fe and S-Fe-S angles being 98.3(1)° and 80.1(1)°, respectively. These values are in good agreement with that of 2.262(6)Å, 98° and 81° respectively, as observed in the structure of $[Fe_2Cp_2^*(CO)_2(\mu\text{-}SPh)_2]$.[223] The Fe-C distance (C of Cp^* ligand) in **1** range between 2.084(6) and 2.125(5)Å and average 2.103Å. This distance is slightly longer than the Fe-C distance of 2.050(2)Å observed in $[FeCp_2^*]$.[224]

As was discussed in Section 2.3.2.1, the mode of packing associated with the metallocene based charge transfer salts have a profound influence on the magnetic properties of the compound. In order to gain some insight into possible intermolecular interactions which might be present in crystals of $[Fe_2Cp_2^*(CO)_2(\mu\text{-}SEt)_2]$ and which might also have an influence on the packing of charge transfer compounds resulting from its reactions with polycyano acceptor molecules, the molecular packing of the compound was studied. Although the molecular structure of $[Fe_2Cp_2(CO)_2(\mu\text{-}SPh)_2]$ has been reported,[223] its molecular packing was not discussed.

A view of the unit cell contents of $[Fe_2Cp_2^*(CO)_2(\mu\text{-}SEt)_2]$ as projected on the ac-plane (see Figure 2.3), reveals that the molecules occur in ordered rows or stacks which are at an angle of *ca.* 50° with the [c]-axis. Isolating one of these "rows" and adding analogous "rows" produced by a unit cell translation in both the positive and negative direction along the [b]-axis, produces Figure 2.4. This diagram reveals that the $[Fe_2Cp_2^*(CO)_2(\mu\text{-}SEt)_2]$ molecules within each of the rows pack in such a way that the Cp^* ligands of adjacent molecules are arranged "face-to-face".

The planes defined by two neighbouring Cp^* ligands participating in this arrangement are exactly parallel to each other, this being enforced by the fact that each $[Fe_2Cp_2^*(CO)_2(\mu\text{-}SEt)_2]$ molecule is related to its closest neighbour within the row through a crystallographic centre of inversion situated midway between the two Cp^* ligands under discussion.

78
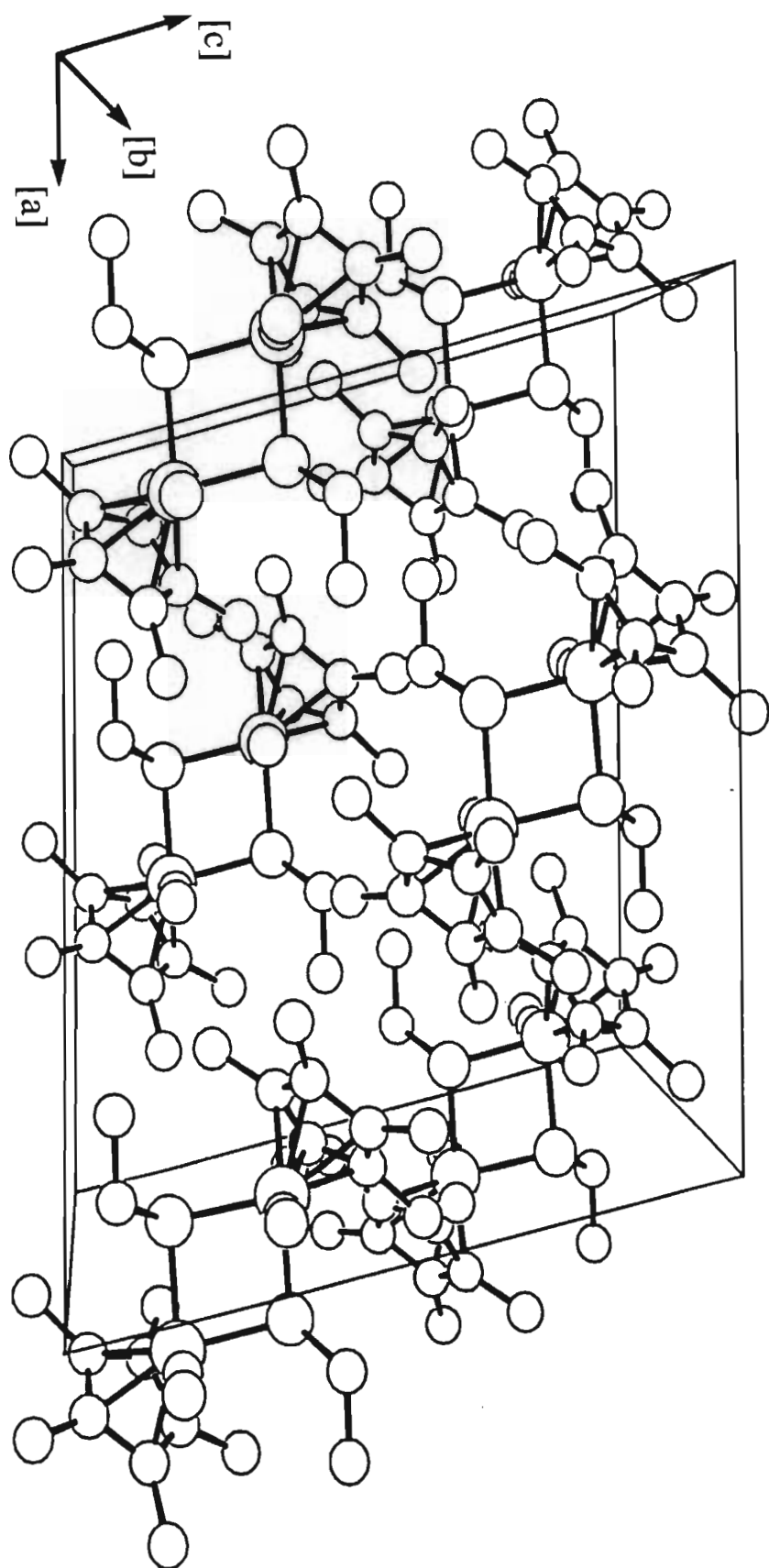
Figure 2.3   A view of the unit cell contents of [Fe₂Cp₂*(CO)₂(μ-SEt)₂] (**1**) as seen in a projection onto the ac-plane.
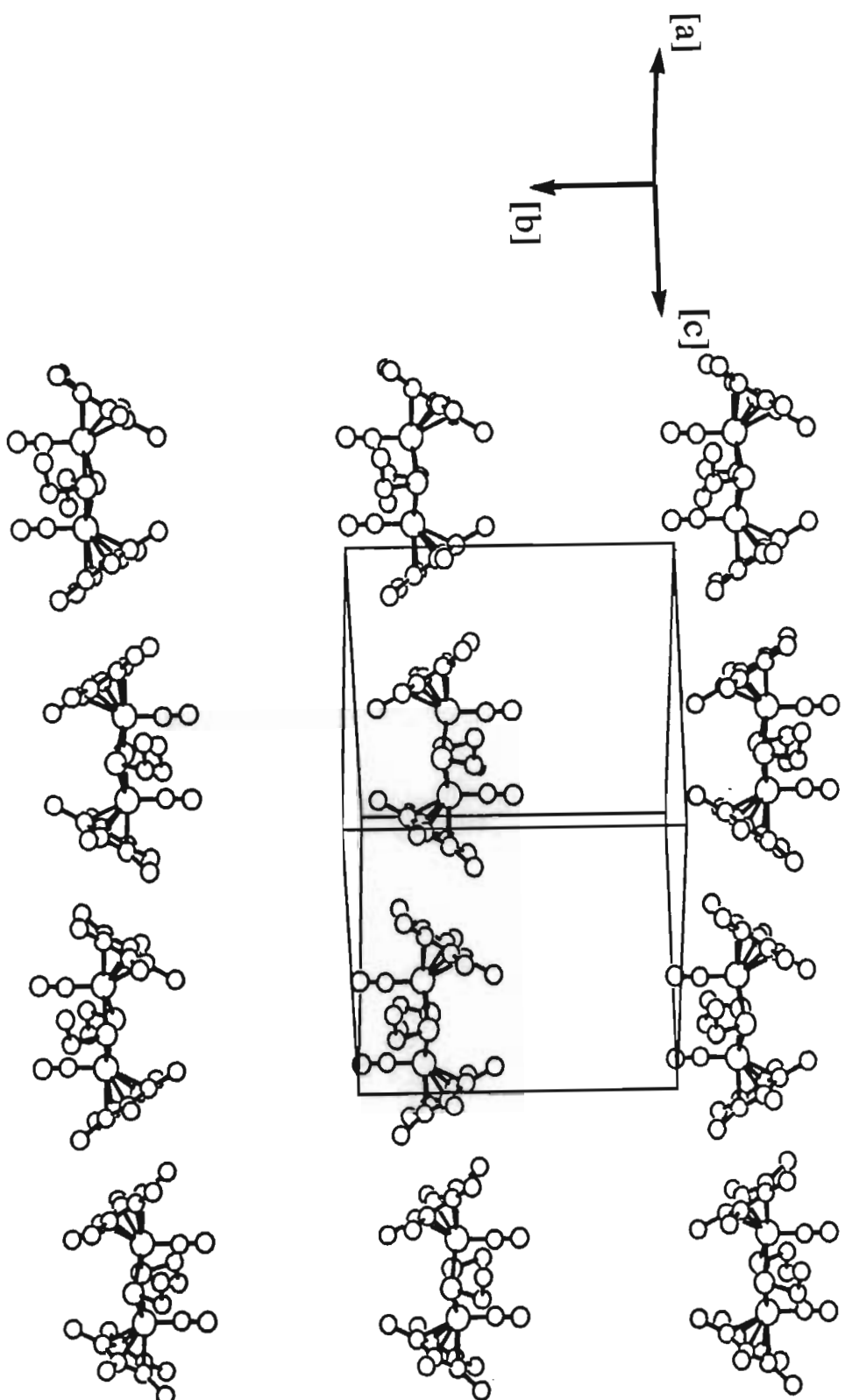
Figure 2.4   The arrangement of the neutral molecules in "rows" in the crystal lattice of [Fe$_2$Cp$_2$*(CO)$_2$(μ-SEt)$_2$] (**1**).

The interplanar distance between the planes defined by the C atoms of two Cp* ligands in such a "face-to-face" pair, is 3.65Å. This, together with the fact that there is some delocalized π-electron density associated with Cp* ligands, could be taken to suggest some π-π interaction between every pair of adjacent Cp* ligands. However, the distance between the centroids of the ligands in these pairs equals 4.69Å, indicating substantial slipping of the ligands with respect to each other and thus ruling out the possibility of any ring-ring overlap and π-π interaction between the Cp* ligands. The absence of ring-ring overlap is aptly illustrated by a projection of such a pair of Cp* ligands onto a plane parallel to that of the ligands (see Figure 2.5).
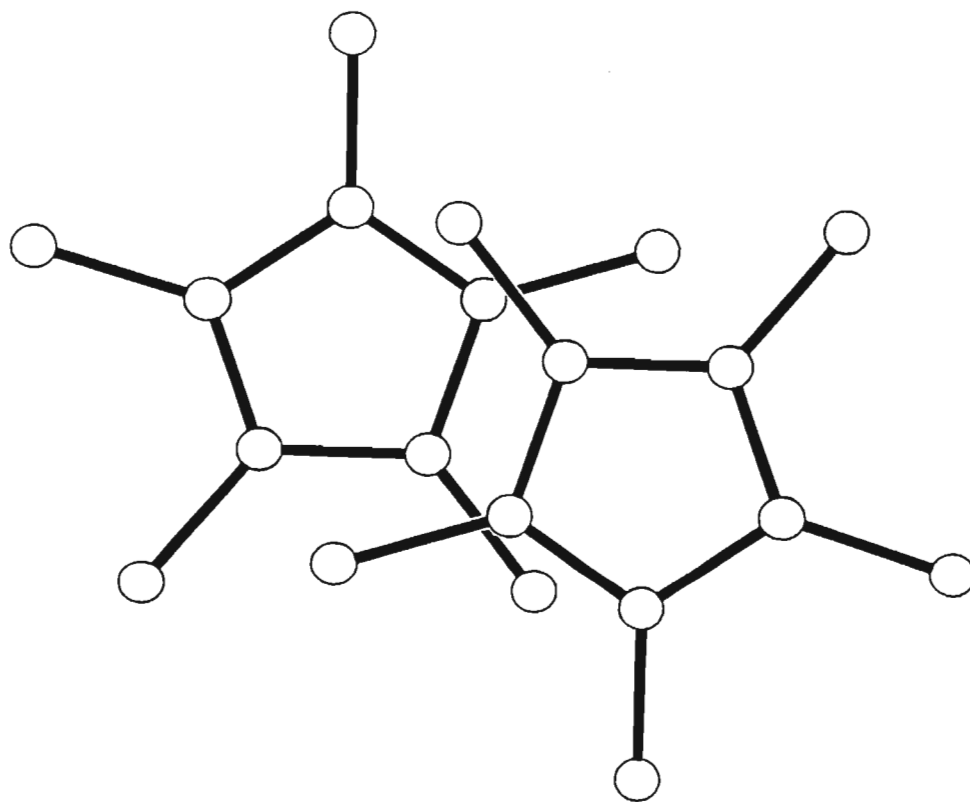
Figure 2.5   *A projection of a pair of Cp* ligands (arranged face-to-face) onto a plane parallel to that of the ligands*

A further important structural feature of $[Fe_2Cp_2^*(CO)_2(\mu\text{-}SEt)_2]$, is that due to the cis configuration of the Cp^* ligands, a line constructed from the centroid of one Cp^* ligand through the Fe-atoms to the centroid of the other ligand, defines a boat shape. This is in marked contrast to the mononuclear metallocene donor molecules utilized in all previously reported studies, where the same construction yields a straight line.

2.4.3 $[Fe_2Cp_2^*(CO)_2(\mu\text{-}SEt)_2](2,5\text{-}Me_2\text{-}DCNQI)$ (2)

2.4.3.1 Synthesis and spectroscopic studies on $[Fe_2Cp_2^*(CO)_2(\mu\text{-}SEt)_2](2,5\text{-}Me_2\text{-}DCNQI)$ (2)

The electrochemical properties of 2,5-Me$_2$-DCNQI have been studied previously.[225] However, in order to allow for a direct comparison of the half-wave potential of the (2,5-Me$_2$-DCNQI)/(2,5-Me$_2$-DCNQI)$^-$ couple with that of the $[Fe_2Cp_2^*(CO)_2(\mu\text{-}SEt)_2]/[Fe_2Cp_2^*(CO)_2(\mu\text{-}SEt)_2]^+$ couple, E_{1D}, the electrochemical behaviour of 2,5-Me$_2$-DCNQI was reinvestigated. In accordance with the literature results, the cyclic voltammogram of 2,5-Me$_2$-DCNQI, recorded in CH_2Cl_2, was found to consist of two reversible, one electron reduction waves, E_{1A} occurring at a potential of +0.08 V (see Table 2.1). As pointed out in section 2.4.2.1, this potential is substantially anodic to that associated with the $[Fe_2Cp_2^*(CO)_2(\mu\text{-}SEt)_2]/[Fe_2Cp_2^*(CO)_2(\mu\text{-}SEt)_2]^+$ couple (E_{1D} equals -0.27 V), implying that the electron transfer between **1** and 2,5-Me$_2$-DCNQI will be spontaneous. The charge transfer is also expected to be complete since the difference in potentials, $|E_{1A}\text{-}E_{1D}|$ which equals 0.35 V is significantly larger than the "cut-off" value of 0.25 V for complete charge transfer suggested by Wheland.[140] Based on these electrochemical data, the charge transfer salt $[Fe_2Cp_2^*(CO)_2(\mu\text{-}SEt)_2](2,5\text{-}Me_2\text{-}DCNQI)$ was expected to be stable with respect to disproportionation to its starting materials.

Slow addition of an equimolar amount of **1**, dissolved in toluene, to a cooled toluene solution of 2,5-Me$_2$-DCNQI resulted in the formation of a green solution from which the crude product precipitated on reducing the volume of the solution *in vacuo*. The product was extracted from this precipitate with CH_3CN, affording shiny blue-black crystals on reducing the volume of the extracts and subjecting it to slow cooling over *ca.* 2 days. The material obtained in this way was analytically pure; elemental analysis for C, H and N being consistent with the empirical formula $[Fe_2Cp_2^*(CO)_2(\mu\text{-}SEt)_2](2,5\text{-}Me_2\text{-}DCNQI)$.

The infrared spectroscopic data for **2** is presented in Table 2.2.

The infrared spectrum of **2**, recorded in CH_2Cl_2 solution, exhibits two peaks (at 2120 and 2092 cm^{-1}) in the C-N stretching region and two peaks (at 1983 and 1946 cm^{-1}) in the C-O stretching region. A similar peak pattern is observed in the solid state infrared spectrum recorded as a KBr pellet, but whereas the C-N stretching peaks occur at the same wavenumbers when the spectrum is recorded in CH_2Cl_2 or KBr, the C-O stretching peaks, as observed in the solid state spectrum, shift to wavenumbers 15 to 20 cm^{-1} lower than that observed in CH_2Cl_2 solution. A single peak occurs in the C-N stretching region of the solid state infrared spectrum of the neutral 2,5-Me$_2$-DCNQI molecule, recorded as a KBr pellet. This peak occurs at 2168 cm^{-1}, which implies that there is a 48 cm^{-1} decrease in the vibrational frequency of this C-N stretching peak upon reducing the 2,5-Me$_2$-DCNQI molecule to its mono-anion. (This comparison considered only the stronger of the two peaks in the C-N stretching region in the solid state infrared spectrum of **2**.) Similar shifts of between 0 and 70 cm^{-1} have been observed to be associated with the formation of the DCNQI$^-$ anion in reactions between TTF and a range of substituted DCNQI molecules.[184] The shift can be attributed to the increase in electron density in the LUMO of the neutral DCNQI molecule which is antibonding with respect to the C and N atoms of the C≡N bonds.

A comparison of the peaks in the C-O stretching region in the infrared spectra of [Fe$_2$Cp$_2^*$(CO)$_2$(μ-SEt)$_2$](2,5-Me$_2$-DCNQI) with that observed for the neutral molecule [Fe$_2$Cp$_2^*$(CO)$_2$(μ-SEt)$_2$] (recorded in both CH_2Cl_2 and KBr), reveals a shift of between 50 and 70 cm^{-1} to higher wavenumbers in going from the neutral to the cationic derivative. A similar shift of *ca.* 50 cm^{-1} has been reported for [Fe$_2$Cp$_2$(CO)$_2$(μ-SMe)$_2$] and its cationic derivative,[226] and has been attributed to the lower electron density on the cation, resulting in a diminished back donation of electron density into the π* orbitals of the C-O ligands. These π* orbitals are antibonding in nature, so that the decreased back donation results in an increase in the C-O bond order which manifests itself in an increase in the C-O vibrational frequency.

The CH_2Cl_2 solution infrared spectra of [Fe$_2$Cp$_2^*$(CO)$_2$(μ-SEt)$_2$] and **2** furthermore differ in that the spectrum of the neutral molecule exhibits essentially one peak with a weak

shoulder in the C-O stretching region, whereas the spectrum of the cationic derivative exhibits two pronounced peaks in this region. This difference has also been reported for the cis isomers of $[Fe_2Cp_2(CO)_2(\mu-SR_2)]$ (R = Me, Ph)[220] and their monocationic derivatives and is attributed to the cationic derivatives occurring as a mixture of at least two conformers or isomers in solution.

2.4.3.2 Structural studies on $[Fe_2Cp_2^*(CO)_2(\mu-SEt)_2](2,5-Me_2-DCNQI)$ (2)

Single crystals of **2** were grown by slow cooling of a saturated CH_3CN solution of the compound.

$[Fe_2Cp_2^*(CO)_2(\mu-SEt)_2](2,5-Me_2-DCNQI)$, like the neutral donor molecule $[Fe_2Cp_2^*(CO)_2(\mu-SEt)_2]$, crystallizes in the monoclinic space group $C2/c$ with four formula units per unit cell. The unit cell dimensions, a full list of internuclear distances and angles and other crystallographic data are presented in Tables 2.15 to 2.19 at the end of this chapter.

The structure presents the first example of a full characterization of a metallocene-based charge transfer salt utilizing a member of the DCNQI series as the acceptor molecule. Miller and co-workers reported the synthesis of $[MCp_2^*](2,5-Me_2-DCNQI)$ (M = Fe, Mn) which presents the only other examples of metallocene based DCNQI - charge transfer salts synthesized to date. However, they have not been able to obtain suitable crystals of either salts for a crystallographic analysis.

As in the case of the neutral molecule **1**, the $[Fe_2Cp_2^*(CO)_2(\mu-SEt)_2]^+$ cation in **2** comprises two crystallographically identical $FeCp^*(CO)$ moieties which are symmetrically bridged by the ethyl-mercapto ligands and are related by a crystallographically imposed two-fold rotation axis (see Figure 2.6). This implies that, as has been described for the neutral molecule **1**, (see section 2.4.2.2) the Cp^* and CO ligands occur in a cis configuration with respect to the Fe-Fe vector and the S-C bonds of the ethyl-mercapto ligands are syn-disposed, whereas the C-C bonds of the ethyl-mercapto ligands occur in an anti-conformation with respect to the S-S vector.

A further comparison of the molecular structure of the $[Fe_2Cp_2^*(CO)_2(\mu-SEt)_2]^+$ cation with the neutral molecule, reveals a decrease of *ca.* 0.36Å in the Fe-Fe distance from
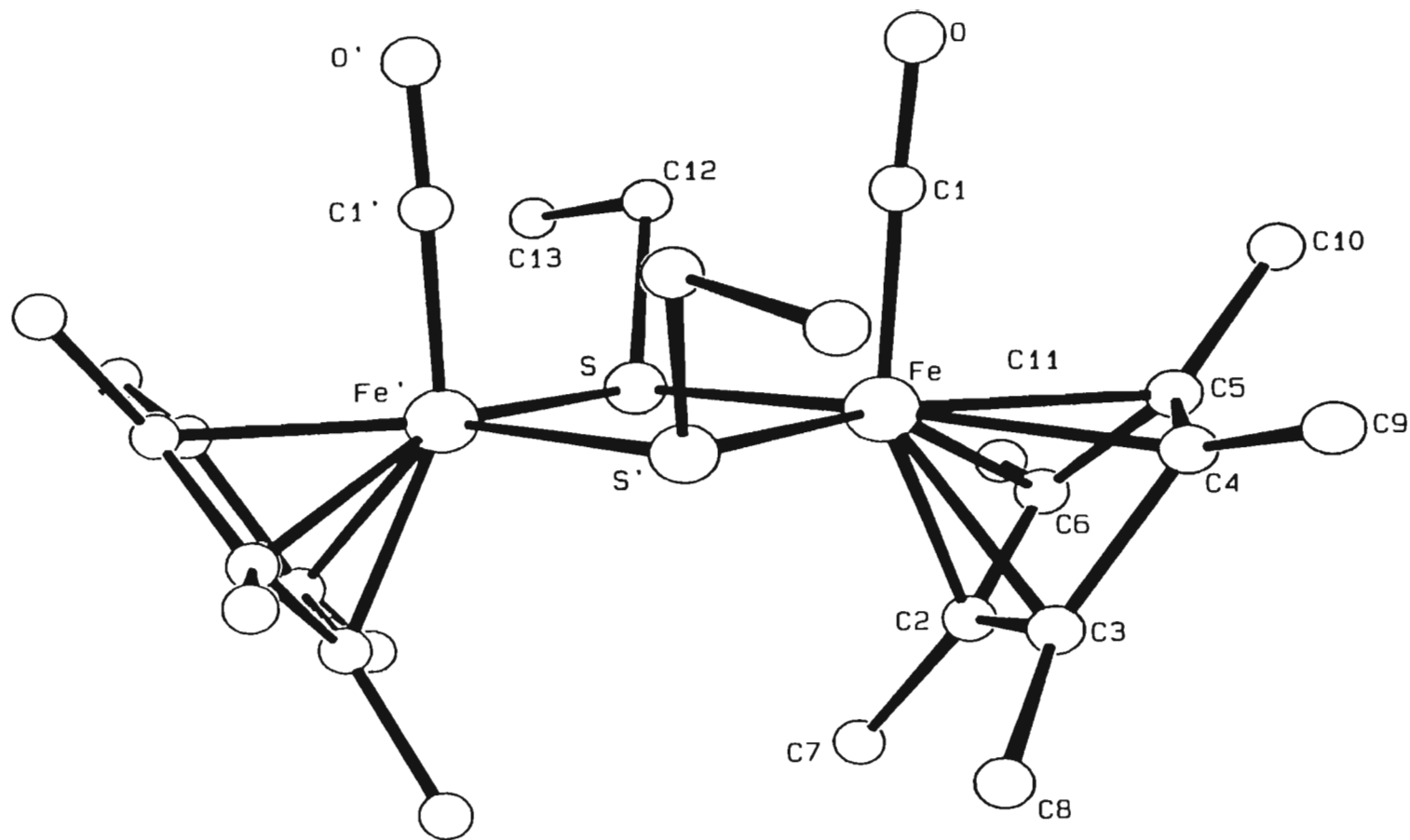
Figure 2.6   *The molecular structure and numbering scheme employed for the cation in [Fe$_2$Cp$_2^*$(CO)$_2$(μ-SEt)$_2$](2,5-Me$_2$-DCNQI) (**2**).*

3.444(1)Å in (**1**) to 3.083(1)Å in the cation. Connelly and Dahl[226] compared the structure of the neutral species [$Fe_2Cp_2(CO)_2(\mu\text{-SPh})_2$] with that of the cation [$Fe_2Cp_2(CO)_2(\mu\text{-SMe})_2$]$^+$ and found the Fe-Fe distance in the cationic species to be 0.46Å shorter than that in the neutral molecule.

The decrease in the Fe-Fe distance on the oxidation of [$Fe_2Cp_2^*(CO)_2(\mu\text{-SR})_2$] has been explained[220,226] by utilizing the bonding scheme which Mason and Mingos have proposed[228] for bridged dinuclear systems containing an M_2X_2 moiety (M = metal, X = bridging ligand, as illustrated in Figure 2.7).

In this scheme the metal d_z^2, d_{xz} and d_{yz} participate in bridge bonding. The same is true of the s and p orbitals of the bridging ligands The highest occupied molecular orbital is derived from mainly the metal d_{yz} orbitals and is orthogonal to a rough plane defined by the M_2X_2 moiety. Furthermore, this orbital is strongly antibonding with respect to the metal

__Figure 2.7:__   *Structural formula for a bridged dinuclear system*
containing an M_2X_2 moiety (M = metal, X = bridging
ligand, L_n = terminal ligand)[228]
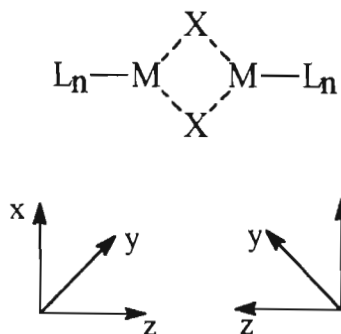
atoms. In a one electron oxidation, the electron is removed from this orbital, leaving one electron in this antibonding orbital and two electrons in the bonding metal σ orbital. This implies that the net metal-metal bond order is 0.5 which has been interpreted [226] as being indicative of a one-electron metal-metal bond. Further support for this assertion is provided by the fact that the Fe-Fe distance in *e.g.* [$Fe_2Cp_2^*(CO)_2(\mu\text{-SMe})_2$]$^+$ [2.925(4)Å] and [$Fe_2Cp_2^*(CO)_2(\mu\text{-SEt})_2$]$^+$ [3.083(1)Å in **2**], is intermediate between that associated with [$Fe_2Cp_2(CO)_2(\mu\text{-SPh})_2$] (3.39Å) or [$Fe_2Cp_2^*(CO)_2(\mu\text{-SEt})_2$] [3.444(1)Å], where there is no

Fe-Fe interaction, and that in *e.g.* [Fe$_2$Cp$_2$(CO)$_4$] (2.533Å) which possesses a two-electron Fe-Fe bond.[226]

The shortened Fe-Fe distance in [Fe$_2$Cp$_2^*$(CO)$_2$(μ-SEt)$_2$]$^+$ is accompanied by a decrease in the Fe-S-Fe angle from 98.3(1)° in (**1**)to 86.3(1)° in the cation and a concomitant increase in the S-Fe-S angle from 80.1(1)° in the neutral species to 93.4(1)° in the cation. A further structural change associated with the decrease in the Fe-Fe distance is that the dihedral angle between the planes defined by the two bridging S atoms and each one of the two Fe atoms, increases from 163.4(3)° in the neutral species, to 172.4(8)° in the cation. The latter angle is in sharp contrast to that of 153° observed in the [Fe$_2$Cp$_2$(CO)$_2$(μ-SMe)$_2$]$^+$ cation[226]. This difference most probably is the result of non-bonded repulsions between the more bulky Cp* ligands when compared to the unsubstituted Cp ligands. (Recall that the Cp* and Cp ligands occur in a cis configuration.)

The Fe-S distances in the [Fe$_2$Cp$_2^*$(CO)$_2$(μ-SEt)$_2$]$^+$ cation are 2.258(2)Å and 2.248(2)Å. This represents a decrease of 0.024Å when compared to the average value of 2.277(1)Å observed for the neutral molecule **1**. An analogous variation of the Fe-S bond distance upon ionization of members of the [Fe$_2$Cp$_2$(CO)$_2$(μ-SR)$_2$] series have not been documented previously, since the structures of both the neutral and monocationic forms of a single member of this series have not been determined to date. The Fe-C (C of Cp* ligand) distances in [Fe$_2$Cp$_2^*$(CO)$_2$(μ-SEt)$_2$]$^+$ varies between 2.105(8) and 2.163(8)Å with an average value of 2.139Å. This value represents an elongation of 0.036Å of the average Fe-C distance when compared to that of 2.103Å observed in the neutral molecule. Again a comparison with members of the [Fe$_2$Cp$_2^*$(CO)$_2$(μ-SR)$_2$] series is not possible. A similar elongation of the average Fe-C bond distance has however been reported to occur on the oxidation of [FeCp$_2^*$], where the average Fe-C distance increases by 0.046Å, from 2.050Å in the neutral molecule, to 2.096Å in the cation.[201]

The (2,5-Me$_2$-DCNQI)$^{n-}$ anion is situated on a crystallographic centre of inversion. The molecular structure and numbering scheme employed for the anion is provided in Figure 2.8. The principal internuclear distances and angles of the anion are provided in Table 2.5 together with that of the neutral unsubstituted DCNQI molecule,[229] that associated with the unsubstituted DCNQI$^-$ anion as found in (TTF)(DCNQI).2H$_2$O[230] and that of the
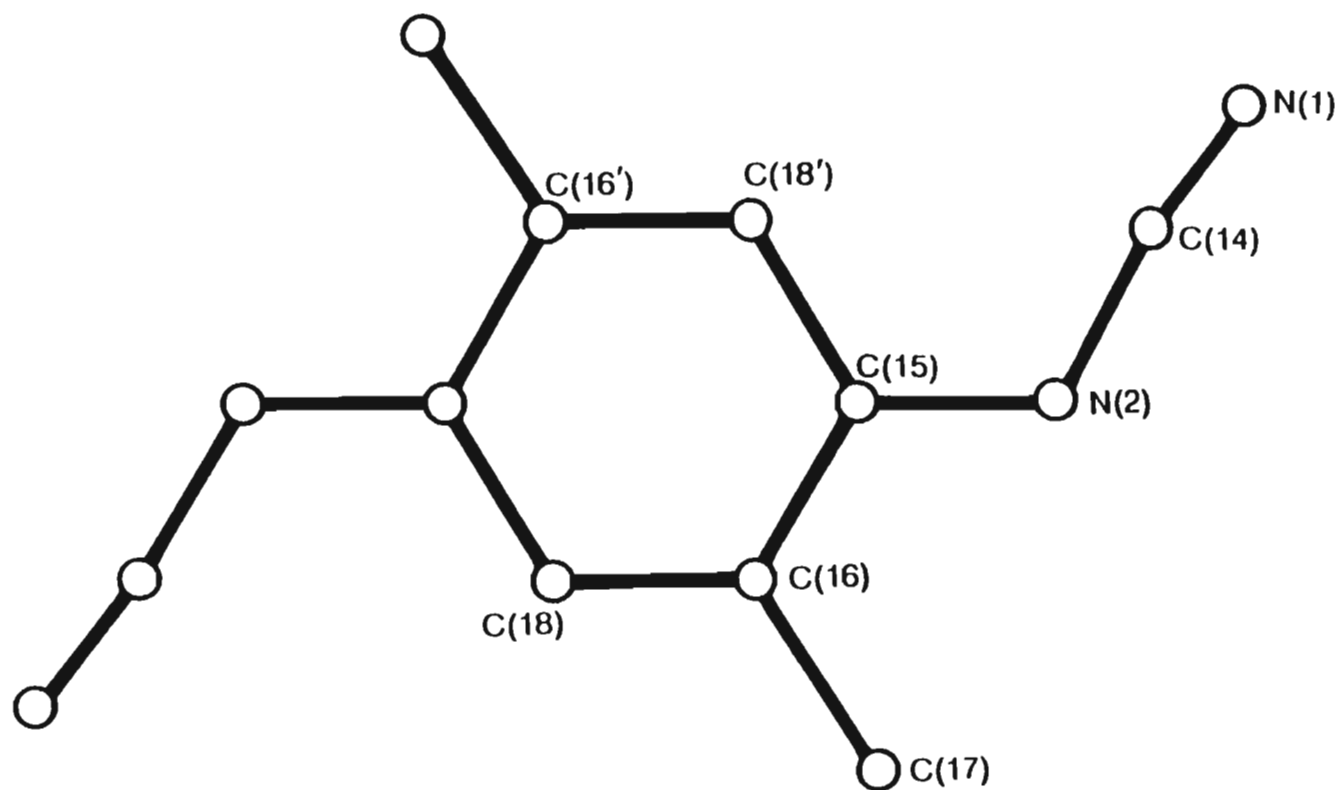
Figure 2.8   _The molecular structure and numbering scheme employed for the anion in [Fe$_2$Cp$_2$(CO)$_2$(μ-SEt)$_2$](2,5-Me$_2$-DCNQI) (_**_2_**_)._

Table 2.5 *Bond parameters for selected DCNQI species (Å)*

Compound	X	a[a]	b	c	d	e	f	Charge on DCNQI
[Fe₂Cp₂*(CO)₂(μ-SEt)₂](2,5-Me₂-DCNQI) (**2**)	Me	1.09(2)	1.38(2)	1.35(1)	1.41(1)	1.43(1)	1.38(1)	[b]
(2,5-Me₂-DCNQI)₂Cu	Me	1.159(6)	1.312(6)	1.342(6)	1.433(6)	1.442(6)	1.350(6)	> -¹/₂
H₄-DCNQI	H	1.150(2)	1.334(2)	1.303(2)	1.446(2)	1.450(2)	1.336(2)	0
(TTF)(H₄-DCNQI).2H₂O	H	1.150(7)	1.328(6)	1.348(7)	1.424(6)	1.427(6)	1.356(7)	-1

(a)
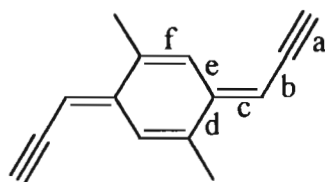
[b] Charge can not be deduced accurately due to relatively large standard errors.

2,5-Me$_2$-DCNQI moiety of (2,5-Me$_2$-DCNQI)$_2$Cu.[191] Aümuller and co-workers have reported[230] an increase in the length of bonds (c) and (f) (see diagram with Table 2.5) on the reduction of the neutral unsubstituted DCNQI molecule to its mono-anionic derivative. Similar variations in the bond lengths have been observed by Kato and co-workers;[191] however they reported the most significant variations to occur in the lengths of bonds (b) and (c), with the length of (b) decreasing and that of (c) increasing, on comparing the bond lengths and angles of the 2,5-Me$_2$-DCNQI moiety in (2,5-Me$_2$-DCNQI)$_2$Cu with that of the neutral unsubstituted DCNQI molecules. A comparison of the (2,5-Me$_2$-DCNQI)$^{n-}$ anion in **2** with the DCNQI compounds reported in the literature, shows that the observed bond lengths and angles are in good agreement with that in the literature. The increase in bond lengths (c) and (f) reported by Aümuller and co-workers is also observed upon comparing the anion in **2** with the neutral unsubstituted DCNQI molecule. However, because of the relatively large standard errors associated with the bond parameters of the anion in **2**, it is not possible to base any firm conclusions about the charge on the anion on these comparisons, as Kato and co-workers have done.

Viewing the unit cell contents down the [b]-axis (see Figure 2.9) reveals that, as in the case of the neutral [Fe$_2$Cp$_2^*$(CO)$_2$(μ-SEt)$_2$] molecule, the [Fe$_2$Cp$_2^*$(CO)$_2$(μ-SEt)$_2$] cations in **2** are arranged in rows or channels. These are at an angle of *ca.* 28° with the [a]-axis in this instance. The (2,5-Me$_2$-DCNQI)$^{n-}$ anion is positioned between the Cp* ligands of two neighbouring cations within these rows. Isolating one of these rows and adding the analogous rows produced by unit cell translations along the [b]-axis produces Figure 2.10 This figure reveals that the [Fe$_2$Cp$_2^*$(CO)$_2$(μ-SEt)$_2$]$^{n+}$ cation participates in essentially the same mode of packing as that observed for the neutral molecule (compare Figures 2.4 and 2.9). Within this arrangement, the (2,5-Me$_2$DCNQI)$^{n-}$ anion is "slipped in" between the Cp* ligands of two neighbouring cations, to form part of a "face-to-face" arrangement which can be represented as Cp*,(2,5-Me$_2$-DCNQI)$^{n-}$,Cp*. It is also important to note that both of the Cp* ligands of each cation participate in this arrangement, thus implying that all the cations in the rows are "linked" to each other through this arrangement. Based on purely structural considerations [Fe$_2$Cp$_2^*$(CO)$_2$(μ-SEt)$_2$](2,5-Me$_2$-DCNQI) can thus be classified as possessing long-range one dimensional order. However, in order to ascertain whether this long-range structural order also induces extended electronic interactions in the solid

90
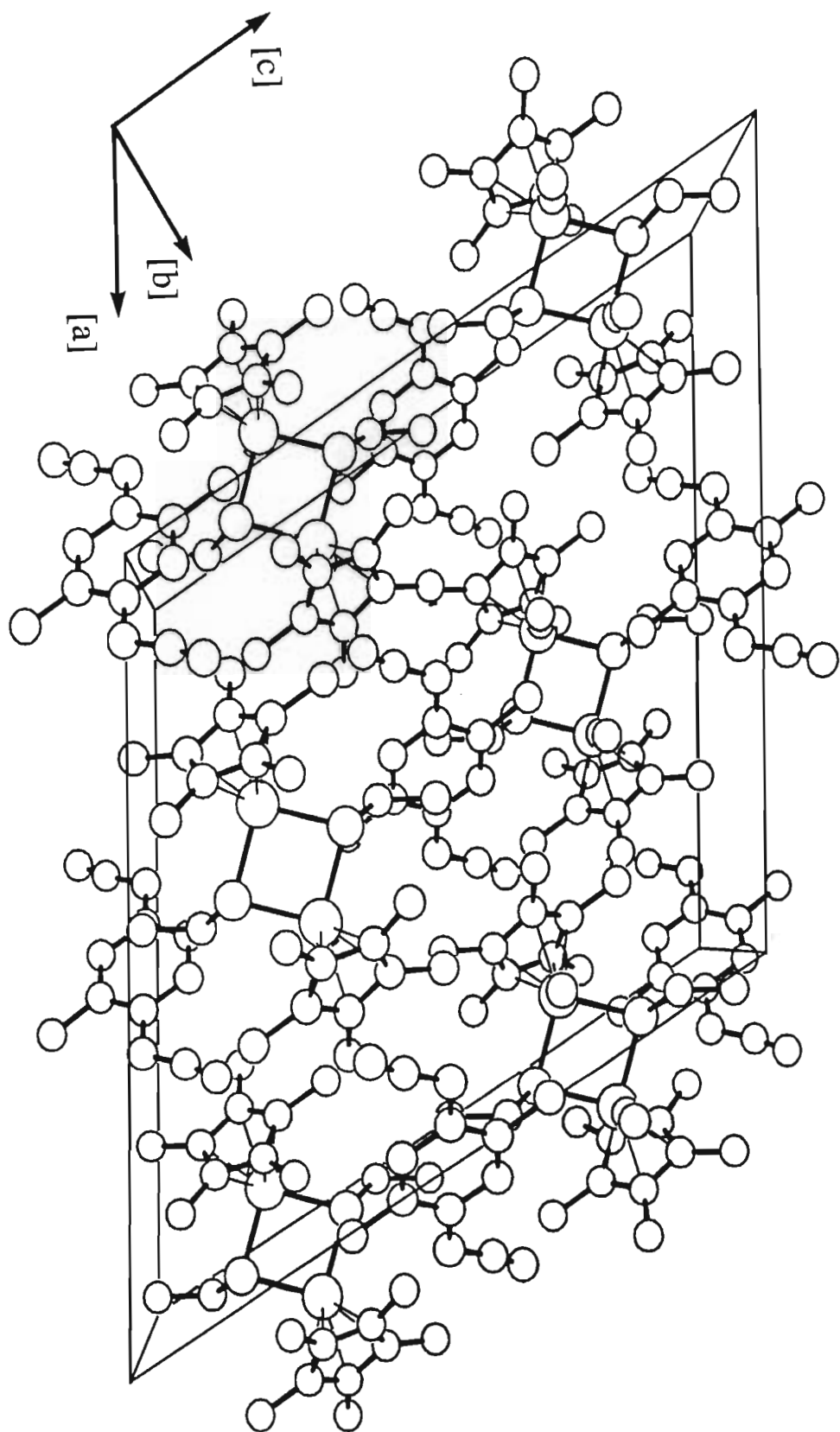
Figure 2.9 *The unit cell contents of [Fe₂Cp₂*(CO)₂(μ-SEt)₂](2,5-Me₂-DCNQI) (2) as seen in a view along the [b]-axis.*
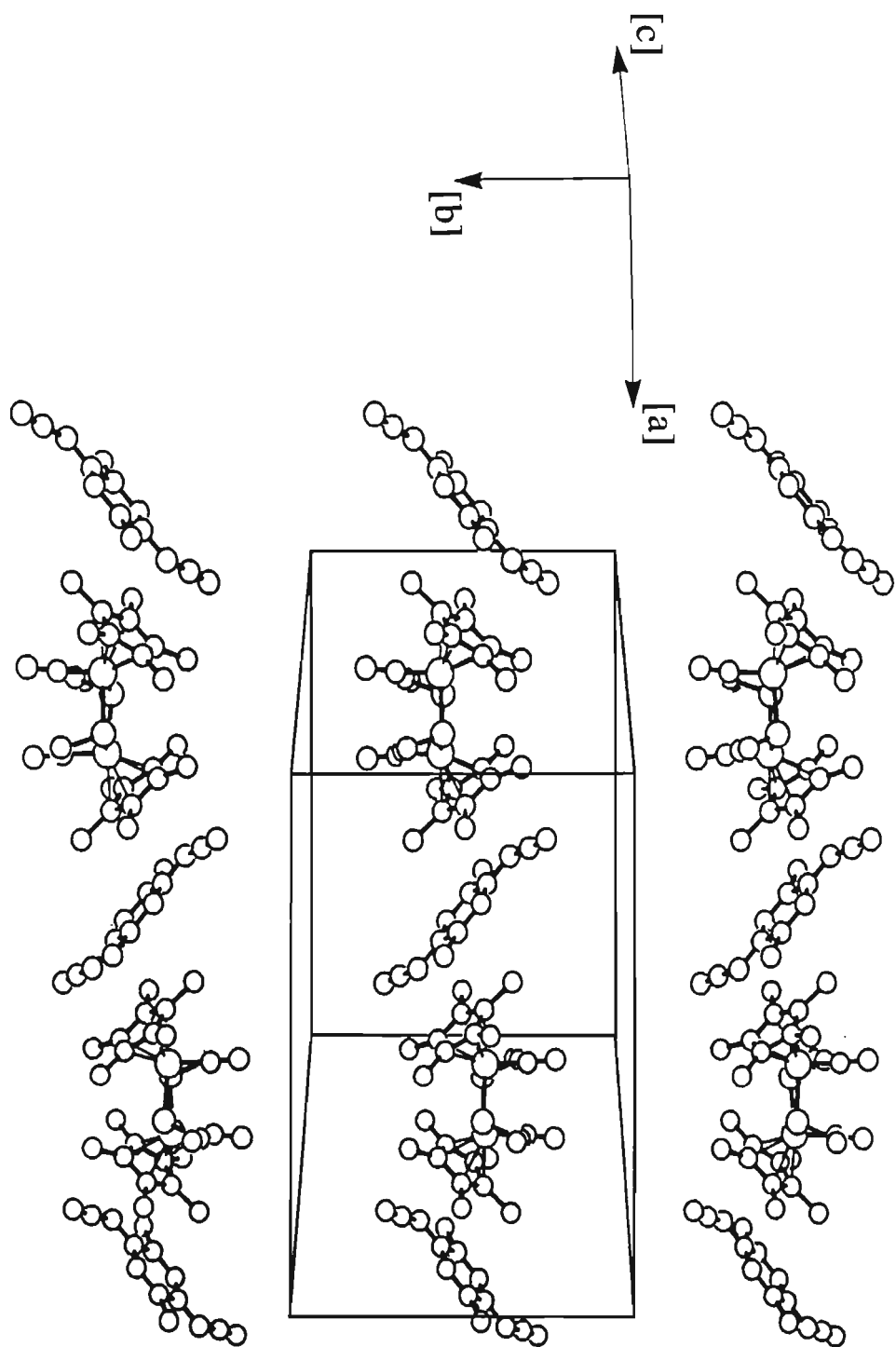
Figure 2.10   The "rows" of alternating cations and anions in the crystal lattice of [Fe₂Cp₂*(CO)₂(µ-SEt)₂](2,5-Me₂-DCNQI) (2).

state, the possibility of any π-π interaction within the $Cp^*,(2,5-Me_2-DCNQI)^{n^-},Cp^*$ sequence is of interest. The Cp^* ligands of the $Cp^*,(2,5-Me_2-DCNQI)^{n^-},Cp^*$ arrangement are positioned such that the best planes defined by the atoms constituting each of the two ligands are exactly parallel to each other. This arrangement is enforced by the fact that these two Cp^* ligands are interrelated by the crystallographic centre of inversion which is situated between the ligands and is coincident with the centre of the quinone ring of the $(2,5-Me_2-DCNQI)^{n^-}$ anion. The orientation of the plane defined by the constituent atoms of the $(2,5-Me_2-DCNQI)^{n^-}$ anion, however is not uniquely defined by any symmetry element. In fact, calculation of the mean plane defined by the atoms of the anion, revealed that the dihedral angle between the $(2,5-Me_2-DCNQI)$-plane and that of the Cp^* ligand is $11.4°$. This limits the extent of any π-π interaction within the $Cp^*,(2,5-Me_2-DCNQI)^{n^-},Cp^*$ arrangement. Furthermore, projecting the Cp^* ligands and the anion onto a plane parallel to that of the anion (see Figure 2.11) reveals that there is no overlap of the Cp^* ligands with the quinone ring or the exocyclic $C=N$ bond of the $(2,5-Me_2-DCNQI)^{n^-}$ anion, as would be expected for conventional π-π interaction. The Cp^* ligands are however positioned directly above and below the $C\equiv N$ groups of the anion; the distances from the C and N atoms of the $C\equiv N$ group to the plane of the Cp^* ring being 3.27 and 3.12Å respectively (see Figure 2.12). These distances are considerably smaller than 3.45Å, the Van der Waal's spacing for π-aromatic species in a face-to-face arrangement[242] and could be indicative of some electronic interaction between the $C\equiv N$ groups of the $(2,5-Me_2-DCNQI)^{n^-}$ anion and the Cp^* ligands.

In short, the crystal structure of **2** can thus be described as consisting of extended alternating stacks of donor and acceptor ions, *i.e.* $...D^{n^+}A^{n^-}D^{n^+}A^{n^-}...$ This extended $...D^{n^+}A^{n^-}D^{n^+}A^{n^-}...$ structural arrangement presents an exact match to that required for the stabilization of ferromagnetic coupling (see section 2.3.2.1). The second prerequisite for the stabilization of such coupling is that the charge transfer between the donor and acceptor molecules should be complete. A quick way of assessing the extent of charge transfer, involves comparing the observed bond lengths and angles, which are known to change on ionization of the donor and acceptor molecules, with that of the neutral and ionized molecules as found in the literature. As has already been pointed out, the standard errors

93
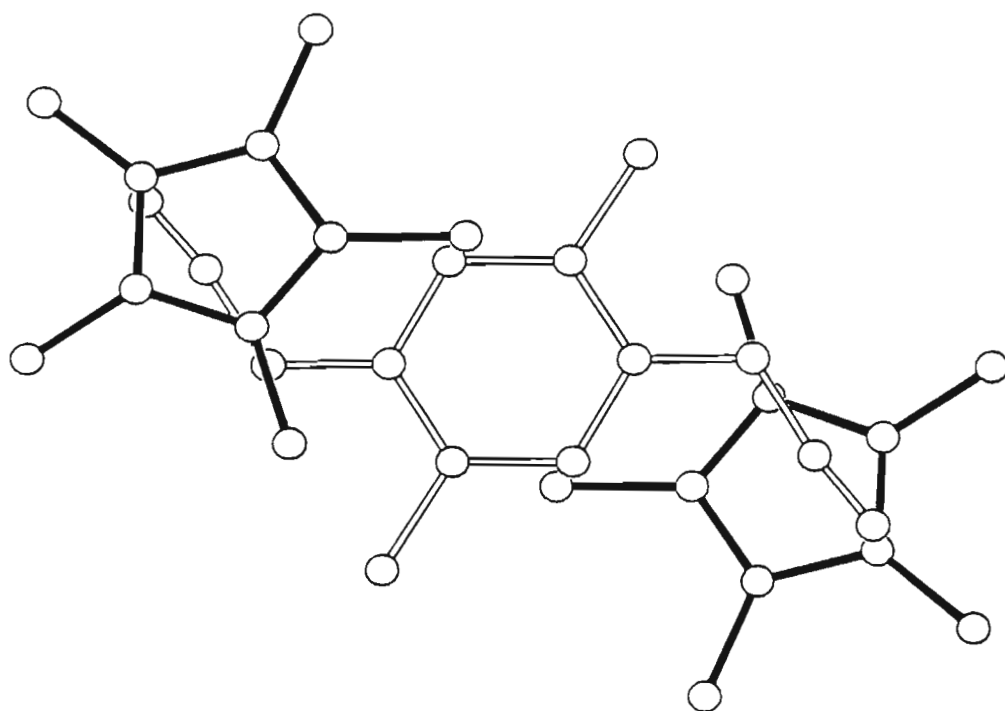
Figure 2.11   *Projection of the Cp* * *ligands and (2,5-Me₂-DCNQI) anion in [Fe₂Cp₂*-* *(CO)₂(μ-SEt)₂](2,5-Me₂-DCNQI) onto a plane parallel to that of the anion.*
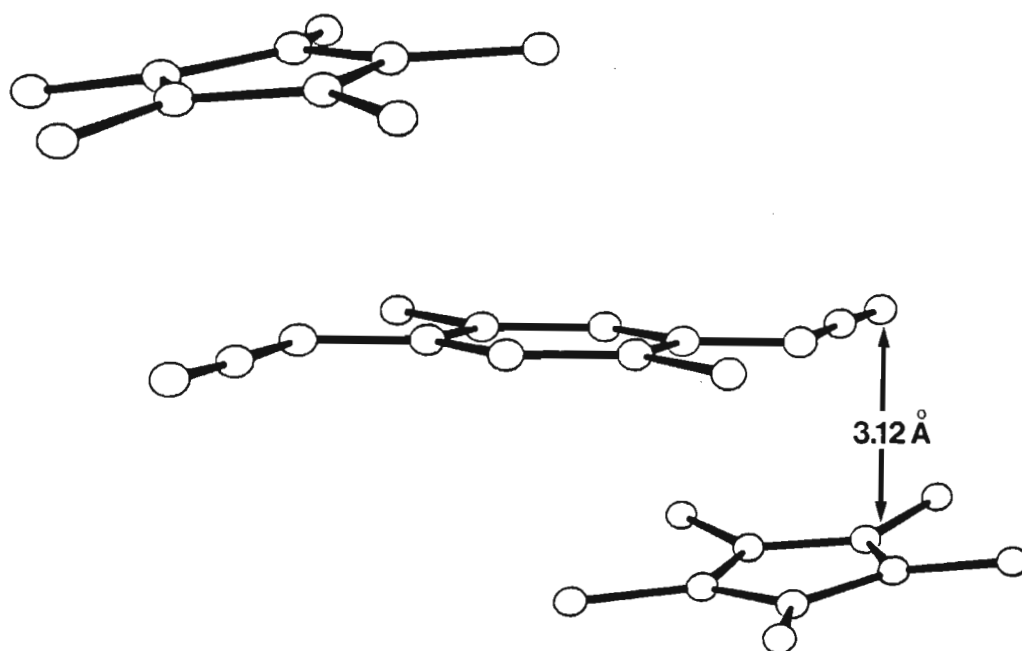
Figure 2.12   *An alternative view of the Cp*,(2,5-Me₂-DCNQI)⁻,Cp* arrangement in* *[Fe₂Cp₂*(CO)₂(μ-SEt)₂](2,5-Me₂-DCNQI) (2).*

associated with the observed bond lengths and angles of the (2,5-Me$_2$-DCNQI)$^{n-}$ anion in **2** are too large to allow for any definite conclusions to be drawn about the charge on the anion. However, as discussed above, Fe-Fe distances in [Fe$_2$Cp$_2$(CO)$_2$(μ-SR)$_2$] compounds vary significantly on oxidation of the neutral molecule. Furthermore, the Fe-Fe distance in the cation in **2** [3.083(1)Å] has been determined with a high enough degree of precision to allow for meaningful comparisons with literature results. Of particular significance in this regard is that the Fe-Fe distance in the cation of **2** is significantly shorter than that observed for the neutral molecule [3.444(1)Å] and in good agreement with that observed [2.925(4)Å] in the cation of [Fe$_2$Cp$_2$(CO)$_2$(μ-SMe)$_2$](BF$_4$). The BF$_4$$^-$ anion carries a full electron charge, *i.e.* -1, which implies that the charge on the [Fe$_2$Cp$_2$*(CO)$_2$(μ-SMe)$_2$]$^+$ cation equals +1. Due to the similarity in the Fe-Fe distances, the charge on the cation in **2**, in all likelihood also equals +1. In order to preserve electrical neutrality, it then follows that the charge on the (2,5-Me$_2$-DCNQI)$^{n-}$ anion in **2** must equal -1, which implies that full electron transfer occurs between the donor and acceptor molecules in **2**.

2.4.3.3 Magnetic studies on [Fe$_2$Cp$_2$*(CO)$_2$(μ-SEt)$_2$](2,5-Me$_2$-DCNQI) (**2**)

From the discussion in section 2.4.3.2 it is clear that [Fe$_2$Cp$_2$*(CO)$_2$(μ-SEt)$_2$](2,5-Me$_2$-DCNQI) meets both of the requirements for the stabilization of ferromagnetic interactions between the unpaired electron spins on its constituent radical ions. The magnetic susceptibilty (over the range 2 to 320K) of **2** was thus determined[231] by the Faraday method[232] and was found to obey the Curie-Weiss law, $\chi = C.(T - \theta)^{-1}$. A plot of the inverse molar susceptibilty versus temperature, corrected for diamagnetic contributions (see Figure 2.13), displays no obvious deviation from linearity at low temperature values, as would be expected if significant coupling between the unpaired electron spin density on the donor and acceptor ions was present. The Curie-Weiss constant, θ, derived from the above plot, equals +0.41 K. This value is substantially smaller than that typically associated with ferromagnetic coupling $\{\theta = +30$ K for [FeCp$_2$*](TCNE)[203], see section 2.3.2.1} and is comparable to the value of 0.5 ± 2.2 K, observed for [Fe(C$_5$Me$_4$H)$_2$](BF$_4$)[233], which has been suggested to be indicative of very weak magnetic interactions. The effective magnetic moment μ_{eff} [$= (8\chi.T)^{1/2}$] equals 2.720 μ_B and, in accordance with the presence of only very weak, if any, magnetic interactions, does not exhibit any temperature dependence
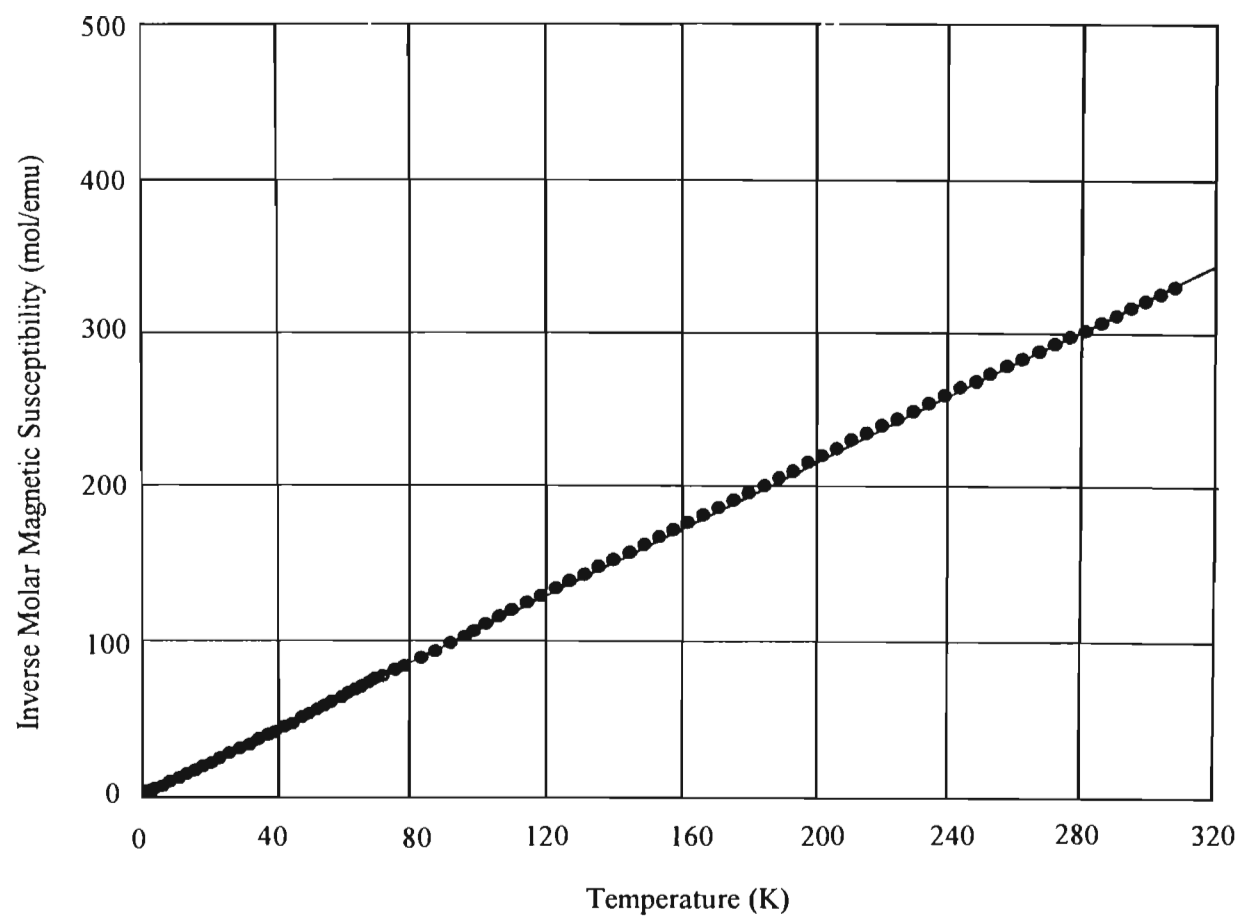
Figure 2.13 _The inverse molar susceptibilty of [Fe$_2$Cp$_2^*$(CO)$_2$(μ-SEt)$_2$](2,5-Me$_2$-DCNQI) (**2**) plotted as a function of temperature._
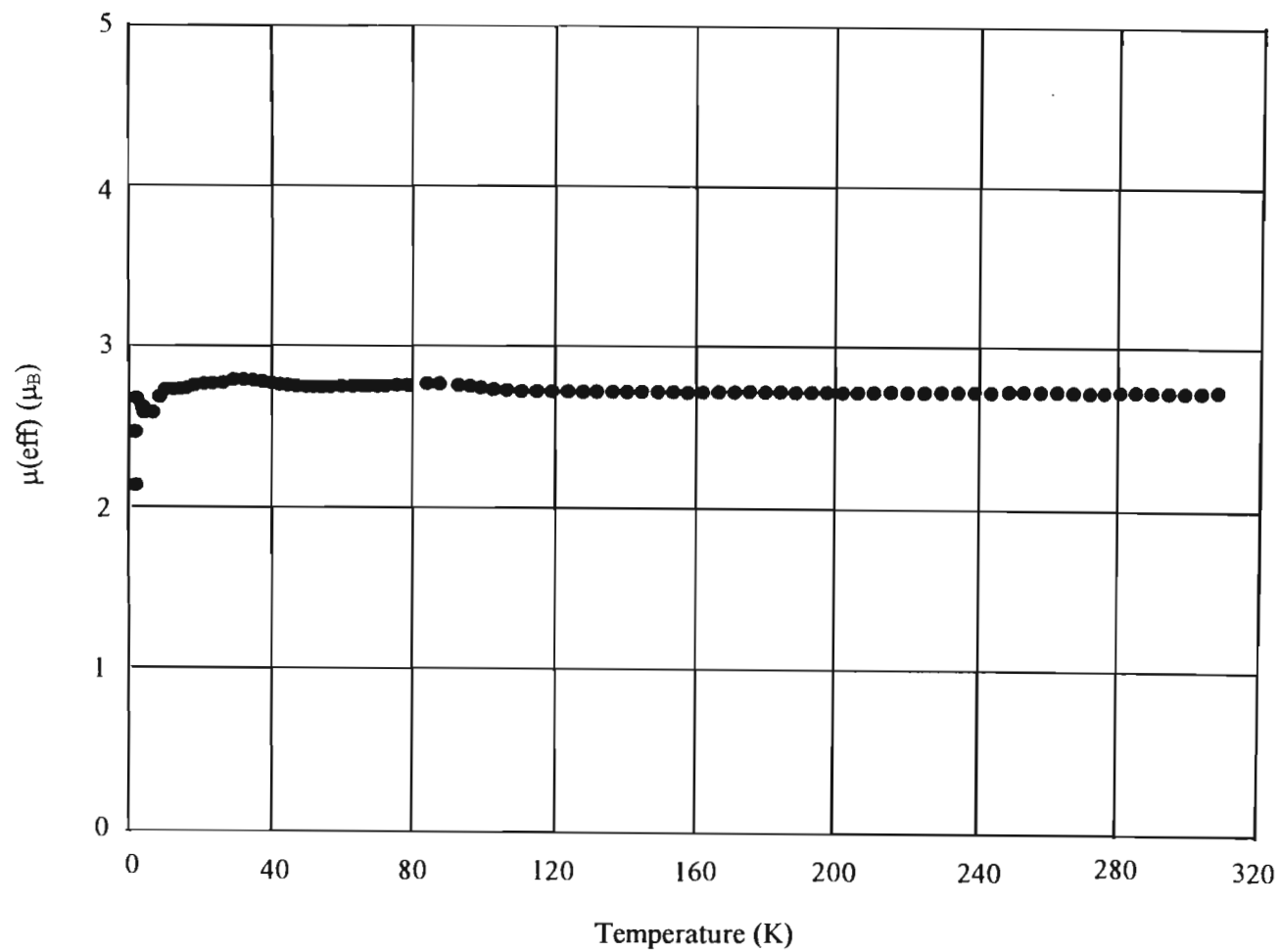
Figure 2.14 *The effective magnetic moment of [Fe$_2$Cp$_2^{\bullet}$(CO)$_2$(μ-SEt)$_2$](2,5-Me$_2$-DCNQI) (**2**) plotted as a function of temperature.*

(see Figure 2.14). This value (2.270 μ_B) however, is significantly different from the spin-only value of 2.45 μ_B predicted for two independent, non-interacting spins per formula unit.[232] The difference between the observed and predicted values most probably arises as a result of orbital angular momentum contributions from the cation to the magnetic moment of **2**. Such contributions are known to cause the Lande g-values for ferrocinium cations to be significantly different from the free-electron g-value of 2, utilized in the prediction of the spin-only effective magnetic moment.[233] A theoretical value for the effective magnetic moment, taking orbital angular momentum contributions into account, can be determined if the Lande g-values for the cation, containing the transition metal atom(s), and corresponding to different orientations with respect to the magnetic field, are known.[233] These g-values are commonly determined through EPR spectroscopy. However, since the EPR spectra of ferrocinium cations, and most probably that of $[Fe_2Cp_2^*(CO)_2(\mu-SEt)_2]^+$, are only observable in dilute diamagnetic glasses at liquid-helium temperatures, and since $[Fe_2Cp_2^*(CO)_2(\mu-SEt)_2](2,5-Me_2-DCNQI)$ does not exhibit significant magnetic interactions between the unpaired electrons of its constituent radical ions, it was decided not to pursue this line of study.

It was suggested in the introduction to this section that $[Fe_2Cp_2^*(CO)_2(\mu-SEt)_2](2,5-Me_2-DCNQI)$ meets both of the prerequisites for the stabilization of ferromagnetic coupling between the unpaired electron spins on its constituent radical ions. The fact that this salt exhibits only very weak, if any, magnetic interactions, again serves to illustrate that meeting these prerequisites is necessary, but not sufficient, to guarantee the stabilization of such interactions. Some suggestions attempting to explain the lack of significant magnetic interactions in **2** are provided in the following discussion.

The magnetic behaviour of $[Fe_2Cp_2^*(CO)_2(\mu-SEt)_2](2,5-Me_2-DCNQI)$ is in marked contrast to that of $[FeCp_2^*](2,5-Me_2-DCNQI)$,[227] where significant ferromagnetic interactions, as indicated by a Curie-Weiss constant, θ, of +15 K, occurs. Since the crystal structure of $[FeCp_2^*](2,5-Me_2-DCNQI)$ is not known, comparisons between this salt and **2** are limited to a consideration of the donor cations. Two major differences exist between $[FeCp_2^*]^+$ and $[Fe_2Cp_2^*(CO)_2(\mu-SEt)_2]^+$.

Firstly, the $[Fe_2Cp_2^*(CO)_2(\mu\text{-}SEt)_2]$ molecule is dinuclear and occupies a substantially larger volume than that of the mononuclear $[FeCp_2^*]$ molecule. This implies that the spin density on the $S = \frac{1}{2}$ $[Fe_2Cp_2^*(CO)_2(\mu\text{-}SEt)_2]^+$ cation, and thus the overall spin density in salts containing this ion, is lower than that on the $S = \frac{1}{2}$ $[FeCp_2^*]$ cation and its associated salts. As previously observed in the cases of $[FeCp_2^*](TCNQ)$ and $[FeCp_2^*](TCNE)$ (see section 2.3.2.1), a lower overall spin density in a charge transfer salt can result in a decrease in the strength of the ferromagnetic interactions between the unpaired electrons in that salt, when compared to related species with a higher overall spin density.

Secondly, as mentioned in section 2.4.2.2 a line drawn from the centroid of one Cp^* ligand through the Fe-atoms to the centroid of the other Cp^* ligand, defines a boat shape in the $[Fe_2Cp_2^*(CO)_2(\mu\text{-}SEt)_2]$ molecule and cation, whereas a similar construction for the $[FeCp_2^*]$ molecule and cation yields a straight line. This implies that in an extended ...$D^{n+}A^{n-}D^{n+}A^{n-}$.... stack with a face-to-face arrangement of the Cp^* ligands and planar acceptor radical ions, a line joining all the Fe-atoms within a stack will tend to be straight in the case of $[FeCp_2^*](A)$ (A = acceptor ion), but will have a distinct wave-like nature in the case of $[Fe_2Cp_2^*(CO)_2(\mu\text{-}SEt)_2](A)$, as observed in **2** (see Figure 2.10). It is not known at present what influence this geometrical feature might have on the magnetic interactions in the salt. The reason for this is two-fold; firstly, the magnetic properties of dinuclear metallocene-based charge transfer salts have not been reported previously, thus preventing any comparisons with established analogues. Secondly, the wave-like geometry constitutes only one of several possible features which could explain the lack of significant magnetic interactions in **2**.

A projection of the Cp^* ligands and the $(2,5\text{-}Me_2\text{-}DCNQI)^-$ anion of the $Cp^*,(2,5\text{-}Me_2\text{-}DCNQI)^-,Cp^*$ arrangement in $[Fe_2Cp_2^*(CO)_2(\mu\text{-}SEt)_2](2,5\text{-}Me_2\text{-}DCNQI)$, onto a plane parallel to that of the anion (see Figure 2.11), revealed that there is a substantial lateral displacement of the planar units constituting the face-to-face arrangements. As a consequence, a line drawn between the centroids of the Cp^* ligands is not normal to the planes of the ligands. The same geometrical arrangement is evident in the crystal structure of $[FeCp_2^*][Ni\{S_2C_2(CF_3)_2\}_2]$,[207] in contrast to $[FeCp_2^*][Pt\{S_2C_2(CF_3)_2\}_2]$ where this lateral displacement does not occur (see section 2.3.2.1), and causes an increase in the Fe-Fe separation from 10.94Å in the former compound, to 11.19Å in the latter. This increased

M-M separation was cited as the origin for the diminished ferromagnetic interactions in [Fe$_2$Cp$_2^*$][Ni{S$_2$C$_2$(CF$_3$)$_2$}$_2$] as compared with those of the Pt-analogue and could well play a role in the magnetic properties of [Fe$_2$Cp$_2^*$(CO)$_2$(μ-SEt)$_2$](2,5-Me$_2$-DCNQI).

It is clear that the factors suggested above to explain the lack of significant magnetic interactions in **2**, fall into two categories. The first is uniquely associated with the molecular ions constituting the salt. The donor cation for instance is dinuclear, boat-shaped and of lower spin density than *e.g.* [FeCp$_2^*$]. The second category concerns structural features centred around the packing of the donor and acceptor ions in the crystal, *e.g.* the lateral displacement of the planar units of the Cp*,(2,5-Me$_2$-DCNQI)$^-$, Cp* sequence. Since crystal packing is directly influenced, and to a great extent determined by the steric aspects associated with the molecular units involved in the packing, the above two categories are closely interrelated.

Bearing the above relationship in mind, and with the aim of eliminating, or at least modifying, structural aspects which could diminish ferromagnetic interactions, and which are associated with the crystal packing, [Fe$_2$Cp$_2^*$(CO)$_2$(μ-SEt)$_2$] was reacted with a range of other polycyano acceptor molecules. The following sections describe the synthesis and characterization of the resulting charge transfer salts. Since our access to equipment for the measurement of magnetic susceptibility as a function of temperature is limited, such studies were only performed on salts for which the solid state structure had been determined and which met the fundamental prerequisites for the stabilization of ferromagnetic coupling (integrated stacking and complete charge transfer between the donor and acceptor molecules).

2.4.4 [Fe$_2$Cp$_2^*$(CO)$_2$(μ-SEt)$_2$](2-Cl-5-Me-DCNQI) (3)

2.4.4.1 Synthesis and spectroscopic studies on [Fe$_2$Cp$_2^*$(CO)$_2$(μ-SEt)$_2$](2-Cl-5-Me-DCNQI) (3)

The acceptor molecule 2,5-Me$_2$-DCNQI is centrosymmetric and, as reported in section 2.4.3.2, it is thus possible for the (2,5-Me$_2$-DCNQI)$^-$ anion to be situated on a crystallographic centre of inversion, as observed in the salt **2**. In an attempt to modify the crystal packing, and as a result, possibly the magnetic properties of the charge transfer salt as well, 2-Cl-5-Me-DCNQI was employed as the acceptor molecule in the reaction with the

donor molecule $\underline{1}$. The 2-Cl-5-Me-DCNQI molecule is not centrosymmetric, which implies that if the salt resulting from this reaction crystallizes with the same ...$D^{n+}A^{n-}D^{n+}A^{n-}$.... motif as $\underline{2}$, the Cp^*,$(DCNQI)^{n-}$,Cp^* sequence will no longer possess a centre of inversion located at the centroid of the quinone ring and different modes of overlap between the units participating in this arrangement might be observed.

In order to make a direct comparison between the potentials, E_{1A} associated with the (2-Cl-5-Me-DCNQI)/(2-Cl-5-Me-DCNQI)$^-$ couple and E_{1D} of the $[Fe_2Cp_2^*(CO)_2(\mu\text{-SEt})_2]$/$[Fe_2Cp_2^*(CO)_2(\mu\text{-SEt})_2]^+$ couple, the electrochemistry of this acceptor molecule was investigated. As reported in the literature,[225] the cyclic voltammogram of 2-Cl-5-Me-DCNQI, recorded in CH_2Cl_2, consists of two reversible one-electron reduction waves. The potential E_{1A} was found to equal +0.22 V (see Table 2.1). This value is 0.14 V more anodic than that determined for the 2,5-dimethyl analogue, which is as expected where the more electron withdrawing chlorine substituent replaces the methyl group on the quinone ring. The difference $|E_{1A}\text{-}E_{1D}|$ for the combination of 2-Cl-5-Me-DCNQI and $[Fe_2Cp_2^*(CO)_2(\mu\text{-SEt})_2]$ equals 0.49 V, indicating that complete electron transfer between the donor and acceptor molecules is feasible.[140]

The reaction of 2-Cl-5-Me-DCNQI with $[Fe_2Cp_2^*(CO)_2(\mu\text{-SEt})_2]$, as well as attempts at crystallizing the resulting product, has been carried out in a range of solvents and solvent combinations. The reaction in toluene affords the expected product $[Fe_2Cp_2^*(CO)_2(\mu\text{-SEt})_2]$(2-Cl-5-Me-DCNQI), together with a CH_3CN and CH_2Cl_2 insoluble product which could result from a side reaction or decomposition of the product. Attempts at extracting $[Fe_2Cp_2^*(CO)_2(\mu\text{-SEt})_2]$(2-Cl-5-Me-DCNQI) from this mixture with either CH_3CN or CH_2Cl_2 resulted in it decomposing substantially. The reaction conditions which were found to consistently afford $[Fe_2Cp_2^*(CO)_2(\mu\text{-SEt})_2]$(2-Cl-5-Me-DCNQI) in the highest yield and greatest purity involve the slow addition of a methylcyclohexane solution of $[Fe_2Cp_2^*(CO)_2(\mu\text{-SEt})_2]$ (5% excess) to a stirred CH_2Cl_2 solution of 2-Cl-5-Me-DCNQI, followed by a reduction of the volume (*in vacuo*) of the reaction mixture to a minimum without effecting precipitation. Cooling the solution overnight resulted in the precipitation of a small amount of $[Fe_2Cp_2^*(CO)_2(\mu\text{-SEt})_2]$(2-Cl-5-Me-DCNQI) together with a large amount of the insoluble side product. Removing the mother liquor by filtration, reducing its volume *in vacuo* and cooling it overnight, afforded the product as dark blue-black crystals.

Elemental analysis for C, H and N confirmed the composition of these crystals to correspond to the empirical formula $[Fe_2Cp_2^*(CO)_2(\mu\text{-SEt})_2](2\text{-Cl-5-Me-DCNQI})$.

The solid state infrared spectrum of the salt $[Fe_2Cp_2^*(CO)_2(\mu\text{-SEt})_2](2\text{-Cl-5Me-DCNQI})$ recorded as a KBr pellet, exhibits two peaks in each of the C-N stretching (peaks at 2132 and 2108 cm^{-1}) and C-O stretching regions (peaks at 1967 and 1936 cm^{-1}, see Table 2.2). Compared to the solid state spectrum of the neutral acceptor molecule (recorded as a KBr pellet), which exhibits a single peak at 2184 cm^{-1}, the frequency of the C-N stretching modes is shifted on average by an amount of 69 cm^{-1} towards lower wavenumbers. As discussed earlier for the solid state infrared spectrum of **2** (see section 2.4.3.2), this shift is consistent with the increased electron density on the DCNQI anion resulting in a decrease in the bond strength of the C≡N bonds. A comparison of the peaks in the C-O stretching region with that observed for the neutral donor molecule **1** reveals that, in exact accordance with the spectrum of the (2,5-Me$_2$-DCNQI) salt **2**, the positions of the peaks are shifted by *ca.* 80 cm^{-1} to higher wavenumbers in going from the neutral to the cationic derivative. As in the case of **2**, this shift is the result of the decreased electron density on the cation, resulting in decreased back donation to the CO ligands which leads to an increased C-O bond order and thus, the shift towards higher wavenumbers of the C-O stretching modes (see section 2.4.3.2).

The CH$_2$Cl$_2$ solution infrared spectrum of an analytically pure, freshly prepared sample of $[Fe_2Cp_2^*(CO)_2(\mu\text{-SEt})_2](2\text{-Cl-5-Me-DCNQI})$ exhibits three peaks in the C-N stretching region (peaks at 2127, 2120 and 2110 cm^{-1}) and two peaks in the C-O stretching region (peaks at 1984 and 1949 cm^{-1}). The relative intensities, and to some extent the position of the C≡N peaks, were however found to depend on the age of sample used to record the spectrum. This variation was also found to occur on consecutive recordings of the spectrum of the same sample, which suggests that the (2-Cl-5-Me-DCNQI) anion might be unstable in CH$_2$Cl$_2$ solution, since the C-O stretching peaks associated with the cation, did not exhibit the same variation. As was observed in the solid state spectrum of **3**, the C-O stretching peaks in the solution spectrum of this salt, are shifted towards higher wavenumbers on oxidizing the $[Fe_2Cp_2^*(CO)_2(\mu\text{-SEt})_2]$ molecule. This shift of C-O stretching peaks was also observed on comparing the CH$_2$Cl$_2$ solution spectrum of **2** with that of the neutral donor molecule.

Single crystals, as evidenced by X-ray oscillation photographs, were obtained from the synthetic procedure as outlined above. These crystals were found to be weakly diffracting however and moreover decomposed, as evidenced by the appearance of powder rings in the oscillation photographs, even when mounted in sealed capillary tubes to minimize any exposure to the atmosphere.

2.4.5 $[Fe_2Cp_2^*(CO)_2(\mu\text{-SEt})_2](2\text{-Me-DCNQI})$ (4)

2.4.5.1 Synthesis and spectroscopic studies on $[Fe_2Cp_2^*(CO)_2(\mu\text{-SEt})_2](2\text{-Me-DCNQI})$ (4)

Based on the fact that the instability of $[Fe_2Cp_2^*(CO)_2(\mu\text{-SEt})_2](2\text{-Cl-5-Me-DCNQI})$ appeared to be associated with the radical anion, it was deemed appropriate to change the acceptor molecule to 2-Me-DCNQI. Similar to 2-Cl-5-Me-DCNQI, 2-Me-DCNQI is non-centrosymmetric, allowing for alternative modes of overlap to that observed in the Cp^*,DCNQI,Cp^* arrangement in $[Fe_2Cp_2^*(CO)_2(\mu\text{-SEt})_2](2,5\text{-Me}_2\text{-DCNQI})$.

The cyclic voltammogram of 2-Me-DCNQI in CH_2Cl_2 solution was recorded in order to allow the difference $|E_{1A}-E_{1D}|$ to be calculated for the reaction with $[Fe_2Cp_2^*(CO)_2(\mu\text{-SEt})_2]$. Consistent with the literature results,[225] the voltammogram consists of two reversible one-electron reduction waves. The potential E_{1A}, associated with the (2-Me-DCNQI)/(2-Me-DCNQI)$^-$ couple, was found to be equal to +0.12 V (see Table 2.1), which implies that the difference $|E_{1A}-E_{1D}|$ is 0.39 V and that complete charge transfer is thus expected to occur between the donor and acceptor molecules.[140]

The addition of $[Fe_2Cp_2^*(CO)_2(\mu\text{-SEt})_2]$ (10% excess) dissolved in methylcyclohexane, to a toluene solution of 2-Me-DCNQI resulted in the precipitation of $[Fe_2Cp_2^*(CO)_2(\mu\text{-SEt})_2](2\text{-Me-DCNQI})$ which was isolated through filtration. Washing the precipitate with petroleum ether and drying it *in vacuo* afforded an analytically pure purple-blue product, the composition of which was established by elemental analysis for C, H and N to be consistent with the formulation $[Fe_2Cp_2^*(CO)_2(\mu\text{-SEt})_2](2\text{-Me-DCNQI})$.

The solid state infrared spectrum of 4, recorded as a KBr pellet, exhibits two peaks in each of the C-N stretching (peaks at 2120 and 2096 cm^{-1}) and C-O stretching regions (peaks at 1967 and 1930 cm^{-1}) (see Table 2.2). A comparison of the frequencies of the C-N

stretching peaks of **4** with that of the single peak at 2168 cm^{-1}, observed in the solid state spectrum of the (2-Me-DCNQI) molecule, reveals a shift of *ca.* 50 cm^{-1} towards lower wavenumbers on reducing the neutral molecule. This shift is consistent with the inreased electron density on the anion causing a weakening of the C≡N bonds as described in section 2.4.3.1. The peaks in the C-O stretching region, when compared to that of the neutral molecule, exhibit the 50 to 70 cm^{-1} shift towards higher wavenumbers associated with the decreased electron density on the cation (see section 2.4.3.1). The solution spectrum of **4** recorded in CH$_2$Cl$_2$ exhibits peaks at 2128 and 2104 cm^{-1} in the C-N stretching region and at 1983 and 1946 cm^{-1} in the C-O stretching region. As observed in the solid state spectrum, the C-O stretching peaks in the solution spectrum are shifted towards higher wavenumbers.

All attempts at obtaining single crystals of **4** suitable for X-ray analysis were unsuccessful with the recrystallization process frequently affording oils which, as evidenced by infrared spectroscopy, result from extensive decomposition of the salt. Based on these problems it was decided to abandon further studies on [Fe$_2$Cp$_2$˙(CO)$_2$(μ-SEt)$_2$](2-Me-DCNQI).

2.4.6 [Fe$_2$Cp$_2$˙(CO)$_2$(μ-SEt)$_2$](H$_4$-DCNQI) (5)

2.4.6.1 Synthesis and spectroscopic studies on [Fe$_2$Cp$_2$˙(CO)$_2$(μ-SEt)$_2$](H$_4$-DCNQI) (5)

Since none of the attempts aimed at synthesizing a charge transfer salt comprising the [Fe$_2$Cp$_2$˙(CO)$_2$(μ-SEt)$_2$]$^+$ cation in combination with a non-centrosymmetric DCNQI anion, afforded crystals suitable for a crystal structure determination, it was decided to revert back to the use of a centrosymmetric DCNQI molecule, namely the unsubstituted DCNQI moiety, represented here as H$_4$-DCNQI.

The cyclic voltammogram of H$_4$-DCNQI, dissolved in CH$_2$Cl$_2$, was recorded. As reported in the literature,[225] the cyclic voltammogram consists of two reversible waves. The potential E_{1A}, associated with the (H$_4$-DCNQI)/(H$_4$-DCNQI)˙ couple was found to equal +0.14 V (see Table 2.1) giving a difference $|E_{1A}-E_{1D}|$ of 0.41 V. This value is substantially larger than the minimum value of 0.25 V for complete electron transfer,[140] thus suggesting that the charge transfer between [Fe$_2$Cp$_2$˙(CO)$_2$(μ-SEt)$_2$] and H$_4$-DCNQI will be complete.

Slow addition of $[Fe_2Cp_2^*(CO)_2(\mu\text{-}SEt)_2]$, dissolved in toluene, to a toluene solution of an equimolar amount of H_4-DCNQI results in the precipitation of a dark blue-black crude product. Attempts at recrystallizing this product from $CHCl_3$ or CH_3CN/THF mixtures for instance, generally resulted in extensive decomposition. The most efficient purification procedure involves adding a minimum amount of CH_3CN to a suspension of the product in toluene until it is completely dissolved. Filtration and reduction of the volume of this solution followed by slow cooling over *ca.* 36 hours results in the crystallization of the product as small dark-blue shiny plate-like crystals. The crystallization is however accompanied by the precipitation of small amounts of a brown powdery decomposition compound from which the product crystals have to be separated manually. Elemental analysis for C, H and N on the material thus obtained, is in agreement with an empirical formula $[Fe_2Cp_2^*(CO)_2(\mu\text{-}SEt)_2](H_4\text{-}DCNQI)$.

The solid state and solution infrared spectra of **5**, recorded as a KBr pellet or in CH_2Cl_2 solution, exhibits three peaks in the C-N stretching region (at 2160, 2124 and 2092 cm^{-1} in the solid state spectrum and at 2164, 2124 and 2098 cm^{-1} in the solution spectrum) and two peaks in the C-O stretching region (at 1978 and 1946 cm^{-1} in the solid state spectrum and at 1984 and 1947 cm^{-1} in the solution spectrum) as reported in Table 2.2. As was observed for all the other $[Fe_2Cp_2^*(CO)_2(\mu\text{-}SEt)_2](DCNQI)$ salts reported here, the increased electron density on the $(H_4\text{-}DCNQI)$ anion in **5** results in the $C\equiv N$ stretching peaks in its solid state spectrum to be shifted towards lower wavenumbers when compared with that observed for the neutral molecule (a single peak at 2176 cm^{-1} in the solid state spectrum). The peaks in the C-O stretching region in the solution spectrum of **5** occur at the same frequency as that observed for the other $[Fe_2Cp_2^*(CO)_2(\mu\text{-}SEt)_2](DCNQI)$ salts reported here. In the solid state spectrum however, these peaks are shifted by *ca.* 10 cm^{-1} towards higher wavenumbers when compared to the other $[Fe_2Cp_2^*(CO)_2(\mu\text{-}SEt)_2](DCNQI)$ salts (see Table 2.2). Although the exact cause for this shift is not known, it most probably is associated with a solid state packing effect.

Single crystals of the salt **5**, suitable for X-ray analysis could not be grown, since attempts at growing such crystals generally resulted in extensive decomposition of the salt.

The instability of the metallocene based dicyanoquinonediimine (DCNQI) charge transfer salts described in sections 2.4.4.1, 2.4.5.1 and 2.4.6.1 is not unprecedented. The only other reported examples of salts of this type, utilizing DCNQI's as acceptor molecules, are $[MCp_2^*](2,5-Me_2-DCNQI)^{(227)}$ (M = Fe, Mn). These salts are unstable in CH_2Cl_2 at room temperature and have to be prepared at -70°C. However, no explanation was offered for the observed instability.

In contrast to the DCNQI salts, the closely related TCNQ and TCNE salts of $[FeCp_2^*]^{(200, 201, 203)}$ do not exhibit the instability referred to in the above discussion. The same applies to the TCNQ and TCNE salts of $[Fe_2Cp_2^*(CO)_2(\mu-SEt)_2]$ (see sections 2.4.7 and 2.4.8). Based on these considerations and the evidence provided by the infrared spectroscopic studies on $[Fe_2Cp_2^*(CO)_2(\mu-SEt)_2](2-Cl-5-Me-DCNQI)$, it would seem that the instability of the metallocene based charge transfer salts of the DCNQI's stem from the instability of the acceptor anions.

Reports$^{(184, 230)}$ of charge transfer salts prepared from the reaction of TTF with various substituted DCNQI acceptor molecules contradict the above suggestion. Although the TTF salts were synthesized using dry solvents under an atmosphere of nitrogen, the products were obtained analytically pure directly from the reaction between the donor and acceptor molecules. No mention was made of any unusual instability associated with the products. In fact, single crystals of $(TTF)(H_4-DCNQI).2H_2O$ have been grown from wet chlorobenzene.$^{(230)}$. The yield of this crystallization was however reported to be very low.

From the above considerations, it would appear that the observed instability of the metallocene-based charge transfer salts of the DCNQI's cannot be attributed to either the donor or acceptor ions in isolation, but results from the unique combination of the molecular constituents in these salts.

One property which is associated with the unique combination of molecular units, is the lattice-energy associated with the crystallization of the salt. The more exothermic the lattice energy, the greater the stabilization of the crystalline state. Since the lattice energy is uniquely determined by the steric and electronic properties of the molecular constituents, differences in the lattice energies might explain why single crystals of $[Fe_2Cp_2^*(CO)_2(\mu-$

SEt)$_2$](2-Cl-5-Me-DCNQI) lose their internal order, whereas crystals of [Fe$_2$Cp$_2$*(CO)$_2$(μ-SEt)$_2$](2,5-Me$_2$-DCNQI) appear to be reasonably stable.

Considering the observed and reported instability of the metallocene-based charge transfer salts of the dicyanoquinonediimines, it was decided to utilize the well-known acceptor molecules 7,7,8,8-tetracyanoquinodimethane (TCNQ) and tetracyanoethylene (TCNE), which are known to form stable metallocene-based charge transfer salts,[200, 201, 203] in reactions with [Fe$_2$Cp$_2$*(CO)$_2$(μ-SEt)$_2$].

2.4.7 [Fe$_2$Cp$_2$*(CO)$_2$(μ-SEt)$_2$]$_2$(TCNQ)$_2$ (6)

2.4.7.1 Synthesis and spectroscopic studies on [Fe$_2$Cp$_2$*(CO)$_2$(μ-SEt)$_2$]$_2$(TCNQ)$_2$ (6)

A number of studies on the electrochemical properties of TCNQ have been published.[225, 234, 235] However, in order to make a direct comparison between the potentials, E$_{1A}$ associated with the (TCNQ)/(TCNQ)$^-$ couple and E$_{1D}$ of the [Fe$_2$Cp$_2$*(CO)$_2$(μ-SEt)$_2$]/ [Fe$_2$Cp$_2$*(CO)$_2$(μ-SEt)$_2$]$^+$ couple, the electrochemistry of TCNQ in CH$_2$Cl$_2$ solution was investigated. In accordance with the literature results, the cyclic voltammogram was found to consist of two reversible, one-electron reduction waves. The potential E$_{1A}$, associated with the (TCNQ)/(TCNQ)$^-$ couple was found to be equal to +0.14 V (see Table 2.1). The difference $|E_{1A}-E_{1D}|$ thus equals 0.41 V. Based on this difference in potentials, the charge transfer between [Fe$_2$Cp$_2$*(CO)$_2$(μ-SEt)$_2$] and TCNQ was expected to be complete.[140]

Slow addition of a 10% excess of [Fe$_2$Cp$_2$*(CO)$_2$(μ-SEt)$_2$], dissolved in a 1:4 CH$_3$CN/toluene mixture, to a solution of TCNQ in toluene, afforded an emerald green solution from which the product precipitated as a dark green microcrystalline solid upon reducing the volume of the solution *in vacuo*. The mother liquid was removed by filtration and the product washed with petroleum ether before drying it *in vacuo*. The material thus obtained was analytically pure, elemental analysis for C, H and N being consistent with the empirical formula [Fe$_2$Cp$_2$*(CO)$_2$(μ-SEt)$_2$](TCNQ).

The solid state and solution infrared spectra of **6** recorded as a KBr pellet or in CH$_2$Cl$_2$ solution, exhibits two peaks in each of the C-N stretching (peaks at 2178 and 2156 cm^{-1} in the solid state spectrum and at 2182 and 2154 cm^{-1} in the solution spectrum) and C-O

stretching regions (peaks at 1978 and 1941 cm^{-1} in the solid state spectrum and at 1984 and 1949 cm^{-1}, in the solution spectrum) as reported in Table 2.2.

In analogy with the observations for the DCNQI acceptor molecules, the reduction of TCNQ to $TCNQ^{-}$ and $TCNQ^{2-}$ results in a weakening of the $C \equiv N$ bonds as a consequence of electron density being placed in the LUMO of the TCNQ molecule, which is antibonding with respect to the $C \equiv N$ bonds. In the case of $TCNQ^{n-}$ (n = 0, -1, -2) a definite correlation between the charge, n, on the molecule and the frequencies of its C-N vibrational modes has been established.[236] This enables the deduction of the charge on a TCNQ moiety[237] by comparison of the vibrational frequencies of its C-N stretching modes with that of TCNQ species where the exact charge is known. These comparisons are normally made for infrared spectra recorded as a Nujol mull.

Despite the fact that the infrared spectra of $[Fe_2Cp_2^{*}(CO)_2(\mu\text{-}SEt)_2]_2(TCNQ)_2$ have been recorded in other media, the C-N vibrational frequencies associated with the salt **6** is in excellent agreement with those reported for $TCNQ^{-}$ and is substantially different from those reported for $TCNQ^{0}$ and $TCNQ^{2-}$ (see Table 2.6). This result confirms the suggestion based on the preliminary electrochemical investigation, that the reaction between $[Fe_2Cp_2^{*}(CO)_2(\mu\text{-}SEt)_2]$ and TCNQ will involve a complete one-electron transfer from the donor to the acceptor molecule.

The $C \equiv O$ stretching peaks in both the solid state and solution infrared spectra of $[Fe_2Cp_2^{*}(CO)_2(\mu\text{-}SEt)_2]_2(TCNQ)_2$ are shifted by between 70 and 90 cm^{-1} towards higher wavenumbers when compared with the neutral molecule. As noted for the DCNQI salts (see *e.g.* section 2.4.3.1) this shift is a result of the decreased electron density on the $[Fe_2Cp_2^{*}(CO)_2(\mu\text{-}SEt)_2]^{+}$ cation when compared to the neutral molecule **1**. It is also interesting to note that the frequencies of the C-O stretching modes in the solid state spectrum of this salt **6**, similar to that of $[Fe_2Cp_2^{*}(CO)_2(\mu\text{-}SEt)_2](H_4\text{-}DCNQI)$ (see section 2.4.6), occur at wavenumbers *ca.* 10 cm^{-1} higher than that of the other DCNQI salts reported (see Table 2.2). As in the case for the (H_4-DCNQI) salt, the exact reason for the difference is not known, and again is tentatively attributed to a solid state packing effect.

Table 2.6: _Infrared C≡N vibrational frequencies of TCNQ^n (n = 0, -1, -2) and **6**_

	C≡N Vibrational frequency (cm^{-1})
TCNQ^0	2226(m), 2222(m) [a]
TCNQ$^-$	2179(s), 2153(m) [a]
TCNQ^{2-}	2150(s), 2105(s) [a]
[Fe$_2$Cp$_2$*(CO)$_2$(μ-SEt)$_2$]$_2$(TCNQ)$_2$	2178(s), 2156(mw) [b]
[Fe$_2$Cp$_2$*(CO)$_2$(μ-SEt)$_2$]$_2$(TCNQ)$_2$	2182(s), 2154(w) [c]

[a]   Recorded as a Nujol mull[236].

Vibrational frequencies for TCNQ$^-$ and TCNQ^{2-} are averaged values,[236]

obtained from a consideration of a range of TCNQ$^-$ and TCNQ^{2-} salts.

[b]   Recorded as a KBr pellet.

[c]   Recorded as a CH$_2$Cl$_2$ solution.

2.4.7.2 Structural studies on [Fe$_2$Cp$_2$*(CO)$_2$(μ-SEt)$_2$]$_2$(TCNQ)$_2$ (**6**)

Single crystals of [Fe$_2$Cp$_2$*(CO)$_2$(μ-SEt)$_2$]$_2$(TCNQ)$_2$ were grown by dissolving the salt in a minimum amount of a 1:1 CH$_3$CN/toluene mixture at room temperature, heating the solution and reducing its volume _in vacuo_. On cooling this solution overnight to _ca._ -6°C, single dark-green block-like crystals were obtained.

[Fe$_2$Cp$_2$*(CO)$_2$(μ-SEt)$_2$]$_2$(TCNQ)$_2$ crystallizes in the space group _C2/c_. This is the same space group as found for the neutral donor molecule **1** and the (2,5-Me$_2$-DCNQI) salt **2**; however, the assymmetric unit in crystals of **1** comprises one half of the [Fe$_2$Cp$_2$*(CO)$_2$(μ-SEt)$_2$] molecule, and half of the cation and half of the anion in **2**, whereas the assymmetric unit in [Fe$_2$Cp$_2$*(CO)$_2$(μ-SEt)$_2$]$_2$(TCNQ)$_2$ comprises one full [Fe$_2$Cp$_2$*(CO)$_2$(μ-SEt)$_2$]$^+$ cation and a TCNQ moiety. The unit cell dimensions, a full list of internuclear distances and angles and other crystallographic data can be found in Tables 2.20 to 2.24 at the end of this chapter.

A diagram displaying the geometry of the cation and the numbering scheme employed, is provided in Figure 2.15 The $[Fe_2Cp_2^*(CO)_2(\mu\text{-}SEt)_2]^+$ cation is situated in a general equivalent position which implies that there are no crystallographically imposed symmetry relations between any of the constituent atoms or ligands in the cation. This again is in contrast to the structures of both the neutral molecule **1**, and the cation in the salt **2**, where a crystallographically imposed two-fold rotation axis passes through the centre of the Fe_2S_2 rhomboid. The cation in **6** can be considered to consist of two nearly identical $FeCp^*(CO)$- moieties bridged by two ethyl-mercapto ligands. The Cp^* ligands occur in a cis configuration with respect to the Fe-Fe vector and are staggered with respect to one another. A cis arrangement is also observed for the two carbonyl ligands with respect to the Fe-Fe vector, while the two S-C bonds of the ethyl-mercapto ligands define a syn conformation with respect to the S-S vector. The molecular geometry of the cation described thus far is analogous to that of the neutral molecule **1** and the cation in **2**. The difference in geometry between the cation in **6** and the latter two cases lies in the fact that the ethyl portions of the thio-ethyl ligands in **6** are syn-disposed with respect to the S-S vector, whereas the ethyl portions in **1** and **2** define an anti-relationship, as enforced by the two-fold rotation axis passing through the Fe_2S_2 rhomboid.

The Fe-Fe distance in the cation is 3.076(2)Å which represents a decrease of *ca.* 0.37Å when compared to the Fe-Fe distance in the neutral molecule **1**. The Fe-Fe distance in the (2,5-Me_2-DCNQI)-salt **2** is 3.083(1)Å. As was discussed for the (2,5-Me_2-DCNQI)-salt (see section 2.4.3.2), this decrease in the Fe-Fe distance in the $[Fe_2Cp_2^*(CO)_2(\mu\text{-}SEt)_2]^+$ cation is a result of the removal of an electron from the HOMO of the neutral molecule. Since this molecular orbital is antibonding with respect to the Fe atoms, the Fe-Fe bond order increases as manifested by the shortening of the Fe-Fe distance. Accompanying the decrease in the Fe-Fe distance is not only a decrease of the Fe-S-Fe angles from 98.3(1)° for the symmetry enforced equivalent angles in the neutral molecule to 86.2(1)° for both of the non-equivalent angles in the cation, but also a concomitant increase in the S-Fe-S angles from 80.1(1)° in the neutral molecule to 94.3(1)° and 93.3(1)°, with an average of 93.8°, in the cation. Both the Fe-S-Fe angles and the S-Fe-S angles in **6** are in good agreement with those observed in **2**. The dihedral angle between the planes defined by the two bridging S atoms and each of the two Fe atoms equals 179(6)°. This value is in
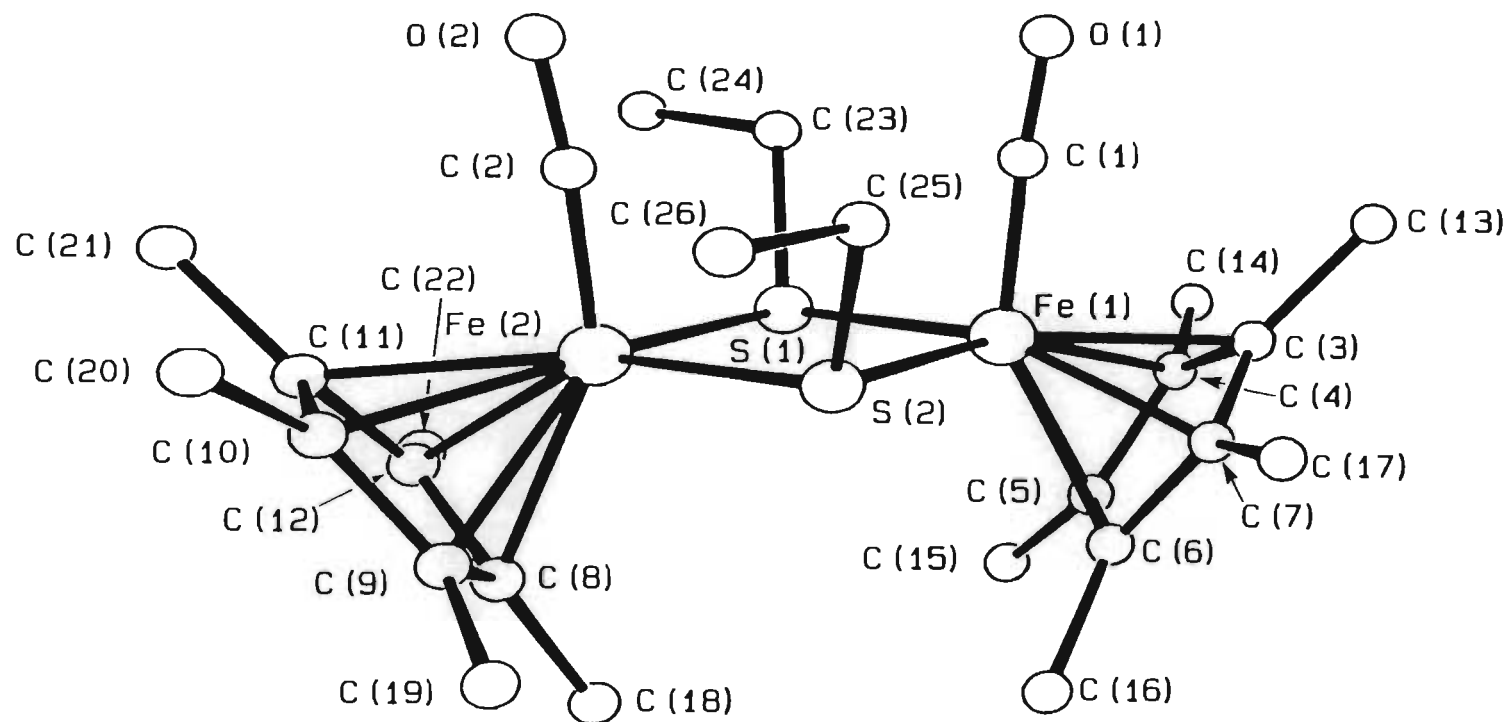
Figure 2.15 *The molecular geometry and numbering scheme employed for the cation in [Fe₂Cp₂·(CO)₂(μ-SEt)₂]₂(TCNQ)₂ (6).*
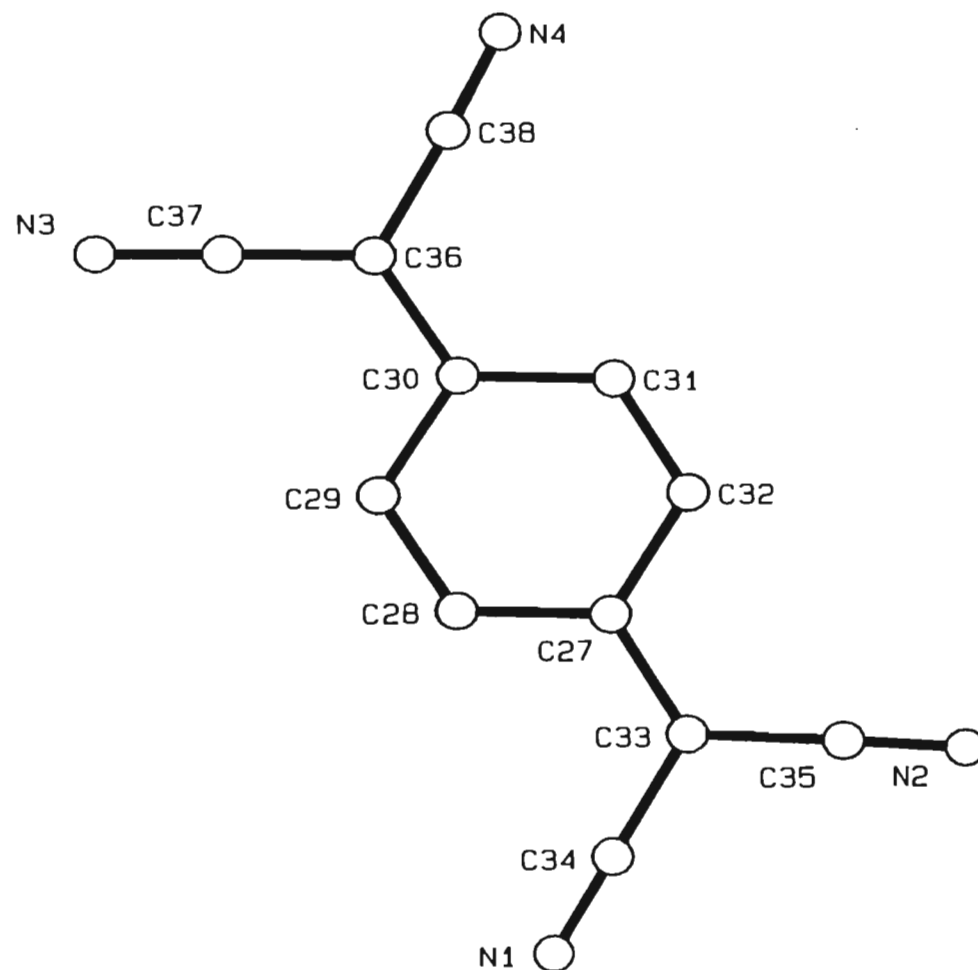
Figure 2.16 *The molecular geometry and numbering scheme employed for the anion in* $[Fe_2Cp_2^*(CO)_2(\mu\text{-}SEt)_2]_2(TCNQ)_2$ *(**6**).*

Table 2.7 *Bond parameters for selected TCNQ species (Å)*[a]

Compound	a	b	c	d	e	Charge	Reference
TCNQ	1.346	1.448	1.374	1.441	1.140	0	239
[TTP][TCNQ]	1.354	1.434	1.396	1.428	1.17	-½	240
RbTCNQ	1.373	1.423	1.420	1.416	1.153	-1	241
[CoCp*]₂[TCNQ]	1.382	1.403	1.457	1.413	1.165	-2	201
[Fe₂Cp₂˙(CO)₂(μ-SEt)₂]₂(TCNQ)₂ (**6**)	1.372	1.430	1.429	1.417	1.129	-1	This study
Theoretical	1.350	1.457	1.361	1.464	-	0	241
Theoretical	1.365	1.433	1.395	1.448	-	-1	241
Theoretical	1.39	1.42	1.44	1.42	1.145	-2	201

113

a)
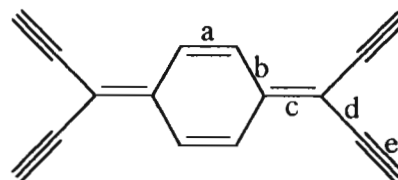
reasonable agreement with that of 172° observed in **2** and confirms the increase in the dihedral angle on oxidation of the $[Fe_2Cp_2^*(CO)_2(\mu\text{-SEt})_2]$ molecule. The Fe-S distances vary between 2.233(3) and 2.207(2)Å with an average of 2.250Å. This corresponds to the average Fe-S distance of 2.253Å observed in **2** and represents a decrease of 0.027Å when compared to the average Fe-S distance in the neutral molecule **1**. The Fe-C distances for the two non-equivalent Fe-Cp* moieties vary between 2.092(9) and 2.177(9)Å with an average of 2.135Å for Fe(1) and between 2.125(10) and 2.174(9)Å with an average of 2.147Å for Fe(2). These values are in accordance with those observed in **2** and confirm the elongation of the Fe-C bond distance (also observed in **2**) upon oxidizing the neutral molecule **1**.

A diagram displaying the molecular geometry of the TCNQ moiety and the numbering scheme employed is provided in Figure 2.16 The TCNQ species is situated in a generally equivalent position and is essentially planar with the C≡N groups showing a slight deviation from the plane defined by the other constituent atoms (maximum displacement of a nitrogen atom from the mean plane equals *ca.* 0.2Å). This deviation in all likelihood results from a combination of molecular packing and electrostatic factors as will be described below. From the fact that the charge on the $[Fe_2Cp_2^*(CO)_2(\mu\text{-SEt})_2]^+$ cation is +1, and as suggested from the electrochemical and infrared spectroscopic studies, the charge on the TCNQ moiety equals -1. Further confirmation for this assertion can be obtained from a comparison of the observed structural parameters of the TCNQ species with those derived from theoretical considerations and observed in TCNQ moieties with a charge equal to 0, -½, -1, or -2.[201, 202] The averaged bond parameters observed in the present case (with exclusion of the C≡N bonds) are in good agreement with those observed in RbTCNQ (see Table 2.7) and strongly support the notion of a full negitive charge per TCNQ moiety.

A consideration of the unit cell contents, as seen in a view along the [b]-axis (see Figure 2.17) reveals that, as in the case of the neutral molecule **1** and the (2,5-Me$_2$-DCNQI)-salt **2**, the formula units are arranged in rows within the unit cell, these rows being at an angle of *ca.* 33° with the [a]-axis. Isolating one of these rows and adding an analogous row produced by a unit cell translation along the [b]-axis (see Figure 2.18), reveals that the rows comprise isolated $D^+A_2^{2-}D^+$ units "strung" together to produce the overall $...[D^+(A_2)^{2-}D^+][D^+(A_2)^{2-}D^+][D^+(A_2)^{2-}D^+]...$ structure. The formation of the $D^+(A_2)^{2-}D^+$

114
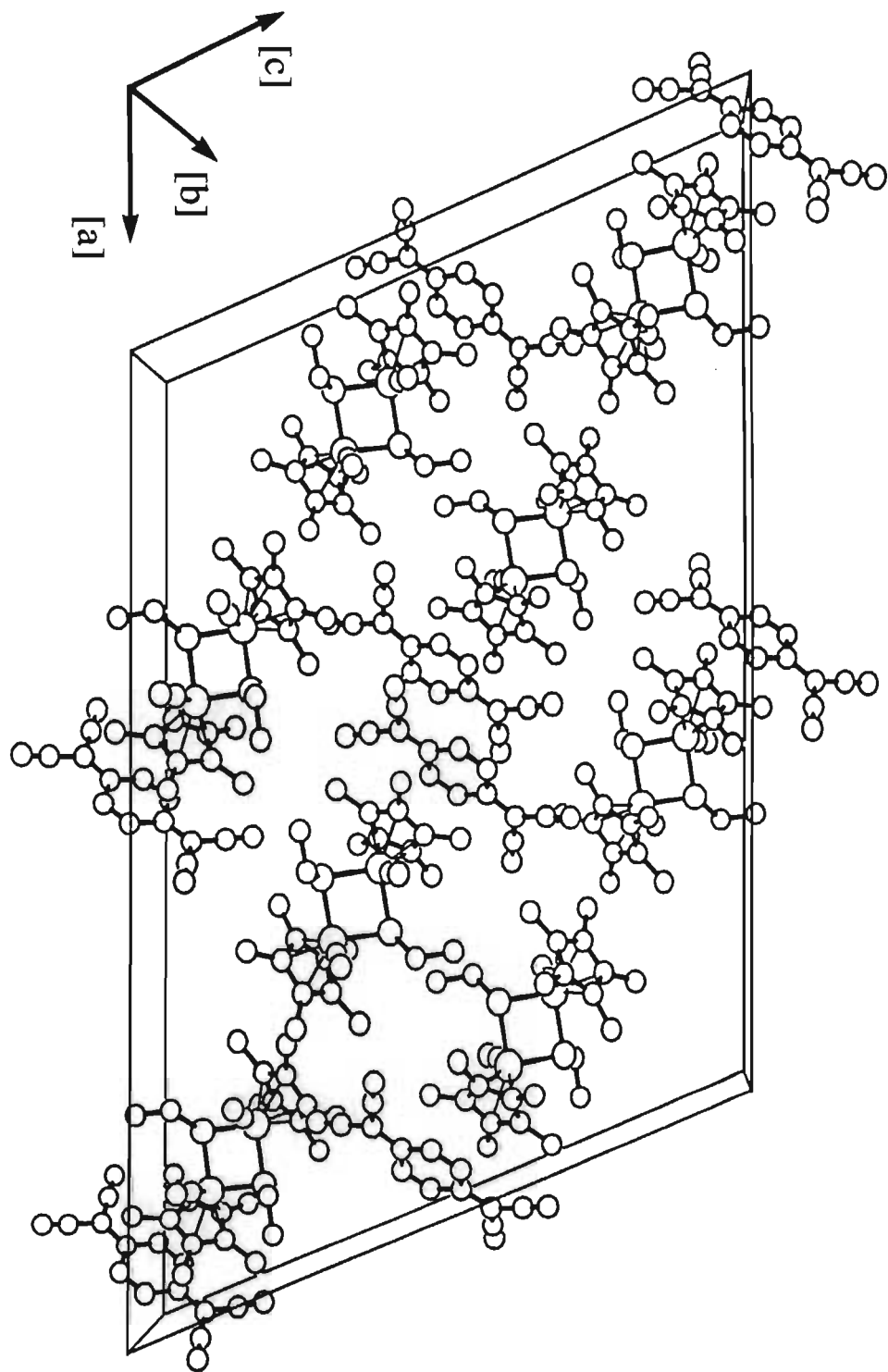
Figure 2.17 The unit cell contents of [Fe₂Cp₂*(CO)₂(μ-SEt)₂]₂(TCNQ)₂ (6) as seen in a view along the [b]-axis.
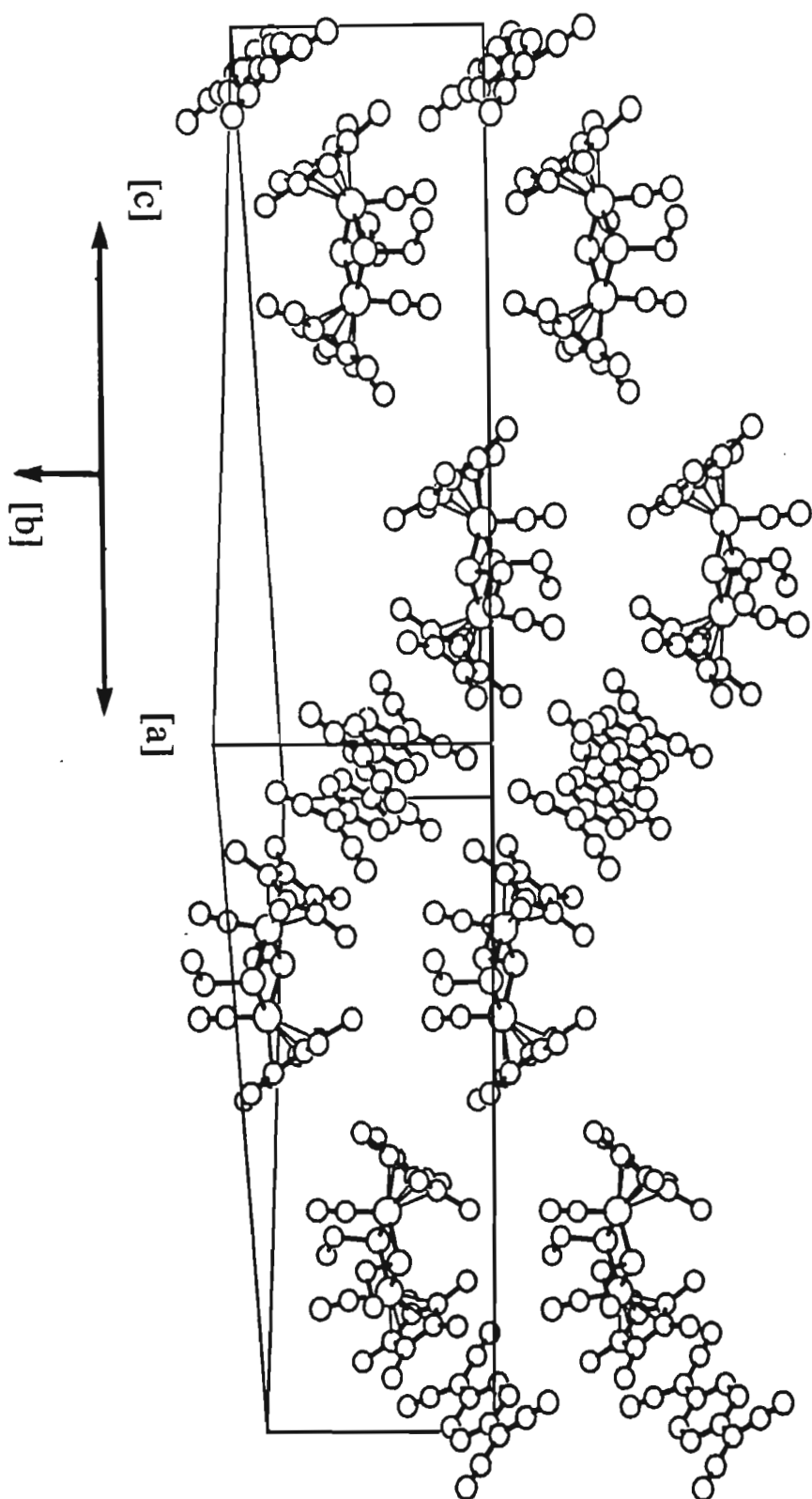
Figure 2.18 The "rows" of cations and anions comprising the crystal lattice of [Fe$_2$Cp$_2$$^\bullet$(CO)$_2$($\mu$-SEt)$_2$]$_2$(TCNQ)$_2$ (**6**).

tetradic units have been ascribed [200] to the complete transfer of a unit negative charge (e) between the donor and TCNQ to produce the TCNQ^{-} radical anion, together with a strong tendency of this anion to dimerize. The isolated nature of the $D^{+}(A_2)^{2-}D^{+}$ units results from the fact that one of the Cp* ligands of each cation in the unit is arranged virtually perpendicular to the analogous Cp* ligand of its neighbouring cation from the next $D^{+}(A_2)^{2-}$ D^{+} unit. As a consequence of this arrangement, there are no extended interactions associated with this mode of packing in $[Fe_2Cp_2^{*}(CO)_2(\mu\text{-}SEt)_2]_2(TCNQ)_2$. The second Cp* ligand of the cation participates in a face-to-face arrangement which can be represented as $Cp^{*},(TCNQ)_2^{2-},Cp^{*}$. Despite the difference in the environment of the two Cp* ligands on the cation, a comparison of the structural parameters associated with the ligands, revealed no obvious difference between the two ligands.

The Cp* ligands, and similarly the TCNQ^{-} anions in the $Cp^{*},(TCNQ)_2^{2-},Cp^{*}$ arrangement are interelated by a crystallographically imposed centre of inversion, situated midway between the TCNQ^{-} anions. The presence of this centre implies that the planes defined by the consitutent atoms of the two Cp* ligands are necessarily parallel to each other. The same applies to the planes of the TCNQ^{-} anions, the interplanar distance between the anions being 3.262Å, which is substantially smaller than 3.45Å, the Van der Waals spacing for π-aromatic species occuring in a face-to-face arrangement. [242]

The small intermolecular distance between the TCNQ anions is indicative of substantial π-π interaction between the anions. This interaction, together with the parallel arrangement of the TCNQ^{-} anions confirm that the anions do not exist as two separate entities, but rather as a dimeric $(TCNQ)_2^{2-}$ anion. The existence of such TCNQ anion dimers is well established in the literature, two examples being $[Nb_3(\mu\text{-}Cl)_6(C_6Me_6)_3]^{2+}(TCNQ)_2^{2-}$ [243] and $[FeCp_2^{*}]_2^{+}(TCNQ)_2^{2-}$ [200]. The interplanar distance between the anions in these dimers is somewhat shorter than that of 3.262Å observed in the present study; the interplanar distance in $[Nb_3(\mu\text{-}Cl)_6(C_6Me_6)_3]^{2+}(TCNQ)_2^{2-}$ being 3.10Å and that in $[FeCp_2^{*}]_2^{+}(TCNQ)_2^{2-}$ being 3.147Å.

A projection of the $(TCNQ)_2^{2-}$ dimer in **6** onto a plane parallel to that of the constituent anions (see Figure 2.19), reveals that the TCNQ anions are offset along the long molecular axis, giving rise to ring-over-exocyclic-double-bond type overlap. This is analogous to the
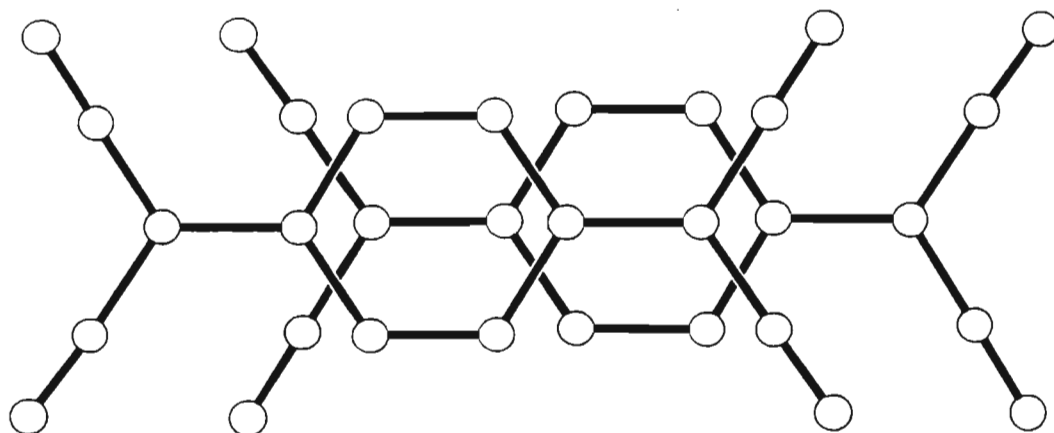
Figure 2.19 _A projection of the (TCNQ)$_2{}^{2-}$ dimer in [Fe$_2$Cp$_2{}^*$(CO)$_2$(μ-SEt)$_2$]$_2$(TCNQ)$_2$_

(**6**) onto a plane parallel to that of the constituent anions

situation observed in [Nb$_3$(μ-Cl)$_6$(C$_6$Me$_6$)$_3$]$^{2+}$(TCNQ)$_2{}^{2-}$, but contrasts to that in [FeCp$_2$*]$_2{}^+$(TCNQ)$_2{}^{2-}$, where the offset is along the short molecular axis, resulting in ring-ring overlap. The C≡N moieties in **6**, as mentioned in the discussion of the molecular geometry of the TCNQ⁻ anions, deviate slightly from the plane defined by the rest of the anion. This deviation is also observed in the dimeric anions of both [Nb$_3$(μ-Cl)$_6$(C$_6$Me$_6$)$_3$]$^{2+}$(TCNQ)$_2{}^{2-}$ and [FeCp$_2$*]$_2{}^+$(TCNQ)$_2{}^{2-}$, and is such that the C≡N moieties bend away from the second member in the dimer. The reason for this deviation from planarity is most probably associated with Coulombic repulsions between the electron density residing on the cyano groups of the TCNQ⁻ anions.

In the earlier discussion, the planes of the Cp* ligands, and similarly those of the TCNQ⁻ anions of the Cp*,(TCNQ)$_2{}^{2-}$,Cp* sequence were described as being parallel as a consequence of symmetry resulting from the presence of a crystallogaphically enforced centre of inversion. This symmetry restriction however, does not apply to the orientation of the planes of the Cp* ligands with respect to that of the (TCNQ)$_2{}^{2-}$ anion. Nonetheless, the plane of the Cp* ligands arc virtually parallel to that of the (TCNQ)$_2{}^{2-}$ dimer, the dihedral angle being 2.04° with the avarage interplanar spacing between the Cp* ligand and the closest TCNQ⁻ anion being 3.617Å (see Figure 2.20). This distance is slightly longer than

that of 3.554Å observed in the analogous $Cp^{\bullet}$,$(TCNQ)_2^{2-}$,$Cp^{\bullet}$ arrangement in $[FeCp_2^{\bullet}]_2(TCNQ)_2$.

3,617Å

3,262 Å

3,617Å
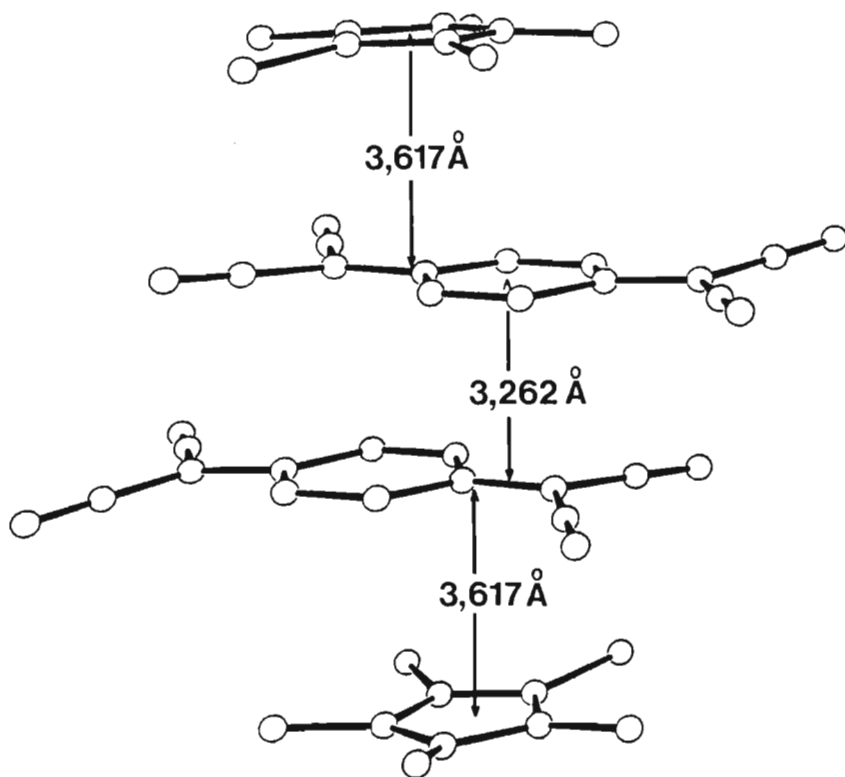
Figure 2.20   *Pertinent distances associated with the $Cp^{\bullet}$,$(TCNQ)_2^{2-}$,$Cp^{\bullet}$ arrangement in $[Fe_2Cp_2^{\bullet}(CO)_2(\mu\text{-}SEt)_2]_2(TCNQ)_2$*

The crystal structure of **6**, as described above, is virtually identical to that of $[FeCp_2^*]_2(TCNQ)_2$. The structure of the latter also consists of isolated $D^+(A_2)^2D^+$ units in which one of the $Cp^{\bullet}$ ligands of each cation is arranged virtually perpendicular to that of a cation from the neighbouring $D^+(A_2)^2D^+$ unit, whilst the other form part of a $Cp^{\bullet}$,$(TCNQ)_2^{2-}$,$Cp^{\bullet}$ sequence. One of the most noticeable differences between the structures of **6** and $[FeCp_2^*]_2(TCNQ)_2$ is that whereas the $D^+(A_2)^2D^+$ units in $[FeCp_2^*]_2(TCNQ)_2$ approximate to being linear, the analogous units in **6** exhibit distinct deviations from linearity as a result of the cis configuration of the $Cp^{\bullet}$ ligands on the $[Fe_2Cp_2^{\bullet}(CO)_2(\mu\text{-}SEt)_2]^+$ cation. Furthermore, as pointed out above, the overlap of the $TCNQ^{\bullet}$ anions in the $(TCNQ)_2^{2-}$ dimers, as well as the interplanar distances between the $Cp^{\bullet}$ ligands and the $(TCNQ)_2^{2-}$ dimer, and between the $TCNQ^{\bullet}$ anions constituting the $(TCNQ)_2^{2-}$ dimers, are different.

It is clear that although there is complete charge transfer between the donor and acceptor molecules in **6**, the arrangement of the donor and acceptor ions in isolated $D^+(A_2)^{2-}D^+$ units does not comply with the prerequisite of extended .... $D^+A^-D^+A^-$.... chains required for the achievement of extended ferromagnetic interactions in the solid state. Based on this consideration, only the room temperature magnetic susceptibility of **6** was determined.

2.4.7.3 Magnetic studies on $[Fe_2Cp_2^*(CO)_2(\mu-SEt)_2]_2(TCNQ)_2$ (**6**)

Based on the lack of extended interactions in the solid state structure of **6**, and the close analogy between its structure and that of $[Fe_2Cp_2^*]_2(TCNQ)_2$ where the magnetic susceptibility varies with temperature according to the Curie Law, *i.e.* no magnetic interaction between the unpaired electron spins in the salt, it is to be expected that there will be no magnetic coupling between the unpaired electron spins in $[Fe_2Cp_2^*(CO)_2(\mu-SEt)_2]_2(TCNQ)_2$ either.

The room temperature effective magnetic moment, μ_{eff} [$= (8\chi.T)^{\frac{1}{2}}$], corrected for diamagnetic contributions from both the donor and acceptor ions, has been determined as 2.76 μ_B, which approximates to the spin only value of 2.45 μ_B predicted for two independent spins per formula unit. However, it is significantly smaller than 3.46 μ_B, the spin only value corresponding to 4 independent spins per formula unit. The fact that the observed susceptibility approximates to two independent spins per $[Fe_2Cp_2^*(CO)_2(\mu-SEt)_2]_2(TCNQ)_2$ unit, and not four, is a consequence of the dimerization of the $TCNQ^-$ radical ions. On dimerization, the two unpaired electrons on the $TCNQ^-$ anions are paired and occupy a dimer bonding orbital, resulting in the dimeric $(TCNQ)_2^{2-}$ anion being a S = 0 system. This leaves only two unpaired electrons, one on each cation per $[Fe_2Cp_2^*(CO)_2(\mu-SEt)_2]_2(TCNQ)_2$ unit. The same situation is found in $[Fe_2Cp_2^*]_2(TCNQ)_2$, where strong antiferromagnetic coupling between the unpaired electrons on the constituent $TCNQ^-$ anions of the dimeric anion, results in the only observed coupling being the very weak interaction between the unpaired electrons on the $[Fe_2Cp_2^*]^+$ cations. This is reflected by the observed effective magnetic moment, μ_{eff} for $[Fe_2Cp_2^*]_2(TCNQ)_2$ of 2.54 μ_B which, as that reported here for $[Fe_2Cp_2^*(CO)_2(\mu-SEt)_2]_2(TCNQ)_2$, approximates to the spin only value for two independent spins per formula unit.

The effective magnetic moment in **6** (= 2.76μ_B), as mentioned above and observed in **2** (= 2.72 μ_B), is somewhat larger than the value predicted using a spin-only approach (2.45 μ_B). In the case of **2** the increased magnetic moment was attributed to an angular momentum contribution form the cation (see section 2.4.3.3). The [Fe$_2$Cp$_2^*$(CO)$_2$(μ-SEt)$_2$]$^+$ cation is common to both **2** and **6**, so that due to this contribution from the cation, the magnetic moment in **6** would in fact be expected to be somewhat larger than that predicted from a spin-only treatment.

In an attempt to increase the overall spin density of the charge transfer salt and to possibly avoid the dimerization of the acceptor anions, it was deemed appropriate to replace TCNQ with tetracyanoethylene, TCNE, in the reaction with [Fe$_2$Cp$_2^*$(CO)$_2$(μ-SEt)$_2$].

2.4.8 [Fe$_2$Cp$_2^*$(CO)$_2$(μ-SEt)$_2$](TCNE) (**7**)

2.4.8.1 Synthesis and spectroscopic studies on [Fe$_2$Cp$_2^*$(CO)$_2$(μ-SEt)$_2$](TCNE) (**7**)

The electrochemical properties of TCNE were investigated in order to determine the potential difference $|E_{1A}-E_{1D}|$ for the reaction of TCNE with [Fe$_2$Cp$_2^*$(CO)$_2$(μ-SEt)$_2$]. As reported in the literature[234,243], the cyclic voltammogram of TCNE, recorded in CH$_2$Cl$_2$, consists of 2 reversible one-electron reduction waves. The potential E_{1A} was found to equal +0.21 V (see Table 2.1). The difference $|E_{1A}-E_{1D}|$ for the combination of [Fe$_2$Cp$_2^*$(CO)$_2$(μ-SEt)$_2$] and TCNE thus equals 0.48 V, indicating that complete electron transfer between the donor and acceptor molecules is feasible[140].

Slow addition of TCNE, dissolved in toluene, to a *ca.* 5% excess of [Fe$_2$Cp$_2^*$(CO)$_2$(μ-SEt)$_2$] in toluene, afforded [Fe$_2$Cp$_2^*$(CO)$_2$(μ-SEt)$_2$](TCNE) as a green-black microcrystalline material which was isolated through filtration. Subsequent purification involved washing with toluene and diethyl ether to obtain an analytically pure product with a composition, as confirmed by elemental analysis for C,H and N, conforming with the empirical formula [Fe$_2$Cp$_2^*$(CO)$_2$(μ-SEt)$_2$][TCNE].

The solid state and solution infrared spectra of the salt **7**, recorded as a KBr pellet or in the CH$_2$Cl$_2$ solution, exhibits two peaks in each of the C-N stretching (peaks at 2188 and 2148 cm^{-1} in the solid state spectrum and at 2187 and 2147 cm^{-1} in the solution

spectrum) and C-O stretching regions (peaks at 1978 and 1946 cm^{-1} in the solid state and 1983 and 1947 cm^{-1} in the solution spectrum, see Table 2.2).

Reduction of the TCNE molecule to its corresponding mono- and dianion involves placing electron density in the LUMO which, in exact analogy to TCNQ and members of the DCNQI series, is antibonding with respect to the C and N of the C≡N bonds and results in a weakening of these bonds. This weakening of the C≡N bonds manifests itself in a decrease of the frequencies of the C-N stretching modes associated with the species, and in the case of TCNE and TCNQ, have been established as a means of deducing the charge on a polycyano moiety.[236, 237] The frequencies of the C-N stretching modes observed in the infrared spectra of [Fe$_2$Cp$_2$*(CO)$_2$(μ-SEt)$_2$](TCNE), together with that for TCNE^0, TCNE$^-$ and TCNE^{2-}, as found in the literature [236], are listed in Table 2.8.

Table 2.8 *Infrared C≡N vibrational frequencies for TCNE^n (n = 0, -1, -2) and* ___7___

	C≡N Vibrational frequency (cm^{-1})
TCNE^0	2259(s), 2221(m)[a]
TCNE$^-$	2183(s), 2144(s)[a]
TCNE^{2-}	2104(s), 2069(s)[a]
[Fe$_2$Cp$_2$*(CO)$_2$(μ-SEt)$_2$](TCNE)	2188(mw), 2148(m)[b]
[Fe$_2$Cp$_2$*(CO)$_2$(μ-SEt)$_2$](TCNE)	2187(w), 2147(m)[c]

[a]   From reference 236, recorded as a Nujol mull

[b]   This work, recorded as a KBr pellet

[c]   This work, recorded in CH$_2$Cl$_2$ solution

Although the frequencies of the C-N stetching modes of TCNE^n (n = 0, -1, -2) in Table 2.8, are for spectra recorded as Nujol mulls, the C-N stretching peak positions observed in the infrared spectra of ___7___, both in the solid state and solution spectra, are in excellent agreement

with that reported for TCNE⁻ and substantially different from the values associated with TCNE⁰ and TCNE²⁻. Based on this result, it can be concluded that one full unit of negative charge (e) is associated with the TCNE anion and thus that, as predicted from the preliminary electrochemical investigation, the reaction between $[Fe_2Cp_2^*(CO)_2(\mu\text{-SEt})_2]$ and TCNE involves complete transfer of one electron from the donor to the acceptor molecule.

The C-O stretching peaks in both the solid state and solution spectra of $[Fe_2Cp_2^*(CO)_2(\mu\text{-SEt})_2]$(TCNE) are shifted by between 60 and 90 cm⁻¹ towards higher wavenumbers when compared to the spectrum of the neutral molecule. This shift has been observed in the spectra of all the other charge transfer salts studied in this work (see section 2.4.3.1 for instance) and is consistent with the decreased electron density on the cation when compared to the neutral molecule. It is also of interest to note that frequencies of the C-O stretching modes in the solid state spectrum of $[Fe_2Cp_2^*(CO)_2(\mu\text{-SEt})_2]$(TCNE), analogous to that in the (TCNQ) **6** and (H₄-DCNQI)-salt **5**, occur at wavenumbers ca. 10 cm⁻¹ higher than that associated with the (2,5-Me₂-DCNQI) **2**, (2-Cl-5-Me-DCNQI) **3** and (2-Me-DCNQI) **4** salts. This effect is not observed in the solution infrared spectra (see Table 2.2), suggesting that its origin most probably is associated with a solid state effect. A more exact assignment will however not be attempted here.

2.4.8.2 Structural studies on $[Fe_2Cp_2^*(CO)_2(\mu\text{-SEt})_2]$(TCNE) (**7**)

Single crystals of $[Fe_2Cp_2^*(CO)_2(\mu\text{-SEt})_2]$(TCNE) were grown by dissolving the salt in a minimum amount of a 1:1 CH₃CN/toluene mixture, heating the solution and reducing the volume *in vacuo*. Cooling the solution to ca. -20°C and storing it at this temperature for a period in excess of two weeks resulted in the formation of dark green-black needle-like crystals.

$[Fe_2Cp_2^*(CO)_2(\mu\text{-SEt})_2]$(TCNE) crystallizes in the space group $P2_1/n$, in contrast to the neutral donor molecule **1**, the (2,5-Me₂-DCNQI) and the (TCNQ) salts which all crystallize in the space group $C2/c$. The unit cell of $[Fe_2Cp_2^*(CO)_2(\mu\text{-SEt})_2]$(TCNE) contains four formula units, with one full formula unit per asymmetric unit. The unit cell dimensions, a full list of bond lengths, angles and other crystallographic data are collated in Tables 2.25 to 2.29 at the end of this chapter.

A diagram, displaying the molecular geometry of the cation and the numbering scheme employed, is provided in Figure 2.21. The cation is located in a general equivalent position. This is exactly analogous to [Fe₂Cp₂*(CO)₂(μ-SEt)₂](TCNQ) **6**, and implies that, in contrast to the neutral molecule **1** and the (2,5-Me₂-DCNQI) salt **2**, there are no crystallographically enforced symmetry relations between any of the constituent atoms or ligands of the cation in **7**. The cation in the present case, as in the salts **2** and **6** and the neutral molecule **1**, can be considered to consist of two nearly identical FeCp*(CO) moieties bridged by the two ethyl-mercapto ligands. The two Cp* ligands occur in a cis arrangement with respect to the Fe-Fe vector and define a staggered configuration. A cis arrangement is also observed for the two carbonyl ligands with respect to the Fe-Fe vector, and similarly for the S-C bonds of the ethyl-mercapto ligands with respect to the S-S vector. The ethyl groups of the ethyl-mercapto ligands occur in an anti conformation with respect to the S-S vector. This is analogous to the anti arrangement in the neutral molecule **1** and the (2,5-Me₂-DCNQI) salt **2** where this arrangement is the result of crystallographically enforced symmetry, but contrasts to the syn arrangement of the ethyl groups observed in [Fe₂Cp₂*(CO)₂(μ-SEt)₂](TCNQ), where, as in the present case, there are no crystallographically enforced symmetry restrictions imposed on the cation.

The Fe-Fe distance is 3.068(2)Å, which is comparable to the distances of 3.083(1)Å and 3.076(2)Å observed in **2** and **6** respectively, but is *ca.* 0.38Å shorter than that observed in the neutral molecule **1**. As discussed in section 2.4.3.2, this shortening of the Fe-Fe distance is the result of the removal of an electron from the HOMO which is antibonding with respect to the Fe atoms. The decrease in the Fe-Fe distance on oxidation results in a decrease in the Fe-S-Fe angles from 98.3(1)° in the neutral molecule to 86.0(1)° and 86.2(1)° with an average of 86.1° in the cation and a concomitant increase in the S-Fe-S angles from 80.1(1)° before oxidation, to 93.9(1)° for both angles in the cation. The Fe-S-Fe and S-Fe-S angles in **7** are in good agreement with that observed in both **2** and **6**. In [Fe₂Cp₂*(CO)₂(μ-SEt)₂](TCNE), the dihedral angle between the planes defined by the two bridging S atoms and each one of the two Fe atoms equals 177(1)°. This is in good agreement with the vaules of 172° and 179° observed in **2** and **6** respectively. The Fe-S bond distance varies between 2.243(3) and 2.252(3)Å with an average of 2.248Å, compared to distances of 2.253 and 2.250Å in **2** and **6** respectively, and represent a
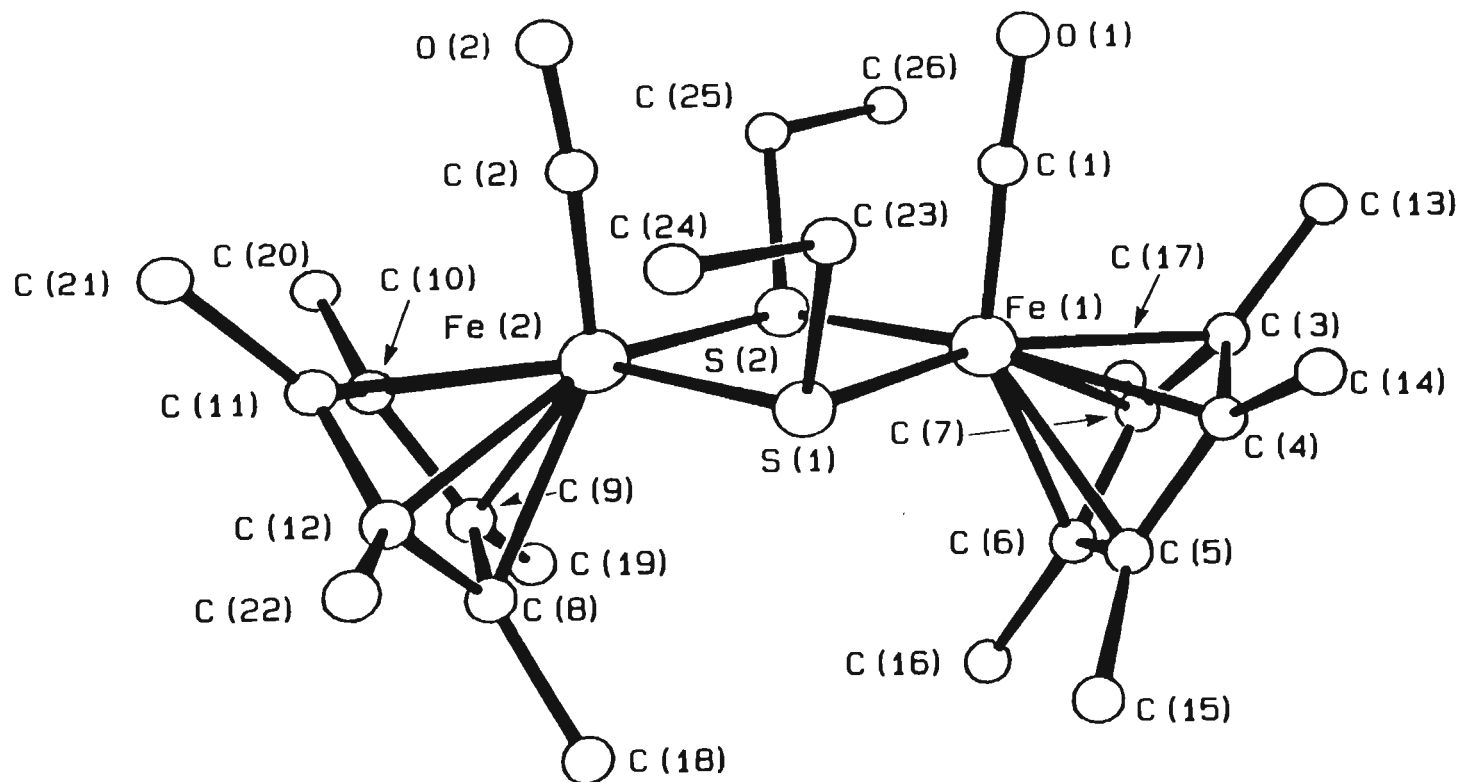
Figure 2.21   *The molecular geometry and the numbering scheme employed for the cation in [Fe₂Cp₂*(CO)₂(μ-SEt)₂](TCNE) (7).*

decrease of 0.029Å when compared to the Fe-S distance in the neutral molecule. The Fe-C distances (C of Cp* ligand) vary between 2.104(11) and 2.166(11)Å with an average of 2.134Å on Fe(1), and between 2.100(11) and 2.171(11)Å with an average of 2.130Å on Fe(2). Again these values are consistent with those observed in **2** and **6** and confirm an elongation of *ca.* 0.034Å in the Fe-C distance on oxidation of the neutral molecule.

The asymmetric unit contains two separate TCNE half-units, which implies that two crystallographically independent groups of TCNE ions exist in the crystal lattice. The TCNE ions from each of these groups are situated on crystallographic centres of inversion. In order to distinguish between TCNE ions from the two different groups, they will be referred to as A and B in the subsequent discussion, with members from either group being denoted as $TCNE_A$ or $TCNE_B$.
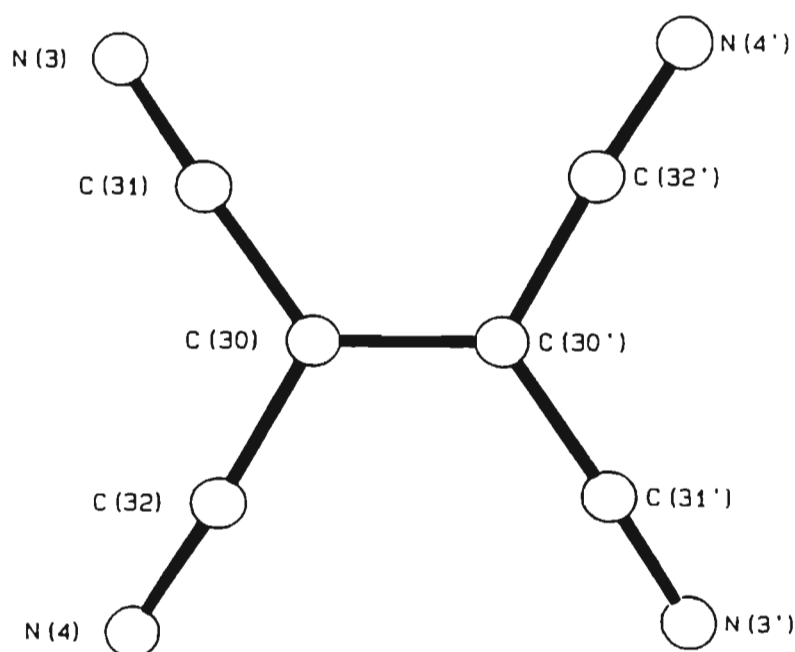
Figure 2.22   *The molecular geometry and numbering scheme employed for $TCNE_A$*
in [Fe$_2$Cp$_2$(CO)$_2$(μ-SEt)$_2$](TCNE) (**7**)*

A diagram depicting the molecular geometry and the numbering scheme employed for $TCNE_A$ is provided in Figure 2.22. The ion is essentially planar (the maximum deviation from the least squares plane being 0.050Å) with a central C=C bond distance of 1.326Å. The C-CN bond distances are 1.426(22) and 1.421(23)Å and average 1.424Å, whilst the C≡N bond distances are 1.085(19) and 1.141(31)Å with an average of 1.113Å. Similar to

126

what was described for TCNQ (see section 2.4.7.2), and members of the DCNQI series (see section 2.4.3.2), the charge, n, on a $TCNE^n$ species can be confirmed through comparison of the observed structural parameters of the species with that found in the literature for TCNE species of known charge. In this way, Miller has noted [245] an increase of 0.08Å in the length of the central C=C bond and concomitant decreases of 0.03Å and 0.02Å in the lengths of the C-CN and C≡N bonds respectively, on reduction of the neutral TCNE molecule to the mono-anionic species. The averaged bond lengths observed for $TCNE_A$ in **7**, together with those reported for $TCNE^0$, $TCNE^-$ and $TCNE^{2-}$, are provided in Table 2.9.

Table 2.9: *Bond parameters for selected TCNE species (Å)[a]*

Compound	a	b	c	Charge	Reference
TCNE	1.355	1.1431	1.160	0	244
$[FeCp_2^*](TCNE)$	1.392	1.417	1.140	-1	203
$[CoCp_2^*]_2(TCNE)$	1.49	1.392	1.166	-2	245
$TCNE_A$ in **7**	1.326	1.424	1.113	-1	This study

(a)
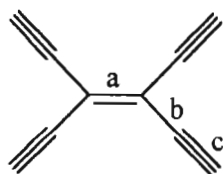
Although the bond lengths observed for $TCNE_A$ generally are in good agreement with the literature results, no firm conclusions about the charge on the anion can be based on these lengths because of the size of the standard errors associated with the bond lengths in the present structure.

A detailed discussion of the molecular geometry of $TCNE_B$ is also inappropriate since the anion was not well resolved. As evidenced by the thermal factors associated with the

constituent atoms of $TCNE_B$ (see Table 2.27), the lack of resolution can be attributed to thermal disorder.

The overall structure of $[Fe_2Cp_2^*(CO)_2(\mu\text{-}SEt)_2](TCNE)$ can be described as consisting of sheets of donor and acceptor ions which are parallel to the ab-plane. Each of these sheets consists of rows of alternating donor and acceptor ions. A diagram depicting this arrangement as projected onto the ab-plane, is provided in Figure 2.23. This figure also reveals that only one of the Cp^* ligands of each cation participates in a face-to-face arrangement which can be represented as $Cp^*,TCNE,Cp^*$ and involves the $TCNE_B$ anion. The cations and anions in one sheet are related to those in the next through n-glide planes. As a consequence of this symmetry relationship, the rows in which the cations and anions occur in one sheet, is virtually at right angles to the rows from the next sheet when projected onto the ab-plane (see Figure 2.24).

The Cp^* ligands within the face-to-face arrangement are related by a crystallographically enforced centre of inversion, which implies that the planes defined by their constituent atoms are necessarily parallel. The $TCNE_B$ anion is situated on the centre of the inversion, thus implying that there is no crystallographically enforced orientation for the plane defined by its constituent atoms relative to the plane of the Cp^* ligands. The plane of the $TCNE_B$ anion nonetheless is close to being parallel to that of the Cp^* ligands, the dihedral angle between the planes being 4.1° with an average interplanar spacing (Cp^* to $TCNE_B$) of ca. 3.68Å. This distance is slightly larger than the 3.51Å separation reported for $[FeCp_2^*](TCNE)$[203] and that of 3.45Å predicted from Van der Waals radii as an upper limit for π-aromtic interaction.[242]

The second Cp^* ligand on each cation also forms part of a $Cp^*, TCNE^{n-}, Cp^*$ sequence, in this instance involving the $TCNE_A$ anion. The Cp^* ligands in this sequence, similar to those in the sequence involving $TCNE_B$, are related by a crystallographically imposed centre of inversion, thus implying that the planes defined by their constituent atoms are necessarily parallel. Furthermore, the $TCNE_A$ anion, analogous to the $TCNE_B$, is situated on a crystallographically imposed centre of inversion. Despite these similarities, the Cp^* ligands and the $TCNE_A$ anion are not arranged face-to-face. The reason for this is two-fold. Firstly, the lateral displacement of the Cp^* ligands, i.e. parallel to the planes of the ligands,
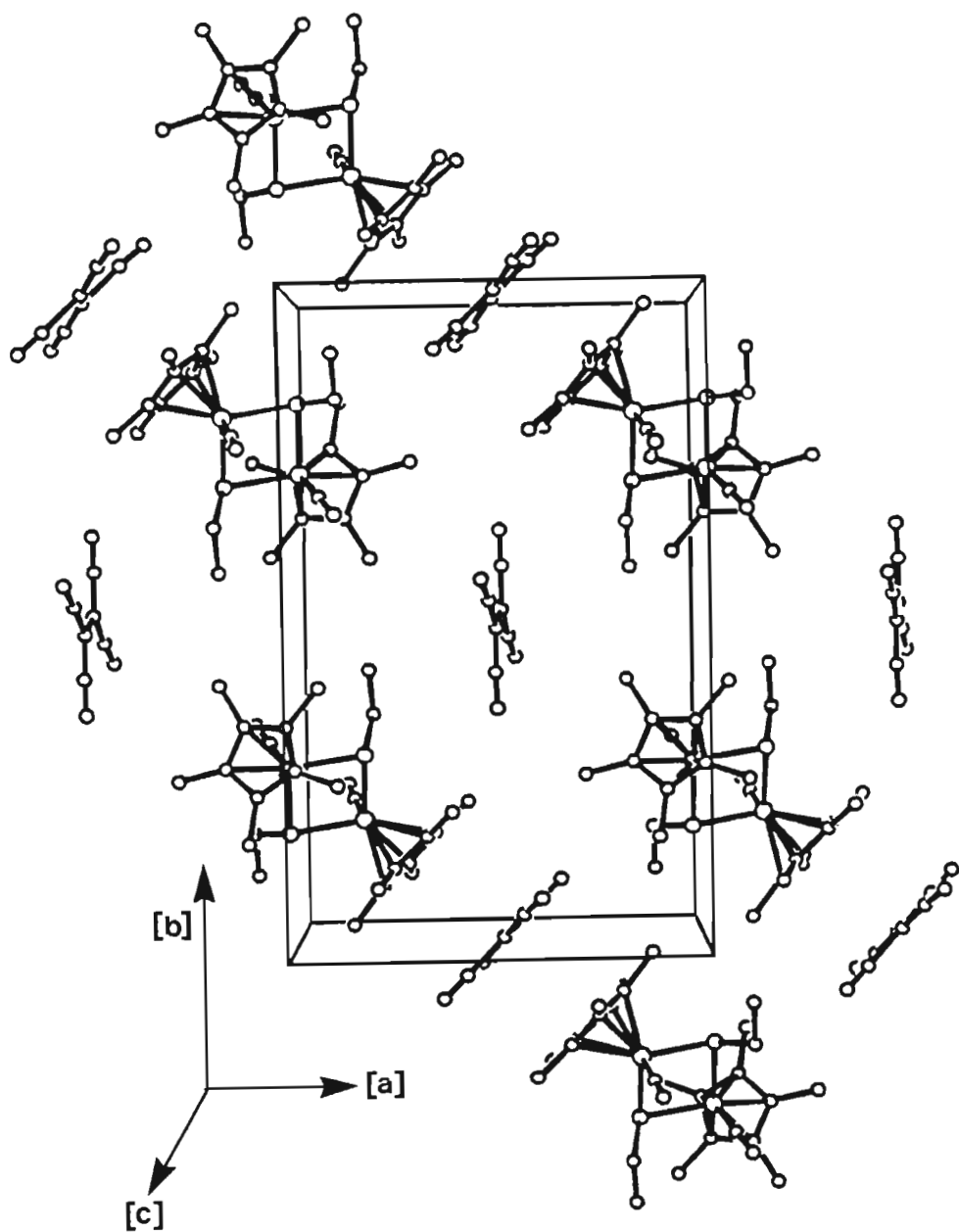
Figure 2.23   *A single sheet of donor and acceptor ions from [Fe₂Cp₂˙(CO)₂(µ-*

SEt)₂](TCNE) (7) as seen in projection onto the ab-plane.
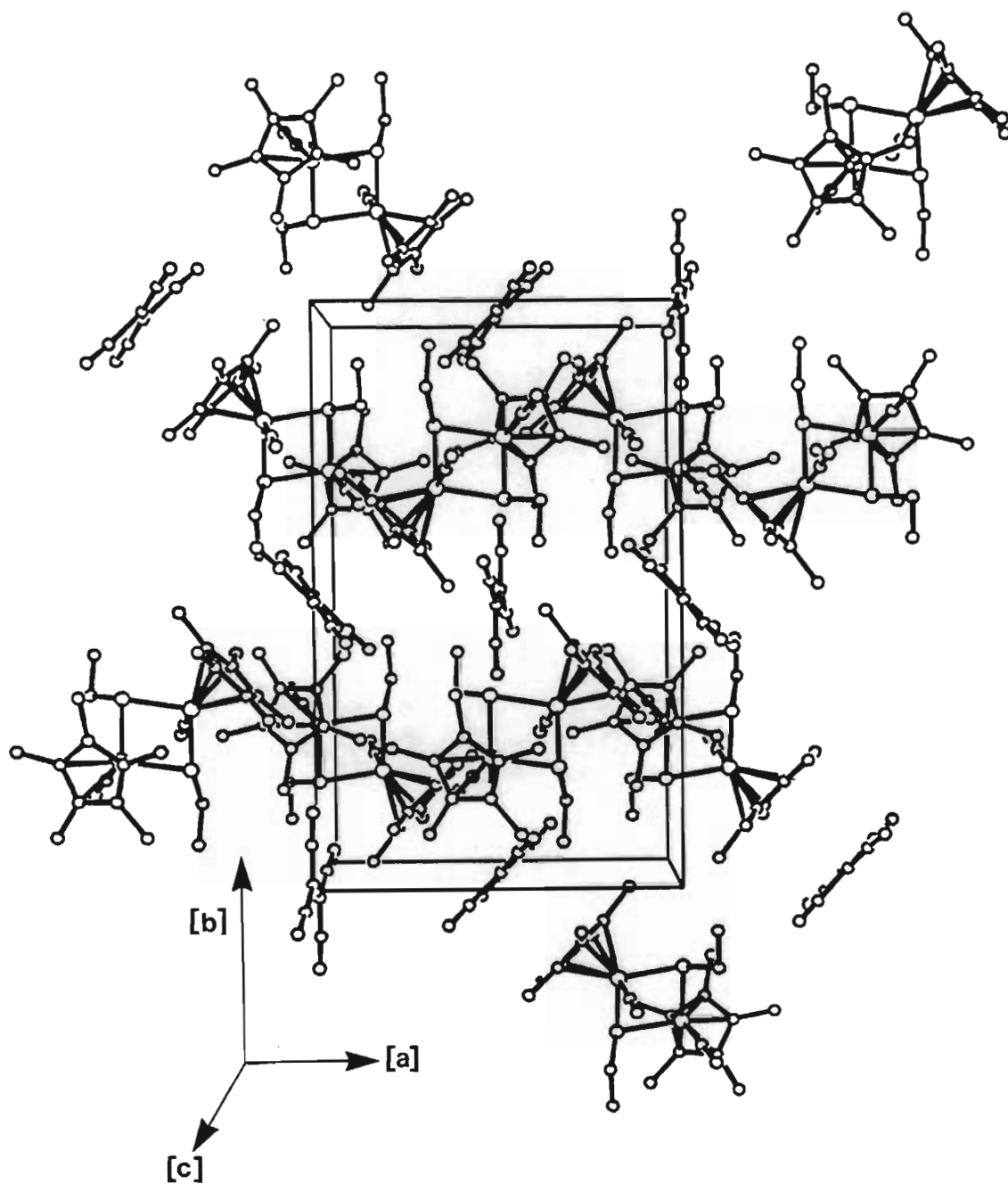
Figure 2.24 _Two consecutive sheets of donor and acceptor ions from_ _[Fe₂Cp₂*(CO)₂(μ-SEt)₂](TCNE) (**7**) as seen in projection onto the ab-plane._

is too large to accommodate any significant ligand-anion-ligand overlap. Secondly, the dihedral angle between the plane defined by the constituent atoms of the $TCNE_A$ anion and that of the Cp^* ligands is $71.6°$ thus prohibiting a face-to-face arrangement. Close scrutiny of one of these "non-participating" Cp^* ligands and its immediate environment in the crystal lattice reveals that the "non-participating" Cp* ligand of the next cation in the "row" is not its closest neighbouring Cp^* ligand. In fact, the closest neighbouring Cp^* ligand to any "non-participating" Cp^* ligand is that participating in the face-to-face $Cp^*, TCNE_B, Cp^*$ arrangement. The latter Cp^* ligand forms part of a cation which is related to that of the "non-participating" Cp^* ligand, by an n-glide plane. The dihedral angle between the planes of these two ligands is $77.4°$, again eliminating the possibility of a "face-to-face" arrangement.

Considering the lattice structure of $[Fe_2Cp_2^*(CO)_2(\mu-SEt)_2](TCNE)$ as described above, it is clear that there are no extended chains present in the structure. Instead, the lattice comprises isolated $D^+A_B^-D^+$ units which are arranged in rows; the rows in turn, being arranged in sheets. Within the rows, the $D^+A_B^-D^+$ units are separated by anions A_A^-, which act as spectator ions and preserve the electrical neutrality of the lattice.

The overall structure of $[Fe_2Cp_2^*(CO)_2(\mu-SEt)_2](TCNE)$ can thus be represented as $....(D^+A_B^-D^+)A_A^-(D^+A_B^-D^+)A_A^-....$ As far as can be ascertained, this is the first example of a metallocene based charge transfer salt of TCNE, exhibiting this structural motif. Generally, the metallocene based charge transfer salts of the TCNE crystallize either with extended integrated chains of donor and acceptor ions, i.e. $....D^+A^-D^+A^-....$ as is observed in $[Fe(C_5Me_4H)_2](TCNE)$,[233] or with a one-dimensional $....D^+(A)_2^2D^+, D^+(A)_2^2D^+....$ arrangement, containing the $(TCNE)_2^{2-}$ anion, as observed in $[Cr(C_6H_6)_2](TCNE)$.[245]

2.4.8.3 Magnetic studies on $[Fe_2Cp_2^*(CO)_2(\mu-SEt)_2](TCNE)$ (7)

A consideration of the structural and spectroscopic data as discussed in section 2.4.8.1 and 2.4.8.2, reveals that a full unit of negative charge (e) is transferred from the donor to the acceptor molecule during the reaction between $[Fe_2Cp_2^*(CO)_2(\mu-SEt)_2]$ and TCNE. This is in exact accordance with the requirements for the stabilization of ferromagnetic interactions between the unpaired spins in the resulting charge transfer salt. Although the donor and acceptor radical ions in 7 are arranged in, what on first consideration would appear to be an

integrated chain structure, there are no extended interactions within these "chains". As such, the condition that the donor and acceptor ions are to be arranged in extended chains in order to stabilize ferromagnetic interactions, is not met.

The magnetization data for $\underline{7}$ recorded from 5.0 K to 310.0 K and plotted as the inverse molar susceptibility (χ_m^{-1}) and the effective magnetic moment (μ_{eff}) as a function of temperature, are shown in Figures 2.25 and 2.26 respectively. The observed molar susceptibility χ_m, expressed as a function of T, can be fitted to the sum of a Curie-Weiss term $\chi_{cw} = C.(T-\theta)^{-1}$ and a temperature independent diamagnetic term χ_d, $i.e.$ $\chi_m = C.(T-\theta)^{-1} + \chi_d$. Compensating for the contribution of χ_d to the observed susceptibility, by plotting $(\chi_m-\chi_d)^{-1}$ vs T, thus affords a straight line. The Curie-Weiss constant, θ, derived from such a linearized plot of $(\chi_m-\chi_d)^{-1}$ vs T, equals +0.08 K. This value is substantially smaller than that typically associated with ferromagnetic coupling ($\theta = +30$ K for $[FeCp_2^*](TCNE)$,[208] see section 2.3.2.1) and is indicative of very weak, if any, magnetic interactions between the unpaired electrons of the $[Fe_2Cp_2^*(CO)_2(\mu\text{-}SEt)_2]^+$ and $TCNE^-$ ions. This lack of substantial interaction is not unexpected, since as was discussed above, the lattice structure of $\underline{7}$ comprises isolated tetrameric $D^+A_B^-D^+$ units separated by A_A^- spectator ions, and does not possess any extended interactions.

In accordance with the above mentioned lack of magnetic interactions, the effective magnetic moment, μ_{eff} $[=(8\chi T)^{0.5}]$, is essentially constant over the temperature range ~50 K to 310 K. Furthermore, it has an average value of 3.41 μ_B. This value is substantially larger than that of 2.45 μ_B predicted for two independent non-interacting spins, each with an associated Lande g-value of 2. Orbital angular momentum contributions to the magnetic moment associated with a compound can, as pointed out in section 2.4.3.3, result in Lande g-values which are substantially larger than the free-electron g-value of 2, and consequently in observed values of μ_{eff} which are in excess of that predicted from the free-electron g-value of 2. Such orbital angular momentum contributions are known to play a part in the magnetic properties of ferrocinium cations[233] and could be operative in this instance too. A second and probably more significant factor which could account for the large difference between the observed and predicted values of the effective magnetic moment, is associated with the sample orientation relative to the magnetic field. The effective magnetic
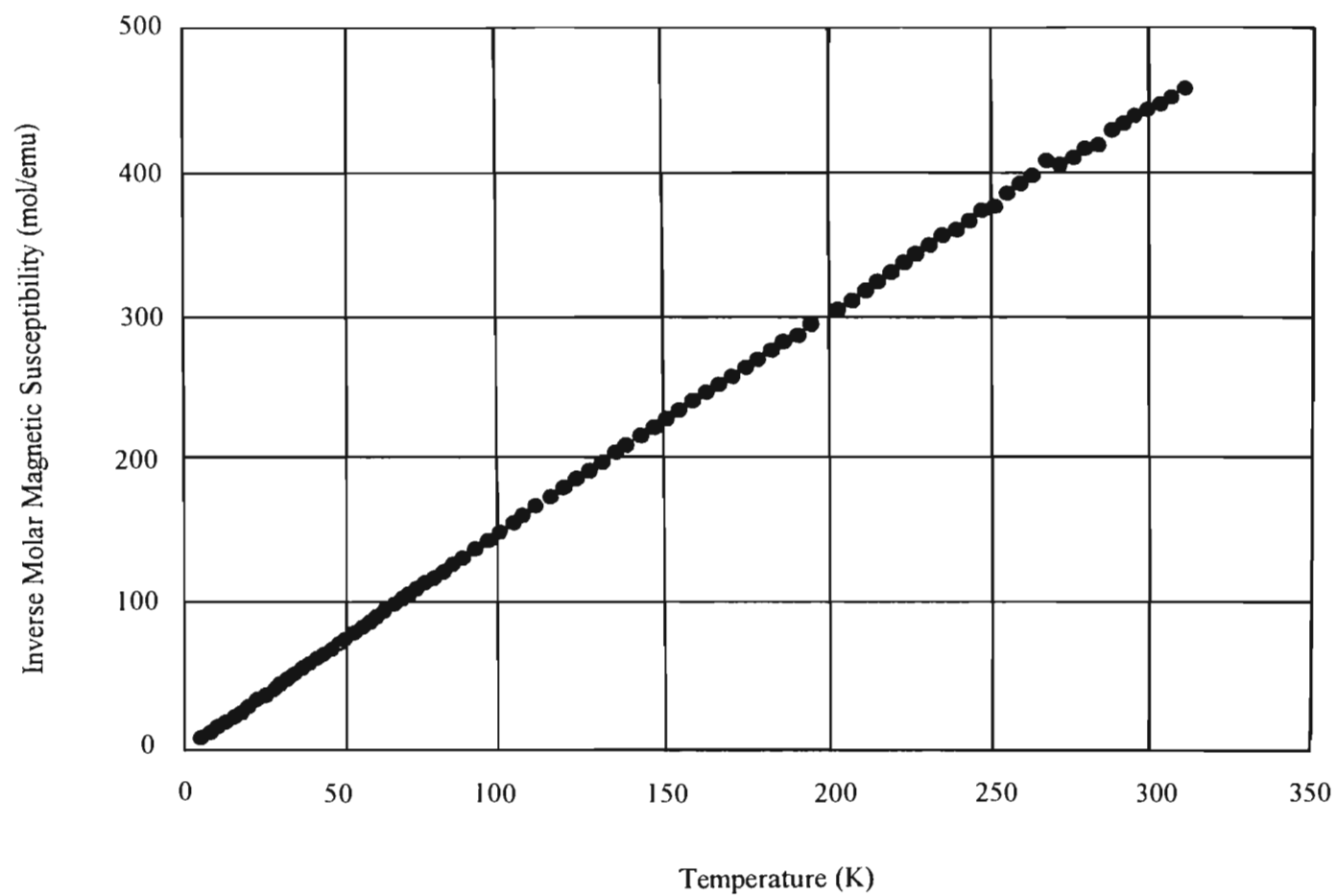
Figure 2.25 _The inverse molar susceptibility of [Fe₂Cp₂*(CO)₂(μ-SEt)₂](TCNE) (**7**) plotted as a function of temperature._

Figure 2.26 *The effective magnetic moment of [Fe$_2$Cp$_2$$^\bullet$(CO)$_2$($\mu$-SEt)$_2$](TCNE) (7) plotted as a function of temperature.*

moments for $[Fe(C_5Et_5)_2](X)$ ($X^- = PF_6^-$, $TCNE^-$ and $TCNQ^-$) were 3.37, 3.15 and 3.65 μ_B respectively.[237] These values are comparable to the value of 3.46 μ_B observed for __7__, but are significantly larger than 2.34 μ_B predicted for a randomly oriented sample with g = 2.71. They are however, less than 4.0 μ_B, the value expected for a sample oriented with the C_5 axis parallel to the magnetic field (g = 4.6), and substantially larger than 1.07 μ_B expected for a sample oriented with the C_5 axis perpendicular to the magnetic field (g = 1.24). These discrepancies between the observed and predicted effective magnetic moments in $[Fe(C_5Et_5)_2](X)$ ($X^- = PF_6^-$, $TCNE^-$ and $TCNQ^-$) are attributed to a field-induced orientation of the sample. A similar mechanism might be invoked to explain the magnitude of the observed effective magnetic moment in $[Fe_2Cp_2^*(CO)_2(\mu\text{-}SEt)_2](TCNE)$.

2.5 Conclusion

In this study charge transfer salts resulting from the reaction of the pentamethylcyclo-pentadienyl electron donor molecule $[Fe_2Cp_2^*(CO)_2(\mu\text{-}SEt)_2]$ with various polycyano-acceptor molecules were synthesized. In particular, members of the DCNQI series, TCNQ and TCNE were utilized as acceptor molecules. The crystal structures of the 2,5-Me_2-DCNQI, TCNQ and TCNE charge transfer salts were determined and reconciled with the observed magnetic properties of the salts. The crystal structure of $[Fe_2Cp_2^*(CO)_2(\mu\text{-}SEt)_2](2,5\text{-}Me_2\text{-}DCNQI)$ provides the first example of a structure of a metallocene based, DCNQI charge transfer salt reported to date.

$[Fe_2Cp_2^*(CO)_2(\mu\text{-}SEt)_2]$ was reacted with 4 members of the DCNQI series, in particular 2,5-Me_2-DCNQI, 2-Cl-5-Me-DCNQI, 2-Me-DCNQI and H_4-DCNQI. In accordance with other examples of metallocene based DCNQI charge transfer salts reported in the literature, most of the charge transfer salts reported here were found either to be inherently unstable, *i.e.* decompose in the solid state despite being isolated from the atmosphere, or to be prone to decomposition in solution. $[Fe_2Cp_2^*(CO)_2(\mu\text{-}SEt)_2](2,5\text{-}Me_2\text{-}DCNQI)$ proved to be an exception to this trend. The salt crystallizes with extended chains of alternating donor and acceptor radical ions, *i.e.* a ...$D^+AD^+A^-$... motif, with a full unit of positive or negative charge residing on each of the cations and anions respectively. As such the salt meets both of the essential prerequisites for the stabilization of ferromagnetic interactions between the unpaired electrons on the constituent radical cations and anions. The magnetic behaviour of

135

$[Fe_2Cp_2^{\bullet}(CO)_2(\mu\text{-SEt})_2](2,5\text{-Me}_2\text{-DCNQI})$ obeys the Curie-Weiss law with a Curie-Weiss constant θ, of $+0.41$ K. This relatively low value of θ is indicative of very weak, if any, ferromagnetic interaction between the unpaired electron spins on the $[Fe_2Cp_2^{\bullet}(CO)_2(\mu\text{-SEt})_2]^+$ and $(2,5\text{-Me}_2\text{-DCNQI})^-$ radical ions.

The charge transfer reaction between $[Fe_2Cp_2^{\bullet}(CO)_2(\mu\text{-SEt})_2]$ and TCNQ affords a stable salt which crystallizes with a lattice structure consisting of isolated $D^+(A)_2^{2-}D^+$ tetradic units. Within these units, the $TCNQ^-$ anions exist as spinless $i.e.$ $S = 0$ dimeric $(TCNQ)_2^{2-}$ anions, the only unpaired electron density residing on the $S = \frac{1}{2}$, $[Fe_2Cp_2^{\bullet}(CO)_2(\mu\text{-SEt})_2]^+$ radical cations. Support for this assertion was obtained from room temperature magnetic susceptibility measurements from which an effective magnetic moment equal to 2.76 μ_B, expected for 2 unpaired electrons per $D^+(A_2)^{2-}D^+$ unit, $i.e.$ one per cation was calculated. As a result of the isolated nature of the $D^+(A_2)^{2-}D^+$ units and the spin pairing of the unpaired electrons on the $TCNQ^-$ anions in the $(TCNQ)_2^{2-}$ dimer, $[Fe_2Cp_2^{\bullet}(CO)_2(\mu\text{-SEt})_2]_2(TCNQ)_2$ is not expected to exhibit any cooperative magnetic interactions.

The charge transfer salt $[Fe_2Cp_2^{\bullet}(CO)_2(\mu\text{-SEt})_2](TCNE)$ crystallizes with a lattice structure which can be represented schematically as $....(D^+A_B^-D^+)A_A^-(D^+A_B^-D^+)....$ and consists of rows of isolated $D^+A_B^-D^+$ trimeric units separated by A_A^- anions. A full unit of positive or negative charge resides on each of the cations and anions respectively. The magnetic behaviour of the salt obeys the Curie-Weiss law with a Curie-Weiss constant, θ, equal to $+0.08$ K. This low value of θ is consistent with virtually no ferromagnetic interaction between the unpaired electrons on the constituent radical ions. The lack of ferromagnetic interactions can be attributed to the absence of an extended chain structure in the solid state.

Considering the results of this study as outlined above, it is clear that the molecular co-crystallization approach utilized here, as in the case of the oxidized metalloporphyrins (see section 1.3.3.2), does not allow for rigorous structural enforcement. In this respect Marks' remarks,[73] although referring to electrical conductivity in stacked metallomacrocles, is also of relevance in this instance: "Without rigorous structural enforcement of the metallomacrocyclic stacking it is impossible to affect controllable and informative variations

in stacking architecture or in donor-acceptor spatial-electronic relationships. Clearly, the packing forces operative in most molecular conductors are rather delicate."

The influence of utilizing a dinuclear, rather than mononuclear, metallocene donor molecule on the magnetic properties of charge transfer salts resulting from its reaction with polycyano acceptor molecules, has not been fully clarified by the study. This is primarily due to the tendency of these salts to decompose and the uncontrollable nature of the packing forces determining the lattice architecture in these compounds. These two factors resulted in this study producing only one salt satisfying the prerequisites for the stabilization of ferromagnetic spin-spin interactions between unpaired spins.

As discussed above, $[Fe_2Cp_2^*(CO)_2(\mu-SEt)_2](2,5-Me_2-DCNQI)$ satisfied both of the prerequisites for the stabilization of ferromagnetic interactions between the unpaired electrons in the salt, yet no such interactions were observed. This lack of ferromagnetic interactions could be the result of a lower overall spin density resulting from the increased bulk of the dinuclear donor molecule when compared to the mononuclear derivatives. A second possibility is that the "boat-like" shape of the $[Fe_2Cp_2^*(CO)_2(\mu-SEt)_2]$ molecule imparts a distinct wave-like nature to integrated stacks of the donor cation and acceptor anion. This wave-like nature results in the Fe atoms in the stacks not all being co-linear, which could influence the spin-spin interactions.

Based on these considerations, it would seem appropriate that any further effort directed towards dinuclear metallocene-based charge transfer salts should attempt to increase the overall spin density of the charge transfer salt, either through decreasing the steric bulk of particularly the donor molecule, or by increasing the number of unpaired electrons on the donor molecule. Secondly, the probability of ferromagnetic interactions might also be increased by utilizing donor molecules which are essentially columnar in shape, i.e. a line joining the centroids of the Cp or Cp* ligands should also pass through the metal atoms.

2.6 Experimental

2.6.1 Synthesis

2.6.1.1 Synthesis of [Fe$_2$Cp$_2^*$(CO)$_2$(μ-SEt)$_2$] (1)

A 50% excess of ethyl disulfide (Et$_2$S$_2$) (0.184 cm^3; 1.49 mmol) was added to [Fe$_2$Cp$_2^*$(CO)$_2$(μ-CO)$_2$] (0.472 g; 0.96 mmol) suspended in toluene (50 cm^3). The mixture was heated under reflux for 22 hours, ensuring that the temperature of the oil bath, used for heating, did not exceed 134°C. The solution was allowed to cool to room temperature and the solvent removed *in vacuo*. The residue was extracted with petroleum ether (boiling range: 60 to 80°C) and the volume of the extract reduced *in vacuo*. Slow cooling of this solution to 0°C and storage at this temperature overnight resulted in the crystallization of the product as shiny dark brown-black cubically shaped crystals.

Yield: 70 - 80%

Molecular Mass: 560.42 g.mol^{-1}

Elemental Analysis: Calculated: C: 55.71   H: 7.14   N: 0.00

Found :   C: 55.71   H: 7.14   N: 0.00

2.6.1.2 Synthesis of [Fe$_2$Cp$_2^*$(CO)$_2$(μ-SEt)$_2$](2,5-Me$_2$-DCNQI) (2)

A solution of [Fe$_2$Cp$_2^*$(CO)$_2$(μ-SEt)$_2$] (0.100 g; 0.18 mmol), in toluene (70 cm^3), was added dropwise over *ca.* 30 min to a stirred solution of an equimolar amount of 2,5-Me$_2$-DCNQI (0.033 g; 0.18 mmol) in toluene (50 cm^3), at 0°C. The colour of the reaction mixture changed from yellow-brown to green as the solution of 2,5-Me$_2$-DCNQI was added. On completion of the addition, the reaction mixture was allowed to warm to room temperature and the volume of the solution reduced *in vacuo*, resulting in the precipitation of the product as a blue-black solid. The crude product was isolated by filtration and washed with diethyl ether before drying it *in vacuo*. The material so obtained was extracted with acetonitrile and the volume of the extracts reduced *in vacuo*. Slow cooling of this solution to *ca.* -15°C and storing it at this temperature for 3 days resulted in the crystallization of the product as shiny blue-black crystals.

Yield: 60 - 70%

Molecular Mass: 744.62 g.mol^{-1}

138

Elemental Analysis: Calculated: C: 58.07   H: 6.50   N: 7.52

Found :   C: 58.77   H: 6.56   N: 7.69

2.6.1.3 Synthesis of [Fe$_2$Cp$_2$*(CO)$_2$(μ-SEt)$_2$](2-Cl-5-Me-DCNQI) (3)

A solution of a 5% excess of [Fe$_2$Cp$_2$*(CO)$_2$(μ-SEt)$_2$] (0.420 g; 0.075 mmol), in methylcyclohexane (12 cm^3) was added dropwise to a stirred solution of 2-Cl-5-Me-DCNQI (0.0146 g; 0.071 mmol) in dichloromethane (8 cm^3) at room temperature. On completion of the additon, the volume of the reaction mixture was reduced to a minimum (*in vacuo*) and stored overnight at *ca.* 0°C thus effecting the precipitation of a decomposition product and a small amount of the desired product. This material was separated by filtration and the volume of the filtrates reduced *in vacuo*. Storage of this solution at *ca.* 0°C overnight resulted in the separation of the analytically pure product as shiny dark blue-black crystals.

Yield: 25 - 35%

Molecular Mass: 765.03 g.mol^{-1}

Elemental Analysis: Calculated: C: 54.95   H: 5.93   N: 7.32

Found :   C: 54.38   H: 5.19   N: 7.35

2.6.1.4 Synthesis of [Fe$_2$Cp$_2$*(CO)$_2$(μ-SEt)$_2$](2-Me-DCNQI) (4)

A solution of a 10% excess of [Fe$_2$Cp$_2$*(CO)$_2$(μ-SEt)$_2$] (0.050 g; 0.089 mmol), in methylcyclohexane (15 cm^3) was added dropwise over *ca.* 30 min to a stirred solution of 2-Me-DCNQI (0.014 g; 0.082 mmol) in toluene (6 cm^3) at room temperature. The blue-black precipitate resulting from the addition was removed by filtration, washed with petroleum ether (boiling range: 60- 80°C) until the washings were colourless and the precipitate then dried *in vacuo*. The blue-black microcrystalline material obtained thus was analytically pure.

Yield: 60 - 70%

Molecular Mass: 730.59 g.mol^{-1}

Elemental Analysis: Calculated: C: 57.54   H: 6.35   N: 7.67

Found :   C: 58.02   H: 6.26   N: 8.25

2.6.1.5 Synthesis of [Fe₂Cp₂*(CO)₂(μ-SEt)₂](H₄-DCNQI) (5)

A solution of $[Fe_2Cp_2^*(CO)_2(\mu\text{-SEt})_2]$ (0.040 g; 0.071 mmol), in toluene (15 cm³) was added dropwise to a stirred solution of an equimolar amount of H_4-DCNQI (0.011 g; 0.071 mmol) in toluene (10 cm³) at room temperature. On completion of the addition, the reaction mixture was stirred for an additional hour before the precipitate, resulting from the addition, was dissolved by adding a minimum amount of acetonitrile to the reaction mixture. The volume of the solution was reduced *in vacuo* and the solution stored at *ca.* -15°C for 36 hours. This resulted in the separation of the product as aggregates of very small dark blue plate-like crystals together with small quantities of a brown powdery decomposition product from which the analytically pure crystals were separated manually.

Yield: 50 - 60%

Molecular Mass: 716.56 g.mol⁻¹

Elemental Analysis:　Calculated:　C: 56.99　H: 6.19　N: 7.82

　　　　　　　　　　Found :　　C: 57.10　H: 5.95　N: 7.50

2.6.1.6 Synthesis of [Fe₂Cp₂*(CO)₂(μ-SEt)₂]₂(TCNQ)₂ (6)

A solution of a 10% excess of $[Fe_2Cp_2^*(CO)_2(\mu\text{-SEt})_2]$ (0.056 g; 0.010 mmol), in toluene (10 cm³) was added dropwise over *ca.* 10 minutes to a stirred solution of TCNQ (0.018 g; 0.09 mmol) in a 1:4 acetonitrile/toluene mixture (5 cm³), at room temperature. On completion of the addition, the volume of the reaction mixture was reduced *in vacuo*, resulting in the separation of the product as a green microcrystalline powder. The product was isolated by filtration, washed with petroleum ether (boiling range: 60 - 80°C) and dried *in vacuo*.

Yield: 65 - 75%

Molecular Mass: 764.61 g.mol⁻¹

Elemental Analysis:　Calculated:　C: 59.69　H: 5.80　N: 7.33

　　　　　　　　　　Found :　　C: 59.12　H: 5.89　N: 7.26

2.6.1.7 Synthesis of [Fe₂Cp₂*(CO)₂(μ-SEt)₂](TCNE) (7)

A solution of TCNE (0.017 g; 0.13 mmol) in toluene (7 cm³) was added dropwise over 30 minutes to a stirred solution of a *ca.* 6% excess of $[Fe_2Cp_2^*(CO)_2(\mu\text{-SEt})_2]$ (0.079; 0.014 mmol), in toluene (10 cm³), at room temperature. The product separated as a dark green

microcrystalline precipitate which was isolated through filtration and washed with toluene and ether, in this order, before drying it *in vacuo*.

Yield: 75 - 85%

Molecular Mass: 688.51 g.mol^{-1}

Elemental Analysis: Calculated: C: 55.82   H: 5.86   N: 8.14

Found :   C: 55.79   H: 5.81:   N: 7.88

2.6.2 Crystal Structure Determinations

2.6.2.1 Single crystal X-ray diffraction study of $[Fe_2Cp_2^*(CO)_2(\mu\text{-}SEt)_2]$ ($\underline{1}$)

Dark brown block-shaped crystals of $\underline{1}$ suitable for X-ray diffraction studies, were obtained by slow cooling of a saturated petroleum ether (boiling range: 60 - 80°C) solution of the compound.

The general procedure for the intensity data collection and the general approach to structure solution and refinement are described in sections A.5.1 and A.5.2 of Appendix A, respectively.

Crystal data, as well as details specific to the data collection, structure solution and refinement for $\underline{1}$ are provided in Table 2.10. Anisotropic refinement was applied to all of the constituent non-H atoms of the molecule. H atoms were not located. The fractional atomic coordinates are listed in Table 2.11 and anisotropic thermal factors in Table 2.12. The interatomic distances are provided in Table 2.13 and the interatomic angles in Table 2.14. The observed and calculated structure factors for $\underline{1}$ may be found on microfiche in an envelope attached to the inside back cover.

Table 2.10   *Crystal Data and Details of the Crystallographic Analysis for*

$[Fe_2Cp_2^*(CO)_2(\mu\text{-}SEt)_2]$ (1)

Formula	$Fe_2S_2O_2C_{26}H_{40}$
Molecular Mass	560.12
Crystal Dimensions (mm)	0.35 x 0.15 x 0.19
Crystal System	Monoclinic
Space Group	$C2/c$
a (Å)	15.075(3)
b (Å)	14.519(2)
c (Å)	13.016(1)
α (°)	90
β (°)	103.74(1)
γ (°)	90
V (Å^3)	2767.3(7)
Z	4
D_c (g.cm^{-3})	1.34
F(000)	1184
λ(Mo - Kα) (Å)	0.71069
Scan Mode	ω - 2θ
ω scan angle	$0.6 + 0.46\tan\theta$
Horizontal Aperture Width (mm)	$2.7 + 0.1\tan\theta$
Scattering range (°)	$2 \leq \theta \leq 23$
μ (cm^{-1})	12.34
Absorption Corrections	Semi empirical
Measured Intensities	2117
Unique Intensities	1779
Unique Intensities with [I > 3σ(I)]	1524
Structure Solution	Direct & Fourier Methods
Weighting Scheme	$1/[\sigma^2(F) + 0.002442F^2]$
$R = \Sigma|F_o - F_c|/\Sigma F_o$	0.0443
$R_w = \Sigma w^{1/2}|F_o - F_c|/\Sigma w^{1/2}F_o$	0.0489
$(\Delta/\sigma)_{max}$	0.110
$\Delta\rho_{max}$ (e.Å^{-3})	0.478
Number of parameters	145

Table 2.11   *Fractional Coordinates (x 10^4) for [Fe$_2$Cp$_2^*$(CO)$_2$(μ-SEt)$_2$] (**1**)*

	x/a	y/b	z/c
Fe	756	2022(1)	1695(1)
S	-766(1)	2206(1)	1565(1)
O	821(3)	34(3)	1745(4)
C(1)	764(3)	835(4)	1744(4)
C(2)	1863(4)	2943(4)	1754(5)
C(3)	2008(4)	2130(4)	1264(5)
C(4)	1264(4)	2037(4)	340(5)
C(5)	692(4)	2781(4)	309(4)
C(6)	1048(4)	3349(4)	1204(5)
C(7)	2495(6)	3379(7)	2730(6)
C(8)	2833(5)	1499(6)	1541(8)
C(9)	1187(7)	1285(6)	-493(7)
C(10)	-148(5)	3002(7)	-589(7)
C(11)	657(6)	4255(5)	1447(8)
C(12)	-1326(3)	1226(4)	756(5)
C(13)	-2349(4)	1172(5)	719(6)

Table 2.12 *Anisotropic Temperature Factors ($\mathring{A}^2$, x 10^3) for $[Fe_2Cp_2^*(CO)_2(\mu\text{-}SEt)_2]$ (1)*

	U(11)	U(22)	U(33)	U(23)	U(13)	U(12)
Fe	33(1)	41(1)	55(1)	-1(1)	3(1)	-1(1)
S	33(1)	46(1)	52(1)	-2(1)	1(1)	3(1)
O	71(3)	41(3)	142(5)	-2(2)	20(3)	7(2)
C(1)	39(3)	52(4)	75(4)	-2(3)	11(3)	3(2)
C(2)	48(3)	69(4)	64(3)	0(3)	12(3)	-28(3)
C(3)	36(3)	60(4)	80(4)	11(3)	14(3)	4(2)
C(4)	66(4)	57(3)	70(4)	-13(3)	32(3)	-13(3)
C(5)	42(3)	84(4)	56(3)	19(3)	10(3)	1(3)
C(6)	67(4)	44(3)	75(4)	9(3)	24(3)	-3(3)
C(7)	95(5)	138(7)	73(4)	-20(4)	11(4)	-75(5)
C(8)	58(4)	115(6)	160(8)	46(6)	52(5)	40(4)
C(9)	146(8)	97(6)	111(6)	-52(5)	64(6)	-40(5)
C(10)	60(4)	181(9)	88(5)	62(5)	-4(4)	0(5)
C(11)	147(8)	49(4)	158(7)	18(4)	93(7)	22(4)
C(12)	38(3)	71(4)	74(4)	-29(3)	0(3)	-11(3)
C(13)	40(3)	90(4)	89(4)	-15(4)	1(3)	-13(3)

Table 2.13   *Interatomic distances (Å) for [Fe$_2$Cp$_2^{\bullet}$(CO)$_2$(μ-SEt)$_2$] (**1**)*

Fe-Fe	3.444(1)	Fe-S	2.276(1)
Fe-S	2.278(1)	Fe-C(1)	1.725(6)
Fe-C(2)	2.125(5)	Fe-C(3)	2.098(5)
Fe-C(4)	2.084(6)	Fe-C(5)	2.098(5)
Fe-C(6)	2.109(6)	S-C(12)	1.851(5)
O-C(1)	1.168(7)	C(2)-C(3)	1.384(8)
C(2)-C(6)	1.398(8)	C(2)-C(7)	1.532(9)
C(3)-C(4)	1.444(9)	C(3)-C(8)	1.518(8)
C(4)-C(5)	1.377(8)	C(4)-C(9)	1.524(9)
C(5)-C(6)	1.426(9)	C(5)-C(10)	1.539(9)
C(6)-C(11)	1.505(9)	C(12)-C(13)	1.533(8)

Table 2.14   *Interatomic angles (°) for [Fe₂Cp₂*(CO)₂(μ-SEt)₂] (1)*

Fe-S-Fe	98.3(1)	S-Fe-S	80.1(1)
S-Fe-C(1)	96.8(2)	S-Fe-C(2)	134.2(2)
C(1)-Fe-C(2)	129.0(2)	S-Fe-C(3)	157.8(2)
C(1)-Fe-C(3)	94.9(2)	C(2)-Fe-C(3)	38.3(2)
S-Fe-C(4)	120.1(2)	C(1)-Fe-C(4)	92.3(2)
C(2)-Fe-C(4)	65.2(2)	C(3)-Fe-C(4)	40.4(2)
S-Fe-C(5)	92.0(2)	C(1)-Fe-C(5)	123.7(3)
C(2)-Fe-C(5)	64.9(2)	C(3)-Fe-C(5)	65.9(2)
C(4)-Fe-C(5)	38.4(2)	S-Fe-C(6)	98.6(2)
C(1)-Fe-C(6)	157.5(2)	C(2)-Fe-C(6)	38.5(2)
C(3)-Fe-C(6)	65.5(2)	C(4)-Fe-C(6)	65.7(2)
C(5)-Fe-C(6)	39.6(2)	Fe-S-Fe	98.3(1)
Fe-S-C(12)	105.5(2)	S-Fe-S	80.1(1)
Fe-C(1)-O	175.3(5)	Fe-C(2)-C(3)	69.8(3)
Fe-C(2)-C(6)	70.1(3)	C(3)-C(2)-C(6)	109.8(5)
Fe-C(2)-C(7)	128.1(4)	C(3)-C(2)-C(7)	126.9(7)
C(6)-C(2)-C(7)	123.2(7)	Fe-C(3)-C(2)	71.9(3)
Fe-C(3)-C(4)	69.3(3)	C(2)-C(3)-C(4)	106.7(5)
Fe-C(3)-C(8)	129.0(4)	C(2)-C(3)-C(8)	128.0(6)
C(4)-C(3)-C(8)	124.9(6)	Fe-C(4)-C(3)	70.3(3)
Fe-C(4)-C(5)	71.3(3)	C(3)-C(4)-C(5)	108.0(5)
Fe-C(4)-C(9)	127.9(4)	C(3)-C(4)-C(9)	125.0(6)
C(5)-C(4)-C(9)	126.9(7)	Fe-C(5)-C(4)	70.2(3)
Fe-C(5)-C(6)	70.6(3)	C(4)-C(5)-C(6)	108.6(5)
Fe-C(5)-C(10)	128.7(4)	C(4)-C(5)-C(10)	125.7(7)
C(6)-C(5)-C(10)	125.6(6)	Fe-C(6)-C(2)	71.4(3)

Table 2.14   *(continued)*

Fe-C(6)-C(5)	69.8(3)	C(2)-C(6)-C(5)	106.8(5)
Fe-C(6)-C(11)	127.9(4)	C(2)-C(6)-C(11)	127.0(6)
C(5)-C(6)-C(11)	126.0(6)	S-C(12)-C(13)	112.1(4)

2.6.2.2 Single crystal X-ray diffraction study on $[Fe_2Cp_2^{\bullet}(CO)_2(\mu-SEt)_2](2,5-Me_2-DCNQI)$ (2)

Dark blue-black block-like crystals of **2** were grown by slow cooling of a saturated acetonitrile solution of the salt.

The general approach used for the intensity data collection is described in section A.5.1 of Appendix A and the general procedure involved in structure solution and refinement in section A.5.2 of the same appendix.

Crystal data, together with details specific to the data collection, structure solution and refinement for **2** are provided in Table 2.15. The unit cell dimensions suggest that the structure of **2** might have hexagonal or trigonal symmetry. These symmetries were specifically tested for by comparing the intensities of reflections which under hexagonal or trigonal symmetry would necessarily be equivalent. From the comparison it was clearly evident that no such symmetry was present. All non-H atoms, both of the cation and anion, were refined anisotropically. H atoms were not located. The fractional atomic coordinates are listed in Table 2.16 and anisotropic thermal factors in Table 2.17. The interatomic distances are provided in Table 2.18 and the interatomic angles in Table 2.19. The observed and calculated structure factors for **2** may be found on microfiche in an envelope fixed to the inside back cover.

Table 2.15   _Crystal Data and Details of the Crystallographic Analysis for_

   [Fe₂Cp*₂(CO)₂(µ-SEt)₂](2,5-Me₂-DCNQI) (**2**)

Formula	$Fe_2S_2O_2C_{36}H_{48}N_4$
Molecular Mass	744.62
Crystal Dimensions (mm)	0.27 x 0.23 x 0.06
Crystal System	Monoclinic
Space Group	$C2/c$
a (Å)	18.391(2)
b (Å)	12.978(1)
c (Å)	18.436(2)
α (°)	90
β (°)	121.02(7)
γ (°)	90
V (Å^3)	3771.3(7)
Z	4
D_c (g.cm^{-3})	1.31
F(000)	1568
λ(Mo - Kα) (Å)	0.71069
Scan Mode	ω - 2θ
ω scan angle	0.6 + 0.35tanθ
Horizontal Aperture Width (mm)	2.7 + 0.1tanθ
Scattering range (°)	2 ≤ θ ≤ 23
μ (cm^{-1})	9.32
Absorption Corrections	Semi empirical
Measured Intensities	2858
Unique Intensities	2354
Unique Intensities with [I > 3σ(I)]	1800
Structure Solution	Direct & Fourier Methods
Weighting Scheme	$1/[\sigma^2(F) + 0.001961F^2]$
$R = \Sigma|F_o - F_c|/\Sigma F_o$	0.0663
$R_w = \Sigma w^{1/2}|F_o - F_c|/\Sigma w^{1/2}F_o$	0.0717
$(\Delta/\sigma)_{max}$	0.061
$\Delta\rho_{max}$ (e.Å^{-3})	0.748
Number of parameters	208

Table 2.16   *Fractional Coordinates (x 10⁴) for [Fe₂Cp₂*(CO)₂(μ-SEt)₂](2,5-Me₂-DCNQI) (2)*

	x/a	y/b	z/c
Fe	5978(1)	696(1)	2991(1)
S	4981(1)	617(2)	1601(1)
O	6121(5)	2912(5)	3085(5)
C(1)	6027(6)	2027(7)	3025(6)
C(2)	6468(6)	-821(6)	2995(7)
C(3)	6662(6)	-578(8)	3816(7)
C(4)	7152(6)	352(7)	4081(5)
C(5)	7294(5)	652(7)	3432(6)
C(6)	6876(5)	-61(7)	2759(6)
C(7)	6003(7)	-1743(8)	2466(9)
C(8)	6456(8)	-1257(10)	4363(9)
C(9)	7560(7)	841(11)	4944(6)
C(10)	7847(6)	1540(8)	3431(8)
C(11)	6909(7)	-46(10)	1934(7)
C(12)	5051(6)	1792(7)	1067(6)
C(13)	4584(8)	1642(9)	127(6)
N(1)	7967(7)	-2511(9)	3722(7)
N(2)	8882(7)	-1425(8)	4966(6)
C(14)	8384(9)	-2001(11)	4242(10)
C(15)	9432(6)	-723(8)	4985(6)
C(16)	9981(7)	-185(8)	5740(6)
C(17)	9914(8)	-400(9)	6530(7)
C(18)	10543(7)	538(7)	5765(6)

Table 2.17   *Anisotropic Temperature Factors ($\mathring{A}^2$, x 10^3) for [Fe$_2$Cp$_2$*(CO)$_2$(μ-SEt)$_2$]-*
*(2,5-Me$_2$-DCNQI) (**2**)*

	U(11)	U(22)	U(33)	U(23)	U(13)	U(12)
Fe	51(1)	48(1)	52(1)	-1(1)	20(1)	3(1)
S	56(1)	56(1)	49(1)	0(1)	22(1)	-7(1)
O	94(6)	58(4)	112(6)	-5(4)	36(5)	-2(4)
C(1)	60(6)	56(6)	67(6)	-3(5)	21(5)	-3(5)
C(2)	57(6)	40(5)	99(8)	2(5)	37(5)	7(4)
C(3)	71(6)	67(6)	83(7)	28(6)	42(5)	33(6)
C(4)	57(6)	66(6)	47(5)	4(4)	13(5)	18(4)
C(5)	45(5)	56(5)	79(6)	5(5)	26(5)	6(4)
C(6)	53(5)	68(6)	68(6)	-6(5)	24(5)	14(5)
C(7)	76(7)	56(6)	155(12)	-37(7)	45(8)	-10(5)
C(8)	119(10)	112(9)	145(11)	79(9)	87(10)	50(8)
C(9)	76(7)	138(10)	61(6)	-19(6)	13(5)	34(7)
C(10)	63(7)	76(7)	133(10)	-7(7)	41(7)	-13(5)
C(11)	96(8)	137(10)	74(7)	-6(7)	55(6)	15(7)
C(12)	78(6)	80(6)	65(6)	17(5)	35(5)	-21(5)
C(13)	129(10)	112(9)	56(6)	22(6)	32(7)	-23(8)
N(1)	88(8)	107(8)	115(9)	-23(7)	43(7)	13(6)
N(2)	112(8)	88(6)	95(7)	18(6)	66(7)	22(6)
C(14)	100(10)	85(9)	121(12)	8(8)	67(10)	24(7)
C(15)	82(7)	60(6)	84(7)	14(6)	56(6)	24(6)
C(16)	98(7)	74(6)	55(6)	16(5)	51(6)	36(6)
C(17)	148(11)	108(9)	75(7)	25(6)	78(8)	23(8)
C(18)	88(7)	66(6)	71(6)	20(5)	49(6)	30(6)

Table 2.18   _Interatomic distances (Å) for [Fe$_2$Cp$_2$*(CO)$_2$(μ-SEt)$_2$](2,5-Me$_2$-DCNQI) (**2**)_

Fe-S	2.258(2)	Fe-C(1)	1.729(9)
Fe-C(2)	2.163(8)	Fe-C(3)	2.159(9)
Fe-C(4)	2.105(8)	Fe-C(5)	2.121(8)
Fe-C(6)	2.145(9)	Fe-Fe	3.083(1)
S-C(12)	1.855(8)	Fe-S	2.248(2)
C(2)-C(3)	1.402(13)	O-C(1)	1.158(10)
C(2)-C(7)	1.502(13)	C(2)-C(6)	1.435(13)
C(3)-C(8)	1.526(14)	C(3)-C(4)	1.432(13)
C(4)-C(9)	1.505(13)	C(4)-C(5)	1.406(12)
C(5)-C(10)	1.537(13)	C(5)-C(6)	1.415(12)
C(12)-C(13)	1.498(14)	C(6)-C(11)	1.555(13)
N(2)-C(14)	1.38(2)	N(1)-C(14)	1.09(2)
C(15)-C(16)	1.413(14)	N(2)-C(15)	1.349(13)
C(16)-C(18)	1.379(13)	C(16)-C(17)	1.549(12)

Table 2.19   *Interatomic angles (°) for [Fe₂Cp₂*(CO)₂(μ-SEt)₂](2,5-Me₂-DCNQI) (2)*

Table 2.19   Interatomic angles (°) for [Fe$_2$Cp$_2^*$(CO)$_2$(μ-SEt)$_2$](2,5-Me$_2$-DCNQI) (2)

Fe-S-Fe	86.3(1)	S-Fe-S	93.4(1)
S-Fe-C(1)	94.8(3)	S-Fe-C(2)	93.2(3)
C(1)-Fe-C(2)	153.5(4)	S-Fe-C(3)	127.1(3)
C(1)-Fe-C(3)	137.6(4)	C(2)-Fe-C(3)	37.8(4)
S-Fe-C(4)	155.2(3)	C(1)-Fe-C(4)	99.7(4)
C(2)-Fe-C(4)	65.4(3)	C(3)-Fe-C(4)	39.2(3)
S-Fe-C(5)	122.2(3)	C(1)-Fe-C(5)	89.1(4)
C(2)-Fe-C(5)	65.4(3)	C(3)-Fe-C(5)	64.8(4)
C(4)-Fe-C(5)	38.9(3)	S-Fe-C(6)	90.6(2)
C(1)-Fe-C(6)	115.7(4)	C(2)-Fe-C(6)	38.9(3)
C(3)-Fe-C(6)	63.9(4)	C(4)-Fe-C(6)	65.0(3)
C(5)-Fe-C(6)	38.8(3)	Fe-S-Fe	86.3(1)
Fe-S-C(12)	109.1(3)	S-Fe-S	93.4(1)
Fe-C(1)-O	175.2(8)	Fe-C(2)-C(3)	70.9(5)
Fe-C(2)-C(6)	69.9(5)	C(3)-C(2)-C(6)	106.9(8)
Fe-C(2)-C(7)	128.8(7)	C(3)-C(2)-C(7)	128.6(10)
C(6)-C(2)-C(7)	124.3(10)	Fe-C(3)-C(2)	71.3(5)
Fe-C(3)-C(4)	68.4(5)	C(2)-C(3)-C(4)	108.8(8)
Fe-C(3)-C(8)	130.9(7)	C(2)-C(3)-C(8)	124.9(10)
C(4)-C(3)-C(8)	126.0(10)	Fe-C(4)-C(3)	72.4(5)
Fe-C(4)-C(5)	71.2(5)	C(3)-C(4)-C(5)	107.7(8)
Fe-C(4)-C(9)	128.9(7)	C(3)-C(4)-C(9)	126.9(10)
C(5)-C(4)-C(9)	124.9(10)	Fe-C(5)-C(4)	70.0(5)
Fe-C(5)-C(6)	71.6(5)	C(4)-C(5)-C(6)	108.0(8)
Fe-C(5)-C(10)	127.2(6)	C(4)-C(5)-C(10)	128.5(9)
C(6)-C(5)-C(10)	123.4(9)	Fe-C(6)-C(2)	71.2(5)

Table 2.19 *(continued)*

Fe-C(6)-C(5)	69.7(5)	C(2)-C(6)-C(5)	108.5(8)
Fe-C(6)-C(11)	127.7(7)	C(2)-C(6)-C(11)	126.5(9)
C(5)-C(6)-C(11)	124.8(9)	S-C(12)-C(13)	110.6(7)
C(14)-N(2)-C(15)	120.3(10)	N(1)-C(14)-N(2)	173(2)
N(2)-C(15)-C(16)	120.3(9)	C(15)-C(16)-C(17)	118.4(10)
C(15)-C(16)-C(18)	120.8(8)	C(17)-C(16)-C(18)	120.8(10)

2.6.2.3 Single crystal X-ray diffraction study on [Fe$_2$Cp$_2^*$(CO)$_2$(μ-SEt)$_2$]$_2$(TCNQ)$_2$ (<u>6</u>)

Dark green cube shaped crystals suitable for X-ray diffraction studies, were grown by dissolving the salt in a minimum of a 1:1 acetonitrile/tetrahydrofuran mixture, reducing the volume of the solution *in vacuo* and cooling this solution to *ca.* -6°C.

The general procedure used for the intensity data collection is described in section A.5.1 of Appendix A and the general approach to structure solution and refinement in section A.5.2 of the same appendix.

Crystal data, as well as details specific to the data collection, structure solution and refinement for <u>6</u> are provided in Table 2.20. The Fe and S atoms of the cation, and all of the non-H atoms of the anion, were refined anisotropically. The remaining non-H atoms wre assigned individual isotropic temperature factors. H atoms were not located. The fractional atomic coordinates and isotropic thermal factors are listed in Table 2.21 and anisotropic thermal factors in Table 2.22. The interatomic distances are provided in Table 2.23 and the interatomic angles in Table 2.24. The observed and calculated structure factors for <u>6</u> may be found on microfiche in an envelope attached to the inside back cover.

Table 2.20   *Crystal Data and Details of the Crystallographic Analysis for*

  [Fe₂Cp₂(CO)₂(μ-SEt)₂]₂(TCNQ)₂ (**6**)*

Formula	$Fe_4S_4O_4C_{76}H_{88}N_8$
Molecular Mass	1528.32
Crystal Dimensions (mm)	0.23 x 0.27 x 0.27
Crystal System	Monoclinic
Space Group	$C2/c$
a (Å)	34.406(3)
b (Å)	9.224(1)
c (Å)	25.539(2)
α (°)	90
β (°)	111.45(6)
γ (°)	90
V (Å³)	7544(1)
Z	4
D_c (g.cm⁻³)	1.35
F(000)	3200
λ(Mo - Kα) (Å)	0.71069
Scan Mode	ω - 2θ
ω scan angle	$0.6 + 0.41\tan\theta$
Horizontal Aperture Width (mm)	$2.7 + 0.1\tan\theta$
Scattering range (°)	$2 \le \theta \le 23$
μ (cm⁻¹)	9.37
Absorption Corrections	Semi empirical
Measured Intensities	5764
Unique Intensities	4774
Unique Intensities with $[I > 3\sigma(I)]$	3531
Structure Solution	Direct & Fourier Methods
Weighting Scheme	$1/[\sigma^2(F) + 0.003020F^2]$
$R = \Sigma\|F_o - F_c\|/\Sigma F_o$	0.0755
$R_w = \Sigma w^{1/2}\|F_o - F_c\|/\Sigma w^{1/2}F_o$	0.0868
$(\Delta/\sigma)_{max}$	0.356
$\Delta\rho_{max}$ (e.Å⁻³)	0.950
Number of parameters	293

Table 2.21 *Fractional Coordinates (x 10⁴) and Isotropic Thermal Factors (Å², x 10³)*
for [Fe₂Cp₂(CO)₂(μ-SEt)₂]₂(TCNQ)₂ (**6**)*

	x/a	y/b	z/c	$\underline{U}_{eq}$
Fe(1)	3256	-350(1)	1771(1)	44
Fe(2)	3775	-427(1)	1014(1)	48
S(1)	3926(1)	122(3)	1933(1)	53(1)
S(2)	3100(1)	-902(2)	859(1)	46(1)
O(1)	2977(3)	2619(9)	1537(3)	94(2)*
O(2)	3622(3)	2526(11)	621(4)	106(3)*
N(1)	5311(3)	-4771(13)	1724(4)	100(3)
N(2)	5512(3)	-1102(13)	800(4)	89(3)
N(3)	3256(3)	-7286(14)	-1018(5)	114(4)
N(4)	3449(3)	-3871(10)	-2044(4)	78(2)
C(1)	3112(3)	1433(12)	1644(4)	65(3)*
C(2)	3677(3)	1323(13)	799(5)	72(3)*
C(3)	2872(3)	-467(10)	2260(4)	55(2)*
C(4)	3288(3)	-672(9)	2610(3)	48(2)*
C(5)	3432(3)	-1979(10)	2434(4)	52(2)*
C(6)	3103(3)	-2512(9)	1954(3)	45(2)*
C(7)	2760(3)	-1551(10)	1836(3)	50(2)*
C(8)	4091(3)	-2505(10)	1105(4)	56(2)*
C(9)	3812(3)	-2351(11)	555(4)	61(3)*
C(10)	3917(3)	-1129(11)	312(4)	61(3)*
C(11)	4281(3)	-495(11)	721(4)	65(3)*
C(12)	4386(3)	-1346(10)	1217(4)	56(2)*

158

Table 2.21   *(continued)*

	x/a	y/b	z/c	$\underline{U}_{eq}$
C(13)	2569(4)	708(13)	2321(5)	83(3)*
C(14)	3529(3)	181(12)	3136(5)	71(3)*
C(15)	3853(3)	-2648(11)	2740(4)	65(3)*
C(16)	3097(3)	-3923(11)	1655(4)	61(3)*
C(17)	2332(3)	-1794(12)	1385(4)	66(3)*
C(18)	4130(4)	-3782(14)	1487(5)	88(3)*
C(19)	3471(4)	-3405(14)	241(5)	88(3)*
C(20)	3713(4)	-616(14)	-291(6)	95(4)*
C(21)	4537(4)	795(14)	641(5)	92(4)*
C(22)	4767(4)	-1146(14)	1744(5)	90(4)*
C(23)	4036(4)	2095(13)	2089(5)	81(3)*
C(24)	4470(7)	2470(23)	2189(9)	170(8)*
C(25)	2727(3)	449(12)	401(4)	70(3)*
C(26)	2627(4)	98(14)	-202(5)	91(4)*
C(27)	4773(3)	-3923(10)	307(3)	52(2)
C(28)	4544(3)	-5183(10)	324(4)	55(2)
C(29)	4207(3)	-5641(10)	-137(4)	54(2)
C(30)	4081(3)	-4801(10)	-641(4)	54(2)
C(31)	4323(3)	-3561(10)	-670(4)	54(2)
C(32)	4653(3)	-3111(10)	-214(4)	54(2)
C(33)	5114(3)	-3444(11)	787(4)	60(3)
C(34)	5227(3)	-4197(12)	1308(4)	65(3)
C(35)	5336(3)	-2132(14)	789(4)	67(3)

Table 2.21 *(continued)*

	x/a	y/b	z/c	$\underline{U}_{eq}$
C(36)	3712(3)	-5230(11)	-1104(4)	57(2)
C(37)	3463(3)	-6355(12)	-1060(5)	73(3)
C(38)	3573(3)	-4454(11)	-1630(4)	62(3)

* isotropic temperature factor

$$\underline{U}_{eq.} = \tfrac{1}{3} \Sigma_i \Sigma_j \underline{U}_{ij} a_i{}^* a_j{}^* (a_i . a_j)$$

Table 2.22 *Anisotropic Temperature Factors ($Å^2$, x 10^3) for [Fe$_2$Cp$_2^*$(CO)$_2$(μ-SEt)$_2$]$_2$(TCNQ)$_2$ (6)*

	U(11)	U(22)	U(33)	U(23)	U(13)	U(12)
Fe(1)	54(1)	37(1)	39(1)	-1(1)	16(1)	6(1)
Fe(2)	62(1)	40(1)	45(1)	3(1)	23(1)	0(1)
S(1)	59(1)	53(1)	44(1)	-6(1)	15(1)	-8(1)
S(2)	57(1)	42(1)	36(1)	-3(1)	14(1)	6(1)
N(1)	108(8)	122(9)	63(6)	20(6)	24(6)	-13(7)
N(2)	88(7)	94(8)	81(7)	-17(6)	26(5)	-35(6)
N(3)	68(7)	117(9)	131(10)	20(8)	7(7)	-18(7)
N(4)	84(6)	75(6)	56(5)	13(5)	3(5)	10(5)
C(27)	57(6)	56(5)	47(5)	-2(4)	24(5)	-1(5)
C(28)	53(5)	55(6)	62(6)	-1(5)	29(5)	5(5)
C(29)	49(5)	65(6)	53(6)	2(5)	23(5)	8(5)
C(30)	57(6)	59(6)	54(5)	0(4)	30(5)	9(5)
C(31)	52(5)	55(6)	55(6)	2(4)	20(5)	2(5)
C(32)	51(5)	62(6)	54(5)	-2(5)	22(5)	-1(5)
C(33)	50(6)	77(7)	52(6)	-2(5)	18(5)	-5(5)
C(34)	61(6)	81(8)	55(6)	-12(6)	25(5)	-6(5)
C(35)	54(6)	86(8)	55(6)	-6(6)	14(5)	-12(6)
C(36)	42(5)	62(6)	62(6)	2(5)	14(4)	2(5)
C(37)	49(6)	64(7)	87(8)	4(6)	4(6)	-6(6)
C(38)	53(6)	64(7)	64(7)	-11(6)	16(5)	2(5)

Table 2.23   *Interatomic Distances (Å) for [Fe₂Cp₂*(CO)₂(μ-SEt)₂]₂(TCNQ)₂ (6)*

Fe(1)-Fe(2)	3.076(2)	Fe(1)-S(1)	2.233(3)
Fe(1)-S(2)	2.248(2)	Fe(1)-C(1)	1.714(11)
Fe(1)-C(3)	2.125(9)	Fe(1)-C(4)	2.125(8)
Fe(1)-C(5)	2.177(9)	Fe(1)-C(6)	2.157(8)
Fe(1)-C(7)	2.092(9)	Fe(2)-S(1)	2.267(2)
Fe(2)-S(2)	2.252(3)	Fe(2)-C(2)	1.699(12)
Fe(2)-C(8)	2.174(9)	Fe(2)-C(9)	2.156(10)
Fe(2)-C(10)	2.125(10)	Fe(2)-C(11)	2.133(10)
Fe(2)-C(12)	2.147(9)	S(1)-C(23)	1.872(12)
S(2)-C(25)	1.862(11)	O(1)-C(1)	1.181(12)
O(2)-C(2)	1.187(12)	N(1)-C(34)	1.127(13)
N(2)-C(35)	1.122(13)	N(3)-C(37)	1.146(13)
N(4)-C(38)	1.121(12)	C(3)-C(4)	1.396(11)
C(3)-C(7)	1.419(12)	C(3)-C(13)	1.551(14)
C(4)-C(5)	1.437(12)	C(4)-C(14)	1.514(13)
C(5)-C(6)	1.419(11)	C(5)-C(15)	1.502(13)
C(6)-C(7)	1.418(11)	C(6)-C(16)	1.506(12)
C(7)-C(17)	1.518(12)	C(8)-C(9)	1.388(12)
C(8)-C(12)	1.428(12)	C(8)-C(18)	1.504(14)
C(9)-C(10)	1.396(13)	C(9)-C(19)	1.511(14)
C(10)-C(11)	1.431(13)	C(10)-C(20)	1.52(2)

Table 2.23   *(continued)*

C(11)-C(12)	1.420(13)	C(11)-C(21)	1.54(2)
C(12)-C(22)	1.507(14)	C(23)-C(24)	1.46(2)
C(25)-C(26)	1.49(2)	C(27)-C(28)	1.414(13)
C(27)-C(32)	1.450(12)	C(27)-C(33)	1.421(12)
C(28)-C(29)	1.383(13)	C(29)-C(30)	1.427(12)
C(30)-C(31)	1.431(12)	C(30)-C(36)	1.437(12)
C(31)-C(32)	1.360(12)	C(33)-C(34)	1.422(14)
C(33)-C(35)	1.43(2)	C(36)-C(37)	1.376(14)
C(36)-C(38)	1.441(14)		

Table 2.24   _Interatomic Angles (°) for [Fe$_2$Cp$_2$*(CO)$_2$(μ-SEt)$_2$]$_2$(TCNQ)$_2$ (**6**)_

Fe(2)-Fe(1)-S(1)	47.3(1)	Fe(2)-Fe(1)-S(2)	46.9(1)
S(1)-Fe(1)-S(2)	94.3(1)	Fe(2)-Fe(1)-C(1)	95.5(3)
S(1)-Fe(1)-C(1)	93.1(3)	S(2)-Fe(1)-C(1)	94.5(3)
Fe(2)-Fe(1)-C(3)	175.0(2)	S(1)-Fe(1)-C(3)	136.3(3)
S(2)-Fe(1)-C(3)	129.3(3)	C(1)-Fe(1)-C(3)	87.8(4)
Fe(2)-Fe(1)-C(4)	143.3(2)	S(1)-Fe(1)-C(4)	99.8(2)
S(2)-Fe(1)-C(4)	156.5(2)	C(1)-Fe(1)-C(4)	103.3(4)
C(3)-Fe(1)-C(4)	38.4(3)	Fe(2)-Fe(1)-C(5)	114.3(2)
S(1)-Fe(1)-C(5)	90.9(2)	S(2)-Fe(1)-C(5)	122.8(2)
C(1)-Fe(1)-C(5)	142.1(4)	C(3)-Fe(1)-C(5)	64.2(3)
C(4)-Fe(1)-C(5)	39.0(3)	Fe(2)-Fe(1)-C(6)	111.0(2)
S(1)-Fe(1)-C(6)	117.2(2)	S(2)-Fe(1)-C(6)	91.7(2)
C(1)-Fe(1)-C(6)	148.4(4)	C(3)-Fe(1)-C(6)	64.7(3)
C(4)-Fe(1)-C(6)	65.1(3)	C(5)-Fe(1)-C(6)	38.2(3)
Fe(2)-Fe(1)-C(7)	135.8(2)	S(1)-Fe(1)-C(7)	155.0(2)
S(2)-Fe(1)-C(7)	94.0(2)	C(1)-Fe(1)-C(7)	109.6(4)
C(3)-Fe(1)-C(7)	39.3(3)	C(4)-Fe(1)-C(7)	65.8(3)
C(5)-Fe(1)-C(7)	64.9(3)	C(6)-Fe(1)-C(7)	38.9(3)
Fe(1)-Fe(2)-S(1)	46.4(1)	Fe(1)-Fe(2)-S(2)	46.8(1)
S(1)-Fe(2)-S(2)	93.3(1)	Fe(1)-Fe(2)-C(2)	95.2(4)
S(1)-Fe(2)-C(2)	93.8(4)	S(2)-Fe(2)-C(2)	93.4(4)
Fe(1)-Fe(2)-C(8)	109.7(2)	S(1)-Fe(2)-C(8)	99.8(2)

164

Table 2.24   *(continued)*

S(2)-Fe(2)-C(8)	107.0(2)	C(2)-Fe(2)-C(8)	154.7(4)
Fe(1)-Fe(2)-C(9)	121.6(3)	S(1)-Fe(2)-C(9)	135.2(3)
S(2)-Fe(2)-C(9)	90.4(3)	C(2)-Fe(2)-C(9)	130.6(4)
C(8)-Fe(2)-C(9)	37.4(3)	Fe(1)-Fe(2)-C(10)	154.6(3)
S(1)-Fe(2)-C(10)	154.8(3)	S(2)-Fe(2)-C(10)	109.5(3)
C(2)-Fe(2)-C(10)	95.5(5)	C(8)-Fe(2)-C(10)	63.9(4)
C(9)-Fe(2)-C(10)	38.1(4)	Fe(1)-Fe(2)-C(11)	163.2(3)
S(1)-Fe(2)-C(11)	117.5(3)	S(2)-Fe(2)-C(11)	148.8(3)
C(2)-Fe(2)-C(11)	90.3(5)	C(8)-Fe(2)-C(11)	64.5(4)
C(9)-Fe(2)-C(11)	64.3(4)	C(10)-Fe(2)-C(11)	39.3(3)
Fe(1)-Fe(2)-C(12)	126.8(2)	S(1)-Fe(2)-C(12)	90.2(3)
S(2)-Fe(2)-C(12)	145.2(3)	C(2)-Fe(2)-C(12)	120.9(4)
C(8)-Fe(2)-C(12)	38.6(3)	C(9)-Fe(2)-C(12)	63.8(3)
C(10)-Fe(2)-C(12)	64.9(3)	C(11)-Fe(2)-C(12)	38.8(3)
Fe(1)-S(1)-Fe(2)	86.2(1)	Fe(1)-S(1)-C(23)	110.1(4)
Fe(2)-S(1)-C(23)	112.9(4)	Fe(1)-S(2)-Fe(2)	86.2(1)
Fe(1)-S(2)-C(25)	110.4(3)	Fe(2)-S(2)-C(25)	114.1(3)
Fe(1)-C(1)-O(1)	174.0(9)	Fe(2)-C(2)-O(2)	175.3(11)
Fe(1)-C(3)-C(4)	70.8(5)	Fe(1)-C(3)-C(7)	69.1(5)
C(4)-C(3)-C(7)	108.9(8)	Fe(1)-C(3)-C(13)	127.5(7)
C(4)-C(3)-C(13)	126.8(9)	C(7)-C(3)-C(13)	124.3(8)
Fe(1)-C(4)-C(3)	70.8(5)	Fe(1)-C(4)-C(5)	72.5(5)
C(3)-C(4)-C(5)	107.7(8)	Fe(1)-C(4)-C(14)	129.2(6)
C(3)-C(4)-C(14)	126.7(8)	C(5)-C(4)-C(14)	125.0(8)
Fe(1)-C(5)-C(4)	68.5(5)	Fe(1)-C(5)-C(6)	70.1(5)

Table 2.24   *(continued)*

C(4)-C(5)-C(6)	107.6(7)	Fe(1)-C(5)-C(15)	129.1(7)
C(4)-C(5)-C(15)	123.9(8)	C(6)-C(5)-C(15)	128.4(8)
Fe(1)-C(6)-C(5)	71.7(5)	Fe(1)-C(6)-C(7)	68.1(5)
C(5)-C(6)-C(7)	107.9(7)	Fe(1)-C(6)-C(16)	130.4(6)
C(5)-C(6)-C(16)	126.5(8)	C(7)-C(6)-C(16)	125.4(8)
Fe(1)-C(7)-C(3)	71.6(5)	Fe(1)-C(7)-C(6)	73.0(5)
C(3)-C(7)-C(6)	107.8(7)	Fe(1)-C(7)-C(17)	127.7(6)
C(3)-C(7)-C(17)	127.0(8)	C(6)-C(7)-C(17)	124.7(8)
Fe(2)-C(8)-C(9)	70.6(6)	Fe(2)-C(8)-C(12)	69.7(5)
C(9)-C(8)-C(12)	107.7(8)	Fe(2)-C(8)-C(18)	133.0(7)
C(9)-C(8)-C(18)	126.9(9)	C(12)-C(8)-C(18)	124.6(9)
Fe(2)-C(9)-C(8)	72.0(6)	Fe(2)-C(9)-C(10)	69.8(6)
C(8)-C(9)-C(10)	109.7(9)	Fe(2)-C(9)-C(19)	129.0(7)
C(8)-C(9)-C(19)	126.0(9)	C(10)-C(9)-C(19)	124.1(9)
Fe(2)-C(10)-C(9)	72.2(6)	Fe(2)-C(10)-C(11)	70.7(6)
C(9)-C(10)-C(11)	107.7(9)	Fe(2)-C(10)-C(20)	126.7(8)
C(9)-C(10)-C(20)	127.2(9)	C(11)-C(10)-C(20)	124.8(10)
Fe(2)-C(11)-C(10)	70.1(6)	Fe(2)-C(11)-C(12)	71.2(6)
C(10)-C(11)-C(12)	107.1(8)	Fe(2)-C(11)-C(21)	127.2(7)
C(10)-C(11)-C(21)	127.5(9)	C(12)-C(11)-C(21)	125.2(9)
Fe(2)-C(12)-C(8)	71.7(5)	Fe(2)-C(12)-C(11)	70.1(5)
C(8)-C(12)-C(11)	107.7(8)	Fe(2)-C(12)-C(22)	128.5(7)
C(8)-C(12)-C(22)	126.4(9)	C(11)-C(12)-C(22)	125.6(9)
S(1)-C(23)-C(24)	112.4(11)	S(2)-C(25)-C(26)	110.6(8)
C(28)-C(27)-C(32)	118.6(8)	C(28)-C(27)-C(33)	121.5(8)

Table 2.24 *(continued)*

C(32)-C(27)-C(33)	120.0(8)	C(27)-C(28)-C(29)	121.9(9)
C(28)-C(29)-C(30)	119.1(9)	C(29)-C(30)-C(31)	119.3(8)
C(29)-C(30)-C(36)	118.5(9)	C(31)-C(30)-C(36)	122.2(8)
C(30)-C(31)-C(32)	121.3(8)	C(27)-C(32)-C(31)	119.8(8)
C(27)-C(33)-C(34)	120.8(9)	C(27)-C(33)-C(35)	122.5(9)
C(34)-C(33)-C(35)	116.5(9)	N(1)-C(34)-C(33)	178.3(12)
N(2)-C(35)-C(33)	178.8(12)	C(30)-C(36)-C(37)	121.9(9)
C(30)-C(36)-C(38)	121.5(9)	C(37)-C(36)-C(38)	116.5(9)
N(3)-C(37)-C(36)	179.3(14)	N(4)-C(38)-C(36)	177.3(11)

2.6.2.4 Single crystal X-ray diffraction study on $[Fe_2Cp_2^{*}(CO)_2(\mu\text{-}SEt)_2](TCNE)$ (7)

Single crystals of 7, suitable for X-ray diffraction studies, were grown by dissolving the salt in a minimum amount of a 1:1 acetonitrile/toluene solution and reducing the volume *in vacuo*. Cooling this solution to *ca.* -20°C and storing it at this temperature for longer than 2 weeks resulted in the separation of dark green-black needle-like crystals.

The general procedure for the intensity data collection and the general approach to structure solution and refinement are described in sections A.5.1 and A.5.2 of Appendix A, respectively.

The crystal data, as well as details specific to the data collection, structure solution and refinement for 7 are provided in Table 2.25. The Fe and S atoms of the cation, and all of the non-H atoms of the anions, were refined anisotropically. The remaining non-H atoms were assigned individual isotropic temperature factors. H atoms were not located. The fractional atomic coordinates and isotropic thermal factors are listed in Table 2.26 and anisotropic thermal factors in Table 2.27. The interatomic distances are provided in Table 2.28 and the interatomic angles in Table 2.29. The observed and calculated structure factors for 7 may be found on microfiche in an envelope attached to the inside back cover.

Table 2.25   *Crystal Data and Details of the Crystallographic Analysis for*

   $[Fe_2Cp_2^*(CO)_2(\mu\text{-}SEt)_2](TCNE)$ (7)

Formula	$Fe_2S_2O_2C_{32}H_{40}N_4$
Molecular Mass	688.51
Crystal Dimensions (mm)	0.08 x 0.04 x 0.27
Crystal System	Monoclinic
Space Group	$P2_1/n$
a (Å)	11.815(3)
b (Å)	19.916(4)
c (Å)	14.535(3)
α (°)	90
β (°)	98.56(2)
γ (°)	90
V ($Å^3$)	3382(1)
Z	4
D_c (g.cm^{-3})	1.35
F(000)	1440
λ(Mo - Kα) (Å)	0.71069
Scan Mode	ω - 2θ
ω scan angle	0.6 + 0.59tanθ
Horizontal Aperture Width (mm)	2.7 + 0.1tanθ
Scattering range	$2 \leq \theta \leq 23$
μ (cm^{-1})	10.31
Absorption Corrections	Semi empirical
Measured Intensities	4956
Unique Intensities	3699
Unique Intensities with $[I > 3\sigma(I)]$	2484
Structure Solution	Direct & Fourier Methods
Weighting Scheme	$1/[\sigma^2(F) + 0.002303F^2]$
$R = \Sigma\|F_o - F_c\|/\Sigma F_o$	0.0704
$R_w = \Sigma w^{1/2}\|F_o - F_c\|/\Sigma w^{1/2}F_o$	0.0757
$(\Delta/\sigma)_{max}$	1.184*
$\Delta\rho_{max}$ (e.$Å^{-3}$)	0.814
Number of parameters	259

* Associated with disordered TCNE⁻ see Section 2.4.8.2.

Table 2.26   *Fractional Coordinates (x 10⁴) and Isotropic Thermal Factors (Å², x 10³)*
for [Fe₂Cp₂(CO)₂(μ-SEt)₂](TCNE) (**7**)*

	x/a	y/b	z/c	$\underline{U}_{eq}$
Fe(1)	1616(1)	1866(1)	4216(1)	40
Fe(2)	-201(1)	2728(1)	4960(1)	43
S(1)	1651(3)	2904(2)	4836(2)	45(1)
S(2)	-215(2)	1681(2)	4385(2)	42(1)
O(1)	1147(9)	2356(5)	2318(6)	81(3)
O(2)	-1109(10)	3356(6)	3216(7)	99(4)
C(1)	1321(10)	2165(6)	3098(11)	56(4)
C(2)	-711(11)	3096(7)	3892(9)	56(3)
C(3)	2679(11)	1146(6)	3714(9)	55(3)*
C(4)	3360(10)	1655(6)	4208(8)	45(3)*
C(5)	3180(10)	1634(6)	5140(8)	47(3)*
C(6)	2367(10)	1144(6)	5238(8)	48(3)*
C(7)	2062(10)	829(6)	4349(8)	48(3)*
C(8)	38(11)	2732(7)	6452(9)	57(3)*
C(9)	-922(10)	2337(6)	6140(8)	52(3)*
C(10)	-1723(10)	2749(6)	5543(8)	46(3)*
C(11)	-1250(11)	3408(6)	5559(8)	50(3)*
C(12)	-174(10)	3386(6)	6115(8)	54(3)*
C(13)	2719(13)	940(8)	2718(11)	80(5)*
C(14)	4188(12)	2116(7)	3794(10)	70(4)*
C(15)	3814(13)	2040(7)	5931(10)	70(4)*
C(16)	1992(12)	877(7)	6139(10)	68(4)*

Table 2.26   *(continued)*

	x/a	y/b	z/c	$\underline{U}_{eq}$
C(17)	1318(13)	208(8)	4185(10)	76(4)*
C(18)	1079(13)	2517(8)	7144(11)	83(5)*
C(19)	-1128(12)	1619(7)	6412(9)	65(4)*
C(20)	-2892(12)	2554(7)	5082(10)	70(4)*
C(21)	-1858(14)	4031(8)	5136(11)	89(5)*
C(22)	630(15)	3991(9)	6377(12)	98(5)*
C(23)	1854(12)	3522(7)	3909(10)	71(4)*
C(24)	1763(15)	4221(9)	4255(12)	103(6)*
C(25)	-1173(11)	1635(7)	3280(9)	61(4)*
C(26)	-1117(14)	946(8)	2821(11)	86(5)*
N(1)	3538(14)	-873(9)	6006(14)	129(6)
N(2)	5959(16)	727(10)	6734(12)	142(6)
C(27)	5066(26)	91(16)	5347(15)	170(10)
C(28)	4078(19)	-549(12)	5669(17)	118(8)
C(29)	5547(15)	447(9)	6108(13)	83(5)
N(3)	9952(19)	1375(9)	672(15)	152(7)
N(4)	9641(23)	-620(11)	1786(13)	186(10)
C(30)	9941(14)	129(10)	410(10)	86(5)
C(31)	9915(18)	838(10)	548(14)	102(6)
C(32)	9774(18)	-299(11)	1161(14)	113(7)

* isotropic temperature factor

$$\underline{U}_{eq.} = {}^{1}/_{3}\ \Sigma_i\Sigma_j\underline{U}_{ij}a_i{}^{*}a_j{}^{*}(a_i.a_j)$$

Table 2.27   _Anisotropic Temperature Factors ($\mathring{A}^2$, x 10^3) for [Fe$_2$Cp$_2$*(CO)$_2$(μ-_
SEt)$_2$](TCNE) (**7**)

	U(11)	U(22)	U(33)	U(23)	U(13)	U(12)
Fe(1)	34(1)	49(1)	35(1)	2(1)	6(1)	0(1)
Fe(2)	39(1)	53(1)	36(1)	-6(1)	4(1)	2(1)
S(1)	42(2)	46(2)	47(2)	-5(1)	9(1)	-5(1)
S(2)	34(2)	53(2)	39(2)	-7(1)	5(1)	-6(1)
O(1)	106(9)	101(8)	37(5)	10(5)	9(5)	5(7)
O(2)	112(9)	130(10)	52(6)	10(7)	-5(6)	44(8)
C(1)	33(7)	61(9)	74(10)	-17(8)	6(7)	8(6)
C(2)	62(9)	63(9)	40(7)	-11(7)	1(6)	3(7)
N(1)	96(12)	131(15)	169(17)	29(13)	53(11)	-9(11)
N(2)	159(18)	141(16)	111(13)	-67(12)	-26(12)	36(13)
C(27)	161(22)	197(26)	130(23)	-84(21)	-51(22)	150(21)
C(28)	90(16)	111(19)	159(21)	23(15)	39(15)	24(14)
C(29)	90(13)	75(12)	80(13)	-13(10)	-4(10)	33(10)
N(3)	197(21)	82(13)	192(19)	-41(14)	81(16)	-5(14)
N(4)	307(33)	159(20)	97(14)	52(14)	49(17)	12(19)
C(30)	75(11)	116(15)	69(10)	-6(10)	21(9)	6(10)
C(31)	122(16)	65(12)	125(16)	-20(12)	42(13)	9(13)
C(32)	136(16)	122(18)	80(13)	7(13)	9(12)	9(14)

Table 2.28   _Interatomic Distances (Å) for [Fe₂Cp₂*(CO)₂(μ-SEt)₂](TCNE) (**7**)_

Fe(1)-Fe(2)	3.068(2)	Fe(1)-S(1)	2.252(3)
Fe(1)-S(2)	2.243(3)	Fe(1)-C(1)	1.72(2)
Fe(1)-C(3)	2.108(12)	Fe(1)-C(4)	2.104(11)
Fe(1)-C(5)	2.166(11)	Fe(1)-C(6)	2.161(11)
Fe(1)-C(7)	2.133(11)	Fe(2)-S(1)	2.249(3)
Fe(2)-S(2)	2.247(3)	Fe(2)-C(2)	1.740(13)
Fe(2)-C(8)	2.145(12)	Fe(2)-C(9)	2.171(11)
Fe(2)-C(10)	2.100(11)	Fe(2)-C(11)	2.110(12)
Fe(2)-C(12)	2.126(12)	S(1)-C(23)	1.866(14)
S(2)-C(25)	1.824(13)	O(1)-C(1)	1.185(14)
O(2)-C(2)	1.148(13)	C(3)-C(4)	1.42(2)
C(3)-C(7)	1.41(2)	C(3)-C(13)	1.51(2)
C(4)-C(5)	1.403(14)	C(4)-C(14)	1.53(2)
C(5)-C(6)	1.39(2)	C(5)-C(15)	1.51(2)
C(6)-C(7)	1.43(2)	C(6)-C(16)	1.54(2)
C(7)-C(17)	1.52(2)	C(8)-C(9)	1.40(2)
C(8)-C(12)	1.40(2)	C(8)-C(18)	1.53(2)
C(9)-C(10)	1.44(2)	C(9)-C(19)	1.51(2)
C(10)-C(11)	1.43(2)	C(10)-C(20)	1.50(2)
C(11)-C(12)	1.40(2)	C(11)-C(21)	1.52(2)
C(12)-C(22)	1.55(2)	C(23)-C(24)	1.49(2)
C(25)-C(26)	1.53(2)	N(1)-C(28)	1.08(2)
N(2)-C(29)	1.11(2)	C(27)-C(28)	1.84(4)
C(27)-C(29)	1.37(3)	C(27)-C(27)	1.06(4)
N(3)-C(31)	1.09(2)	N(4)-C(32)	1.14(2)
C(30)-C(31)	1.43(2)	C(30)-C(32)	1.42(2)
C(30)-C(30)	1.33(3)		

Table 2.29   *Interatomic Angles (°) for [Fe$_2$Cp$_2$*(CO)$_2$(μ-SEt)$_2$](TCNE) (__7__)*

Fe(2)-Fe(1)-S(1)	47.0(1)	Fe(2)-Fe(1)-S(2)	46.9(1)
S(1)-Fe(1)-S(2)	93.9(1)	Fe(2)-Fe(1)-C(1)	94.9(4)
S(1)-Fe(1)-C(1)	92.8(4)	S(2)-Fe(1)-C(1)	95.6(4)
Fe(2)-Fe(1)-C(3)	170.8(3)	S(1)-Fe(1)-C(3)	141.9(3)
S(2)-Fe(1)-C(3)	124.0(3)	C(1)-Fe(1)-C(3)	87.5(5)
Fe(2)-Fe(1)-C(4)	148.3(3)	S(1)-Fe(1)-C(4)	103.1(3)
S(2)-Fe(1)-C(4)	158.2(3)	C(1)-Fe(1)-C(4)	97.2(5)
C(3)-Fe(1)-C(4)	39.4(4)	Fe(2)-Fe(1)-C(5)	118.6(3)
S(1)-Fe(1)-C(5)	89.2(3)	S(2)-Fe(1)-C(5)	130.1(3)
C(1)-Fe(1)-C(5)	134.0(5)	C(3)-Fe(1)-C(5)	64.6(4)
C(4)-Fe(1)-C(5)	38.3(4)	Fe(2)-Fe(1)-C(6)	111.6(3)
S(1)-Fe(1)-C(6)	110.8(3)	S(2)-Fe(1)-C(6)	96.8(3)
C(1)-Fe(1)-C(6)	152.4(5)	C(3)-Fe(1)-C(6)	65.2(4)
C(4)-Fe(1)-C(6)	64.5(4)	C(5)-Fe(1)-C(6)	37.5(4)
Fe(2)-Fe(1)-C(7)	133.3(3)	S(1)-Fe(1)-C(7)	149.6(3)
S(2)-Fe(1)-C(7)	93.4(3)	C(1)-Fe(1)-C(7)	115.7(5)
C(3)-Fe(1)-C(7)	38.8(4)	C(4)-Fe(1)-C(7)	65.1(4)
C(5)-Fe(1)-C(7)	63.9(4)	C(6)-Fe(1)-C(7)	39.0(4)
Fe(1)-Fe(2)-S(1)	47.1(1)	Fe(1)-Fe(2)-S(2)	46.8(1)
S(1)-Fe(2)-S(2)	93.9(1)	Fe(1)-Fe(2)-C(2)	95.1(4)
S(1)-Fe(2)-C(2)	94.3(4)	S(2)-Fe(2)-C(2)	94.4(4)
Fe(1)-Fe(2)-C(8)	111.4(3)	S(1)-Fe(2)-C(8)	95.6(3)
S(2)-Fe(2)-C(8)	111.8(4)	C(2)-Fe(2)-C(8)	151.2(5)
Fe(1)-Fe(2)-C(9)	117.0(3)	S(1)-Fe(2)-C(9)	128.3(3)

Table 2.29   *(continued)*

S(2)-Fe(2)-C(9)	88.8(3)	C(2)-Fe(2)-C(9)	137.0(5)
C(8)-Fe(2)-C(9)	37.8(4)	Fe(1)-Fe(2)-C(10)	147.1(3)
S(1)-Fe(2)-C(10)	158.6(3)	S(2)-Fe(2)-C(10)	102.1(3)
C(2)-Fe(2)-C(10)	98.5(5)	C(8)-Fe(2)-C(10)	65.4(4)
C(9)-Fe(2)-C(10)	39.4(4)	Fe(1)-Fe(2)-C(11)	171.7(3)
S(1)-Fe(2)-C(11)	124.9(3)	S(2)-Fe(2)-C(11)	141.0(3)
C(2)-Fe(2)-C(11)	87.2(5)	C(8)-Fe(2)-C(11)	65.0(5)
C(9)-Fe(2)-C(11)	65.2(4)	C(10)-Fe(2)-C(11)	39.6(4)
Fe(1)-Fe(2)-C(12)	133.9(3)	S(1)-Fe(2)-C(12)	93.9(3)
S(2)-Fe(2)-C(12)	149.8(3)	C(2)-Fe(2)-C(12)	114.1(5)
C(8)-Fe(2)-C(12)	38.3(4)	C(9)-Fe(2)-C(12)	63.8(4)
C(10)-Fe(2)-C(12)	65.3(4)	C(11)-Fe(2)-C(12)	38.7(4)
Fe(1)-S(1)-Fe(2)	86.0(1)	Fe(1)-S(1)-C(23)	108.3(5)
Fe(2)-S(1)-C(23)	113.0(4)	Fe(1)-S(2)-Fe(2)	86.2(1)
Fe(1)-S(2)-C(25)	113.2(4)	Fe(2)-S(2)-C(25)	110.1(4)
Fe(1)-C(1)-O(1)	177.6(10)	Fe(2)-C(2)-O(2)	175.2(12)
Fe(1)-C(3)-C(4)	70.1(7)	Fe(1)-C(3)-C(7)	71.6(7)
C(4)-C(3)-C(7)	107.3(10)	Fe(1)-C(3)-C(13)	128.4(9)
C(4)-C(3)-C(13)	125.5(11)	C(7)-C(3)-C(13)	126.8(12)
Fe(1)-C(4)-C(3)	70.4(7)	Fe(1)-C(4)-C(5)	73.2(6)
C(3)-C(4)-C(5)	108.0(10)	Fe(1)-C(4)-C(14)	124.6(8)
C(3)-C(4)-C(14)	125.3(10)	C(5)-C(4)-C(14)	126.6(11)
Fe(1)-C(5)-C(4)	68.5(6)	Fe(1)-C(5)-C(6)	71.0(7)
C(4)-C(5)-C(6)	109.1(10)	Fe(1)-C(5)-C(15)	129.6(9)
C(4)-C(5)-C(15)	126.1(10)	C(6)-C(5)-C(15)	124.7(10)

Table 2.29   *(continued)*

Fe(1)-C(6)-C(5)	71.4(7)	Fe(1)-C(6)-C(7)	69.5(7)
C(5)-C(6)-C(7)	107.4(10)	Fe(1)-C(6)-C(16)	132.4(8)
C(5)-C(6)-C(16)	128.4(11)	C(7)-C(6)-C(16)	123.4(10)
Fe(1)-C(7)-C(3)	69.7(7)	Fe(1)-C(7)-C(6)	71.6(7)
C(3)-C(7)-C(6)	108.1(10)	Fe(1)-C(7)-C(17)	130.3(9)
C(3)-C(7)-C(17)	127.4(11)	C(6)-C(7)-C(17)	124.1(11)
Fe(2)-C(8)-C(9)	72.1(7)	Fe(2)-C(8)-C(12)	70.1(7)
C(9)-C(8)-C(12)	108.4(11)	Fe(2)-C(8)-C(18)	129.5(9)
C(9)-C(8)-C(18)	126.1(12)	C(12)-C(8)-C(18)	125.1(12)
Fe(2)-C(9)-C(8)	70.1(7)	Fe(2)-C(9)-C(10)	67.6(6)
C(8)-C(9)-C(10)	107.6(10)	Fe(2)-C(9)-C(19)	130.0(8)
C(8)-C(9)-C(19)	127.0(11)	C(10)-C(9)-C(19)	125.4(10)
Fe(2)-C(10)-C(9)	72.9(6)	Fe(2)-C(10)-C(11)	70.6(7)
C(9)-C(10)-C(11)	107.1(10)	Fe(2)-C(10)-C(20)	127.1(8)
C(9)-C(10)-C(20)	127.0(11)	C(11)-C(10)-C(20)	125.5(11)
Fe(2)-C(11)-C(10)	69.8(7)	Fe(2)-C(11)-C(12)	71.3(7)
C(10)-C(11)-C(12)	107.5(10)	Fe(2)-C(11)-C(21)	129.0(9)
C(10)-C(11)-C(21)	125.8(11)	C(12)-C(11)-C(21)	126.4(12)
Fe(2)-C(12)-C(8)	71.6(7)	Fe(2)-C(12)-C(11)	70.1(7)
C(8)-C(12)-C(11)	109.3(11)	Fe(2)-C(12)-C(22)	127.7(9)
C(8)-C(12)-C(22)	124.5(12)	C(11)-C(12)-C(22)	126.0(12)
S(1)-C(23)-C(24)	110.5(10)	S(2)-C(25)-C(26)	111.5(10)
C(28)-C(27)-C(29)	111(2)	N(1)-C(28)-C(27)	167(3)
N(2)-C(29)-C(27)	178(2)	C(31)-C(30)-C(32)	119(2)
N(3)-C(31)-C(30)	176(3)	N(4)-C(32)-C(30)	177(2)

2.6.3 Magnetic Susceptibility measurements

2.6.3.1 [Fe$_2$Cp$_2^*$(CO)$_2$(μ-SEt)$_2$](2,5-Me$_2$-DCNQI) (2)

Variable temperature magnetic susceptibility measurements on polycrystalline samples of **2** were performed by J.S. Miller and co-workers of E.I. du Pont de Nemours and Company, Inc, utilizing the Faraday method. A full description of the apparatus involved, typical sample size and experimental conditions may be found in reference 232.

2.6.3.2 [Fe$_2$Cp$_2^*$(CO)$_2$(μ-SEt)$_2$](TCNQ) (6)

The room temperature magnetic susceptibility of polycrystalline samples of **6** was determined using a Sherwood Scientific Magnetic Susceptibility Balance. Measurements were conducted in air. The conventional HgCo(SCN)$_4$ standard was used to calibrate the apparatus. Samples, typically ranging in mass between *ca.* 0.08 and 0.12 g, were contained in glass tubes. The diamagnetic contribution of these tubes to the observed susceptibility was determined and corrected for. Further correction factors include the diamagnetic core corrections of -355 x 10^{-6} emu/mol for the cation[246] and -98 x 10^6 emu/mol for the TCNQ$^-$ anion.[233]

2.6.3.3 [Fe$_2$Cp$_2^*$(CO)$_2$(μ-SEt)$_2$](TCNE) (7)

The magnetic dipole moment of a polycrystalline sample of **7** as a function of temperature, was determined with a superconducting quantum interference device (SQUID) magnetometer. The sample (of mass 0.0325 g) was contained in a glass capsule which was packed in a glovebox under a nitrogen atmosphere. The capsule was placed in an extended plastic tube with a thin platform, consisting of two pieces of thin cotton thread, across the middle of the tube dividing the tube into two equal lengths. With this design only the platform and a minimal amount of the glass from the sample capsule contribute to the background. The magnetic dipole data were not corrected for sample holder or core diamagnetism. Instead the observed magnetic susceptibility χ_m, as a function of temperature, calculated from the dipole data, was fitted to the sum of a Curie-Weiss term $\chi_{cw} = C/(T-\theta)$ and a diamagnetic term χ_d, *i.e.* $\chi_m = C/(T-\theta) + \chi_d$.[247]

CHAPTER THREE

Square planar bipyridyl and terpyridyl complexes of platinum(II)

3.1 Introduction

Square planar bipyridyl and terpyridyl complexes of Pt(II) form part of the broader category of platinum haloamine complexes, the first examples of which were synthesized in the late 1800's (see Section 1.2.2.3). However, detailed studies of the physical properties of these complexes were, first undertaken in 1951.[41] The possibility of their exhibiting high electrical conductivity did attract some attention, but the interest was short-lived, since most of these complexes display semiconducting or insulating behaviour.[42]

Current interest in platinum haloamine complexes, and in particular in bipyridyl and terpyridyl complexes of platinum(II), centres around the photoluminescent properties of these complexes and in particular in their excited state chemistry, the ultimate goal being to utilize them as photocatalysts for C-H and C-X (X = halogen) bond activation[248] or as microheterogeneous photosensitizers to drive energy storage redox reactions.[249] A further line of interest involves the biological activity of the platinum(II) complexes; specifically as anti-tumour agents.[250]

3.2 Aims of this work

At present the main interest in polypyridyl complexes of platinum(II) is centred around their excited state chemistry and their biological activity. As a consequence, the majority of photoluminescent studies are conducted on solutions of the platinum(II) complexes, with less attention being paid to their solid state emission properties.

As explained in Chapter 1, a variety of extended interactions are possible for low-dimensional materials in the solid state, examples being metal-metal and ligand-ligand interactions. The bulk physical properties of the majority of low-dimensional materials can be attributed to such solid state interactions. It is thus of crucial importance to assess and understand the interactions present in a low-dimensional solid if the solid

state structure of such a compound, on a molecular level, is to be reconciled with its bulk physical properties on a macroscopic level. Since the studies on the photoluminescent properties of the platinum(II) complexes in solution is specifically aimed at probing the properties of these complexes as monomeric units, dimerization and oligomerization of the complexes in solution is often specifically avoided. This implies that, whereas a wealth of information is being collected on the luminescence of these complexes in solution, less attention is being paid to the extended interactions which could occur in the solid state. In the light of this, it was deemed appropriate to embark on a line of research specifically aimed at probing the extended interactions in square planar bipyridyl and terpyridyl complexes of platinum(II) in the solid state.

The specific goals of this study thus included the following:

1) The synthesis and characterization of square planar bipridyl and terpyridyl complexes of Pt(II).

2) The determination of their solid state structures.

3) The investigation of their photoluminescent properties particularly in the solid state, but also in solution for comparative purposes.

4) The reconciliation of the observed bulk physical properties of these materials with their solid state structures.

A comparison of the goals outlined for this study with those cited for the dinuclear metallocene-based charge transfer salts described in Chapter 2, reveals that the goals are essentially the same. The only difference between the two studies is that, whereas the magnetic properties of the metallocene-based charge transfer salts were reconciled with their solid state structures, the physical property investigated and to be reconciled in this instance, is the photoluminescence of the bi- and terpyridyl Pt(II) complexes.

In order to place the results of this study in context, it is necessary to first consider some of the basic theoretical considerations associated with absorption and luminescence spectroscopy. This will be followed by a brief overview of selected literature results pertaining to luminescent square planar Pt(II) complexes. No attempt will be made at being comprehensive. Instead, results illustrating fundamental principles will be discussed.

The final section of this chapter will consist of a report and discussion of the results obtained in this study of bi- and terpyridyl complexes of Pt(II).

3.3 Background

3.3.1 Fundamental theoretical considerations

The absorption and emission of electromagnetic radiation in the form of light by a molecule are two closely related processes. Absorption constitutes the uptake of radiation energy to produce an electronically excited state of the absorbing species, whereas emission (or radiative decay) implies the relaxation of the excited state species back to its ground state through the emission of energy in the form of light. radiative decay however, is only one of a variety of pathways which could be available to the excited state species to return to its ground state.

The amount of monochromatic radiation absorbed by a material in relation to the concentration of the sample, is described by the Beer-Lambert law, which can be written as:

$$A = \log_{10}(I \, / \, I_t) = \varepsilon bc$$

The symbols used in the above formulation and the conditions under which the law applies are well-known, and will not be discussed.

As mentioned above, the absorption of ultraviolet or visible radiation by a molecule produces an electronically excited state. In the case of a transition metal complex, the excited state most frequently arises from one or more of the following electronic transitions:

1)   Ligand field or d-d transitions.

2)   Intraligand transitions.

3)   Charge transfer transitions.

Ligand field or d-d transitions imply the promotion of an electron in a metal d orbital to an empty or partially occupied d orbital. Such transitions are Laporte forbidden, *i.e.* the molar extinction coefficient, ε, associated with these transitions is relatively small, typically in the range of 1 to 100 $dm^3mol^{-1}cm^{-1}$. For molecules in solution, the energy

of these transitions is independent of the nature of the solvent. Furthermore, if the d orbital to which the electron is excited is antibonding in nature, the excited state molecule may be susceptible to ligand substitution reactions.

Intraligand transitions involve the excitation of electrons from the highest occupied ligand orbital to the lowest unoccupied or partially occupied ligand orbital. Depending on the relative energies associated with the various ligand orbitals, this lowest energy transition could be a $\pi \rightarrow \pi^*$, $n \rightarrow \pi^*$, $n \rightarrow \sigma^*$ or a $\sigma \rightarrow \sigma^*$ transition. In this context, the lowest energy transition for an uncoordinated pyridine ligand is a $n \rightarrow \pi^*$ transition, involving excitation of a nonbonding electron into the ring system. On coordination, with the nonbonding electrons participating in a σ bond to the metal ion, the energy of these electrons is lowered beyond that of the highest occupied π orbital on the pyridine ligand. This implies that the lowest energy intraligand transition associated with a coordinated pyridine ligand is a $\pi \rightarrow \pi^*$ transition; this transition being commonly encountered in studies involving pyridine or pyridine-based coordinated ligands. The molar extinction coefficient, ε, associated with intraligand transitions, generally occurs in the range of 10^4 to 10^5 $dm^3mol^{-1}cm^{-1}$. Intraligand transitions are furthermore generally associated with the absorption of light from the ultraviolet region of the spectrum and are not greatly affected by the presence or absence of other ligands coordinated to the metal atom.

The third type of transition associated with the absorption of ultraviolet or visible radiation is charge transfer transitions. These transitions involve the transfer of electrons from one part of the molecule, which functions as the donor, to another, functioning as the acceptor. As such, charge transfer transitions can be described as "internal oxidation-reduction" processes. If the transfer of the electron during the transition is from a metal centre to a ligand, the transition is known as a metal-to-ligand charge transfer (MLCT) transition; conversely, if the transfer is from the ligand to the metal centre, a ligand-to-metal charge transfer (LMCT) transition is implied. The molar extinction coefficient, ε, associated with these transitions typically ranges from 10^3 to *ca.* 10^4 $dm^3mol^{-1}cm^{-1}$. For molecules in solution, the energy associated with these transitions can be quite sensitive to the polarity of the solvent. Exceptions to this trend do however exist.

The time scale on which absorption of radiation takes place, is typically in the order of 10^{-15} s, which is much too short for any change in the relative positions of the nuclei within the molecule. This is known as the Frank-Condon principle and implies that during absorption, a molecule is frequently excited from the ground state to a vibrationally excited state of the electronic excited state. Following the absorption of radiation, molecules will thus undergo vibrational relaxation from the vibrationally excited state to the lowest energy vibrational level of the electronic excited state. This process is often 100% efficient before the occurrence of any emission and has led Kasha to propose that: "the emitting electronic level of a given multiplicity is the lowest excited level of that multiplicity".[251]

The relaxation pathway from the excited state to the ground state, described above, is not the only pathway which might be available to the excited state molecule. In fact, the majority of known compounds and especially metal complexes, do not relax from the electronically excited state through radiative decay, but instead undergo non-radiative decay. This includes processes such as vibrational relaxation, internal conversion, intersystem crossing and photochemical processes *e.g.* dissociation.

At this stage it is appropriate to consider a few of the pertinent aspects regarding radiative decay or emission.

Radiative relaxation from the electronic excited state terminates in the excited vibrational levels of the ground state. If these levels are reasonably well separated in energy and there is no major distortion of the molecular geometry accompanying the transition between the ground and electronic excited state, each of the transitions from the lowest vibrational level of the electronically excited state to the different vibrational excited levels of the ground state will have a unique energy value associated with it. This implies that the emission spectrum will exhibit peaks at distinct frequencies corresponding to those energy values. Such an emission spectrum is said to possess vibrational structure.

As mentioned above, absorption frequently gives rise to a vibrationally excited state of the electronic excited state, resulting in non-radiative decay to the lowest energy vibrational level of the electronic excited state from which emission can then occur.

Furthermore, radiative relaxation can terminate in a vibrationally excited state of the ground electronic state which implies that further non-radiative decay occurs before the lowest vibrational level of the ground state, from which the electron was originally excited, is reached. Considering these pathways, it is clear that due to non-radiative processes, the energy associated with excitation (*i.e.* absorption) could be greater than that associated with emission. It is therefore possible for the wavelength of an emission resulting form excitation at a specific wavelength, to be red-shifted with respect to the excitation wavelength. This wavelength shift is known as the Stokes' shift.

Two distinct types of emission exist, these being fluorescence and phosphorescence. Fluorescence is the result of the radiative decay of an electron from a singlet excited state to a singlet ground state. In this case, the electron in the electronic excited state has opposite spin to the one remaining in the electronic ground state. Thus, the return of the electronic excited state electron to the electronic ground state does not require spin change of the electron and is "spin allowed". Phosphorescence implies emission resulting from a triplet excited state relaxing to a singlet ground state. Here, the electron in the electronic excited state has the same spin as the one remaining in the electronic ground state, implying that return of the molecule to the ground state requires the spin of the electron involved to be flipped. This process is "spin forbidden". In heavy metal complexes however, the selection rules are weakened considerably by spin-orbit coupling, thus allowing these "spin forbidden" transitions to be observed in practice.

Since emission is essentially the reciprocal of the absorption process, the transitions responsible for emission are first of all, the reciprocals of transitions associated with light absorption. Thus, emission can arise from excited states derived from ligand field (d-d), intraligand and charge transfer transitions. However, emission can also originate from excited state dimers (excimers) and metal-centred dinuclear excited states, *vide infra.*

3.3.2 Luminescence in square planar complexes of Pt(II): Selected examples from the literature

As discussed above, luminescence results from the radiative decay of an electronically excited state. In the case of Pt(II) complexes, emission has been observed from the radiative decay of intraligand, ligand field, metal-to-ligand charge transfer, interligand charge transfer, excimeric and metal-centred dinuclear excited states. The discussion below will deal with luminescence originating from each of these excited states and will highlight examples of square planar Pt(II) complexes exhibiting luminescence from each type of state.

3.3.2.1 Radiative decay of intraligand (IL) excited states

The observation of luminescence from square planar Pt(II) complexes in fluid solution is relatively rare,[252] and in the majority of instances where luminescence is in fact observed, the emissive state has been assigned as a $^3(\pi\text{-}\pi^*)$ intraligand (IL) state.

In the case of diimine ligands coordinated to Pt(II), emission from the lowest energy ^{3}IL diimmine state is typically associated with a small Stokes' shift from the related absorption. Furthermore, the emission band profile usually exhibits well-resolved vibronic structure, even at room temperature.

Microcrystalline powders of $[Pt(bipy)(en)](ClO_4)_2$ (en = ethylenediamine) exhibit room temperature luminescence[253] with an electronic origin at 458 nm and an excited state lifetime of 1.4 ± 0.2 µs. The emission band profile shows a well-resolved vibrational pattern which is in excellent agreement with the phosphorescence spectrum of $Zn(bipy)_3^{2+}$. Based on this analogy, the emissive state was assigned to be the $^3(\pi\text{-}\pi^*)$ state. Further comparison of the emission spectra of $[Pt(bipy)(en)](ClO_4)_2$ and $Zn(bipy)_3^{2+}$ revealed that the Pt complex's emission is red-shifted by ~1200 cm^{-1} with respect to that of the latter. This shift was interpreted as possibly resulting from a perturbation of the bipyridine π^* orbital by the Pt(II) d and p_z orbitals. It is important to note that both bipyridine and ethylenediamine are relatively strong field ligands resulting in a reasonably large ligand field splitting of the Pt d orbitals in $[Pt(bipy)(en)](ClO_4)_2$. Consequently, the energy associated with the lowest energy

ligand field (d-d) transition is elevated to a level above that associated with the $^3(\pi\text{-}\pi^*)$ transition. The same reasoning applies to the emission exhibited by dilute ($\sim10^{-5}$M) CH_2Cl_2 solutions of [Pt(4,7-diphenyl-1,10-phenanthroline)(CN)$_2$].[254] As a result of the strong σ bonding and π back bonding of the phenanthroline and cyanide ligands, the ligand field splitting is large enough to allow the $^3(\pi\text{-}\pi^*)$ IL transition to be the lowest energy electronic transition present in the monomeric molecule.

The structured luminescence observed for CH_3CN solutions of [Pt(bipy)(NH$_3$)$_2$](PF$_6$)$_2$ at room temperature, has also been assigned to originate from a $^3(\pi\text{-}\pi^*)$ IL excited state.[255] The radiative decay of a $^3(\pi\text{-}\pi^*)$ IL excited state has also been suggested to be responsible for the luminescence exhibited by the quinolinolate[256] and quaterpyridine[257] complexes of Pt(II). The assignment in the latter two cases is not absolutely certain, since the authors could not rule out the possibility that the luminescence might originate from a triplet metal-to-ligand charge transfer (^{3}MLCT) state.

3.3.2.2 Radiative decay of ligand field (LF) excited states

In strong field complexes such as [Pt(bipy)(en)](ClO$_4$)$_2$, the lowest energy ^{3}LF excited state is much higher in energy than the lowest energy ^{3}IL excited state, as discussed above. However, in weaker field complexes, $e.g.$ [Pt(diimine)X$_2$] (X = halogen), the ligand field splitting is smaller. As a consequence, the energy associated with the lowest energy LF transition is reduced, resulting in the energy of the lowest energy ^{3}LF excited state becoming comparable to that of the lowest energy ^{3}IL transition. The band profile of emission from a LF excited state typically is broad and Guassian in shape with the wavelength associated with the maximum emission intensity, $\lambda(em)_{max}$, being nearly independent of temperature.

^{3}LF emission has been observed for [Pt(tmen)Cl$_2$] (tmen = N,N,N',N'-tetramethyl-ethylenediamine), for both the solid and low-temperature glassy solution (ethanol/methanol, 77K).[258] The emission band profile is broad and Guassian-shaped and does not exhibit any vibrational structure. At low temperature the emission peak is narrower than that observed at room temperature with very little shift of the intensity maximum.

Similar emission spectra have been recorded for samples of [Pt(4,4'-Me$_2$-bipy)Cl$_2$], [Pt(phen)Cl$_2$], [Pt(bipy)I$_2$] and the yellow form of [Pt(bipy)Cl$_2$][258] (in the solid state, in glassy and in frozen solutions). In all of the cases the emission has been assigned as originating from ^{3}LF excited states. A comparison of the emission spectra of the yellow form of [Pt(bipy)Cl$_2$] with that of [Pt(bipy)I$_2$] reveals a substantial red-shift in the emission maximum of the latter. This is consistent with the ^{3}LF assignment for the observed emissions, since the iodine ligand is a weaker field ligand than Cl, thus resulting in a smaller ligand field splitting in [Pt(bipy)I$_2$] than that associated with [Pt(bipy)Cl$_2$] (yellow form). Consequently, the energy of the ^{3}LF excited state of [Pt(bipy)I$_2$] is lower than that of [Pt(bipy)Cl$_2$] (yellow form), resulting in the observed red-shift.

The low-temperature emission observed for single crystals of K$_2$[PtCl$_4$] has also been assigned to the radiative decay of a LF excited state.[259] Despite the high symmetry and apparent simplicity of the square planar [PtCl$_4$]$^{2-}$ anion, the interpretation of its vibronically structured emission spectrum is not straightforward and the involvement of multiple-mode excited state distortions have been suggested.

An examination of the examples of LF emission cited above, reveals that all of those quoted involve luminescence from samples in rigid media with no examples of LF emission from Pt(II) monomers in fluid solution. This observation is generally true for LF emission from Pt(II) monomers. In fact, McMillin *et al.* state that "there are few, if any, reports of d-d emissions from platinum(II) monomers in fluid solution".[260] The reason offered for this observation is that some of the LF excited states of d^8 complexes readily undergo D_{2d} distortions, thus facilitating non-radiative decay of the electronically excited state. A further explanation offered involves solvent interactions with the coordinatively unsaturated Pt(II) ion at axial sites, thus allowing for quenching of the excited state monomer in solution.[260]

3.3.2.3 Radiative decay of metal-to-ligand charge transfer (MLCT) excited states

From the discussion of the radiative decay of the LF and IL excited states of the Pt(II) diimines (Sections 3.3.2.1 and 3.3.2.2), it is evident that the energy associated with the 5d metal orbitals is very similar to that of the π orbitals of the diimmine ligands. Thus

by employing strong or weak field ligands, it is possible to manipulate the energy of the 5d metal orbitals in the Pt(II) complexes and in so-doing to switch between emission from a IL excited state to a LF excited state. A second variable available for modification of the electronic structure of the Pt(II) diimine complexes, involves the utilization of substituted diimine ligands. This approach allows for the manipulation of the energy levels of the π-π^* diimine orbitals relative to those of the metal-centred 5d orbitals. Consequently it is possible to arrive at a situation where the HOMO of a complex is metal-centred, whereas the LUMO is essentially ligand-centred. In such a case the lowest energy electronic excited state is a MLCT state.

The emission observed from the dicarbomethoxy-substituted bipyridine derivative, [Pt{3,3'-(CH$_3$OCO)$_2$bipy}Cl$_2$] has been assigned to the radiative decay of a ^{3}MLCT excited state.[258] The emission band profile associated with solid samples of this complex differs from that associated with ^{3}LF emission, in that it has a highly asymmetric shape compared to the Guassian shape observed for the latter. At 300 K, the emission spectrum of [Pt{3,3'-(CH$_3$OCO)$_2$bipy}Cl$_2$] does not exhibit any vibrational structure, however on cooling solid samples to 10 K, a broad vibronic structure, which is attributed to an "average" vibrational mode of the substituted bipyridine ligand, develops. This vibrational structure is not as sharp as that associated with ^{3}IL emissions. A further feature distinguishing the ^{3}MLCT emission of [Pt{3,3'-(CH$_3$OCO)$_2$bipy}Cl$_2$] from the ^{3}IL emission, is the Huang-Rhys factor, S, which is defined as $S = I_{1,0} / I_{0,0}$ where $I_{1,0}$ and $I_{0,0}$ represent the intensities associated with the $1 \rightarrow 0$ and $0 \rightarrow 0$ vibrational transitions. In the case of [Pt{3,3'-(CH$_3$OCO)$_2$bipy}Cl$_2$], the Huang-Rhys ratio is close to 1, whereas for ^{3}IL emissions, the ratio tends to be larger. [Pt{3,3'-(CH$_3$OCO)$_2$bipy}Cl$_2$] was found to be non-emissive in both CH$_3$CN or degassed CH$_2$Cl$_2$ solutions at room temperature.

In contrast to [Pt{3,3'-(CH$_3$OCO)$_2$bipy}Cl$_2$], [Pt(terpy)(OMe)](BPh$_4$) and [Pt(terpy)(NCS)](BF$_4$) luminesce in CH$_3$CN solution at room temperature, the maximum emission intensities being observed at wavelengths λ(em)$_{max}$ of 654 and 588 nm, respectively.[260] The band profiles in both instances are broad and devoid of any vibrational structure. The emissive state for both complexes has been assigned to a ^{3}MLCT state. On lowering the temperature and changing from fluid solution to a

glassy solution, the emission changes from the ^{3}MLCT emission to $^3(\pi\text{-}\pi^*)$ emission from the coordinated terpyridine ligand.

3.3.2.4 Radiative decay of ligand-to-ligand charge transfer (LLCT) or interligand excited states

Ligand-to-ligand charge transfer transitions can occur in mixed ligand complexes where one ligand is oxidizing with respect to another on the same metal centre, *i.e.* one ligand possesses empty low-lying orbitals whereas another on the same metal centre, possesses filled high-lying orbitals.

This situation is observed in [Pt(bipy)(3,4-toluenedithiolate)] in which the platinum(II) centre is coordinated to bipyridine and the 3,4-toluenedithiolate dianion.[261] The UV-visible spectrum of this complex exhibits an intense long-wavelength absorption band which is strongly solvent dependent. This absorption band was assigned to a LLCT transition in which charge is transferred from the dithiolate dianionic ligand to the bipyridine ligand. Studies on the analogous Ni and Pd complexes[262] revealed that the band is independent of the nature of the metal centre, thus providing further support for the LLCT assignment. The excitation of [Pt(bipy)(3,4-toluenedithiolate)] in an ethanol glass at 77 K, led to the observation of a strong emission signal centred at 654 nm. This emission was assigned to the radiative decay of the LLCT excited state.

3.3.2.5 Radiative decay from excimeric excited states

Excimer formation is the result of dimerization of an excited state and a ground state molecule[263] or two excited state molecules[264] in solution. Once formed, a variety of pathways exist for the excimer to return to the ground state. This includes radiationless decay, dissociation to the original excited state and ground state monomers and in some instances, radiative decay. However, as a result of the interactions between the constituent molecules, the electronic structure and thus any possible luminescence originating from the excimer, is substantially different to that associated with the excited state monomer. Certain guidelines have been proposed[254] for the design of molecules that might exhibit excimeric emission in solution. These include that the complex should be designed such that there is a driving force *e.g.* metal-metal or ligand-ligand interaction promoting the excited state dimerization, that the complex

should preferably be neutral in order to minimize Coulombic repulsions between them and finally, the molecules should be sufficiently soluble (since excimer formation is generally associated with reasonably high concentrations).

In dilute CH_2Cl_2 solutions ($\sim10^{-5}$M), [Pt(4,7-diphenyl-1,10-phenanthroline)(CN)$_2$] exhibits an emission with $\lambda(em)_{max}$ equal to 520 nm and which originates from a monomeric $^3(\pi$-$\pi^*)$ excited state, as discussed in Section 3.3.2.1. Changing the solvent to polyethylene glycol and increasing the concentration, results in the appearance of a new emission peak centred at 630 nm which grows at the expense of the peak centred at 530 nm as the concentration is increased[254] [a small shift of $\lambda(em)_{max}$ was reported to accompany the change in solvent]. At intermediate concentrations both emissions are observed, but at sufficiently high concentrations the emission centred at 630 nm completely replaces that centred at 530 nm. The emission centred at 630 nm has been assigned to the radiative decay of an excimer which possesses a metal-metal bond, the formation of which promotes the dimerization. Although the authors did not discount the possibility of ligand-ligand interaction, the formation of a metal-metal bond was considered to be a more probable alternative.[254] As described above, the luminescence of the excimer is shifted to a longer wavelength than that originating from the excited state monomer. This shift was attributed to the formation of a new low-energy excited state which is associated with the proposed metal-metal interaction in the excimer.

Che and co-workers[264] have similarly studied excimeric emission from [Pt{4,4'-(^{t}Bu)$_2$-bipy}(CN)$_2$]. In dilute CH_3CN and CH_2Cl_2 solutions (10^{-6} to 10^{-5} M) at room temperature, the complex exhibits an emission centred at $ca.$ 500 nm, which originates from a $^3(\pi$-$\pi^*)$ excited state. The emission is vibronically structured with a vibronic spacing of 1100 to 1200 cm^{-1}. Changing the solvent to 1,2-dichloroethane and increasing the complex concentration to 10^{-4} to 10^{-3} M results in a red-shift of the emission to afford a peak centred at 565 nm with very little evidence of vibronic structure. As in the case of [Pt(4,7-diphenyl-1,10-phenanthroline)(CN)$_2$], this red-shift of the luminescence is attributed to excimer formation. Taking the steric bulk of the ^{t}Bu-substituents on the diimmine ligand into consideration, the possibility of pure metal-metal interaction being present in the excimer was discounted. Instead it was

suggested that the true species responsible for the excimeric emission might be a mixture of metal d_{z^2} and π-π^* ligand-based excimers.

The two complexes discussed above both exhibit excimeric emission in fluid solution. Excimeric emission has also been invoked to explain the solid state luminescence exhibited by $[Pt(phen)_2]Cl_2$.[253] The emission spectrum of $[Pt(phen)_2]Cl_2$ in glassy solution at 77 K is completely analogous to that of $[Pt(bipy)(en)](ClO_4)_2$ (see Section 3.3.2.1) recorded under the same conditions. The emission is vibronically structured and is centred at $ca.$ 500 nm. Based on these observations, the emission exhibited by $[Pt(phen)_2]Cl_2$ in a low-temperature glassy solution was assigned to the radiative decay of a monomeric $^3(\pi$-$\pi^*)$ excited state. The emission spectrum of solid $[Pt(phen)_2]Cl_2$ is highly dependent on the sample preparation and history. However, the emission from all microcrystalline samples of $[Pt(phen)_2]Cl_2$ is significantly red-shifted [$\lambda(em)_{max}$ typically $ca.$ 630 nm] with respect to that observed in glassy solution. Furthermore, the band profiles of the emission from the microcrystalline solids are unstructured and much broader than that observed from glassy solutions. $[Pt(phen)_2]Cl_2.3H_2O$ is known to crystallize with the cations occurring in discrete, weakly interacting face-to-face dimers.[265] The Pt-Pt separation within these dimers is 3.710Å. This distance is too long to facilitate any significant metal-metal interaction, but is short enough to allow overlap of the phenanthroline π^* orbitals. Based on these considerations, the solid state emission of $[Pt(phen)_2]Cl_2$ was assigned to a classical excimeric interaction of the phenanthroline ligands in the two monomers.

3.3.2.6 Radiative decay of dinuclear metal-based excited states

Through the utilization of the appropriate bridging ligands, it is possible to construct dinuclear metal complexes in which the two metal centres, in this case Pt(II), are "locked together" in close proximity to each other. Such short internuclear distances allow for metal-metal interactions which can have a profound influence on the electronic structure and excited state properties of the complexes involved.

An example of a complex to which the above applies, is $K_4[Pt_2(\mu$-$P_2O_5H_2)_4]$.[266] The complex is described as being d^8-d^8 with the complex consisting of two Pt(II) centres held together by four bridging dianionic pyrophosphite ligands. The Pt-Pt separation

within the anion is 2.925Å, thus allowing for extensive metal-metal interaction. In aqueous solutions, the complex exhibits an intense phosphorescence centred at 514 nm (with a lifetime of *ca.* 9 μs) and a fluorescence centred at 407 nm (with a much shorter lifetime of 8 to 40 ps). Both emissions have been assigned to the radiative decay of a metal-centred ($d_{\sigma^*} \rightarrow p_\sigma$) excited state, a triplet state being associated with the emission centred at 514 nm and a singlet state with that at 407 nm. The ($d_{\sigma^*} \rightarrow p_\sigma$) excited states are produced by electronic transitions from the occupied d_{σ^*} orbital, which is the result of an antibonding interaction between the $5d_{z^2}$ orbitals of the two Pt(II) centres, to the unoccupied p_σ orbital, which arises from a bonding interaction of the $6p_z$ orbitals of the Pt(II) centres.

A similar situation is prevalent in the luminescent $[Pt_2(dppm)_2(CN)_4]$ complex[267] [dppm = bis(diphenylphosphino)methane]. The complex is also described as being d^8-d^8 with the two Pt(II) centres held together by two bridging dppm ligands. The coordination sphere around each Pt centre is completed by two cyanide ligands. The Pt-Pt distance in the complex is 3.201Å, which is somewhat longer than that observed in $K_4[Pt_2(\mu$-$P_2O_5H_2)_4]$ and is indicative of a weaker Pt-Pt interaction. Excitation of degassed methanolic solutions of $[Pt_2(dppm)_2(CN)_4]$ at room temperature, results in an intense emission centred at 425 nm with a shoulder at 530 nm. The emission centred at 425 nm has been assigned to the radiative decay of a $^1(d_{\sigma^*} \rightarrow p_\sigma)$ excited state and the shoulder to the decay of the analogous triplet excited state. The lifetime of the singlet excited state was estimated to be less than 6 ns whereas that of the $^3(d_{\sigma^*} \rightarrow p_\sigma)$ state was found to be 0.23 μs. This implies that the triplet excited state lifetime of $[Pt_2(dppm)_2(CN)_4]$ is *ca.* 40 times shorter than that of $K_4[Pt_2(\mu$-$P_2O_5H_2)_4]$, thus rendering it less attractive for photochemical applications.

3.4 Results and Discussion

3.4.1 Preliminary Considerations

As outlined in Section 3.2, one of the aims of this study is to reconcile the photoluminescent properties of selected bipiridyl and terpyridyl complexes of Pt(II) with their solid state structures. One of the obvious factors to consider in this

reconciliation is the influence of extended solid state interactions on the electronic structure of the constituent monomeric moieties. The effects of such interactions on the photoluminescent properties of Pt(II) complexes have been reported previously.[268] However, the report by Houlding and Miskowski concentrated on the Pt(II)diimine moiety, as found in neutral complexes and double salts, *i.e.* salts where the cation and anion carry a +2 or -2 charge respectively and where both the cation and anion involve a Pt atom.

In contrast to the above mentioned report, the present study is primarily concerned with terpyridyl complexes of Pt(II). All the complexes considered are ionic and involve non-planar, non-Pt-containing counterions.

Although the first Pt(II) complexes of terpyridine were reported in 1934,[269] more detailed investigations into the use of the platinum terpyridine moiety, Pt(terpy), as a metallointercalation reagent,[270] and regarding the general synthesis and charaterization of Pt(terpy) complexes,[271] appeared only some forty years later. Several reports of complexes containing the Pt(terpy) moiety have appeared more recently (see references 260, 263, 272, and 273 for representative examples). All of these studies involving Pt(terpy) complexes, have utilized [Pt(terpy)Cl]Cl[274] as the starting material and have relied on the labilization of the coordinated Cl⁻ ligand by a π-trans effect[275] to achieve ligand exchange at the Pt(II) centre. Lippard and co-workers[270] reported that they removed the chlorine moieties from both the inner and outer coordination sphere by reaction with silver nitrate to generate what is believed to be [Pt(terpy)(H₂O)](NO₃)₂. However, the complex was prepared *in situ* and used as an intermediate and was thus not isolated.

In an attempt to gain increased control over ligand substitution reactions at the Pt(II) centre and to possibly broaden the range of accessible complexes containing the Pt(terpy) moiety, it was deemed appropriate to attempt the synthesis and isolation of the solvento species [Pt(terpy)(CH₃CN)](X)₂ (X = non-coordinating anion). In this complex the coordinated Cl⁻ ligand is replaced by the neutral CH₃CN molecule. This modification was expected to increase the complex's susceptibility to ligand-exchange reactions. Furthermore, with a neutral ligand in the fourth coordination site, the

preservation of electrical neutrality requires that the complex possesses two counterions in its outer coordination sphere. This requirement implies that the effect of the counterions on the packing architecture of the complex is effectively "doubled" when compared to related Pt(terpy) complexes containing an anionic ligand in the fourth coordination site and one counterion in the outer coordination sphere. Furthermore, since both the terpyridine and the CH_3CN ligands are essentially planar, the $[Pt(terpy)(CH_3CN)]^{2+}$ chromophore presented an ideal opportunity for studying the influence of the steric requirements of the counterion on the linear chain structure and photoluminescent properties of Pt(II) complexes.

3.4.2 $[Pt(terpy)(CH_3CN)](SbF_6)_2$ (8)

3.4.2.1 Synthesis and Characterization

Initial attempts at synthesizing $[Pt(terpy)(CH_3CN)](SbF_6)_2$ (**8**) relied on the substitution of three of the CH_3CN molecules on the tetrakis-acetonitrile species, $[Pt(CH_3CN)_4]^{2+\ (276)}$ with the chelating terpyridine ligand.

The first description of the synthesis of $[Pt(CH_3CN)_4]^{2+}$, is a brief communication[277] by Panunzi and co-workers who reported that $[Pt(CH_3CN)_4](BF_4)_2$ catalyses the dimerization of a number of olefins. The synthesis of $[Pt(CH_3CN)_4](BF_4)_2$ involved the reaction of $[Pt(CH_3CN)_2Cl_2]$ with two molar equivalents of $AgBF_4$ in anhydrous acetonitrile, followed by evaporation of the solvent and extraction of the salt with nitromethane, from which it is reported to have crystallized as colourless needles. The report does not disclose any further details of the experimental conditions, or the yield of the reaction. The characterization of the complex salt was limited to elemental analysis and ^{1}H-NMR spectroscopy, the details of which were not reported either.

A subsequent report involving the synthesis of $[Pt(CH_3CN)_4]^{2+}$, was published by Hartley and co-workers who utilized the perchlorate salt $[Pt(CH_3CN)_4](ClO_4)_2$, as a precursor in the synthesis of monomeric complexes of Pt(II) with chelating open-chain tetrathioether ligands.[278] According to these authors, $[Pt(CH_3CN)_4](ClO_4)_2$ was synthesized by treating a solution of $[Pt(CH_3CN)_2Cl_2]$ in acetonitrile with two equivalents of $AgClO_4$, dissolved in CH_3CN, and heating the mixture to reflux for two hours, "until the original yellow solution of $[Pt(CH_3CN)_2Cl_2]$ had turned colourless".

The product resulting from this reaction was used *in situ*, consequently no characterization data or yield was reported for $[Pt(CH_3CN)_4](ClO_4)_2$.

During initial attempts at synthesizing $[Pt(terpy)(CH_3CN)](SbF_6)_2$, the procedure described above was adopted to synthesize the $[Pt(CH_3CN)_4](SbF_6)_2$ precursor. However, instead of $[Pt(CH_3CN)_2Cl_2]$, the benzonitrile equivalent $[Pt(C_6H_5CN)_2Cl_2]$, dissolved in acetonitrile, was treated with two equivalents of $AgSbF_6$ and the mixture heated to reflux for 2 hours. In analogy with the report by Hartley *et al.*,[278] the yellow solution, in this case due to the colour of the dissolved $[Pt(C_6H_5CN)_2Cl_2]$, turned colourless during this period. The precipitated silver chloride was removed by filtration, one equivalent of 2,2',6',2"-terpyridine added and the mixture heated to reflux for an additional 24 hours. A small amount of silver chloride, which precipitated during this period, was removed by filtration. Reducing the volume of the filtrates *in vacuo* and cooling the solution overnight, resulted in the formation of very fine orange needle-like crystals. However, the values obtained from elemental analysis for C, H and N on the material obtained from a number of attempts utilizing the above procedure, were consistent with an empirical formula $[Pt(terpy)Cl](SbF_6)$, rather than $[Pt(terpy)(CH_3CN)](SbF_6)_2$. Further evidence suggesting that the material obtained *via* the above synthetic procedure might contain Cl^- rather than CH_3CN coordinated to the Pt(II) centre, was provided by the absence of any C-N stretching bands in the solid state infrared spectrum.

Based on the above results and observations, it would seem that the reaction between $[Pt(C_6H_5CN)_2Cl_2]$, CH_3CN and $AgSbF_6$ does not result in the displacement of both Cl^- ligands from the Pt(II) coordination sphere to afford $[Pt(CH_3CN)_4](SbF_6)_2$, but rather that only one Cl^- ligand is displaced, affording a species which can be represented as $[Pt(C_6H_5CN)_{3-n}(CH_3CN)_nCl](SbF_6)$ (n = 1, 2 or 3). During the subsequent reaction with the terpyridine ligand, the coordinated nitrile ligands are displaced, resulting in the formation of $[Pt(terpy)Cl](SbF_6)$.

Reports by Mureinik and Bidani,[271] Lippard and co-workers[270] and Che and co-workers[263] do however suggest that the Cl^- ligand on the $[Pt(terpy)Cl]^+$ chromophore can be displaced by neutral ligands *viz.* pyridine, H_2O and NH_3 respectively. In view of

these reports and the problems experienced during the initial attempts at synthesizing [Pt(terpy)(CH₃CN)](SbF₆)₂, it was thus decided to rather use [Pt(terpy)Cl](SbF₆) as starting material and attempt to displace the Cl⁻ ligand with CH₃CN.

As mentioned earlier, the studies by Mureinik and Bidani, [271] Lippard and co-workers[270] and Che and co-workers,[263] all utilized [Pt(terpy)Cl]Cl as starting material. Water was employed as solvent. However, since [Pt(terpy)Cl](SbF₆) is insoluble in H₂O, the reaction has to be performed in CH₃CN. This requires that the concentration of [Pt(terpy)Cl](SbF₆) should be kept as low as possible, whilst maintaining the highest possible concentration of Ag⁺ relative to that of [Pt(terpy)Cl](SbF₆). Should this not be the case, it is possible that Cl⁻ ions liberated from the ligand displacement reaction, can combine with [Pt(terpy)Cl]⁺ ions to afford [Pt(terpy)Cl]Cl. This compound is virtually insoluble in CH₃CN and could precipitate from the reaction mixture, thus removing [Pt(terpy)Cl]⁺ ions from the reaction mixture and consequently decreasing the overall yield of [Pt(terpy)(CH₃CN)](SbF₆)₂.

The synthesis of [Pt(terpy)(CH₃CN)](SbF₆)₂ thus involves synthesizing [Pt(terpy)Cl]-(SbF₆) as a first step. The latter was obtained by treating [Pt(C₆H₅CN)₂Cl₂] with a 10% excess of AgSbF₆ in refluxing acetonitrile, followed by the addition of a 10% excess of terpyridine ligand and heating the mixture under reflux for an additional 15 hours. The resulting mixture, containing precipitated AgCl, was allowed to cool before its volume was reduced *in vacuo*, leading to the precipitation of [Pt(terpy)Cl](SbF₆). The solids were removed by filtration, placed in a specially designed vapour extraction apparatus (see Section A.2.1.2 of Appendix A) and the [Pt(terpy)Cl](SbF₆) content extracted into a refluxing acetonitrile solution, containing at least two equivalents of AgSbF₆ (based on the quantity of [Pt(C₆H₅CN)₂Cl₂] used in the first step). The mixture was allowed to reflux for an additional 4 hours before it was cooled, the precipitated AgCl removed by filtration and the volume reduced *in vacuo*, leading to the precipitation of unreacted [Pt(terpy)Cl](SbF₆). The mother liquor was removed, evaporated to dryness (*in vacuo*) and the residue thoroughly washed with acetone and ether before drying it *in vacuo*. Redissolving the solid obtained thus in acetonitrile and allowing the solvent to evaporate slowly, resulted in the formation of light yellow block-shaped crystals of

Table 3.1   *Infrared stretching frequencies (quoted in cm⁻¹) for the Pt polypyridyl salts investigated in this study.*[a]

Compound	C≡N or C≡C	Polypyridine	Counterion
[Pt(terpy)(CH₃CN)](SbF₆)₂ (**8**)	2332 (mw), 2304 (w)	1611 (s), 1574 (m), 1510 (w), 1485 (ms), 1455 (s), 1408 (m), 1322 (ms), 1250 (m), 1036 (m), 783 (vs)	656(vs)
[Pt(terpy)Cl](SbF₆) (**9**)	-	1607 (s), 1480 (ms), 1456 (s), 1442 (m), 1400 (m), 1317 (m), 1035 (m), 773 (vs)	655 (vs)
[Pt(terpy)Cl](CF₃SO₃) (**10**)	-	1606 (s), 1480 (s), 1456 (s), 1443 (m, sh), 1402 (ms), 1317 (m), 777(vs)	1266 (vs), 1158 (vs), 1030 (vs)
[Pt(terpy)Cl](BF₄) (**11**)	-	1606 (s), 1478 (ms), 1454 (s), 1443 (m, sh), 1401 (m), 774 (vs)	1054 (vs)
[Pt(bipy)₂](SbF₆)₂ (**12**)	-	1616 (s), 1504 (m), 1475 (s), 1456 (s), 1435 (m), 1318 (w), 1248 (m), 1169 (m), 779 (vs)	660 (vs)
[Pt(bipy)₂](CF₃SO₃)₂ (**13**)	-	1611 (s), 1470 (m), 1456 (m), 1433 (w), 1174 (s)785 (vs)	1265 (vs), 1164 (vs), 1030 (vs)
[Pt(4'-Ph-terpy)Cl](SbF₆) (**14**)	-	1611 (s), 1556 (m), 1480 (ms),1417 (s), 1034 (mw), 884 (mw), 774 (vs)	658 (vs)
[Pt(terpy)(C≡CPh)](SbF₆) (**15**)	2128 (w)	1605 (s), 1487 (m), 1478 (m), 1454 (s), 1439 (s), 1400 (s), 1035 (m), 772 (s)	658 (vs)
[Pt(4'-Ph-terpy)(C≡CPh)](SbF₆) (**16**)	2124 (w)	1610 (s), 1558 (m), 1487 (m), 1476 (m), 1417 (s), 1032 (mw), 884 (m), 764 (vs)	658 (vs)

[a]   All spectra were recorded on KBr pellets.

Key: vs = very strong, s = strong, ms = medium to strong, m = medium, mw = medium to weak, w = weak, sh = shoulder.

which the elemental analysis for C, H and N corresponds to an empirical formula of [Pt(terpy)(CH$_3$CN)](SbF$_6$)$_2$.

The solid state infrared spectrum of [Pt(terpy)(CH$_3$CN)](SbF$_6$)$_2$, recorded as a KBr pellet, exhibits two peaks in the C-N stretching region (at 2330 and 2302 cm^{-1}) which are attributed to the CH$_3$CN ligand (see Table 3.1). A similar peak pattern has been reported for the solid state spectrum of [Pt(CH$_3$CN)$_2$Cl$_2$],[279] with peaks occurring at 2332.8 and 2304.7 cm^{-1}. The C-N vibrational frequencies of [Pt(terpy)(CH$_3$CN)]-(SbF$_6$)$_2$ occur at wavenumbers which on average are 50 cm^{-1} higher than that associated with "free" acetonitrile (C-N stretching peak at 2266 cm^{-1})[280]. This shift in frequency has been attributed to three factors, *viz*. the ionic character of the C≡N bond,[279] kinematic coupling[279,280] and most importantly, a significant increase in the C≡N force constant on coordination of the CH$_3$CN ligand.[280] The solid state infrared spectrum of [Pt(terpy)(CH$_3$CN)](SbF$_6$)$_2$ also exhibits a number of peaks in the range 1650 to 780 cm^{-1} which can be assigned to the terpyridine ligand. The wavenumbers associated with these peaks are in good agreement with those reported for the solid state spectrum of [Pt(terpy)(SCH$_2$CO$_2$CH$_2$CH$_3$)](PF$_6$)[270] for instance. The spectrum also exhibits the customary peak at *ca*. 655 nm associated with the SbF$_6^-$ anion.

3.4.2.2 Structural studies on [Pt(terpy)(CH$_3$CN)](SbF$_6$)$_2$ (**8**)

Single cubically-shaped light yellow crystals of [Pt(terpy)(CH$_3$CN)](SbF$_6$)$_2$, suitable for X-ray diffraction studies, were grown by dissolving the crude product in CH$_3$CN and allowing the solvent to evaporate over a period of *ca*. 1 week.

Compound **8** crystallizes in the space group $P2_1/c$. There are four formula units per unit cell, implying that the asymmetric unit consists of one [Pt(terpy)(CH$_3$CN)]$^{2+}$ cation and two SbF$_6^-$ anions. The unit cell dimensions, a full list of interatomic distances and angles and other crystallographic data are collected in Tables 3.7 to 3.11 at the end of this chapter.

To the best of our knowledge, the crystal structure determination of [Pt(terpy)(CH$_3$CN)](SbF$_6$)$_2$ described here, is the first reported example of a structure determination of a terpyridyl complex of Pt(II) with a neutral ligand in the fourth coordination site.
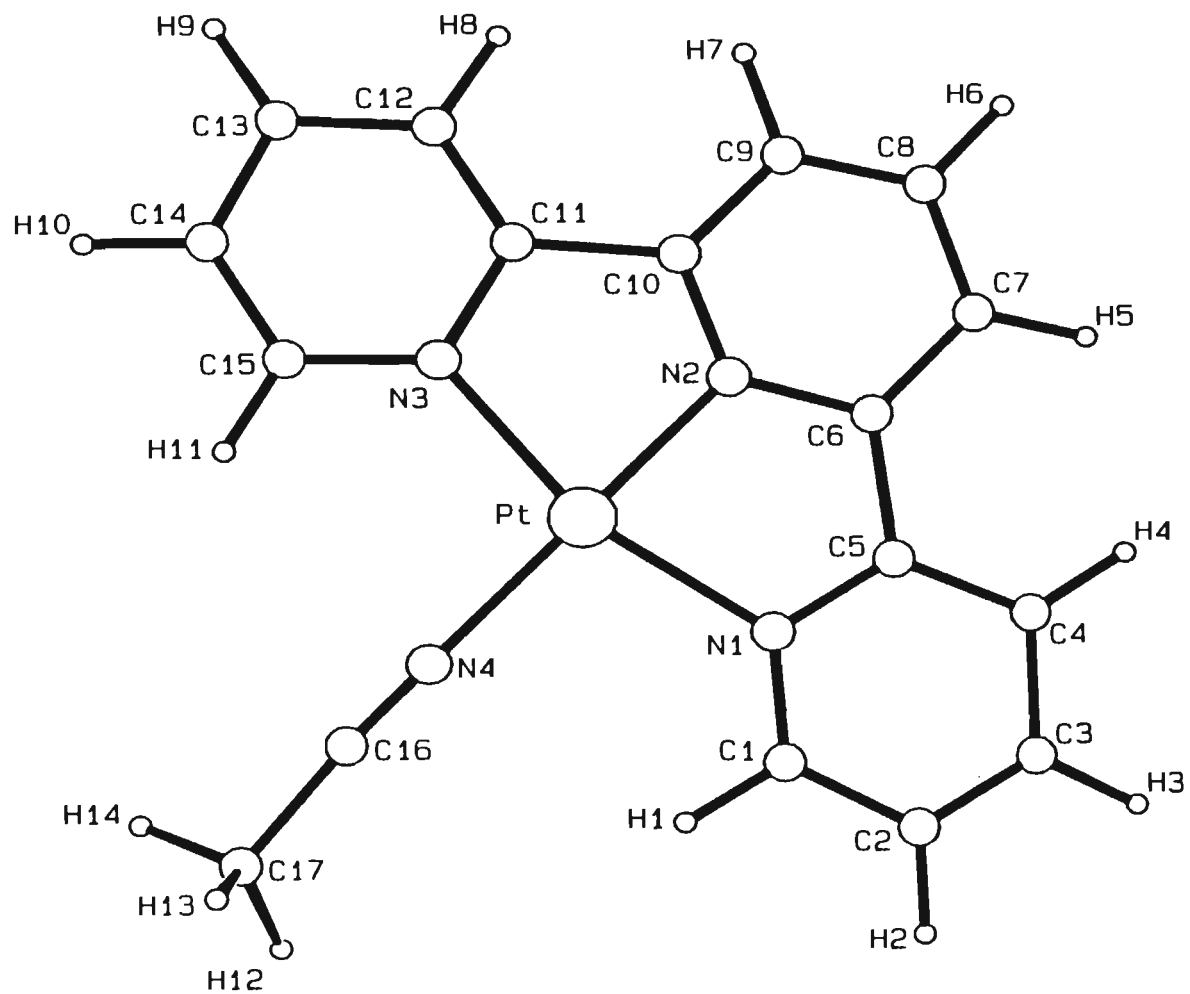
Figure 3.1   *The molecular geometry and numbering scheme employed for the [Pt(terpy)(CH₃CN)]²⁺ cation.*

A diagram displaying the molecular geometry of the cation and the numbering scheme employed, is provided in Figure 3.1. The [Pt(terpy)(CH₃CN)]²⁺ cation is located in a general equivalent position, which implies that there are no crystallographically imposed symmetry relations between any of the atoms constituting the cation. The cation consists of the Pt(II) centre to which is coordinated the tridentate terpyridine ligand and the N atom of the CH₃CN ligand. The coordination geometry around the Pt(II) centre is essentially square planar with the metal and the four coordinated N atoms defining a mean plane. The maximum displacement from this plane is exhibited by the Pt atom and equals 0.012Å. Furthermore, the coordination deviates from being square planar in that the N-Pt-N angles differ from the idealized value of 90°, *vide infra*.

The interatomic distances between the Pt centre and the N atoms N(1), N(2) and N(3) of the terpyridine ligand are 2.05(1), 1.94(1) and 2.04(1)Å, respectively, with the distance from the platinum atom to the bridgehead N atom, N(2), being *ca.* 0.09Å shorter than those from the platinum to atoms N(1) and N(3). The Pt-N distances reported here are in excellent agreement with, and show an analogous variation in length to those established for [Pt(terpy)(SCH₂CH₂OH)](NO₃), [Pt(terpy)-Cl](CF₃SO₃) and [Pt(terpy)(OMe)](BPh₄), see Table 3.2.

Table 3.2 *Pt-N distances[a] for selected Pt(terpy) salts*

Salt	Pt-N	Pt-N*[b]	Pt-N	Reference
[Pt(terpy)(CH₃CN)](SbF₆)₂ (**8**)	2.05(1)	1.94(1)	2.01(1)	This work
[Pt(terpy)(SCH₂CH₂OH)](NO₃)	2.303(5)	1.968(5)	2.033(5)	270
[Pt(terpy)Cl](CF₃SO₃)	2.030(5)	1.930(4)	2.018(5)	263
[Pt(terpy)(OMe)](BPh₄)	2.04(1)	1.92(1)	2.10(1)	260

[a] N of terpyridine ligand, distances quoted in Å

[b] N* = "bridgehead" N atom.

The variation in the length of the Pt-N distances is a result of the geometric constraints imposed by the terpyridine ligand. These constraints also manifest themselves in the N-Pt-N angles (N atoms of the terpyridine ligand) deviating from the ideal value of 90°. The N-Pt-N angles in [Pt(terpy)(CH$_3$CN)](SbF$_6$)$_2$ were found to be 81.7(6) and 80.8(6)°, which compare well with the corresponding values of 80.6(2) and 80.8(2)° for [Pt(terpy)-(SCH$_2$CH$_2$OH)](NO$_3$),[270] 81.1(2)°and 80.8(2)° for [Pt(terpy)Cl]-(CF$_3$SO$_3$)[263] and 79.1(6) and 80.5(7)° for [Pt(terpy)(OMe)](BPh$_4$).[260] The internal bond lengths and angles associated with the terpyridine ligand are in good agreement with those reported for [Pt(terpy)(SCH$_2$CH$_2$OH)](NO$_3$)[270] for example, and will not be discussed here in any further detail. The ligand is slightly ruffled though, the mean planes of the terminal pyridine rings defining dihedral angles of 2.1 and 3.2° with that of the central pyridine ring. These angles are not unusual. The analogous angles for the [Pt(terpy)(OMe)]$^+$ chromophore, as reported by McMillin and co-workers,[260] equal 3.6° and 6.6°.

The Pt-N(4) distance (N of CH$_3$CN ligand) is 2.00(2)Å. This distance is in exact accordance with the Pt-N distance of 2.00(1)Å determined from the X-ray absorption edge and the extended X-ray absorption fine structure (EXAFS) spectra of [Pt(CH$_3$CN)$_4$](CF$_3$SO$_3$)$_2$ in CH$_3$CN solution.[281] The Pt-N(4) distance is also comparable to the average Pt-N distance of 1.98(1)Å established for [Pt(CH$_3$CN)$_2$Cl$_2$][279] and that of 1.940(22)Å reported for [Pt(L)(CH$_3$CN)](PF$_6$).[282] The latter contains the cyclometallated [Pt(L)(CH$_3$CN)]$^+$ cation, where L represents the 6-phenyl-2,2'-bipyridine ligand. The Pt-N distance for the coordinated CH$_3$CN ligand, as observed here, and reported for [Pt(CH$_3$CN)$_4$](CF$_3$SO$_3$)$_2$ and [Pt(CH$_3$CN)$_2$Cl$_2$], is marginally shorter than the Pt-N distances reported for *cis*-dichlorobis(N-cyclobutylamine)platinum [2.06(3)Å] and its trans isomer.[283] This decrease in the Pt-N distance for the coordinated CH$_3$CN ligand has been attributed to a smaller ionic radius of the nitrile nitrogen and to the possibility of back bonding from the filled metal d orbitals to the empty π^* orbitals of the acetonitrile ligand.[279, 281]

From the above suggestion, one would expect the C$\equiv$N bond of the acetonitrile ligand to be weakened on coordination to platinum in much the same way as observed for the carbonyl ligands in metal carbonyl complexes. However, as reported in Section 3.4.2.1

and in the literature,[279, 284] spectroscopic studies indicate that the $C \equiv N$ bond is strengthened, rather than weakened, when CH_3CN coordinates through the N atom. This observation is further supported by X-ray crystallographic studies.[270] A comparison of the N-C and C-C distances for the CH_3CN ligands in $[Pt(CH_3CN)_2Cl_2]$ (see Table 3.3) with those obtained from the rotational spectra of free CH_3CN[284] and from averaging the N-C and C-C distances for structures containing CH_3CN not bound to metal atoms (*i.e.* lattice CH_3CN), revealed a marginal contraction of the N-C distance and a similarly small elongation of the C-C bond of the CH_3CN ligand on coordination.[279] Similar results were obtained when the study was extended to include other metal complexes containing coordinated CH_3CN and is consistent with a strengthening of the $C \equiv N$ bond and a weakening of the C-C bond on coordination.

Table 3.3 $C \equiv N$ *and C-C bond distances[a] for free, "lattice" and coordinated CH_3CN*

	$C \equiv N$	C-C	Reference
Free CH_3CN	1.16	1.46	285
"Lattice" CH_3CN (averaged)[b]	1.14	1.42	279
$[Pt(CH_3CN)_2Cl_2]$ (averaged)	1.11	1.47	279
$[Pt(terpy)(CH_3CN)](SbF_6)_2$	1.09(2)	1.51(3)	This study

[a] Bond distances quoted in Å

[b] Averaged value calculated from a number of structures containing "lattice" CH_3CN

A consideration of the $C \equiv N$ and C-C distances in $[Pt(terpy)(CH_3CN)](SbF_6)_2$ reveals that these distances are comparable with those observed in $[Pt(CH_3CN)_2Cl_2]$, but that the decrease in the $C \equiv N$ distance and the concomitant increase in the C-C distance, on coordination of the CH_3CN ligand, are more substantial than those observed in $[Pt(CH_3CN)_2Cl_2]$.

The Pt-N-C angle of the CH_3CN ligand equals 179(2)° and does not exhibit any substantial deviation from the 180° expected for idealized geometry. Small deviations of this angle from 180° have been reported previously[279] and have been attributed to the use of orbitals of partial sp^2 character by the nitrogen atom. The N-C-C angle of the CH_3CN ligand equals 177(2)°, deviating marginally from the expected value of 180°. This small deviation is not unprecedented, an angle of 176.9(8)° having been reported for the CH_3CN ligand in the $[(C_5H_5)(dppe)Fe(CH_3CN)]^+$ cation[286] [dppe = 1,2-bis(diphenylphosphino)ethane].

The crystal lattice of $[Pt(terpy)(CH_3CN)](SbF_6)_2$ consists of sheets of cations and anions. A diagram depicting the packing architecture in one such sheet is provided in Figure 3.2. The $[Pt(terpy)(CH_3CN)]^{2+}$ and SbF_6^- ions within a sheet are arranged in alternating rows of cations and anions which extend along the [b]-axis. The cations in one such a row are interrelated by a unit cell translation along the [b]-axis and occur in a side-by-side arrangement. As a consequence of this arrangement no π-π or metal-metal interaction is expected between the cations in a row.

An alternative projection depicting the unit cell contents and the packing architecture, as viewed along the [b]-axis, is provided in Figure 3.3. In this figure, the cation and anion rows extend into and out of the plane of the page. The sheets resulting from the combination of these rows extend in the horizontal direction and into and out of the plane of the page. The individual sheets are interrelated by c-glide planes, which results in their being "slipped" with respect to each other. As a consequence of this slipped arrangement, a row of anions is situated directly above and below each row of cations. This results in the interatomic distances between cations in adjoining sheets being too long to allow for any interaction beween these ions. (The Pt-Pt distances between neighbouring cations from adjacent sheets are all greater than 4.90Å.) Similarly, the C-C distances between these cations all exceed 3.50Å, the sum of the Van der Waal's radii for π-aromatic species in a face-to-face arrangement being 3.45Å. Since there are no metal-metal or π-π interactions between the cations within a row or between cations in rows from neighbouring sheets, the $[Pt(terpy)(CH_3CN)]^{2+}$ chromophore can be considered as existing in a monomeric environment in $[Pt(terpy)(CH_3CN)](SbF_6)_2$.
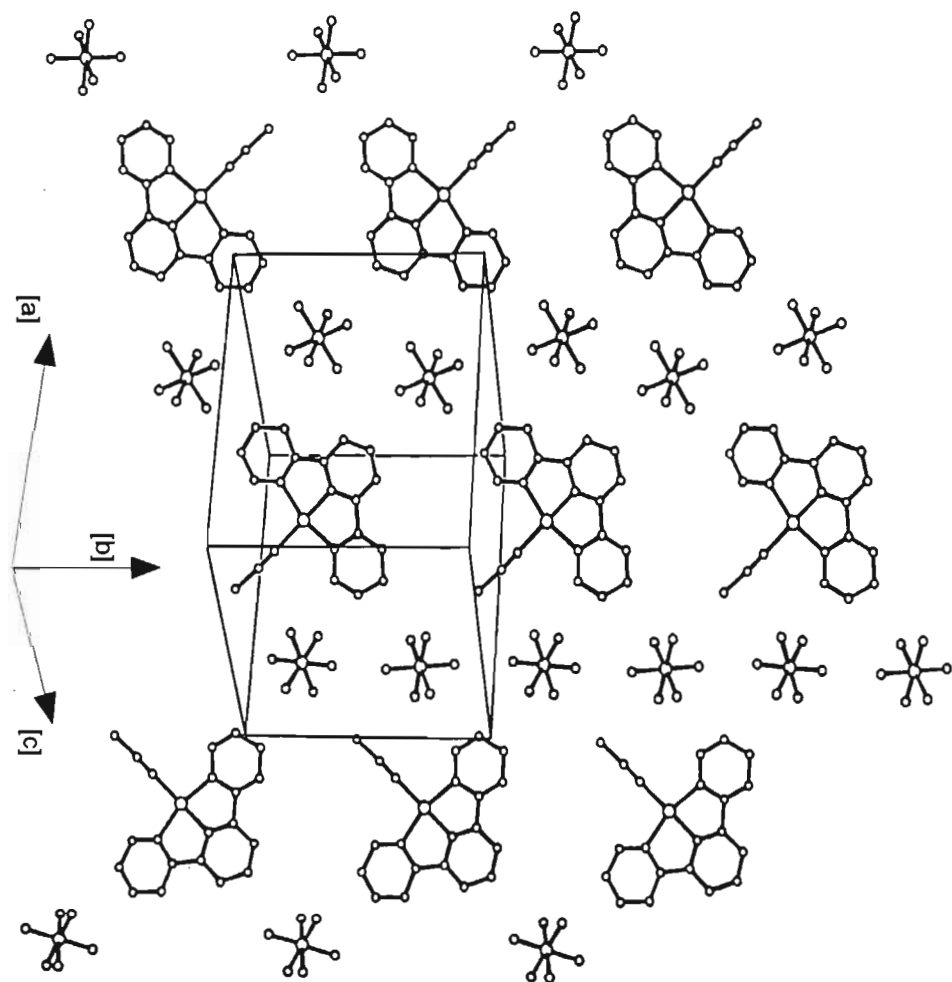
Figure 3.2 The packing architecture in a sheet of cations and anions in [Pt(terpy)(CH₃CN)](SbF₆)₂.
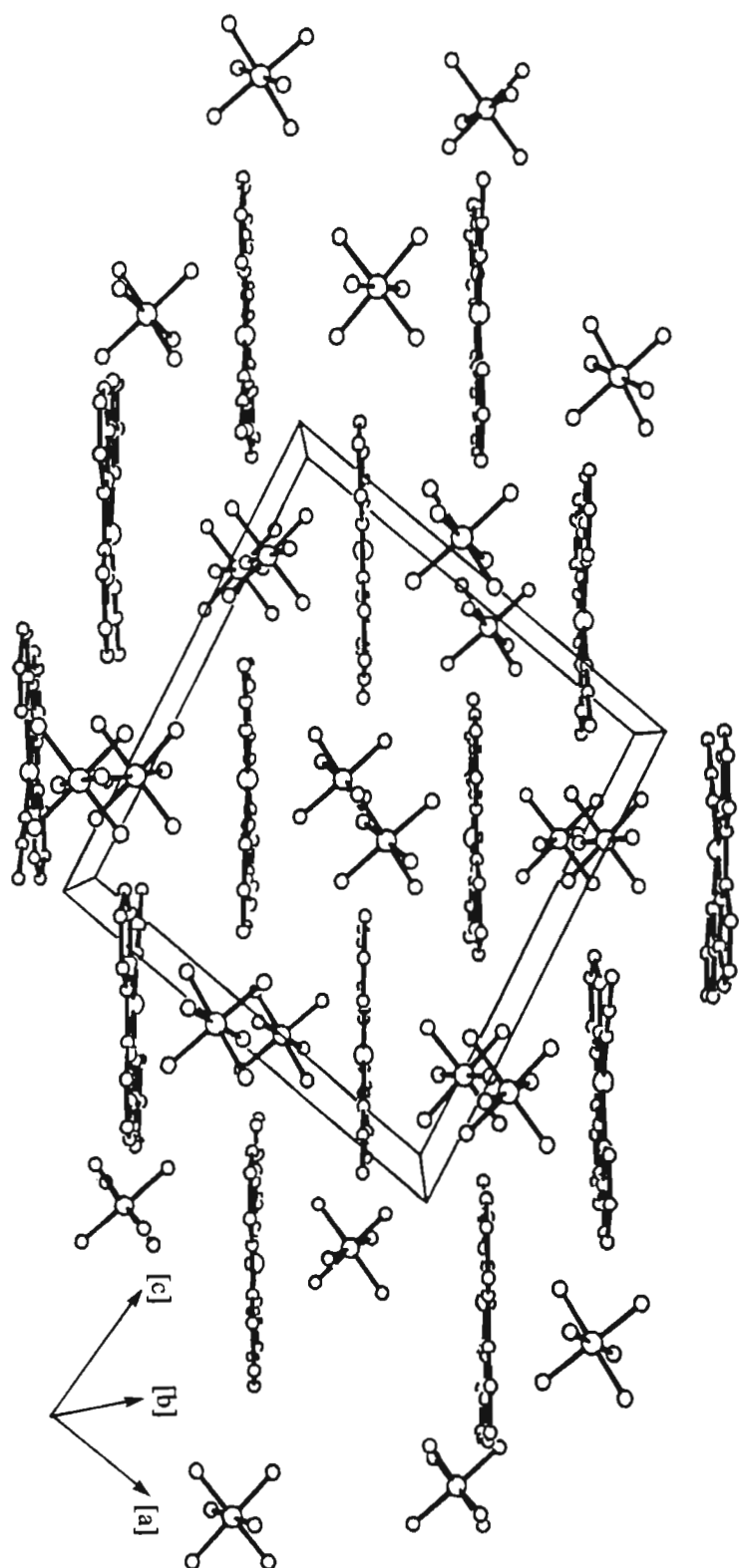
Figure 3.3 The unit cell contents of [Pt(terpy)(CH₃CN)](SbF₆)₂ as seen in a view along the [b]-axis.

3.4.2.3 Photophysical studies on [Pt(terpy)(CH₃CN)](SbF₆)₂ (8)

The room temperature absorption spectrum of a CH_3CN solution of **8** is depicted in Figure 3.4. The wavelengths $\lambda(abs)_{max}$ associated with the absorption maxima, are listed in Table 3.4.

The absorption spectrum consists of three features, *viz.* a relatively sharp transition at 273 nm with a shoulder at 293 nm, a pair of maxima [$\lambda(abs)_{max}$ equal 324 and 338 nm] and two peaks at wavelengths greater than 350 nm [$\lambda(abs)_{max}$ equal 367 and 386 nm]. Both McMillin and co-workers[260] and Che and co-workers[263] have observed the same features in the spectra of [Pt(terpy)Cl]Cl, [Pt(terpy)(OH)](BF₄) and [Pt(terpy)(NH₃)](PF₆)₂ for example. The assignment of these absorption features thus follows that reported in the aforementioned studies. By analogy to the absorption spectrum of $[Zn(terpy)_2]^{2+}$,[287,288] the sharp transition at 273 nm, as well as the maxima at 324 and 338 nm can be assigned to π-π^* transitions of the coordinated terpyridine ligand. It is known that the absorption spectrum of $[Zn(terpy)_2]^{2+}$ does not to possess any features originating from metal-to-ligand charge transfer (MLCT) transitions[288] and that it does not exhibit any absorption features at wavelengths greater than 350 nm. Thus, the two peaks at 367 and 386 nm in the spectrum of [Pt(terpy)(CH₃CN)](SbF₆)₂ (**8**), are tentatively assigned to MLCT transitions. It is also interesting to note that both of these peaks are narrow with distinct absorption maxima. This is analogous to the shape of the MLCT features Che and co-workers[263] reported in the absorption spectrum of the $[Pt(terpy)(NH_3)]^{2+}$ chromophore, but contrasts with that observed in the spectra of other Pt(terpy) chromophores where the fourth coordination site is occupied by ligands such as I^-,[263] Cl^-, OH^- or NCS^-.[260] In the latter instance the bands are broad and do not exhibit well-defined maxima. The I^-, Cl^-, OH^- and NCS^- ligands do of course differ from CH_3CN and NH_3 in that they are anionic ligands, whereas both CH_3CN and NH_3 are neutral. The higher electron density associated with these anionic ligands, can contribute to a greater stabilization of the excited state resulting from Pt→terpy metal-to-ligand charge transfer, compared to that achieved by the neutral ligands. As a result some influence
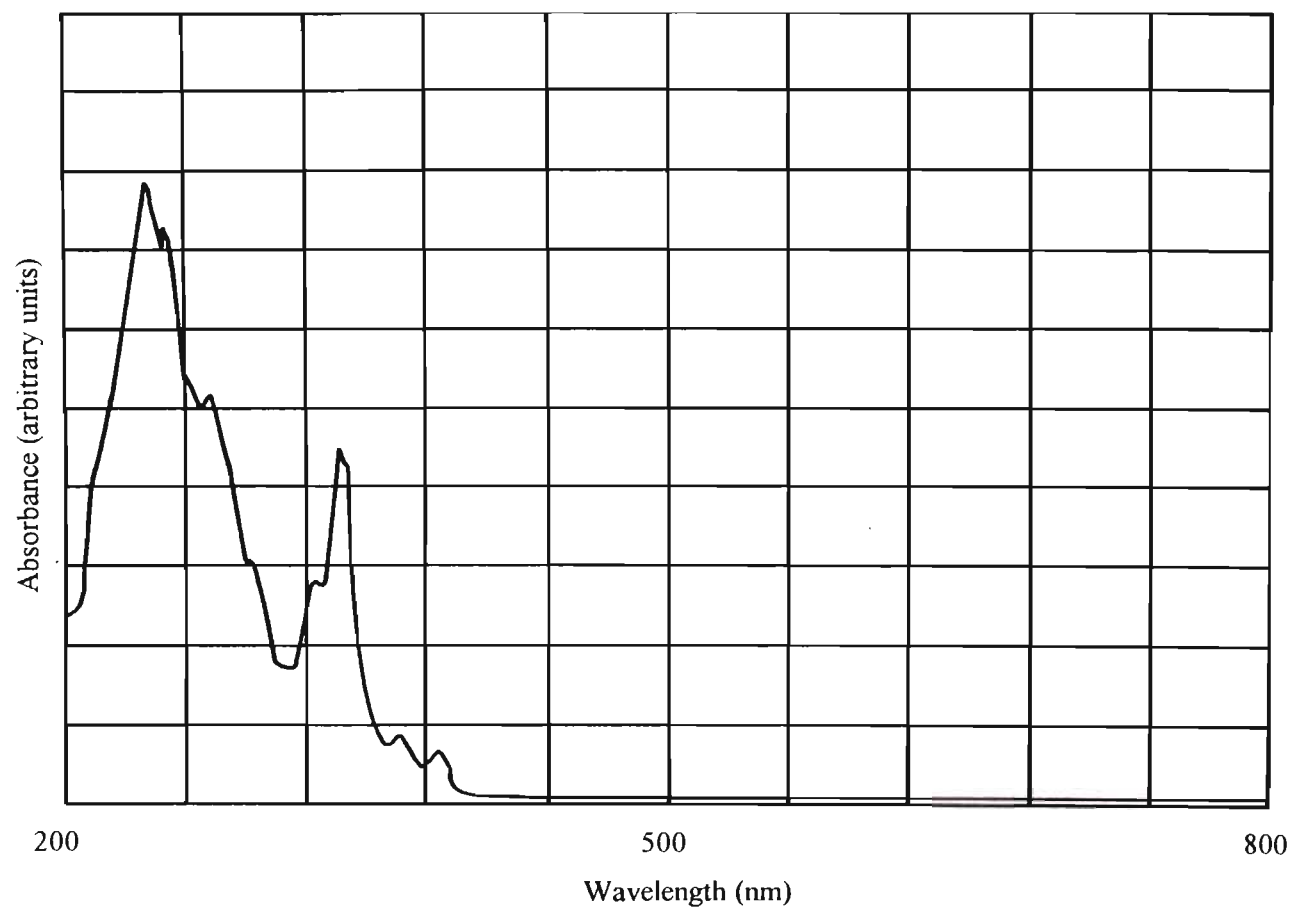
Figure 3.4   *The absorption spectrum of a CH₃CN solution of [Pt(terpy)(CH₃CN)](SbF₆)₂ recorded at room temperature.*

Table 3.4 *The Wavelengths, $\lambda(abs)_{max}$, associated with the absorption maxima in the solution spectra of some of the complex salts studied in this work.*

Compound	$\lambda(abs)_{max}$ (nm)	Assignment
[Pt(terpy)(CH₃CN)](SbF₆)₂	273, 324, 338	$^1(\pi\text{-}\pi^*)$ (terpy)
	367, 386	MLCT [Pt(5d) → terpy(π^*)]
[Pt(terpy)Cl](SbF₆)	305, 319, 332, 349	$^1(\pi\text{-}\pi^*)$ (terpy)
	379, 393	MLCT [Pt(5d) → terpy(π^*)]
[Pt(bipy)₂](SbF₆)₂	220, 256, 310, 320, 348	$^1(\pi\text{-}\pi^*)$ (bipy)
[Pt(4-Ph'-terpy)Cl](SbF₆)	282, 304, 320, 333, 351	$^1(\pi\text{-}\pi^*)$ (4-Ph'-terpy)
	384, 403	MLCT [Pt(5d) → 4-Ph'-terpy(π^*)]
[Pt(terpy)(C≡CPh)](SbF₆)	261	$^1(\pi\text{-}\pi^*)$ (-C≡C**Ph**)
	284, 311, 329, 343	$^1(\pi\text{-}\pi^*)$ (terpy)
	440	Uncertain
[Pt(4-Ph'-terpy)(C≡CPh)](SbF₆)	262	$^1(\pi\text{-}\pi^*)$ (-C≡C**Ph**)
	289, 309, 332	$^1(\pi\text{-}\pi^*)$ (4-Ph'-terpy)
	405	MLCT [Pt(5d) → 4-Ph'-terpy(π^*)]
	458	Uncertain

on the width of the MLCT bands in the absorption spectra of the Pt(terpy) chromophores might be expected.

The emission behaviour of [Pt(terpy)(CH$_3$CN)](SbF$_6$)$_2$ was studied in the solid state, in a butyronitrile glass at 77 K and in CH$_3$CN solution at room temperature.

The solid state emission spectrum of [Pt(terpy)(CH$_3$CN)](SbF$_6$)$_2$, was recorded at 40 K intervals over the temperature range 80 to 280 K. The overlaid spectra displaying the relative intensities of the emissions are depicted in Figure 3.5 and the individual spectra corresponding to temperatures of 240 and 280 K in Figure 3.6.

One of the most noticeable features in the series of overlaid spectra is the general increase in the intensity of the emission associated with a decrease in the temperature of the sample. This phenomenon can be explained by the presence of a metal-centred d-d excited state, which is slightly higher in energy than the emissive excited state(s). The existence of such d-d states is well established in the literature.[289, 290] In the case of Pt(II) (a d^8 centre) population of such an excited state involves transfer of an electron to the Pt d$_{x^2-y^2}$ orbital. As pointed out by McMillin et al.,[260] this orbital is antibonding with respect to the metal-to-ligand bonds, thus implying that the d-d excited state will be subject to strong molecular distortions. Consequently, the chromophore can undergo rapid non-radiative decay from the d-d excited state, once populated. Since this state is suggested to be very close in energy to the emitting state(s), electron transfer from the emitting state to the d-d state can be thermally activated. Decreasing the temperature of the sample results in less thermal energy being available for the population of the d-d state, which in turn implies that a larger fraction of excited chromophores will undergo radiative decay from the emitting state(s), thus leading to the observed increase in the emission intensity.

Although the intensity of the emission at 280 K is extremely weak when compared to that observed at 80 K, it is nonetheless possible to resolve four vibrational features on the high energy side of the band envelope (see Figure 3.6). The low energy side of the band envelope is dominated by a broad unresolved feature. The vibrational features occur at wavelengths, λ(em)$_{max}$, of ca. 465, 497, 546 and 580 nm. It is however, difficult to accurately determine the position of these features due to the low intensity

(a) 80 K, (b) 120 K, (c) 160 K, (d) 200K, (e) 240K, (f) 280K
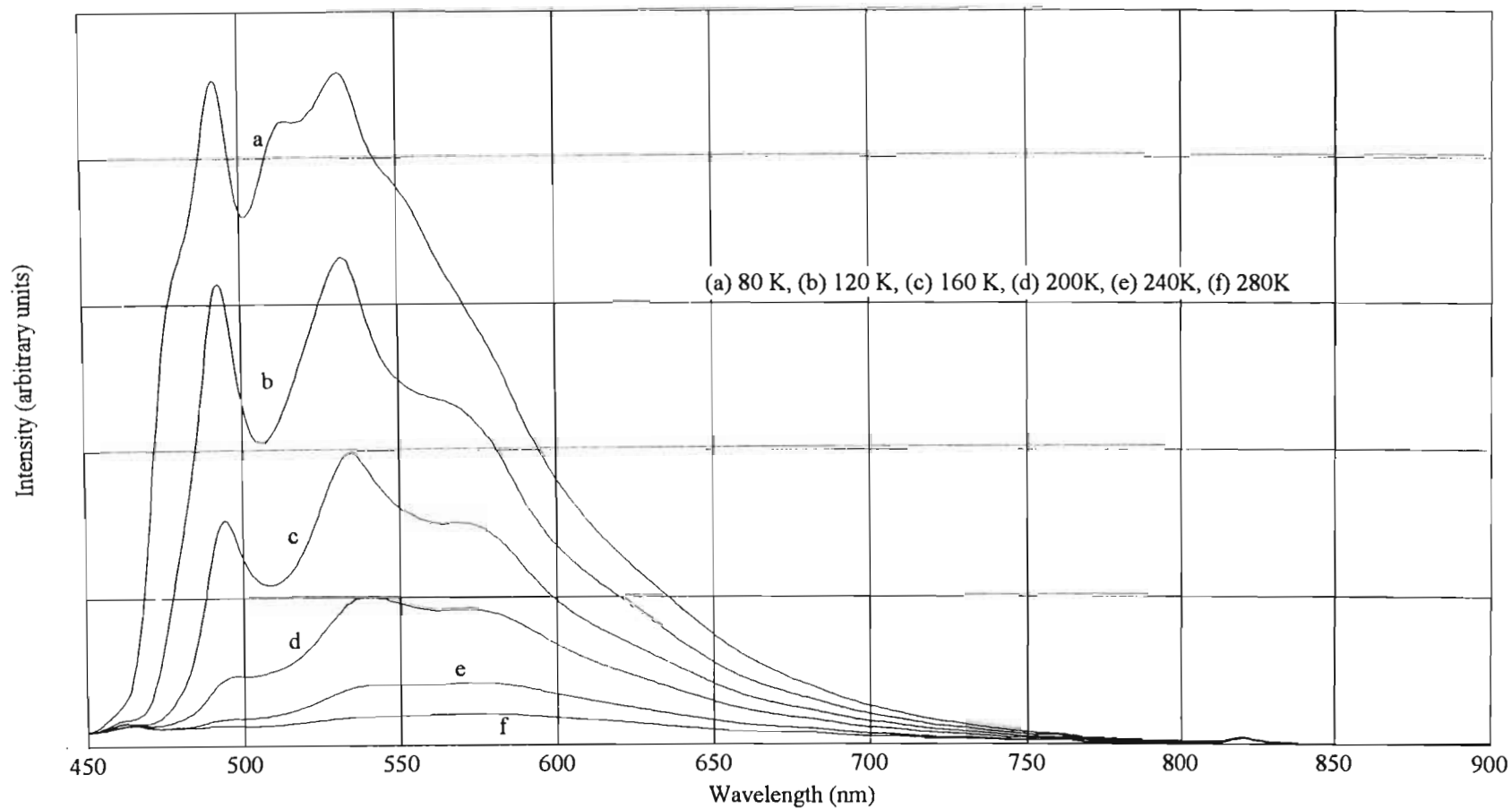
Figure 3.5   *The solid state emission spectrum of [Pt(terpy)(CH₃CN)](SbF₆)₂ recorded at 40 K intervals over the range 80 to 280 K.*
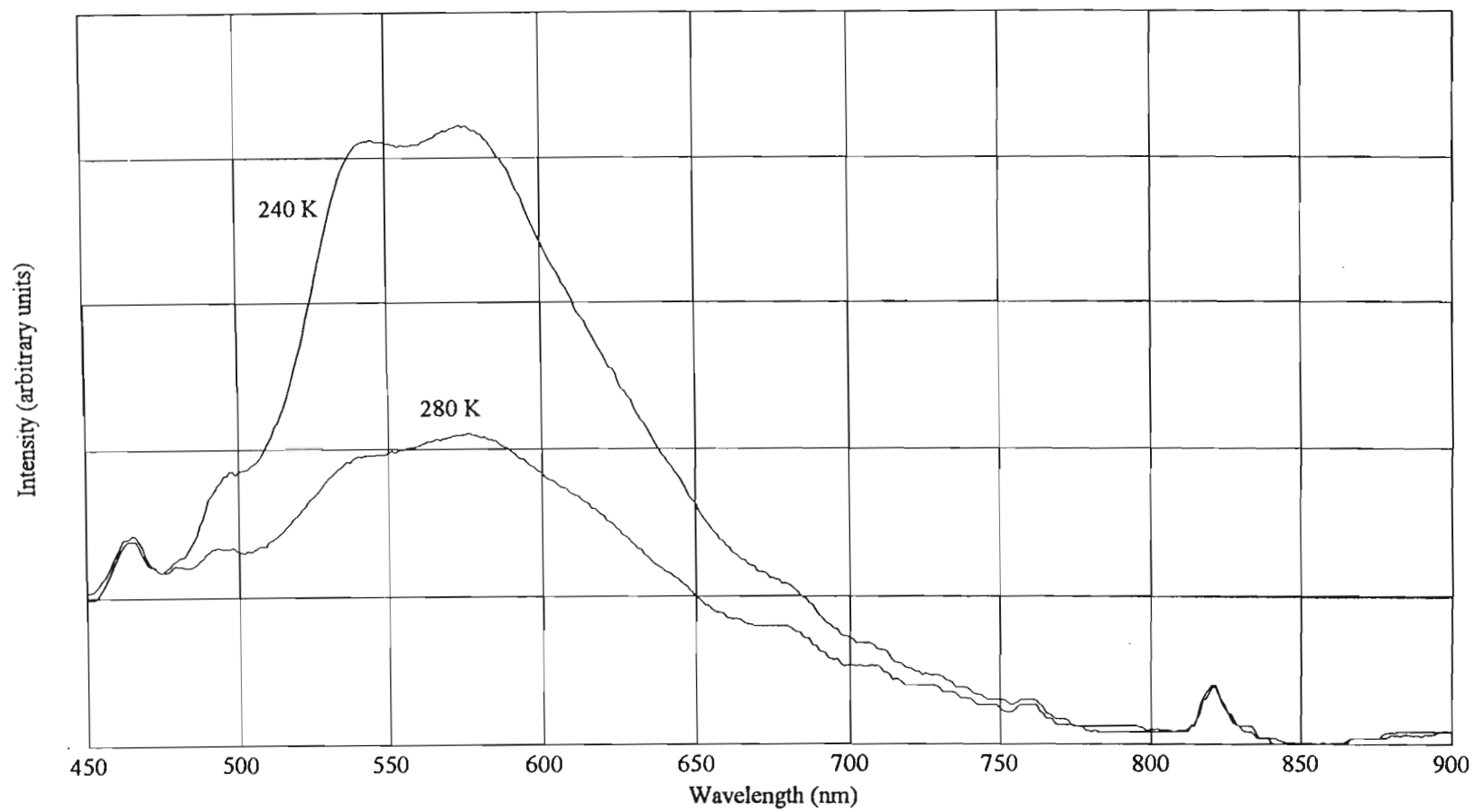
Figure 3.6   *The solid state emission spectrum of [Pt(terpy)(CH₃CN)](SbF₆)₂ recorded at 240 K and 280 K.*

of the emission, which decreases the signal to noise ratio; moreover these features overlap with and obscure the broad unresolved feature which could result in their being shifted from their true positions. The wavelengths, $\lambda(em)_{max}$, of these features are nonetheless in good agreement with those of analogous features observed in a low-temperature butyronitrile glass emission spectrum of [Pt(terpy)Cl](SbF$_6$) (see Section 3.4.3.3); they do however display a small shift of between 0 and 15 nm towards shorter wavelengths when compared to those in the emission spectrum of {[Pt(terpy)]$_2$(μ-pyrazole)}(PF$_6$)$_3$ in a CH$_3$CN glass at 77 K.[291] The emission observed from both of these complex salts originates from the radiative decay of a terpyridine based $^3(\pi$-$\pi^*)$ excited state. By analogy, the vibrational features on the high energy side of the solid state emission spectrum of [Pt(terpy)(CH$_3$CN)](SbF$_6$)$_2$ are also assigned to originate from a $^3(\pi$-$\pi^*)$ excited state. Some structure is also observed to be superimposed on the broad unresolved feature on the low energy side of the emission band profile. The origin of these features are uncertain. It is however, possible that they could be a result of the low signal to noise ratio associated with the spectrum; certainly these features are not present in any of the solid state spectra of [Pt(terpy)(CH$_3$CN)](SbF$_6$)$_2$ which were recorded at lower temperatures and display higher emission intensities.

As mentioned above, the emission intensity of [Pt(terpy)(CH$_3$CN)](SbF$_6$)$_2$ increases as the temperature of the sample is decreased. More specifically, the intensity of the second, third and fourth vibrational features, in order of decreasing energy, increases over the interval 280 to 240 K, whereas the intensity of the vibrational feature of highest energy remains virtually unaffected. Further decreasing the temperature over the interval 240 to 120 K results in the second and third vibrational features displaying marked increases in emission intensity, with the intensity of the first vibrational feature remaining virtually constant and the fourth feature displaying a smaller increase. This results in the band profile of the emission spectrum recorded at 120 K, being dominated by the second and third vibrational features, with the first and fourth features existing as shoulders to the aforementioned features. The increase in the intensity of the second and third vibrational features also exceeds that of the obscured, broad and unresolved feature observed in the spectrum recorded at 280 K. Decreasing the temperature of the sample to 80 K effects a further increase in the intensity of the

second and third vibrational features, along with the appearance of additional vibrational structure.

As such, the solid state emission spectrum of [Pt(terpy)(CH$_3$CN)](SbF$_6$)$_2$, recorded at 80 K closely resembles that reported for microcrystalline samples of [Pt(bipy)$_2$](ClO$_4$)$_2$ recorded at 30 K.[253] In their assessment of the emission spectrum of [Pt(bipy)$_2$](ClO$_4$)$_2$, Miskowski and Houlding[252] found the energy separation between the vibrational features on the high energy side of the band to be consistent with bipyridine vibrational modes, thus providing further support for the terpyridine $^3(\pi\text{-}\pi^*)$ assignment proposed for [Pt(terpy)(CH$_3$CN)](SbF$_6$)$_2$.

The broad concealed feature on the low energy side of the band envelope of the solid state emission spectrum of [Pt(terpy)(CH$_3$CN)](SbF$_6$)$_2$ is more difficult of assign. Miskowski and Houlding suggested that an analogous feature in the solid state spectrum of [Pt(bipy)$_2$](ClO$_4$)$_2$ could either be the result of the [Pt(bipy)$_2$]$^{2+}$ chromophore emitting from multiple states, or of "excimer-like emission from neighbouring complexes that are brought into electronic contact by the crystal packing". However, the authors conceded that their assignment is restricted to conjecture since they were unable to obtain any solution emission data and the crystal structure of [Pt(bipy)$_2$](ClO$_4$)$_2$ is unknown.

Excimer-like emission can be ruled out in the assignment of the broad unresolved feature on the low energy side of the emission band envelope of solid samples of [Pt(terpy)(CH$_3$CN)](SbF$_6$)$_2$, since the crystal lattice of this complex salt is known to contain the [Pt(terpy)(CH$_3$CN)]$^{2+}$ chromophore in a monomeric environment with no possibility of any metal-metal or ligand-ligand interaction (see Section 3.4.2.2).

Further evidence ruling out the possibility of excimer-like emission is provided by the emission spectrum of the [Pt(terpy)(CH$_3$CN)]$^{2+}$ chromophore in a dilute, low-temperature butyronitrile glass (see Figure 3.7). The spectrum is dominated by a broad feature which occurs on the low energy side of the band envelope at *ca.* 613 nm. This is most probably the same feature as the obscured and unresolved feature which was observed in the solid state spectra of [Pt(terpy)(CH$_3$CN)](SbF$_6$)$_2$. The fact that this feature is present, and in fact is more dominant in the emission spectrum of the
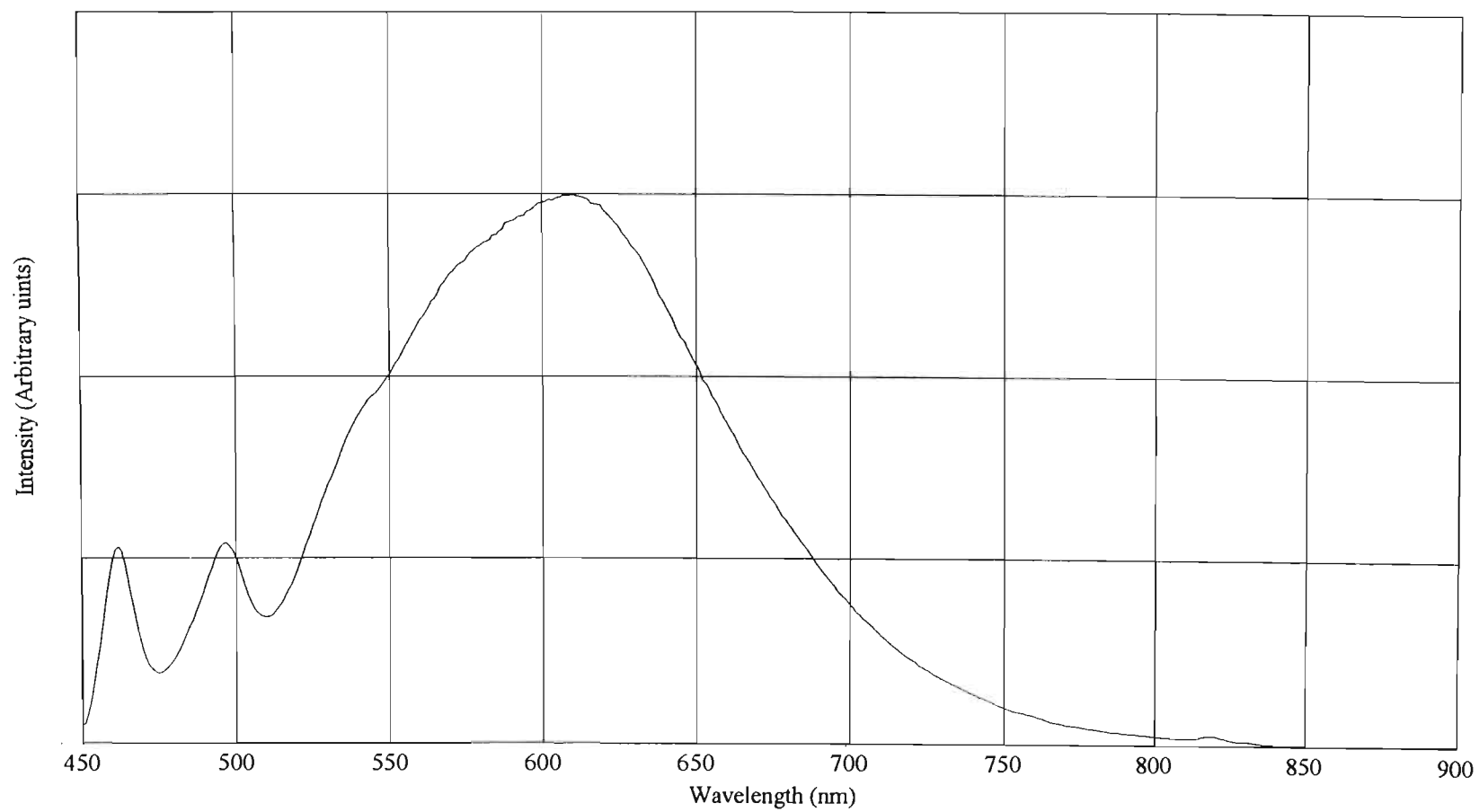
Figure 3.7   _The emission spectrum of a dilute low-temperature butyronitrile glass of [Pt(terpy)(CH₃CN)](SbF₆)₂._
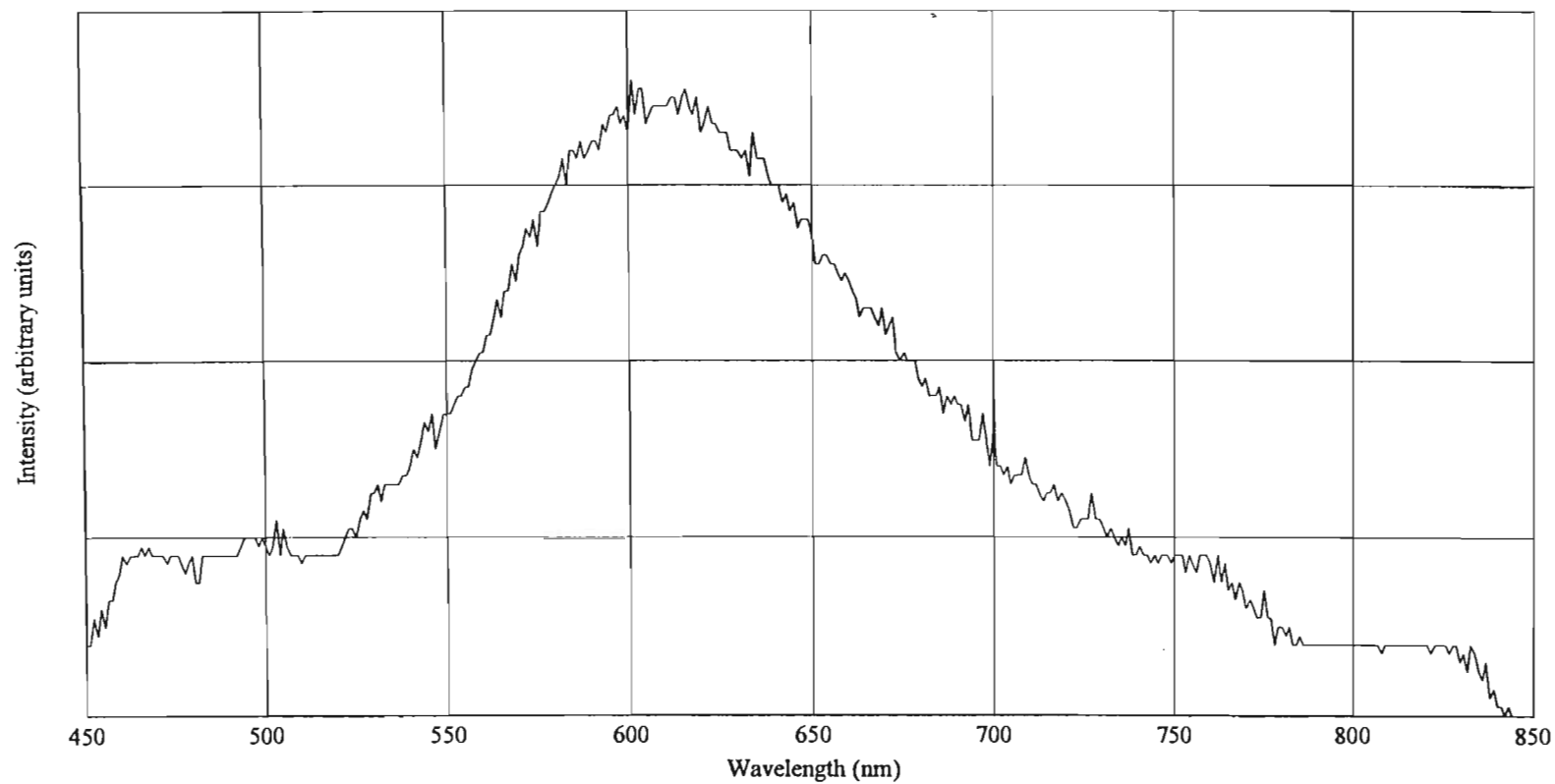
Figure 3.8   *The emission spectrum of a degassed CH₃CN solution of [Pt(terpy)(CH₃CN)](SbF₆)₂ recorded at room temperature.*

chromophore in a glassy solution when compared to the solid state spectra, suggests that this feature does not originate from excimer-like emission, since electronic interactions would be expected to decrease when comparing glassy solutions to the solid state. The high energy side of the emission spectrum of $[Pt(terpy)(CH_3CN)](SbF_6)_2$ in glassy solution displays vibronic structure. Four vibrational features occurring at ca. 462, 497, 543 and 583 nm respectively, can be resolved. These wavelengths are in good agreement with those observed in the solid state emission spectra of $[Pt(terpy)(CH_3CN)](SbF_6)_2$.

The argument against excimer-like emission being the origin of the broad feature observed in the solid state and glassy solution spectra of $[Pt(terpy)(CH_3CN)](SbF_6)_2$ is further supported by a consideration of the emission spectrum of the $[Pt(terpy)(CH_3CN)]^{2+}$ chromophore in CH_3CN solution at room temperature (see Figure 3.8). Although the emission intensity is very low, the spectrum can be resolved to consist of a single broad feature centred at ca. 610 nm. This is in good agreement with the wavelength associated with the broad feature observed in the emission spectrum obtained from the low-temperature butyronitrile glass. Since metal-metal and ligand-ligand interactions are expected to be minimal in fluid solution at room temperature, it would seem that excimer-like emission can be discounted as the origin of the broad emission features observed in spectra recorded on samples in the solid state and in glassy and fluid solution.

These arguments would thus suggest that both solid samples and glassy butyronitrile solutions of $[Pt(terpy)(CH_3CN)](SbF_6)_2$ exhibit multiple state emission. However, before such an assignment can be made with any certainty, it is necessary to eliminate certain factors[292, 293] which could lead to the observation of multiple emissions from a sample containing the chromophore of interest.

The first of these factors involves intrinsic heterogeneity of the sample and includes the trivial case where impurity emissions are present. The sample utilized in the study of the emission behaviour of $[Pt(terpy)(CH_3CN)](SbF_6)_2$ was crystalline and elemental analysis for C, H and N have confirmed the sample to be analytically pure. However, as pointed out by DeArmond and Carlin,[290] "use of elemental analysis and NMR

spectra and IR spectra alone cannot be expected properly to verify purity when the phenomenon of interest is luminescence".

It is thus necessary to consider possible sources of contamination of samples of $[Pt(terpy)(CH_3CN)](SbF_6)_2$. The salt is reasonably stable with respect to air and moisture, the first signs of any deterioration only being detectable after prolonged exposure over a period of several weeks. Samples used in the photophysical studies were freshly prepared, stored under an atmosphere of nitrogen and photophysical studies were completed within days of the sample having been synthesized. The possibility of any impurity emissions arising from decomposition of the salt can thus be ruled out. Another possible source of contamination is that of unreacted starting materials, these being $AgSbF_6$ and $[Pt(terpy)Cl](SbF_6)$. The silver salt is non-emissive, the platinum complex on the other hand, is emissive both in the solid state and in glassy butyronitrile solutions (see Section 3.4.3.3). Although the solid state emission spectrum of $[Pt(terpy)Cl](SbF_6)$ displays a relatively broad feature centred at $ca.$ 552 nm, which could be responsible for the broad unresolved feature in the solid state spectra of $[Pt(terpy)(CH_3CN)](SbF_6)_2$, should the sample contain small amounts of $[Pt(terpy)Cl](SbF_6)$, the band profile of the emission of the latter in dilute glassy butyronitrile solutions displays distinct vibronic structure with no evidence of the broad feature at 552 nm. Since the broad feature is observed in the emission spectra of $[Pt(terpy)(CH_3CN)](SbF_6)_2$, both in the solid state and in glassy solution, it cannot be attributed to the presence of impurity emissions from $[Pt(terpy)Cl](SbF_6)$.

A second factor which could result in multiple emissions, is that of microenvironmental effects. When the energy of an excited state is sensitive to the microenvironment, multiple emission can arise as a consequence of discrete environments producing spectrally distinct emissions. Although microenvironmental effects are usually associated with solvent heterogeneity in solution spectra,[292, 293] it is clear that these effects also extend to the solid state where the lattice contains the chromophore in two or more crystallographically distinct environments. This does not apply to $[Pt(terpy)(CH_3CN)](SbF_6)_2$, since as pointed out in the discussion of the structure of this salt (see Section 3.4.2.2), the asymmetric unit contains only one

$[Pt(terpy)(CH_3CN)]^{2+}$ chromophore, thus implying that the microenvironment of each of the chromophores in the lattice is identical.

Based on these considerations, it would thus seem that the $[Pt(terpy)(CH_3CN)]^{2+}$ chromophore does indeed exhibit multiple state emission, both in the solid state and in dilute butyronitrile glasses. In the preceding discussion the vibrationally structured component of the emission observed from the chromophore in the solid state or in glassy solution, was assigned to originate from a $^3(\pi\text{-}\pi^*)$ state. The broad structureless component of the emission, although extremely weak, is best resolved in spectra recorded on the chromophore in CH_3CN solution, where it is not obscured by the $^3(\pi\text{-}\pi^*)$ emission (see Figure 3.8).

The energy and the broad band shape associated with this feature, closely corresponds to that of $[Pt(terpy)(OH)]^+$ in CH_3CN solution, as observed by McMillin and co-workers.[260] The reasoning applied in assigning this feature thus follows that reported by the aforementioned authors. The energy and the broad band shape of the feature is substantially different from that associated with the $^3(\pi\text{-}\pi^*)$ component, thus suggesting that it does not originate from a purely ligand-based electronic transition. In fact, it is more consistent with emission from a ^{3}d-d or triplet charge transfer (^{3}CT) state.

Emission from ^{3}d-d states is rarely observed from Pt(II) complexes since, as mentioned in the earlier discussion and pointed out by McMillin et al.,[260] "Populating a ^{3}d-d state involves promoting an electron into the metal-ligand antibonding $d_{x^2\text{-}y^2}$ orbital. As a result these excited states are subject to strong distortions and are likely to be substitution active and short-lived." In the light of this, and considering the fact that the feature is observed at room temperature in fluid CH_3CN solution, the medium in which excited state distortions would be expected to be most prevalent, it would seem that the broad emission feature in all probability originates from the radiative decay of a ^{3}CT state. Furthermore, since both the terpyridine and acetonitrile ligands are classified as being π-acceptor ligands, the charge transfer state is most likely to possess extensive metal-to-ligand character, i.e. a ^{3}MLCT state is suggested to be involved.

Repeated attempts at synthesizing the tetrafluoroborate salt, [Pt(terpy)(CH$_3$CN)]-(BF$_4$)$_2$, were unsuccessful. Attempts at utilizing the tetrakis-acetonitrile species [Pt(CH$_3$CN)$_4$](BF$_4$)$_2$ as an intermediate, consistently afforded [Pt(terpy)Cl](BF$_4$), whilst attempts at displacing the coordinated Cl$^-$ ligand on [Pt(terpy)Cl](BF$_4$) with acetonitrile, as utilized in the synthesis of [Pt(terpy)(CH$_3$CN)](SbF$_6$)$_2$, afforded a product which was contaminated with [Pt(terpy)Cl](BF$_4$). All attempts at isolating the product from this mixture were unsuccessful.

The synthetic difficulties encountered in the preparation of the [Pt(terpy)(CH$_3$CN)]$^{2+}$ salts, in contrast to those of [Pt(terpy)Cl]$^+$, together with the fact that the colours of the [Pt(terpy)Cl]$^+$ salts display a marked dependence on the nature of the counterion, *vide infra*, prompted us to turn our attention away from the [Pt(terpy)(CH$_3$CN)]$^{2+}$ salts and to focus on salts of the [Pt(terpy)Cl]$^+$ chromophore.

3.4.3 [Pt(terpy)Cl](X) [X$^-$ = SbF$_6^-$ (9), CF$_3$SO$_3^-$ (10), BF$_4^-$ (11)]

3.4.3.1 Preliminary considerations

As discussed in Section 3.4.1, the [Pt(terpy)Cl]$^+$ chromophore is well-known and its chloride salt, [Pt(terpy)Cl]Cl, has been utilized extensively as a starting material in the preparation of complexes containing the Pt(terpy) moiety.

The emission properties of the [Pt(terpy)Cl]$^+$ chromophore have also received attention. McMillin and co-workers[260] reported that the [Pt(terpy)Cl]$^+$ chromophore is non-emissive in acetonitrile solution at 25°C. In a more detailed study, Che and co-workers[263] prepared [Pt(terpy)Cl](CF$_3$SO$_3$) (compound **10** in this work) and investigated its emission properties both in the solid state and in a low-temperature butyronitrile glass.

The studies of McMillin and co-workers[260] and Che and co-workers[263] focused on characterizing the emission behaviour of the [Pt(terpy)Cl]$^+$ chromophore in various media, and on determining the influence of temperature variations on the emission behaviour of the CF$_3$SO$_3^-$ salt in the solid state. In contrast, this study considers the influence of counterions with different steric demands on the solid state emission behaviour of the [Pt(terpy)Cl]$^+$ chromophore as found in the various salts. To the best

of our knowledge, no such study involving a Pt(II) polypyridyl chromophore has been performed before.

3.4.3.2 Synthesis and characterization of [Pt(terpy)Cl](X) [X⁻ = SbF₆⁻ (9), CF₃SO₃⁻ (10) and BF₄⁻ (11)]

In synthesizing [Pt(terpy)Cl](CF₃SO₃) (**10**), Che and co-workers[263] employed [Pt(terpy)Cl]Cl as starting material and obtained the $CF_3SO_3^-$ salt by performing a metathesis reaction utilizing $AgCF_3SO_3$ in an aqueous solution.

The synthesis employed here differs from that of Che and co-workers and constitutes the first step of the procedure utilized in synthesizing the $[Pt(terpy)(CH_3CN)]^{2+}$ chromophore. $[Pt(C_6H_5CN)_2Cl_2]$ was treated with an equimolar amount of the appropriate silver salt in refluxing acetonitrile. As was discussed in Section 3.4.2.1, this most probably results in the formation of a species which can be represented as $[PtCl(C_6H_5CN)_{3-n}(CH_3CN)_n](X)$ (X⁻ = SbF_6^-, $CF_3SO_3^-$, BF_4^-, n = 1, 2 or 3). The precipitated silver chloride was removed by filtration, a small excess of terpyridine {based on $[Pt(C_6H_5CN)_2Cl_2]$} added and the mixture heated under reflux. Subsequent removal of the solvent *in vacuo*, extraction into CH_3CN, crystallization and washing with acetone and/or diethyl ether afforded air and moisture stable analytically pure products. Elemental analysis for C, H, and N corresponded with the empirical formulas [Pt(terpy)Cl](SbF₆) (**9**), [Pt(terpy)Cl](CF₃SO₃) (**10**) and [Pt(terpy)Cl](BF₄) (**11**).

From the colours of the three salts **9**, **10** and **11**, it is immediately evident that the counterions have a distinct influence on the optical properties of the salts. The SbF_6^- salt **9**, when precipitated from CH_3CN has a bright orange colour. However, on isolating the salt from the mother liquor, a slow conversion to a yellow phase immediately sets in, irrespective of whether the salt is stored in air or under an inert atmosphere. An instantaneous conversion from the meta-stable orange modification to the yellow polymorph can be achieved by washing the orange form with acetone. The $CF_3SO_3^-$ salt **10**, is orange in colour and in contrast to the SbF_6^- salt, does not exhibit any polymorphic behaviour. The same applies to the BF₄⁻ salt **11**, which has an orange-red colour. From the observations made regarding these three salts it would seem that

the colour of the $[Pt(terpy)Cl]^+$ salts tend towards the red part of the visible spectrum as the steric demands of the counterions decrease.

The meta-stable polymorphic behaviour of $[Pt(terpy)Cl](SbF_6)$ (**9**) is not unusual. A similar observation was made by Che and co-workers,[263] who reported that the colour of $[Pt(terpy)(NH_3)](PF_6)_2$ changes from red, when freshly prepared, to a dull yellow on standing in air for *ca.* 1 day. $[Pt(terpy)(N_3)](PF_6)$ was also reported to change colour over a few days.[263]

The solid state infrared spectra of the salts **9** ,**10** and **11** were recorded as KBr pellets, the most prominent peaks being listed in Table 3.1. The solid state KBr spectrum of $[Pt(terpy)Cl]Cl$ was also recorded and compared with the spectra of the aforementioned salts. The spectra of **9** ,**10**, **11** and $[Pt(terpy)Cl]Cl$ are essentially identical, the only difference between them being that associated with the different counterions. A further comparison of the solid state spectra of these salts with that of $[Pt(terpy)(CH_3CN)](SbF_6)_2$ (**8**) reveals that the positions of the peaks associated with the coordinated terpyridine ligand in **9** ,**10** and **11** and $[Pt(terpy)Cl]Cl$ are consistently displaced by *ca.* 6 cm^{-1} towards lower wavenumbers when compared to **8**. Although this displacement might appear to be small when compared to the uncertainty in peak position associated with the instrumentation utilized in this study, the fact that all the peaks associated with the coordinated terpyridine ligand exhibit this displacement, might suggest that the π-donating character of the Cl$^-$ ligand versus the more π-accepting character of the CH$_3$CN ligand, could influence the vibrational modes of the terpyridine ligand through modifying the electron density on the platinum centre.

The crystal structure of $[Pt(terpy)Cl](CF_3SO_3)$ (**10**) has been reported by Che and co-workers.[263] Despite repeated attempts, single crystals of neither the BF$_4^-$, nor the SbF$_6^-$ salt, suitable for X-ray crystallographic studies could be obtained. This is largely due to the fact that crystals of the BF$_4^-$ salt have a needle-like morphology resulting in the crystals being prone to twinning. In the case of the SbF$_6^-$ salt, the meta-stable behaviour of the salt precludes the isolation of suitable single crystals. Although single crystals of the orange phase were isolated, and the phase transition to the yellow phase of the salt did not seem to be accompanied by any loss in crystallinity, as evidenced by

X-ray oscillation photography, all attempts at obtaining the crystal structure of this salt through X-ray diffractometric techniques proved unsuccessful.

3.4.3.3 Photophysical studies on [Pt(terpy)Cl](X) [X⁻ = SbF₆⁻ (9), CF₃SO₃⁻ (10), BF₄⁻ (11)]

The absorption spectrum of the $[Pt(terpy)Cl]^+$ chromophore in CH_3CN solution at room temperature has been studied by both McMillin and co-workers[260] and Che and co-workers.[263] As mentioned in Section 3.4.2.3, the spectrum was reported to consist of a sharp transition at 280 nm and a vibronically structured band with maxima in the range of 300 to 350 nm. Both of these features were attributed to $^1(\pi-\pi^*)$ transitions associated with the coordinated terpyridine ligand. In addition to these peaks, two poorly resolved bands with $\lambda(abs)_{max}$ greater than 350 nm were observed in the absorption spectrum. These bands were assigned to $Pt(5d) \rightarrow terpy(\pi^*)$ MLCT transitions. As would be expected, the room temperature absorption spectra of CH_3CN solutions of $[Pt(terpy)Cl](SbF_6)$ (9), $[Pt(terpy)Cl](CF_3SO_3)$ (10) and $[Pt(terpy)Cl]$-(BF_4) (11) were found to be identical to each other and to that of the $[Pt(terpy)Cl]^+$ chromophore, as reported by the aforementioned authors. A similar assignment to that suggested by these authors is thus proposed.

None of the three $[Pt(terpy)Cl](X)$ salts $[X^- = SbF_6^-$ (9), $CF_3SO_3^-$ (10), BF_4^- (11)] investigated in this study, exhibit luminesence from degassed CH_3CN solutions of the salt. This observation corresponds to that of McMillin and co-workers[260] who also found that the $[Pt(terpy)Cl]^+$ chromophore is non-emissive in solution. The salts 9, 10 and 11 do however luminesce in the solid state and their solid state luminescent behaviour was studied over the temperature range 100 to 280 K.

The solid state emission spectrum of the yellow polymorph of $[Pt(terpy)Cl](SbF_6)$ (9), recorded at 30 K intervals over the temperature range specified above, is depicted in Figure 3.9. The emission at 280 K is weak, the emission spectrum consisting of a broad, poorly resolved peak. It is difficult to determine the wavelength, $\lambda(em)_{max}$, corresponding to the maximum emission intensity for this broad peak. On cooling the sample, the intensity of the emission increases, resulting in improved resolution with the broad peak observed at 280 K, developing a definite maximum, $\lambda(em)_{max}$, at 552
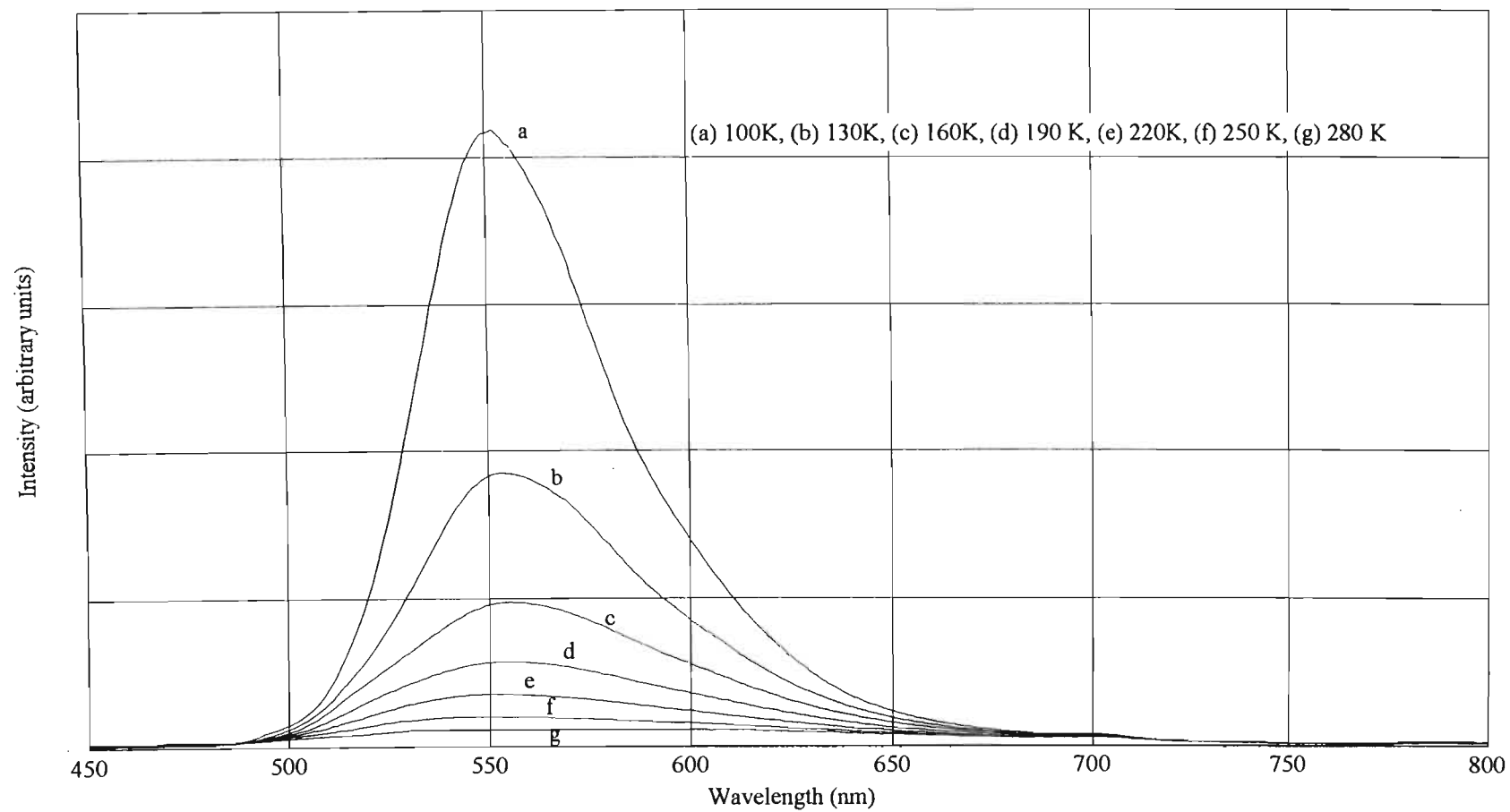
Figure 3.9   *The solid state emission spectrum of [Pt(terpy)Cl](SbF₆) recorded at 30 K intervals over the range 100 to 280 K.*
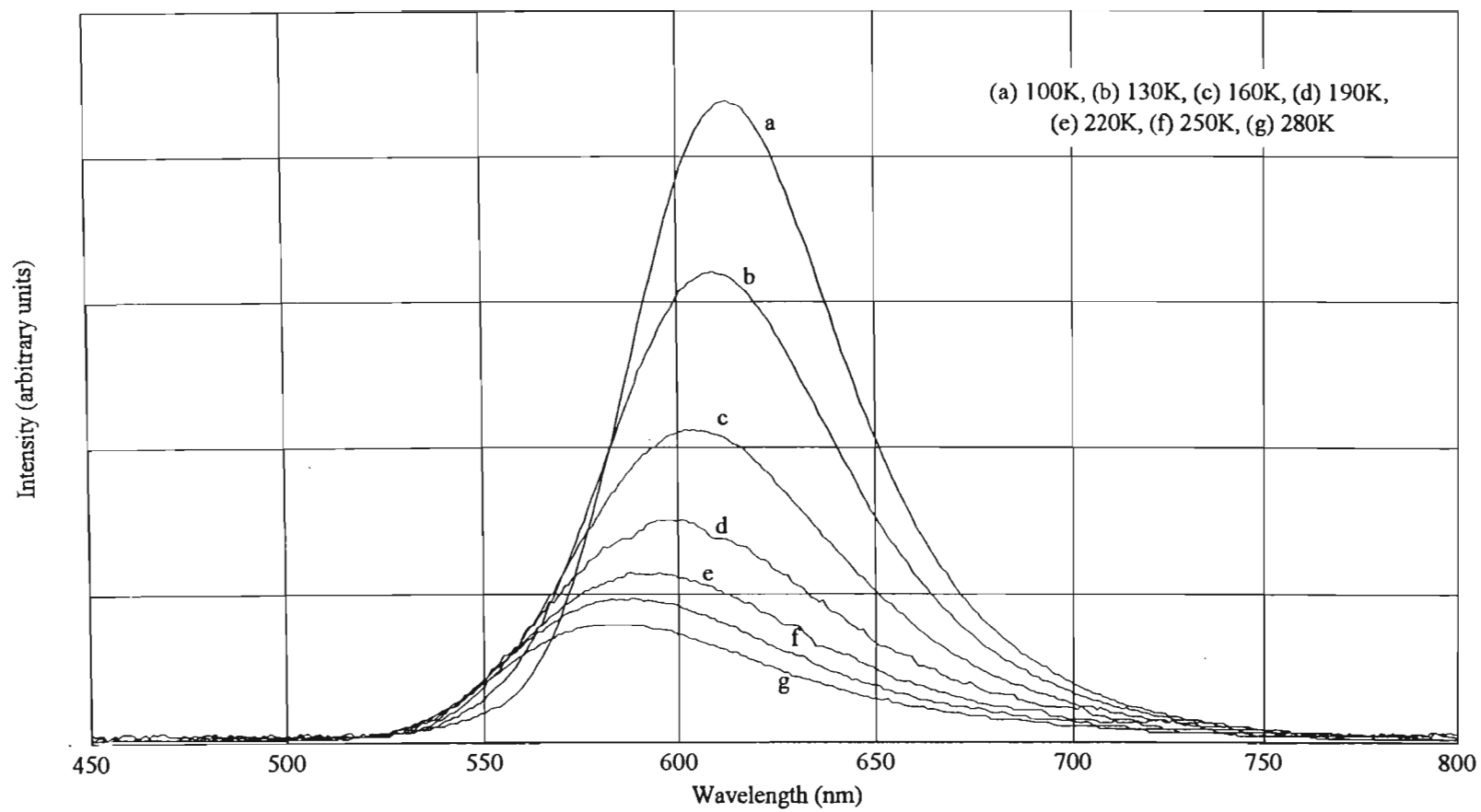
Figure 3.10   *The solid state emission spectrum of [Pt(terpy)Cl](CF₃SO₃) recorded at 30 K intervals over the range 100 to 280 K.*

(a) 100K, (b) 130K, (c) 160K, (d) 190K, (e) 220K, (f) 250 K, (g) 280 K
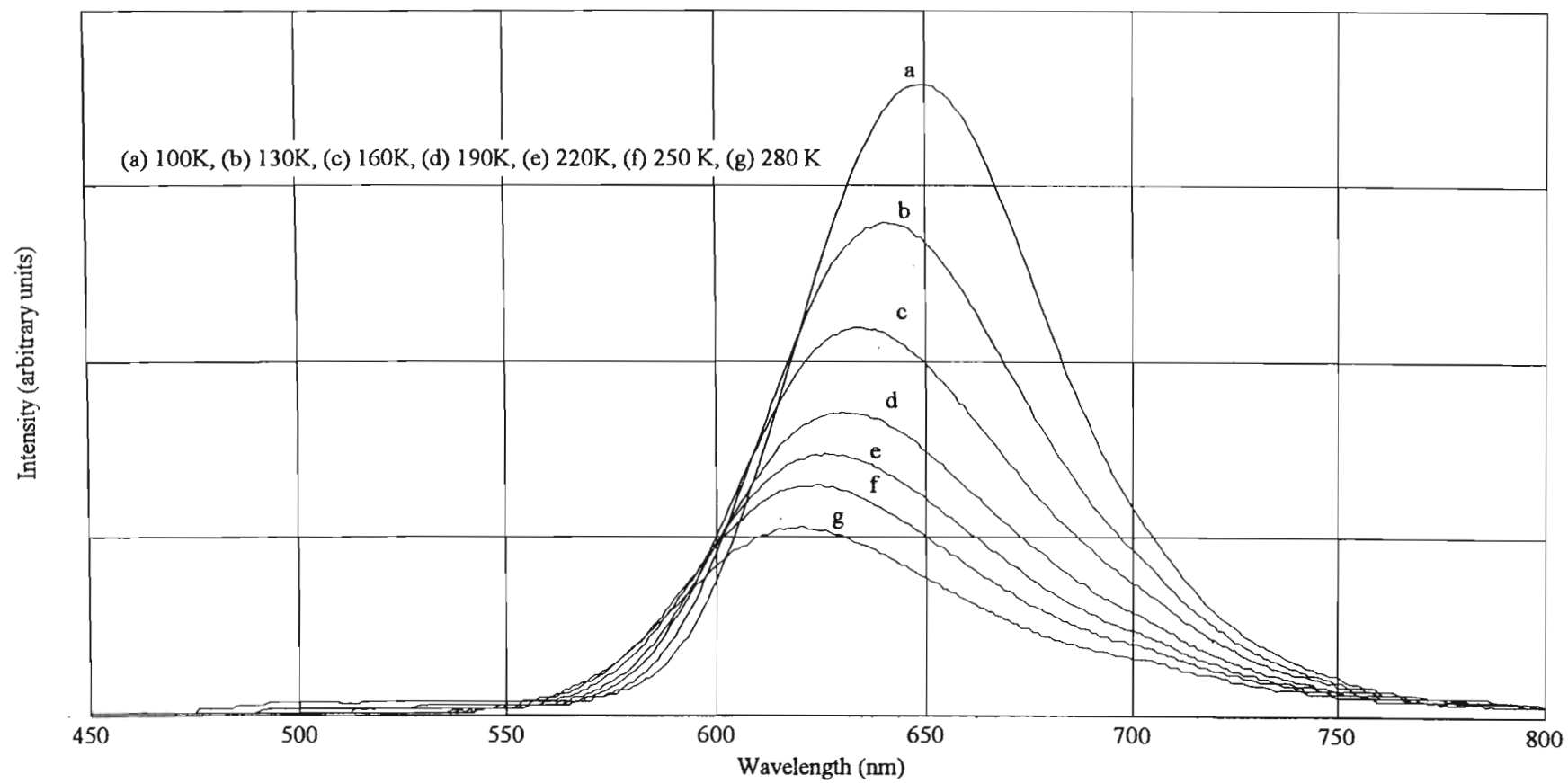
Figure 3.11   _The solid state emission spectrum of [Pt(terpy)Cl](BF₄) recorded at 30 K intervals over the range 100 to 280 K._

nm. Further decreases in the temperature of the sample result in progressive increases in the emission intensity. The peak remains quite broad however, and is devoid of any vibrational structure. Furthermore, the peak position does not vary as the temperature of the sample is decreased, $\lambda(em)_{max}$ remaining constant at 552 nm.

The solid state emission spectra of $[Pt(terpy)Cl](CF_3SO_3)$ (**10**) and $[Pt(terpy)Cl](BF_4)$ (**11**), also recorded at 30 K intervals over the temperature range 100 to 280 K are provided in Figures 3.10 and 3.11 respectively. In contrast to the weak, poorly resolved emission feature observed for the SbF_6^- salt at 280 K, the emission spectra of the $CF_3SO_3^-$ and BF_4^- salts at the same temperature, each exhibit a well-resolved asymmetric peak. The maximum emission intensities for these peaks occur at wavelengths $\lambda(em)_{max}$ equal to 585 nm for the $CF_3SO_3^-$ salt and at 618 nm for the BF_4^- salt.

Che and co-workers[263] have reported the emission spectra of solid samples of $[Pt(terpy)Cl](CF_3SO_3)$ (**10**), both at room temperature and at 77 K. The emission spectrum of $[Pt(terpy)Cl](CF_3SO_3)$ obtained in this study, differs from that in the above report, in that the maximum emission intensity was observed to occur at a wavelength *ca.* 15 nm lower than that reported by Che *et al.* Furthermore, the report by Che and co-workers makes mention of a poorly resolved shoulder on the low energy side of the aforementioned peak, whereas this feature was not observed in the present study. Both of these differences can most probably be attributed to differences in the instrumentation used in these two studies.

On decreasing the temperature of the $CF_3SO_3^-$ and BF_4^- salts, the band width narrows when compared to that in the correponding spectra recorded at 280 K. Furthermore, the emission intensities of both salts increases in an analogous way to that observed for the SbF_6^- salt. However, in contrast to the SbF_6^- salt where $\lambda(em)_{max}$ remained unchanged at 552 nm on cooling the sample, $\lambda(em)_{max}$ in the case of the $CF_3SO_3^-$ and BF_4^- salts is red-shifted as the temperature of the sample is decreased. At 100 K, $\lambda(em)_{max}$ of both salts (**10** and **11**) is red-shifted by *ca.* 30 nm with respect to the values observed at 280 K. A similar shift was observed by Che and co-workers on

comparing the solid state emission spectrum of the $CF_3SO_3^-$ salt, recorded at room temperature, with that recorded at 77 K.

A comparison of the emission spectra of the three salts **9**, **10** and **11**, recorded at 100 K, furthermore reveals that $\lambda(em)_{max}$ for the $CF_3SO_3^-$ salt is red-shifted by 61 nm, and that of the BF_4^- salt by 98 nm, with respect to the value of $\lambda(em)_{max}$ observed for the SbF_6^- salt. Table 3.5 lists the values of $\lambda(em)_{max}$ for each of the SbF_6^-, $CF_3SO_3^-$ and BF_4^- salts as observed at 100 and 280 K, along with the shifts observed between the different emission spectra.

Table 3.5 *The wavelengths, $\lambda(em)_{max}$, and shifts (quoted in nm) associated with the solid state emission spectra of the [Pt(terpy)Cl](X) (X = SbF$_6^-$, CF$_3$SO$_3^-$ and BF$_4^-$) salts.*

[Pt(terpy)Cl](X)	280K[a]	Shift[b]	100K[a]
X = SbF$_6^-$	ca. 552[d]	0	552
Shift[c]	33	-	61
X = CF$_3$SO$_3^-$	585	28	613
Shift[c]	33	-	37
X = BF$_4^-$	618	32	650

[a] Temperature at which spectrum was recorded.

[b] Shift in $\lambda(em)_{max}$ associated with change in temperature.

[c] Shift in $\lambda(em)_{max}$ associated with change in counterion.

[d] Broad peak with poorly defined maximum.

Che and co-workers assigned the emission observed from solid samples of [Pt(terpy)Cl](CF$_3$SO$_3$) (**10**) to the radiative decay of a ^{3}MLCT [Pt $\rightarrow$ terpy(π^*)] excited state and proposed the molecular orbital bonding scheme depicted in Figure 3.12.

In this scheme the Pt $5d_{z^2}$ orbitals of the monomeric chromophores interact to give rise to a sigma bonding (d_σ) and antibonding orbital ($d_{\sigma*}$). The terpy π and π^* orbitals similarly interact to give rise to a set of bonding and antibonding orbitals. Support for the proposed Pt-Pt and terpyridine interactions in $[Pt(terpy)Cl](CF_3SO_3)$ was obtained from a crystal structure determination which revealed that the $[Pt(terpy)Cl]^+$ chromophores occur in a head-to-tail stacked configuration with the intermolecular Pt-Pt separation being $3.329(1)$Å.
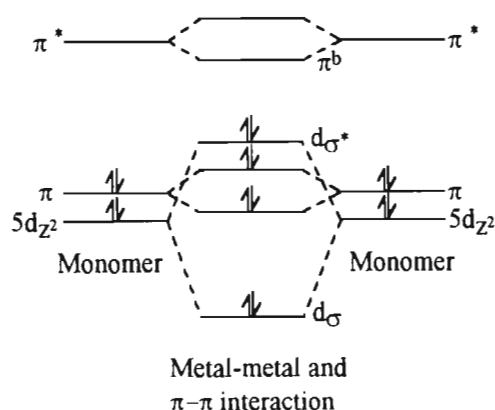
Figure 3.12   _Molecular orbital scheme as proposed by Che et al._[263] _for monomeric [Pt(terpy)Cl]$^+$ and for chromophores with Pt-Pt and π-π interaction._

With the above molecular orbital scheme in mind, Che and co-workers[263] specifically assigned the luminescence observed from solid samples of $[Pt(terpy)Cl](CF_3SO_3)$ (**10**) to a ($\pi^b \rightarrow d_{\sigma*}$) transition. Further confirmation of this assignment is provided by the red-shift in the position of the emission maximum, $\lambda(em)_{max}$, observed on decreasing the temperature of the sample. Such a red-shift is believed to be typically associated[258] with linear chain type compounds, since the decreasing temperature affects a lattice contraction, resulting in a decrease in the metal-metal separation. This in turn manifests itself in increased metal-metal interaction which further destabilizes the $d_{\sigma*}$ orbital, resulting in the observed red-shift. The red polymorph of $[Pt(bipy)Cl_2]$, which is known to posess a linear chain structure[294] (Pt-Pt separation of 3.45Å), has been reported to exhibit an analogous temperature dependent red-shift.[258]

Although the maximum emission intensity associated with [Pt(terpy)Cl](BF$_4$) (**11**) is lower in energy than that associated with the CF$_3$SO$_3^-$ salt discussed above, the band profiles of the emission spectra of the two salts are identical. Furthermore, the emission spectrum of the BF$_4^-$ salt also exhibits the temperature dependent red-shift described above. Based on the chemical similarity, as well as the closely corresponding luminescent behaviour of [Pt(terpy)Cl](BF$_4$) (**11**) and the CF$_3$SO$_3^-$ salt **10**, the emission observed from solid samples of **11** can thus be assigned to the radiative decay of a ^{3}MLCT excited state and more specifically, to a ($\pi^b \rightarrow d_{\sigma^*}$) transition.

A comparison of the variable temperature solid state emission spectra of the SbF$_6^-$ salt [Pt(terpy)Cl](SbF$_6$) (**9**) with that of the CF$_3$SO$_3^-$ and BF$_4^-$ salts, revealed that the band profiles of all three salts are essentially identical. This, together with the chemical similarity of the three salts, would suggest that the emission observed from solid samples of the SbF$_6^-$ salt also originates from a ($\pi^b \rightarrow d_{\sigma^*}$) transition. This assignment is also consistent with the molecular orbital scheme utilized by Che *et al.*[263] in assessing the emission of *e.g.* the CF$_3$SO$_3^-$ salt **10**. Following the logic of this molecular orbital scheme, emission from the [Pt(terpy)Cl]$^+$ chromophore would be expected to either originate from a ($\pi^b \rightarrow d_{\sigma^*}$) transition, in cases where there are interactions between the chromophores, or else from a ($\pi^* \rightarrow \pi$) transition in instances where the chromophores exist in their monomeric state, *i.e.* there are no interactions between the chromophores. Emission originating from a ($\pi^b \rightarrow d_{\sigma^*}$) transition, as was observed from solid samples of [Pt(terpy)Cl](CF$_3$SO$_3$) and [Pt(terpy)Cl](BF$_4$), results in a band profile which is devoid of any well-resolved vibrational structure. This is in contrast to the vibrationally structured band profile expected to result from a ($\pi^* \rightarrow \pi$) transition, which according to the molecular orbital scheme of Che *et al.*,[263] would be associated with the [Pt(terpy)Cl]$^+$ chromophore in its monomeric state.

This line of reasoning can be further assessed by following an approach established by Miskowski and Houlding,[253] which involves recording the emission spectrum of the chromophore in a dilute low-temperature glassy solution and comparing it with the solid state emission spectrum of the chromophore at the same temperature. Both matrices are rigid. However, dilute glassy solutions are believed to contain the chromophore in its monomeric state and thus, a comparison of the glassy solution and

solid state emission spectra, was suggested to allow for the evaluation of the influence of solid state interactions on the electronic structure of the chromophore. Using this approach, Miskowski and Houlding[253] compared the emission spectrum of $[Pt(phen)_2]^{2+}$ in dilute glassy solution at 77 K with that of microcrystalline $[Pt(phen)_2]Cl_2.3H_2O$ at the same temperature. The former possesses distinct vibronic structure, whereas the latter approximates to being of Guassian shape, is devoid of any resolved structure and is significantly red-shifted relative to the emission from the glassy solution. Based on these observations, and the crystal structure of $[Pt(phen)_2]Cl_2.3H_2O$, Miskowski and Houlding[253] suggested that the solid state emission of this salt is due to classical eximeric interaction between the phenanthroline ligands of neighbouring $[Pt(phen)_2]^{2+}$ chromophores.

In accordance with this approach, the emission spectra of butyronitrile glasses containing varying concentrations of $[Pt(terpy)Cl](SbF_6)$ (**9**) at 77 K, were recorded. Figure 3.13 depicts the emission spectra corresponding to concentrations of 6.6×10^{-5} and 3.3×10^{-4} M. The spectra at both concentrations are blue-shifted with respect to that of the solid state emission spectrum recorded at the same temperature and is highly structured.

The emission spectrum corresponding to the 6.6×10^{-5} M glass is identical to that reported by Che and co-workers[263] for $[Pt(terpy)Cl](CF_3SO_3)$ (**10**) in a butyronitrile glass at 77 K, and by Gray and co-workers[291] for a 10:10:1 $CH_3OH:CH_3CH_2OH:DMF$ glass containing the $\{[Pt(terpy)]_2(\mu\text{-pyrazole})\}^{3+}$ chromophore. Whereas Gray and co-workers favoured a $^3(\pi - \pi^*)$ excited state as the emitting state in the $\{[Pt(terpy)]_2(\mu\text{-pyrazole})\}^{3+}$ chromophore under the conditions mentioned above, the assignment made by Che et al. is not quite clear. In accordance with the assignment made by Gray et al., the emission observed here from the 6.6×10^{-5}M butyronitrile glass of $[Pt(terpy)Cl](SbF_6)$ at 77 K, is also assigned to the radiative decay of a $^3(\pi - \pi^*)$ excited state.

The high energy side of the band profile of the emission spectrum corresponding to the 3.3×10^{-4} M glass of $[Pt(terpy)Cl](SbF_6)$, is identical to that of the 6.6×10^{-5} M glass and is accordingly assigned to originate from a $^3(\pi - \pi^*)$ excited state. However, the emission spectrum of the 3.3×10^{-4} M glass also contains a relatively broad feature
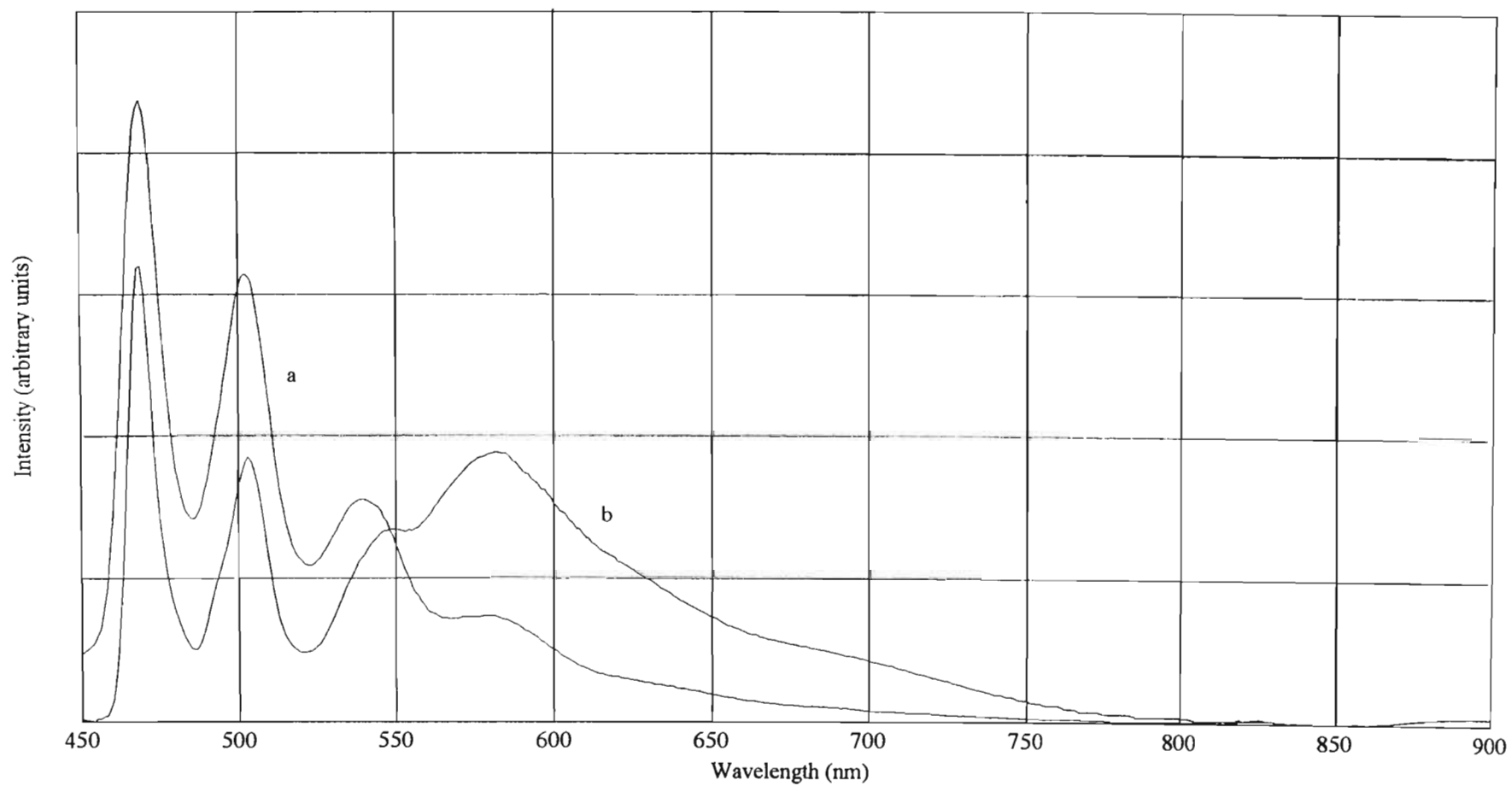
Figure 3.13 *The emission spectra of low-temperature butyronitrile glasses of $[Pt(terpy)Cl](SbF_6)$ [(a) $6.6 \times 10^{-5}M$, (b) 3.3×10^{-4} M].*

centred at *ca.* 590 nm and a shoulder at *ca.* 552 nm. The position of the latter coincides with the wavelength associated with the maximum emission intensity in the solid state emission spectrum of the yellow polymorph of [Pt(terpy)Cl](SbF$_6$). The shoulder at *ca.* 552 nm could thus arise as a result of emission from small amounts of solid of the yellow modification of [Pt(terpy)Cl](SbF$_6$) caused by the aggregation of small numbers of cations and anions at the higher concentration under consideration. The profile of the broad feature and its peak position [$\lambda(em)_{max}$ = 590 nm] correspond closely with that of the solid state emission spectrum of the CF$_3$SO$_3^-$ salt **10** at low temperatures. Thus, this feature can most probably be assigned to a ($\pi^b \rightarrow d_{\sigma*}$) transition associated with small aggregates of the orange modification of [Pt(terpy)Cl](SbF$_6$) which results from the higher concentration utilized here. Recall that [Pt(terpy)Cl](SbF$_6$), when first precipitated from CH$_3$CN solutions, exists as the orange polymorph (see Section 3.4.3.2).

Summarizing the above, the emission observed from solid state samples of the yellow polymorph of [Pt(terpy)Cl](SbF$_6$) can be assigned to a ($\pi^b \rightarrow d_{\sigma*}$) transition, whereas that from dilute butyronitrile glasses at low temperatures would be attributed to the radiative decay of a $^3(\pi - \pi^*)$ excited state. These assignments were made utilizing the documented approach of Miskowski and Houlding[253] for assessing the influence of solid state interactions on the electronic structure of a specific chromophore and are consistent with the molecular orbital bonding scheme utilized by Che *et al.*[263] in studying the luminescent behaviour of [Pt(terpy)Cl](CF$_3$SO$_3$). However, from the above assignment it is not evident why the solid state emission spectrum of [Pt(terpy)Cl](SbF$_6$) (**9**) does not display a red-shift of the emission maximum on decreasing the temperature of the sample, whereas both the CF$_3$SO$_3^-$ (**10**) and the BF$_4^-$ (**11**) salts do. This is of even greater relevance if it is borne in mind that in the preceding discussion, the solid state emission of all three salts were assigned to originate from ($\pi^b \rightarrow d_{\sigma*}$) transitions. Two explanations are possible.

The first explanation is that the extent of interactions between the [Pt(terpy)Cl]$^+$ chromophores in the yellow polymorph of [Pt(terpy)Cl](SbF$_6$) (**9**) is minimal and that the crystal structure of this salt is such that whereas decreasing the temperature of the salt might result in a lattice contraction, such a contraction does not translate into an

increased extent of interaction between the $[Pt(terpy)Cl]^+$ chromophores. Consequently, no red-shift of the emission maximum would be expected on decreasing the temperature of the salt. The yellow colour of the SbF_6^- salt, when compared to the orange and orange-red colours of the $CF_3SO_3^-$ and BF_4^- salts, certainly supports the suggestion of minimal interactions between the chromophores in the yellow polymorph of $[Pt(terpy)Cl](SbF_6)$. However, without knowing the exact structure of this polymorph, this explanation is merely speculative.

The second explanation involves the $[Pt(terpy)Cl]^+$ chromophores in the yellow polymorph of $[Pt(terpy)Cl](SbF_6)$ (**9**) existing in a monomeric environment, *i.e.* there are no orbital interactions between the chromophores in the solid state. Like the first explanation provided above, this suggestion is also consistent with the colour differences observed for solid samples of the three $[Pt(terpy)Cl]^+$ salts considered here. However, as in the case of the first explanation, exact knowledge of the crystal structure of the salt is required to elevate this explanation above the level of being purely speculative. Suggesting that there are no orbital interactions between the $[Pt(terpy)Cl]^+$ chromophores in the yellow modification of $[Pt(terpy)Cl](SbF_6)$ (**9**), implies that the emission observed from solid samples of this salt cannot be assigned to originate from a $(\pi^b \rightarrow d_{\sigma^*})$ transition and that an alternative assignment has to be made.

The energy and band profile of the emission spectrum of solid samples of the yellow modification of $[Pt(terpy)Cl](SbF_6)$ are clearly distinct from that observed for the low-temperature glass spectra discussed above. The possibility of a $^3(\pi - \pi^*)$ excited state as the emitting state can thus be ruled out. The band profile is more consistent with emission from either a charge transfer, ligand field or excimer excited state. Of these, excimeric emission can also be ruled out, since this line of reasoning deals specifically with the $[Pt(terpy)Cl]^+$ chromophores existing in a monomeric environment. Emission from interligand charge transfer states on the other hand are extremely rare and can probably also be discounted. This leaves a ^3MLCT or triplet ligand field (^3LF) excited state as the emitting state. As discussed in Section 3.3.2.2, the band profile associated with ^3LF emission is typically Guassian in shape. This is clearly different from the asymmetric shape of the band profile associated with the emission from solid state

samples of the yellow polymorph of [Pt(terpy)Cl](SbF$_6$). Based on these considerations and the supposition that the [Pt(terpy)Cl]$^+$ chromophores exist in a monomeric environment in the yellow modification of the SbF$_6^-$ salt, the emission from solid samples of this salt can be assigned to originate from the radiative decay of a ^{3}MLCT excited state. The difference in the emission from solid state samples of this salt and that from dilute glasses would then not stem from electronic interactions between the chromophores modifying their electronic configuration, since both are suggested to contain the chromophores in a monomeric environment, but rather from the different media influencing the relative energies of the emitting states. Such behaviour is not unprecedented. McMillin and co-workers[260] reported that the [Pt(terpy)(OH)]$^+$, [Pt(terpy)(OCH$_3$)]$^+$ and [Pt(terpy)(NCS)]$^+$ chromophores all exhibited ^{3}MLCT emission in e.g. CH$_3$CN solution, whereas the complexes generally displayed $^3(\pi$ -$\pi^*)$ emission from the coordinated terpyridine ligand in low-temperature alcohol glasses. In both these matrices the chromophores would have existed in their monomeric state. This behaviour is also exhibited by the [Pt(terpy)(CH$_3$CN)]$^{2+}$ chromophore where ^{3}MLCT emission was observed from the chromophore in fluid CH$_3$CN solution at room temperature, but both ^{3}MLCT and $^3(\pi-\pi^*)$ emission was observed from a dilute low-temperature butyronitrile glass (see Section 3.4.2.3).

In the light of these suggestions it is necessary to reconsider the molecular orbital scheme utilized by Che and co-workers[263]. As described above, Che et al. suggested the π orbital of the coordinated terpyridine ligand to be higher in energy than the 5d$_{z^2}$ orbital of the platinum atom, resulting in a $^3(\pi$ - $\pi^*)$ state being the lowest energy excited state associated with the monomeric [Pt(terpy)Cl]$^+$ chromophore. However, if one accepts the line of reasoning suggested in the preceding discussion, it follows that the Pt 5d$_{z^2}$ and terpyridine π orbital have to be very similar in energy, with the electronic transition of lowest energy being determined by the nature of the medium surrounding the monomeric chromophore. The ordering of the energy levels associated with chromophores exhibiting metal-metal and ligand-ligand interactions is not affected by this line of reasoning, a ($\pi^b \rightarrow d_{\sigma^*}$) transition still being the lowest energy transition associated with interacting [Pt(terpy)Cl]$^+$ chromophores as found in the CF$_3$SO$_3^-$ and BF$_4^-$ salts.

In an attempt to gain further insight into the influence the steric demands of the counterions could have on lattice architecture and thus on the interactions between, and the electronic configuration of the constituent chromophores, it was decided to study the structural and photoluminescent properties of salts containing the $[Pt(bipy)_2]^{2+}$ chromophore in combination with various counterions.

3.4.4 $[Pt(bipy)_2](X)_2$ [X⁻ = SbF$_6^-$ (12) and CF$_3$SO$_3^-$ (13)]

3.4.4.1 Synthesis and characterization of $[Pt(bipy)_2](SbF_6)_2$

Salts of the $[Pt(bipy)_2]^{2+}$ chromophore were first synthesized by Morgan and Burnstall[295]. Their method has since been modified by Bielli and co-workers[296] who synthesized $[Pt(bipy)_2](ClO_4)_2$ by treating $[Pt(bipy)Cl_2]$ with 2,2'-bipyridine and sodium perchlorate.

The synthesis for $[Pt(bipy)_2](SbF_6)_2$ reported here, differs from that of Bielli and co-workers and employs the same type of methodology as that employed in the synthesis of the $[Pt(terpy)Cl]^+$ salts. The synthesis involves treating $[Pt(C_6H_5CN)_2Cl_2]$ suspended in boiling CH_3CN with a twice molar amount of $AgSbF_6$. Following the removal of the precipitated AgCl, a twice molar amount of 2,2'-bipyridine was added to the reaction mixture which was then heated further under reflux. Any additional precipitated AgCl was removed by filtration before reducing the volume of the reaction mixture *in vacuo* to afford a lemon yellow crystalline product. The material thus obtained was isolated, washed with CH_3CN and diethyl ether and dried *in vacuo*. Elemental analysis for C, H, and N is consistent with the empirical formulation $[Pt(bipy)_2](SbF_6)_2$. In contrast to $[Pt(terpy)Cl](SbF_6)_2$ (**9**), no evidence of polymorphism was observed for $[Pt(bipy)_2](SbF_6)_2$.

It is also interesting to note the outcome of this reaction in contrast to the attempts at synthesizing the $[Pt(terpy)(CH_3CN)]^{2+}$ chromophore from $[Pt(C_6H_5CN)_2Cl_2]$. Recall that in the latter case, the reaction afforded the $[Pt(terpy)Cl]^+$ chromophore, thus suggesting that the intermediate involved has at least one Cl⁻ ligand coordinated to the platinum centre and that the coordinating properties of the acetonitrile ligand is such that it does not readily displace the coordinated Cl⁻ ligand. The bipyridine ligand in

contrast, seems to readily displace the Cl ligand, this displacement most probably being aided by the chelating nature of the bipyridine ligand.

In subsequent studies, the analogous $CF_3SO_3^-$ salt, $[Pt(bipy)_2](CF_3SO_3)_2$ (**13**), has also been prepared in our laboratories[297]. The synthetic procedure employed is identical to that described for $[Pt(bipy)_2](SbF_6)_2$. However, the product obtained has a golden orange colour compared to the lemon yellow colour observed for the SbF_6^- salt.

The solid state infrared spectrum of $[Pt(bipy)_2](SbF_6)_2$, recorded as a KBr pellet, exhibits a number of peaks in the range 1650 to 770 cm^{-1} which are attributed to the coordinated 2,2'-bipyridine ligands (see Table 3.1). A similar peak pattern was observed for the $CF_3SO_3^-$ salt[297]. The solid state spectrum of $[Pt(bipy)_2](SbF_6)_2$ also exhibits the customary peak at *ca.* 655 nm associated with the SbF_6^- counterion.

3.4.4.2 Structural Studies on $[Pt(bipy)_2](SbF_6)_2$ (12)

Single light yellow cube-shaped crystals of **12** were grown by slow cooling of concentrated CH_3CN solutions of the salt.

$[Pt(bipy)_2](SbF_6)_2$ crystallizes in the triclinic space group $P\bar{1}$. The asymmetric unit consists of one half of the $[Pt(bipy)_2]^{2+}$ cation and one SbF_6^- anion, implying that there is one formula unit per unit cell. The unit cell dimensions, a full list of interatomic distances and angles and other crystallographic data are collected in Tables 3.12 to 3.16 at the end of this chapter.

A diagram depicting the molecular geometry of the cation and the numbering scheme employed, is provided in Figure 3.14. The cation is situated in a special position, the Pt atom being coincident with a crystallographic centre of inversion. As a consequence, symmetry requires that the Pt atom and the four coordinated N atoms are strictly co-planar. This is analogous to the geometry reported for the $[Pt(bipy)_2]^{2+}$ cation in $[Pt(bipy)_2](TCNQ)_3$ which also crystallizes in the space group $P\bar{1}$ with the Pt atom situated on a crystallographic centre of inversion[298]. However, it contrasts with the geometry reported for the cation in $[Pt(bipy)_2](NO_3)_2.2H_2O$, where the Pt coordination sphere exhibits a tetrahedral distortion resulting in the planes constituted by the Pt and the two N atoms of each bipyridine ligand defining a dihedral angle of 24.0(3)° with
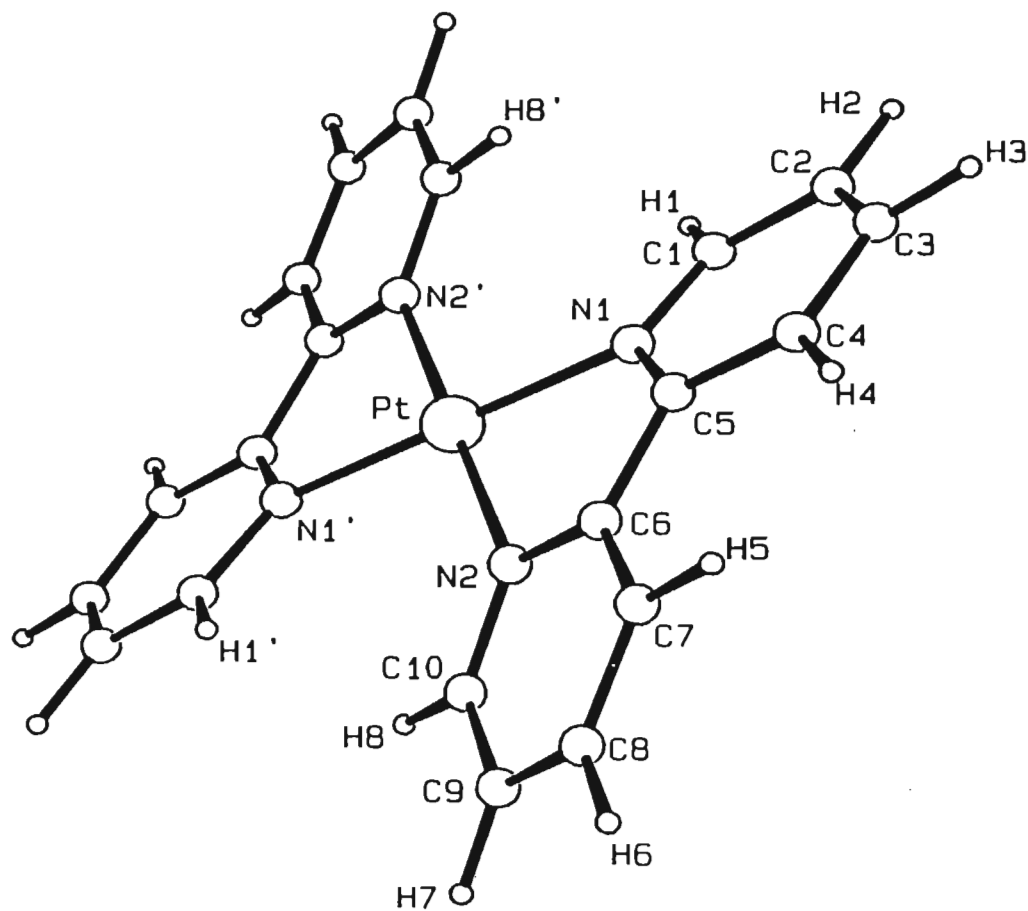
Figure 3.14   *The molecular geometry and numbering scheme employed for the cation in [Pt(bipy)$_2$](SbF$_6$)$_2$.*

respect to each other[299]. This distortion is believed to occur in order to minimize the non-bonded repulsions between the hydrogen atoms in the 6 and 6' positions on one ligand and the analogous atoms on the other. Hazell and co-workers refer to this distortion as a "twist" in contrast to a "bow" or a "tilt" distortion[299], *vide infra*. The Pt-N distances in $[Pt(bipy)_2](SbF_6)_2$ equal 2.023(3)Å and 2.025(3)Å with an average of 2.024Å. This is in good agreement with the distances of 2.02(2)Å and 2.01(2)Å reported for $[Pt(bipy)_2](TCNQ)_3$ and 2.025(4)Å and 2.028(5)Å in $[Pt(bipy)_2](NO_3)_2.2H_2O$. The N(1)-Pt-N(2) angle in $[Pt(bipy)_2](SbF_6)_2$ equals 78.7(1)° which is substantially smaller than the idealized value of 90° expected for square planar geometry. This deviation is the result of the chelating effect of the bipyridine ligand. Similar deviations from idealized geometry have been reported for the $[Pt(bipy)_2]^{2+}$ cation in $[Pt(bipy)_2](TCNQ)_3$ [N-Pt-N angle equals 77(1)°][298] and $[Pt(bipy)_2](NO_3)_2.2H_2O$ [N-Pt-N angles equal 80.1(2) and 80.0(2)°][299].

Despite the strictly planar configuration of the Pt centre and the four coordinated N atoms, the $[Pt(bipy)_2]^{2+}$ cation is decidedly non-planar. This stems from distortions which in terms of Hazell's terminology[299] can be referred to as "bow" and "tilt" distortions (see Figure 3.15).

(a)   (b)   (c)
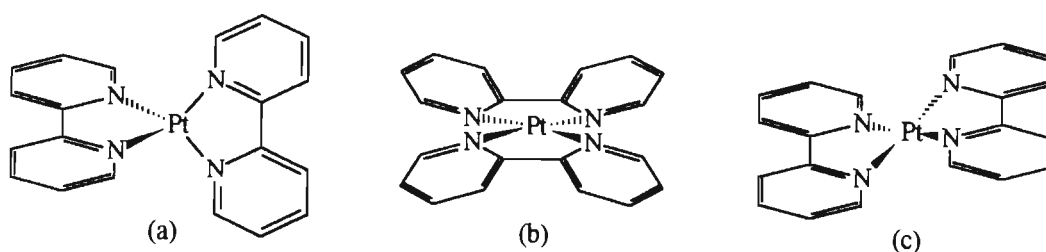
Figure 3.15   *Distortions resulting in the non-planarity of the $[Pt(bipy)_2]^{2+}$ cation[299]:*

(a) Twist

(b) Bow

(c) Tilt

The bow distortion in $[Pt(bipy)_2](SbF_6)_2$ results in the constituent pyridine rings of the bipyridyl ligands defining a dihedral angle of 22.7(3)° with respect to each other.

Similar distortions have been observed in [Pt(bipy)$_2$](TCNQ)$_3$ (dihedral angle = 21°)[298], [Pt(bipy)$_2$](TCNQ)$_2$ (dihedral angle = 22.7°)[300] and the complex palladium salt, [Pd(bipy)$_2$](pic)$_2$ (dihedral angle = 21.3°, pic = picrate)[301]. Based on the stacked structures of [Pt(bipy)$_2$](TCNQ)$_2$ and [Pd(bipy)$_2$](pic)$_2$, in which bipyridyl-TCNQ or bipyridyl-picrate stacking interactions are observed, Okawa and co-workers suggested that the bow-distortion of the bipyridyl ligands occurs as a result of these interactions[301]. However, this suggestion is contradicted by the fact that bow-distortions are also observed in [Pt(bipy)$_2$](TCNQ)$_3$[299] and in the hexafluoroantimonate salt discussed here. In both [Pt(bipy)$_2$](TCNQ)$_3$ and [Pt(bipy)$_2$](SbF$_6$)$_2$, *vide infra*, the [Pt(bipy)$_2$]$^{2+}$ cations exist as isolated entities with no stacking interactions between the cations and anions. As an alternative to Okawa's suggestion, it is thus proposed that the bow distortions of the bipyridyl ligands in [Pt(bipy)$_2$]$^{2+}$ and its palladium analogue should rather be attributed to a minimization of the non-bonded interligand repulsions of the hydrogen atoms in the 6 and 6' positions on the bipyridyl fragment (H1' and H8, and H1 and H8' with reference to Figure 3.14).

In addition to the bow distortion, the bipyridyl ligands in [Pt(bipy)$_2$](SbF$_6$)$_2$ are tilted [see Figure 3.15(c)] by a rotation of 20.0(4)° about their N-N vectors out of the PtN$_4$ plane. A similar distortion has been reported to occur in the [Ru(phen)$_2$(py)$_2$]$^{2+}$ cation, the "tilting angle" being 15.6(2)° [302]. As in the case of the bow distortion, the tilting of the bipyridyl ligands from the PtN$_4$ plane most probably occurs as a consequence of the minimization of the interligand non-bonded repulsions between the α-hydrogens.

Whereas both the above distortions are believed to arise as a result of interligand H-H repulsions, intraligand repulsions (between H4 and H5 in Figure 3.14) are believed to result in an in-plane bending of the bipyridyl ligand effecting a decrease in the angles N1-C5-C6 [114.6(3)°] and N2-C6-C5 [113.8(3)°] from the idealized value of 120°. This decrease in the N-C-C angles is accompanied by an increase in the angles C4-C5-C6 [122.9(3)°] and C5-C6-C7 [123.7(3)°]. Analogous distortions have been reported to occur in [Pt(bipy)$_2$](TCNQ)$_3$ [N-C-C angles equal 111(2) and 114(2)° and C-C-C angles equal 123(2) and 128(2)°][298] and [Pt(bipy)$_2$](NO$_3$)$_2$.2H$_2$O [N-C-C angles equal 114.0(2) and 114.6(3)° and C-C-C angles equal 123.3(3) and 124.2(3)°][299].
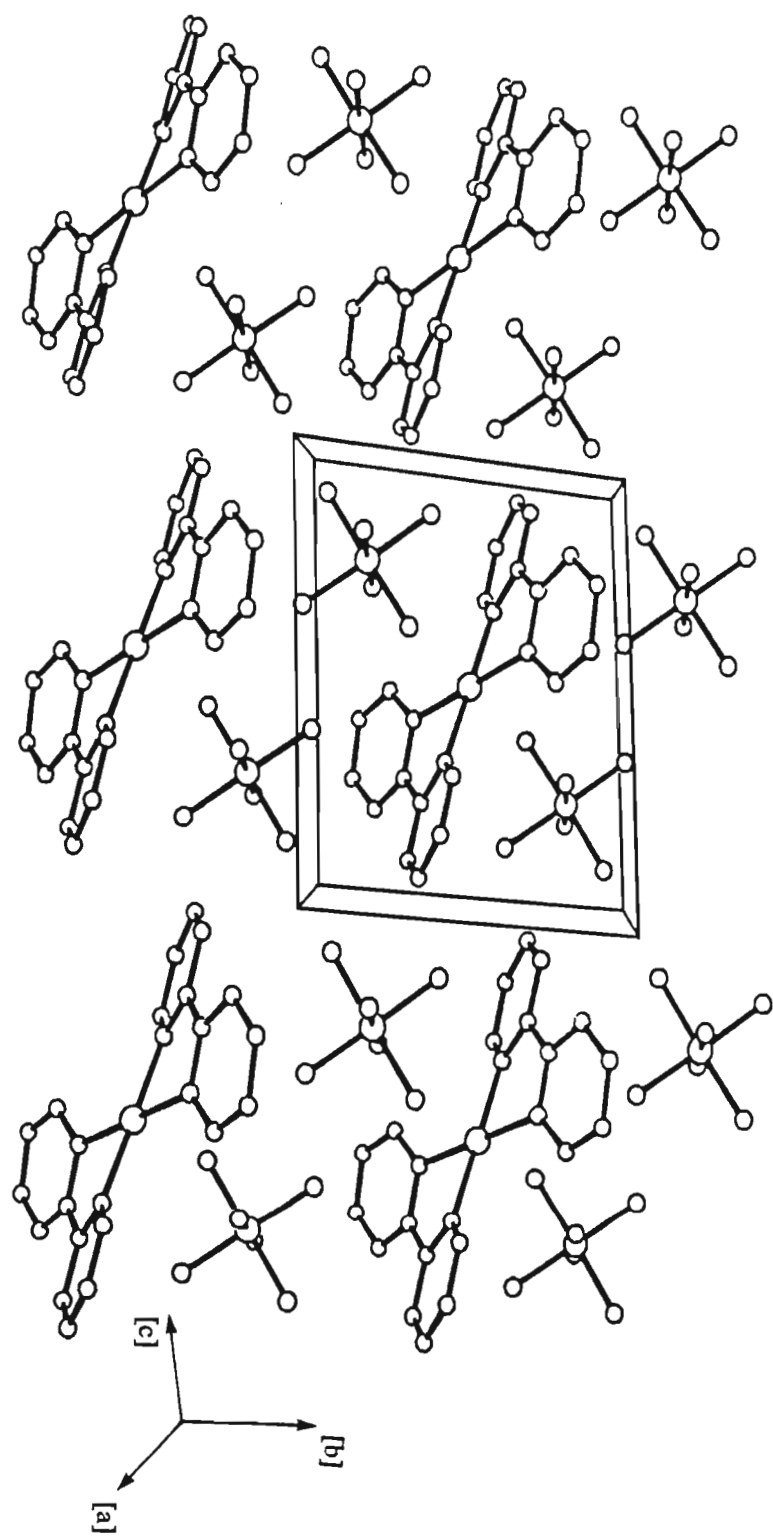
Figure 3.16   _The packing architecture of the [Pt(bipy)$_2$](SbF$_6$)$_2$ salt._

239
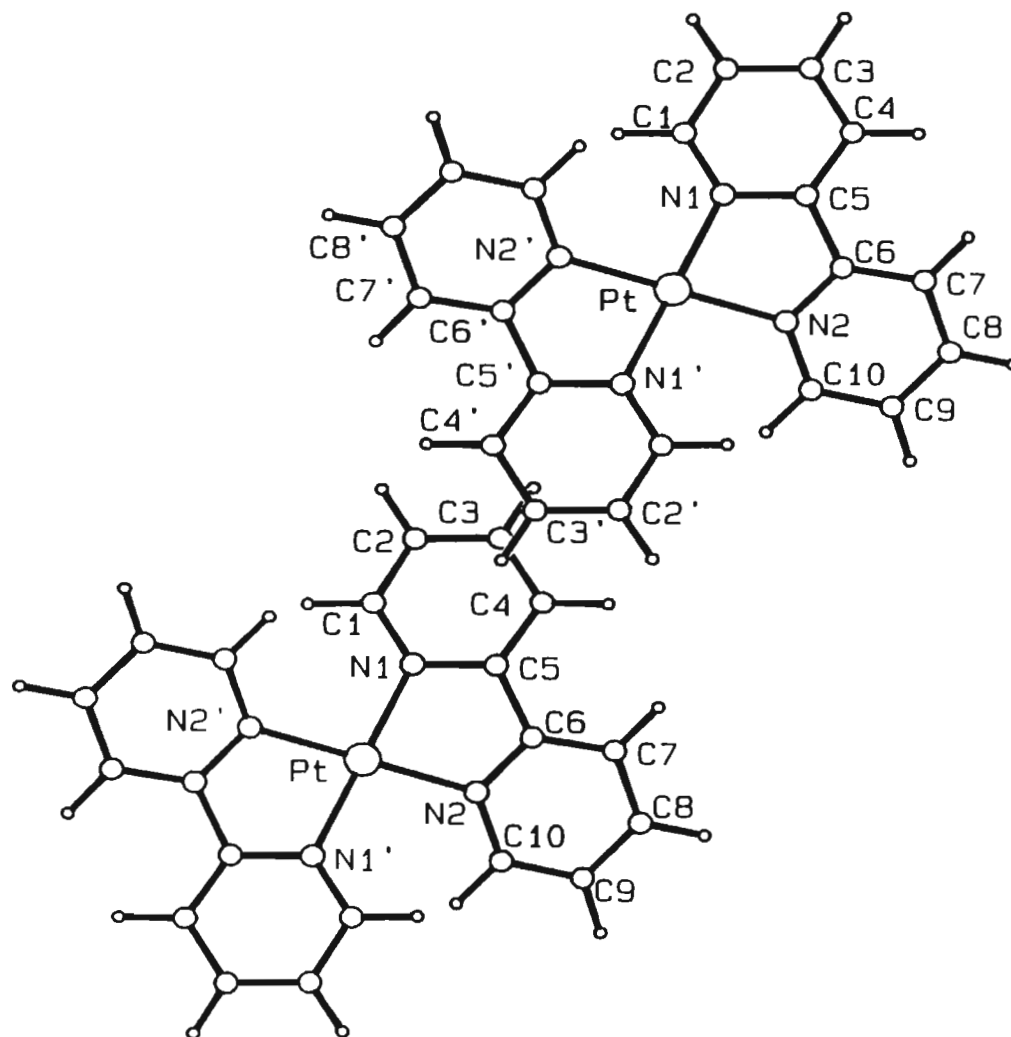
Figure 3.17 *Lateral offset of the [Pt(bipy)$_2$]$^{2+}$ cations in [Pt(bipy)$_2$](SbF$_6$)$_2$ (as seen in a view perpendicular to the planes of the closest neighbouring bipyridine ligands).*

A diagram depicting the packing architecture in $[Pt(bipy)_2](SbF_6)_2$ is provided in Figure 3.16. From this figure it is clear that the $[Pt(bipy)_2]^{2+}$ cations and SbF_6^- anions are arranged in rows which extend along the [a]-axis, the individual cations and anions within these rows being interrelated by unit cell translations along the [a]-axis. However, as reported for the packing architecture of $[Pt(terpy)(CH_3CN)](SbF_6)_2$ (**9**) (see Section 3.4.2.2), the cations occur in a side-by-side arrangement within these rows, thus precluding the possibility of π-π interactions between the bipyridyl ligands of neighbouring $[Pt(bipy)_2]^{2+}$ cations within these rows. Each of the cation rows is surrounded and effectively encapsulated by six neighbouring anion rows, thus limiting the possibility of any π-π interaction between cations from neighbouring rows. The shortest inter-cation C-C separation is associated with neighbouring cations which are interrelated by both a unit cell translation along the [c]-axis and a crystallographic centre of inversion situated at (0.5, 0.5, 0.0). As a result of this relation between the cations along the [c]-axis, the planes of the pyridine rings defined by N1 and C1 to C5 of these cations necessarily are parallel to each other. The shortest C-C distance within this arrangement equals 3.363Å and occurs between C3 and the analogous C3 atom of the symmetry related pyridine ring of the neighbouring cation. Although this distance is smaller than 3.45Å, the Van der Waal's spacing for π-aromatic species occurring in a face-to-face arrangement[242], the possibility of any π-π interaction between the symmetry related pyridine rings can be discounted since, as seen in Figure 3.17, the rings exhibit a substantial lateral offset, resulting in all the other C-C and C-N separations between the rings, exceeding 3.50Å. As such, the $[Pt(bipy)_2]^{2+}$ cations in $[Pt(bipy)_2](SbF_6)_2$ can thus be regarded as existing as isolated monomeric units.

The crystal structure of $[Pt(bipy)_2](CF_3SO_3)_2$ has also been determined in our laboratories[297]. In exact analogy to the hexafluoroantimonate salt, $[Pt(bipy)_2](CF_3SO_3)_2$ was found to crystallize in the space group $P\bar{1}$ with the Pt atom situated on a crystallographic centre of inversion. This implies that, as in the case of $[Pt(bipy)_2](SbF_6)_2$, the Pt atom and the four coordinated N atoms are strictly co-planar. The Pt-N distances average 2.024Å, with the N(1)-Pt-N(2) angle being equal to 78.9(2)°. The analogous dimensions for $[Pt(bipy)_2](SbF_6)_2$ are 2.024 Å and 78.7(1)°. The similarities between the $[Pt(bipy)_2]^{2+}$ cations in the triflate and
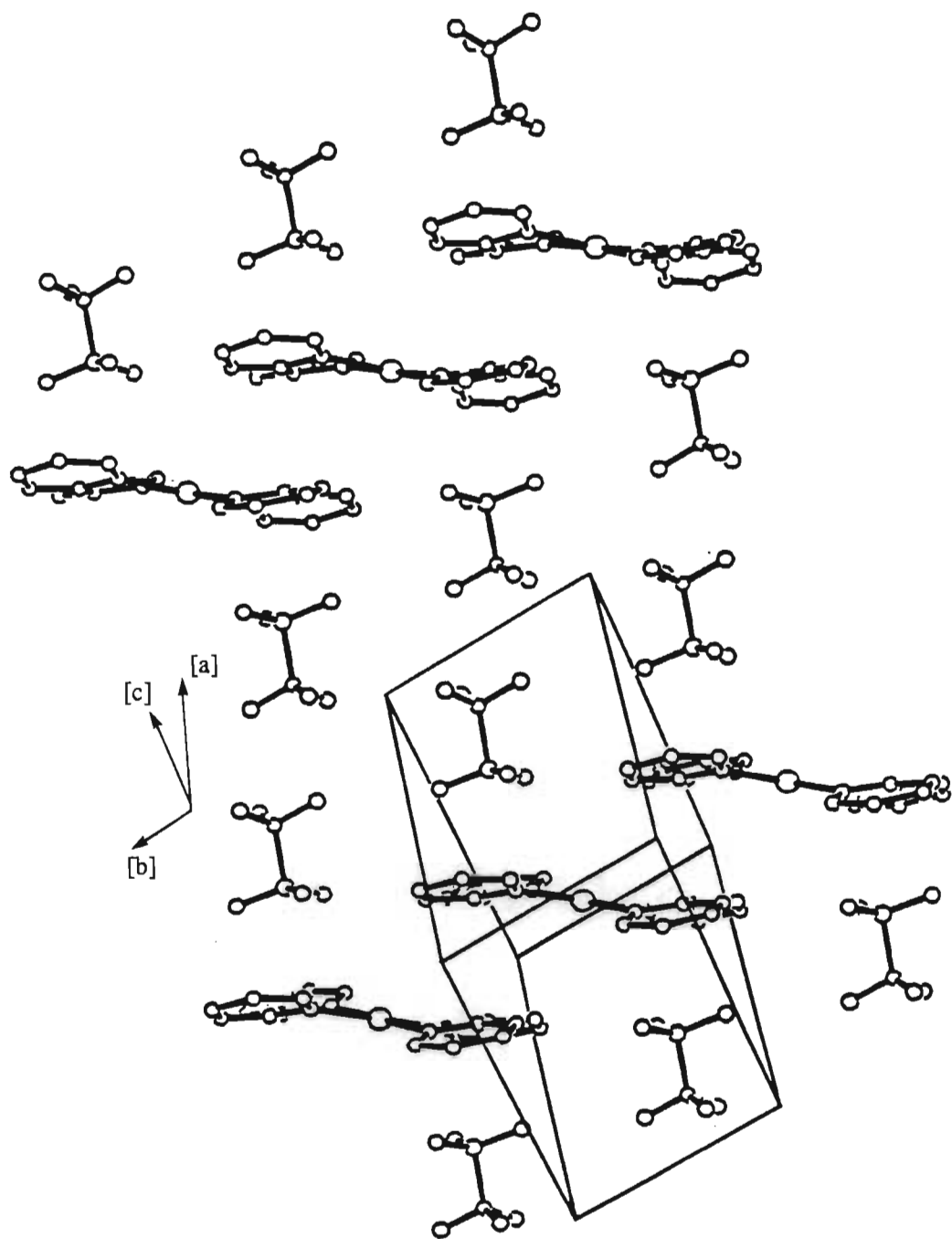
Figure 3.18 _The packing architecture of the [Pt(bipy)₂](CF₃SO₃)₂ salt._
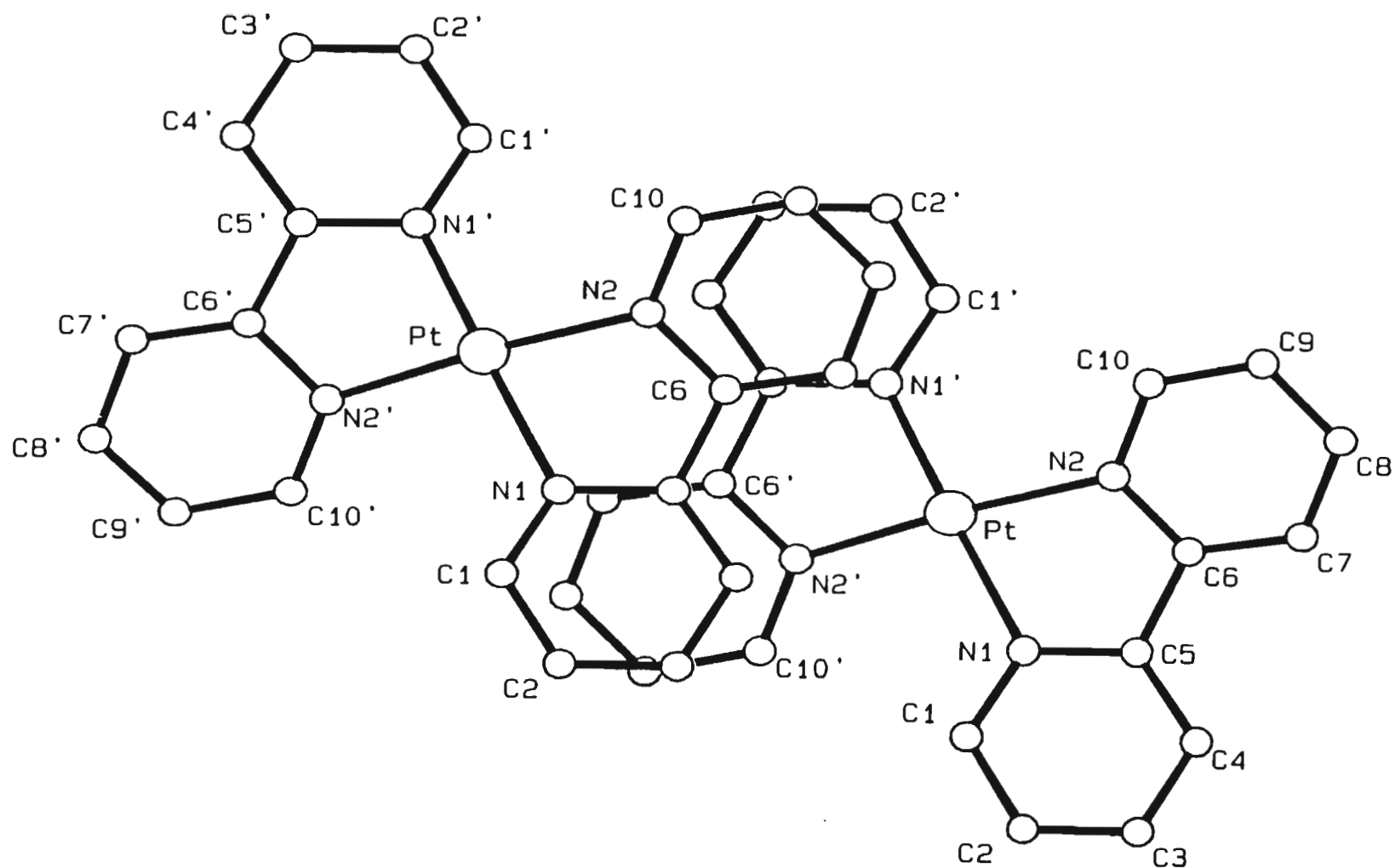
Figure 3.19 *Ligand-ligand overlap between neighbouring [Pt(bipy)₂]²⁺ cations in [Pt(bipy)₂](CF₃SO₃)₂ (as seen in a view perpendicular to the planes of the overlapping bipyridine ligands).*

hexafluoroantimonate salts furthermore include that the cation in the former also exhibits bow distortions of the bipyridyl ligands, the dihedral angle between the constituent pyridine rings being 23.5(5)°. This angle is only marginally larger than that of 22.7(3)° observed for the hexafluoroantimonate salt. The in-plane bending of the bipyridyl ligand observed for $[Pt(bipy)_2](SbF_6)_2$ is also present for the triflate salt, resulting in the N-C-C angles being equal to 113.9(6)° and 114.0(6)°and the C-C-C angles being 123.4(6)° and 123.1(6)°; the analogous angles for $[Pt(bipy)_2](SbF_6)_2$ equal 113.8(3)° and 114.6(3)° (N-C-C angles) and 122.9(3)° and 123.7(2)° (C-C-C angles).

The cations and anions in $[Pt(bipy)_2](CF_3SO_3)_2$ are arranged in rows which extend along the [b]-axis (see Figure 3.18). Neighbouring cations within these rows are interrelated by both a unit cell translation along the [b]-axis, as well as by a crystallographic centre of inversion situated at (0.5, 0.0, 0.5). In contrast to $[Pt(bipy)_2](SbF_6)_2$, where there is no overlap of the bipyridyl ligands from neighbouring cations, both the bipyridyl ligands of the $[Pt(bipy)_2]^{2+}$ cation in the triflate salt participate in a face-to-face arrangement with the bipyridyl ligands from neighbouring cations. A diagram[297] depicting the overlap of the bipyridyl ligands within this arrangement is provided in Figure 3.19. As a result of the crystallographic centre of inversion situated midway between these ligands, the mean planes defined by their constituent atoms are necessarily parallel, the separation between the planes being 3.5Å. This value borders on that of 3.45Å, the Van der Waal's separation for π-aromatic species in a face-to-face arrangement[242]. This data suggest that some π-π interaction is possible between the bipyridyl ligands from neighbouring cations. Further support for this suggestion is provided by the colour difference between the hexafluoroantimonate (lemon yellow) and the triflate salt (golden orange, the colour of both being independent of crystal size), as well as the solid state emission spectra of the two salts, *vide infra*.

3.4.3.3 Photophysical studies on $[Pt(bipy)_2](X)_2$ ($X^- = SbF_6^-$ and $CF_3SO_3^-$)

The room temperature absorption spectra of CH_3CN solutions of both the $[Pt(bipy)_2](SbF_6)_2$ and $[Pt(bipy)_2](CF_3SO_3)_2$ salts were recorded. As expected the spectra are identical. Table 3.4 lists the wavelengths, $\lambda(abs)_{max}$, associated with the

absorption maxima of the hexafluoroantimonate salt. Identical absorption spectra have been reported for CH_3CN solutions of $[Pt(bipy)_2](PF_6)_2$[303] and aqueous solutions of the perchlorate salt[252]. In their assignment of the peaks in the absorption spectrum of $[Pt(bipy)_2](PF_6)_2$, Maestri, Von Zelewsky and co-workers[303] compared the absorption spectrum of the complex salt with that of the free bipyridyl ligand and assigned all the peaks with $\lambda(abs)_{max} < 350$ nm to ligand-centred (LC) transitions which to a greater or lesser extent have been perturbed by coordination to the Pt(II) centre. The MLCT bands were suggested to be obscured by the intense LC bands. This overlap of the MLCT and LC bands was proposed to be the result of a blue-shift of the MLCT bands when compared to Pt(II) diimine complexes where the coordination sphere is completed by anionic ligands and which exhibit distinct MLCT bands in their absorption spectra.

The proposed blue-shift of the MLCT bands of the $[Pt(bipy)_2]^{2+}$ chromophore was attributed to the +2 charge on the Pt centre in combination with the neutral bipyridyl ligands which are unable to effect a significant stabilization of the MLCT excited state[303]. Miskowski and Houlding[252] compared the absorption spectrum of $[Pt(bipy)_2](ClO_4)_2$ with that of $[Zn(bipy)_3]^{2+}$ and assigned the vibrationally structured feature maximizing at $ca.$ 320 nm to the lowest energy $^1(\pi\text{-}\pi^*)$ transition of the bipyridyl ligand. The shoulder observed at $ca.$ 350 nm was suggested to form part of a second weaker structured feature which has its origin in a $^3(\pi\text{-}\pi^*)$ transition. The intensity of the peak associated with this transition is enhanced relative to that of $[Zn(bipy)_3]^{2+}$ due to platinum spin-orbit coupling[252]. The $[Pt(bipy)_2]^{2+}$ chromophore is common to both the SbF_6^- and $CF_3SO_3^-$ salts described here, and the PF_6^- and ClO_4^- salts reported in the literature. Furthermore, the absorption spectra of all four salts are identical and thus, the assignment of the absorption features for the latter two salts, as discussed above, also pertain to the hexafluoroantimonate and triflate salts.

Some attention has been paid to the emission behaviour of the $[Pt(bipy)_2]^{2+}$ chromophore. Maestri, Von Zelewski and co-workers studied the emission behaviour of $[Pt(bipy)_2](PF_6)_2$ in a butyronitrile glass at 77 K. The band structure was found to be quite similar to that of the free bipyridyl ligand. Based on this observation, together with a consideration of the lifetime and energy associated with the luminescence, the

emission was assigned to the radiative decay of a ligand-centred $^3(\pi\text{-}\pi^*)$ excited state[303]. In a subsequent study, Miskowski and Houlding considered the emission observed from a microcrystalline sample of $[Pt(bipy)_2](ClO_4)_2$ at 30 K[252]. As mentioned in Section 3.4.2.3, a complicated pattern of vibronic structure suggested to be consistent with bipyridine vibrational modes, was observed on the high-energy side of the band whereas the low energy side was found to be asymmetric and suggested to conceal a broad structureless emission. This feature was proposed to either be indicative of multiple state emission from the $[Pt(bipy)_2]^{2+}$ chromophore or to originate from excimer-like emission similar to that suggested to be associated with solid samples of $[Pt(phen)_2]Cl_2.3H_2O$.

The solid state emission spectra of microcrystalline samples of $[Pt(bipy)_2](SbF_6)_2$, recorded at 40 K intervals over the temperature range 80 to 280 K are provided in Figure 3.20. The emission from CH_3CN solutions of $[Pt(bipy)_2](SbF_6)_2$ at room temperature, like that observed for the perchlorate salt, is vanishingly weak.

At 280 K the emission spectrum of microcrystalline samples of $[Pt(bipy)_2](SbF_6)_2$ does not exhibit any well-defined features. However, on reducing the temperature of the sample, the luminescent intensity increases. This behaviour is analogous to that observed for the $[Pt(terpy)(CH_3CN)]^{2+}$ and $[Pt(terpy)Cl]^+$ chromophores and most probably is indicative of the presence of an efficient thermally activated non-radiative deactivation pathway. At 80 K a well-defined band with distinct vibrational structure on the high energy side is observed. The individual vibrational features occur at wavelengths, $\lambda(em)_{max}$ of *ca.* 463, 495 and 534 nm. These wavelengths are only approximate since the vibrational features occur as shoulders rather than distinct peaks with well-defined maxima. Furthermore, overlap with a broad structureless emission feature which coincides with these features, *vide infra*, could result in peak shifts of the vibrational features. The wavelength representation provided in Figure 3.20 was converted to an energy representation by multiplying the emission intensity at each wavelength with the wavelength squared in order to account for the energy dependence of the band-pass function[304]. From this representation the energy separations between the vibrational features were found to be *ca.* 1400 and 1480 cm^{-1} respectively. Again these values are approximate due to the difficulty associated with
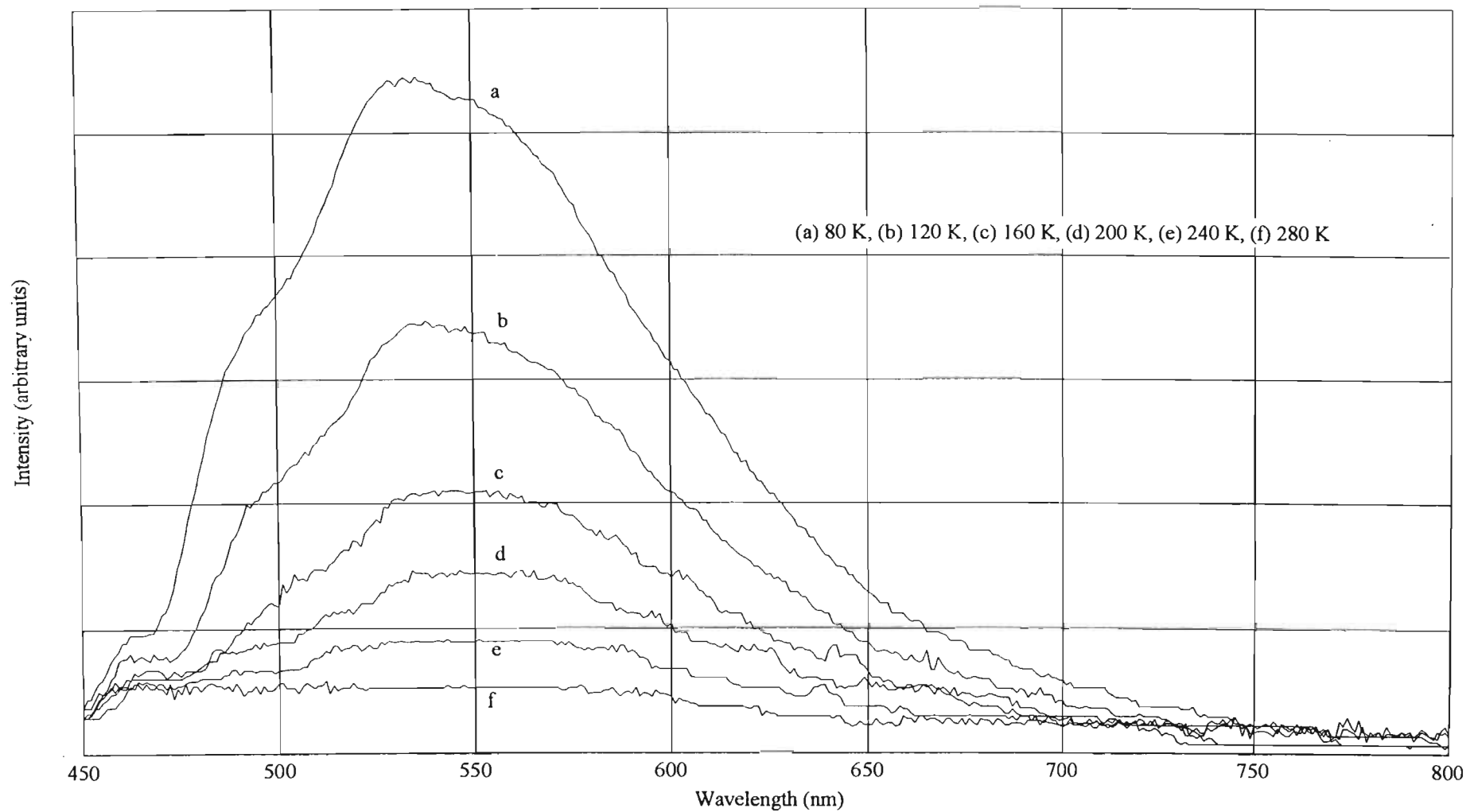
Figure 3.20 _The solid state emission spectrum of [Pt(bipy)₂](SbF₆)₂ recorded at 40 K intervals over the range 80 to 280 K._

The chart shows Intensity (arbitrary units) on the vertical axis versus Wavelength (nm) on the horizontal axis (450 to 800 nm). Curves are labelled a–f:

(a) 80 K, (b) 120 K, (c) 160 K, (d) 200 K, (e) 240 K, (f) 280 K

determining the true peak positions of the vibrational features. The energy separations nonetheless suggest that the observed vibrational structure has its origin in the excitation of progressions of a 1400 cm^{-1} vibration which occurs in the spectra of many aromatic molecules[305], in this case the bipyridyl ligands. The wavelengths associated with the vibrational features furthermore are in reasonable agreement with that reported for [Pt(bipy)$_2$](PF$_6$)$_2$ in a rigid butyronitrile matrix[303] and provide further support for the suggestion that, like the PF$_6^-$ salt, the structured emission from the hexafluoroantimonate salt originates from the radiative decay of a ligand-centred excited state, and in particular from the $^3(\pi\text{-}\pi^*)$ excited state.

A comparison of the solid state emission spectra of [Pt(bipy)$_2$](SbF$_6$)$_2$ with that reported for [Pt(bipy)$_2$](ClO$_4$)$_2$ reveals that the spectra are essentially identical, but that the vibrational structure observed in the spectrum of the perchlorate salt is much more pronounced than that observed for the hexafluoroantimonate salt. This difference could stem from the fact that the emission spectrum of the perchlorate salt was recorded at 30 K, whereas the minimum temperature achievable with the apparatus utilized in recording the spectra of the hexafluoroantimonate salt, was 77 K. A consideration of the series of variable temperature emission spectra of the SbF$_6^-$ salt, presented in Figure 3.20, does in fact suggest that the resolution of the vibrational structure improves as the temperature of the sample is decreased.

Furthermore, comparing the emission spectrum of microcrystalline [Pt(bipy)$_2$](SbF$_6$)$_2$ with that of the PF$_6^-$ salt in butyronitrile glass, reveals that the band envelope associated with the hexafluoroantimonate salt is much broader than that of the PF$_6^-$ salt and that, as has been suggested for the spectrum recorded on a microcrystalline sample of [Pt(bipy)$_2$](ClO$_4$)$_2$[252], a broad structureless emission is most probably concealed on the low-energy side of the band. As discussed earlier, Miskowski and Houlding proposed that this feature could indicate multiple-state emission from the [Pt(bipy)$_2$]$^{2+}$ chromophore or "that it is an excimer-like emission from neighbouring complexes that are brought into electronic contact by the crystal packing." However, since the crystal structure of the ClO$_4^-$ salt has not been determined and solution emission data were not available, the authors conceded that their assignment is restricted to conjecture.

As pointed out in the discussion of the crystal structure of $[Pt(bipy)_2](SbF_6)_2$ (see Section 3.4.3.2), the $[Pt(bipy)_2]^{2+}$ chromophores exist as isolated monomeric entities in the crystal lattice with no ligand-ligand, metal-metal or metal-ligand interactions between the individual cations. Miskowski and Houlding's suggestion that the structureless feature concealed on the low-energy side of the solid state emission band envelope of the $[Pt(bipy)_2]^{2+}$ chromophore, as observed for $[Pt(bipy)_2](ClO_4)_2$ and $[Pt(bipy)_2](SbF_6)_2$, is excimeric in origin, can thus be discounted. Further evidence contradicting the suggested excimer-like emission is provided by the solid-state emission spectra of $[Pt(bipy)_2](CF_3SO_3)_2$.

The solid state emission spectra of the triflate salt recorded on microcrystalline samples at 40 K intervals over the temperature range 80 to 280 K, are presented in Figure 3.21. The emission from CH_3CN solutions of $[Pt(bipy)_2](CF_3SO_3)_2$, like that of the hexafluoroantimonate and perchlorate salts, is vanishingly weak.

The emission of microcrystalline samples of $[Pt(bipy)_2](CF_3SO_3)_2$ at 280 K is extremely weak and does not exhibit any well-defined features. However, as described for the SbF_6^- salt, the luminescent intensity increases as the temperature of the sample is decreased, consistent with the presence of an efficient thermally activated non-radiative deactivation pathway. At 80 K a well-defined band with distinct vibrational structure on the high energy side is observed. In contrast to the spectrum of the hexafluoroantimonate salt, where the vibrational features were present as shoulders, the vibrational structure in the spectrum of the triflate salt is present as distinct peaks. The individual features occur at wavelengths, $\lambda(em)_{max}$, of ca. 465, 508 and 546 nm. As in the case of the hexafluoroantimonate salt, the wavelengths associated with the latter two vibrational features might be shifted from their true positions as a result of overlap with a broad structureless emission feature concealed on the low energy side of the band envelope.

Further comparison of the series of variable temperature solid state emission spectra reveal that the wavelengths associated with the well defined vibrational features in the spectra of the triflate salt (508 and 546 nm) are red-shifted by ca. 12 nm when compared to that of the analogous features in the spectra of the hexafluoroantimonate
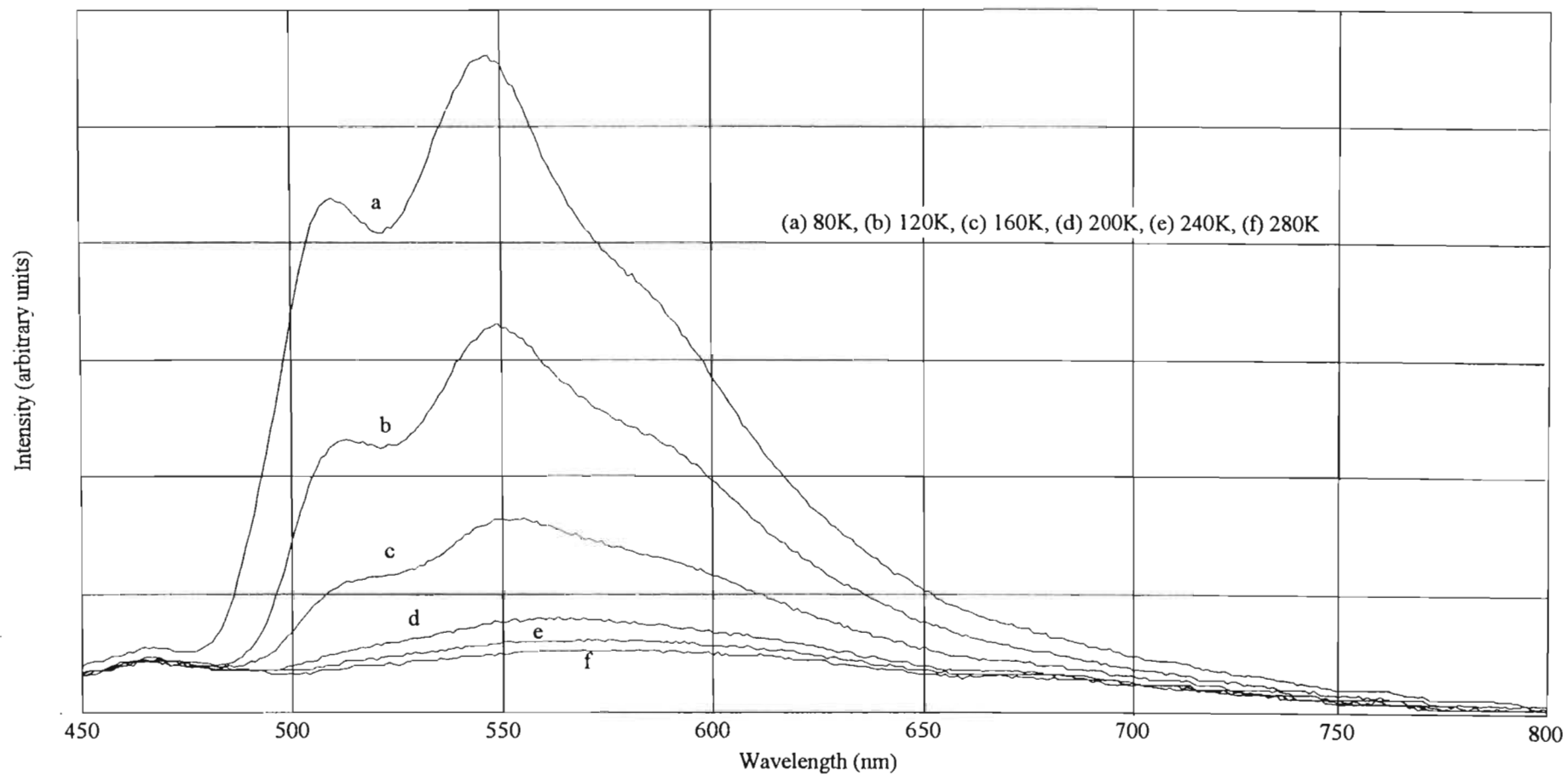
Figure 3.21 *The solid state emission spectrum of $[Pt(bipy)_2](CF_3SO_3)_2$ recorded at 40 K intervals over the range 80 to 280 K.*

salt (495 and 534 nm). The broad concealed emission feature also seems to be red-shifted when comparing the spectra of the two salts. However, due to the extensive overlap between this feature and the vibrational features in the spectra of both salts, the exact wavelength associated with the maximum emission intensity cannot be determined from these spectra, thus complicating the assessment of any shifts in the peak position of this feature. The observed red-shift of the vibrational features and proposed shift in the position of the broad concealed feature, is consistent with and provides further support for the π-π interaction between the bipyridine ligands of neighbouring $[Pt(bipy)]^{2+}$ chromophores, as suggested from the crystal structure of $[Pt(bipy)_2](CF_3SO_3)_2^{(297)}$ (see Section 3.4.3.2).

A schematic representation of the energy levels associated with the $[Pt(bipy)_2]^{2+}$ chromophore and the influence of the proposed π-π ligand interaction on the energy of these levels, is provided in Figure 3.22. This scheme is essentially that as proposed by Miskowski and Houlding[253] for $[Pt(phen)_2]Cl_2.3H_2O$. However, Miskowski and Houlding's proposed scheme provides for interaction between the metal p_z orbitals although they do state that the Pt-Pt distance in $[Pt(phen)_2]Cl_2.3H_2O$ (3.710Å) is too long to support significant metal-metal interaction. A similar cation arrangement to that of $[Pt(phen)_2]Cl_2.3H_2O$ (i.e. ligand-ligand and no metal-metal interaction) is present in the lattice of $[Pt(bipy)_2](CF_3SO_3)_2$, thus leading to the scheme depicted below with no interaction between the metal-centred d_{z^2} or p_z orbitals.
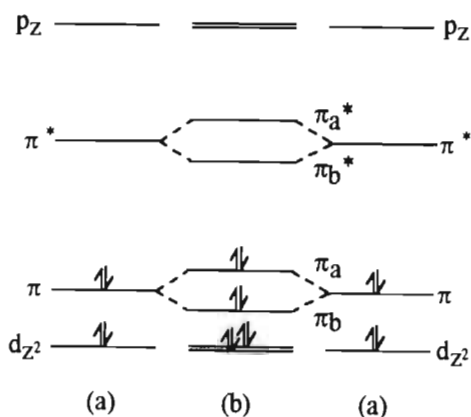
Figure 3.22 *Schematic representation of selected energy levels for:*

(a) [Pt(bipy)₂](SbF₆)₂ (monomeric cationic moieties)

(b) [Pt(bipy)₂](CF₃SO₃)₂ (π-π interacting moieties)

251

In $[Pt(bipy)_2](CF_3SO_3)_2$ the bipyridine-centred π and π^* orbitals from neighbouring $[Pt(bipy)_2]^{2+}$ chromophores interact to produce a set of bonding (e.g. π_b) and antibonding (e.g. π_a) orbitals. As a result of this interaction, the energy associated with the lowest energy excited state for samples in the solid state decreases in going from $[Pt(bipy)_2](SbF_6)_2$ to $[Pt(bipy)_2](CF_3SO_3)_2$, thus causing the observed red-shift in the emission spectra of the triflate salt when compared to that of the hexafluoroantimonate analogue.

It is also important to note that the band profile of the solid state emission of the SbF_6^- and the $CF_3SO_3^-$ salts are essentially identical, the only difference being that the vibrational structure is better resolved in the spectra of the triflate salt. If the broad concealed feature in the spectra of both of these salts did originate from excimeric emission, this feature would have been expected to be much more pronounced in the spectrum of the triflate salt, where π-π ligand-ligand interaction does occur, when compared to the hexafluoroantimonate salt where little, if any, interaction between the bipyridine ligands of neighbouring $[Pt(bipy)_2]^{2+}$ cations is possible.

Having eliminated the possibility that the concealed, broad and unstructured emission from the $[Pt(bipy)_2]^{2+}$ chromophore is excimeric in origin, the possibility of multiple emission has to be considered. However, as mentioned in the discussion on the emission behaviour of the $[Pt(terpy)(CH_3CN)]^{2+}$ chromophore, certain factors which could be responsible for the observation of multiple emissions from a sample containing the chromophore of interest have to be eliminated before a chromophore is suggested to emit from multiple excited states of the same multiplicity[292, 293].

The first of these factors involves intrinsic heterogeneity of the sample and includes the trivial case where impurity emissions are present. As a first step, elemental analysis for C, H and N have confirmed the samples of $[Pt(bipy)_2](SbF_6)_2$ and $[Pt(bipy)_2](CF_3SO_3)_2$, utilized in the emission studies to be analytically pure. However, as pointed out by DeArmond and Carlin[290], and discussed in Section 3.4.2.3, the use of elemental analysis is not sufficient to guarantee sample purity when the phenomenon of interest is luminescence. It thus is necessary to consider possible sources of contamination and to evaluate the effects and likelihood of such contamination.

As mentioned in the preceding discussion, the low-temperature solid state emission spectra of both $[Pt(bipy)_2](SbF_6)_2$ and $[Pt(bipy)_2](CF_3SO_3)_2$ reported here , as well as that of the perchlorate salt reported by Miskowski and Houlding, exhibit the concealed broad unstructured feature on the low energy side of the emission band. This would imply that unless two or more different luminescent impurities can all give rise to the same broad unstructured emission feature, the impurity from which this feature originates, has to be common to the synthetic routes employed in the preparation of all three salts. The only possible impurities in this context are the uncoordinated bipyridine ligand and $[Pt(bipy)Cl_2]$. Impurity emission from free bipyridine molecules can be ruled out, since the material utilized in the luminescence studies reported here and in the literature[253], was washed extensively to remove uncoordinated ligand molecules. Furthermore, emission from the uncoordinated bipyridine moiety would be vibrationally stuctured and would occur at energies which are *ca.* 950 cm^{-1} higher than that of the $^3(\pi\text{-}\pi^*)$ emission from the $[Pt(terpy)(CH_3CN)]^{2+}$ chromophore[303]. The luminescent properties of $[Pt(bipy)Cl_2]$ have been reported previously[253, 258], the maximum emission intensity of the yellow polymorph occurring at a wavelength, $\lambda(em)_{max}$ of *ca.* 630 nm[253]. This emission is substantially red-shifted with respect to that of the concealed unstructured feature observed in the low-temperature solid state emission spectra of either $[Pt(bipy)_2](SbF_6)_2$ or $[Pt(bipy)_2](CF_3SO_3)_2$ (see Figures 3.20 and 3.21). Emission from the red polymorph of $[Pt(bipy)Cl_2]$ red-shifts on reducing the temperature of the sample. If the concealed unstructured emission feature in the low-temperature solid state emission spectra of $[Pt(bipy)_2](X)_2$ ($X^- = SbF_6^-$ or $CF_3SO_3^-$) did originate from an impurity emission from red $[Pt(bipy)Cl_2]$, a temperature dependent change of the band profile of the solid state emission spectra would be expected. However, the series of variable temperature spectra provided in Figures 3.20 and 3.21 present no evidence of such a temperature dependent change of the band profile. Sample heterogeneity can also arise as a result of ligand redistribution equilibria involving solvent molecules, but can be discounted since the spectra considered here were recorded on solid state samples.

A second factor which could result in multiple emissions is that of microenvironmental effects. As mentioned in the discussion of the luminescence of $[Pt(terpy)(CH_3CN)](SbF_6)_2$ (see Section 3.4.2.3), multiple spectra can arise as a

consequence of discrete environments producing spectrally distinct emissions when the energy of an excited state is sensitive to the microenvironment. Although these effects are usually associated with solvent-chromophore interactions[292, 293], it was pointed out in the aforementioned discussion that such effects also extend to the solid state where the lattice contains the chromophore in two or more crystallographically distinct environments or where the two halves of a symmetrical chromophore, like $[Pt(bipy)_2]^{2+}$, occur in crystallographically distinct sites. However, as pointed out in the discussion of the crystal structures of $[Pt(bipy)_2](SbF_6)_2$ and $[Pt(bipy)_2](CF_3SO_3)_2$ (see Section 3.4.4.2), the asymmetric unit consists of one anion and half of the $[Pt(bipy)_2]^{2+}$ chromophore. It thus follows that the crystallographic environment of the two halves of the $[Pt(bipy)_2]^{2+}$ chromophore, as well as that of all the chromophores in the lattice, necessarily are identical. Based on these considerations, together with Miskowski and Houlding's earlier suggestion[253], it would seem that solid samples of the hexafluoroantimonate, triflate and perchlorate salts of the $[Pt(bipy)_2]^{2+}$ chromophore do indeed exhibit multiple state emission. Further assessment of the nature of the emitting state without resource to spectra obtained in other media is difficult, but might be possible through the use of time-resolved spectra and excited state lifetime determinations. However, as a result of our limited access to apparatus required for the study of luminescent behaviour, it was not possible to conduct such studies.

In conclusion, it also interesting to note that whereas the solid state spectra of $[Pt(bipy)_2](SbF_6)_2$, $[Pt(bipy)_2](CF_3SO_3)_2$ and $[Pt(bipy)_2](ClO_4)_2$ exhibit the broad concealed emission feature, this feature has not been observed in emission spectra recorded for $[Pt(bipy)_2](PF_6)_2$ in a rigid butyronitrile matrix[303]. This difference in the emission spectra could be a consequence of the $[Pt(bipy)_2]^{2+}$ chromophore adopting different equilibrium geometries in the solid state and rigid glassy matrix. Such differences in geometry are clearly evident in comparing the crystal structure of $[Pt(bipy)_2](NO_3)_2.H_2O$[299], where a tetrahedral distortion of the platinum coordination sphere occurs, to that of $[Pt(bipy)_2](SbF_6)_2$ and $[Pt(bipy)_2](CF_3SO_3)_2$, where the $[Pt(bipy)_2]^{2+}$ chromophore exhibit bow and tilting distortions (see Section 3.4.4.2). An interesting extension of the results presented here would involve a study of the solid state luminescent behaviour of $[Pt(bipy)_2](NO_3)_2.H_2O$ to ascertain what influence the

difference in equilibrium geometry will have on the luminescent behaviour, and in particular, on the suggested multiple state emission of the $[Pt(bipy)_2]^{2+}$ chromophore.

3.4.5 [Pt(4'-Ph-terpy)Cl](SbF₆) (14)

3.4.5.1 Preliminary considerations

The reasons for studying [Pt(4'-Ph-terpy)Cl](SbF₆) **14** are three-fold:

1. A method for the synthesis of [Pt(terpy)Cl]Cl involves reacting 2,2',6',6"-terpyridine with K_2PtCl_4 in aqueous solution. Che and co-workers extended the scope of this reaction to include substituted terpyridine ligands, in particular 4'-R-terpyridines such as 4'-(4'-OMe-Ph)-terpy, 4'-(4'-Me-Ph)-terpy, 4'-(4'-Br-Ph)-terpy and 4'-(4'-CN-Ph)-terpy, to produce [Pt(4'-R-terpy)Cl](ClO₄)[263]. However, it is interesting to note that all the ligands utilized by Che *et al.*, include a substituent in a position para to the carbon atom through which the phenyl ring is bonded to the central pyridine ring of the terpyridine moiety. Thus, although 4'-Ph-terpy would be a logical choice to broaden the range of substituted terpyridine ligands utilized in the synthesis of square planar Pt(II) complexes, Che and co-workers did not include this ligand in their study. Preliminary attempts at extending the synthetic procedure reported by Che *et al.* to include 4'-Ph-terpy were unsuccessful. This most probably is the result of the insolubility of [Pt(4'-Ph-terpy)Cl]Cl in common solvents, thus hampering its isolation from a variety of insoluble side products resulting from the reaction. These solubility problems could also explain why all the ligands utilized in the aforementioned study included the para-substituent on the 4'-phenyl substituent on the terpyridine moiety, since such substituents could improve the solubility of the resulting Pt(II) complex.

2. The 4'-Ph-terpy ligand is not planar, the phenyl ring being twisted about the interannular bond such that it makes an angle of $10.9°^{[306]}$ with respect to the plane of the central pyridine ring on the free ligand. This deviation from planarity arises as a consequence of a minimization of the non-bonded repulsions between the protons situated in the ortho positions on the phenyl ring and the analogous protons on the central pyridine ring of the terpyridine moiety (see figure 3.23)
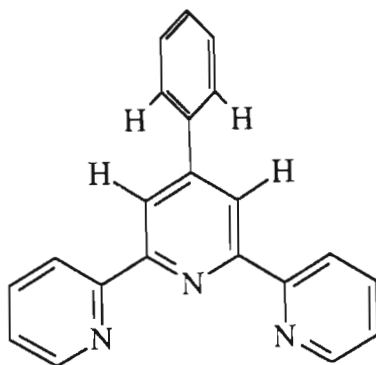
Figure 3.23 *Structural formula of the 4'-Ph-terpy ligand showing hydrogens in ortho positions.*

Whereas the series of complex salts [Pt(terpy)Cl](X) (X⁻ = SbF₆⁻, CF₃SO₃⁻ and BF₄⁻) (see Section 3.4.2) focused on the effect of the counterion of the packing architecture and luminescent properties of the [Pt(terpy)Cl]⁺ chromophore, the introduction of deviations from planarity presents a further perturbation which can influence the molecular packing and ultimately, the luminescent behaviour of the salt.

3. In addition to the increased steric demands of the 4'-Ph-terpy ligand, resulting from the introduction of the phenyl substituent, the electronic properties of the ligand could also differ from that of the unsubstituted terpyridine ligand, since the phenyl substituent can form an extended π-conjugated system with the rest of the terpyridine moiety.

3.4.5.2 Synthesis and characterization of [Pt(4'-Ph-terpy)Cl](SbF₆) (14)

The synthetic procedure utilized in the preparation of [Pt(4'-Ph-terpy)Cl](SbF₆) is essentially identical to that employed in the synthesis of [Pt(terpy)Cl](X) (X⁻ = BF₄⁻, CF₃SO₃⁻ and SbF₆⁻). It involves treating [Pt(C₆H₅CN)₂Cl₂], suspended in CH₃CN, with an equimolar amount of AgSbF₆ and heating the mixture to reflux for *ca.* 15 hours. Following the removal of the precipitated AgCl, a 5% excess of 4'-phenylterpyridine was added to the reaction mixture and the mixture heated under reflux for a further 15 hours during which time the product, [Pt(4'-Ph-terpy)Cl](SbF₆), occasionally precipitated as a fine yellow powder. On completion of the reaction, the temperature of the reaction mixture was kept close to the boiling point of the solvent whilst adding

enough CH_3CN to completely dissolve any precipitated [Pt(4'-Ph-terpy)Cl](SbF_6). The resulting solution was filtered to remove additional AgCl which might have precipitated during the second reflux, before reducing the volume of the solvent *in vacuo*. The precipitated product was isolated through filtration and washed in order, with cold CH_3CN, acetone and diethyl ether. Subsequent purification involved reprecipitating the product by dissolving it in hot CH_3CN, filtering the solution and allowing it to slowly cool to room temperature. The resulting yellow solid was washed with CH_3CN and diethyl ether before drying it *in vacuo*. Elemental analysis for C, H and N was consistent with the proposed empirical formula [Pt(4'-Ph-terpy)Cl](SbF_6). It is also interesting to note that the product does not exhibit any evidence of the yellow/orange polymorphic behaviour associated with the analogous unsubstituted terpyridine derivative [Pt(terpy)Cl](SbF_6).

The solid state infrared spectrum of [Pt(4'-Ph-terpy)Cl](SbF_6) was recorded as a KBr pellet, the most prominent peaks being listed in Table 3.1. A comparison of this spectrum with that of [Pt(terpy)Cl](SbF_6) reveals that the two spectra are nearly identical, the only differences being in the relative intensities of the bands at 1456 and 1441 cm^{-1} and the wavenumber of a band in the range 1400 to 1420 cm^{-1}. Whereas the solid state infrared spectrum of the unsubstituted terpyridine derivative exhibits two very well resolved bands at 1456 and 1441 cm^{-1} respectively, these bands appear as a broad, weak and poorly resolved band in the spectrum of [Pt(4'-Ph-terpy)Cl](SbF_6) (**14**). Furthermore, a band which appears at 1400 cm^{-1} in the spectrum of [Pt(terpy)Cl](SbF_6), is shifted to higher wavenumbers in the spectrum of [Pt(4'-Ph-terpy)Cl](SbF_6) and appears at 1417 cm^{-1}. Both these differences are associated with bands which originate from vibrational modes of the coordinated polypyridyl ligand and in all probability result from the introduction of the phenyl substituent in the 4' position on the 4'-phenylterpyridine ligand. The spectrum also displays the customary peak at *ca.* 655 nm associated with the SbF_6^- anion.

Despite repeated attempts, single crystals of [Pt(4'-Ph-terpy)Cl](SbF_6), suitable for X-ray diffractometric studies could not be grown. Vapour diffusion techniques, as well as slow cooling of saturated solutions of the salt, resulted in the formation of powdery material. Very small amounts of crystalline material was obtained from slow

evaporation of solutions containing the salt. However, these crystals were too small to conduct X-ray diffractometric studies.

3.4.5.3 Photophysical studies on [Pt(4'-Ph-terpy)Cl](SbF$_6$) (14)

The room temperature absorption spectrum of a CH$_3$CN solution of 14 was recorded and is presented in Figure 3.24. Table 3.4 lists the wavelengths, λ(em)$_{max}$, associated with the absorption maxima. The spectrum can be divided into three features, *viz.* a narrow band at *ca.* 280 nm, a broad band with distinct vibronic structure between 300 and 350 nm and two broad bands between 350 and 420 nm. As such the peak pattern and wavelengths associated with these features is comparable to that of the [Pt(terpy)Cl]$^+$ chromophore and the assignment of the absorption features again follows that as reported by McMillin and co-workers[260] and Che and co-workers[263].

The absorption feature at 282 nm, as well as the vibronically structured band between 300 and 350 nm, can be assigned to ^{1}(π-π*) transitions of the coordinated 4'-phenylterpyridine ligand, based on the analogy between these peaks and that of [Pt(terpy)Cl]$^+$. The possibility that the bands with λ(abs)$_{max}$ greater than 350 nm also originate from intraligand π-π* transitions can most probably be discounted since the absorption spectrum of the uncoordinated ligand does not exhibit any bands at wavelengths higher than 350 nm. Based on the similarity in the relative intensities and the wavelengths of these bands and analogous bands in the absorption spectra of the [Pt(terpy)Cl]$^+$, [Pt(terpy)(OH)]$^+$ and [Pt(terpy)(NCS)]$^{+}$ [260, 263] chromophores, it does not seem unreasonable to suggest that the bands with λ(abs)$_{max}$ higher than 350 nm, like those in the absorption spectrum of the latter three chromophores, originate from metal-to-ligand charge transfer transitions.

Preliminary studies on the solid state luminescent behaviour of [Pt(4'-Ph-terpy)Cl](SbF$_6$), utilizing a hand held ultraviolet lamp providing blanket radiation in the range 300 to 380 nm, revealed that carefully handled samples (avoiding crushing of the sample) display a bright yellow luminescence on irradiation at room temperature. Cooling the sample had no influence on the colour of the luminescence as perceived by eye. However, on crushing and grinding the sample, the colour of the luminescence at room temperature changed from bright yellow to bright orange. Cooling such a

258
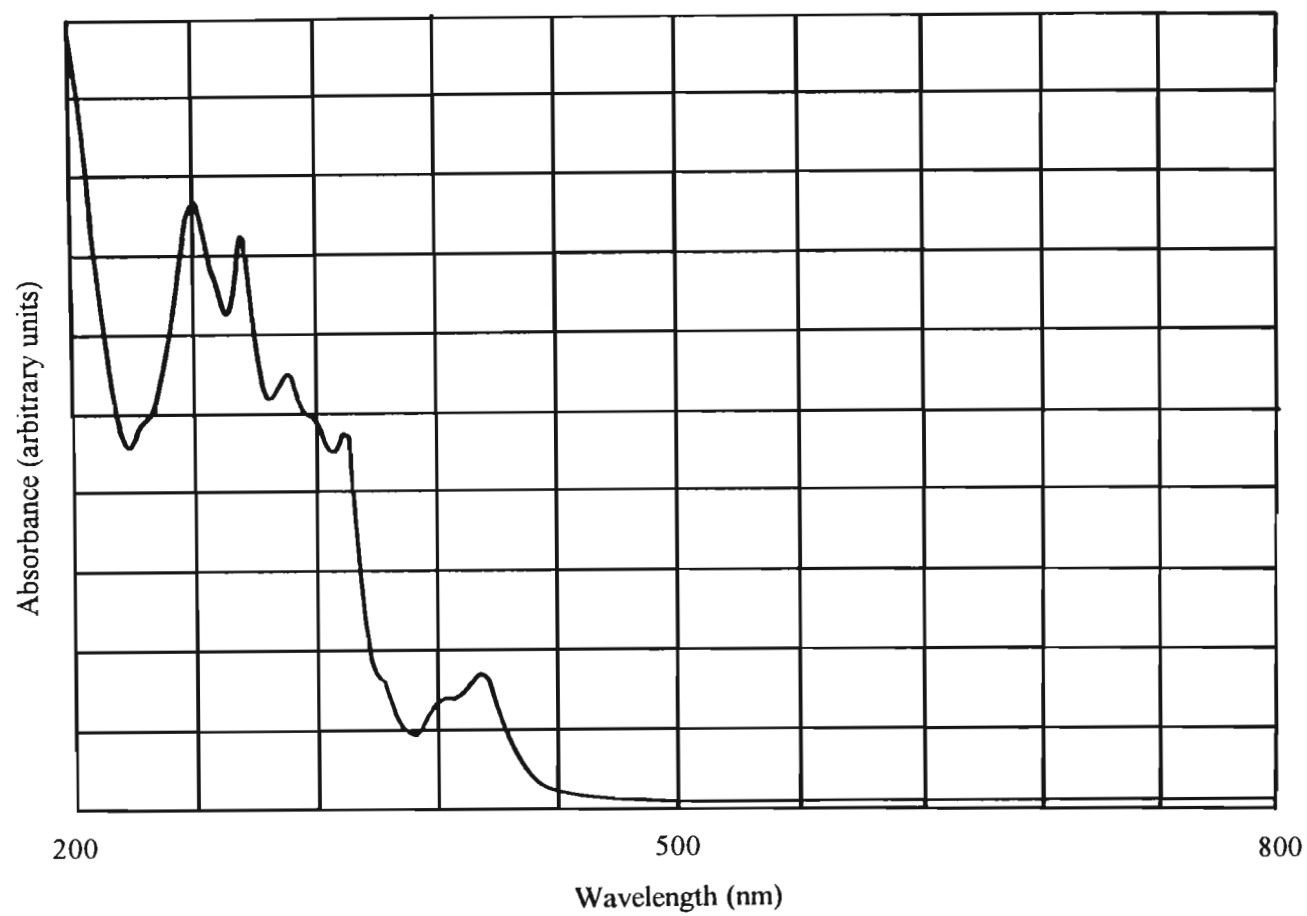
Figure 3.24 *The absorption spectrum of a CH₃CN solution of [Pt(4'-Ph-terpy)Cl](SbF₆) recorded at room temperature.*

crushed sample to liquid nitrogen temperatures resulted in the colour of the luminescence changing back to the original yellow colour. Further heating/cooling cycles revealed that this temperature dependent change in the luminescent colour is completely reversible.

The solid state emission spectrum of an uncrushed sample of [Pt(4'-Ph-terpy)Cl](SbF$_6$) was recorded at 80 K and thereafter at 30 K intervals over the range 100 to 280 K. The series of spectra measured at different temperatures are presented in Figure 3.25. At 280 K, the emission band profile is vibrationally structured with two vibrational features occurring at 522 and 557 nm respectively. The energy separation between these features is *ca.* 1200 cm^{-1}. A broad structureless band centred at *ca.* 640 nm is also observed. On reducing the temperature of the sample, the emission intensity increases, consistent with the presence of an efficient thermally activated deactivation pathway. Lowering the temperature of the sample also results in the two vibrational features undergoing a blue-shift, the feature centred at 522 nm in the spectrum recorded at 280 K, being shifted by *ca.* 8 nm to 514 nm in the spectrum recorded at 80 K, the other undergoing an analogous shift of *ca.* 6 nm from 557 to 551 nm. Furthermore, the broad structureless feature centred at 640 nm red-shifts on decreasing the temperature, whilst a third vibrational feature is resolved at 599 nm in spectra recorded at temperatures between 130 and 80 K. Examining the sample employed in recording these spectra under blanket ultraviolet irradiation, did however reveal that despite extreme care taken to avoid the conversion to the orange luminescent phase induced by crushing the sample, sample handling did actually result in the sample being contaminated with a small amount of the orange luminescent phase. The spectra presented in Figure 3.25 thus are a composite of the emissions from the yellow and trace amounts of the orange luminescent forms.

The crystal structure of [Pt(4'-Ph-terpy)Cl](SbF$_6$) has not been determined. The yellow colour of the material, together with the yellow luminescence under ultraviolet irradiation, would however, suggest that there is minimal, if any, interaction between the chromophores in the yellow luminescent phase of the salt.

In order to further explore the validity of this suggestion, the emission spectrum of the [Pt(4'-Ph-terpy)Cl]$^+$ chromophore in a CH$_3$CN solution at room temperature was
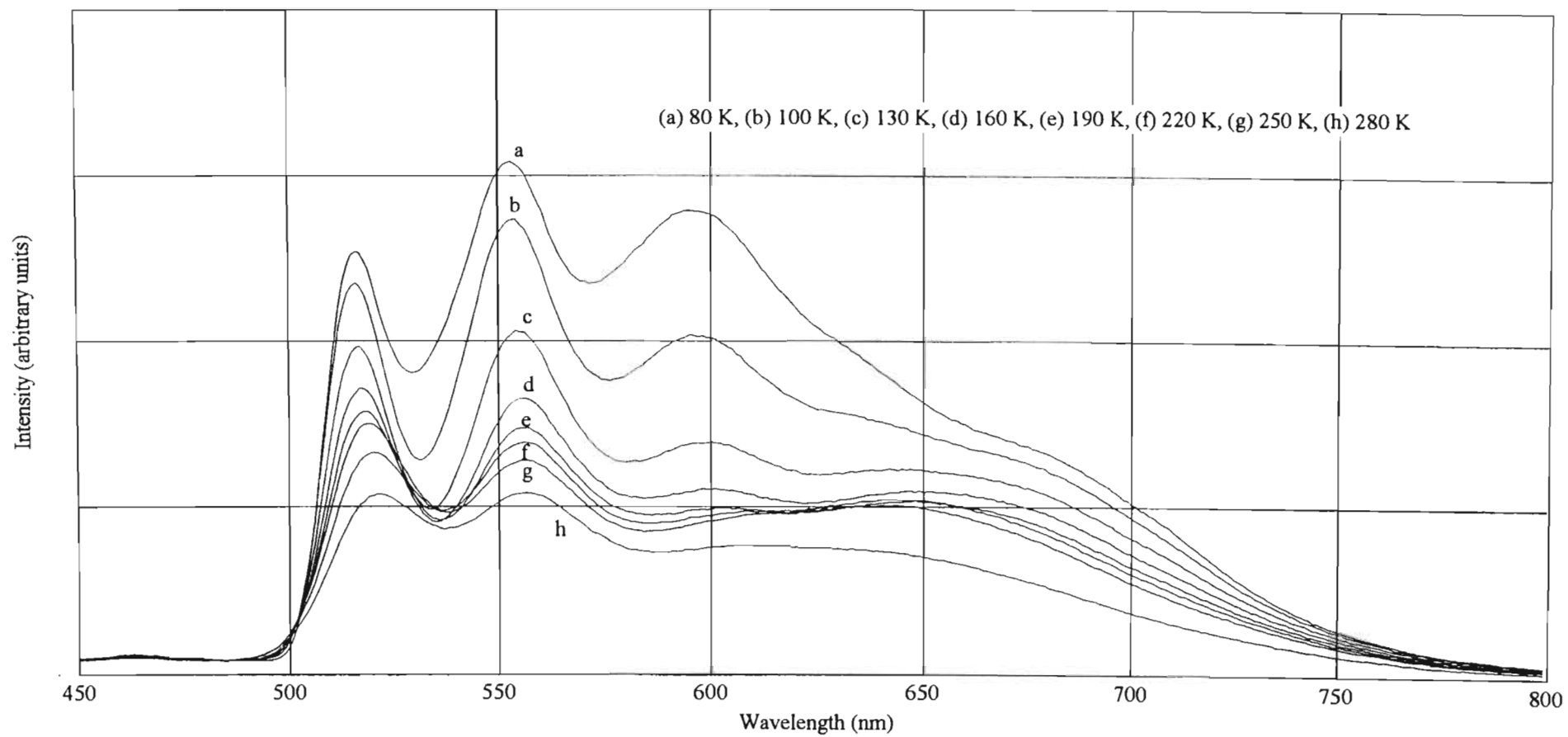
Figure 3.25 *The solid state emission spectrum of an uncrushed sample of [Pt(4'Ph-terpy)Cl](SbF₆) recorded over the range 80 to 280 K.*
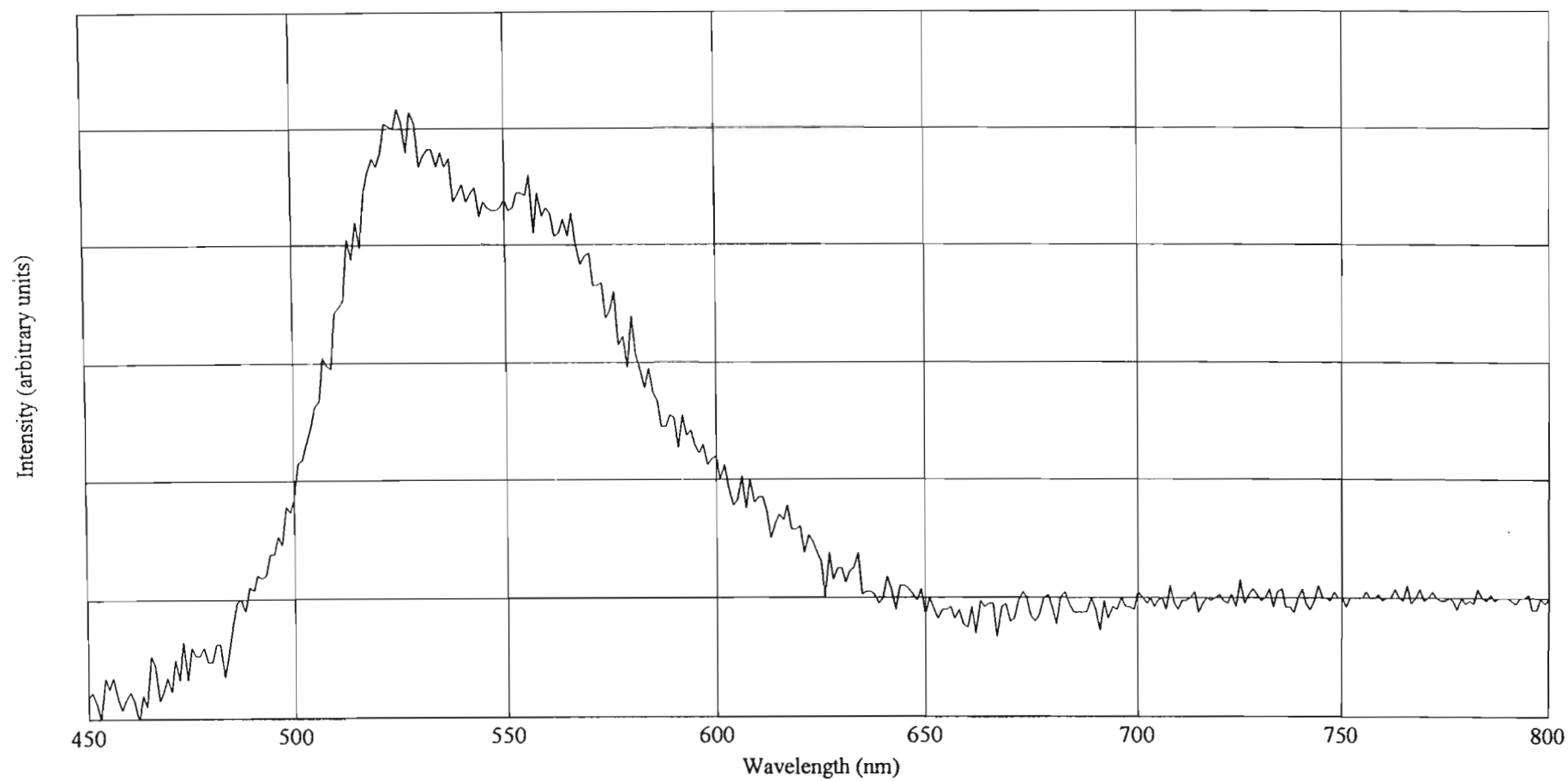
Figure 3.26   *The emission spectrum of a CH₃CN solution of [Pt(4'-Ph-terpy)Cl](SbF₆) recorded at room temperature.*

recorded and is presented in Figure 3.26. The emission in solution is weak, but a definite vibrationally structured peak with two vibrational features occurring at *ca.* 525 and 555 nm is observed. The uncertainty in the wavelengths associated with these features stems from the high level of background noise superimposed on the signal. Increasing the concentration of the sample solution to the solubility limit, or decreasing the concentration to where emission was barely detectable, did not reveal any changes in the shape or position of the band profile. Based on these considerations, it would seem that the emission from CH_3CN solutions of $[Pt(4'-Ph-terpy)Cl](SbF_6)$ can be assumed to be representative of the emission from the $[Pt(4'-Ph-terpy)Cl]^+$ chromophore in a monomeric environment. Further support for this suggestion is provided by the solid state emission spectra of the orange luminescent phase of the chromophore, recorded at different temperatures, *vide infra*.

A comparison of the emission spectrum of $[Pt(4'-Ph-terpy)Cl](SbF_6)$ in CH_3CN solution at room temperature, with that of the contaminated yellow phase discussed above, reveals that there is excellent agreement between the wavelengths associated with the vibrational features in the solution spectrum (*ca.* 525 and 555 nm) and that of the two highest energy features in the solid state emission spectrum of the contaminated yellow phase (522 and 557 nm). From these considerations it would appear that the broad unstructured emission centred at *ca.* 640 nm actually is an impurity emission originating from the orange luminescent form of $[Pt(4'-Ph-terpy)Cl](SbF_6)$.

The vibrational structure observed in both the emission spectra of $[Pt(4'-Ph-terpy)Cl](SbF_6)$ in CH_3CN solution at room temperature and of the yellow luminescent form in the solid state at various temperatures, suggests some ligand involvement in the electronic excited state. In this regard, three types of excited state come to mind, these being (i) a ligand-to-ligand charge transfer (LLCT), (ii) a metal-to-ligand charge transfer (MLCT) or (iii) an intraligand (IL) excited state. The first of these can be discounted since the Cl⁻ ligand is regarded as a weak π-donating ligand which together with the π-accepting nature of the terpyridine ligand, implies that the difference in redox potentials between the terpyridine and Cl⁻ ligands will be relatively large, thus limiting the likelihood of a LLCT excited state. The band envelope associated with

emission from a MLCT excited state in platinum polypyridyl complexes usually is devoid of any vibrational structure. One notable exception in this regard is [Pt{3,3'-(CH$_3$OCO)$_2$bipy}Cl$_2$] which exhibits vibrationally structured emission from a unimolecular MLCT excited state[258]. At 300 K the solid state emission band profile is broad with little evidence of any well resolved vibrational structure. However, on decreasing the temperature to 10 K, broad vibrational structure with a 1300 cm^{-1} spacing develops. This behaviour contrasts with that of the yellow luminescent form of [Pt(4'-Ph-terpy)Cl](SbF$_6$) where the vibrational structure in the solid state spectrum appears much sharper and is clearly evident over the entire temperature range from 80 to 280 K. Furthermore, the Huang-Rhys ratio (S = I$_{1-0}$/I$_{0-0}$) associated with the emission from [Pt(4'-Ph-terpy)Cl](SbF$_6$) in fluid CH$_3$CN solution is larger than 1, the value associated with the vibrationally structured emission from [Pt{3,3'-(CH$_3$OCO)$_2$bipy}Cl$_2$]. As such the emission behaviour of the yellow luminescent form of [Pt(4'-Ph-terpy)Cl](SbF$_6$) in the solid state (disregarding the impurity emission from the orange luminescent form) and in CH$_3$CN solution at room temperature, is more consistent with ^{3}IL emission as described by Miskowski, Houlding, Che and Wang[258] than with vibrationally structured MLCT emission as described by the same authors. The emission of [Pt(4'-Ph-terpy)Cl](SbF$_6$) both as the yellow luminescent form in the solid state and in fluid CH$_3$CN solution, is thus assigned to originate from a $^3(\pi$-$\pi^*)$ 4'-phenylterpyridine based excited state.

In order to study the luminescent behaviour of the orange luminescent phase of [Pt(4'-Ph-terpy)Cl](SbF$_6$) and to further assess its influence as an impurity emission on the variable temperature spectra of the yellow luminescent phase, a sample of the yellow phase was ground until examination under blanket ultraviolet irradiation revealed no traces of the yellow luminescent form. The solid state emission spectrum of this sample was recorded at 80 K and thereafter at 30 K intervals over the range 100 to 280 K. The series of spectra, recorded at different temperatures, are presented in Figure 3.27. At 280 K the solid state emission spectrum consists of a broad unstructured peak centred at 644 nm with two weak and poorly resolved vibrational features at the high energy side of the band at 521 and 554 nm respectively. The position of both the unstructured peak, as well as the two weak vibrational features, are in good agreement with the analogous features observed in the emission spectrum of the contaminated
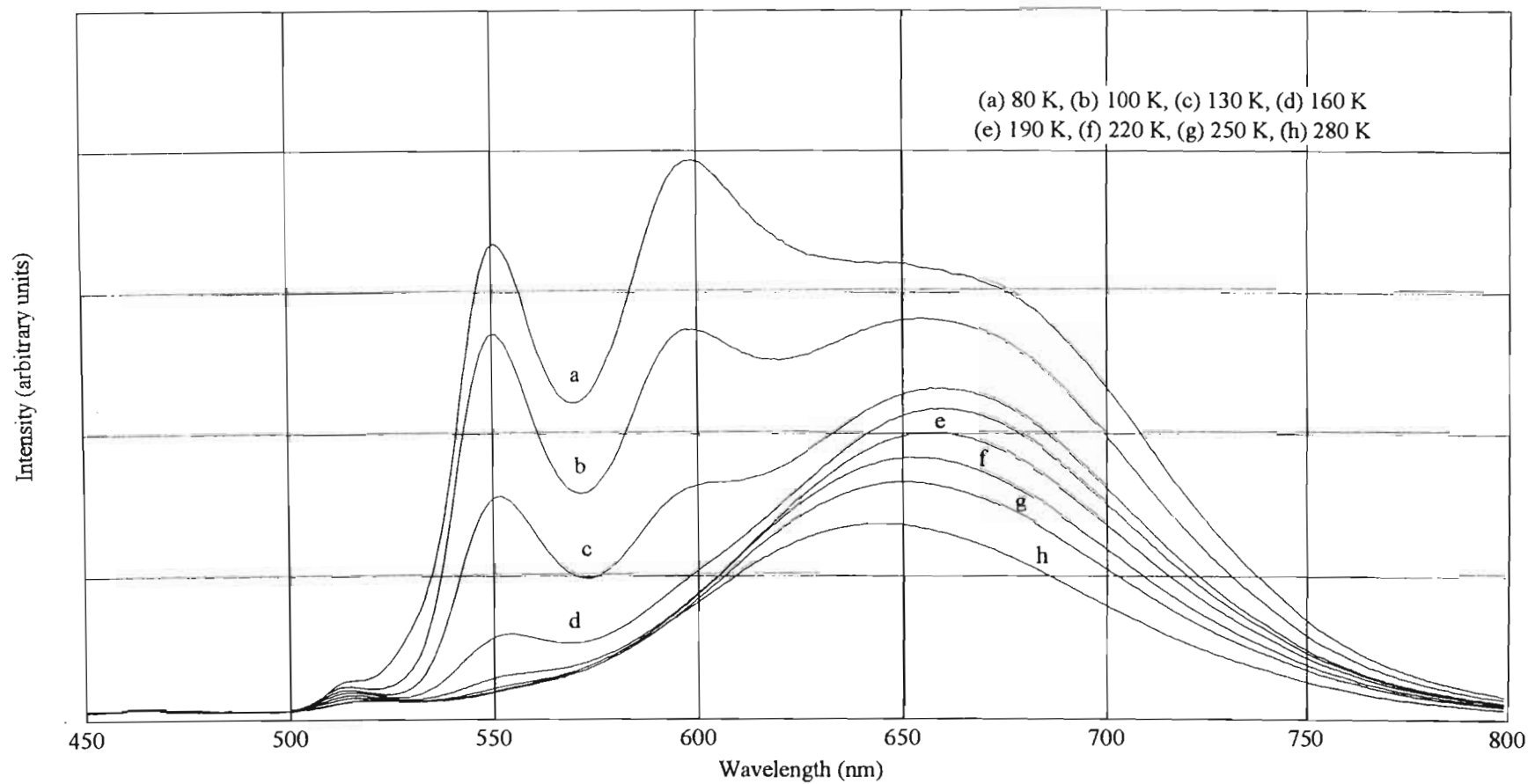
Figure 3.27 *The solid state emission spectrum of a crushed sample of [Pt(4'Ph-terpy)Cl](SbF₆) recorded over the range 80 to 280 K.*

yellow phase, recorded at 280 K (broad peak at *ca.* 640 nm with two vibrational features at 522 and 557 nm respectively). However, the intensities of the peaks in the two spectra are markedly different. Whereas the vibrational features in the emission spectrum of the yellow luminescent phase are well-resolved (see Figure 3.25), these features are poorly resolved in the spectrum of the orange luminescent phase and tend to be vanishingly weak when compared to the broad unstructured feature.

On decreasing the temperature of a crushed sample of [Pt(4'-Ph-terpy)Cl](SbF$_6$), the luminescent intensity increases (see Figure 3.27). Similar observations have been made for the [Pt(terpy)Cl]$^+$ and [Pt(bipy)$_2$]$^{2+}$ chromophores, as well as for the yellow luminescent phase of [Pt(4'-Ph-terpy)Cl](SbF$_6$), and is interpreted as being indicative of the presence of a thermally activated non-radiative deactivation pathway (see Section 3.4.2.3). Accompanying the increased luminescent intensity, a red-shift of 18 nm in the position of the broad feature (from 644 to 662 nm) occurs on decreasing the temperature of the sample from 280 to 160 K. As a result of peak overlap between this peak and a third vibrational feature which appears in the emission spectrum at temperatures below 160 K, an accurate assessment of any shifts in the position of the broad unstructured peak is not possible for sample temperatures below 160 K. A comparison of the red-shift in this case with that observed for of [Pt(terpy)Cl](CF$_3$SO$_3$), reveals that for the latter, the shift in peak position associated with the same variation in temperature also equals 18 nm. The analogous shift in the case of [Pt(terpy)Cl](BF$_4$) equals 14 nm (see Section 3.4.2.3). Furthermore, on decreasing the temperature of the crushed sample of [Pt(4'-Ph-terpy)Cl](SbF$_6$), the intensity of the highest energy vibrational feature [λ(em)$_{max}$ = 521 nm] increases only slightly whereas the second vibrational feature [λ(em)$_{max}$ = 554 nm] exhibits a substantial increase in luminescent intensity. These increases in luminescent intensity are accompanied by a blue-shift in the peak positions of both the vibrational features, the highest energy feature being shifted by 5 nm from 521 nm in the spectrum recorded at 280 K, to 516 nm in that recorded at 80 K. The second feature is also shifted by 5 nm, from 554 nm (280 K) to 549 nm (80 K). A third vibrational feature is resolved at temperatures between 160 and 80 K. Decreasing the temperature of the sample effects substantial increases in the intensity of this feature as well. An accurate assessment of any shift in the position of this feature is not possible due to overlap between it and the

broad unstructured feature, as discussed above. Nonetheless, indications are that this feature, like the other two vibrational features, also exhibits a blue-shift of the peak position on decreasing the temperature of the sample.

A comparison of the vibrational structure on the high energy side of the band envelope of the solid state emission spectrum of the orange luminescent form of [Pt(4'-Ph-terpy)Cl](SbF$_6$), recorded at 80 K, with the vibrational structure in the analogous spectrum of the yellow luminescent form, reveals that the peak positions and therefore the energy separation between the features are identical. The vibrational structure on the high energy side of the band envelope in the solid state emission spectra of [Pt(4'-Ph-terpy)Cl](SbF$_6$), recorded at different temperatures, is thus assigned to originate from the radiative decay of a $^3(\pi\text{-}\pi^*)$ 4'-phenylterpyridine excited state. The broad feature on the low energy side of the band envelope on the other hand, is identical in shape to the broad bands observed in the solid state emission spectra of [Pt(terpy)Cl](CF$_3$SO$_3$) (**10**) and [Pt(terpy)Cl](BF$_4$) (**11**) and, as pointed out above, displays an analogous red-shift in peak position on decreasing the temperature of the sample. Similar behaviour has been reported for [Pt(bipy)(CN)$_2$], [Pt(phen)(CN)$_2$] and the red polymorph of [Pt(bipy)Cl$_2$] and, as pointed out in Section 3.4.3.3, has been interpreted as being indicative of emission from a ($d_{\sigma^*} \rightarrow \pi^b$) transition associated with linear chain type compounds with metal-metal interactions between the stacked chromophores.[268] Emission from the $^3(d_{\sigma^*} \rightarrow \pi^b)$ excited state most probably comes into play in crushed samples of [Pt(4'-Ph-terpy)Cl](SbF$_6$) as a result of the crushing and grinding causing a modification of the lattice structure. This modification most probably involves a change-over from a situation where there are minimal, if any Pt-Pt interactions between the [Pt(4'-Ph-terpy)Cl]$^+$ chromophores in uncrushed samples of the salt, to a situation where definite Pt-Pt interactions are present in crushed samples.

From the above discussion it is clear that the luminescence from crushed samples of [Pt(4'-Ph-terpy)Cl](SbF$_6$) in the solid state, originates from separate excited states. A trivial situation which could give rise to a sample emitting from two separate excited states is that where the sample contains a luminescent impurity. Elemental analysis for C, H and N has confirmed the samples of [Pt(4'-Ph-terpy)Cl](SbF$_6$) used in the photophysical studies to be analytically pure. However, as pointed out in Section

3.4.2.3, the use of elemental analysis alone is not sufficient to guarantee sample purity when the phenomenon of interest is luminescence.[290] Since the $^3(\pi-\pi^*)$ component of the emission is also observed in the spectra of both uncrushed samples of [Pt(4'-Ph-terpy)Cl](SbF$_6$) and CH$_3$CN solutions containing the chromophore, it seems highly unlikely that this component of the emission spectrum originates from a luminescent impurity. This leaves the $(d_{\sigma^*} \to \pi^b)$ component. This component of the emission is only observed on crushing the sample and by its nature implies that chromophores exhibiting metal-metal interactions are involved. From this line of reasoning it follows that if samples of [Pt(4'-Ph-terpy)Cl](SbF$_6$) did contain a luminescent impurity, it had to be non-luminescent or exhibit vanishingly weak luminescence, both in the uncrushed solid state and in CH$_3$CN solution, and had to be present in a low enough concentration not to be detected by elemental analysis. Yet, on crushing the solid samples, sufficiently large amounts of the impurity chromophore had to be present to go from a situation where no metal-metal interactions are present to one where definite interactions are observed. Although these arguments cannot provide absolute proof that samples of [Pt(4'-Ph-terpy)Cl](SbF$_6$) did not contain trace amounts of a luminescent impurity, they do suggest that the likelihood of this having happened, is extremely limited.

This would suggest that the chromophores either exist in two crystallographically distinct environments in the crushed sample, the one with metal-metal interactions between the stacked chromophores and the other without, or that the chromophores all exist in a stacked type lattice with metal-metal interactions between them and furthermore exhibit simultaneous emission from both a $^3(\pi \to \pi^*)$ and a $(d_{\sigma^*} \to \pi^b)$ excited state. The only absolute way to distinguish between these two scenarios would be through single crystal X-ray diffractometric analysis. However, since *crushed* samples of [Pt(4'-Ph-terpy)Cl](SbF$_6$) are being considered here, such an analysis is not possible.

With respect to the first scenario, *i.e.* chromophores existing in two crystallographically distinct environments, one obvious suggestion is that only a fraction of the chromophores is converted from the yellow to the orange luminescent form during crushing and that the emission spectrum of a crushed sample of [Pt(4'-Ph-

terpy)Cl](SbF$_6$) actually is a superposition of the emission spectra of the pure yellow and orange luminescent forms. This suggestion can most probably be discounted since the intensity of the vibrational feature of highest energy in the variable temperature solid state emission spectra of the orange luminescent form, is considerable lower than that of the same feature in the corresponding spectra of the yellow luminescent form. This difference in the solid state spectra would rather suggest that some molecular distortion is associated with the $^3(\pi \rightarrow \pi^*)$ excited state from which the vibrationally structured component of the emission from crushed samples originates. The first explanation for the luminescence from crushed samples of [Pt(4'-Ph-terpy)Cl](SbF$_6$) thus involves the chromophores existing in two crystallographically distinct environments; one with the chromophores displaying very little, if any, metal-metal interaction and emitting from a distorted $^3(\pi-\pi^*)$ excited state, the other with the chromophores arranged in a stacked configuration with metal-metal interactions between the chromophores and emitting from a $(d_{\sigma^*} \rightarrow \pi^b)$ excited state. Both the distorted $^3(\pi-\pi^*)$ IL and the $(d_{\sigma^*} \rightarrow \pi^b)$ MLCT excited state is associated with thermally activated deactivation pathways, thus explaining the increases in luminescent intensity observed on decreasing the temperature of the sample.

The second explanation suggested above involves all the [Pt(4'-Ph-terpy)Cl]$^+$ chromophores existing in a stacked configuration with metal-metal interactions between them. In this scenario the chromophores are suggested to simultaneously emit from both the $^3(\pi-\pi^*)$ IL and the $(d_{\sigma^*} \rightarrow \pi^b)$ MLCT excited states.

At this point the temperature dependence of the emission spectrum is of interest. As pointed out in the above discussion, the $^3(\pi-\pi^*)$ component in spectra of the orange luminescent phase, recorded at higher temperatures, is of considerably lower intensity than that in spectra recorded at lower temperatures. Furthermore, the $^3(\pi-\pi^*)$ component tends towards being vanishingly weak when compared to the $(d_{\sigma^*} \rightarrow \pi^b)$ component at temperatures of ca. 280 K. This reduction in luminescent intensity of the $^3(\pi-\pi^*)$ component at increased temperatures, probably is the result of either an interconversion with the $(d_{\sigma^*} \rightarrow \pi^b)$ state becoming more efficient, or of other radiationless processes increasing in efficiency. To distinguish between these relaxation pathways would require quite sophisticated photophysical experiments. Recall that

emission from crushed samples in the solid state, which most probably contain the chromophores in a distorted state, is being considered, thus ruling out the possibility of comparative or quenching studies in solution where the chromophore is bound to exist in a different molecular environment. On the other hand, the temperature dependence of the emission spectra of crushed samples of [Pt(4'-Ph-terpy)Cl](SbF$_6$) is remarkably similar to that of the [Cu(2,9-Me$_2$-1,10-phen)(PPh$_3$)$_2$]$^+$ chromophore.[307] It is also analogous to the substituent dependent variation in the emission spectra of the [Cu(5-X-phen)(PPh$_3$)$_2$]$^+$ and [Cu(4,7-X$_2$-phen)(PPh$_3$)$_2$]$^+$ chromophores (X = H, CH$_3$, Cl or Ph).[302] For each of the latter three chromophores an interconversion between the $^3(\pi\text{-}\pi^*)$ and a triplet charge transfer (^{3}CT) state was invoked to explain the variation in their emission spectra. Based on the strong resemblance between the variable temperature emission spectra of crushed samples of [Pt(4'-Ph-terpy)Cl](SbF$_6$) and the spectra of these three chromophores, it is tempting to suggest that the temperature dependent variation in the emission spectrum of the platinum containing chromophore is attributable to a similar mechanism, *i.e.* interconversion between the $^3(\pi\text{-}\pi^*)$ and $(d_{\sigma^*}\rightarrow\pi^b)$ states.

In this regard it is important to realise that whereas the $^3(\pi\text{-}\pi^*)$ IL transition involves electron transfer between ligand-based orbitals, the $(d_{\sigma^*}\rightarrow\pi^b)$ MLCT transition involves charge transfer from orbitals which are metal-based to orbitals which are ligand-based. The latter transition thus formally involves the generation of a Pt(III) centre and one can thus expect that there is some difference between the equilibrium geometries of the $^3(\pi\text{-}\pi^*)$ IL and the $(d_{\sigma^*}\rightarrow\pi^b)$ MLCT excited states. At the appropriate temperatures however, the thermal energy available to the molecules might be sufficient to enable vibronic interactions to couple the two states and allow for the interconversion between the $^3(\pi\text{-}\pi^*)$ IL and the $(d_{\sigma^*}\rightarrow\pi^b)$ MLCT excited states. In such an instance radiative decay from the lowest energy excited state, *i.e.* the $(d_{\sigma^*}\rightarrow\pi^b)$ MLCT excited state in this case, will predominate. Conversely, at low temperatures in a rigid matrix, the interconversion will be inhibited and one would expect to observe radiative decay from both excited states, *i.e.* $^3(\pi\text{-}\pi^*)$ IL and $(d_{\sigma^*}\rightarrow\pi^b)$ MLCT in this case.

270

3.4.6 [Pt(terpy)(C≡CPh)](SbF₆) (15)

3.4.6.1 Synthesis and characterization

A large number of reports describing the luminescence of platinum-polypyridyl complexes have been published. Similarly, the luminescent properties of complexes containing the Pt-C≡CPh moiety have also received some attention, yet the synthesis and photophysical properties of chromophores in which both of these ligands are coordinated to the same platinum centre have remained virtually unexplored. A literature search in this regard has revealed only one report on a chromophore of this type, the compound of interest being [Pt(phen)(C≡CPh)₂].[509] As a logical extension to the work presented here, it was decided to pursue the synthesis and study of the luminescent properties of the [Pt(terpy)(C≡CPh)]⁺ chromophore. Both the terpyridine and phenylacetylide ligands are planar. This, together with the square planar coordination geometry of the Pt centre provides for the possibility that the [Pt(terpy)(C≡CPh)]⁺ chromophore could be completely planar, which in turn implies that the possibility of face-to-face stacking in the solid state and extended interactions between such stacked chromophores exists.

Two methods for the synthesis of [Pt(terpy)(C≡CPh)](SbF₆) have been developed. Both of these rely on displacing the coordinated Cl⁻ ligand on the [Pt(terpy)Cl]⁺ chromophore with the phenylacetylide ligand.

The first method involves treating a suspension of [Pt(terpy)Cl](SbF₆) in pyridine with a 5% excess of AgC≡CPh.[308] Allowing the reaction mixture to stir for *ca.* 15 hours resulted in the suspension changing colour from yellow-orange to bright red. The solid component of the suspension was isolated by filtration, washed with diethyl ether and dried *in vacuo*. This resulted in the solid changing colour from bright red to a pale brown. The brown material was placed in the vapour extraction apparatus depicted in Section A.2.1.2 of Appendix A and the [Pt(terpy)(C≡CPh)](SbF₆) content extracted into boiling CH₃CN. Reducing the volume of this solution to a minimum and slowly cooling it to *ca.* -10°C resulted in the product precipitating as a dark purple-brown

microcrystalline solid. Elemental analysis for C, H and N was consistent with the empirical formula, $[Pt(terpy)(C{\equiv}CPh)](SbF_6)$.

The second and preferred method involves adding an approximately twice molar amount of $Bu_3SnC{\equiv}CPh$, obtained by treating $HC{\equiv}CPh$ with Bu_3SnCl,[309] to a suspension of $[Pt(terpy)Cl](SbF_6)$ in CH_3CN and heating the mixture to reflux for 4 to 6 hours. During this period the product precipitated as an orange microcrystalline solid. Allowing the solution to cool to room temperature resulted in more of the product precipitating out. The precipitate was isolated through filtration, washed with *n*-hexane, cold acetonitrile and diethyl ether and dried *in vacuo*. Elemental analysis for C, H and N confirmed the composition of the product to be consistent with the empirical formula $[Pt(terpy)(C{\equiv}CPh)](SbF_6)$.

From the different colours of the product obtained from the two synthetic methods outlined above, it is clear that $[Pt(terpy)(C{\equiv}CPh)](SbF_6)$ exhibits polymorphic behaviour. The orange polymorph obtained from the second synthetic route can be converted to the purple-brown form by preparing a hot, saturated CH_3CN solution of the product and slowly cooling it to *ca.* -10°C, resulting in the precipitation of the purple-brown polymorph. However, since we have managed to grow single crystals of the orange polymorph and determine its crystal structure, subsequent attention focused mainly on this polymorph. Despite repeated efforts utilizing a variety of crystal growth and precipitation techniques, we have not been able to devise a high-yielding method for converting the purple-brown polymorph to the orange form.

The solid state infrared spectrum of $[Pt(terpy)(C{\equiv}CPh)](SbF_6)$, was recorded as a KBr pellet, a list of the most prominent peaks being provided in Table 3.1. The spectrum displays a single weak, but well-defined peak at 2124 cm^{-1} which is assigned to the $C{\equiv}C$ stretching vibration of the phenylacetylide ligand. This is not dissimilar to the spectrum of $[Pt_2(\mu\text{-}C{=}CHPh)(C{\equiv}CPh)(PEt_3)_3Cl]$[310] for instance, where a weak band was resolved between 2110 and 2115 cm^{-1} and the same assignment was favoured. The spectrum of $[Pt(terpy)(C{\equiv}CPh)](SbF_6)$ also displays a number of peaks in the range 1650 to 780 cm^{-1}, which by comparison with other Pt(terpy) complexes included in this study, can be assigned to originate from the coordinated terpyridine ligand. The

wavelengths are also in good agreement with those reported for the solid state spectrum of [Pt(terpy)(SCH$_2$CO$_2$CH$_2$CH$_3$)](PF$_6$),[270] for instance. Close scrutiny of the peaks in this range did, however, reveal that the spectrum of [Pt(terpy)Cl](SbF$_6$) displays a single peak at 1480 cm^{-1}, whereas the spectrum of [Pt(terpy)(C≡CPh)]-(SbF$_6$) displays two peaks with wavenumbers 1485 and 1476 cm^{-1}, respectively. This difference most probably is the result of a solid state effect. The spectrum of **15** also displays the customary peak at *ca.* 655 nm associated with the SbF$_6^-$ anion.

3.4.6.2 Structural studies on [Pt(terpy)(C≡CPh)](SbF$_6$) (**15**)

Orange needle-like single crystals of [Pt(terpy)(C≡CPh)](SbF$_6$), suitable for X-ray diffractometric studies, were grown by dissolving the salt in CH$_3$CN and allowing the solvent to evaporate slowly over a period of several days.

[Pt(terpy)(C≡CPh)](SbF$_6$) crystallizes in the monoclinic space group $P2_1/n$. Both the complex cation and the anion are situated in general equivalent positions with the asymmetric unit consisting of one cation and one anion. This implies that the unit cell is comprised of four formula units and that there are no crystallographically imposed symmetry relationships between any of the atoms constituting the complex cation or the anion. The unit cell dimensions, a full list of interatomic distances and angles and other pertinent crystallographic data are collected in Tables 3.17 to 3.21 at the end of this chapter.

The molecular geometry of the [Pt(terpy)(C≡CPh)]$^+$ cation and the numbering scheme employed is provided in Figure 3.28. The cation comprises a Pt(II) centre to which the three nitrogen atoms of the chelating terpyridine ligand and the terminal C atom of the phenylacetylide ligand are coordinated. As such the coordination geometry around the Pt centre is essentially square planar, with any deviations from idealized geometry being the result of the geometric constraints imposed by the terpyridine ligand, *vide infra*.

The interatomic distances between the Pt centre and the nitrogen atoms N(1), N(2) and N(3) are 2.06(3), 1.94(3) and 2.05(3)Å respectively, with the angles N(1)-Pt-N(2) and N(2)-Pt-N(3) being 84(1)° and 79(1)°. Although the standard errors associated with the bond lengths and angles quoted here are somewhat larger than those associated
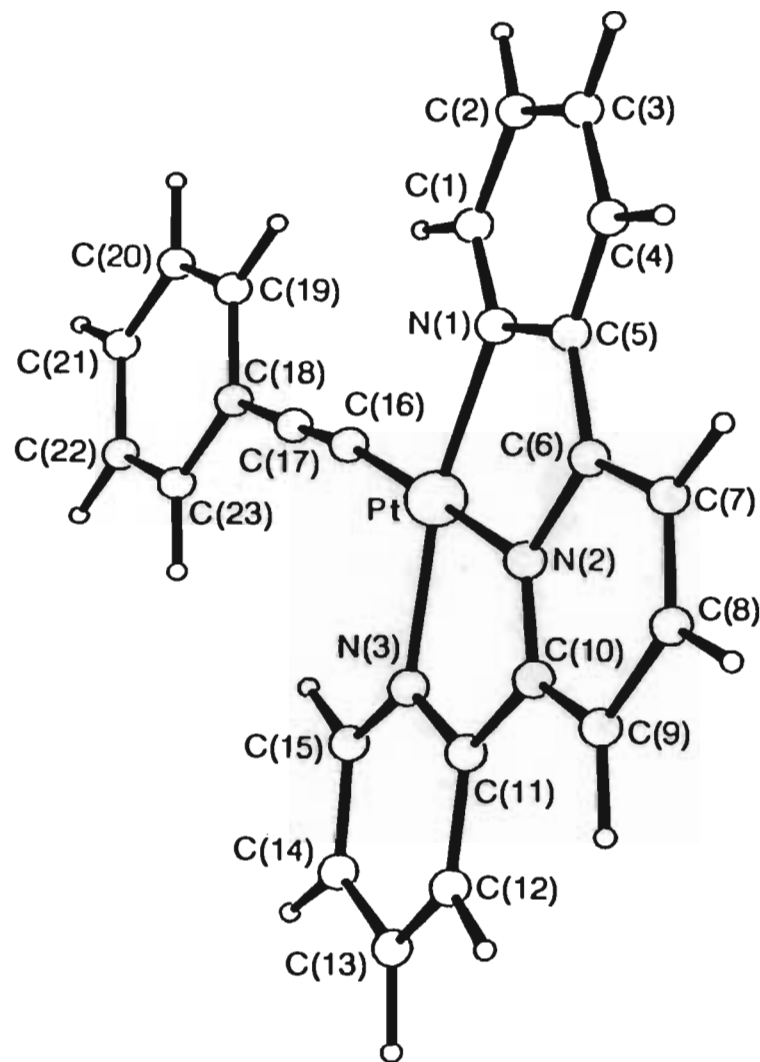
Figure 3.28 *The molecular geometry and numbering scheme employed for the [Pt(terpy)(C≡CPh)]⁺ cation.*

with the structure determination of $[Pt(terpy)(CH_3CN)](SbF_6)_2$ (**8**) for instance, the values are still in good agreement with those reported for the latter compound. Furthermore, the Pt-N bond distances display the by now familiar variation in bond lengths associated with Pt(terpy) complexes, with the distance from the platinum atom to the "bridgehead" nitrogen atom, N(2) being *ca.* 0.1 Å shorter than those between the platinum and nitrogen atoms N(1) and N(3) (see Section 3.4.2.2). This variation in bond length is the result of the geometric constraints imposed by the terpyridine ligand which also manifests itself in the N-Pt-N angles deviating from the idealized value of 90°, *vide supra*. The terpyridine ligand is slightly ruffled, the mean planes of the terminal pyridine rings defining dihedral angles of 2.6 and 3.4° with that of the central pyridine ring. These values are not unusual. The analogous angles associated with the $[Pt(terpy)(CH_3CN)]^{2+}$ chromophore equal 2.1 and 3.2° respectively (see Section 3.4.2.2), whereas in the case of the $[Pt(terpy)(OMe)]^+$ chromophore, as reported by McMillin and co-workers,[260] the angles are equal 3.6° and 6.6°.

The internal bond lengths and angles associated with the terpyridine ligand are in good agreement with those reported for $[Pt(terpy)(SCH_2CH_2OH)](NO_3)^{(270)}$ for instance, and will not be discussed here in any further detail.

The phenylacetylide ligand exhibits small deviations from the mean plane defined by the Pt centre and the terpyridine ligand. The phenyl ring of the ligand defines a dihedral angle of 2.9° with the latter plane, whereas C(18) deviates by 0.08Å from the plane. However, these deviations are small in comparison to the standard errors associated with them and would indicate that to all intents and purposes, the $[Pt(terpy)(C\equiv CPh)]^+$ chromophore can be regarded as being essentially planar.

The Pt-C(16) distance [C(16) being the coordinated "acetylide carbon"] equals 1.94(4)Å. This value is comparable to that of 2.00Å predicted by Lappert, Muir and co-workers[311] for the length of a Pt-C(*sp*) single bond, and is well within the range of values found in the literature, these values ranging between 1.92(1)Å, as observed in $[\{Pt(NCS)(PEt_3)_2\}_2\{p\text{-}C_6H_4(C\equiv C)_2\}]^{(312)}$ for instance, and 2.05(2)Å as found in $[Pt_2(\mu\text{-}C=CHPh)(C\equiv CPh)(PEt_3)_3Cl]^{(310)}$ The C≡C bond length in compound **15** [C(16) to C(17)] is equal to 1.23(4)Å. This value is in good agreement with that of 1.212Å,

the C≡C bond length of acetylene as determined from electron diffraction in the gas phase.[311] Similar values have also been reported for the C≡C bonds of the *trans*-[Pt(C≡CPh)(NH$_2$C$_6$H$_4$F)(PPh$_3$)$_2$]$^+$ cation [C≡C bond length = 1.21(5)][314] and [(PhC≡C)$_2$(Et$_3$P)$_2$Pt{1,4-(4-NO$_2$C$_6$H$_4$)$_2$N$_4$}] [C≡C bond lengths = 1.20(2) and 1.19(2)].[315]

Each of the [Pt(terpy)(C≡CPh)]$^+$ chromophores participate in "face-to-face" stacking with its closest neighbouring cation, thus generating a series of extended stacks running parallel to the [a]-axis. A diagram depicting one such stack, as seen in a view along the [a]-axis, is provided in Figure 3.29. The individual chromophores within each of these stacks are interrelated by centres of inversion, the latter being separated by 3.765 Å, *i.e.* half the length of the [a]-axis. As a consequence of this relationship between the chromophores within a stack, symmetry dictates that the mean planes of these chromophores necessarily are parallel to each other. Mean plane calculations have revealed the interplanar spacing between the stacked chromophores to be uniform, and to be equal to 3.23Å (see Figure 3.30). This distance is substantially smaller than 3.45Å, the Van der Waal's separation for π-aromatic species occurring in a face-to-face arrangement,[242] and would strongly suggest that there are some orbital interactions present between neighbouring chromophores within the stacks, *vide infra*. It is also interesting to note that the uniform spacing of the chromophores within the stacks is not enforced by symmetry.

A comparison of the interplanar spacing between the chromophores with the spacing of the centres of inversion relating each of the chromophores within the face-to-face stacked arrangement, reveals that the interplanar spacing is substantially smaller than the latter. This difference in spacing results from the fact that the normals to the planes of the stacked chromophores are not parallel to the [a]-axis, *i.e.* the stacking axis. In fact, the angle between the normal to the plane defined by the Pt, the three N atoms of the terpyridine ligand and the terminal C atom of the phenylacetylide ligand of any chromophore and the [a]-axis equals 28.7°. A further consequence of the inversion symmetry relating adjacent chromophores in the face-to-face arrangement, is that the chromophores occur in a head-to-tail arrangement. This, together with the fact that the Pt-centres are laterally offset from the stacking axis, implies that the Pt-Pt separation
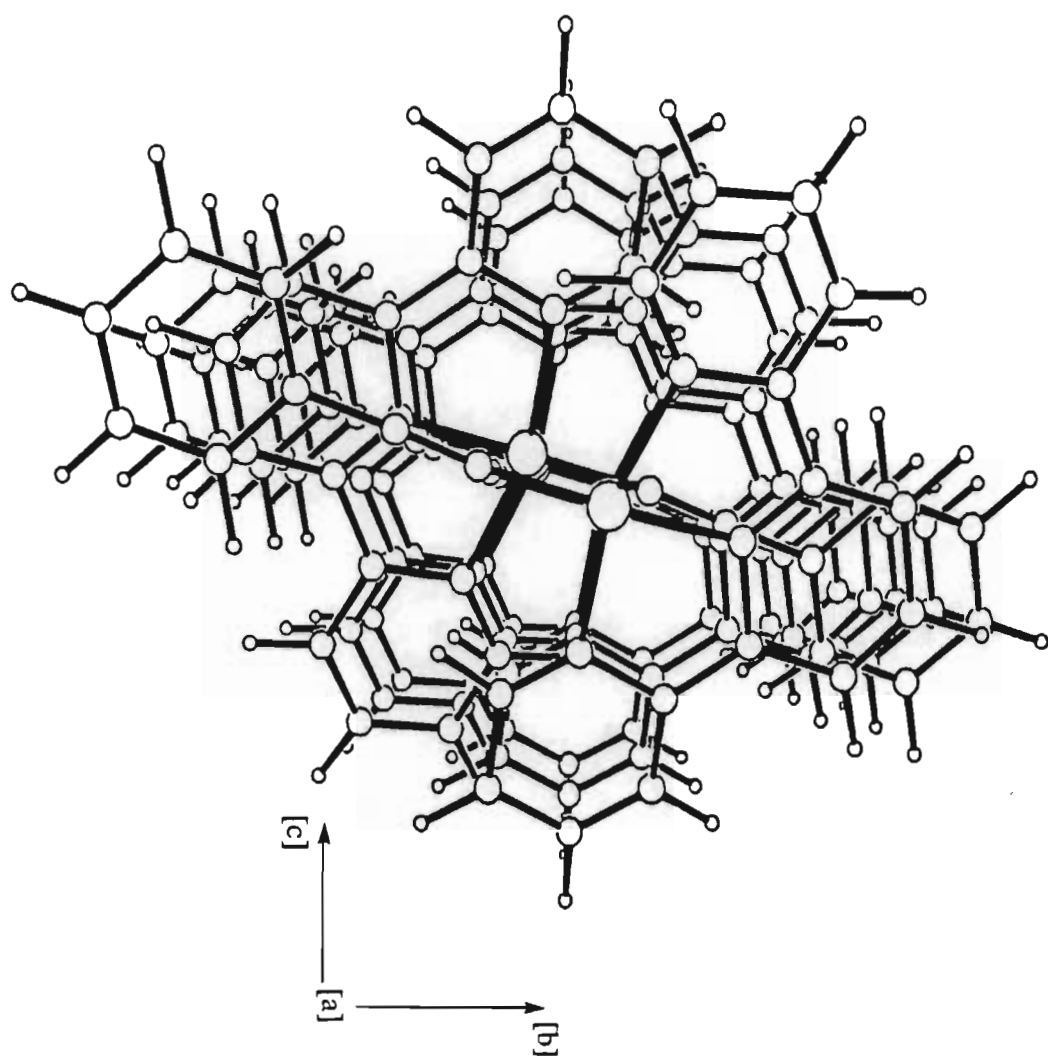
Figure 3.29   A stack of [Pt(terpy)(C≡CPh)]+ cations as seen in a view along the [a]-axis.
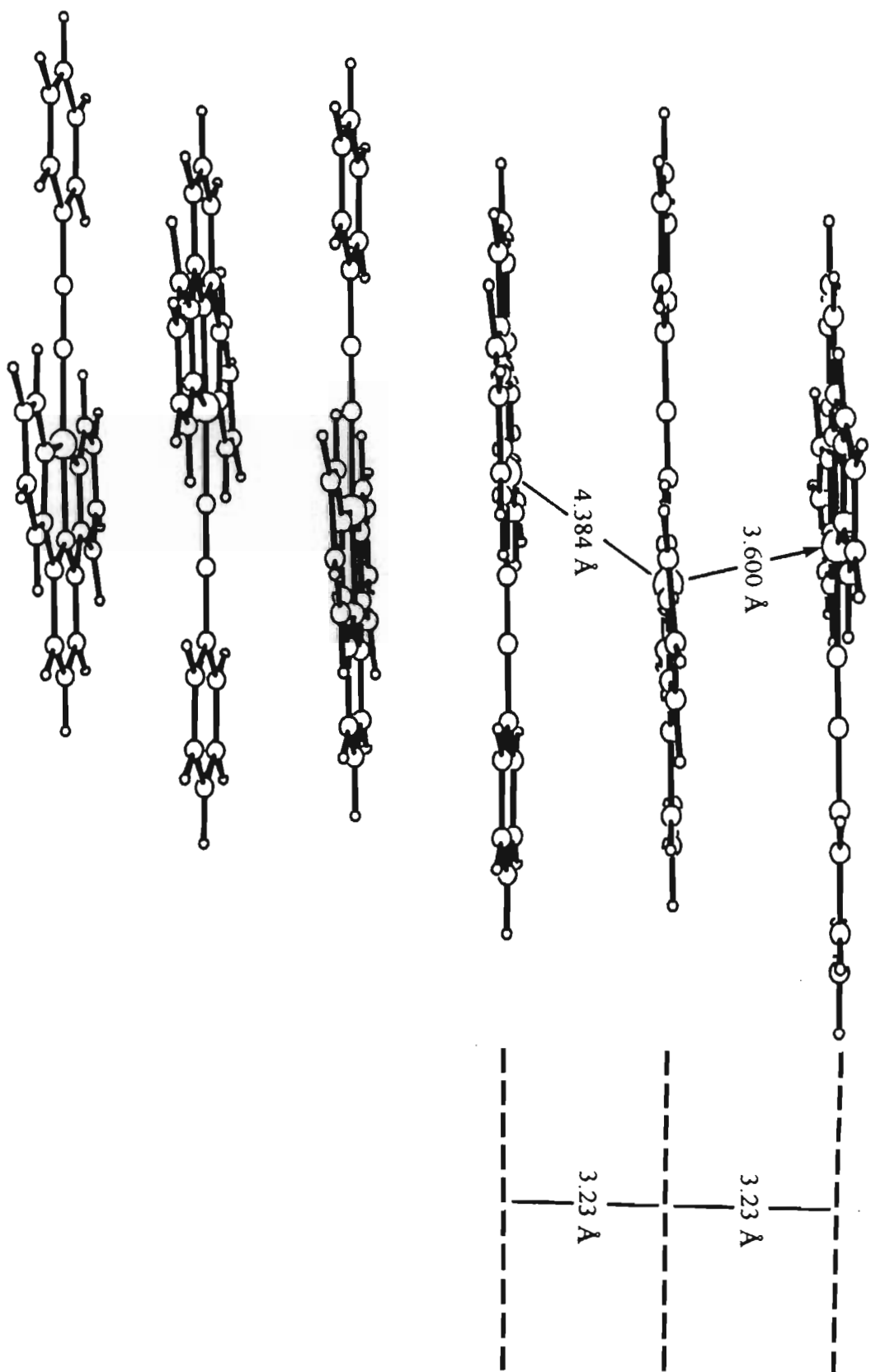
Figure 3.30 An alternative view of the stacked [Pt(terpy)(C≡CPh)]⁺ chromophores in [Pt(terpy)(C≡CPh)](SbF₆).

Labels within figure: 4.384 Å, 3.600 Å, 3.23 Å, 3.23 Å
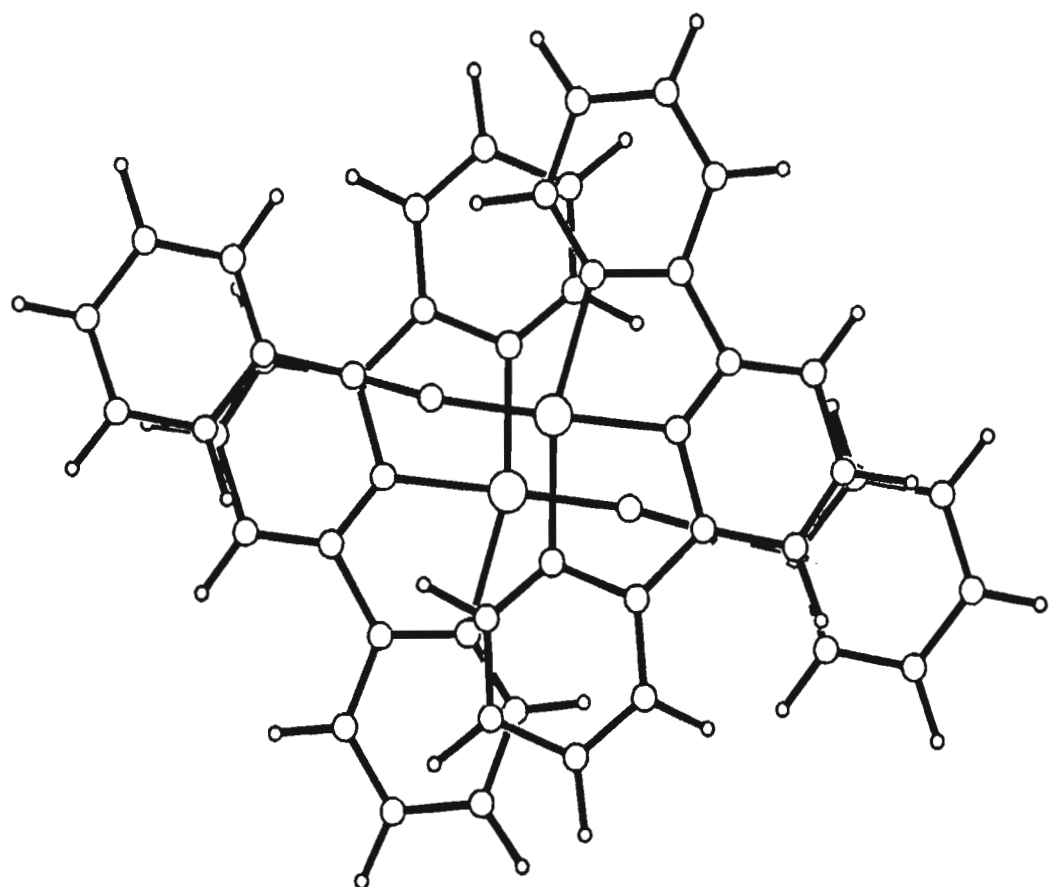
Figure 3.31 Overlap between neighbouring [Pt(terpy)(C≡CPh)]⁺ chromophores in [Pt(terpy)(C≡CPh)](SbF₆) (Pt–Pt distance = 3.600Å).
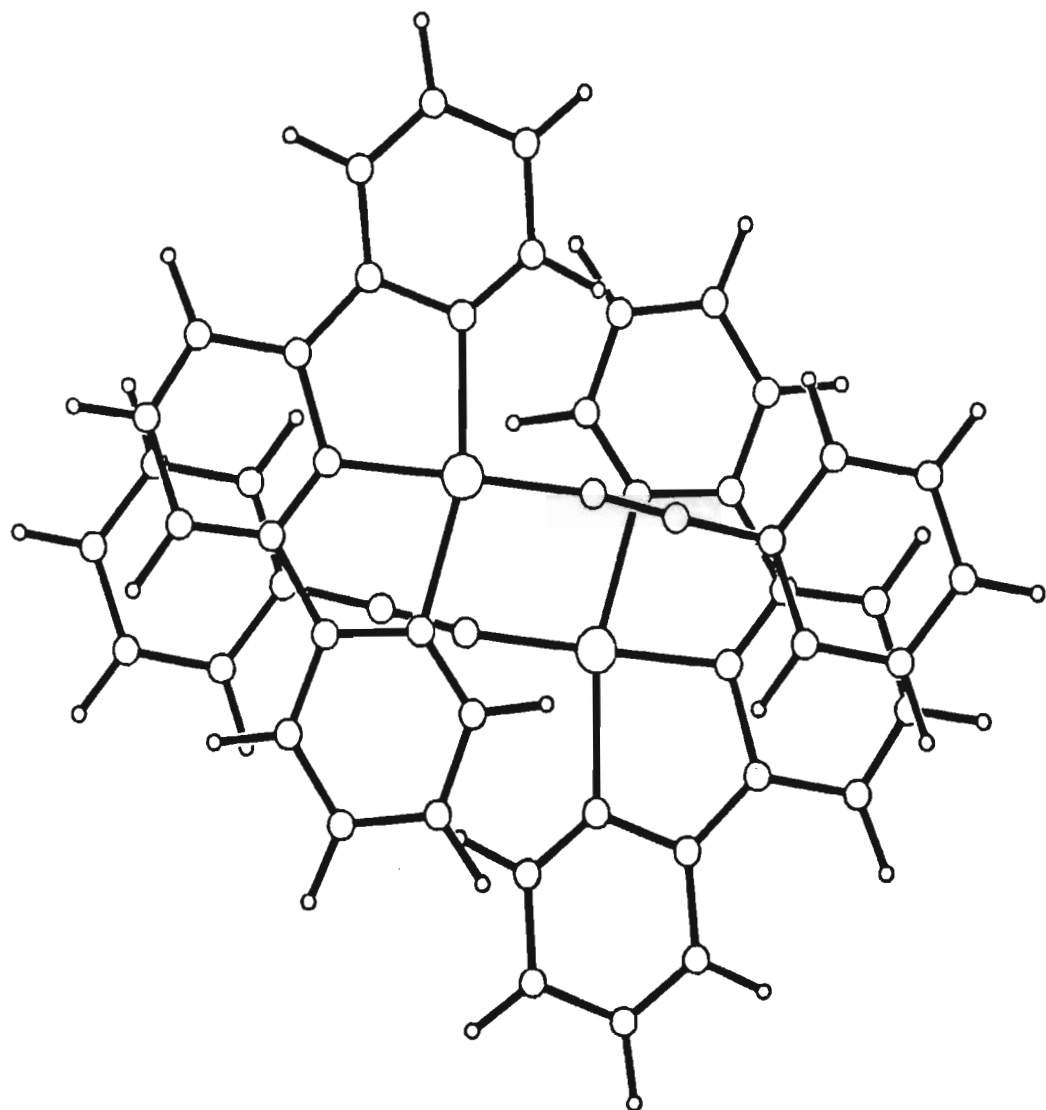
Figure 3.32   *Overlap between neighbouring [Pt(terpy)(C≡CPh)]⁺ chromophores in [Pt(terpy)(C≡CPh)](SbF₆) (Pt-Pt distance = 4.384Å).*

within the extended stacks are not uniform. Instead, two distinct Pt-Pt separations are observed to alternate along the stacks, these distances being 3.600 and 4.384 Å (see Figure 3.30). The shorter of these two distances is comparable to the Pt-Pt separation of 3.5721(8)Å, reported for [Pt(terpy)(SCH$_2$CH$_2$OH)](NO$_3$),[270] but is significantly longer than that of 3.329(1)Å observed in [Pt(terpy)Cl](CF$_3$SO$_3$)[263] and that of 3.45Å, reported for the red form of [Pt(bipy)Cl$_2$].[258]

Considering the variation in Pt-Pt separation against the backdrop of the uniform interplanar distance between the stacked chromophores, this distance being less than the Van der Waal's separation for π-aromatic species in a face-to-face arrangement, it is evident that two different modes of orbital overlap are present and alternate along the extended stacks. Figure 3.31 displays the overlap between two chromophores with a Pt-Pt separation of 3.600Å as seen in a view perpendicular to the mean planes of the chromophores. Within this arrangement the carbon atoms C(17), C(18) and C(19) of the acetylide ligand of one [Pt(terpy)(C≡CPh)]$^+$ cation are positioned directly above the carbon atoms C(6), C(7) and C(8) of the central pyridine ring of the other cation's terpyridine ligand. Similarly, the N-C bond between N(3) and C(15) of one chromophore is positioned directly above the C-C bond between C(1) and C(2) of the other.

A diagram displaying the overlap between two chromophores with a Pt-Pt separation of 4.384Å, as seen in a view perpendicular to the mean plane of the chromophores, is provided in Figure 3.32. In this instance the acetylide C≡C bond between C(16) and C(17) is positioned directly above the nitrogen atom N(3) of one of the outer pyridine rings of the other cation's terpydine ligand. Furthermore there is partial ring-ring overlap between the phenyl ring [C(18), C(22) and C(23)] of the acetylide ligand on one chromophore, with the central pyridine ring [C(8), C(9) and C(10)] of the terpyridine ligand of the other.

3.4.6.3 Photophysical studies on [Pt(terpy)(C≡CPh)](SbF$_6$) (15)

The room temperature absorption spectrum of a CH$_3$CN solution of 15 is depicted in Figure 3.33 and the wavelengths, λ(abs)$_{max}$, associated with the absorption maxima are listed in Table 3.4.
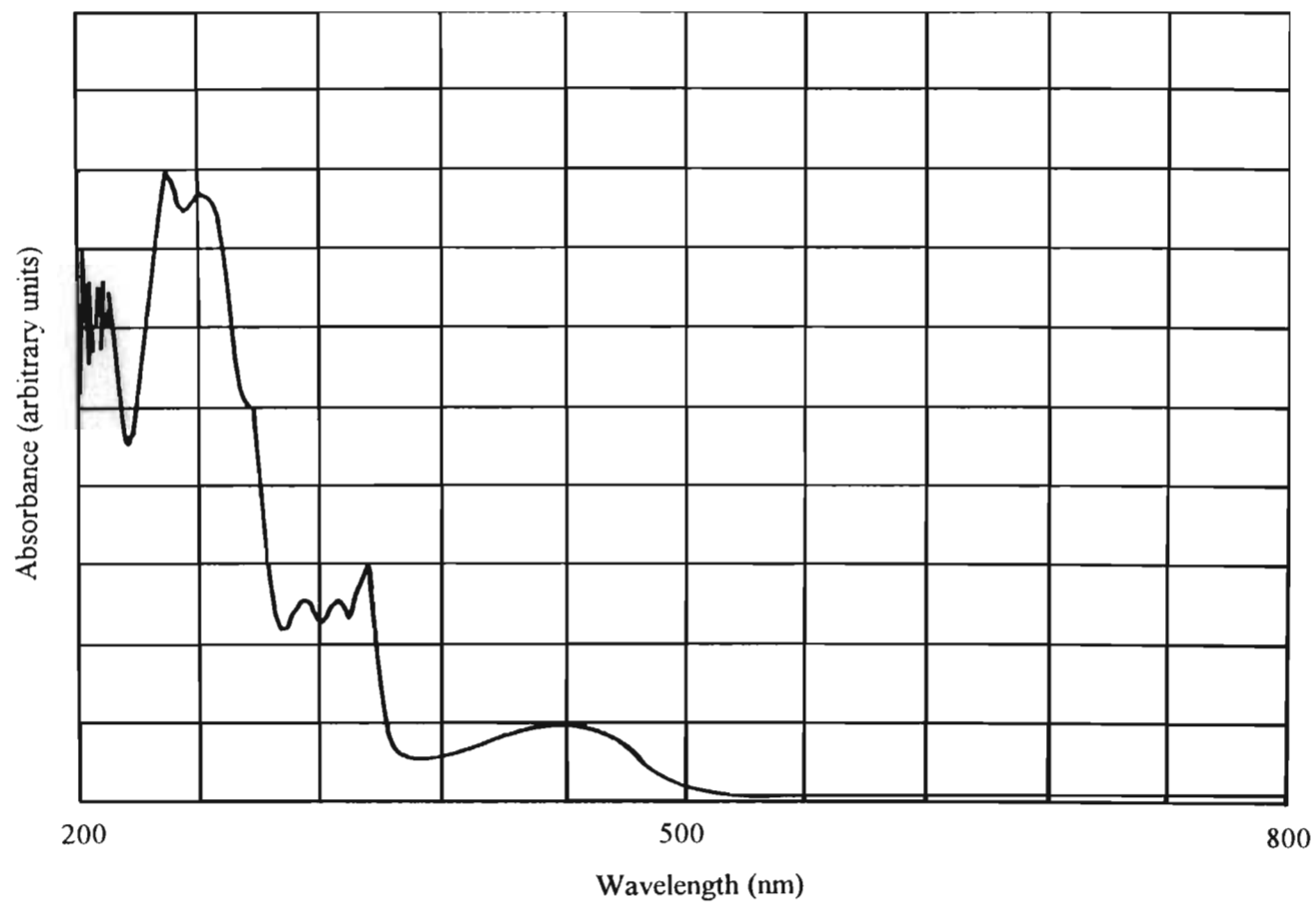
Figure 3.33   *The absorption spectrum of a CH₃CN solution of [Pt(terpy)(C≡CPh)](SbF₆) recorded at room temperature.*

A comparison of the absorption spectrum of [Pt(terpy)(C≡CPh)](SbF$_6$) with that of the [Pt(terpy)Cl]$^+$ chromophore as reported here and by McMillin and co-workers,[260] reveals that the spectra are essentially identical at wavelengths lower than 350 nm, the only differences being an increase in the absorption at 261 nm and a reduction in the relative intensity of the sharp transition observed at 280 nm in the spectrum of the [Pt(terpy)Cl]$^+$ chromophore. The latter feature appears as a shoulder at 284 nm in the absorption spectrum of [Pt(terpy)(C≡CPh)](SbF$_6$). In accordance with the assignment of the absorption features in the spectrum of the [Pt(terpy)Cl]$^+$ chromophore, the shoulder at 284 nm, as well as the vibrationally structured band between 310 and 345 nm, can be assigned to π-π* transitions of the coordinated terpyridine ligand. The increased absorption at 261 nm, as well as the reduction in the relative intensity of the band at 284 nm, most probably results from π-π* transitions of the phenyl group of the phenylacetylide ligand, the associated bands of which overlap with and partially obscure the bands associated with the coordinated terpyridine ligand. This suggestion is consistent with the absorption spectrum of phenylacetylene which exhibits bands at 272, 248 and 238 nm.[310] In addition to the features discussed above, the absorption spectrum of [Pt(terpy)(C≡CPh)](SbF$_6$) also exhibits a single very broad feature with λ(abs)$_{max}$ at 440 nm.

The absorption spectrum of [Zn(terpy)$_2$]$^{2+}$, which is known not to possess any absorption features originating from charge transfer transitions, does not display any peaks with λ(abs)$_{max}$ higher than 350 nm. It is thus possible that the broad feature at 440 nm originates from a charge transfer transition. Che and co-workers[248] have observed an analogous broad feature centred at 394 nm in the absorption spectrum of [Pt(phen)(C≡CPh)$_2$], recorded in CH$_3$CN solution, and have assigned it to a Pt→π*(phen) MLCT transition. The corresponding transition in the case of the [Pt(terpy)(C≡CPh)]$^+$ chromophore would be a Pt→π*(terpy) MLCT transition. However, the wavelength (440 nm) associated with the broad feature in the spectrum of [Pt(terpy)(C≡CPh)](SbF$_6$) is substantially higher than that associated with both the Pt→π*(phen) MLCT transition of [Pt(phen)(C≡CPh)$_2$][248] and the Pt→π*(terpy) MLCT transition of the [Pt(terpy)Cl]$^+$ chromophore.[260, 263]

Another possibility is that the transition could result from a Pt→C≡CPh type MLCT transition. In this context, Che and co-workers[313] have assigned a band centred at 345 nm in the absorption spectrum of [Pt(dppm)$_2$(C≡CPh)$_2$] to a transition, which is a hybrid of the Pt(5d)→C≡CPh MLCT and acetylide intraligand π-π* transitions. Furthermore, a band with λ(abs)$_{max}$ at 387 nm in the spectrum of [(C≡CPh)$_2$Pt(dppm)$_2$Au](PF$_6$) was assigned to a ^{1}(d$_{\sigma^*}$→1π*) MMLCT transition, *i.e.* a metal-metal bond to ligand charge transfer transition,[313] where the 1π* orbital originates from the phenylacetylide ligand. However, the wavelengths associated with the transitions mentioned above are also substantially lower than that associated with the broad feature in the absorption spectrum of the [Pt(terpy)(C≡CPh)]$^+$ chromophore.

A third possibility is that of a ligand-to-ligand charge transfer transition. The phenylacetylide ligand is known to be a good σ-donor ligand, whereas the terpyridine ligand is classified as a π-acceptor ligand. The proposed LLCT state would thus involve the transfer of electron density from the phenylacetylide ligand to the terpyridine ligand. Although LLCT states have been reported previously,[261, 262] the frequency of the occurrence of such transitions are quite low when compared to that of MLCT transitions.

Yet another possibility is that the band originates from absorption by dimeric or even oligomeric species in solution. Although the solutions used in recording the absorption spectra were dilute, the possibility of dimer or even oligomer formation in solution can not be discounted. The orbital interactions associated with such dimers or oligomers will give rise to a new low energy excited state, thus explaining the high wavelength or low energy associated with the band.

It might also be suggested that the broad feature has its origin in absorption by an impurity. Elemental analysis for C, H, and N have confirmed the sample used in recording the absorption spectrum to be analytically pure. Although this does not provide absolute proof that the sample was spectroscopically pure, it does suggest that if there was an impurity present in the sample, it had to be present in exceedingly low concentrations. Furthermore, an analogous feature, centred at 458 nm, is observed in the absorption spectrum of [Pt(4'-Ph-terpy)(C≡CPh)](SbF$_6$) (**16**) recorded in CH$_3$CN

solution (see Section 3.4.7.3), thus suggesting that the broad feature in the absorption spectrum of **15** does not originate from absorption by an impurity.

From the above discussion it is clear that the broad low-energy feature could originate from one or even a combination of different charge transfer transitions. Unfortunately, an unequivocal assignment of such a charge transfer transition(s) to a specific orbital origin is not possible without the aid of molecular orbital calculations or other supporting evidence.

The emission properties of [Pt(terpy)(C≡CPh)](SbF$_6$) were studied both in fluid solution at room temperature and in the solid state at 40 K intervals over the temperature range 80 to 280 K.

The emission spectra of **15**, in fluid solution, are presented in Figure 3.34. The spectrum recorded in CH$_3$CN solution consists of a single asymmetric band with no vibrational structure, the maximum emission intensity occurring at 608 nm. On the other hand, the spectrum recorded in CH$_2$Cl$_2$ solution also consists of a single broad asymmetric band, but seems to possess some unresolved structure concealed on the high-energy side of the band envelope. Furthermore, the latter spectrum is red-shifted by 11 nm with respect to that recorded in CH$_3$CN, the maximum emission intensity occurring at 619 nm.

Che and co-workers[248] have reported an identical band shape to that of the spectrum of **15** in CH$_3$CN, for the emission spectrum of [Pt(phen)(C≡CPh)$_2$], recorded in an ethanol solution at room temperature. However, the wavelength associated with the maximum emission intensity for the latter is somewhat lower than that of the [Pt(terpy)(C≡CPh)]$^+$ chromophore. In CH$_2$Cl$_2$ solution the emission maximum occurs at 578 nm, whilst in CH$_3$CN solution the maximum occurs at 581 nm. It is also interesting to note that, for [Pt(phen)(C≡CPh)$_2$] changing the solvent was reported to have almost no influence on the wavelength $\lambda(em)_{max}$ of the emission,[248] whereas a shift of *ca.* 11 nm, as discussed above, was observed in the emission spectrum of [Pt(terpy)(C≡CPh)](SbF$_6$) on changing the solvent. Furthermore, the emission intensity of a CH$_2$Cl$_2$ solution of the salt was found to be higher than that of a CH$_3$CN solution of roughly equal concentration. It would thus seem that emission from the
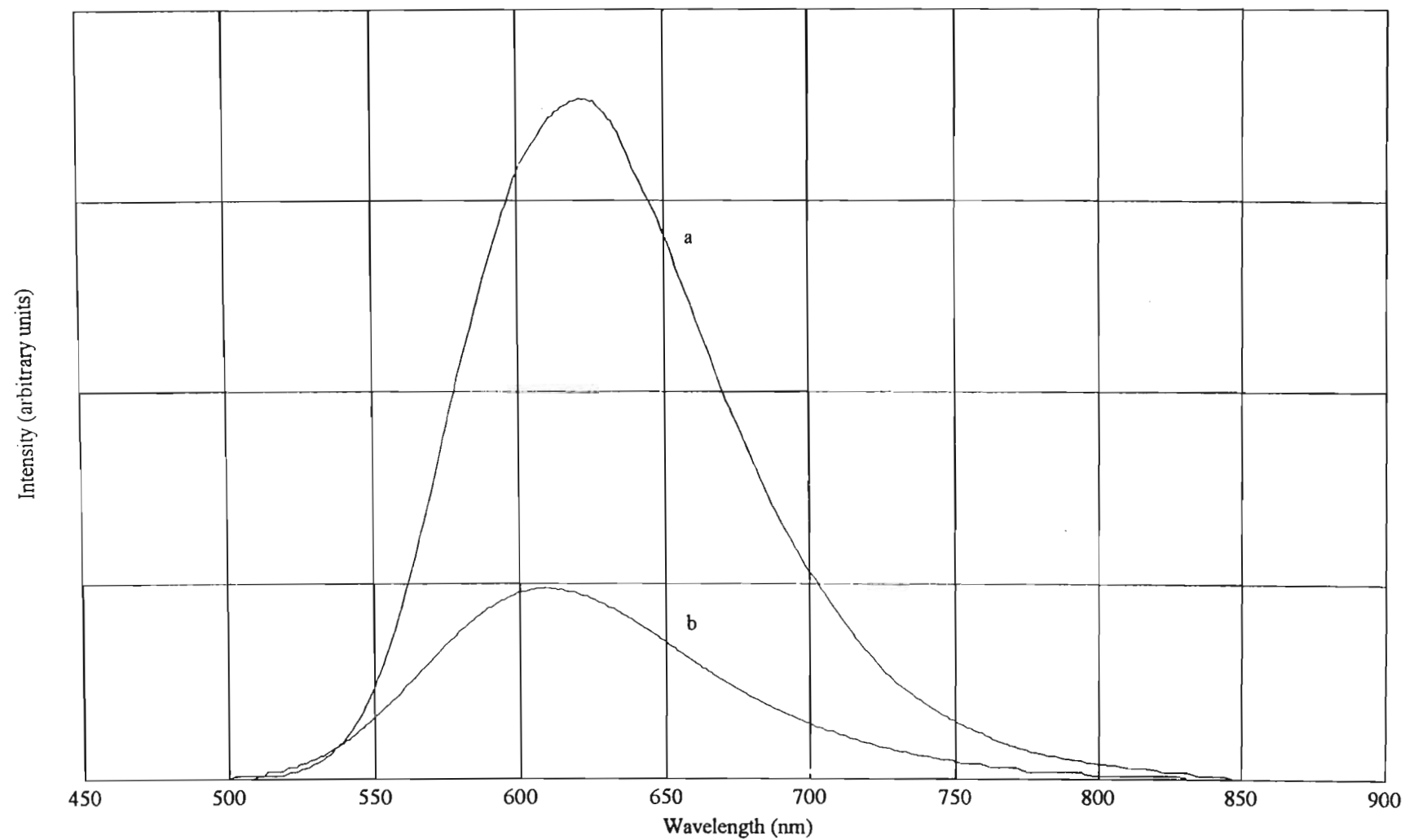
Figure 3.34   The emission spectra of degassed solutions of [Pt(terpy)(C≡CPh)](SbF₆) recorded at room temperature [(a) CH₂Cl₂ solution and (b) CH₃CN solution].

[Pt(terpy)(C≡CPh)]$^+$ chromophore in fluid solution is partially quenched by acetonitrile. This observation was confirmed by studying the luminescence of a CH_2Cl_2 solution of the chromophore before and after the addition of equal volumes of CH_2Cl_2 or CH_3CN. The addition of CH_2Cl_2 resulted in a minimal reduction in the emission intensity due to dilution, whereas a substantial reduction in emission intensity was observed on adding the same volume of CH_3CN.

The broad band shape of the emission observed from both CH_3CN and CH_2Cl_2 solutions of [Pt(terpy)(C≡CPh)](SbF$_6$) is clearly distinct from the highly structured band profiles associated with the radiative decay of ^{3}IL excited states, and is more consistent with emission from either a ^{3}CT, a ^{3}LF or even an excimeric excited state. The latter can probably be ruled out, since the dilution experiments performed as part of the quenching studies did not reveal any change in the wavelength, or the shape of the band profile associated with the emission, as would be expected on reducing the concentration of the chromophore, if excimeric emission was involved. The asymmetric shape of the band profile also differs from the Guassian shape normally associated with ^{3}LF emission.[258] Furthermore, as pointed out by McMillin et al.,[260] the population of a ^{3}LF excited state in a Pt(II) system would involve promoting an electron to the metal-ligand antibonding $d_{x^2-y^2}$ orbital, thus rendering the excited state prone to strong molecular distortions. Consequently, ^{3}LF excited states in Pt(II) systems are expected to be substitution active and short-lived in solution. Based on these considerations it would seem that the emission from [Pt(terpy)(C≡CPh)](SbF$_6$) both in CH_3CN and CH_2Cl_2 solution, originates from a ^{3}CT and in particular, a metal-to-ligand charge transfer state. This assignment is consistent with that of Che and co-workers,[248] who favoured an analogous assignment for the emission from [Pt(phen)(C≡CPh)$_2$] in fluid solution. The ^{3}MLCT assignment is also consistent with the emission being partially quenched by acetonitrile, since metal-to-ligand charge transfer will formally produce a Pt(III) centre. This centre can be regarded as a highly reactive 17 electron metal-based radical and will be prone to attack by coordinating solvents such as acetonitrile.

The solid state emission spectrum of [Pt(terpy)(C≡CPh)](SbF$_6$) was recorded at 40 K intervals over the range 80 to 280 K, the overlaid spectra being depicted in Figure
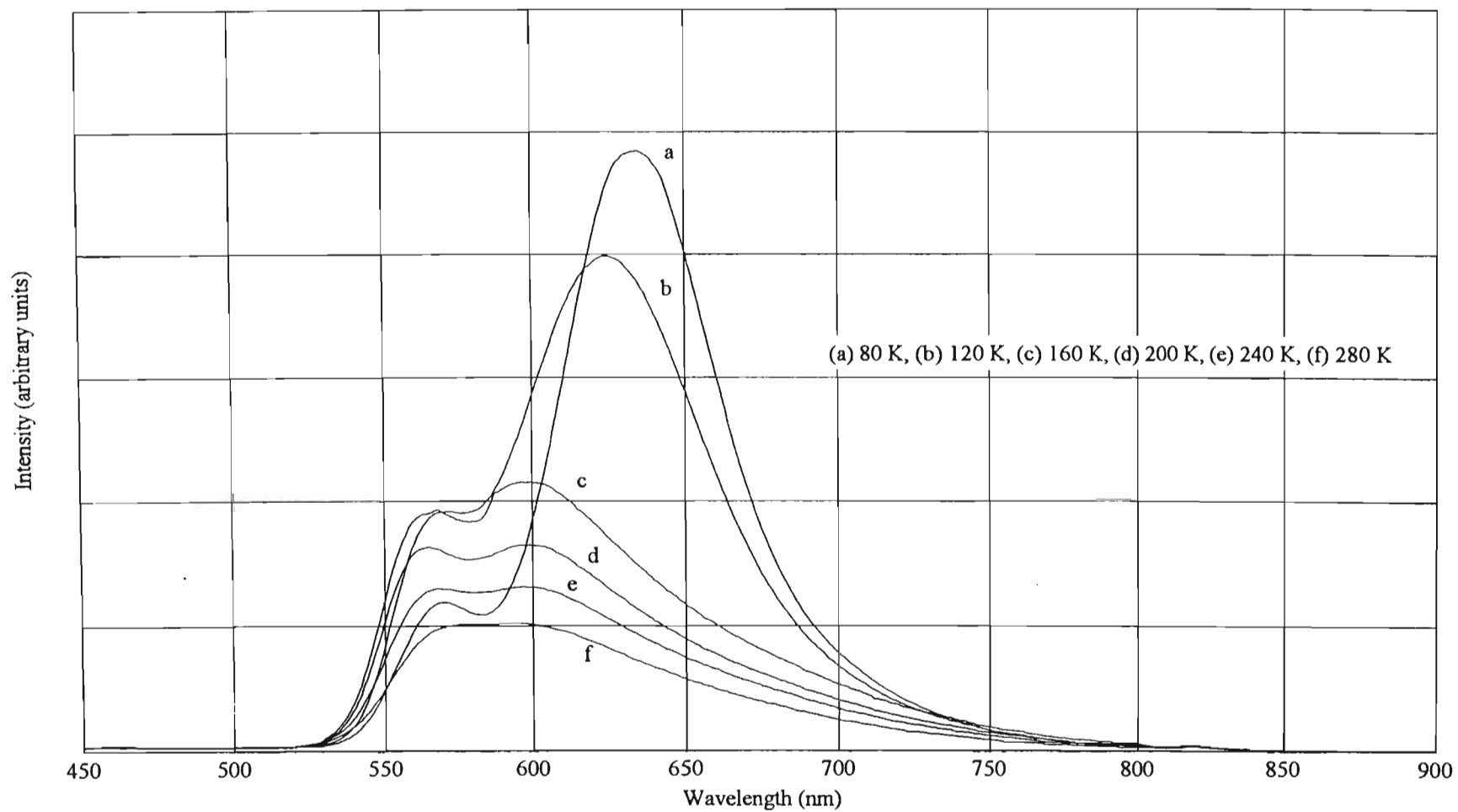
Figure 3.35 *The solid state emission spectrum of [Pt(terpy)(C≡CPh)](SbF₆) recorded at 40 K intervals over the range 80 to 280 K.*

3.35. At 280 K the emission spectrum comprises a single very broad, but well-defined asymmetric band with the maximum emission intensity occurring at *ca.* 585 nm. The emission intensity increases on reducing the temperature of the sample and at 240 K, this broad band can be resolved to consist of two overlapping components of equal intensity, the wavelengths, $\lambda(em)_{max}$, associated with these components being *ca.* 566 and 597 nm. Further decreasing the temperature of the sample results in further increases in the luminescent intensity with the lower energy component displaying a series of red-shifts, whereas the higher energy component displays a number of blue-shifts. At 160 K the two components exist as two well-separated features, the wavelength, $\lambda(em)_{max}$, associated with the component of higher energy being 562 nm, whilst that associated with the lower energy component, equals 602 nm. Decreasing the temperature of the sample from 160 to 80 K results in a narrowing of the bandwidth and a marked increase in the intensity of the lower energy component. This increase in intensity is accompanied by a further red-shift of the emission maximum, such that at 80 K, the wavelength, $\lambda(em)_{max}$, of the lower energy component equals 637 nm. The intensity of the higher energy component on the other hand, remains essentially constant on lowering the temperature of the sample from 160 to 120 K, but decreases dramatically on reducing the sample temperature from 120 to 80 K. These decreases in luminescent intensity are accompanied by a red-shift of this component, from 562 nm at 160 K, to 566 nm at 120 K and finally to 568 nm at 80 K.

The different temperature dependent variations in the band position and luminescent intensity of the two components in the solid state emission spectrum of [Pt(terpy)(C≡CPh)](SbF$_6$), suggest that the components originate from two different excited states. As discussed in Section 3.4.5.3 for instance, a trivial situation which could give rise to emission from different excited states, is that where the sample contains a luminescent impurity. The samples used in studying the luminescent properties of [Pt(terpy)(C≡CPh)](SbF$_6$) were analytically pure, as confirmed by elemental analysis for C, H and N. However, since elemental analysis cannot provide adequate proof of purity when the phenomenon of interest is luminescence, it is also relevant to consider possible sources of trace contamination of the samples of [Pt(terpy)(C≡CPh)](SbF$_6$). These would either be unreacted starting materials, *i.e.*

[Pt(terpy)Cl](SbF$_6$) or Bu$_3$SnC≡CPh, or products resulting from the decomposition of [Pt(terpy)(C≡CPh)](SbF$_6$). [Pt(terpy)Cl](SbF$_6$) exhibits a single broad peak at 552 nm in its solid state emission spectrum recorded at 80 K. Furthermore, the spectrum does not exhibit any temperature dependent shifts, thus eliminating [Pt(terpy)Cl](SbF$_6$) as a possible source of contamination. Bu$_3$SnC≡CPh exists as a liquid at room temperature, and even if luminescent, would have been removed by washing the sample as part of the work-up procedure during the synthesis. Decomposition products can in all likelihood also be ruled out, since [Pt(terpy)(C≡CPh)](SbF$_6$) was found to be air and moisture stable in the solid state. Samples used in photophysical studies were nonetheless stored under an atmosphere of dinitrogen and photophysical studies were completed within the shortest time possible. The argument against contamination by a luminescent impurity is further strengthened by the fact that the solid state emission spectrum of the 4'-phenylterpyridine analogue, [Pt(4'-Ph-terpy)(C≡CPh)](SbF$_6$), also consists of two components originating from different excited states (see Section 3.4.7.3). Furthermore, the two components in the variable temperature solid state spectra of both [Pt(terpy)(C≡CPh)](SbF$_6$) and [Pt(4'-Ph-terpy)(C≡CPh)](SbF$_6$), exhibit similar temperature dependent variations.

A further situation which could be responsible for the observation of emission from different excited states, is that where the emitting chromophores exist in two crystallographically distinct states. This possibility can be discounted for [Pt(terpy)(C≡CPh)](SbF$_6$), since as pointed out in Section 3.4.6.2, the asymmetric unit contains only one formula unit, thus implying that the crystallographic environment of all the chromophores in the crystal lattice is identical.

From these considerations it would thus appear that, in solid state samples of [Pt(terpy)(C≡CPh)](SbF$_6$), the [Pt(terpy)(C≡CPh)]$^+$ chromophore exhibits simultaneous emission from at least two different excited states.

The decrease in bandwidth and concomitant red-shift of the low-energy component in the solid state emission spectrum of [Pt(terpy)(C≡CPh)](SbF$_6$), resulting from decreasing the temperature of the sample, is typical of emission from a $^3(d_{\sigma*}\rightarrow\pi^b)$ MLCT excited state. Similar temperature dependent shifts and variations in the width

of the emission band envelope have been reported for [Pt(bipy)(CN)$_2$], [Pt(phen)(CN)$_2$], [Pt(terpy)Cl](CF$_3$SO$_3$)[263] and the red form of [Pt(bipy)Cl$_2$][268]. In each of these instances the emission was assigned to originate from the radiative decay of a ^{3}(d$_{\sigma^*}$→π^b) MLCT excited state.

An accurate determination of the origin of the higher energy component of the solid state emission spectrum is more difficult with the data available. If the emission originated from the radiative decay of a ^{3}(π-π*) IL excited state with the higher energy component considered here representing the highest energy vibrational feature, one would expect to observe the vibrational features of lower energy superimposed on the high energy side of the band envelope of the ^{3}(d$_{\sigma^*}$→π^b) component. However, the band envelope of the latter does not exhibit any evidence of superimposed vibrational structure, thus ruling out the possibility of a ^{3}(π-π*) IL excited state. Several other possibilities remain though, examples being; emission from a unimolecular type ^{3}MLCT excited state, a ligand-to-ligand charge transfer excited state, with electron density being transferred from the phenylacetylide to the terpyridine ligand, or even excimer type emission distinct from that of the ^{3}(d$_{\sigma^*}$→π^b) component, in that only ligand-ligand interactions, and no metal-metal interactions, are involved. With respect to the latter, recall that the interplanar distance between the head-to-tail stacked chromophores in [Pt(terpy)(C≡CPh)](SbF$_6$) is uniform and less than the Van der Waal's separation for π-interacting aromatic moieties. The platinum centres on the other hand, display a lateral offset from the stacking axis thus giving rise to a longer and a shorter Pt-Pt separation, the longer distance being such that minimal Pt-Pt interaction would be expected.

From the above discussion it is clear that further studies would be required to fully explain the solid state luminescent behaviour of the [Pt(terpy)(C≡CPh)]$^+$ chromophore. In this regard one might consider recording the excitation spectra at the wavelengths corresponding to maximum emission intensity for each of the two components in the solid state emission spectra of [Pt(terpy)(C≡CPh)](SbF$_6$). However, since there is extensive overlap of the band envelopes of the two components, it is unlikely that an unequivocal assignment of the electronic origin of the higher energy component will be possible based on this data alone. A further experiment would be to attempt to

determine the lifetimes associated with each of the two components. This might provide grounds for the elimination of some of the possible excited states. Furthermore, if the lifetimes of the $^3(d_{\sigma^*} \rightarrow \pi^b)$ and the higher energy component are sufficiently different, it might be possible to separate and view each of the components independently through use of either a phosphoroscope, to suppress relatively short-lived components (typically ^{3}CT components), or pulsed laser excitation with the emission being sampled with a boxcar averager, to suppress any long-lived components. Further synthetic studies could include preparing the palladium analogue, [Pd(terpy)(C≡CPh)](SbF$_6$). This salt could exhibit different stacking modes, and since the metal centre is being varied, might provide some insight into the influence of both the metal centre, and the stacking interactions between the chromophores, on the solid state luminescence. Similar studies would involve varying the counterion, as has been demonstrated here for the [Pt(terpy)Cl]$^+$ and [Pt(bipy)$_2$]$^{2+}$ chromophores.

Due to our limited access to the equipment required for advanced photophysical investigations, it was decided to attempt the synthesis of [Pt(4'-Ph-terpy)(C≡CPh)](SbF$_6$). Not only would this complex salt allow us to further explore the luminescent properties of chromophores containing both polypyridyl and acetylide ligands coordinated to a single platinum centre, but it would also permit an investigation into the influence of the introduction of a non-planar ligand on the solid state packing and consequently, on the solid state luminescent properties of these chromophores.

3.4.7. [Pt(4'-Ph-terpy)(C≡CPh)](SbF$_6$) (16)

3.4.7.1. Synthesis and characterization

Both methods developed for the synthesis of [Pt(terpy)(C≡CPh)](SbF$_6$) can be utilized to synthesize [Pt(4'-Ph-terpy)(C≡CPh)](SbF$_6$) (see Section 3.4.6.1). The route employing Bu$_3$SnC≡CPh as starting material, however, affords a mixture of products from which [Pt(4'-Ph-terpy)(C≡CPh)](SbF$_6$) is more readily separated than that using AgC≡CPh and thus is the method of choice.

The method described below is similar to that for the synthesis of the unsubstituted terpyridine derivative and involves treating a suspension of [Pt(4'-Ph-terpy)Cl](SbF$_6$)

in CH_3CN with $Bu_3SnC{\equiv}CPh$ and heating the mixture to reflux for 4 to 6 hours. Reducing the volume of the solution *in vacuo* resulted in the precipitation of an orange microcrystalline solid which was isolated by filtration, washed with *n*-hexane, cold acetonitrile and diethyl ether and dried *in vacuo*. The solid was placed in the vapour extraction apparatus described in Section A.2.1.2 of Appendix A and the [Pt(4'-Ph-terpy)(C${\equiv}$CPh)](SbF_6) content extracted into boiling CH_3CN. Allowing the saturated solution obtained thus to cool to room temperature, resulted in [Pt(4'-Ph-terpy)(C${\equiv}$CPh)](SbF_6) crystallizing as orange-red block-shaped crystals. Elemental analysis for C, H and N was consistent with the empirical formula [Pt(4'-Ph-terpy)(C${\equiv}$CPh)](SbF_6).

The solid state infrared spectrum of [Pt(4'-Ph-terpy)(C${\equiv}$CPh)](SbF_6) was recorded as a KBr pellet, the most prominent peaks being listed in Table 3.1. The spectrum displays a single weak, but well defined peak in the C${\equiv}$C stretching region at 2124 cm^{-1} and is accordingly assigned to originate from the C${\equiv}$C stretching vibration of the phenylacetylide ligand. The position and relative intensity of this peak is identical to that associated with the analogous peak in the solid state infrared spectrum of [Pt(terpy)(C${\equiv}$CPh)](SbF_6) (**15**). Furthermore, the peak position and intensity is not dissimilar to that of the C${\equiv}$C stretching vibration in [Pt$_2$(μ-C${\equiv}$CPh)(C${\equiv}$CPh)(PEt$_3$)$_3$Cl],[310] which was resolved as a weak band between 2110 and 2115 cm^{-1}. The infrared spectrum of [Pt(4'-Ph-terpy)(C${\equiv}$CPh)](SbF_6) also displays a number of peaks in the range 1650 to 780 cm^{-1}, which by comparison with those in the spectrum of [Pt(4'-Ph-terpy)Cl](SbF_6) and other complexes containing the terpyridine moiety coordinated to a platinum centre, can be assigned to originate from vibrational modes of the 4'-phenylterpyridine ligand. Although the peaks in this range in the spectra of [Pt(4'-Ph-terpy)(C${\equiv}$CPh)](SbF_6) and [Pt(4'-Ph-terpy)Cl](SbF_6) are virtually identical, close scrutiny of the peaks did reveal that, the spectrum of the latter displays a single peak at 1479 cm^{-1}, whereas the spectrum of the phenylacetylide derivative displays two peaks with wavenumbers 1486 and 1476 cm^{-1} respectively. This difference in spectra was also observed on comparing the solid state infrared spectra of [Pt(terpy)Cl](SbF_6) and [Pt(terpy)(C${\equiv}$CPh)](SbF_6) and was attributed to a a solid state

effect. The spectrum of [Pt(4'-Ph-terpy)(C≡CPh)](SbF$_6$) also displays the customary peak at *ca.* 655 nm associated with the SbF$_6^-$ anion.

3.4.7.2 Structural studies on [Pt(4'-Ph-terpy)(C≡CPh)](SbF$_6$) (16)

Orange-red block-shaped crystals of compound **16** were grown by extracting the complex salt from a crude reaction mixture into boiling CH$_3$CN using the vapour extraction apparatus described in Section A.2.1.2 of Appendix A and allowing the saturated solution to slowly cool to room temperature over a period of *ca.* 24 hours.

[Pt(4'-Ph-terpy)(C≡CPh)](SbF$_6$), analogous to the unsubstituted terpyridine derivative **15**, crystallizes in the monoclinic space group *P*2$_1$/*n*. Furthermore, as in the case of [Pt(terpy)(C≡CPh)](SbF$_6$) (**15**), both the complex cation and the anion are situated in general equivalent positions with the asymmetric unit consisting of one cation and one anion. It thus follows that the unit cell contains four formula units with no crystallographically imposed symmetry relationships between any of the atoms constituting the complex cation or the anion. The unit cell dimensions, a full list of the interatomic distances and angles and other relevant crystallographic data are presented in Tables 3.22 to 3.26 at the end of this chapter.

A diagram displaying the molecular geometry of the [Pt(4'-Ph-terpy)(C≡CPh)]$^+$ cation and the numbering scheme employed, is provided in Figure 3.36. As in the case of [Pt(terpy)(CH$_3$CN)]$^{2+}$ and [Pt(4'-Ph-terpy)(C≡CPh)]$^+$, the coordination geometry around the Pt(II) centre can be described as being essentially square planar, with any deviation from the idealized geometry being the result of the geometric constraints imposed by the 4'-phenylterpyridine ligand.

The interatomic distances between the Pt centre and the nitrogen atoms N(1), N(2) and N(3) are 2.00(1), 1.96(1) and 2.01(1)Å respectively, with the N(1)-Pt-N(2) and N(2)-Pt-N(3) angles being 80.0(4) and 81.0(4)°. The geometric constraints imposed by the chelating tridentate 4'-phenylterpyridine ligand is clearly evident in the shorter bond distance between the platinum centre and the nitrogen atom N(2) of the central pyridine ring when compared to the analogous bond distances pertaining to the terminal pyridine rings of the ligand. These geometric constraints are also manifested in the N-Pt-N angles deviating from the idealized value of 90°, expected for square planar

294
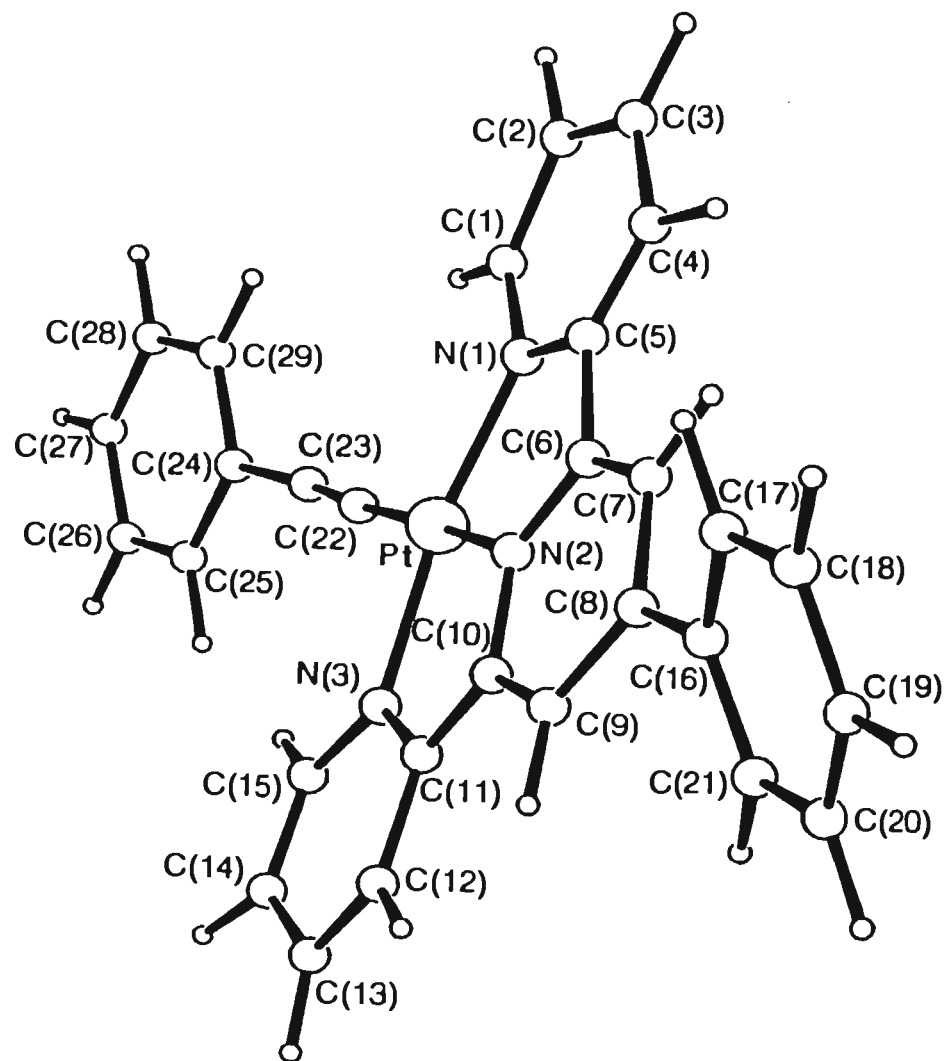
Figure 3.36   _The molecular geometry and numbering scheme employed for the [Pt(4'-Ph-terpy)(C≡CPh)]⁺ cation._

geometry. As such the Pt-N bond lengths and N-Pt-N angles reported here are in good agreement with those of [Pt(terpy)(CH₃CN)](SbF₆) (**8**), [Pt(terpy)(C≡CPh)](SbF₆) (**15**), [Pt(terpy)(SCH₂CH₂OH)](NO₃)[270] and [Pt(terpy)Cl](CF₃SO₃),[263] as examples. This contrasts with the results reported by Constable, Lewis and co-workers[306] who found that the bond lengths (1.986 and 1.983Å) between the nickel centre and the nitrogen atoms of the central pyridine rings of the 4'-phenylterpyridine ligands in [Ni(4'-Ph-terpy)₂]Cl₂.10H₂O, are shorter than those (2.016 and 2.009Å) associated with the [Ni(terpy)₂](PF₆) complex. The difference was attributed to a greater "π-bonding component" associated with the 4'-phenylterpyridine ligand when compared to the unsubstituted terpyridine ligand. The fact that this difference in Pt-N distance is not observed when comparing the [Pt(4'-Ph-terpy)(C≡CPh)]⁺ cation to cations containing the unsubstituted terpyridine ligand, could be associated with the larger covalent radius of the platinum centre in contrast to that of a nickel centre.

The bond lengths and angles associated with the terpyridine fragment of the coordinated 4'-phenylterpyridine ligand closely resemble that observed in other complexes containing the unsubstituted terpyridine ligand. The terpyridine fragment is slightly ruffled however, the terminal pyridine rings defining dihedral angles of 5.3 and 2.0° with the central pyridine ring. These angles are not significant, interannular angles of between 3.9 and 8.2° having been reported for [Ni(4'-Ph-terpy)₂]Cl₂.10H₂O.[306] The phenyl ring exhibits a much larger twist about the interannular C-C bond, a dihedral angle of 33.5° being defined between the planes of the phenyl ring and the central pyridine ring of the ligand. This deviation from planarity in all probability arises as a consequence of minimizing the non-bonded interactions between the hydrogen atoms bonded to the carbon atoms in the ortho positions to the interannular bond between the phenyl ring and the central pyridine ring of the ligand. The analogous angles in the [Ni(4'-Ph-terpy)₂]²⁺ cation are 16.7 and 17.8°.[306] The twist of the phenyl ring from the plane of the rest of the 4'-phenylterpyridine ligand is accompanied by a shortening of the interannular C-C bond, the interatomic distance between C(16) and C(8) being equal to 1.46(2)Å, when compared to the analogous distance of 1.492(4)Å reported for the uncoordinated 4'-phenylterpyridine ligand.[306] Constable, Lewis and co-workers also reported a shortening of this bond on coordination, the bond distances in [(Ni(4'-

Ph-terpy)$_2$]Cl$_2$.10H$_2$O being 1.485(5) and 1.483(5)Å. The shortening of the interannular bond was attributed to an electrostatic effect associated with the positively charged metal centre,[306] since the twist about the interannular bond is expected to reduce the extent of π-π interaction across the bond and consequently result in a lengthening of this bond,[316] *vide infra*. An electrostatic effect analogous to that proposed by Constable, Lewis *et al.* probably is responsible for the short phenyl to terpyridine interannular C-C distance observed in the [Pt(4'-Ph-terpy)(C≡CPh)]$^+$ chromophore.

The phenylacetylide ligand bends from the mean plane defined by the platinum centre and the terpyridine fragment of the 4'-phenylterpyridine ligand, C(23), C(24) and C(25) being displaced respectively by 0.05, 0.24 and 0.64Å from this plane. Furthermore, the ligand is twisted about the Pt-C(22) bond, the dihedral angle between the phenyl ring and the mean plane of the platinum-terpyridine fragment being 16.0°. These deviations from planarity most probably result from a minimization of the non-bonded interactions between the phenylacetylide ligand and the phenyl moiety of the 4'-phenylterpyridine ligand of an adjacent chromophore within the stacked arrangement observed in [Pt(4'-Ph-terpy)(C≡CPh)](SbF$_6$), *vide infra*.

The Pt-C(22) distance [C(22) being the terminal carbon atom of the C≡C functionality of the phenylacetylide ligand] equals 2.02(2)Å. This value is comparable to the value of 2.00Å predicted for a Pt-C(*sp*) single bond, and that of 2.05(2)Å reported for the analogous bond length in [Pt$_2$(μ-C=CHPh)(C≡CPh)(PEt$_3$)$_3$Cl].[310] The C≡C bond length [C(22) to C(23)] equals 1.07(2)Å. This value is somewhat smaller than that of 1.212Å, the C≡C bond length of acetylene as determined from electron diffraction studies in the gas phase.[311] It is also smaller than the values of 1.17(2) and 1.18(3) reported for the C≡C bond lengths in [Pt$_2$(μ-C=CHPh)(C≡CPh)(PEt$_3$)$_3$Cl][310] and *trans*-[PtCl(C≡CPh)-(PEt$_2$Ph)$_2$],[311] both compounds having Pt-C(*sp*) single bond lengths close to, or greater than that observed in compound **16**. An exact explanation for the short C≡C bond length observed in [Pt(4'-Ph-terpy)(C≡CPh)](SbF$_6$) cannot be provided at this stage.

The Pt-C(22)-C(23) and C(22)-C(23)-C(24) angles are equal to 175(1) and 178(2)° respectively. These angles are somewhat smaller than the idealized value of 180° expected for *sp*-hybridized C atoms, but are not unusual, values as low as 172.5(9) and 173(1)° having been reported for the analogous angles in $[(PhC\equiv C)_2(Et_3P)_2Pt\{1,4\text{-}(4\text{-}NO_2C_2H_4)_2N_4\}]^{(315)}$ for instance. As in the case of $[Pt(terpy)(C\equiv CPh)](SbF_6)$, the phenyl ring of the phenylacetylide ligand was refined as a rigid group and thus the internal bond lengths and angles associated with this ring will not be discussed here.

The $[Pt(4'\text{-}Ph\text{-}terpy)(C\equiv CPh)]^+$ chromophores in compound **16** are arranged in extended stacks along the [a]-axis, each of the chromophores stacking face-to-face with its closest neighbouring cation. A diagram depicting this stacked arrangement, as seen in a view along the [a]-axis is provided in Figure 3.37. As in the case of $[Pt(terpy)(C\equiv CPh)]^+$ (**15**), the individual chromophores within one such stack are interrelated by centres of inversion, these being located on the [a]-axis at intervals equal to half the length of the axis, *i.e.* 3.645Å in this case, as compared to 3.765Å for the unsubstituted terpyridine derivative. This symmetry relationship between the chromophores dictates that the mean planes defined by the Pt-terpy moieties of neighbouring cations within each stack are necessarily parallel to each other. Mean plane calculations have revealed the interplanar spacing between the chromophores to be uniform along the stack and to equal 3.43Å (see Figure 3.38), compared to 3.23Å in compound **15**. The larger interplanar spacing between the chromophores observed for **16**, compared to that in compound **15**, is in contrast to the smaller spacing between the centres of inversion relating neighbouring cations within the stack in compound **16**, when compared to $[Pt(terpy)(C\equiv CPh)](SbF_6)$ (**15**). This is a consequence of the normals to the planes of the stacked chromophores in compound **16** being closer to being parallel to the stacking axis [a], than the normals to the planes of the $[Pt(terpy)(C\equiv CPh)]^+$ chromophores in **15**. This difference is clearly evident when comparing the angle between the [a]-axis and normals to the planes defined by the Pt, the three N atoms and the terminal C of the phenylacetylide ligand, in the two compounds. In $[Pt(4'\text{-}Ph\text{-}terpy)(C\equiv CPh)](SbF_6)$ (**16**) this angle is equal to 21.9°, whereas the same angle in $[Pt(terpy)(C\equiv CPh)](SbF_6)$ (**15**) equals 28.7°. The distance of 3.43Å between the mean planes defined by the Pt-terpy fragments of the stacked
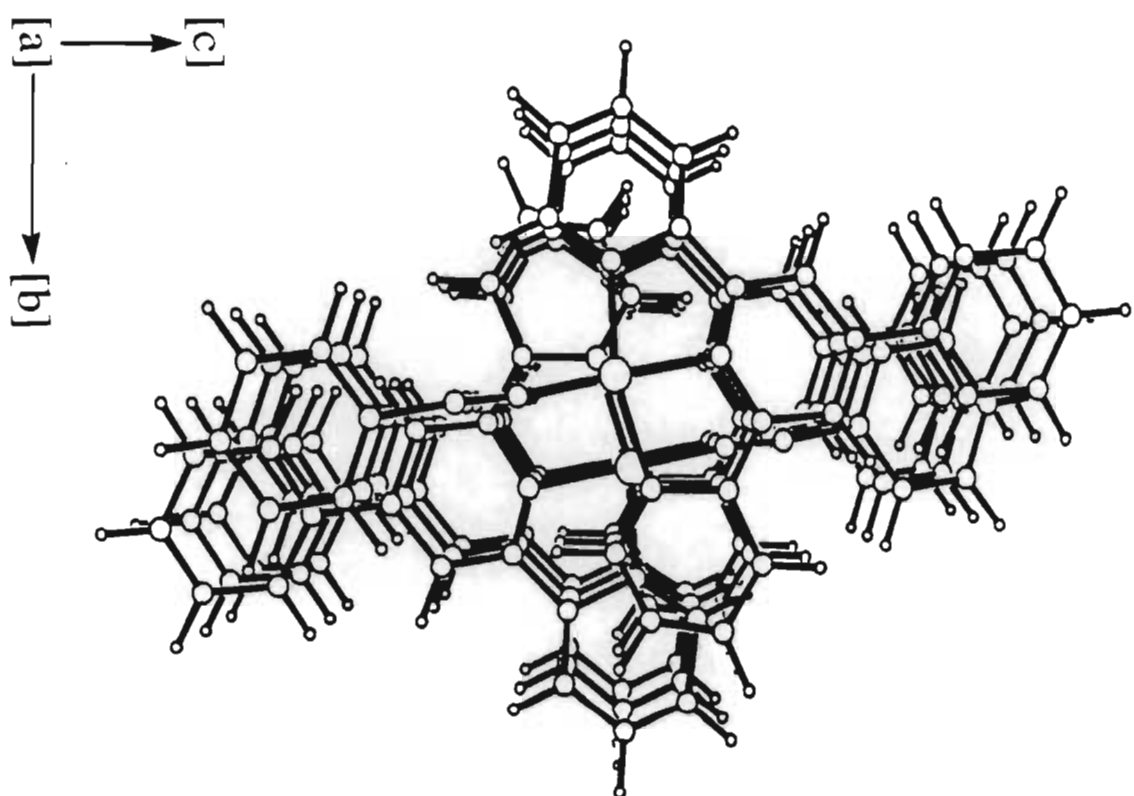
Figure 3.37 A stack of [Pt(4'-Ph-terpy)(C≡CPh)]⁺ cations as seen in a view along the [a]-axis.

3.43 Å

3.43 Å

3.490 Å

4.474 Å

[a]

[b]

[c]
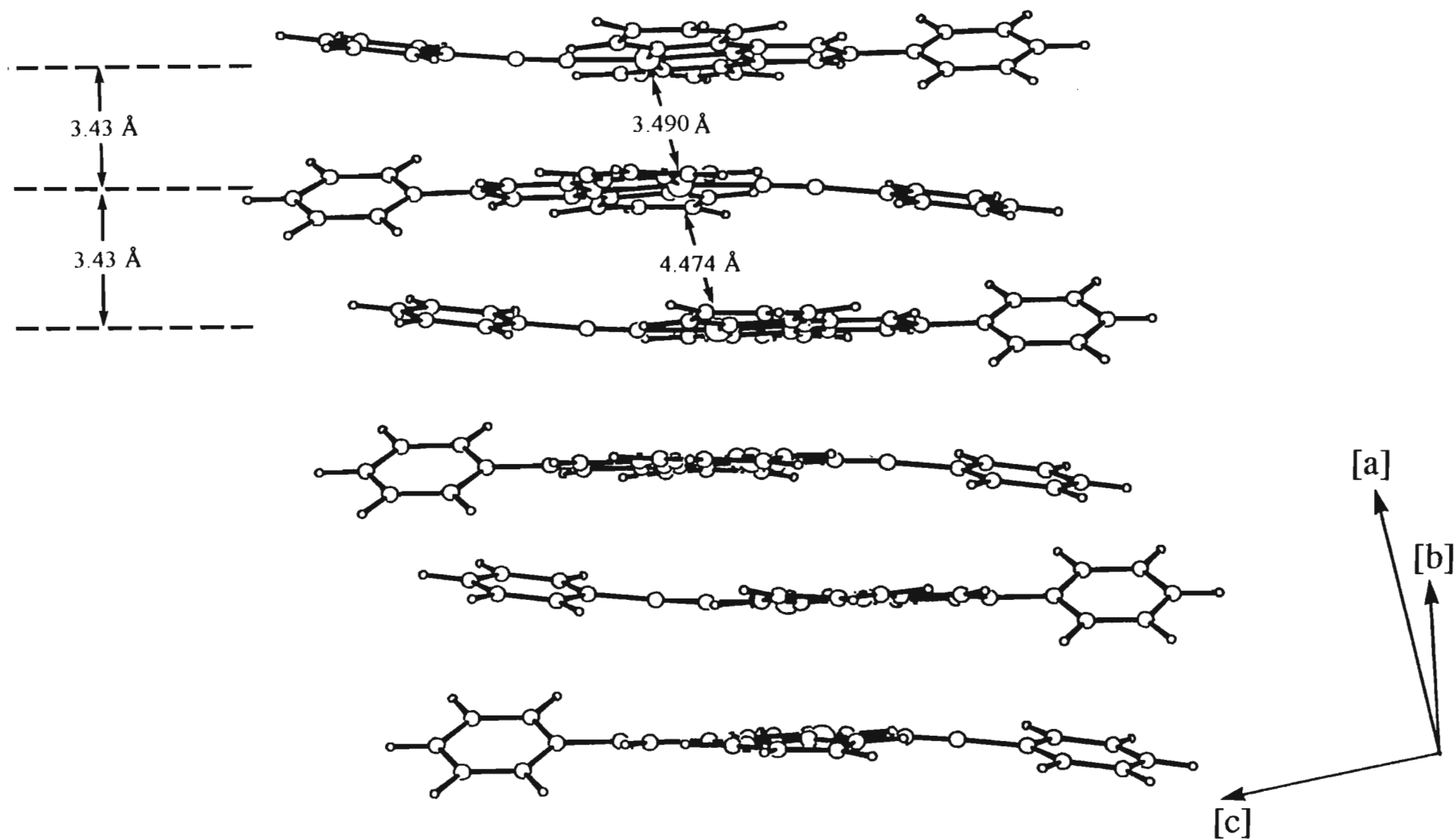
Figure 3.38 An alternative view of the stacked [Pt(4'-Ph-terpy)(C≡CPh)]⁺ chromophores in [Pt(4'-Ph-terpy)(C≡CPh)](SbF₆).
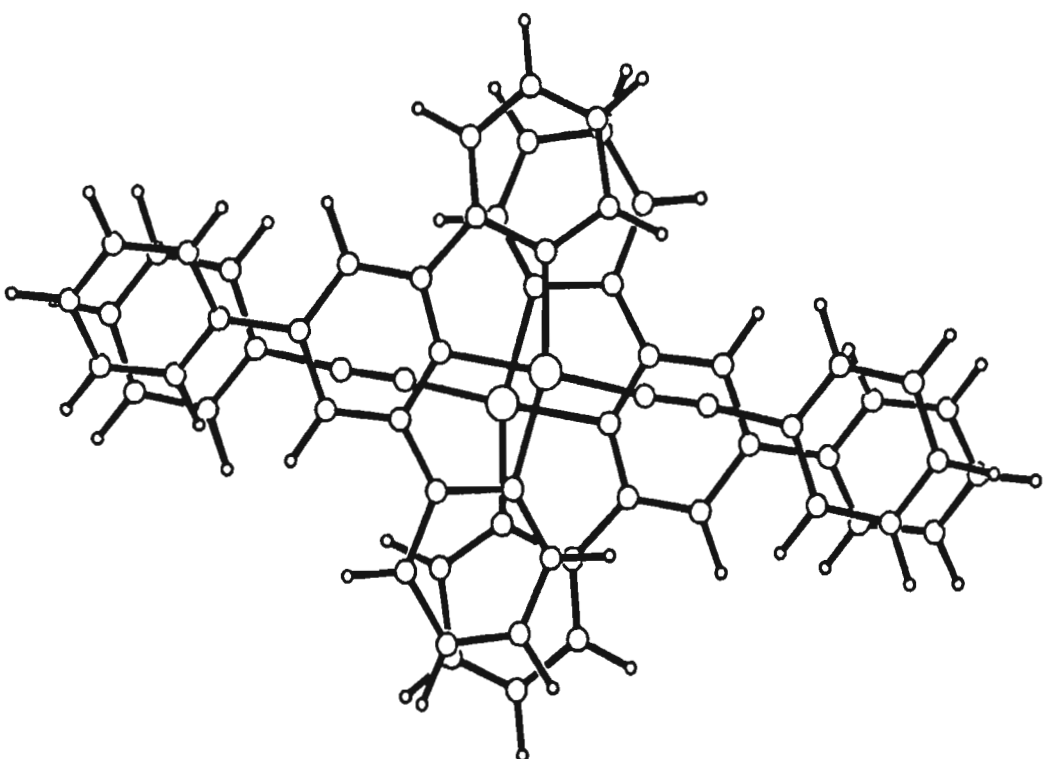
Figure 3.39 Overlap between neighbouring [Pt(4'-Ph-terpy)(C≡CPh)]⁺ chromophores in [Pt(4'-Ph-terpy)(C≡CPh)](SbF₆) (Pt–Pt distance = 3.490Å).
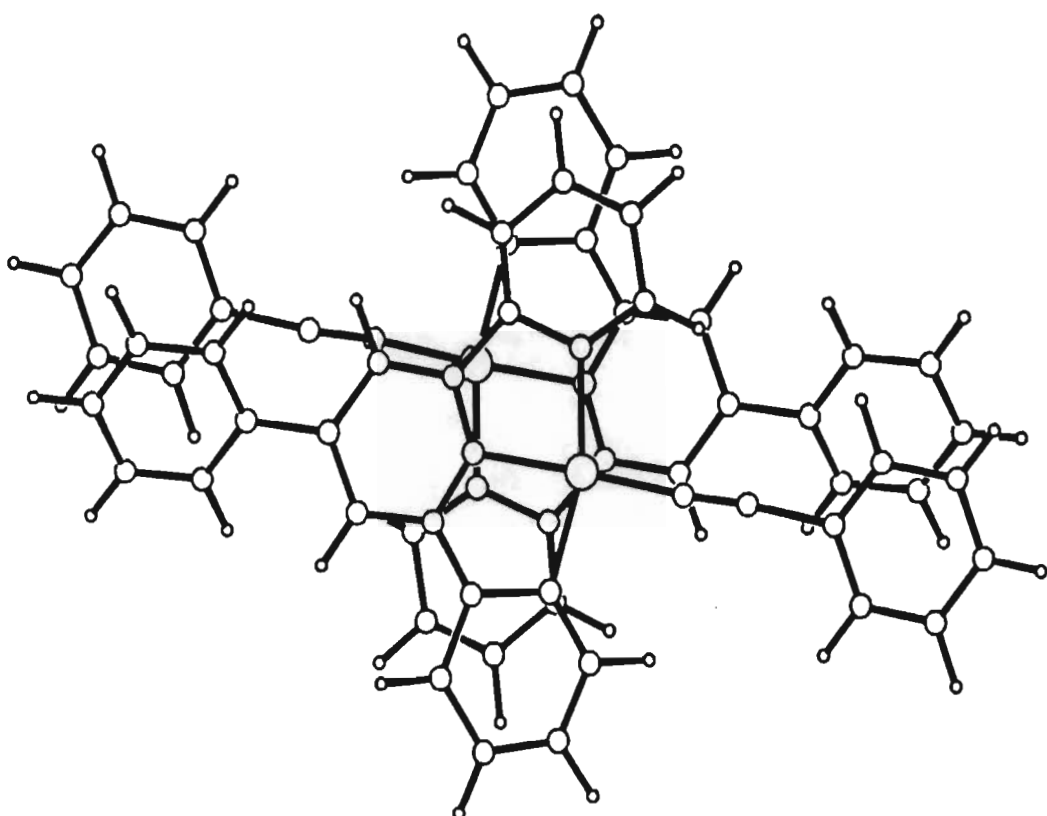
Figure 3.40 Overlap between neighbouring $[Pt(4'-Ph-terpy)(C{\equiv}CPh)]^+$ chromophores in $[Pt(4'-Ph-terpy)(C{\equiv}CPh)](SbF_6)$ (Pt-Pt distance = 4.474Å).

[Pt(4'-Ph-terpy)(C≡CPh)]⁺ chromophores, closely approximates to 3.45Å, the Van der Waal's separation between π-aromatic species occurring in a face-to-face arrangement,[242] thus suggesting that there could be some orbital interaction between the stacked chromophores. Neighbouring complexes within the stacked arrangement in [Pt(4'-Ph-terpy)(C≡CPh)](SbF₆) are arranged head-to-tail. This is identical to the arrangement found in the unsubstituted terpyridine derivative and is enforced by the inversion symmetry relating neighbouring chromophores within the stacked arrangement in both compounds. The similarity further includes that the platinum centres in [Pt(4'-Ph-terpy)(C≡CPh)](SbF₆) also exhibit a lateral offset from the stacking axis, which together with the head-to-tail arrangement of the chromophores, results in the Pt-Pt separation not being uniform along the extended stacks. Instead, two different separations, these being 3.490 and 4.474Å, are observed to alternate along the stacks. The shorter of these two distances is comparable to the value of 3.45Å reported for the Pt-Pt separation in the red form of [Pt(bipy)Cl₂]. The analogous values for [Pt(terpy)(C≡CPh)](SbF₆) (**15**) are 3.600 and 4.384Å. This variation in Pt-Pt separation furthermore implies that two different modes of orbital overlap alternate along the stacked arrangement of the cations. A diagram depicting the arrangement of two chromophores with a Pt-Pt separation of 3.490Å, as seen in a view perpendicular to the Pt(4'-Ph-terpy) fragment, is provided in Figure 3.39. In this figure the terminal pyridine rings of the 4'-phenylterpyridine ligand can be observed to participate in partial ring-ring overlap with the analogous rings of its neighbouring chromophore whilst the C≡C acetylide functionality of one chromophore is positioned directly above or below the central pyridine ring of the terpyridine functionality of the other. An analogous diagram to that described above, and depicting the arrangement of two chromophores with a Pt-Pt separation of 4.474Å, is provided in Figure 3.40. In this case the overlap is predominantly between the terminal pyridine rings on one chromophore, each of which partially overlaps with both a terminal pyridine ring and the five membered ring defined by the Pt centre and one of the chelating N-C-C-N fragments of the terpyridine moiety of the other chromophore.

3.4.7.3 Photophysical studies on [Pt(4'-Ph-terpy)(C≡CPh)](SbF$_6$) (**16**)

The room temperature absorption spectrum of a CH$_3$CN solution of [Pt(4'-Ph-terpy)(C≡CPh)](SbF$_6$) is depicted in Figure 3.41 and the wavelengths λ(abs)$_{max}$, associated with the absorption maxima are listed in Table 3.4.

A comparison of this spectrum with that of [Pt(4'-Ph-terpy)Cl](SbF$_6$) (**14**) reveals that the two spectra are virtually identical at wavelengths lower than 350 nm, the only differences being the relative intensities of the peak at 289 nm and the resolution of the bands between 300 and 340 nm. As in the case of [Pt(4'-Ph-terpy)Cl](SbF$_6$) (**14**) the peak at 288 nm, as well as the vibrationally structured band between 300 and 340 nm, can be assigned to π-π* transitions of the coordinated 4'-phenylterpyridine ligand. The decrease in the relative intensity of the peak at 289 nm in going from the Cl$^-$ to the PhC≡C$^-$ derivative is most probably the result of increased absorption at *ca.* 262 nm which is associated with the π-π* transitions of the phenyl group of the phenylacetylide ligand. The same assignment was suggested to explain an analogous decrease in relative intensity when comparing the absorption spectra of [Pt(terpy)Cl](SbF$_6$) and [Pt(terpy)(C≡CPh)](SbF$_6$) (see Section 3.4.6.3) and is consistent with the absorption spectrum of phenylacetylide which exhibits bands at 272, 248 and 238 nm.[310] In addition to the features discussed above, the absorption spectrum of [Pt(4'-Ph-terpy)(C≡CPh)](SbF$_6$) also exhibits two broad bands with absorption maxima at 405 and 458 nm respectively. The wavelength of the former of these two bands closely corresponds to that of 403 nm associated with the Pt→π*(terpy) MLCT transition in the absorption spectrum of [Pt(terpy)Cl](SbF$_6$) (**14**). Furthermore, the relative intensities of these features are very similar, thus suggesting that the band centred at 405 nm in the spectrum of [Pt(4'-Ph-terpy)(C≡CPh)](SbF$_6$) (**16**) might have its origin in a Pt→π*(terpy) MLCT transition. The band centred at 458 nm is more difficult to assign however and, as in the case of the analogous band centred at 440 nm in the spectrum of [Pt(terpy)(C≡CPh)](SbF$_6$) (**15**), could originate from either a Pt→π*(4'-Ph-terpy) MLCT, a Pt→C≡CPh type MLCT, an acetylide to 4'-phenylterpyridine LLCT transition or even from absorption by dimeric or oligomeric species in solution. The reader is referred to Section 3.4.6.3 for a more comprehensive discussion of these
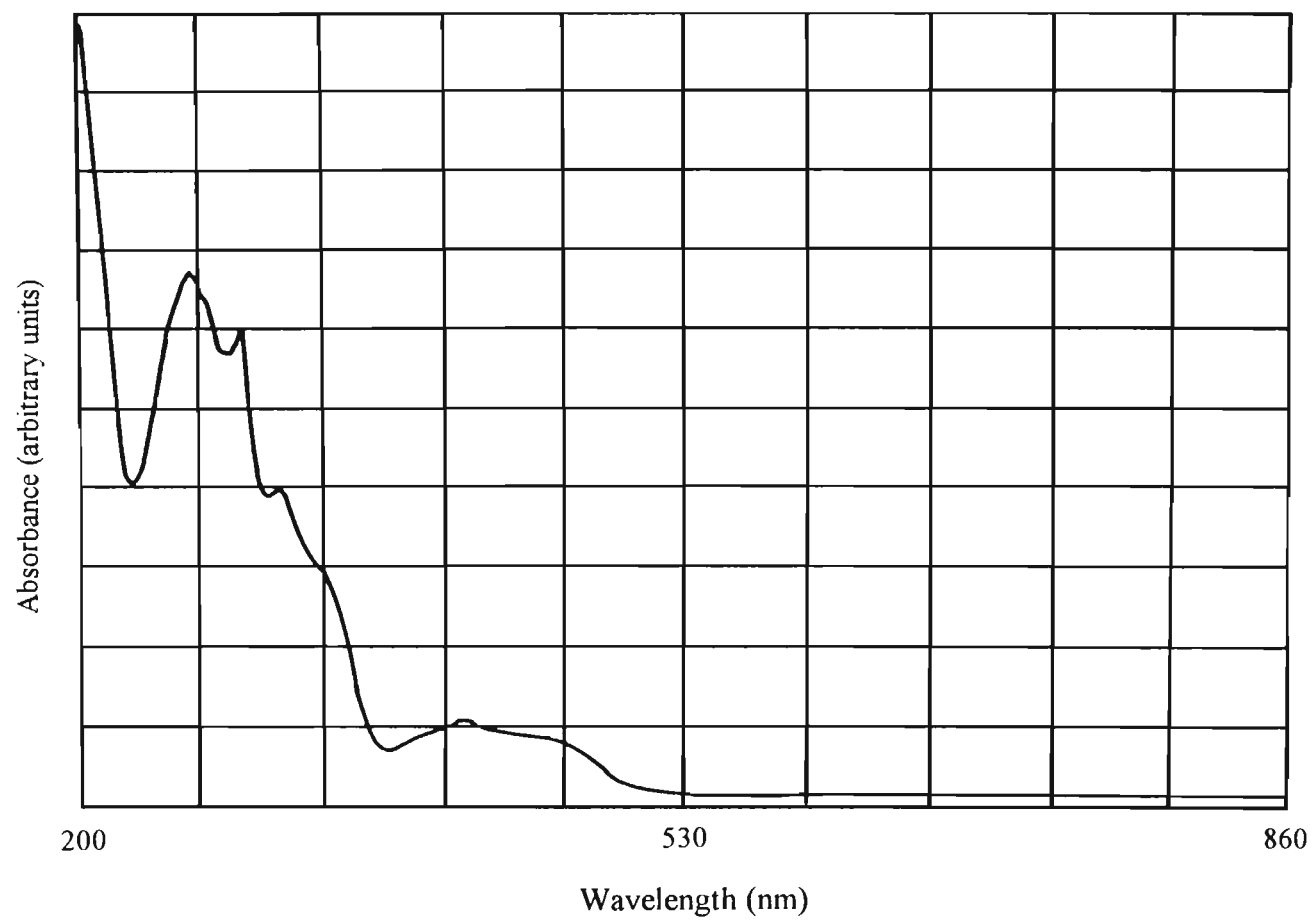
Figure 3.41   *The absorption spectrum of a CH₃CN solution of [Pt(4'-Ph-terpy)(C≡CPh)](SbF₆) recorded at room temperature.*

possibilities. It is clear however, that any attempt to assign the band at 458 nm to a specific electronic transition, without the aid of molecular orbital calculations, or other supporting evidence, would be restricted to the realm of being purely speculative.

The emission behaviour of [Pt(4'-Ph-terpy)(C≡CPh)](SbF₆) (**16**) was studied both in degassed CH_2Cl_2 and CH_3CN solution at room temperature, as well as in the solid state at 40 K intervals over the range 80 to 280 K.

The emission spectra of degassed CH_2Cl_2 and CH_3CN solutions of [Pt(4'-Ph-terpy)(C≡CPh)](SbF₆) (**15**), recorded at room temperature, are provided in Figure 3.42. The emission spectrum recorded in CH_3CN solution consists of a single broad, asymmetric band, the maximum emission intensity occurring at 613 nm. This is similar to the analogous spectrum of the unsubstituted terpyridine derivative, [Pt(terpy)-(C≡CPh)](SbF₆), the only difference being that the wavelength associated with the maximum emission intensity in the spectrum of the 4'-phenylterpyridine derivative is red-shifted by 5 nm with respect to that of the latter. The shape of the emission band envelope also matches that reported for an ethanol solution of [Pt(phen)(C≡CPh)₂][248] recorded at room temperature, with the emission of the 4'-phenylterpyridine derivative occurring 32 nm to the red of that of the phenanthroline derivative. The emission spectrum of a CH_2Cl_2 solution of [Pt(4'-Ph-terpy)(C≡CPh)](SbF₆) displays pronounced differences to that recorded in CH_3CN solution. The band envelope is blue-shifted with respect to that of the spectrum recorded in CH_3CN solution, and displays some poorly resolved structure on the low energy side of the band. The maximum emission intensity is observed at 580 nm with the concealed and poorly resolved feature centred at *ca.* 608 nm. This blue-shift observed in the solution emission spectrum of [Pt(4'-Ph-terpy)(C≡CPh)](SbF₆) on changing the solvent from CH_3CN to CH_2Cl_2, is in contrast with the emission behaviour of the unsubstituted terpyridine derivative, where changing the solvent from CH_3CN to CH_2Cl_2 effected a small red-shift of the emission band envelope. Furthermore, the emission band envelope in the CH_2Cl_2 solution spectrum of [Pt(4'-Ph-terpy)(C≡CPh)](SbF₆) displays some poorly resolved structure, whereas the analogous spectrum of the unsubstituted terpyridine derivative displayed only hints of some unresolved structure, if any. Similar behaviour was reported for the [Pt(phen)(C≡CPh)₂] chromophore,[248] the emission spectrum of which displays no
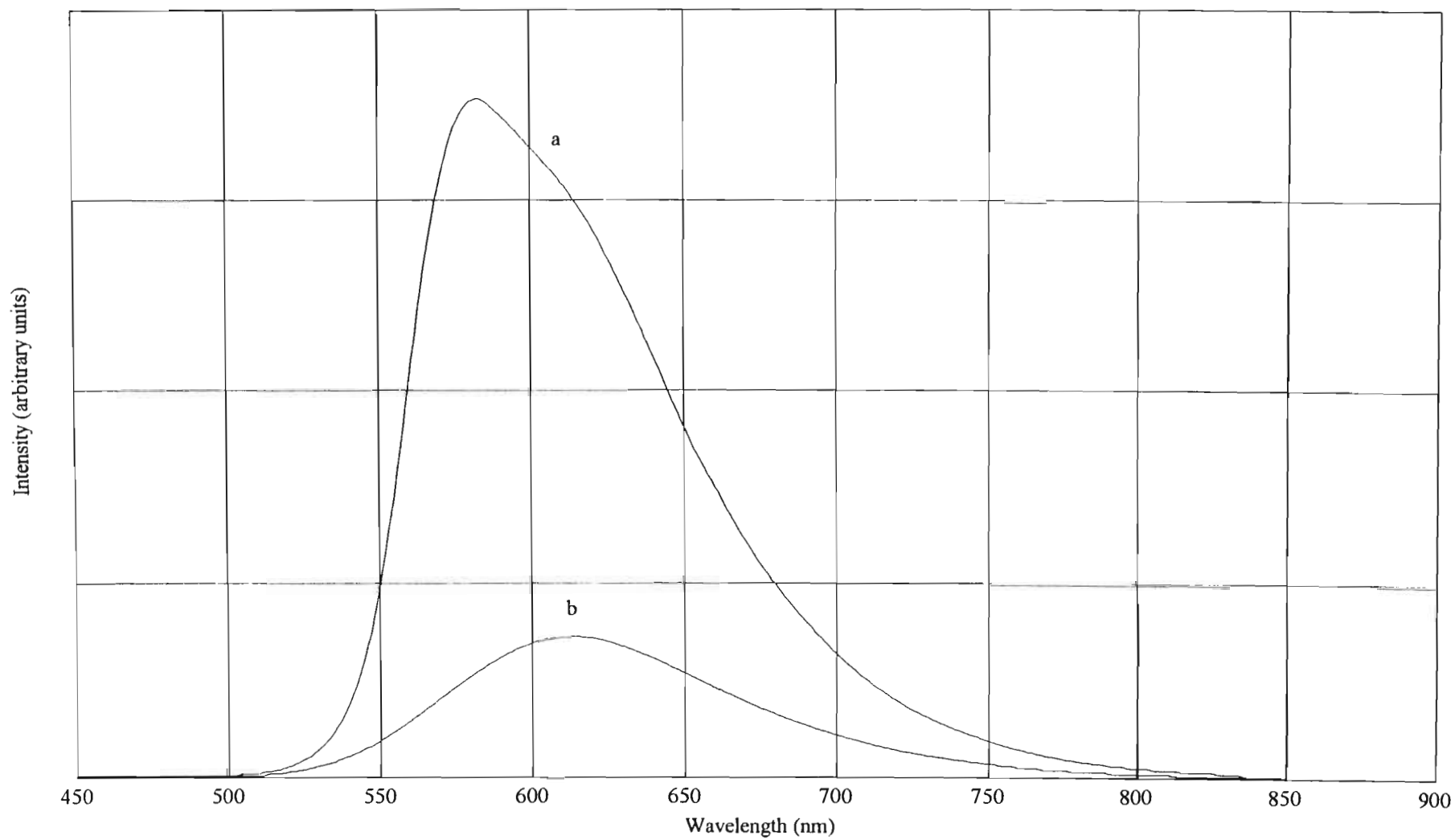
Figure 3.42   _The emission spectra of degassed solutions of [Pt(4'-Ph-terpy)(C≡CPh)](SbF₆) recorded at room temperature [(a) CH₂Cl₂_
solution and (b) CH₃CN solution].

structure when recorded in ethanol solution at room temperature. However, decreasing the temperature of such a solution to 77 K, results in the appearance of some vibrational structure in the emission spectrum. It is also interesting to note that, as in the case of the [Pt(terpy)(C≡CPh)]⁺ chromophore, emission from the [Pt(4'-Ph-terpy)(C≡CPh)]⁺ chromophore in fluid solution, is partially quenched by acetonitrile.

Based on the chemical similarity between the [Pt(4'-Ph-terpy)(C≡CPh)]⁺ and the [Pt(terpy)(C≡CPh)]⁺ chromophores, as well as their closely corresponding emission spectra recorded in CH₃CN solution, it follows that the reasoning employed in assigning the emission from the [Pt(4'-Ph-terpy)(C≡CPh)]⁺ chromophore in fluid solution, closely follows that employed in the case of the unsubstituted terpyridine derivative (**15**), as discussed in Section 3.4.6.3. Thus, considering the shape of the emission band profile, the fact that ³LF excited states for Pt(II) systems are generally relatively short-lived and that the dilution experiments performed as part of the quenching studies, did not reveal any significant changes in the band shape of the emission, the luminescence observed from fluid CH₃CN and CH₂Cl₂ solutions of [Pt(4'-Ph-terpy)(C≡CPh)](SbF₆) (**16**) is assigned to originate from the radiative decay of a unimolecular ³MLCT excited state. As in the case of the unsubstituted terpyridine derivative, this assignment is consistent with the fact that the emission in fluid solution is partially quenched by CH₃CN. The partially resolved structure observed in the emission spectrum of the chromophore dissolved in CH₂Cl₂, does not contradict this assignment. As mentioned above, the emission spectrum of an ethanol solution of [Pt(phen)(C≡CPh)₂], recorded at 77K, was reported to exhibit some vibrational structure.[248] Che and co-workers[248] nonetheless favoured a [(dπ*)(π*_phen)] excited state as the emitting state. Vibrationally structured emission from a unimolecular ³MLCT excited state has also been observed for the [Pt{3,3'-CH₃OCO)₂bipy}Cl₂] chromophore.[258]

The solid state emission spectrum of [Pt(4'-Ph-terpy)(C≡CPh)](SbF₆) was recorded at 40 K intervals over the temperature range 80 to 280 K. The overlaid spectra are presented in Figure 3.43. At 280 K the emission spectrum consists of a single very broad and distinctly asymmetric band, the maximum emission intensity occurring at *ca.* 600 nm. Decreasing the temperature of the sample results in a progressive increase in
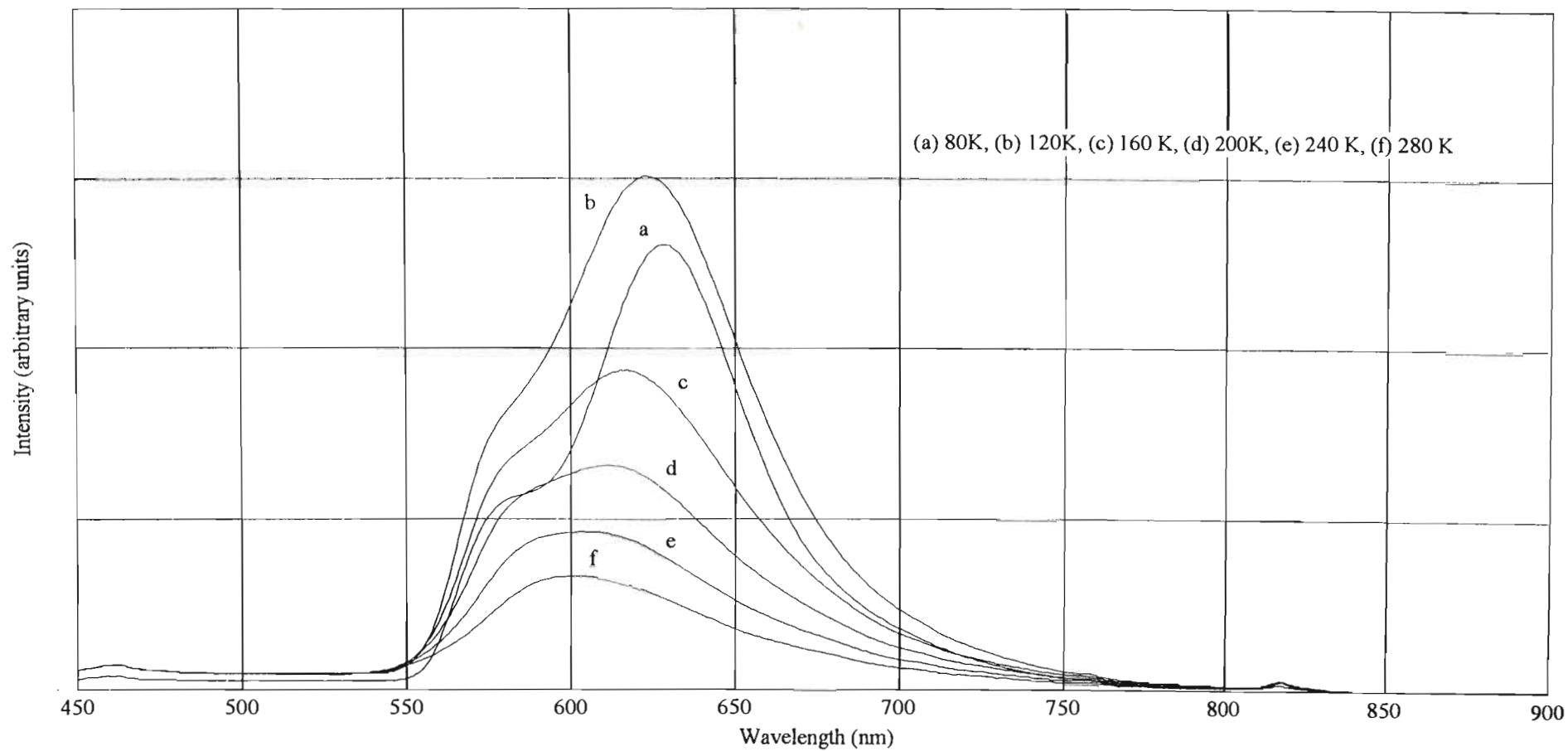
Figure 3.43 _The solid state emission spectrum of [Pt(4'-Ph-terpy)(C≡CPh)](SbF₆) recorded at 40 K intervals over the range 80 to 280 K._

the overall emission intensity with a concomitant widening of the band envelope. At temperatures between 200 and 160 K. it is evident that the band is actually comprised of two components, as in the case of the unsubstituted terpyridine derivative. The widening of the band envelope on reducing the sample temperature from 280 to 200 K, can thus be attributed to the higher energy component undergoing a blue-shift, whilst the lower energy component undergoes a red-shift. At 160 K the lower energy component exhibits maximum emission intensity at 616 nm. Due to extensive peak overlap with this component, it is more difficult to accurately determine the peak position of the higher energy component. Nonetheless, the maximum emission intensity for the latter component appears to occur at *ca.* 582 nm at 160 K. Decreasing the temperature of the sample to 120 K results in a further increase in the luminescent intensity of both components, with the lower energy component undergoing a further red-shift to 622 nm, whereas the higher energy component is blue-shifted to *ca.* 578 nm. However, this trend towards increasing overall luminescent intensity with decreasing temperature, does not apply on reducing the temperature of the sample from 120 to 80 K. Instead, the luminescent intensity of both components of the emission spectrum decrease as a result of the reduced sample temperature. Furthermore, although the lower energy component exhibits a further red-shift to 627 nm, the higher energy component does not display a further blue-shift in the position of its emission maximum. At 80 K the two components are clearly resolved, partly as a consequence of the diverging shifts of the two components on decreasing the sample temperature, but also as a result of a narrowing of the band envelope of the component of lower energy.

The different temperature dependent shifts in the positions of the emission maxima of the two components in the solid state emission spectrum of [Pt(4'-Ph-terpy)(C≡CPh)](SbF$_6$) (**16**), together with the strong similarity between the variable temperature solid state emission spectra of the [Pt(4'-Ph-terpy)(C≡CPh)](SbF$_6$) and [Pt(terpy)(C≡CPh)](SbF$_6$) (**15**) salts, suggest that as in the case of the latter, the two components in the emission spectrum of [Pt(4'-Ph-terpy)(C≡CPh)](SbF$_6$) originate from two different excited states. In this context the possibility of an impurity emission, or of emission from chromophores in different crystallographic environments being

responsible for the separate components has to be investigated, as was done in the case of [Pt(terpy)(C≡CPh)](SbF$_6$) (see Section 3.4.6.3). The possibility of an impurity emission giving rise to one of the components can most probably be discounted, since elemental analysis for C, H, and N has confirmed the samples of [Pt(4'-Ph-terpy)(C≡CPh)](SbF$_6$) used in the photophysical studies to be analytically pure. Impurity emission from trace amounts of starting material, not detected by elemental analysis, is also unlikely. Bu$_3$SnC≡CPh exists in the liquid phase at room temperature and, even if emissive, would have been removed by washing the sample during the purification procedure. On the other hand, the band profile of emission from solid samples of [Pt(4'-Ph-terpy)Cl](SbF$_6$), as discussed in Section 3.4.5.3, is unmistakably different from that of [Pt(4'-Ph-terpy)(C≡CPh)](SbF$_6$) and occurs at wavelengths well to the red of that observed for the latter. The possibility of impurity emissions originating from decomposition products can also be ruled out, since [Pt(4'-Ph-terpy)(C≡CPh)](SbF$_6$) is air and moisture stable in the solid state. The samples used in the photophysical studies were nonetheless stored under an atmosphere of dinitrogen and the experiments completed in the shortest time possible. The suggestion that emission from chromophores in different crystallographic environments within the crystal lattice might give rise to the two components in the emission spectrum can also be discounted since, as pointed out in Section 3.4.7.2, the [Pt(4'-Ph-terpy)(C≡CPh)](SbF$_6$) lattice contains one formula unit per asymmetric unit. This implies that the crystallographic environment of all the chromophores in the lattice are necessarily identical.

A consideration of the arguments presented above suggests that in solid samples of [Pt(4'-Ph-terpy)(C≡CPh)](SbF$_6$) (**16**), the [Pt(4'-Ph-terpy)(C≡CPh)]$^+$ chromophore exhibits simultaneous emission from at least two different excited states.

The lower energy component in the emission spectrum of solid samples of [Pt(4'-Ph-terpy)(C≡CPh)](SbF$_6$) is assigned to the radiative decay of a ^{3}(d$_{\sigma^*}$→π^b) excited state. This assignment is based on the red-shift and concomitant decrease in the bandwidth of this component, observed on decreasing the temperature of the sample. The same assignment was suggested for the analogous feature in the solid state emission spectrum of [Pt(terpy)(C≡CPh)](SbF$_6$). Identical temperature dependent variations

have also been reported to occur in the emission spectra of [Pt(bipy)(CN)$_2$], [Pt(phen)(CN)$_2$], [Pt(terpy)Cl](CF$_3$SO$_3$)[263] and the red form of [Pt(bipy)Cl$_2$].[268] In each of these instances, the authors assigned the emission to the radiative decay of a ^{3}(d$_{\sigma^*} \rightarrow \pi^b$) MLCT excited state.

At this point it is also interesting to compare the temperature dependent variation in the wavelength associated with the maximum emission intensity, λ(em)$_{max}$, for the ^{3}(d$_{\sigma^*} \rightarrow \pi^b$) MLCT component in the solid state emission spectra of [Pt(4'-Ph-terpy)(C≡CPh)](SbF$_6$) and [Pt(terpy)(C≡CPh)](SbF$_6$). At temperatures between 160 and 280 K, the value of λ(em)$_{max}$ for the ^{3}(d$_{\sigma^*} \rightarrow \pi^b$) MLCT component in the spectrum of the 4'-phenylterpyridine derivative is higher , *i.e.* to the red , of that associated with the unsubstituted terpyridine derivative. At 120 K the values for λ(em)$_{max}$ are virtually identical for the two compounds. However, at 80 K the order is reversed and the value of λ(em)$_{max}$ for the 4'-phenylterpyridine derivative is lower than that associated with [Pt(terpy)(C≡CPh)](SbF$_6$). These variations arise as a direct consequence of the differences in the packing architecture of the [Pt(terpy)(C≡CPh)](SbF$_6$) and [Pt(4'-Ph-terpy)(C≡CPh)](SbF$_6$) salts. In both salts the chromophores occur in extended stacks in which they are arranged head-to-tail. However, the shortest Pt-Pt separation in the lattice of the 4'-phenylterpyridine derivative at room temperature, equals 3.485Å, compared to 3.600Å in [Pt(terpy)(C≡CPh)](SbF$_6$). This implies that most probably, there are more substantial metal-metal interactions between the [Pt(4'-Ph-terpy)(C≡CPh)]$^+$ chromophores at room temperature in the solid state, than there are between the [Pt(terpy)(C≡CPh)]$^+$ chromophores under the same conditions. Consequently, the d$_{\sigma^*}$ orbital associated with the 4'-phenylterpyridine derivative (**16**) is most likely higher in energy than that of the unsubstituted terpyridine derivative (**15**), thus resulting in the energy of the ^{3}(d$_{\sigma^*} \rightarrow \pi^b$) MLCT excited state of the former being lower than that of the latter. This effect will be further enhanced by the fact that phenyl substitution in the 4'-position on the terpyridine ligand is also known to decrease the energy of the ^{3}CT state.[317] It is thus not surprising that at temperatures between 160 and 280 K, the wavelength, λ(em)$_{max}$, associated with the ^{3}(d$_{\sigma^*} \rightarrow \pi^b$) component of the emission from solid samples of [Pt(4'-Ph-terpy)(C≡CPh)](SbF$_6$), is higher than that associated with [Pt(terpy)(C≡CPh)](SbF$_6$). On decreasing the temperature of the

samples , the Pt-Pt separations will decrease, thus resulting in more substantial metal-metal interactions and consequently in the red-shift of the emission maxima as observed in the variable temperature solid state spectra. Since the $[Pt(4'-Ph-terpy)(C\equiv CPh)]^+$ chromophore is decidedly non-planar, it follows that with decreasing temperature, the Pt-Pt separation can only decrease to a certain minimum distance, at which point the non-bonded interactions associated with the non-planar substituents will predominate. The $[Pt(terpy)(C\equiv CPh)]^+$ chromophore on the other hand, is essentially planar, thus implying that much smaller Pt-Pt distances can be attained. At 80 K the non-bonded interactions between the $[Pt(4'-Ph-terpy)(C\equiv CPh)]^+$ chromophores are most probably sufficient to affect the Pt-Pt separation in such a way that the energy associated with the $^3(d_{\sigma*}\rightarrow\pi^b)$ MLCT excited state is higher than that associated with the $[Pt(terpy)(C\equiv CPh)]^+$ chromophores. This would explain why at 80 K, the emission maximum associated with the $^3(d_{\sigma*}\rightarrow\pi^b)$ MLCT component of the emission from solid samples of $[Pt(terpy)(C\equiv CPh)](SbF_6)$, occur at higher wavelengths than that of the 4'-phenylterpyridine derivative (**16**).

As in the case of $[Pt(terpy)(C\equiv CPh)](SbF_6)$ (**15**), the currently available data is not sufficient to attempt to make an unequivocal assignment of the higher energy component in the emission spectrum of $[Pt(4'-Ph-terpy)(C\equiv CPh)](SbF_6)$. The possibility of it originating from the radiative decay of a $^3(\pi-\pi*)$ IL excited state can be ruled out, since the high energy side of the band envelope of the $^3(d_{\sigma*}\rightarrow\pi^b)$ MLCT component does not display any evidence of superimposed vibrational structure, as would be expected if the higher energy component of the emission represented the highest energy vibrational feature. However, as mentioned in the discussion of the analogous feature in the solid state emission spectrum of $[Pt(terpy)(C\equiv CPh)](SbF_6)$ (see Section 3.4.6.3), several possibilities remain, examples being emission from a unimolecuar type ^{3}MLCT excited state, a ligand-to-ligand charge transfer state or even from excimer type emission which only involves ligand-ligand and no metal-metal interactions.

The above discussion focused only on the radiative processes associated with the $[Pt(4'-Ph-terpy)(C\equiv CPh)]^+$ chromophore. No attempt was made at explaining the non-

radiative processes involved and their influence in affecting the temperature dependent increases and decreases in luminescent intensity observed in the solid state emission spectra. It is obvious that further studies will be required to obtain enough information to fully understand the electronic processes involved following excitation of the chromophore in the solid state. In this regard, lifetime measurements and time resolved spectra, as suggested in Section 3.4.6.3, might be considered. Furthermore a synthetic programme, aimed at effecting small changes in the molecular structure of the chromophore and its packing architecture, and studying the influence of such perturbations on the solid state luminescence, might provide some further insight. In this context one might consider changing the metal centre, or the counterion as was demonstrated for the $[Pt(terpy)Cl]^+$ and $[Pt(bipy)_2]^{2+}$ chromophores, or the substituents on the terpyridine and acetylide ligands.

3.5 Conclusion

The work described in this chapter is primarily concerned with the solid state luminescent properties of square planar bi- and terpyridyl complexes of Pt(II) and where possible, with reconciling the solid state crystal structure of these complexes with their luminescent properties. To this end the complex salts $[Pt(terpy)(CH_3CN)](SbF_6)_2$, $[Pt(terpy)Cl](X)$ $(X = SbF_6^-,$ $CF_3SO_3^-,$ $BF_4^-)$, $[Pt(bipy)_2](X)_2$ $(X = SbF_6^-$ and $CF_3SO_3^-)$, $[Pt(4'-Ph-terpy)Cl](SbF_6)$, $[Pt(terpy)-(C\equiv CPh)](SbF_6)$ and $[Pt(4'-Ph-terpy)(C\equiv CPh)](SbF_6)$ were synthesized and their emission behaviour studied. The crystal structures of $[Pt(terpy)(CH_3CN)](SbF_6)_2$, $[Pt(bipy)_2](SbF_6)_2$, $[Pt(terpy)(C\equiv CPh)](SbF_6)$ and $[Pt(4'-Ph-terpy)(C\equiv CPh)](SbF_6)$ were determined.

To the best of our knowledge, the structure of $[Pt(terpy)(CH_3CN)](SbF_6)_2$ represents the first example of the structure determination of a terpyridyl complex of Pt(II) with a neutral ligand in the fourth coordination site. The crystal lattice of the yellow salt consists of sheets of alternating rows of cations and anions. However, the cations within each row are arranged side-by-side with no evidence of any orbital interactions between neighbouring cations. Samples of $[Pt(terpy)(CH_3CN)](SbF_6)_2$, both in the solid state and in a dilute butyronitrile glass at 77 K, exhibit simultaneous emission

from both a $^3(\pi\text{-}\pi^*)$ intraligand and a unimolecular ^{3}MLCT excited state. The $^3(\pi\text{-}\pi^*)$ component of the emission is suppressed in CH$_3$CN solution at room temperature, with only emission originating from the radiative decay of the ^{3}MLCT excited state being observed under these conditions. Repeated attempts at obtaining pure samples of [Pt(terpy)(CH$_3$CN)](CF$_3$SO$_3$)$_2$ and [Pt(terpy)(CH$_3$CN)](BF$_4$)$_2$, to study the influence of the counterion on the solid state packing architecture and thus on the luminescence of the [Pt(terpy)(CH$_3$CN)]$^+$ chromophore, were unsuccessful.

The next part of this study focused on the [Pt(terpy)Cl]$^+$ chromophore and the influence of variations in the steric demands of the counterion on the emission behaviour of this chromophore in the solid state. Whereas the solid state emission spectra of both [Pt(terpy)Cl](BF$_4$) and [Pt(terpy)Cl](CF$_3$SO$_3$) display distinct red-shifts of the emission maximum on decreasing the temperature of the sample, the wavelength of the emission maximum in the spectrum of [Pt(terpy)Cl](SbF$_6$) was found to be unaffected by the sample temperature. The emission behaviour of the BF$_4^-$ and the CF$_3$SO$_3^-$ salts is typical of that of linear chain compounds with metal-metal interactions between the individual chromophores and where the emission originates from the radiative decay of a $^3(d_{\sigma^*}\rightarrow\pi^b)$ excited state. The different behaviour of the SbF$_6^-$ salt was interpreted as being a direct consequence of a solid state packing effect. The emission either originates from a $^3(d_{\sigma^*}\rightarrow\pi^b)$ excited state, the linear chain structure being such that no decrease in the Pt-Pt separation is possible on decreasing the sample temperature, and thus no red-shift is observed, or from a unimolecular ^{3}MLCT excited state if there are no orbital interactions between the [Pt(terpy)Cl]$^+$ chromophores. Unfortunately we were unable to obtain the crystal structure of [Pt(terpy)Cl](SbF$_6$), thus complicating the assignment. From these studies it did become apparent however that the utilization of counterions with varying steric demands can substantially influence the luminescent properties of a chromophore in the solid state by modifying the solid state packing motif and thus the electronic interactions between the individual chromophores.

The effect of the steric demands of the counterion on the luminescent properties of platinum polypyridyl salts was further investigated in a study of the solid state luminescence of salts of the [Pt(bipy)$_2$]$^{2+}$ chromophore. Although the emission

behaviour of $[Pt(bipy)_2](ClO_4)_2$ in the solid state has been reported previously, some doubt existed as to whether a broad structureless feature in the emission spectrum originated from excimeric emission, or from multiple state emission from the monomeric chromophore. With the object of further investigating this problem, $[Pt(bipy)_2](SbF_6)_2$ was synthesized and its luminescent behaviour, together with that of its triflate analogue, $[Pt(bipy)_2](CF_3SO_3)_2$, studied. The solid state emission spectra of both salts exhibit the broad structureless feature observed in the spectrum of the ClO_4^- salt. However, a crystal structure determination revealed that the $[Pt(bipy)_2]^{2+}$ chromophores in the SbF_6^- salt exist as monomeric entities with no orbital interactions between them, whereas the chromophores are arranged in extended stacks in the $CF_3SO_3^-$ salt with ligand-ligand overlap between neighbouring chromophores. From these observations it was concluded that the broad structureless feature in the solid state emission spectra of these salts is not excimeric in origin, but results from multiple state emission from the monomeric $[Pt(bipy)_2]^{2+}$ chromophore. A more accurate assignment could not be attempted without the aid of more sophisticated photophysical experiments.

A further perturbation which can impact on the solid state structure and luminescent properties, involves modifying the molecular structure of the chromophore to include small deviations from planarity. With this in mind $[Pt(4'-Ph-terpy)Cl](SbF_6)$ was synthesized. Not only is the phenyl substituent responsible for introducing some non-planarity to the $[Pt(4'-Ph-terpy)Cl]^+$ chromophore, but it also results in a different electronic structure when comparing this chromophore to its unsubstituted terpyridine equivalent. Freshly prepared solid state samples of $[Pt(4'-Ph-terpy)Cl](SbF_6)$ exhibit a bright yellow luminescence which was attributed to the radiative decay of a $^3(\pi-\pi^*)$ excited state. Although the luminescent intensity increases and additional vibrational structure is resolved on decreasing the sample temperature, the electronic origin of the emission is unaffected by these temperature changes. However, on crushing samples of $[Pt(4'-Ph-terpy)Cl](SbF_6)$, the luminescence at room temperature changes from the bright yellow associated with uncrushed samples, to a bright orange, attributable to the radiative decay of a $(d_{\sigma^*} \rightarrow \pi^b)$ excited state, in the crushed samples. On decreasing the temperature of such samples, the $^3(\pi-\pi^*)$ component reappears with the colour of the

luminescence reverting back to the original yellow colour observed for uncrushed samples. Two scenarios were proposed to explain the emission behaviour of crushed samples of [Pt(4'-Ph-terpy)Cl](SbF$_6$). The first involves the [Pt(4'-Ph-terpy)Cl]$^+$ chromophores existing in two crystallographically distinct environments, the one with no interactions between the chromophores and with emission originating from the $^3(\pi$-$\pi^*)$ excited state, the other with distinct orbital interactions between the chromophores and emission originating from the radiative decay of a (d$_{\sigma^*} \to \pi^b$) excited state. The second scenario involves the crystallographic environment of all the chromophores being identical, but with the chromophores exhibiting simultaneous emission from both the $^3(\pi$-$\pi^*)$ and (d$_{\sigma^*} \to \pi^b$) excited states, the two states being coupled by thermally activated vibrational interactions. At room temperature, emission from the (d$_{\sigma^*} \to \pi^b$) excited state predominates, due to the vibrational interactions resulting in interconversion from the $^3(\pi$-$\pi^*)$ to the (d$_{\sigma^*} \to \pi^b$) excited state. The obvious way to determine which of these scenarios apply in practice, would be by determining the solid state structure of the crushed form. However, since a *crushed* sample is involved, the use of single crystal X-ray diffractometry is precluded, thus complicating the assignment.

The last sections of this study focused on the synthesis and luminescent properties of the [Pt(terpy)(C≡CPh)]$^+$ and [Pt(4'-Ph-terpy)(C≡CPh)]$^+$ chromophores in which both an acetylide and a terpyridine ligand are coordinated to a single Pt(II) centre. In both [Pt(terpy)(C≡CPh)](SbF$_6$) and [Pt(4'-Ph-terpy)(C≡CPh)](SbF$_6$) the chromophores are arranged in extended stacks with the interplanar spacing between the chromophores being less than, or comparable to the Van der Waal's separation for π-aromatic species in a face-to-face arrangement. Both chromophores exhibit emission from a unimolecular ^{3}MLCT excited state in degassed solutions of CH$_2$Cl$_2$ and CH$_3$CN at room temperature, the emission being partially quenched by CH$_3$CN. The solid state emission spectra of both salts are comprised of two components originating from the radiative decay of two separate excited states. The lower energy component in the spectra of both salts has been assigned to originate from a ^{3}(d$_{\sigma^*} \to \pi^b$) MLCT excited state. The different temperature dependent behaviour of this feature for the two salts is a direct consequence of the different molecular geometries associated with the

$[Pt(terpy)(C\equiv CPh)]^+$ and $[Pt(4'-Ph-terpy)(C\equiv CPh)]^+$ chromophores effecting differences in the packing architecture, which in turn impact on the electronic interactions between the chromophores. Unfortunately, the currently available data is insufficient to allow an absolute assignment of the higher energy component in the solid state emission spectra of these two chromophores.

From a consideration of the results presented in this study it is obvious that although some understanding of the luminescent properties of the chromophores considered, and the influence of their solid state packing architecture on their emission behaviour (in the solid state) has been gained, a complete understanding of all the electronic transitions following excitation of these chromophores is still lacking. This is due to two factors. Firstly we were unable to obtain the solid state structures of all the complex salts considered here and secondly, our limited access to the equipment required for photophysical studies restricted the number of experiments we could perform. Although more effort can be directed at attempts to obtain some of the solid state structures lacking in this work, a considerable amount of time and effort has already been invested on this front, and the likelihood of success is limited. Effort should rather be directed at more exhaustive photophysical experiments, particularly at determining the lifetimes of the excited states involved and separating and studying the individual components in instances where simultaneous emission from multiple excited states is evident. In the short term, synthetic studies can concentrate on effecting small modifications of the chromophores presented in this study. Such modifications can be the result of changing the metal centre, the ligand in the fourth coordination site, the substituents on the terpyridine moiety or the counterion involved. Comparing and contrasting the emission properties of chromophores resulting from such perturbations might provide further insight into the radiative and non-radiative processes following excitation of these chromophores.

The results presented in this study also revealed that a much larger number of relatively long lived excited states are accessible to polypyridyl complexes of Pt(II) in the solid state, than in solution. This is the consequence of a number of factors, the most important ones being:

1. Most of the orbital interactions between the chromophores in the solid state are absent in solution.

2. Chromophores are more subject to excited state distortions in solution, than in the solid state.

3. Interactions between solvent molecules and the excited state chromophore can reduce the excited state lifetime.

The scarcity of polypyridyl complexes of Pt(II) which do exhibit luminescence in solution, becomes particularly relevant if these platinum complexes, in their excited states, are to be utilized as catalysts or reactive intermediates. Since most chemical reactions occur in solution, it follows that unless these complexes are employed as heterogeneous catalysts or intermediates, *i.e.* in the solid state, it would not be possible to exploit a large number of the excited states accessible by these complexes.

Furthermore, all the complex salts synthesized and studied in this work, utilized the molecular co-crystallization approach, which does not allow for rigorous structural enforcement since, as pointed out by Marks,[73] "the packing forces operative in most molecular conductors (and other low-dimensional materials) are rather delicate".

From these arguments it is evident that in order to overcome these restrictions, a long term synthetic programme should perhaps be directed towards incorporating Pt(II) polypyridyl chromophores into dimeric or oligomeric type complexes. In this regard the work by Gray and co-workers[291] and Che and co-workers[318] on the preparation and luminescent properties of dimeric $\{[Pt(terpy)]_2(\mu\text{-}L)\}^{3+}$ complexes [L = μ-pyrazole, μ-azaindole, μ-diphenylformamidine, μ-arginine[291] or μ-guanidine[318]] constitutes a first step.

3.6 Note

At the time of the submission of this thesis, the following article on the "Electronic spectroscopy of chloro(terpyridine)platinum(II)", *i.e.* the $[Pt(terpy)Cl]^+$ chromophore, appeared on our shelves: J.A. Bailey, M.G. Hill, R.E. Marsh, V.M. Miskowski, W.P. Schaefer and H.B. Gray, *Inorg. Chem.*, (1995), **34**, 4591.

Gray and co-workers prepared the PF_6^-, ClO_4^-, Cl^- and $CF_3SO_3^-$ salts of $[Pt(terpy)Cl]^+$ and studied the absorption of the chromophore in solution, as well as its luminescent behaviour, both in solution and in the solid state. The report also includes a description of the crystal structure of $[Pt(terpy)Cl](ClO_4)$.

In accordance with the results reported in Section 3.4.3.2, Gray and co-workers found that the $[Pt(terpy)Cl]^+$ chromophore precipitates with different counterions to give salts of various colours. The authors also note that precipitation from different solvents can have an influence on the colour of the complex salt. In this context, $[Pt(terpy)Cl](ClO_4)$, precipitated from aqueous solution and vacuum-dried, is deep-red in colour, whereas the Cl^- and PF_6^- salts treated in the same way, are orange and yellow, respectively. Furthermore, the perchlorate salt, when crystallized from DMF/ether, was found to have a rust-orange colour. As described in Section 3.4.3.2, these differences in colour are attributable to differences in the solid state packing architecture, or in the words of Gray *et al.* "it is likely that the range of colours of the $[Pt(terpy)Cl]^+$ salts is due both to variation of metal-metal separations, and to the degree of oligomerization in the solid state".

Table 3.6   *Emission maxima for [Pt(terpy)Cl](X) solids*

X^-	Precipitated or crystallized from	Colour	$\lambda(em)_{max}$ (nm)	
			300K	77K
ClO_4^-	H_2O	Deep red	725	695
ClO_4^-	DMF/Et_2O	Rust-orange	645	640
Cl^-	H_2O	Orange	650	640
$CF_3SO_3^-$	H_2O	Orange	640	625
PF_6^-	H_2O	Yellow	630	565

The emission maxima in the solid state emission spectra of the salts reported by Gray and co-workers are collated in Table 3.6.

The emission from solid samples of the red form of [Pt(terpy)Cl](ClO$_4$), both at room temperature and at 77 K, has been assigned to the radiative decay of a ^{3}MMLCT (metal-metal bond to ligand charge transfer), $i.e.$ a ^{3}(d$_{\sigma^*} \rightarrow \pi^b$) excited state. However, the temperature dependence of the solid state emission of this salt is in marked contrast to that normally associated with metal-chain compounds as has been observed for the [Pt(terpy)Cl](BF$_4$) and [Pt(terpy)Cl](CF$_3$SO$_3$) salts reported in this thesis. Gray and co-workers suggested that the difference originates from the red perchlorate salt possessing an isolated dimer type structure, rather than a linear chain structure with uniform Pt-Pt separations.

The low-temperature (77 K) emission from solid samples of the orange form of the [Pt(terpy)Cl](ClO$_4$) salt, as well as that from [Pt(terpy)Cl](CF$_3$SO$_3$) and [Pt(terpy)Cl]Cl, was assigned to also originate from a ^{3}MMLCT excited state. On the other hand, the broad band observed in the room temperature emission spectra of these salts was suggested to originate from a different electronic state. The authors were uncertain of its exact origin, but based on a previous assignment of a broad band in the solid state emission spectra of the [Pt(bipy)$_2$]$^{2+}$ and [Pt(phen)$_2$]$^{2+}$ chromophores, suggested that the emission originates from an excimeric π-π* intraligand transition. In this respect it is interesting to note that whilst Gray and co-workers reported a blue-shift in the position of the emission maximum, from 640 nm to 625 nm, on cooling solid samples of [Pt(terpy)Cl](CF$_3$SO$_3$) from 300 to 70 K, this study, as well as that of Che and co-workers,[263] revealed a red-shift in the position of the emission maximum on cooling solid state samples of this salt. It is possible that the samples studied here and by Che and co-workers had a different solid state packing motif to that utilized in the study by Gray et $al.$, thus explaining the difference in solid state luminescent behaviour. This suggestion is supported by the fact that the samples of [Pt(terpy)Cl](CF$_3$SO$_3$) utilized in the study by Gray et $al.$ was precipitated from water, whereas the samples utilized in the present study and in that of Che and co-workers, were recrystallized from acetonitrile. However, Gray and co-workers made use of the crystal structure reported by Che et $al.$ in their assignment of the emission from solid

samples of [Pt(terpy)Cl](CF$_3$SO$_3$), but did not offer any explanation for the difference in luminescent behaviour between the samples they studied, and that studied by Che and co-workers.

A further aspect that deserves mention, is the fact that the results presented in this thesis have shown that the broad emission feature in the solid state emission spectra of the [Pt(bipy)$_2$]$^{2+}$ chromophore, as found in [Pt(bipy)$_2$](SbF$_6$)$_2$ (**12**) and [Pt(bipy)$_2$]-(CF$_3$SO$_3$)$_2$ (**13**), does not originate from an excimeric π-π* intraligand transition. A similar result was obtained for the [Pt(terpy)(CH$_3$CN)](SbF$_6$)$_2$ salt. These results raise some doubt concerning the excimeric π-π* intraligand assignment favoured by Gray *et al.* to explain the room temperature solid state luminescence of the orange ClO$_4^-$, Cl$^-$ and CF$_3$SO$_3^-$ salts of [Pt(terpy)Cl]$^+$, and demands some further evidence to substantiate such an assignment.

The temperature dependence of the emission from solid samples of [Pt(terpy)Cl](PF$_6$), a yellow salt, was reported to be markedly different from that of the other salts studied by Gray and co-workers. At temperatures between 295 and 160 K, the emission from the PF$_6^-$ salt exhibits very little change in either λ(em)$_{max}$ (630 nm), or the width of the band envelope. However, on decreasing the temperature of the sample below 160 K, the intensity of the emission centred at 630 nm decreases and a new narrow band, centred at 565 nm, rapidly increases in intensity. At 70 K this band dominates the emission spectrum. Again the luminescence was assigned to originate from an excimeric intraligand π-π* transition with the temperature dependent changes in the spectrum being suggested to be a consequence of the presence of multiple electronic states.

The temperature dependence of the emission from solid samples of [Pt(terpy)Cl](PF$_6$), as described by Gray and co-workers. also differs from the yellow [Pt(terpy)Cl](SbF$_6$) salt described in this thesis. The emission spectrum of the PF$_6^-$ salt seems to be comprised of two separate components, whereas only one component is evident in the solid state emission spectra of the SbF$_6^-$ salt recorded at different temperatures. This component, centred at 552 nm, would seem to correspond to the dominant higher energy component [λ(em)$_{max}$ = 565 nm] in the low-temperature spectra of the PF$_6^-$ salt.

It might thus be that the solid state packing motif in the SbF$_6^-$ salt represents a lower extreme, with minimum interactions between the [Pt(terpy)Cl]$^+$ chromophores, whereas that of the PF$_6^-$ salt represents a cross-over from the situation where some Pt-Pt interactions are evident, as in the structure of the CF$_3$SO$_3^-$ salt for instance, to that of minimal interactions, if any, as suggested for the SbF$_6^-$ salt. This would certainly be consistent with the increased steric bulk of the SbF$_6^-$ anion, when compared to the PF$_6^-$ ion. Furthermore, also recall that the SbF$_6^-$ salt, when precipitated from CH$_3$CN, is orange in colour, similar to the CF$_3$SO$_3^-$ salt, and only reverts to the yellow form on isolation from the mother liquor.

Gray and co-workers also studied the emission behaviour of the [Pt(terpy)Cl]$^+$ chromophore in a low-temperature glassy solution. As reported in this thesis, the emission was found to be highly structured and was assigned to originate from a $^3(\pi\text{-}\pi^*)$ intraligand excited state.

3.7 Experimental

3.7.1 Synthetic procedures

3.7.1.1 [Pt(terpy)(CH$_3$CN)](SbF$_6$)$_2$ (**8**)

A solution of a 10% excess of AgSbF$_6$(0.160 g, 0.466 mmol) in CH$_3$CN (5 to 7 cm^3), was added to a suspension of [Pt(C$_6$H$_5$CN)$_2$Cl$_2$] (0.200 g, 0.424 mmol) in CH$_3$CN (15 cm^3) and the mixture heated to reflux for 4 hours before a 10% excess of 2, 2',6',2''-terpyridine (0.109 g, 0.466 mmol) was added as a solid. The reaction mixture was then heated under reflux for a further 15 hours and allowed to cool to room temperature before the volume was reduced *in vacuo*. The precipitate, containing a mixture of AgCl and [Pt(terpy)Cl](SbF$_6$), was isolated by filtration, placed in the vapour extraction apparatus depicted in Section A.2.1.2 of Appendix A, and the [Pt(terpy)Cl](SbF$_6$) extracted into a refluxing solution of AgSbF$_6$ {0.291 g, 0.848 mmol, a twofold molar equivalent based on the quantity of [Pt(C$_6$H$_5$CN)$_2$Cl$_2$] used in the first step} in CH$_3$CN (10 cm^3). The reaction mixture was heated under reflux for an additional 4 hours after the last traces of [Pt(terpy)Cl](SbF$_6$) was extracted (visually assessed) from the AgCl/[Pt(terpy)Cl](SbF$_6$) mixture. It was then allowed to cool to room temperature and the precipitated AgCl removed by filtration. The volume of the

filtrate was reduced *in vacuo*, resulting in the precipitation of any unreacted [Pt(terpy)Cl](SbF$_6$), which was removed by filtration. The filtrate was evaporated to dryness (*in vacuo*) and the residue thoroughly washed with acetone and diethyl ether before drying under vacuum. The solid material thus obtained was dissolved in CH$_3$CN and the solvent allowed to evaporate over *ca.* 1 week, resulting in the crystallization of [Pt(terpy)(CH$_3$CN)](SbF$_6$)$_2$ as light yellow block-shaped crystals.

Yield: 40 - 50%

Molecular Mass: 940.89 g.mol^{-1}

Elemental Analysis: Calculated: C: 21.70   H: 1.50   N: 5.95

                       Found: C: 21.61   H: 1.39   N: 5.93

3.7.1.2 [Pt(terpy)Cl](X) [X⁻ = SbF$_6$⁻ (9), CF$_3$SO$_3$⁻ (10), BF$_4$⁻ (11)]

An equimolar amount of AgX (0.146 g for X⁻ = SbF$_6$⁻; 0.109 g for X⁻ = CF$_3$SO$_3$⁻ and 0.082 g for X⁻ = BF$_4$⁻, 0.424 mmol) in CH$_3$CN (5 to 7 cm^3) was added to a suspension of [Pt(C$_6$H$_5$CN)$_2$Cl$_2$] (0.200 g, 0.424 mmol) in CH$_3$CN (15 cm^3). The reaction mixture was heated under reflux for 15 hours, the precipitated AgCl removed by filtration and a 5% excess of 2,2',6',2"- terpyridine (0.104 g, 0.445 mmol) added to the filtrate. The resulting mixture was heated under reflux for a further 15 hours after which any additional precipitated AgCl was removed by filtration before the solvent was removed *in vacuo*. The [Pt(terpy)Cl](X) salt was extracted from the residue with hot CH$_3$CN and the volume of the hot extract reduced to a minimum (*in vacuo*). Allowing the solution thus obtained to slowly cool to room temperature resulted in the separation of the salt as an orange crystalline or microcrystalline solid. Subsequent purification involved washing the isolated product with acetone and/or diethyl ether and drying it under vacuum to afford [Pt(terpy)Cl](SbF$_6$) as a yellow solid, whilst the CF$_3$SO$_3$⁻ and BF$_4$⁻ salts retained their original orange colour.

Yield: 70-80%

Molecular Masses:

$[Pt(terpy)Cl](SbF_6)$:   699.6 g.mol^{-1}

$[Pt(terpy)Cl](CF_3SO_3)$:   612.9 g.mol^{-1}

$[Pt(terpy)Cl](BF_4)$:   550.6 g.mol^{-1}

Elemental Analysis:

$[Pt(terpy)Cl](SbF_6)$:	Calculated:	C: 25.75	H: 1.58	N: 6.00
	Found:	C: 25.88	H: 1.67	N: 6.05
$[Pt(terpy)Cl](CF_3SO_3)$:	Calculated:	C: 31.36	H: 1.81	N: 6.86
	Found:	C: 30.27	H: 1.63	N: 7.27
$[Pt(terpy)Cl](BF_4)$:	Calculated:	C: 32.72	H: 2.01	N: 7.63
	Found:	C: 32.28	H: 2.14	N: 7.47
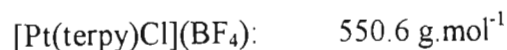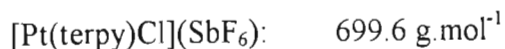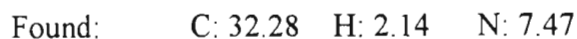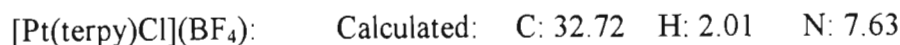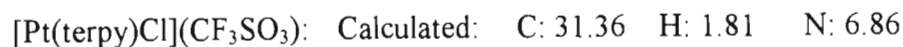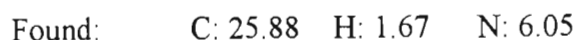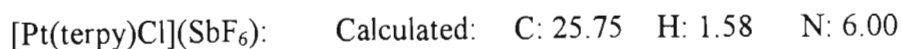
3.7.1.3 [Pt(bipy)₂](SbF₆)₂ (12)

A solution of $AgSbF_6$ (0.298 g, 0.868 mmol, 5% in excess of a twice molar amount) in CH_3CN (10 to 15 cm^3), was added to $[Pt(C_6H_5CN)_2Cl_2]$ (0.200 g, 0.424 mmol) suspended in CH_3CN (15 cm^3). The reaction mixture was heated under reflux for 15 hours after which the precipitated AgCl was removed by filtration and 2,2'- bipyridine (0.136 g, 0.868 mmol, 5% in excess of a twice molar amount) added as a solid. The reaction mixture was heated under reflux for a further 15 hours. If any traces of precipitated product (lemon yellow microcrystalline solid) was evident, the temperature of the mixture was kept close to its boiling point and enough CH_3CN added to dissolve the precipitated product. Any further precipitated AgCl was removed by filtration and the volume of the hot filtrate reduced to a minimum (*in vacuo*). Allowing this solution to slowly cool to room temperature resulted in the crystallization of $[Pt(bipy)_2](SbF_6)_2$ as lemon-yellow block-like crystals. The isolated

crystals were washed , in order, with small aliquots of CH_3CN, acetone and diethyl ether before drying *in vacuo*.

Yield: 75 - 85%

Molecular Mass: 978.9 g.mol⁻¹

Elemental Analysis: Calculated: C: 24.54   H: 1.65   N: 5.72

                       Found: C: 24.89   H: 1.61   N: 5.58

3.7.1.4 [Pt(4'-Ph-terpy)Cl](SbF₆) (14)

An equimolar amount of $AgSbF_6$ (0.146 g, 0.424 mmol) in CH_3CN (5 to 7 cm³) was added to a suspension of $[Pt(C_6H_5CN)_2Cl_2]$ (0.200 g, 0.424 mmol) in CH_3CN (15 cm³). The reaction mixture was heated under reflux for 15 hours, the precipitated AgCl removed by filtration and a 5% excess of 4'-phenylterpyridine (0.138g, 0.445 mmol) added as a solid. The mixture was then heated under reflux for an further 15 hours. If any traces of precipitated product (yellow microcrystalline solid) was evident, the temperature of the mixture was kept close to its boiling point and sufficient CH_3CN added to fully dissolve the precipitated product, added. Any further AgCl which might have precipitated during the second reflux, was removed by filtration and the volume of the hot filtrate reduced to a minimum (*in vacuo*). Allowing this solution to slowly cool to room temperature resulted in the precipitation of $[Pt(4'-Ph-terpy)Cl](SbF_6)$ as a yellow microcrystalline solid. The isolated product was washed, in order, with small aliquots of CH_3CN, acetone and diethyl ether before drying *in vacuo*. Further purification was achieved by redissolving the product it in hot CH_3CN and reprecipitating it from the solution by allowing the solution to slowly cool to room temperature.

Yield: 70 - 80 %

Molecular Mass: 775.7 g.mol⁻¹

Elemental Analysis: Calculated: C: 32.51   H: 1.95   N: 5.42

                       Found: C: 32.55   H: 1.96   N: 5.63

3.7.1.5 [Pt(terpy)(C≡CPh)](SbF$_6$) (**15**)

Method 1:

[Pt(terpy)Cl](SbF$_6$) (0.100g, 0.143 mmol) and AgC≡CPh (0.031 g, 0.150 mmol, 5% excess) was suspended in pyridine (30 cm^3) and the suspension stirred vigorously for 15 hours. The resulting bright red precipitate was isolated by filtration, washed with diethyl ether and dried *in vacuo*. This resulted in the precipitate changing colour from bright red to pale brown. The material was then placed in the vapour extraction apparatus depicted in Section A.2.1.2 of Appendix A and the [Pt(terpy)(C≡CPh)](SbF$_6$) extracted into boiling CH$_3$CN. The volume of the hot extract was reduced to a minimum and the solution then slowly cooled to *ca.* -10° C resulting in the product precipitating as a dark purple-brown microcrystalline solid. The isolated product was washed with small volumes of CH$_3$CN and then with diethyl ether before drying it *in vacuo*.

Yield: 50 - 60 %

Method 2 (Preferred method):

[Pt(terpy)Cl](SbF$_6$) (0.150g, 0.214 mmol) was suspended in CH$_3$CN (10 cm^3) and a twice molar amount of Bu$_3$SnC≡CPh (0.168 g, 0.429 mmol) added. The mixture was heated under reflux for 4 to 6 hours and then allowed to cool to room temperature. The orange microcrystalline precipitate was isolated through filtration, washed with *n*-hexane, cold acetonitrile and then diethyl ether and dried *in vacuo*.

Yield: 60 - 70 %

Molecular Mass: 765.2 g.mol-1

Elemental Analysis: Calculated: C: 36.10   H: 2.11   N: 5.49

Found: C: 36.10   H: 2.25   N: 5.71

3.7.1.6 [Pt(4'-Ph-terpy)(C≡CPh)](SbF$_6$) (**16**)

[Pt(4'-Ph-terpy)Cl](SbF$_6$) (0.150g, 0.193 mmol) was suspended in CH$_3$CN (10 cm^3) and a twice molar amount of Bu$_3$SnC≡CPh (0.151 g, 0.389 mol) added. The mixture

was heated under reflux for 4 to 6 hours and the volume of the solution then reduced *in vacuo*, resulting in the precipitation of the crude product as an orange microcrystalline solid. This material was isolated washed, in order, with *n*-hexane, cold acetonitrile and diethyl ether and dried *in vacuo*. The solid material was placed in the vapour extraction apparatus depicted in Section A.2.1.2 of Appendix A and the [Pt(4'-Ph-terpy)(C≡CPh)](SbF$_6$) extracted into boiling CH$_3$CN. Allowing the hot extract to slowly cool to room temperature, resulted in [Pt(4'-Ph-terpy)(C≡CPh)](SbF$_6$) crystallizing as orange-red block-shaped crystals. These crystals were washed with small aliquots of cold CH$_3$CN and then with diethyl ether before drying it under vacuum.

Yield: 65- 75 %

Molecular Mass: 841.3 g.mol^{-1}

Elemental Analysis: Calculated: C: 41.40   H: 2.40   N: 4.99

Found: C: 40.95   H: 2.25   N: 5.26

3.7.2 Crystal Structure Determinations

3.7.2.1 [Pt(terpy)(CH₃CN)](SbF₆)₂ (8)

Light yellow block-like crystals of **8**, suitable for X-ray diffraction studies were obtained by preparing a CH_3CN solution of the salt and allowing the solvent to slowly evaporate over a period of *ca.* 1 week.

The general procedure for the intensity data collection and the general approach to structure solution and refinement are described in Sections A.5.1 and A.5.2 of Appendix A, respectively.

Crystal data, as well as details specific to the data collection, stucture solution and refinement for **8** are provided in Table 3.7. Anisotropic refinement was applied to all the non-hydrogen atoms of both the cation and the two anions. The hydrogen atoms were not located, but were placed in calculated positions. The two SbF_6^- anions were refined as rigid groups. The fractional coordinates and isotropic thermal factors are listed in Table 3.8 and the anisotropic thermal factors in Table 3.9. the interatomic distances and angles are provided in Tables 3.10 and 3.11 respectivley. The observed and calculated structure factors for **8** may be found on microfiche in an envelope attached to the inside back cover.

Table 3.7   *Crystal Data and Details of the Crystallographic Analysis for*
[Pt(terpy)(CH3CN)](SbF6)2 (8)

Formula	$PtSb_2F_{12}C_{17}H_{14}N_4$
Molecular Mass	940.89
Crystal Dimensions (mm)	0.12 x 0.15 x 0.12
Crystal System	Monoclinic
Space Group	$P2_1/c$
a (Å)	13.705(6)
b (Å)	12.324(4)
c (Å)	14.507(4)
α (°)	90
β (°)	98.27(3)
γ (°)	90
V (Å^3)	2425(1)
Z	4
D_c (g.cm^{-3})	2.58
F(000)	1728
λ(Mo - Kα) (Å)	0.71069
Scan Mode	ω - 2θ
ω scan angle	$0.6 + 0.83\tan\theta$
Horizontal Aperture Width (mm)	$2.7 + 0.1\tan\theta$
Scattering range (°)	$2 \leq \theta \leq 23$
μ (cm^{-1})	84.18
Absorption Corrections	Semi empirical
Measured Intensities	3708
Unique Intensities	2784
Unique Intensities with [I > 3σ(I)]	1988
Structure Solution	Direct & Fourier Methods
Weighting Scheme	$1/[\sigma^2(F) + 0.005795F^2]$
$R = \Sigma|F_o - F_c|/\Sigma F_o$	0.0429
$R_w = \Sigma w^{1/2}|F_o - F_c|/\Sigma w^{1/2}F_o$	0.0502
$(\Delta/\sigma)_{max}$	0.972
$\Delta\rho_{max}$ (e.Å^{-3})	1.225*
Number of parameters	294

* Close to Pt(II) centre

Table 3.8 *Fractional Coordinates (x 10^4) and Isotropic Thermal Factors ($Å^2$, x 10^3) for*

*[Pt(terpy)(CH₃CN)](SbF₆)₂ (**8**)*

	x/a	y/b	z/c	$\underline{U}_{eq}$
Pt	2394	2116(1)	4000	52
N(1)	2987(9)	1174(12)	3058(10)	59(3)
N(2)	2853(9)	3264(11)	3261(9)	56(3)
N(3)	1943(10)	3396(12)	4679(11)	65(4)
N(4)	1909(10)	932(13)	4746(10)	72(4)
C(1)	3044(14)	105(16)	3031(14)	78(5)
H(1)	2747(14)	-370(16)	3552(14)	218(36)*
C(2)	3469(16)	-433(16)	2344(16)	103(6)
H(2)	3497(16)	-1309(16)	2329(16)	218(36)*
C(3)	3853(13)	163(20)	1712(16)	100(6)
H(3)	4166(13)	-244(20)	1163(16)	218(36)*
C(4)	3843(14)	1330(16)	1743(14)	77(5)
H(4)	4174(14)	1831(16)	1261(14)	218(36)*
C(5)	3383(12)	1769(14)	2442(13)	69(4)
C(6)	3317(11)	2963(16)	2547(12)	65(4)
C(7)	3692(13)	3783(23)	2034(14)	99(7)
H(5)	4083(13)	3586(23)	1460(14)	218(36)*

Table 3.8 (continued)

	x/a	y/b	z/c	$\underline{U}_{eq}$
C(8)	3536(16)	4867(20)	2291(16)	99(7)
H(6)	3808(16)	5518(20)	1900(16)	18(36)*
C(9)	3064(15)	5102(16)	3007(13)	90(5)
H(7)	2955(15)	5935(16)	3200(13)	18(36)*
C(10)	2712(12)	4276(16)	3503(11)	72(5)
C(11)	2165(11)	4372(14)	4307(12)	57(4)
C(12)	1900(14)	5328(16)	4656(17)	78(6)
H(8)	2120(14)	6071(16)	4348(17)	218(36)*
C(13)	1385(15)	5376(18)	5386(18)	97(6)
H(9)	1141(15)	6132(18)	5652(18)	218(36)*
C(14)	1178(14)	4359(22)	5780(16)	117(7)
H(10)	769(14)	4342(22)	6362(16)	218(36)*
C(15)	1459(12)	3395(16)	5442(13)	69(5)
H(11)	1300(12)	2640(16)	5769(13)	218(36)*
C(16)	1652(12)	270(16)	5180(14)	79(5)
C(17)	1297(15)	-667(17)	5701(14)	97(6)
H(12)	-554(15)	-1348(17)	62(14)	218(36)*

Table 3.8 (continued)

	x/a	y/b	z/c	$\underline{U}_{eq}$
H(13)	-554(15)	-1348(17)	62(14)	218(36)*
H(14)	-554(15)	-1348(17)	62(14)	218(36)*
Sb(1)	4239(1)	-2792(1)	165(1)	72
F(1)	3589(1)	-4063(1)	151(1)	190(5)
F(2)	5288(1)	-3468(1)	-187(1)	257(9)
F(3)	3744(1)	-2570(1)	-1034(1)	261(9)
F(4)	4895(1)	-1520(1)	192(1)	366(11)
F(5)	3195(1)	-2109(1)	524(1)	225(9)
F(6)	4739(1)	-3010(1)	1371(1)	224(7)
Sb(2)	350(1)	6992(1)	7766(1)	81
F(7)	-10(1)	6482(1)	6607(1)	305(10)
F(8)	1552(1)	7317(1)	7493(1)	188(7)
F(9)	-90(1)	8318(1)	7396(1)	219(10)
F(10)	698(1)	7492(1)	8936(1)	202(6)
F(11)	-858(1)	6662(1)	8048(1)	203(6)
F(12)	780(1)	5661(1)	8147(1)	209(8)

* isotropic temperature factor.

$$\underline{U}_{eq.} = \tfrac{1}{3} \, \Sigma_i \Sigma_j \underline{U}_{ij} a_i^* a_j^* (a_i . a_j)$$

Table 3.9   _Anisotropic Temperature Factors ($Å^2$, x 10^3) for [Pt(terpy)(CH$_3$CN)](SbF$_6$)$_2$ (**8**)_

	U(11)	U(22)	U(33)	U(23)	U(13)	U(12)
Pt	45(1)	41(1)	41(1)	4(1)	12(1)	-2(1)
N(1)	43(7)	61(10)	50(9)	5(8)	25(7)	5(7)
N(2)	52(8)	44(8)	33(8)	-2(7)	11(6)	-7(6)
N(3)	52(8)	53(9)	60(10)	-9(8)	15(7)	15(7)
N(4)	60(9)	63(10)	42(9)	13(8)	16(7)	-21(8)
C(1)	92(14)	51(12)	53(12)	8(11)	20(10)	3(11)
C(2)	108(16)	48(13)	93(17)	-20(12)	51(14)	-7(12)
C(3)	52(11)	93(17)	78(16)	-13(14)	13(10)	-13(12)
C(4)	81(12)	60(13)	63(12)	15(11)	30(10)	3(11)
C(5)	49(10)	47(10)	56(12)	0(9)	11(9)	-19(8)
C(6)	47(9)	67(12)	43(10)	4(11)	1(8)	4(9)
C(7)	55(11)	130(22)	62(13)	31(16)	26(10)	-11(13)
C(8)	88(15)	74(17)	73(16)	16(13)	12(12)	-14(13)
C(9)	99(15)	58(13)	42(11)	9(10)	8(11)	-25(12)
C(10)	64(11)	65(12)	27(9)	6(10)	-13(8)	-9(10)
C(11)	55(10)	37(10)	50(10)	2(9)	21(8)	-4(8)
C(12)	57(11)	52(12)	107(18)	5(12)	18(12)	27(10)
C(13)	74(13)	49(13)	111(20)	1(13)	20(14)	-8(11)

Table 3.9 continued on next page...

334

Table 3.9 (continued)

	U(11)	U(22)	U(33)	U(23)	U(13)	U(12)
C(14)	62(12)	115(21)	85(17)	-41(16)	33(11)	-9(13)
C(15)	44(9)	64(12)	61(12)	-10(10)	15(9)	6(9)
C(16)	55(11)	48(12)	75(14)	-22(11)	31(11)	-14(9)
C(17)	83(14)	69(14)	68(14)	8(12)	13(11)	-22(11)
Sb(1)	71(1)	52(1)	54(1)	1(1)	19(1)	0(1)
F(1)	214(17)	94(11)	92(10)	-7(9)	34(11)	-71(11)
F(2)	166(16)	194(20)	307(29)	-70(22)	152(19)	36(16)
F(3)	314(30)	164(18)	113(15)	52(15)	-71(18)	-12(20)
F(4)	472(39)	128(16)	160(17)	-55(14)	159(22)	-183(22)
F(5)	130(13)	210(23)	239(25)	-51(18)	57(15)	65(14)
F(6)	141(13)	226(22)	109(12)	26(14)	-20(10)	-63(14)
Sb(2)	68(1)	66(1)	62(1)	-7(1)	12(1)	9(1)
F(7)	134(13)	435(41)	101(12)	-115(20)	-11(10)	37(21)
F(8)	125(13)	179(18)	178(19)	21(15)	78(13)	-5(12)
F(9)	317(28)	129(16)	269(28)	95(18)	135(23)	123(19)
F(10)	148(13)	173(16)	107(13)	-63(13)	-10(10)	-8(12)
F(11)	92(9)	210(19)	157(15)	-41(15)	39(10)	-20(11)
F(12)	187(18)	88(12)	260(26)	34(15)	-8(18)	34(12)

__Table 3.10__   *Interatomic Distances (Å) for [Pt(terpy)(CH$_3$CN)](SbF$_6$)$_2$ (__8__)*

Pt-N(1)	2.049(13)	Pt-N(2)	1.935(13)
Pt-N(3)	2.004(13)	Pt-N(4)	1.987(14)
N(1)-C(1)	1.32(2)	N(1)-C(5)	1.33(2)
N(2)-C(6)	1.34(2)	N(2)-C(10)	1.32(2)
N(3)-C(11)	1.37(2)	N(3)-C(15)	1.37(2)
N(4)-C(16)	1.12(2)	C(1)-H(1)	1.080(0)
C(1)-C(2)	1.39(3)	C(2)-H(2)	1.080(0)
C(2)-C(3)	1.34(3)	C(3)-H(3)	1.080(0)
C(3)-C(4)	1.44(3)	C(4)-H(4)	1.080(0)
C(4)-C(5)	1.38(3)	C(5)-C(6)	1.48(2)
C(6)-C(7)	1.40(3)	C(7)-H(5)	1.080(0)
C(7)-C(8)	1.41(3)	C(8)-H(6)	1.080(0)
C(8)-C(9)	1.33(3)	C(9)-H(7)	1.080(0)
C(9)-C(10)	1.37(2)	C(10)-C(11)	1.48(2)
C(11)-C(12)	1.35(2)	C(12)-H(8)	1.080(0)
C(12)-C(13)	1.36(3)	C(13)-H(9)	1.080(0)
C(13)-C(14)	1.42(3)	C(14)-H(10)	1.080(0)
C(14)-C(15)	1.36(3)	C(15)-H(11)	1.080(0)
C(16)-C(17)	1.50(3)	Sb(1)-F(1)	1.801(0)

Table 3.10 *(continued)*

Sb(1)-F(2)	1.798(0)	Sb(1)-F(3)	1.794(0)
Sb(1)-F(4)	1.805(0)	Sb(1)-F(5)	1.800(0)
Sb(1)-F(6)	1.805(0)	Sb(2)-F(7)	1.796(0)
Sb(2)-F(8)	1.794(0)	Sb(2)-F(9)	1.797(0)
Sb(2)-F(10)	1.804(0)	Sb(2)-F(11)	1.808(0)
Sb(2)-F(12)	1.803(0)		

Table 3.11   _Interatomic Angles (°) for [Pt(terpy)(CH₃CN)](SbF₆)₂ (**8**)_

N(1)-Pt-N(2)	81.5(6)	N(1)-Pt-N(3)	162.6(6)
N(2)-Pt-N(3)	81.0(6)	N(1)-Pt-N(4)	98.2(6)
N(2)-Pt-N(4)	179.3(5)	N(3)-Pt-N(4)	99.2(6)
Pt-N(1)-C(1)	128.0(13)	Pt-N(1)-C(5)	112.0(12)
C(1)-N(1)-C(5)	120(2)	Pt-N(2)-C(6)	116.9(12)
Pt-N(2)-C(10)	118.2(11)	C(6)-N(2)-C(10)	125(2)
Pt-N(3)-C(11)	113.3(11)	Pt-N(3)-C(15)	128.0(13)
C(11)-N(3)-C(15)	119(2)	Pt-N(4)-C(16)	179(2)
N(1)-C(1)-H(1)	119.3(11)	N(1)-C(1)-C(2)	122(2)
H(1)-C(1)-C(2)	118.8(12)	C(1)-C(2)-H(2)	120.6(12)
C(1)-C(2)-C(3)	118(2)	H(2)-C(2)-C(3)	121.0(12)
C(2)-C(3)-H(3)	119.2(12)	C(2)-C(3)-C(4)	121(2)
H(3)-C(3)-C(4)	119.6(12)	C(3)-C(4)-H(4)	122.9(12)
C(3)-C(4)-C(5)	115(2)	H(4)-C(4)-C(5)	122.1(11)
N(1)-C(5)-C(4)	123(2)	N(1)-C(5)-C(6)	116(2)
C(4)-C(5)-C(6)	120(2)	N(2)-C(6)-C(5)	113(2)
N(2)-C(6)-C(7)	118(2)	C(5)-C(6)-C(7)	129(2)
C(6)-C(7)-H(5)	120.6(13)	C(6)-C(7)-C(8)	118(2)

Table 3.11 (continued)

H(5)-C(7)-C(8)	121.8(12)	C(7)-C(8)-H(6)	119.2(12)
C(7)-C(8)-C(9)	121(2)	H(6)-C(8)-C(9)	119.4(13)
C(8)-C(9)-H(7)	120.7(13)	C(8)-C(9)-C(10)	120(2)
H(7)-C(9)-C(10)	119.7(12)	N(2)-C(10)-C(9)	119(2)
N(2)-C(10)-C(11)	113(2)	C(9)-C(10)-C(11)	128(2)
N(3)-C(11)-C(10)	114.0(14)	N(3)-C(11)-C(12)	122(2)
C(10)-C(11)-C(12)	124(2)	C(11)-C(12)-H(8)	118.6(12)
C(11)-C(12)-C(13)	122(2)	H(8)-C(12)-C(13)	119.5(13)
C(12)-C(13)-H(9)	122.6(13)	C(12)-C(13)-C(14)	116(2)
H(9)-C(13)-C(14)	121.8(13)	C(13)-C(14)-H(10)	119.2(13)
C(13)-C(14)-C(15)	123(2)	H(10)-C(14)-C(15)	118.0(12)
N(3)-C(15)-C(14)	119(2)	N(3)-C(15)-H(11)	120.5(10)
C(14)-C(15)-H(11)	120.5(13)	N(4)-C(16)-C(17)	176(2)
F(1)-Sb(1)-F(2)	90.4(0)	F(1)-Sb(1)-F(3)	90.2(0)
F(2)-Sb(1)-F(3)	90.1(0)	F(1)-Sb(1)-F(4)	179.4(0)
F(2)-Sb(1)-F(4)	89.6(0)	F(3)-Sb(1)-F(4)	90.4(0)
F(1)-Sb(1)-F(5)	89.8(0)	F(2)-Sb(1)-F(5)	179.6(0)
F(3)-Sb(1)-F(5)	90.2(0)	F(4)-Sb(1)-F(5)	90.1(0)
F(1)-Sb(1)-F(6)	90.0(0)	F(2)-Sb(1)-F(6)	89.9(0)

Table 3.11 (continued)

F(3)-Sb(1)-F(6)	179.8(0)	F(4)-Sb(1)-F(6)	89.4(0)
F(5)-Sb(1)-F(6)	89.7(0)	F(7)-Sb(2)-F(8)	90.5(0)
F(7)-Sb(2)-F(9)	90.2(0)	F(8)-Sb(2)-F(9)	90.6(0)
F(7)-Sb(2)-F(10)	179.2(0)	F(8)-Sb(2)-F(10)	90.3(0)
F(9)-Sb(2)-F(10)	90.2(0)	F(7)-Sb(2)-F(11)	89.8(0)
F(8)-Sb(2)-F(11)	179.7(0)	F(9)-Sb(2)-F(11)	89.6(0)
F(10)-Sb(2)-F(11)	89.5(0)	F(7)-Sb(2)-F(12)	90.1(0)
F(8)-Sb(2)-F(12)	90.0(0)	F(9)-Sb(2)-F(12)	179.3(0)
F(10)-Sb(2)-F(12)	89.5(0)	F(11)-Sb(2)-F(12)	89.8(0)

3.7.2.2 [Pt(bipy)$_2$](SbF$_6$)$_2$ (12)

Single, lemon-yellow block-like crystals of 12, suitable for X-ray diffraction studies, were obtained by allowing a hot, concentrated CH$_3$CN solution of the salt to slowly cool to room temperature.

The general procedure for the intensity data collection and the general approach to structure solution and refinement are described in Sections A.5.1 and A.5.2 of Appendix A, respectively.

Crystal data and details specific to the data collection, structure solution and refinement for 12 are provided in Table 3.12. Anisotropic refinement was applied to all non-hydrogen atoms of the asymmetric unit. The hydrogen atoms were placed in calculated postions. Table 3.13 lists the fractional coordinates and isotropic thermal factors, with the anisotropic thermal factors being provided in Table 3.14. The interatomic distances are collated in Table 3.15 and the interatomic angles in Table 3.16. The observed and calculated structure factors for 12 may be found on microfiche in an envelope attached to the inside back cover.

Table 3.12   *Crystal Data and Details of the Crystallographic Analysis for*

   *[Pt(bipy)₂](SbF₆)₂ (**12**)*

Formula	$PtSb_2F_{12}C_{20}H_{16}N_4$
Molecular Mass	978.93
Crystal Dimensions (mm)	0.15 x 0.20 x 0.15
Crystal System	Triclinic
Space Group	$P\bar{1}$
a (Å)	7.992(1)
b (Å)	8.795(1)
c (Å)	10.135(1)
α (°)	90.34(1)
β (°)	105.49(1)
γ (°)	114.34(1)
V (Å³)	620.0(2)
Z	1
D_c (g.cm⁻³)	2.62
F(000)	452
λ(Mo - Kα) (Å)	0.71069
Scan Mode	ω - 2θ
ω scan angle	0.6 + 0.80tanθ
Horizontal Aperture Width (mm)	2.7 + 0.1tanθ
Scattering range (°)	$2 \leq \theta \leq 30$
μ (cm⁻¹)	82.22
Absorption Corrections	Semi empirical
Measured Intensities	3795
Unique Intensities	3433
Unique Intensities with [I > 3σ(I)]	3074
Structure Solution	Direct & Fourier Methods
Weighting Scheme	$1/[\sigma^2(F) + 0.005554F^2]$
$R = \Sigma\|F_o - F_c\|/\Sigma F_o$	0.00267
$R_w = \Sigma w^{1/2}\|F_o - F_c\|/\Sigma w^{1/2}F_o$	0.0341
$(\Delta/\sigma)_{max}$	1.009
$\Delta\rho_{max}$ (e.Å⁻³)	0.491
Number of parameters	179

Table 3.13   *Fractional Coordinates (x 10⁴) and Isotropic Thermal Factors (Å², x 10³)*

for [Pt(bipy)₂](SbF₆)₂ (__12__)

	x/a	y/b	z/c	$\underline{U}_{eq}$
Pt	5000	5000	5000	31
N(1)	4675(5)	5799(4)	6751(4)	36(1)
N(2)	7668(5)	6835(4)	5910(3)	37(1)
C(1)	3030(6)	5555(6)	7012(5)	46(1)
H(1)	1704(6)	5039(6)	6176(5)	51(5)*
C(2)	2986(8)	5947(6)	8328(6)	51(1)
H(2)	1635(8)	5691(6)	8519(6)	51(5)*
C(3)	4685(8)	6667(7)	9389(5)	55(1)
H(3)	4671(8)	6939(7)	10425(5)	51(5)*
C(4)	6425(7)	7040(6)	9111(5)	48(1)
H(4)	7778(7)	7642(6)	9914(5)	51(5)*
C(5)	6360(6)	6611(5)	7765(4)	38(1)
C(6)	8062(6)	7188(5)	7293(4)	37(1)
C(7)	9890(6)	8192(6)	8125(5)	46(1)
H(5)	10190(6)	8385(6)	9233(5)	51(5)*
C(8)	11351(6)	8957(7)	7507(6)	56(1)
H(6)	12806(6)	9731(7)	8134(6)	51(5)*
C(9)	10910(8)	8709(7)	6076(6)	54(1)
H(7)	11992(8)	9350(7)	5571(6)	51(5)*
C(10)	9065(6)	7631(6)	5314(5)	47(1)
H(8)	8726(6)	7416(6)	4205(5)	51(5)*
Sb	7398	11972	7518	41

Table 3.13   (continued)

	x/a	y/b	z/c	$\underline{U}_{eq}$
F(1)	8173(5)	13223(5)	6140(3)	69(1)
F(2)	5022(5)	12023(5)	6974(4)	74(1)
F(3)	6695(6)	10768(5)	8946(4)	86(1)
F(4)	6475(7)	9974(5)	6367(4)	87(1)
F(5)	8360(6)	13969(4)	8691(4)	78(1)
F(6)	9811(5)	11970(6)	8087(4)	87(1)

* isotropic temperature factor

$\underline{U}_{eq.} = {}^{1}/_{3}\ \Sigma_i\Sigma_j\underline{U}_{ij}a_i{}^{*}a_j{}^{*}(a_i.a_j)$

Table 3.14   _Anisotropic Temperature Factors (Å², X 10³) for [Pt(bipy)₂](SbF₆)₂ (**12**)_

	U(11)	U(22)	U(33)	U(23)	U(13)	U(12)
Pt	28(1)	32(1)	34(1)	5(1)	10(1)	12(1)
N(1)	31(2)	36(2)	44(2)	7(1)	12(1)	16(1)
N(2)	34(2)	33(2)	42(2)	8(1)	13(1)	11(1)
C(1)	41(2)	48(2)	56(3)	4(2)	20(2)	22(2)
C(2)	46(2)	45(2)	65(3)	4(2)	26(2)	18(2)
C(3)	64(3)	50(3)	55(3)	6(2)	32(2)	19(2)
C(4)	46(2)	54(3)	38(2)	4(2)	13(2)	16(2)
C(5)	40(2)	32(2)	38(2)	6(1)	9(2)	13(2)
C(6)	34(2)	33(2)	43(2)	7(2)	9(1)	16(2)
C(7)	37(2)	44(2)	46(2)	5(2)	9(2)	9(2)
C(8)	29(2)	55(3)	67(3)	-5(2)	13(2)	5(2)
C(9)	38(2)	54(3)	65(3)	2(2)	21(2)	11(2)
C(10)	37(2)	45(2)	54(2)	7(2)	20(2)	10(2)
Sb	40(1)	40(1)	42(1)	7(1)	11(1)	16(1)
F(1)	74(2)	84(2)	66(2)	33(2)	43(2)	36(2)
F(2)	43(2)	84(2)	105(3)	33(2)	31(2)	30(2)
F(3)	101(3)	73(2)	70(2)	30(2)	31(2)	19(2)
F(4)	115(3)	62(2)	70(2)	-11(2)	12(2)	35(2)
F(5)	79(2)	55(2)	86(2)	-15(2)	33(2)	11(2)
F(6)	56(2)	102(3)	104(3)	8(2)	0(2)	50(2)

Table 3.15   _Interatomic Distances (Å) for [Pt(bipy)$_2$](SbF$_6$)$_2$ (**12**)_

Pt-N(1)	2.023(3)	Pt-N(2)	2.025(3)
N(1)-C(1)	1.341(4)	N(1)-C(5)	1.356(4)
N(2)-C(6)	1.356(4)	N(2)-C(10)	1.350(4)
C(1)-H(1)	1.080(0)	C(1)-C(2)	1.388(6)
C(2)-H(2)	1.080(0)	C(2)-C(3)	1.380(7)
C(3)-H(3)	1.080(0)	C(3)-C(4)	1.398(6)
C(4)-H(4)	1.080(0)	C(4)-C(5)	1.395(5)
C(5)-C(6)	1.455(5)	C(6)-C(7)	1.377(5)
C(7)-H(5)	1.080(0)	C(7)-C(8)	1.399(5)
C(8)-H(6)	1.080(0)	C(8)-C(9)	1.391(6)
C(9)-H(7)	1.080(0)	C(9)-C(10)	1.378(6)
C(10)-H(8)	1.080(0)	Sb-F(1)	1.861(2)
Sb-F(2)	1.850(3)	Sb-F(3)	1.868(3)
Sb-F(4)	1.855(3)	Sb-F(5)	1.861(3)
Sb-F(6)	1.860(3)		

Table 3.16 *Interatomic Angles (°) for [Pt(bipy)₂](SbF₆)₂ (12)*

N(1)-Pt-N(2)	78.7(1)	Pt-N(1)-C(1)	127.7(2)
Pt-N(1)-C(5)	113.2(2)	C(1)-N(1)-C(5)	119.0(3)
Pt-N(2)-C(6)	113.4(2)	Pt-N(2)-C(10)	127.6(3)
C(6)-N(2)-C(10)	118.9(3)	N(1)-C(1)-H(1)	119.1(2)
N(1)-C(1)-C(2)	121.8(4)	H(1)-C(1)-C(2)	119.1(2)
C(1)-C(2)-H(2)	120.3(2)	C(1)-C(2)-C(3)	119.4(4)
H(2)-C(2)-C(3)	120.3(3)	C(2)-C(3)-H(3)	120.3(3)
C(2)-C(3)-C(4)	119.5(4)	H(3)-C(3)-C(4)	120.3(2)
C(3)-C(4)-H(4)	121.0(2)	C(3)-C(4)-C(5)	118.0(4)
H(4)-C(4)-C(5)	121.0(2)	N(1)-C(5)-C(4)	122.0(3)
N(1)-C(5)-C(6)	114.5(3)	C(4)-C(5)-C(6)	122.9(3)
N(2)-C(6)-C(5)	113.8(3)	N(2)-C(6)-C(7)	121.9(3)
C(5)-C(6)-C(7)	123.7(3)	C(6)-C(7)-H(5)	120.7(2)
C(6)-C(7)-C(8)	118.7(4)	H(5)-C(7)-C(8)	120.7(2)
C(7)-C(8)-H(6)	120.4(2)	C(7)-C(8)-C(9)	119.2(3)
H(6)-C(8)-C(9)	120.4(2)	C(8)-C(9)-H(7)	120.6(2)
C(8)-C(9)-C(10)	118.8(4)	H(7)-C(9)-C(10)	120.6(3)
N(2)-C(10)-C(9)	122.2(4)	N(2)-C(10)-H(8)	118.9(2)
C(9)-C(10)-H(8)	118.9(3)	F(1)-Sb-F(2)	92.0(1)
F(1)-Sb-F(3)	178.1(1)	F(2)-Sb-F(3)	89.2(1)
F(1)-Sb-F(4)	91.1(2)	F(2)-Sb-F(4)	91.7(2)
F(3)-Sb-F(4)	90.4(2)	F(1)-Sb-F(5)	89.2(1)
F(2)-Sb-F(5)	89.3(2)	F(3)-Sb-F(5)	89.3(2)
F(4)-Sb-F(5)	179.0(2)	F(1)-Sb-F(6)	87.8(1)
F(2)-Sb-F(6)	178.7(2)	F(3)-Sb-F(6)	91.0(2)
F(4)-Sb-F(6)	89.6(2)	F(5)-Sb-F(6)	89.4(2)

3.7.2.3 [Pt(terpy)(C≡CPh)](SbF$_6$) (15)

Thin orange needle-like crystals of 15, suitable for X-ray diffractometric studies, were obtained by preparing a CH$_3$CN solution of the salt and allowing the solvent to slowly evaporate over a period of days.

The general procedure for the intensity data collection and the general approach to structure solution and refinement are described in Sections A.5.1 and A.5.2 of Appendix A, respectively.

Crystal data and details specific to the data collection, structure solution and refinement for 15 are provided in Table 3.17. Anisotropic refinement was applied to the platinum atom of the cation and all the atoms of the anion. The hydrogen atoms were placed in calculated positions and the SbF$_6^-$ anion and the phenyl ring of the phenylacetylide ligand refined as rigid groups. The fractional coordinates and isotropic thermal factors are listed in Table 3.18 and the anisotropic thermal factors in Table 3.19. The interatomic distances are provided in Table 3.20 and the interatomic angles in Table 3.21. The observed and calculated structure factors for 15 may be found on microfiche in an envelope attached to the inside back cover.

Table 3.17 *Crystal Data and Details of the Crystallographic Analysis for*

*[Pt(terpy)(C≡CPh)](SbF$_6$) (**15**)*

Formula	$PtSbF_6C_{23}H_{16}N_3$
Molecular Mass	765.22
Crystal Dimensions (mm)	0.05 x 0.17 x 0.05
Crystal System	Monoclinic
Space Group	$P2_1/n$
a (Å)	7.529(7)
b (Å)	14.666(7)
c (Å)	20.721(17)
α (°)	90
β (°)	90.814(9)
γ (°)	90
V (Å^3)	2288(3)
Z	4
D_c (g.cm^{-3})	2.22
F(000)	1432
λ(Mo - Kα) (Å)	0.71069
Scan Mode	ω - 2θ
ω scan angle	0.6 + 0.41tanθ
Horizontal Aperture Width (mm)	2.7 + 0.1tanθ
Scattering range (°)	$2 \leq \theta \leq 20$
μ (cm^{-1})	76.87
Absorption Corrections	Semi empirical
Measured Intensities	3423
Unique Intensities	2295
Unique Intensities with [I > 3σ(I)]	1257
Structure Solution	Direct & Fourier Methods
Weighting Scheme	$1/[\sigma^2(F) + 0.001223F^2]$
$R = \Sigma|F_o - F_c|/\Sigma F_o$	0.0630
$R_w = \Sigma w^{1/2}|F_o - F_c|/\Sigma w^{1/2}F_o$	0.0623
$(\Delta/\sigma)_{max}$	0.807
$\Delta\rho_{max}$ (e.Å^{-3})	1.378*
Number of parameters	151

* Close to Pt(II) centre

Table 3.18   _Fractional Coordinates (x 10^4) and Isotropic Thermal Factors_
(Å^2, x 10^3) for [Pt(terpy)(C≡CPh)](SbF$_6$) (**15**)

	x/a	y/b	z/c	$\underline{U}_{eq}$
Pt	2203(2)	403(1)	4831(1)	70
N(1)	966(34)	119(18)	3960(12)	60(8)*
N(2)	1660(38)	1663(21)	4613(14)	77(9)*
N(3)	3287(31)	1075(18)	5610(12)	54(7)*
C(1)	732(48)	-673(25)	3710(19)	78(12)*
H(1)	1235(48)	-1262(25)	3966(19)	124(34)*
C(2)	-139(40)	-810(22)	3117(15)	50(9)*
H(2)	-278(40)	-1474(22)	2896(15)	124(34)*
C(3)	-848(53)	9(29)	2822(20)	96(13)*
H(3)	-1617(53)	-37(29)	2379(20)	124(34)*
C(4)	-570(41)	827(23)	3099(16)	60(9)*
H(4)	-1123(41)	1423(23)	2866(16)	124(34)*
C(5)	402(47)	943(26)	3657(17)	74(10)*
C(6)	761(40)	1759(22)	3990(15)	55(9)*
C(7)	316(47)	2691(24)	3788(19)	73(11)*
H(5)	-361(47)	2832(24)	3336(19)	124(34)*
C(8)	809(52)	3329(29)	4187(20)	95(12)*

Table 3.18 (continued)

	x/a	y/b	z/c	$\underline{U}_{eq}$
H(6)	518(52)	4023(29)	4045(20)	124(34)*
C(9)	1693(42)	3188(26)	4810(17)	80(11)*
H(7)	2036(42)	3750(26)	5124(17)	124(34)*
C(10)	2053(46)	2334(25)	4963(16)	68(10)*
C(11)	3047(44)	1989(27)	5534(18)	73(10)*
C(12)	3662(45)	2524(26)	6038(17)	77(12)*
H(8)	3392(45)	3247(26)	6026(17)	124(34)*
C(13)	4631(48)	2182(27)	6556(18)	77(11)*
H(9)	5205(48)	2629(27)	6917(18)	124(34)*
C(14)	4817(45)	1245(25)	6599(17)	69(10)*
H(10)	5503(45)	935(25)	7004(17)	124(34)*
C(15)	4110(43)	725(25)	6111(17)	73(11)*
H(11)	4233(43)	-8(25)	6139(17)	124(34)*
C(16)	2706(50)	-847(26)	5082(18)	74(11)*
C(17)	3120(43)	-1606(24)	5289(16)	67(10)*
C(19)	3192(28)	-3227(18)	5115(9)	82(11)*
C(20)	3585(28)	-4112(18)	5319(9)	111(14)*

Table 3.18 (continued)

	x/a	y/b	z/c	$\underline{U}_{eq}$
C(21)	4386(28)	-4257(18)	5922(9)	114(15)*
C(22)	4795(28)	-3517(18)	6320(9)	90(12)*
C(23)	4402(28)	-2632(18)	6116(9)	59(9)*
C(18)	3601(28)	-2487(18)	5514(9)	54(9)*
H(12)	2572(28)	-3115(18)	4649(9)	124(34)*
H(13)	3269(28)	-4684(18)	5011(9)	124(34)*
H(14)	4691(28)	-4942(18)	6080(9)	124(34)*
H(15)	5415(28)	-3629(18)	6787(9)	124(34)*
H(16)	4718(28)	-2060(18)	6425(9)	124(34)*
Sb	4234(4)	1187(2)	1938(2)	121(1)
F(1)	4201(4)	2052(2)	1318(2)	215(12)
F(2)	5423(4)	432(2)	1409(2)	559(33)
F(3)	4266(4)	322(2)	2559(2)	565(38)
F(4)	3045(4)	1943(2)	2469(2)	525(25)
F(5)	2150(4)	743(2)	1632(2)	298(14)
F(6)	6318(4)	1632(2)	2246(2)	238(13)

* isotropic temperature factor.

$\underline{U}_{eq.} = {}^{1}/_{3} \Sigma_i\Sigma_j\underline{U}_{ij}a_i{}^*a_j{}^*(a_i.a_j)$

Table 3.19   _Anisotropic Temperature Factors ($Å^2$, x 10^3) for for [Pt(terpy)(C≡CPh)]-_
                  (SbF$_6$) (**15**)

	U(11)	U(22)	U(33)	U(23)	U(13)	U(12)
Pt	52(1)	66(1)	56(1)	10(1)	6(1)	4(1)
Sb	78(2)	122(3)	92(2)	29(2)	-13(2)	-1(2)
F(1)	181(27)	210(34)	134(23)	125(25)	-53(21)	-21(25)
F(2)	273(51)	313(66)	621(112)	-299(78)	219(65)	-93(51)
F(3)	241(41)	504(89)	777(127)	594(101)	-82(59)	-108(51)
F(4)	228(40)	573(93)	188(35)	-213(50)	51(33)	-194(53)
F(5)	153(25)	242(40)	210(34)	-57(29)	-37(24)	-66(26)
F(6)	94(20)	303(45)	190(29)	114(30)	-31(20)	-14(24)

Table 3.20   *Interatomic Distances (Å) for [Pt(terpy)(C≡CPh)](SbF₆) (**15**)*

Pt-N(1)	2.06(3)	Pt-N(2)	1.94(3)
Pt-N(3)	2.05(3)	Pt-C(16)	1.94(4)
N(1)-C(1)	1.28(4)	N(1)-C(5)	1.42(4)
N(2)-C(6)	1.46(4)	N(2)-C(10)	1.26(4)
N(3)-C(11)	1.36(5)	N(3)-C(15)	1.31(4)
C(1)-H(1)	1.080(0)	C(1)-C(2)	1.40(5)
C(2)-H(2)	1.080(0)	C(2)-C(3)	1.45(5)
C(3)-H(3)	1.080(0)	C(3)-C(4)	1.35(5)
C(4)-H(4)	1.080(0)	C(4)-C(5)	1.37(5)
C(5)-C(6)	1.41(5)	C(6)-C(7)	1.47(5)
C(7)-H(5)	1.080(0)	C(7)-C(8)	1.30(5)
C(8)-H(6)	1.080(0)	C(8)-C(9)	1.46(5)
C(9)-H(7)	1.080(0)	C(9)-C(10)	1.32(5)
C(10)-C(11)	1.48(5)	C(11)-C(12)	1.38(5)
C(12)-H(8)	1.080(0)	C(12)-C(13)	1.38(5)
C(13)-H(9)	1.080(0)	C(13)-C(14)	1.38(5)
C(14)-H(10)	1.080(0)	C(14)-C(15)	1.37(5)
C(15)-H(11)	1.080(0)	C(16)-C(17)	1.23(5)
C(17)-C(18)	1.42(5)	C(19)-C(20)	1.395(0)

Table 3.20 (continued)

C(19)-C(18)	1.395(0)	C(19)-H(12)	1.080(0)
C(20)-C(21)	1.395(0)	C(20)-H(13)	1.080(0)
C(21)-C(22)	1.395(0)	C(21)-H(14)	1.080(0)
C(22)-C(23)	1.395(0)	C(22)-H(15)	1.080(0)
C(23)-C(18)	1.395(0)	C(23)-H(16)	1.080(0)
Sb-F(1)	1.807(0)	Sb-F(2)	1.806(0)
Sb-F(3)	1.806(0)	Sb-F(4)	1.807(0)
Sb-F(5)	1.806(0)	Sb-F(6)	1.807(0)

N(1)-Pt-N(2)	84.1(13)	N(1)-Pt-N(3)	162.9(11)
N(2)-Pt-N(3)	78.8(13)	N(1)-Pt-C(16)	97.3(14)
N(2)-Pt-C(16)	178(2)	N(3)-Pt-C(16)	100(2)
Pt-N(1)-C(1)	127(3)	Pt-N(1)-C(5)	110(2)
C(1)-N(1)-C(5)	124(3)	Pt-N(2)-C(6)	113(2)
Pt-N(2)-C(10)	124(3)	C(6)-N(2)-C(10)	123(3)
Pt-N(3)-C(11)	109(3)	Pt-N(3)-C(15)	128(3)
C(11)-N(3)-C(15)	123(3)	N(1)-C(1)-H(1)	119(2)
N(1)-C(1)-C(2)	123(4)	H(1)-C(1)-C(2)	118(2)
C(1)-C(2)-H(2)	123(2)	C(1)-C(2)-C(3)	115(4)
H(2)-C(2)-C(3)	123(2)	C(2)-C(3)-H(3)	120(2)
C(2)-C(3)-C(4)	120(4)	H(3)-C(3)-C(4)	120(3)
C(3)-C(4)-H(4)	118(3)	C(3)-C(4)-C(5)	123(4)
H(4)-C(4)-C(5)	118(2)	N(1)-C(5)-C(4)	115(4)
N(1)-C(5)-C(6)	117(3)	C(4)-C(5)-C(6)	128(4)
N(2)-C(6)-C(5)	116(3)	N(2)-C(6)-C(7)	116(3)
C(5)-C(6)-C(7)	128(3)	C(6)-C(7)-H(5)	122(2)
C(6)-C(7)-C(8)	115(4)	H(5)-C(7)-C(8)	123(3)

Table 3.21 (continued)

C(7)-C(8)-H(6)	117(3)	C(7)-C(8)-C(9)	126(4)
H(6)-C(8)-C(9)	118(3)	C(8)-C(9)-H(7)	122(3)
C(8)-C(9)-C(10)	116(4)	H(7)-C(9)-C(10)	122(3)
N(2)-C(10)-C(9)	124(4)	N(2)-C(10)-C(11)	108(4)
C(9)-C(10)-C(11)	128(4)	N(3)-C(11)-C(10)	120(4)
N(3)-C(11)-C(12)	115(4)	C(10)-C(11)-C(12)	125(4)
C(11)-C(12)-H(8)	119(3)	C(11)-C(12)-C(13)	123(4)
H(8)-C(12)-C(13)	118(3)	C(12)-C(13)-H(9)	121(3)
C(12)-C(13)-C(14)	118(4)	H(9)-C(13)-C(14)	121(3)
C(13)-C(14)-H(10)	121(3)	C(13)-C(14)-C(15)	118(4)
H(10)-C(14)-C(15)	121(3)	N(3)-C(15)-C(14)	123(4)
N(3)-C(15)-H(11)	118(2)	C(14)-C(15)-H(11)	119(3)
Pt-C(16)-C(17)	174(4)	C(16)-C(17)-C(18)	179(4)
C(20)-C(19)-C(18)	120.0(0)	C(20)-C(19)-H(12)	120.0(0)
C(18)-C(19)-H(12)	120.0(0)	C(19)-C(20)-C(21)	120.0(0)
C(19)-C(20)-H(13)	120.0(0)	C(21)-C(20)-H(13)	120.0(0)
C(20)-C(21)-C(22)	120.0(0)	C(20)-C(21)-H(14)	120.0(0)
C(22)-C(21)-H(14)	120.0(0)	C(21)-C(22)-C(23)	120.0(0)
C(21)-C(22)-H(15)	120.0(0)	C(23)-C(22)-H(15)	120.0(0)

357

Table 3.21 (continued)

C(22)-C(23)-C(18)	120.0(0)	C(22)-C(23)-H(16)	120.0(0)
C(18)-C(23)-H(16)	120.0(0)	C(17)-C(18)-C(19)	118(2)
C(17)-C(18)-C(23)	123(2)	C(19)-C(18)-C(23)	120.0(0)
F(1)-Sb-F(2)	90.0(0)	F(1)-Sb-F(3)	180.0(0)
F(2)-Sb-F(3)	90.0(0)	F(1)-Sb-F(4)	90.0(0)
F(2)-Sb-F(4)	180.0(0)	F(3)-Sb-F(4)	89.9(0)
F(1)-Sb-F(5)	90.0(0)	F(2)-Sb-F(5)	90.0(0)
F(3)-Sb-F(5)	90.0(0)	F(4)-Sb-F(5)	90.0(0)
F(1)-Sb-F(6)	90.0(0)	F(2)-Sb-F(6)	90.0(0)
F(3)-Sb-F(6)	90.0(0)	F(4)-Sb-F(6)	90.0(0)
F(5)-Sb-F(6)	179.9(0)		

3.7.2.4 [Pt(4'-Ph-terpy)(C≡CPh)](SbF₆) (16)

Single, orange-red block-like crystals of **16**, suitable for X-ray diffractometric analysis, were obtained by extracting the salt from the crude product with boiling CH_3CN and allowing the hot extract to slowly cool to room temperature.

The general procedure for the intensity data collection and the general approach to structure solution and refinement are described in Sections A.5.1 and A.5.2 of Appendix A, respectively.

Crystal data and details specific to the data collection, structure solution and refinement for **16** are provided in Table 3.22. Anisotropic refinement was applied to all the non-hydrogen atoms of the cation and the SbF_6^- anion. The hydrogen atoms were placed in calculated positions. The anion and the phenyl rings of both the 4'-Ph-terpyridine and the phenylacetylide ligand were refined as rigid groups. A list of the fractional coordinates and isotropic themal factors are provided in Table 3.23. The anisotropic thermal factors are listed in Table 3.24 and the interatomic distances and angles in Tables 3.25 and 3.26. The observed and calculated structure factors for **16** may be found on microfiche in an envelope attached to the inside back cover.

Table 3.22 _Crystal Data and Details of the Crystallographic Analysis for [Pt(4'-Ph-terpy)(C≡CPh)](SbF₆) (**16**)_

Formula	$PtSbF_6C_{29}H_{20}N_3$
Molecular Mass	841.32
Crystal Dimensions (mm)	0.11 x 0.16 x 0.10
Crystal System	Monoclinic
Space Group	$P2_1/n$
a (Å)	7.290(2)
b (Å)	20.164(2)
c (Å)	18.360(3)
α (°)	90
β (°)	94.42(2)
γ (°)	90
V (Å³)	2691(1)
Z	4
D_c (g.cm⁻³)	2.09
F(000)	1664
λ(Mo - Kα) (Å)	0.71069
Scan Mode	ω - 2θ
ω scan angle	$1.0 + 1.5\tan\theta$
Horizontal Aperture Width (mm)	$2.7 + 0.1\tan\theta$
Scattering range (°)	$2 \leq \theta \leq 23$
μ (cm⁻¹)	65.94
Absorption Corrections	Semi empirical
Measured Intensities	4533
Unique Intensities	3403
Unique Intensities with $[I > 3\sigma(I)]$	2572
Structure Solution	Direct & Fourier Methods
Weighting Scheme	$1/[\sigma^2(F) + 0.000886F^2]$
$R = \Sigma|F_o - F_c|/\Sigma F_o$	0.0441
$R_w = \Sigma w^{1/2}|F_o - F_c|/\Sigma w^{1/2}F_o$	0.0473
$(\Delta/\sigma)_{max}$	0.582
$\Delta\rho_{max}$ (e.Å⁻³)	1.37*
Number of parameters	293

* Close to Pt(II) centre

Table 3.23 *Fractional Coordinates (x 10^4) and Isotropic Thermal Factors ($Å^2$, x 10^3) for [Pt(4'-Ph-terpy)(C≡CPh)](SbF$_6$) (**16**)*

	x/a	**y/b**	**z/c**	**U**eq
Pt	2149(1)	385	10093	44
N(1)	1317(13)	1329(6)	10138(6)	44(3)
N(2)	1461(14)	546(5)	9060(6)	45(3)
N(3)	2786(14)	-501(5)	9699(6)	45(3)
C(1)	1345(21)	1723(8)	10725(9)	64(4)
H(1)	1734(21)	1501(8)	11250(9)	85(11)*
C(2)	779(24)	2380(10)	10689(10)	78(5)
H(2)	973(24)	2708(10)	11153(10)	85(11)*
C(3)	267(22)	2634(8)	10005(9)	69(5)
H(3)	-191(22)	3143(8)	9968(9)	85(11)*
C(4)	245(20)	2262(8)	9399(9)	59(4)
H(4)	-318(20)	2465(8)	8885(9)	85(11)*
C(5)	785(18)	1605(8)	9467(8)	53(4)
C(6)	825(17)	1144(7)	8839(7)	45(3)
C(7)	338(18)	1252(8)	8117(8)	53(4)
H(5)	-172(18)	1733(8)	7938(8)	85(11)*

Table 3.23 continued on next page...

Table 3.23 (continued)

	x/a	y/b	z/c	$\underline{U}_{eq}$
C(8)	515(17)	741(7)	7607(7)	46(3)
C(9)	1242(18)	133(7)	7853(8)	45(3)
H(6)	1477(18)	-257(7)	7468(8)	85(11)*
C(10)	1725(15)	23(7)	8583(8)	41(3)
C(11)	2476(18)	-554(6)	8951(8)	44(4)
C(12)	2796(18)	-1125(8)	8595(8)	54(4)
H(7)	2682(18)	-1147(8)	8006(8)	85(11)*
C(13)	3584(22)	-1656(8)	8989(9)	68(5)
H(8)	3708(22)	-2133(8)	8730(9)	85(11)*
C(14)	3897(21)	-1615(8)	9751(9)	62(4)
H(9)	4652(21)	-1998(8)	10057(9)	85(11)*
C(15)	3476(18)	-1034(8)	10060(8)	52(4)
H(10)	3689(18)	-1019(8)	10649(8)	85(11)*
C(17)	275(15)	1460(4)	6502(5)	68(4)
C(18)	-164(15)	1548(4)	5755(5)	90(6)
C(19)	-860(15)	1019(4)	5329(5)	81(5)
C(20)	-1117(15)	402(4)	5649(5)	75(5)

Table 3.23 *(Continued)*

	x/a	y/b	z/c	$\underline{U}_{eq}$
C(21)	-678(15)	314(4)	6395(5)	57(4)
C(16)	18(15)	843(4)	6822(5)	51(4)
H(11)	814(15)	1869(4)	6832(5)	85(11)*
H(12)	34(15)	2026(4)	5507(5)	85(11)*
H(13)	-1200(15)	1088(4)	4751(5)	85(11)*
H(14)	-1655(15)	-7(4)	5319(5)	85(11)*
H(15)	-876(15)	-164(4)	6643(5)	85(11)*
C(22)	2889(18)	217(8)	11158(9)	48(4)
C(23)	3416(20)	130(9)	11711(11)	62(4)
C(25)	4585(16)	-647(6)	12719(7)	72(5)
C(26)	5341(16)	-764(6)	13428(7)	89(6)
C(27)	5717(16)	-234(6)	13905(7)	119(8)
C(28)	5336(16)	414(6)	13672(7)	106(7)
C(29)	4580(16)	531(6)	12962(7)	86(6)
C(24)	4205(16)	1(6)	12486(7)	67(5)
H(16)	4295(16)	-1057(6)	12350(7)	85(11)*
H(17)	5636(16)	-1265(6)	13609(7)	85(11)*

Table 3.23 (continued)

	x/a	y/b	z/c	$\underline{U}_{eq}$
H(18)	6302(16)	-325(6)	14454(7)	85(11)*
H(19)	5627(16)	824(6)	14041(7)	85(11)*
H(20)	4286(16)	1032(6)	12782(7)	85(11)*
Sb	121(2)	2192(1)	3157(1)	71
F(1)	1575(2)	1880(1)	3924(1)	156(5)*
F(2)	-8(2)	2986(1)	3608(1)	215(8)*
F(3)	249(2)	1397(1)	2705(1)	168(6)*
F(4)	-1334(2)	2503(1)	2389(1)	151(5)*
F(5)	2136(2)	2467(1)	2724(1)	237(9)*
F(6)	-1894(2)	1916(1)	3589(1)	275(11)*

* isotropic temperature factor.

$\underline{U}_{eq.} = {}^{1}/_{3} \Sigma_i \Sigma_j \underline{U}_{ij} a_i{}^* a_j{}^* (a_i . a_j)$

Table 3.24 *Anisotropic Temperature Factors (Å², x 10³) for [Pt(4'-Ph-terpy)(C≡CPh)]-(SbF₆) (16)*

	U(11)	U(22)	U(33)	U(23)	U(13)	U(12)
Pt	37(1)	53(1)	44(1)	3(1)	7(1)	-5(1)
N(1)	32(5)	49(7)	51(7)	2(6)	15(5)	-5(5)
N(2)	37(6)	44(8)	54(7)	7(6)	6(5)	-3(5)
N(3)	45(6)	49(8)	37(7)	12(5)	-10(5)	-15(5)
C(1)	66(10)	65(12)	60(10)	-18(9)	4(8)	-3(9)
C(2)	92(13)	80(14)	64(12)	-27(10)	27(10)	0(11)
C(3)	89(12)	61(11)	61(11)	-12(10)	21(9)	9(9)
C(4)	56(9)	55(11)	68(11)	-1(9)	8(8)	4(8)
C(5)	38(8)	63(10)	60(10)	13(9)	22(7)	-7(7)
C(6)	39(7)	52(9)	45(9)	-7(8)	11(6)	3(7)
C(7)	50(8)	53(10)	59(10)	2(8)	14(7)	1(7)
C(8)	44(8)	44(9)	52(9)	13(8)	10(7)	2(7)
C(9)	47(8)	44(8)	46(9)	1(7)	8(7)	-3(7)
C(10)	25(6)	45(9)	54(9)	2(8)	5(6)	-1(6)
C(11)	43(8)	30(9)	58(9)	3(7)	-3(7)	-10(6)
C(12)	49(8)	52(10)	59(9)	5(8)	-1(7)	-3(7)
C(13)	87(12)	43(10)	74(12)	8(9)	-1(9)	-10(9)

Table 3.24 (continued)

	U(11)	U(22)	U(33)	U(23)	U(13)	U(12)
C(14)	61(10)	53(11)	69(11)	-2(9)	-6(8)	3(8)
C(15)	47(8)	63(11)	47(9)	17(8)	10(7)	-5(8)
C(17)	109(13)	41(9)	51(9)	1(8)	-22(9)	-17(9)
C(18)	138(17)	62(12)	68(12)	21(11)	-7(11)	-3(12)
C(19)	110(15)	67(13)	64(11)	-10(10)	-8(10)	17(11)
C(20)	71(11)	98(15)	57(10)	-15(11)	2(8)	9(11)
C(21)	47(8)	66(11)	57(10)	-13(8)	-5(7)	5(7)
C(16)	52(8)	53(10)	49(9)	-4(8)	2(7)	7(7)
C(22)	27(7)	71(11)	48(9)	6(8)	5(7)	-3(7)
C(23)	40(9)	72(12)	73(12)	10(10)	7(8)	-3(8)
C(25)	66(11)	80(12)	72(12)	26(10)	11(9)	13(9)
C(26)	52(10)	126(18)	91(15)	35(14)	20(10)	15(11)
C(27)	108(17)	173(26)	73(15)	10(18)	-18(13)	-34(19)
C(28)	87(14)	171(25)	60(12)	-36(15)	-3(10)	-20(16)
C(29)	77(12)	109(17)	75(12)	-11(12)	17(10)	-3(11)
C(24)	58(10)	85(13)	60(11)	-9(11)	16(8)	-13(10)
Sb	94(1)	66(1)	54(1)	-9(1)	1(1)	-13(1)

Table 3.25   *Interatomic Distances (Å) for [Pt(4'-Ph-terpy)(C≡CPh)](SbF₆) (**16**)*

Pt-N(1)	2.001(11)	Pt-N(2)	1.952(11)
Pt-N(3)	1.997(12)	Pt-C(22)	2.02(2)
Pt-Pt	3.490(1)	N(1)-C(1)	1.34(2)
N(1)-C(5)	1.38(2)	N(2)-C(6)	1.34(2)
N(2)-C(10)	1.39(2)	N(3)-C(11)	1.38(2)
N(3)-C(15)	1.34(2)	C(1)-H(1)	1.080(0)
C(1)-C(2)	1.39(2)	C(2)-H(2)	1.080(0)
C(2)-C(3)	1.38(2)	C(3)-H(3)	1.080(0)
C(3)-C(4)	1.34(2)	C(4)-H(4)	1.080(0)
C(4)-C(5)	1.39(2)	C(5)-C(6)	1.49(2)
C(6)-C(7)	1.36(2)	C(7)-H(5)	1.080(0)
C(7)-C(8)	1.41(2)	C(8)-C(9)	1.40(2)
C(8)-C(16)	1.47(2)	C(9)-H(6)	1.080(0)
C(9)-C(10)	1.38(2)	C(10)-C(11)	1.43(2)
C(11)-C(12)	1.35(2)	C(12)-H(7)	1.080(0)
C(12)-C(13)	1.39(2)	C(13)-H(8)	1.080(0)
C(13)-C(14)	1.40(2)	C(14)-H(9)	1.080(0)
C(14)-C(15)	1.35(2)	C(15)-H(10)	1.080(0)
C(17)-C(18)	1.395(0)	C(17)-C(16)	1.395(0)

Table 3.25 (continued)

C(17)-H(11)	1.080(0)	C(18)-C(19)	1.395(0)
C(18)-H(12)	1.080(0)	C(19)-C(20)	1.395(0)
C(19)-H(13)	1.080(0)	C(20)-C(21)	1.395(0)
C(20)-H(14)	1.080(0)	C(21)-C(16)	1.395(0)
C(21)-H(15)	1.080(0)	C(22)-C(23)	1.07(2)
C(23)-C(24)	1.52(2)	C(25)-C(26)	1.395(0)
C(25)-C(24)	1.395(0)	C(25)-H(16)	1.080(0)
C(26)-C(27)	1.395(0)	C(26)-H(17)	1.080(0)
C(27)-C(28)	1.395(0)	C(27)-H(18)	1.080(0)
C(28)-C(29)	1.395(0)	C(28)-H(19)	1.080(0)
C(29)-C(24)	1.395(0)	C(29)-H(20)	1.080(0)
Sb-F(1)	1.809(0)	Sb-F(2)	1.810(0)
Sb-F(3)	1.810(0)	Sb-F(4)	1.809(0)
Sb-F(5)	1.810(0)	Sb-F(6)	1.810(0)

Table 3.26   *Interatomic Angles (°) for [Pt(4'-Ph-terpy)(C≡CPh)](SbF₆) (**16**)*

N(1)-Pt-N(2)	80.0(5)	N(1)-Pt-N(3)	161.1(4)
N(2)-Pt-N(3)	81.1(4)	N(1)-Pt-C(22)	100.4(5)
N(2)-Pt-C(22)	179.3(5)	N(3)-Pt-C(22)	98.5(5)
Pt-N(1)-C(1)	127.7(10)	Pt-N(1)-C(5)	114.4(9)
C(1)-N(1)-C(5)	117.8(13)	Pt-N(2)-C(6)	120.0(9)
Pt-N(2)-C(10)	116.7(9)	C(6)-N(2)-C(10)	123.3(11)
Pt-N(3)-C(11)	113.9(9)	Pt-N(3)-C(15)	128.8(10)
C(11)-N(3)-C(15)	117.2(12)	N(1)-C(1)-H(1)	117.4(9)
N(1)-C(1)-C(2)	123(2)	H(1)-C(1)-C(2)	119.7(10)
C(1)-C(2)-H(2)	121.8(10)	C(1)-C(2)-C(3)	117(2)
H(2)-C(2)-C(3)	120.0(10)	C(2)-C(3)-H(3)	118.1(10)
C(2)-C(3)-C(4)	122(2)	H(3)-C(3)-C(4)	119.7(10)
C(3)-C(4)-H(4)	119.5(10)	C(3)-C(4)-C(5)	118(2)
H(4)-C(4)-C(5)	121.8(10)	N(1)-C(5)-C(4)	121.6(14)
N(1)-C(5)-C(6)	114.9(13)	C(4)-C(5)-C(6)	123.5(14)
N(2)-C(6)-C(5)	110.7(12)	N(2)-C(6)-C(7)	119.8(13)
C(5)-C(6)-C(7)	129.5(14)	C(6)-C(7)-H(5)	119.9(9)
C(6)-C(7)-C(8)	119.9(14)	H(5)-C(7)-C(8)	120.2(8)

Table 3.26 (continued)

C(7)-C(8)-C(9)	118.7(13)	C(7)-C(8)-C(16)	121.4(12)
C(9)-C(8)-C(16)	119.9(12)	C(8)-C(9)-H(6)	120.1(8)
C(8)-C(9)-C(10)	121.2(13)	H(6)-C(9)-C(10)	118.6(8)
N(2)-C(10)-C(9)	117.0(12)	N(2)-C(10)-C(11)	112.6(12)
C(9)-C(10)-C(11)	130.4(13)	N(3)-C(11)-C(10)	115.7(12)
N(3)-C(11)-C(12)	121.7(13)	C(10)-C(11)-C(12)	122.5(13)
C(11)-C(12)-H(7)	121.0(9)	C(11)-C(12)-C(13)	118.9(14)
H(7)-C(12)-C(13)	119.1(10)	C(12)-C(13)-H(8)	120.1(10)
C(12)-C(13)-C(14)	120(2)	H(8)-C(13)-C(14)	118.6(10)
C(13)-C(14)-H(9)	120.9(10)	C(13)-C(14)-C(15)	117(2)
H(9)-C(14)-C(15)	121.7(9)	N(3)-C(15)-C(14)	125.3(14)
N(3)-C(15)-H(10)	119.5(8)	C(14)-C(15)-H(10)	115.2(9)
C(18)-C(17)-C(16)	120.0(0)	C(18)-C(17)-H(11)	120.0(0)
C(16)-C(17)-H(11)	120.0(0)	C(17)-C(18)-C(19)	120.0(0)
C(17)-C(18)-H(12)	120.0(0)	C(19)-C(18)-H(12)	120.0(0)
C(18)-C(19)-C(20)	120.0(0)	C(18)-C(19)-H(13)	120.0(0)
C(20)-C(19)-H(13)	120.0(0)	C(19)-C(20)-C(21)	120.0(0)
C(19)-C(20)-H(14)	120.0(0)	C(21)-C(20)-H(14)	120.0(0)
C(20)-C(21)-C(16)	120.0(0)	C(20)-C(21)-H(15)	120.0(0)

Table 3.26 *(continued)*

C(16)-C(21)-H(15)	120.0(0)	C(8)-C(16)-C(17)	120.4(6)
C(8)-C(16)-C(21)	119.6(6)	C(17)-C(16)-C(21)	120.0(0)
Pt-C(22)-C(23)	174.5(14)	C(22)-C(23)-C(24)	179(2)
C(26)-C(25)-C(24)	120.0(0)	C(26)-C(25)-H(16)	120.0(0)
C(24)-C(25)-H(16)	120.0(0)	C(25)-C(26)-C(27)	120.0(0)
C(25)-C(26)-H(17)	120.0(0)	C(27)-C(26)-H(17)	120.0(0)
C(26)-C(27)-C(28)	120.0(0)	C(26)-C(27)-H(18)	120.0(0)
C(28)-C(27)-H(18)	120.0(0)	C(27)-C(28)-C(29)	120.0(0)
C(27)-C(28)-H(19)	120.0(0)	C(29)-C(28)-H(19)	120.0(0)
C(28)-C(29)-C(24)	120.0(0)	C(28)-C(29)-H(20)	120.0(0)
C(24)-C(29)-H(20)	120.0(0)	C(23)-C(24)-C(25)	120.0(8)
C(23)-C(24)-C(29)	120.0(8)	C(25)-C(24)-C(29)	120.0(0)
F(1)-Sb-F(2)	90.0(0)	F(1)-Sb-F(3)	90.0(0)
F(2)-Sb-F(3)	180.0(0)	F(1)-Sb-F(4)	180.0(0)
F(2)-Sb-F(4)	90.0(0)	F(3)-Sb-F(4)	90.0(0)
F(1)-Sb-F(5)	90.1(0)	F(2)-Sb-F(5)	90.1(0)
F(3)-Sb-F(5)	89.9(0)	F(4)-Sb-F(5)	89.9(0)
F(1)-Sb-F(6)	89.9(0)	F(2)-Sb-F(6)	89.9(0)
F(3)-Sb-F(6)	90.1(0)	F(4)-Sb-F(6)	90.1(0)
F(5)-Sb-F(6)	180.0(0)		

APPENDIX A

General experimental details

A.1 Characterisation and instrumentation

Elemental analyses for C, H and N for compounds **1** to **6** were performed by the Microanalytical Laboratory, University of Natal , Pietermaritzburg, whilst that for compounds **7** to **16** were performed by Galbraith Laboratories, Inc., Knoxville, Tennessee, USA.

Electrochemical measurements were performed using a PAR 175 universal programmer, a PAR 173 potentiostat, fitted with a PAR 176 current follower and connected to a HP 7045A X-Y recorder and a locally made coulometer (Electronics Workshop, University of Natal).

All infrared spectra, both for solution and for KBr pellets, were recorded using a Shimadzu FT-1400 Fourier transform infrared spectrometer.

UV-visible spectra were recorded on a Shimadzu UV-2101PC UV-visible scanning spectrophotometer. Spectroscopic grade solvents were employed in all instances.

The emission spectra for compounds **8** to **16** were recorded on an SLM-Amino SPF-500C spectrophotometer. Low temperature measurements were obtained with the aid of a quartz finger dewar or an Oxford Instruments Model DN-704 liquid nitrogen cryostat.

A.2 Synthetic procedures

All reactions, unless stated otherwise, were performed under an atmosphere of dry dinitrogen using standard Schlenk techniques.

A.2.1 Chemical reagents

The chemicals used during the course of this investigation were either obtained from commercial suppliers or synthesized by previously published methods as indicted in Appendix B. Chemical reagents obtained commercially were used without further purification.

A.2.2 Vapour extraction apparatus

The vapour extraction apparatus depicted below was used in the synthesis or purification of compounds **8**, **15** and **16**.

To Condensor

Sample to be purified

P4 - Fritte

To flask containing boiling solvent

··········▶ Vapour Path

-------▶ Condensed solvent Path
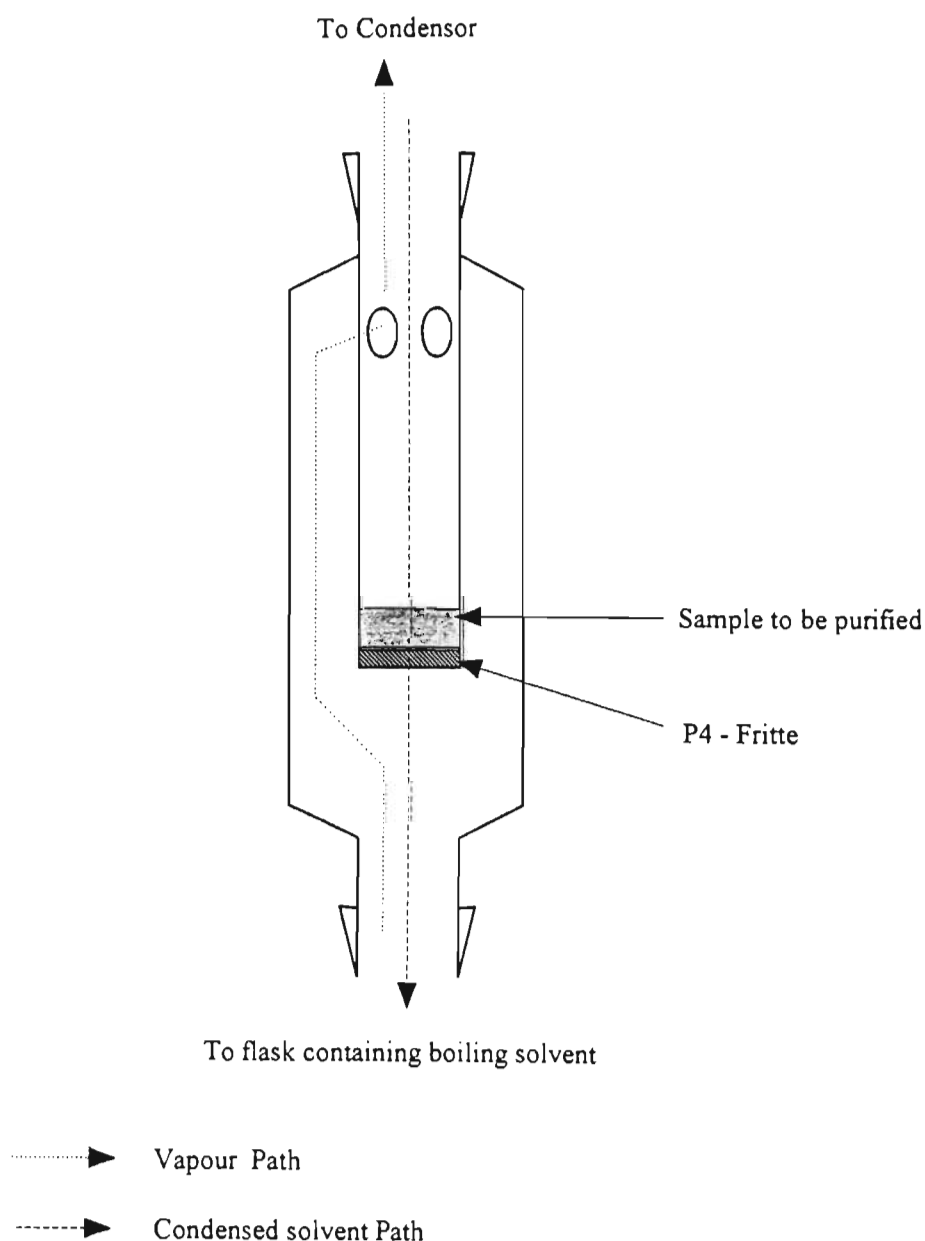
A.2.3 Solvents

All solvents used were freshly distilled and dried before use, utilizing standard procedures, except for acetonitrile which was purified by the method as described by Carlsen and Andersen.[319]

A.3 Electrochemical studies

All experiments were performed under an atmosphere of pure dry argon at room temperature. The solvents required for these studies were purified according to the procedures described by C.K. Mann.[320] The purity of the solvent system was examined before commencement of the electrochemical studies by running a blank voltammogram. Tetrabutylammonium perchlorate (TBAP), recrystallized from a 9:1 ethanol/water mixture and dried *in vacuo* at 100°C, was employed as the supporting electrolyte in a 0.1 M concentration, the sample concentration being 10^{-3} M.

All experiments were performed utilizing a conventional three-electrode cell. The auxiliary and reference electrodes consisted of a platinum spiral wire and an AgCl-coated spiral silver wire respectively, both of which dipped into 0.1 M solutions of TBAP in the appropriate solvent. These solutions were separated from the electrolyte solution by fine frittes. The working electrode was a platinum disc electrode constructed locally (Faculty of Science, Mechanical Instrument Workshop, University of Natal), the surface of which was freshly polished, rinsed and dried before each experiment.

All potentials are quoted relative to the Ag/AgCl reference electrode against which the $[FeCp_2]^\circ/[FeCp_2]^+$ couple had an $E_{1/2}$ value of 0.44 V in benzonitrile. Ferrocene was added to the solution of the compound under investigation at the end of each experiment as an internal standard to check on the stability of the reference electrode.

A.4 Emission studies

All solvents employed in the emission studies were of spectroscopical grade and obtained from commercial suppliers. The solvents were used as obtained from the suppliers. Emission was viewed either through a $\lambda > 400$ nm or $\lambda > 440$ nm long-pass

filter. The excitation wavelength was 350 nm for all the emission spectra reported here, except for that of the solid samples of [Pt(bipy)$_2$](SbF$_6$)$_2$ (**12**) and [Pt(bipy)$_2$](CF$_3$SO$_3$)$_2$ (**13**) where radiation with a wavelength of 315 nm was utilized and that of [Pt(4'-Ph-terpy)Cl](SbF$_6$) (**14**) in CH$_3$CN solution where radiation of 330 nm was utilized to excite the sample. In the variable temperature studies all samples were allowed to equilibrate for 1 hour after the cryostat sensor indicated that the desired temperature had been reached. After this period the emission spectrum was recorded at 10 minute intervals until no change in the luminescent intensity was evident. Once these criteria were met, the spectra presented here, were recorded.

A.5 Crystal Structure Determinations

A.5.1 Data collection

The intensities of the reflections were measured at 22°C with an Enraf-Nonius CAD-4 diffractometer utilizing graphite monochromated Mo-K_α radiation.

Cell constants were obtained by fitting the setting angles of 25 high-order reflections ($\theta > 12°$). Three standard reflections were measured every hour to check on any possible decomposition of the crystal. An ω-2θ scan with a variable speed up to a maximum of 5.49° per minute was used. The ω angle changed as $a_\omega + b_\omega \tan\theta$ (°) and the horizontal aperture as $a_h + b_h \tan\theta$ (mm), but was limited to the range 1.3 to 5.9 mm. The vertical slit was fixed at 4 mm. Optimum values of a_ω, b_ω, a_h and b_h were determined for each crystal by a critical evaluation of the peak shape for several reflections with different values of θ using the program OTPLOT (Omega-Theta plot; Enraf-Nonius diffractometer control program, 1988). Where applicable, a linear decay correction was applied using the mean value of linear curves fitted through three intensity control reflections, measured at regular time intervals. Data were corrected for Lorentz and polarization effects, and where possible for absorption, by the psi-scan (semi - empirical) method.[321]

A.5.2 Structure solution and refinement

The phase problem was solved by utilizing direct methods or the Patterson function. Once a suitable phasing model was found, successive applications of Fourier and difference Fourier techniques allowed the location of the remaining non-hydrogen atoms. The hydrogen atoms in the structures of compounds **8**, **12**, **15** and **16** were placed in idealized positions. All structures were refined using weighted full-matrix least-squares methods, the weighting scheme being chosen so as to find the smallest variation of the mean value of $w(F_o - F_c)^2$ as a function of the magnitude of F_o. R, R_w and the weighting scheme were defined as follows:

$$R = \Sigma \left| F_o\text{-}F_c \right| / \Sigma F_o$$

$$R_w = \Sigma w^{\frac{1}{2}} \left| F_o\text{-}F_c \right| / \Sigma w^{\frac{1}{2}} F_o$$

and $\quad w = 1.0 / [\sigma^2(F) + gF^2]$, where g is variable.

Scattering factor data was obtained from "International Tables for X-ray Crystallography".[322] The programs SHELX-76[323] and SHELX-86[324] were employed for all the structure solution calculations. Mean plane calculations were performed using the programme PLANE of the SDP package,[325] whilst plotting of structures was performed using the program ORTEP-II.[326] The tabulation of fractional coordinates, thermal parameters, interatomic distances and angles was achieved using the program TABLES.[327]

APPENDIX B

B.1 Sources of chemicals

All the chemicals used in preparing the compounds studied in this thesis were either obtained form commercial suppliers or synthesized form commercially available chemicals as indicated in the following table. Chemicals obtained form commercial suppliers (excluding solvents) were used as received, without any further purification. Extreme care was however taken not to use any chemicals (especially relevant to TCNE and the silver salts) where the shelf live has expired, or where sample purity was doubted.

Chemical	Obtained from or synthesized as per reference/section
Et_2S_2	Aldrich Chemical Company Inc.
$[Fe_2Cp_2*(CO)_2(\mu\text{-SEt})_2]$	Strem Chemicals
2,5-Me_2-DCNQI	Reference 181
2-Cl-5-Me-DCNQI	Reference 181
2-Me-DCNQI	Reference 181
H_4-DCNQI	Reference 181
TCNQ	Aldrich Chemical Company Inc.
TCNE	Aldrich Chemical Company Inc.
$[Pt(C_6H_5CN)_2Cl_2]$	Strem Chemicals
$AgSbF_6$	Fluka AG
$AgCF_3SO_3$	Fluka AG
$AgBF_4$	Fluka AG
2,2',6',2''-terpyridine	Strem Chemicals
2,2'-bipyridine	E. Merck
4'-Ph-terpyridine	Reference 306
$AgC{\equiv}CPh$	Reference 308
$Bu_3SnC{\equiv}CPh$	Section B.2.1

B.2 Chemicals synthesized by adaptation of published methods

B.2.1 Bu$_3$SnC≡CPh

BuLi (5.10 cm^3 of a 1.68 M solution, 8.56 mmol) was added dropwise to a vigorously stirred solution of HC≡CPh (0.75 cm^3, 6.85 mmol) in dry THF (20 cm^3) at -78°C. After 10 minutes a solution of Bu$_3$SnCl (2.78 cm^3, 10.28 mmol) was added dropwise to this mixture and the cooling bath removed. The reaction mixture was allowed to heat up to 25°C before the volume was reduced to a minimum (*in vacuo*). The remaining liquid was extracted with hexane (2 x 20 cm^3) and filtered under an atmosphere of dinitrogen using a P4 fritte. The volume of the filtrate was reduced to a minimum (*in vacuo*) affording the product as a clear, light yellow liquid. The infrared spectrum of a CH$_2$Cl$_2$ solution of this product exhibits a distinct peak at 2132 cm^{-1} which is attributed to a C≡C stretching mode.

REFERENCES

1. K. Krogmann, *Angew. Chem. Int. Ed. Engl.*, (1969), **8**, 35.

2. R.E. Rundle, *J. Phys. Chem.*, (1975), **61**, 45.

3. J.R. Miller, *J. Chem. Soc.*, (1965), 713.

4. R.M. Bozorth and L. Pauling, *Phys. Rev.*, (1932), **39**, 537.

5. J.M. Williams, A.J. Schultz, A.E. Underhill and K. Carneiro in: *"Extended Linear Chain Compounds Vol.1"*, (J.S. Miller, *ed.*), Plenum, New York, (1982), 73.

6. F. Fontaine, *Bull. Soc. Roy. Sci. Liege,* (1964), **33**, 178.

7. K. Krogmann and D. Stephan, *Z. Anorg. Chem.*, (1968), **362**, 290.

8. A. Macadre and C. Moncuit, *Compt. Rend.*, (1965), **261 B**, 2339.

9. S. Yamada, *Bull. Chem. Soc. Jpn,* (1951), **24**, 125.

10. C. Moncuit and H. Poulet, *J. Phys. Rad.* (1962), **23**, 353.

11. J.H. O'Neil, A.E. Underhill and G.A. Toombs, *Solid State Commun.*, (1979), **29**, 557.

12. A.E. Underhill in: *"Low Dimensional cooperative phenomena and the possibility of a High Temperature Superconductor"*, NATO Advanced Study Institute, Starnberg, Germany, Sept. 1974, (H.J. Keller *ed.*), Plenum, New York.

13. K.D. Keefer, D.M. Washecheck, N.P. Enright and J.M. Williams, *J. Amer. Chem. Soc.*, (1976), **98**, 233.

14. J.M. Williams and A.J. Schultz in: *"Molecular Metals"*, (W.E. Hatfield *ed.*), Plenum, New York, (1979), 337.

15. J.M. Williams, *Inorg. Nucl. Chem. Lett.*, (1976), **12**, 651.

16. J.M. Williams and A.J. Schultz in: *"Modulated Structures - 1979"*, (J.M. Cowley, J.B. Cohen, M.B. Salamon, B.J. Wuensch *eds.*), American Institute of Physics, New York, (1979), 187.

17. K. Carneiro, A.S. Petersen, A.E. Underhill, D.J. Wood, D.M. Watkins and G.A. MacKenzie, *Phys. Rev. B,* (1979), **19**, 6279.

18. D.J. Wood, A.E. Underhill, A.J. Schultz and J.M. Williams, *Solid State Commun.*, (1979), **30**, 501.

19. J.M. Williams, P.L. Johnson, A.J. Schultz and C. Coffey, *Inorg. Chem.*, (1978), **17**, 834.

20. J.M. Williams, M. Iwata, S.W. Peterson, K.A. Leslie and H.J. Guggenheim, *Phys. Rev. Lett.*, (1975), **34**, 1653.

21. R.K. Brown and J.M. Williams, *Inorg. Chem.*, (1979), **18**, 1922.

22. J.S. Miller and R. Weagley, *Inorg. Chem.*, (1977), **16**, 2965.

23. A.J. Schultz, C.C. Coffey. G.C. Lee and J.M. Williams, *Inorg. Chem.*, (1977), **16**, 2129.

24. R.K. Brown and J.M. Williams, *Inorg. Chem.*, (1978), **17**, 2607.

25. A.J. Schultz, D.P. Gerrity and J.M. Williams, *Acta Cryst. B,* (1978), **34**, 1673.

26. R.E. Peierls, *"Quantum Theory of Solids"*, Oxford Univ. Press, London & New York, (1955), 107.

27. R. Musselman and J.M. Williams, *J. Chem. Soc., Chem. Commun.,* (1977), 186.

28. A.J. Epstein and J.S. Miller, *Solid State Commun.,* (1979), **29**, 345.

29. K. Carneiro, C.S. Jacobson and J.M. Williams, *Solid State Commun.,* (1979), **31**, 837.

30. E.F. Steigmeier, D. Baeriswyl, H. Auderset and J.M. Williams in: *"Quasi-One-Dimensional Conductors II"*, (S. Barisic *et al.* Eds.) Springer-Verlag, Berlin, (1979), 229.

31. K. Krogmann and P. Dodel, *Chem. Ber.,* (1966), **99**, 3402.

32. K. Krogmann and P. Dodel, *Chem. Ber.,* (1966), **99**, 3408.

33. H. Kobayashi, I. Shirotani, A. Kobayashi and Y. Sasaki, *Solid State Commun.,* (1977), **23**, 409.

34. T.W. Thomas, H. Che-Hsiung, M.M. Labes, P.S. Gomm, A.E. Underhill and D.M. Watkins, *J. Chem. Soc. A,* (1972), 2050.

35. A.J. Schultz, A.E. Underhill and J.M. Williams, *Inorg. Chem.,* (1978), **17**, 1313.

36. J.S. Miller, *Science,* (1976), **194**, 189.

37. A. Kobayashi, Y. Sasaki and H. Kobayashi, *Bull. Chem. Soc. Jpn.,* (1979), **52**, 3682.

38. A. Kobayashi, Y. Sasaki, I. Shirotani and H. Kobayashi, *Solid State Commun.*, (1978), **26**, 653.

39. C.S. Jacobsen, D.M. Watkins and A.E. Underhill, *Solid State Commun.*, (1980), **36**, 477.

40. D.W. Bullett, *Solid State Commun.*, (1978), **27**, 467.

41. S. Yamada, *J. Amer. Chem. Soc.*, (1951), **73**, 1579.

42. J.S. Miller and A.J. Epstein, *Prog. Inorg. Chem.*, (1976), **20**, 1.

43. J.D. Bell, J.C. Bowles, H.J. Cumming, D. Hall and R.V. Holland, *Acta Cryst. B*, (1976), **32**, 634.

44. G.H.W. Milburn and M.R. Truter, *J. Chem. Soc. A*, (1966), 1609.

45. L. Chugayev and J. Chernyayev, *Z. Anorg. Allg. Chem.*, (1929), **182**, 159.

46. G.B. Bokii and G.I. Distler, *Chem. Abs.*, (1949), **43**, 3683c.

47. H. Endres, M. El Sharrif, H.J. Keller, R. Martin and U. Traeger in: *"Synthesis and properties of low-dimensional materials"*, (J.S. Miller and A.J. Epstein eds.), *Ann. N.Y. Acad. Sci.*, (1978), **313**, 663.

48. D.S. Martin, L.D. Hunter, R. Kroenig and R.F. Coley, *J. Amer. Chem. Soc.*, (1971), **93**, 5433.

49. R.F. Kroenig, L.D. Hunter, R M. Rush, J.C. Clardy and D.S. Martin, *J. Phys. Chem.*, (1973), **77**, 3077.

50. J.R. Miller, *J. Chem. Soc.*, (1961), 4452.

51. M. Atoji, J.W. Richardson and R.E. Rundle, *J. Amer. Chem. Soc.*, (1957), **79**, 3017.

52. P. Day, F. Orchard, A.J. Thompson and R.J.P. Williams, *J. Chem. Phys.*, (1965), **42**, 1973.

53. C.N.R. Rao and S.N. Bhat, *Inorg. Nucl. Chem. Lett.*, (1969), **5**, 531.

54. L.E. Godycki and R.E. Rundle, *Acta Cryst.*, (1953), **6**, 487.

55. D.E. Williams, G. Wohlauer and R.E. Rundle, *J. Amer. Chem. Soc.*, (1959), **12**, 2132.

56. E. Frasson, C. Panattoni and R. Zannetti, *Acta Cryst.*, (1959), **12**, 1027.

57. C.V. Banks and D.W. Barnum, *J. Amer. Chem. Soc.*, (1958), **80**, 4767.

58. M. Calleri, G. Ferraris and D. Viterbo, *Acta Cryst.*, (1967), **22**, 468.

59. M. Calleri, G. Ferraris and D. Viterbo, *Inorg. Chim. Acta*, (1967), **1**, 297.

60. G. Ferraris and D. Viterbo, *Acta Cryst. B*, (1969), **25**, 2066.

61. E. Frasson and C. Panattoni, *Acta Cryst.*, (1960), **13**, 893.

62. B.G. Anex and F.G. Krist, *J. Amer. Chem. Soc.*, (1967), **89**, 6114.

63. Y. Ohasi, I. Hanazaki and S. Nagakura, *Inorg. Chem.*, (1970), **9**, 2551.

64. J.C. Zahner and H.G. Drickamer, *J. Chem. Phys.*, (1960), **33**, 1625.

65. T.W. Thomas and A.E. Underhill, *J. Chem. Soc., Chem. Commun.*, (1969), 725.

66. A.E. Underhill, D.M. Watkins and R. Pethig, *Inorg. Nucl. Chem. Lett.*, (1973), **9**, 1269.

67. M. Cowie, A. Gleizes, G.W. Grynkewich, D.W. Kalina, M.S. McClure, R.P. Scaringe, R.C. Teitelbaum, S.L. Ruby, J.A. Ibers, C.R. Kannewurf and T.J. Marks, *J. Amer. Chem. Soc.*, (1979), **101**, 2921.

68. A.S. Foust and R.H. Soderberg, *J. Amer. Chem. Soc.*, (1967), **89**, 5507.

69. D.W. Kalina, J.W. Lyding, M.T. Ratajack, C.R. Kannewurf and T.J. Marks, *J. Amer. Chem. Soc.*, (1980), **102**, 7854.

70. L.D. Brown, D.W. Kalina, M.S. McClure, S. Schultz, S.L. Ruby, J.A. Ibers, C.R. Kannewurf and T.J. Marks, *J. Amer. Chem. Soc.*, (1979), **101**, 2937.

71. H. Endres, H.J. Keller, W. Moroni and J. Weiss, *Acta Cryst. B*, (1975), **31**, 2357.

72. J.L. Petersen, C.S. Schramm, D.R. Stojakovic, B.M. Hoffman and T.J. Marks, *J. Amer. Chem. Soc.*, (1977), **99**, 286.

73. T.J. Marks, *Science*, (1985), **227**, 881.

74. C.J. Schramm, R.P. Scaringe, D.R. Stojakovic, B.M. Hoffman, J.A. Ibers and T.J. Marks, *J. Amer. Chem. Soc.*, (1980), **102**, 6702.

75. J. Martinsen. R.L. Greene, S.M. Palmer, B.M. Hoffman, *J. Amer. Chem. Soc.*, (1983), **105**, 677.

76. E.A. Cuellar and T.J. Marks, *Inorg. Chem.*, (1981), **20**, 3766.

77. D.R. Stojakovic, *Ph.D. thesis*, Northwestern University, Evanston, Ilinois, USA, (1978).

78. T. Inabe, S. Nakamura, W.-B. Liang and T.J. Marks, *J. Amer. Chem. Soc.*, (1985), **107**, 7224.

79. B.M. Hoffman, T.E. Phillips, C.J. Schram and S.K. Wright in: *"Molecular Metals"*, (W.E. Hatfield *ed.*), Plenum, New York, (1979), 393.

80. T.E. Phillips and B.M. Hoffman, *J. Amer. Chem. Soc.*, (1977), **99**, 7734.

81. T.E. Phillips, R.P. Scaringe, B.M. Hoffman and J.A. Ibers, *J. Amer. Chem. Soc.*, (1980), **102**, 3435.

82. J. Martinsen, L.J. Pace, T.E. Phillips, B.M. Hoffman and J.A. Ibers, *J. Amer. Chem. Soc.*, (1982), **104**, 83.

83. L.J. Pace, J. Martinsen, A. Ulman, B.M. Hoffman and J.A. Ibers, *J. Amer. Chem. Soc.*, (1983), **105**, 2612.

84. S.K. Wright, C.J. Schramm, T.E. Phillips, D.M. Scholler and B.M. Hoffman, *Synth. Met.*, (1979/1980), **1**, 43.

85. C.J. Schramm, D.R. Stojakovic, B.M. Hoffman and T.J. Marks, *Science*, (1978), **200**, 47.

86. L.J. Pace, A. Ulman and J.A. Ibers, *Inorg. Chem.*, (1982), **21**, 199.

87. L.-S. Lin, T.J. Marks, C.R. Kannewurf, J.W. Lyding, M.S. McClure, M.T. Ratajack and T.-C. Whang, *J. Chem. Soc., Chem. Commun.*, (1980), 954.

88. M.S. McClure, L.-S. Lin, T.-C. Whang, M.T. Ratajack, C.R. Kannewurf and T.J. Marks, *Bull. Amer. Phys. Soc.*, (1980), **25**, 315.

89. J.C. Dabrowiak, D.P. Fisher, F.C. McElroy and D.J. Macero, *Inorg. Chem.*, (1979), **18**, 2304.

90. G.P. Ferrara and J.C. Dabrowiak, *Inorg. Nucl. Chem. Lett.*, (1978), **14**, 223.

91. R.D. Joyner and M.E. Kenney, *Inorg. Chem.*, (1962), **1**, 717.

92. P.M. Kuznesof, K.J. Wynne, R.S. Nohr and M.E. Kenney, *J. Chem. Soc., Chem. Commun.*, (1980), 121.

93. J.P. Linsky, T.R. Paul, R.S. Nohr and M.E. Kenney, *Inorg. Chem.*, (1980), **19**, 3131.

94. R.S. Nohr and K.J. Wynne, *J. Chem. Soc., Chem. Commun.*, (1981), 1210.

95. C.W. Dirk, T. Inabe, K.F. Schoch Jr and T.J. Marks, *J. Amer. Chem. Soc.*, (1983), **105**, 1539.

96. R.S. Nohr, P.M. Kuznesof, K.J. Wynne, M.E. Kenney and P.G. Siebenman, *J. Amer. Chem. Soc.*, (1981), **103**, 4371.

97. K.J. Wynne and R.S. Nohr, *Mol. Cryst. Liq. Cryst.*, (1982), **81**, 243.

98. R.S. Nohr, P. Brant, D. Weber and K.J. Wynne, *Chem. Abs.*, (1984), **100**, 15916.

99. K. Wynne, J. Brant, R.S. Nohr, D. Weber and S. Haupt, *Chem. Abs.*, (1983), 99: 114255.

100. B.N. Diel, T. Inabe, J.W. Lyding, K.F. Schoch Jr, C.R. Kannewurf and T.J. Marks, *J. Amer. Chem. Soc.*,(1983), **105**, 1551.

101. T. Inabe, J.G. Gaudiello, M.K. Moguel, J.W. Lyding, R.L. Burton, W.J. McCarthy, C.R. Kannewurf and T.J. Marks, *J. Amer. Chem. Soc.*, (1986), **108**, 7595.

102. X. Zhou, T.J. Marks and S.H. Carr, *Mol. Cryst. Liq. Crsyt.*, (1985), **118**, 357.

103. X. Zhou, T.J. Marks and S.H. Carr, *J. Polym. Sci. Phys. Ed.*, (1985), **23**, 305.

104. T. Inabe, J.W. Lyding, M.K. Moguel, C.R. Kannewurf and T.J. Marks, *Mol. Cryst. Liq. Cryst.*, (1983), **93**, 355.

105. J.G. Gaudiello, M. Almeida, T.J. Marks, W.J. McCarthy, J.C. Butler and C.R. Kannewurf, *J. Phys. Chem.*, (1986), **90**, 4917.

106. J.G. Gaudiello, G.E. Kellogg, S.M. Tetrik and T.J. Marks, *J. Amer. Chem. Soc.*, (1989), **111**, 5259.

107. M. Almeida, J.G. Gaudiello, G.E. Kellogg, S.M. Tetrick, H.O. Marcy, W.J. McCarthy, J.C. Butler, C.R. Kannewurf and T.J. Marks, *J. Amer. Chem. Soc.*, (1989), **111**, 5271.

108. J.G. Gaudiello, H.O. Marcy, W.J. McCarthy, M.K. Moguel, C.R. Kannewurf and T.J. Marks, *Synth. Met.*, (1986), **15**, 115.

109. M.K. Moguel, L.M. Tonge, H.O. Marcy. W.J. McCarthy, C.R. Kannewurf and T.J. Marks, unpublished results as quoted by T.J. Marks, *Angew. Chem. Int. Ed. Engl.*, (1990), **29**, 857.

110. E. Ciliberto, K.A. Doris, W.J. Pietro, G.M. Reisner, D.E. Ellis, I. Fragalà, F.H. Herbstein, M.A. Ratner and T.J. Marks, *J. Amer. Chem. Soc.*, (1984), **106**, 7748.

111. P.D. Hale, W.J. Pietro, M.A. Ratner, D.E. Ellis, and T.J. Marks, *J. Amer. Chem. Soc.*, (1987), **109**, 5943.

112. W.J. Pietro, T.J. Marks and M.A. Ratner, *J. Amer. Chem. Soc.*, (1985), **107**, 5387.

113. J.P. Collman, J.T. McDevitt, G.T. Yee, C.R. Leidner, L.G. McCullough, W.A. Little and J.B. Torrance, *Proc. Natl. Acad. Sci. USA*, (1986), **83**, 4581.

114. M. Hanack, *Israel Jour. Chem.*, (1985), **25**, 205.

115. J.P. Collman, J.T. McDevitt, C.R. Leidner, G.T. Yee, J.B. Torrance and W.A. Little, *J. Amer. Chem. Soc.*, (1987), **109**, 4606.

116. O. Schneider and M. Hanack, *Angew. Chem. Int. Ed. Engl.*, (1980), **19**, 392.

117. O. Schneider and M. Hanack, *Angew. Chem. Int. Ed. Engl.*, (1982), **21**, 79.

118. W. Kobel and M. Hanack, *Inorg. Chem.*, (1986), **25**, 103.

119. U. Keppeler, S. Deger, A. Lange and M. Hanack, *Angew. Chem. Int. Ed. Engl.*, (1987), **26**, 344.

120. M. Hanack, A. Gül, and L.R. Subramanian, *Inorg. Chem.*, (1992), **31**, 1542.

121. O. Schneider and M. Hanack, *Chem. Ber.*, (1983), **116**, 2088.

122. J. Metz, O. Schneider and M. Hanack, *Spectrochim. Acta, Part A*, (1982), **38A**, 1265.

123. B.N. Diel, T. Inabe, N.K. Jaggi, J.W. Lyding, O. Schneider, M. Hanack, C.R. Kannewurf, T.J. Marks and L. H. Schwartz, *J. Amer. Chem. Soc.*, (1984), **106**, 3207.

124. J. Metz and M. Hanack, *J. Amer. Chem. Soc.*, (1983), **105**, 828.

125. A. Datz, J. Metz, O. Schneider and M. Hanack, *Syn. Met.*, (1984), **9**, 31.

126. H.N. McCoy and W.C. Moore, *J. Amer. Chem. Soc.*, (1911), **33**, 273.

127. J. Ferraris, D.O. Cowan, V. Walatka Jr and J.H. Perlstein, *J. Amer. Chem. Soc.*, (1973), **93**, 948.

128. M. Bryce and L. Murphy, *Nature (London)*, (1984), **309**, 119.

129. L.B. Coleman, M.J. Cohen, D.J. Sandman, F.G. Yamagishi, A.F. Garito and A.J. Heeger, *Solid State Commun.*, (1973), **12**, 1125.

130. T.E. Phillips, R.J. Kistenmacher, J.P. Ferraris and D.O. Cowan, *J. Chem. Soc., Chem. Commun.*, (1973), 471.

131. D. Jérome, A. Mazaud, M. Ribault and K. Bechgaard, *J. Phys. Lett.*, (1980), **41**, L195.

132. D. Jérome, W. Müller and M. Weger, *J. Phys. Lett.*, (1974), **35**, L77.

133. Z.G. Soos, *Annu. Rev. Phys. Chem.*, (1974), **25**, 121.

134. S. Kagoshima, H. Anzai, K. Kajimura and T. Ishiguro, *J. Phys. Soc. Jpn.*, (1975), **39**, 1143.

135. F. Denoyer, R. Comès, A.F. Garito and A.J. Heeger, *Phys. Rev. Lett.*, (1975), **35**, 445.

136. R. Comès, S.M. Shapiro, G. Shirane, A.F. Garito and A J Heeger, *Phys. Rev. Lett.*, (1975), **35**, 1518.

137. H.A. Mook and C.R. Watson Jr, *Phys. Rev. Lett.*, (1976), **36**, 801.

138. B. Rosenau, C. Krieger and H.A. Staab, *Tetrahedron Lett.*, (1985), **26**, 2081.

139. I. Silverman and N.F. Yanoni, *J. Chem. Soc. B*, (1967), 1941.

140. R.C. Wheland, *J. Amer. Chem. Soc.*, (1976), **98**, 3926.

141. A.J. Schultz, G.D. Stucky, R. Craven, M.J. Schaffman and M.B. Salamon, *J. Amer. Chem. Soc.*, (1976), **98**, 5191.

142. J.H. Perlstein, *Angew. Chem. Int. Ed. Engl.*, (1977), **16**, 519.

143. J.H. Perlstein, J.A. Van Allan, L.C. Isett and G.A. Reynolds, *"Synthesis and properties of low-dimensional materials"*, (J.J. Miller and A.J. Epstein, *eds.*), *Ann. N.Y. Acad. Sciences*, (1978), **313**, 61.

144. R.L. Greene and G.B. Street, *Science*, (1984), **226**, 651.

145. D. Jérome, A. Mazaud, M. Ribault and K. Bechgaard, *J. Phys. Lett.*, (1980), **41**, L195.

146. K. Bechgaard, C.S. Jacobsen, K. Mortensen, H.J. Pedersen and N. Thorup, *Solid State Commun.*, (1980), **33**, 1119.

147. K. Bechgaard, K. Carneiro, M. Olsen, F.B. Rasmussen and C.S. Jacobsen, *Phys. Rev. Lett.*, (1981), **46**, 852.

148. K. Bechgaard, F.B. Rasmussen, M. Olsen, G. Rindorf, C.S. Jacobsen, H.J. Pedersen and J.C. Scott, *J. Amer. Chem. Soc.*, (1981), **103**, 2440.

149. J.M. Williams, M.A. Beno, E.H. Appelman, F. Wudl, E. Aharon-Shalom and D. Nalewajek, *Mol. Cryst. Liq. Cryst.*, (1982), **79**, 319.

150. F. Wudl, *J. Amer. Chem. Soc.*, (1981), **103**, 7064.

151. H. Kobayashi, A. Kobayashi, G. Saito and H. Inokuchi, *Chem. Lett.*, (1982), 245.

152. K. Bechgaard, *Mol. Cryst. Liq. Cryst.*, (1982), **79**, 1.

153. M.A. Beno, J.M. Williams, M.M. Lee and D.O. Cowan, *Solid State Commun.*, (1982), **44**, 1195.

154. J.M. Williams, M.A. Beno, J.C. Sullivan, L.M. Banovetz, J.M. Braam, G.S. Blackman, C.D. Carlson, D.L. Greer and D.M. Loesing, *J. Amer. Chem. Soc.*, (1983), **105**, 643.

155. S.S.P. Parkin, F. Creuzet, M. Ribault, D. Jérome, K. Bechgaard and J.M. Fabre, *Mol. Cryst. Liq. Cryst.*, (1982), **79**, 249.

156. M.A. Beno, G.S. Blackman, P.C.W. Leung and J.M. Williams, *Solid State Commun.*, (1983), **48**, 99.

157. J.P. Pouget, G. Shirane, K. Bechgaard and J.M. Fabre, *Phys. Rev. B: Conden. Matter*, (1983), **27**, 5203.

158. D.U. Gubser, W.W. Fuller, T.O. Poehler, J. Stokes, D.O. Cowan, M.M. Lee and A.N. Bloch, *Mol. Cryst. Liq. Cryst.*, (1982), **79**, 225.

159. S.S.P. Parkin, E.M. Engler, R.R. Schumaker, R. Lagier, V.Y. Lee, J.C. Scott and R.L. Greene, *Phys. Rev. Lett.*, (1983), **50**, 270.

160. J.M. Williams, M.A. Beno, H.H. Wang, P.E. Reed, L.J. Azevedo and J.E. Schirber, *Inorg. Chem.*, (1984), **23**, 1790.

161. H. Kobayashi, A. Kobayashi, Y. Sasaki, G. Saito, T. Enoki and H. Inokuchi, *J. Amer. Chem. Soc.*, (1983), **105**, 297.

162. J.M. Williams, T.J. Emge, H.H. Wang, M.A. Beno, P.T. Copps, L.N. Hall, K. D. Carlson and G.W. Crabtree, *Inorg. Chem.*, (1984), **23**, 2558.

163. P.C.W. Leung, T.J. Emge, M.A. Beno, H.H. Wang, J.M. Williams, V. Petricek and P.J. Coppens, *J. Amer. Chem. Soc.*, (1984), **106**, 7644.

164. J.M. Williams, H.H. Wang, M.A. Beno, T.J. Emge, L.W. Sowa, P.T. Copps, F. Behroozi, L.N. Hall, K.D. Carlson and G.W. Crabtree, *Inorg. Chem.*, (1984), **23**, 3839.

165. K.D. Carlson, G.W. Crabtree, L.N. Hall, F. Behroozi, P.T. Copps, L.M. Sowa, L. Nuñez, M.A. Firestone, H.H. Wang, M.A. Beno, T.J. Emge and J.M. Williams, *Mol. Cryst. Liq. Cryst.*, (1985), **125**, 159.

166. A.M. Kini, U. Geiser, H.H. Wang, K.D. Carlson, J.M. Williams, W.K. Kwok, K.G. Vandervoot, J.E. Thompson, D.L. Stupka, D. Jung and M.-H. Whangbo, *Inorg. Chem.*, (1990), **29**, 2555.

167. L. Brossard, M. Ribault, L. Valade and P. Cassoux, *Physica B*, (1986), **143**, 378.

168. M. Bousseau. L. Valade, M.-F. Bruniquel, P. Cassoux, M. Garbauskas, L.V. Interrante and K. Kasper, *Nouv. J. Chim.*, (1984), **8**, 3.

169. M. Bousseau. L. Valade, J.-P. Legros, P. Cassoux, M. Garbauskas and L.V. Interrante, *J. Amer. Chem. Soc.*, (1986), **108**, 1908.

170. J.-P. Legros and L. Valade, *Solid State Commun.*, (1988), **68**, 599.

171. L. Brossard, M. Ribault, L. Valade and P. Cassoux, *J. Phys. (Paris)*, (1989), **50**, 1521.

172. E. Canadell, E.I. Rochidi, S. Ravy, J.-P. Pouget, L. Brossard and J.-P. Legros, *J. Phys. (Paris)*, (1989), **50**, 2967.

173. E. Canadell, S. Ravy, J.-P. Pouget and L. Brossard, *Solid State Commun.*, (1990), **75**, 633.

174. P. Cassoux, L. Valade, H. Kobayashi, A. Kobayashi, R.A. Clark and A.E. Underhill, *Coord. Chem. Rev.*, (1991), **110**, 115.

175. J.-P. Legros, L. Valade and P. Cassoux, *Synth. Met.*, (1988), **27**, B347.

176. H. Kim, A. Kobayashi, Y. Sasaki, R. Kato and H. Kobayashi, *Chem. Lett.*, (1987), 1799.

177. A. Kobayashi, H. Kim, Y. Sasaki, S. Moriyama, Y. Nishio, K. Kajita, W. Sasaki, R. Kato and H. Kobayashi, *Synth. Met.*, (1988), **27**, B339.

178. A. Kobayashi, H. Kim, Y. Sasaki, R. Kato, H. Kobayashi, S. Moriyama, Y. Nishio, K. Kajita and W. Sasaki, *Chem. Lett.*, (1987), 1819.

179. A. Kobayashi, H. Kim, Y. Sasaki, K. Murata, R. Kato and H. Kobayashi, *J. Chem. Soc. Faraday Trans.*, (1990), **86**, 361.

180. G.D. Andreetti, S. Bradamante, P.C. Bizzarri and G.A. Pagani, *Mol. Cryst. Liq. Cryst.*, (1985), **120**, 309.

181. A. Aumüller and S. Hünig, *Liebigs Ann. Chem.*, (1986), 142.

182. S. Hünig, A. Aumüller and U. Schubert, *Liebigs Ann. Chem.*, (1985), 1216.

183. A. Aumüller and S. Hünig, *Liebigs Ann. Chem.*, (1986), 165.

184. A. Aumüller, P. Erk, S. Hünig, H. Meixner, J.-U. von Schütz and H.-P. Werner, *Liebigs Ann. Chem.*, (1987), 997.

185. A. Aumüller, P. Erk, S. Hünig, J.-U. von Schütz, H.-P. Werner and H.C. Wolf, *Mol. Cryst. Liq. Cryst. Inc. Nonlin. Opt.*, (1988), **156**, 215.

186. J.S. Miller and A.J. Epstein, *Angew. Chem. Int. Ed. Engl.*, (1987), **26**, 287.

187. H.-P. Werner, J.-U. von Schütz, H.C. Wolf, R.K. Kremer, M. Gehrke, A. Aumüller, P. Erk and S. Hünig, *Solid State Commun.*, (1989), **69**, 1127.

188. A. Aümuller, P. Erk, G. Klebe, S. Hünig, J.-U. von Schütz and H.-P. Werner, *Angew. Chem. Int. Ed. Engl.*, (1986), **25**, 740.

189. P. Erk, S. Hünig, J.-U. von Schütz, H.-P. Werner and H.C. Wolf, *Angew. Chem. Int. Ed. Engl.*, (1982), **27**, 267.

190. R. Kato, H. Kobayashi, A. Kobayashi, T. Mori and H. Inokuchi, *Chem. Lett.*, (1987), 1579.

191. R. Kato, H. Kobayashi and A. Kobayashi, *J. Amer. Chem. Soc.*, (1989), **111**, 5224.

192. P. Erk, S. Hünig, H. Meixner, J.-U. von Schütz and H.-P. Werner, *Liebigs Ann. Chem.*, (1988), 157.

193. A. Kobayashi, R. Kato, H. Kobayashi, T. Mori and H. Inokuchi, *Solid State Commun.*, (1987), **64**, 45.

194. S. Hünig and P. Erk, *Adv. Mater.*, (1991), **3**, 225.

195. M. Krebs and J.-U. von Schütz, *Bruker Report*, (1994), **1**, 44.

196. T. Mori, K. Imaeda, R. Kato, A. Kobayashi, H. Kobayashi and H. Inokuchi, *J. Phys. Soc. Jpn.*, (1987), **56**, 3429.

197. P. Erk, H.-J. Gross, S. Hünig, U. Langohr, H. Meixner, H.-P. Werner, J.-U. von Schütz and H.C. Wolf, *Angew. Chem. Int. Ed. Engl.*, (1989), **28**, 1245.

198. P. Erk, H. Meixner, T. Metzenthin, S. Hünig, U. Langohr, J.-U. von Schütz, H.-P. Werner, H.C. Wolf, R. Burkett, H.W. Helberg and G. Schaumburg, *Adv. Mater.*, (1991), **3**, 311.

199. K. Sinzger, S. Hünig, M. Jopp, D. Bauer, W. Bietsch, J.-U. von Schütz, H.C. Wolf, R.K. Kremer, T. Metzenthin, R. Bau, S.I. Khan, A. Lindbaum, C.L. Lengauer and E. Tillmanns, *J. Amer. Chem. Soc.*, (1993), **115**, 7696.

200. A.H. Reis, L.D. Preston, J.M. Williams, S.W. Peterson, G.A Candela, L.J. Swartzendruber and J.S. Miller, *J. Amer. Chem. Soc.*, (1979), **101**, 2756.

201. J.S. Miller, J.H. Zhang, W.M. Reiff, D.A. Dixon, L.D. Preston, A.H. Reis, E. Gebert, M. Extine, J. Troup, A.J. Epstein and M.D. Ward, *J. Phys. Chem.*, (1987), **91**, 4344.

202. G.A Candela, L.J. Swatzendruber, J.S. Miller and M.J. Rice, *J. Amer. Chem. Soc.*, (1979), **101**, 2755.

203. J.S. Miller, J.C. Calabrese, H. Rommelmann, S.R. Chittipeddi, J.H. Zhang, W.M. Reiff and A.J. Epstein, *J. Amer. Chem. Soc.*, (1987), **109**, 769.

204. J.L. Robbins, N. Edelstein, B. Spencer, J.C. Smart, *J. Amer. Chem. Soc.*, (1982), **104**, 1882.

205. E. Adman, M. Rosenblum, S. Sullivan, T.N. Margulis, *J. Amer. Chem. Soc.*, (1967), **89**, 4540.

206. J.S. Miller, J.H. Zhang and W.M. Reiff, *Inorg. Chem.*, (1987), **26**, 600.

207. J.S. Miller, J.C. Calabrese and A.J. Epstein, *Inorg. Chem.*, (1989), **28**, 4230.

208. J.S. Miller and A.J. Epstein, *Angew. Chem. Int. Ed. Engl.*, (1994), **33**, 385.

209. W.E Broderick, J.A. Thompson, E.P. Day, B.M. Hoffman, *Science*, (1990), **240**, 401.

210. K.S. Narayan, B.G. Morin, J.S. Miller and A.J. Epstein, *Phys. Rev. B*, (1992), **46**, 6195.

211. J.M. Manriquez, G.T. Yee, R.S. McLean, A.J. Epstein and J.S. Miller, *Science*, (1991), **252**, 1415.

212. J.S. Miller and A.J. Epstein, *Mol. Cryst. Liq. Cryst.*, (1993), **233**, 133.

213. J.S. Miller, J.C. Calabrese, R.S. McLean and A.J. Epstein, *Adv. Mater.*, (1992), **4**, 498.

214. J.S. Miller and A.J. Epstein, *Chem. in Brittian*, (1994), 477.

215. R.B. King, P.M. Treichel and F.G.A. Stone, *J. Amer. Chem. Soc.*, (1961), **83**, 3600.

216. R.B. King and M.B. Bisnette, *Inorg. Chem.*, (1965), **4**, 482.

217. M. Ahmad, R. Bruce and G.R. Knox, *J. Organometal. Chem.*, (1966), **6**,1.

218. R.E. Dessy, F.E. Stary, R.B. King and M. Waldrop, *J. Amer. Chem. Soc.*, (1966), **88**, 471.

219. R.B King and M.B. Bisnette, *Inorg. Chem.*, (1967), **6**, 469.

220. J.A. de Beer, R.J. Haines, R. Greatrex and J.A. van Wyk, *J. Chem. Soc., Dalton Trans.*, (1973), 2341.

221. R.J. Haines, J.A. de Beer and R. Greatrex, *J. Organometal. Chem.*, (1975), **85**, 89.

222. R.B. King and M.B. Bisnette, *J. Organometal. Chem.*, (1967), **8**, 287.

223. G. Ferguson, C. Hannaway and K.M.S. Islam, *J.Chem. Soc., Chem. Commun.*, (1968), 1165.

224. D.P. Freyberg, J.L. Robins, K.N. Raymond and J.C. Smart, *J. Amer. Chem. Soc.*, (1979), **101**, 892.

225. A. Aumüller and S. Hünig, *Liebigs Ann. Chem.*, (1986), 165.

226. N.G. Connelly and L.F. Dahl, *J. Amer. Chem. Soc.*, (1970), **92**, 7472.

227. J.S Miller, C. Vazquez, R.S. McLean, W.M. Reiff, A. Aumüller and S. Hünig, Submitted for publication.

228. R. Mason and D.M.P Mingos, *J. Organometal. Chem.*, (1973), **50**, 53.

229. G.D. Andreetti, S. Bradamante, P.C. Bizzarri and G.A. Pagani, *Mol. Cryst. Liq. Cryst.*, (1985), **120**, 309.

230. A. Aumüller, P. Erk, S. Hünig, J.-U. von Schütz, H.-P. Werner, H.C. Wolf and G. Klebe, *Chem. Ber.*, (1991), **124**, 1445.

231. Magnetic susceptibility measurements performed by J.S. Miller and co-workers at the laboratories of E.I. du Pont de Nemours and Company, Inc., Wilmington, USA.

232. J.S. Miller, D.A. Dixon, J.C. Calabrese, C. Vazquez, P.J. Krusic, M.D. Ward, E. Wasserman and R.L. Harlow, *J. Amer. Chem. Soc.*, (1990), **112**, 381.

233. J.S. Miller, D.T. Glatzhofer, D.M. O'Hare, W.M. Reiff, A. Chakraborty and A.J. Epstein, *Inorg. Chem.*, (1989), **28**, 2930.

234. D.S. Acker and W.R. Hertler, *J. Amer. Chem. Soc.*, (1962), **84**, 3370.

235. R.C. Wheland and J.L. Gillson, *J. Amer. Chem. Soc.*, (1976), **98**, 3916.

236. J.S. Miller and D.A. Dixon, *Science*, (1987), **235**, 871.

237. K.-M. Chi, J.C. Calabrese, W.M. Reiff and J.S. Miller, *Organometallics*, (1991), **10**, 688.

238. S.Z. Goldberg, R. Eisenberg, J.S. Miller and A.J. Epstein, *J. Amer. Chem. Soc.*, (1976), **98**, 5173.

239. R.E. Long, R.A. Sparks, K.N. Trueblood, *Acta Cryst.*, (1965), **18**, 932

240. P. Goldstein, K. Seff, K.N. Trueblood, *Acta Cryst. B*, (1968), **24**, 778.

241. A. Hoekstra, T. Spoelder, A. Vos, *Acta Cryst. B*, (1972), **28**, 14.

242. J.S. Miller, *Ann. N.Y. Acad. of Sci.*, (1978), **313**, 25.

243. S.E. Bell, *M.Sc. Thesis*, Universtiy of Natal, Pietermaritzburg, RSA, (1990).

244. P. Becker, P. Coppens and R.K. Ross, *J. Amer. Chem. Soc.*, (1973), **95**, 7604.

245. J.S. Miller, D. O'Hare, A. Chakraborty and A.J. Epstein, *J. Amer. Chem. Soc.*, (1989), **111**, 7853.

246. Personal correspondence with J.S. Miller

247. D.M. Eichhorn, D.C. Skee, W.M. Broderick and B.M. Hoffman, *Inorg. Chem.*, (1993), **32**, 491.

248. C.-W. Chan, L.-K. Cheng and C.M. Che, *Coord. Chem. Rev.*, (1994), **132**, 87.

249. V.H. Houlding and A.J. Frank, *Inorg. Chem.*, (1985), **24**, 3664.

250. S.E. Sherman, S.J. Lippard, *Chem. Rev.*, (1987), **87**, 1153.

251. M. Kasha, *Faraday Soc. Disc.*, (1950), **9**, 14.

252. J.M. Bevilacqua and R. Eisenberg, *Inorg. Chem.*, (1994), **33**, 2913.

253. V.M Miskowski and V.H. Houlding, *Inorg. Chem.*, (1989), **28**, 1529.

254. H. Kunkely and A. Vogler, *J. Amer. Chem. Soc.*, (1990), **112**, 5625.

255. R. Ballardini, M.T. Gandolfi, V. Balzani, F.H. Kohnke and J.F. Stoddart, *Angew. Chem. Int. Ed. Engl.* (1988), **27**, 692.

256. R. Ballardini, G. Varani, M.T. Indelli and F. Scandola, *Inorg. Chem.*, (1986), **25**, 3858.

257. C.-W. Chan, C.-M. Che, M.-C. Cheng and Y. Wang, *Inorg. Chem.*, (1992), **31**, 4874.

258. V.M. Miskowski, V.H. Houlding, C.-M. Che and Y. Wang, *Inorg. Chem.*, (1993), **32**, 2518.

259. D.M. Preston, W. Günter, A. Lechner, G. Glieman and J.I. Zink, *J. Amer. Chem. Soc.*, (1988), **110**, 5628.

260. T.K. Aldridge, E.M. Stacy and D.R. McMillin, *Inorg. Chem.*, (1994), **33**, 722.

261. A. Vogler and H. Kunkely, *J. Amer. Chem. Soc.*, (1981), **103**, 1559.

262. A. Vogler, H. Kunkely, J. Hlavatsch and A. Merz, *Inorg. Chem.*, (1984), **23**, 506.

263. H.-K. Yip, L.-K. Cheng, K.-K. Cheung and C.-M. Che, *J. Chem. Soc., Dalton Trans.*, (1993), 2933.

264. K.-T. Wan, C.-M. Che and K.-C. Cho, *J. Chem. Soc., Dalton Trans.*, (1991), 1077.

265. A. Hazell and A. Mukhopadhyay, *Acta Cryst. B*, (1980), **36**, 1647.

266. D.M. Roundhill, H.B. Gray and C.-M. Che, *Acc. Chem. Res.*, (1989), **22**, 55.

267. C.-M. Che, V.W.-W. Yam, W.-T. Wong and T.-F. Lai, *Inorg. Chem.*, (1989), **28**, 2908.

268. V.H. Houlding and V.M. Miskowski, *Coord. Chem. Rev.*, (1991), **111**, 145.

269. G.T. Morgan and F.H. Burstall, *J. Chem. Soc.*, (1934), 1498.

270. K.W. Jennette, J.T. Gill, J.A. Sadownick and S.J. Lippard, *J. Amer. Chem. Soc.*, (1976), **98**, 6159.

271. R.J. Mureinik and M. Bidani, *Inorg. Nucl. Chem. Letters*, (1977), **13**, 625.

272. J.A. Bailey and H.B. Gray, *Acta Cryst. C*, (1992), **48**, 1420.

273. E.M.A. Ratilla, H.M. Brothers II and N.M. Kostic, *J. Amer. Chem. Soc.*, (1987), **109**, 4592.

274. M. Howe-Grant and S.J. Lippard in: *"Inorganic Synthesis, Vol. 20"*, (D.H. Busch *ed.*), John Wiley and Sons Inc., (1980), 101.

275. R.J. Mureinik and M. Bidani, *Inorg. Chim. Acta*, (1978), **29**, 37

276. R.J. Cross in: *"Dictionary of Organometallic Compounds, Vol. 2"*, (J. Buckingham, *Exec. Ed.*), Chapman and Hall, London, (1984), 1567.

277. A. de Renzi, A. Panunzi, A. Vitagliano and G. Paiaro, *J. Chem. Soc., Chem. Commun.*, (1976), 47.

278. F.R. Hartley, S.G. Murray and C.A. McAuliffe, *Inorg. Chem.*, (1979), **18**, 1394.

279. F.D. Rochon, R. Melanson, H.E. Howard-Lock, C.J.L. Lock and G. Turner, *Can. J. Chem.*, (1984), **62**, 860.

280. K.F. Purcell and R.S. Drago, *J. Amer. Chem. Soc.*, (1966), **88**, 919.

281. B. Hellquist, L.A. Bengtsson, B. Holmberg, B. Hedman, I. Persson and L.I. Elding, *Acta Chem. Scand.*, (1991), **45**, 449.

282. E.C. Constable, R.P.G. Henney, T.A. Leese and D.A. Tocher, *J. Chem. Soc., Chem. Commun.*, (1990), 513.

283. C.J.L. Lock and M. Zvagulis, *Inorg. Chem.*, (1981), **20**, 1817.

284. C.C. Costain, *J. Chem. Phys.*, (1958), **29**, 864.

285. W. Gerrard, M.F. Lappert, H. Pyszora and J.W. Wallis, *J. Chem. Soc.*, (1960), 2182.

286. P.E. Riley, C.E. Capshew, R. Pettit and R.E. Davis, *Inorg. Chem.*, (1978), **17**, 408.

287. E.M. Stacy, *Ph.D. Thesis*, Purdue University, West Lafayette, Indiana, USA, (1992), 91.

288. T.K. Aldridge, *Ph.D. Thesis*, Purdue University, West Lafayette, Indiana, USA, (1993), 47.

289. J.R. Kirchoff, D.R. McMillin, P.A. Marnot and J.P. Sauvage, *J. Amer. Chem. Soc.*, (1985), **107**, 1138.

290. C.R. Hecker, A.K.I. Gushurst and D.R. McMillin, *Inorg. Chem.*, (1991), **30**, 538.

291. J.A. Bailey, V.M. Miskowski and H.B. Gray, *Inorg. Chem.*, (1993), **32**, 369.

292. M.K. DeArmond and C.M. Carlin, *Coord. Chem. Rev.*, (1981), **36**, 325.

293. D.J. Casadonte Jr and D.R. McMillin, *J. Amer. Chem. Soc.*, (1987), **109**, 331.

294. R.S. Osborn and D. Rogers, *J. Chem. Soc., Dalton Trans.*, (1974), 1002.

295. G.T. Morgan and F.H. Burstall, *J. Chem. Soc.*, (1934), 965.

296. E. Bielli, P.M. Gidney, R.D. Gillard and B.T. Heaton, *J. Chem. Soc., Dalton Trans.*, (1974), 2133.

297. G.C. Summerton, *Honours Project*, University of Natal, Pietermaritzburg, RSA, (1993).

298. H. Endres, H.J. Keller, W. Moroni, D. Nöthe and V. Dong, *Acta Cryst. B*, (1978), **34**, 1823.

299. A. Hazell, O. Simonsen and O. Wernberg, *Acta Cryst. C*, (1986), **42**, 1707.

300. V. Dong, H. Endres, H.J. Keller, W. Moroni,and D. Nöthe, *Acta Cryst. B*, (1977), **33**, 2428.

301. S. Maeda, Y. Nishida, H. Okawa and S. Kida, *Bull. Chem. Soc. Jpn.*, (1986), **59**, 2013.

302. P. Bonneson, J.L. Walsh, W.T. Pennington. A.W. Cordes and B. Durham, *Inorg. Chem.*, (1983), **22**, 1761.

303. M. Maestri, D. Sandrini, V. Balzani, A. von Zelewsky, C. Deuschel-Cornioley and P. Jolliet, *Helv. Chim. Acta*, (1988), **71**, 1053.

304. J.R. Lakowicz, *"Principles of Fluorescence Spectroscopy"*, Plenum Press, New York, (1983), 42.

305. R.G. Bray, J. Ferguson and C.J. Hawkins, *Aust. J. Chem.*, (1969), **22**, 2091.

306. E.C. Constable, J. Lewis, M.C. Liptrot and P.R. Raithby, *Inorg. Chim. Acta*, (1990), **178**, 47.

307. R.A. Rader, D.R. McMillin, M.T. Buckner, T.G. Matthews, D.J. Casadonte, R.K. Lengel, S.B. Whittaker, L.M. Darmon and F.E. Lytle, *J. Amer. Chem. Soc.*, (1981), **102**, 5906.

308. T. Agawa, *J. Amer. Chem. Soc.*, (1961), **83**, 449.

309. $Bu_3SnC{\equiv}CPh$ was synthesized by adapting the method for the synthesis of $Me_3SnC{\equiv}CPhC{\equiv}CSnMe_3$, as obtained from personal correspondence with Prof. J. Lewis, Department of Chemistry, Univesity of Cambridge and outlined in Appendix B.

310. E. Baralt, E.A. Boudreaux, J.N. Demas, P. Galen Lenhert, C.M. Lukehart, A.T. McPhail, D.R. McPhail, J.B. Myers Jr, L. Sacksteder and W.R. True, *Organometallics*, (1989), **8**, 2417.

311. C.J. Cardin, D.J. Cardin, M.F. Lappert and K.W. Muir, *J. Chem. Soc., Dalton Trans.*, (1978), 46.

312. U. Behrens, K. Hoffman, J. Kopf and J. Moritz, *J. Organometal. Chem.*, (1976), **117**, 91.

313. H.-K. Yip, H.-M. Lin, Y. Wang and C.-M. Che, *J. Chem. Soc., Dalton Trans.*, (1993), 2939.

314. U. Croatto, L. Toniolo, A. Immirzi and G. Bombieri, *J. Organometal. Chem.*, (1975), **102**, C31.

315. J. Geisenberger, U. Nagel, A. Sebald and W. Beck, *Chem. Ber.* (1993), **116**, 911.

316. H. Suziki, Bull, *Chem. Soc. Jpn*, (1960), **33**, 109.

317. C.R. Hecker, A.K.I. Gushurst and D.R. McMillin, *Inorg. Chem.* (1991), **30**, 538.

318. H.-K. Yip, C.-M. Che, Z.-Y. Zhou and T.C.W. Mak, *J. Chem. Soc., Chem. Commun.*, (1992), 1369.

319. L. Carlsen, H. Egsgaard and J.R. Andersen, *Analytical Chemistry*, (1979), **51**, 1593.

320. C.K. Mann, *Electroanal. Chem.*, (1969), **3**, 57.

321. A.C.T. North, D.C. Phillips and F.S. Mathews, *Acta. Cryst. A*, (1968), **24**, 351.

322. *"International Tables for X-ray Crystallography"*, Kynoch Press, Birmingham, (1974), **4**, 99 - 149.

323. G.M. Sheldrick, SHELX-76, Program for Crystal Structure Determination, Universtiy of Cambridge, 1976.

324. G.M. Sheldrick, SHELX-86, Program for Crystal Structure Determination, Universtiy of Göttingen, 1986.

325. *Structure Determination Package*, B.A. Frenze and Associates Inc., College Station, Texas 77480, USA; and Enraf-Nonius, Delft, Holland, 1985.

326. C. Johnson, ORTEP-II, A Fortran Thermal Elipsoid Programme for Crystal Structure Illustrations, Oak Ridge National Laboratory, Tennesse, 1976.

327. D. Liles, TABLES, Program for Tabulation of Crystallographic Data, Council for Scientific and Industrial Research (Pretoria), 1988.